

CLEANER TREATMENT TECHNOLOGIES AND PRODUCTIONS IN THE ENERGY INDUSTRY, 2nd Edition

EDITED BY: Jiang Bian, Xuewen Cao, Chuang Wen, Lin Teng and Zheng Li
PUBLISHED IN: Frontiers in Energy Research





frontiers

Frontiers eBook Copyright Statement

The copyright in the text of individual articles in this eBook is the property of their respective authors or their respective institutions or funders. The copyright in graphics and images within each article may be subject to copyright of other parties. In both cases this is subject to a license granted to Frontiers.

The compilation of articles constituting this eBook is the property of Frontiers.

Each article within this eBook, and the eBook itself, are published under the most recent version of the Creative Commons CC-BY licence.

The version current at the date of publication of this eBook is CC-BY 4.0. If the CC-BY licence is updated, the licence granted by Frontiers is automatically updated to the new version.

When exercising any right under the CC-BY licence, Frontiers must be attributed as the original publisher of the article or eBook, as applicable.

Authors have the responsibility of ensuring that any graphics or other materials which are the property of others may be included in the CC-BY licence, but this should be checked before relying on the CC-BY licence to reproduce those materials. Any copyright notices relating to those materials must be complied with.

Copyright and source acknowledgement notices may not be removed and must be displayed in any copy, derivative work or partial copy which includes the elements in question.

All copyright, and all rights therein, are protected by national and international copyright laws. The above represents a summary only. For further information please read Frontiers' Conditions for Website Use and Copyright Statement, and the applicable CC-BY licence.

ISSN 1664-8714

ISBN 978-2-8325-2279-0

DOI 10.3389/978-2-8325-2279-0

About Frontiers

Frontiers is more than just an open-access publisher of scholarly articles: it is a pioneering approach to the world of academia, radically improving the way scholarly research is managed. The grand vision of Frontiers is a world where all people have an equal opportunity to seek, share and generate knowledge. Frontiers provides immediate and permanent online open access to all its publications, but this alone is not enough to realize our grand goals.

Frontiers Journal Series

The Frontiers Journal Series is a multi-tier and interdisciplinary set of open-access, online journals, promising a paradigm shift from the current review, selection and dissemination processes in academic publishing. All Frontiers journals are driven by researchers for researchers; therefore, they constitute a service to the scholarly community. At the same time, the Frontiers Journal Series operates on a revolutionary invention, the tiered publishing system, initially addressing specific communities of scholars, and gradually climbing up to broader public understanding, thus serving the interests of the lay society, too.

Dedication to Quality

Each Frontiers article is a landmark of the highest quality, thanks to genuinely collaborative interactions between authors and review editors, who include some of the world's best academicians. Research must be certified by peers before entering a stream of knowledge that may eventually reach the public - and shape society; therefore, Frontiers only applies the most rigorous and unbiased reviews.

Frontiers revolutionizes research publishing by freely delivering the most outstanding research, evaluated with no bias from both the academic and social point of view. By applying the most advanced information technologies, Frontiers is catapulting scholarly publishing into a new generation.

What are Frontiers Research Topics?

Frontiers Research Topics are very popular trademarks of the Frontiers Journals Series: they are collections of at least ten articles, all centered on a particular subject. With their unique mix of varied contributions from Original Research to Review Articles, Frontiers Research Topics unify the most influential researchers, the latest key findings and historical advances in a hot research area! Find out more on how to host your own Frontiers Research Topic or contribute to one as an author by contacting the Frontiers Editorial Office: frontiersin.org/about/contact

CLEANER TREATMENT TECHNOLOGIES AND PRODUCTIONS IN THE ENERGY INDUSTRY, 2nd Edition

Topic Editors:

Jiang Bian, China University of Petroleum, China

Xuewen Cao, China University of Petroleum, China

Chuang Wen, University of Exeter, United Kingdom

Lin Teng, Fuzhou University, China

Zheng Li, Vanderbilt University, United States

Publisher's note: In this 2nd edition, the following article has been added: Yang C, Han Q, Liu H, Wang Y and Cheng R (2023) Ignition characteristics of methane-air mixture at low initial temperature. *Front. Energy Res.* 10:1003470. doi: 10.3389/fenrg.2022.1003470

Citation: Bian, J., Cao, X., Wen, C., Teng, L., Li, Z., eds. (2023). *Cleaner Treatment Technologies and Productions in The Energy Industry*, 2nd Edition. Lausanne: Frontiers Media SA. doi: 10.3389/978-2-8325-2279-0

Table of Contents

05	<i>Editorial: Cleaner Treatment Technologies and Productions in the Energy Industry</i>
	Jiang Bian, Xuewen Cao and Lin Teng
08	<i>Permeability Enhancement Properties of High-Pressure Abrasive Water Jet Flushing and Its Application in a Soft Coal Seam</i>
	Xinzhe Zhang, Piotr Wiśniewski, Stawomir Dykas and Guojie Zhang
20	<i>Structure and Topology Analysis of Separated Vortex in Forward-Swept Blade</i>
	D. Liang, Y. Li, Z. Zhou, P. Wiśniewski and S. Dykas
31	<i>Study on Dispersion of Carbon Dioxide Over the Shrubbery Region</i>
	Wang Huiru, You Zhanping, Mo Fan, Liu Bin and Han Peng
46	<i>General Optimization Model of Modular Equipment Selection and Serialization for Shale Gas Field</i>
	Bingyuan Hong, Xiaoping Li, Xuemeng Cui, Jingjing Gao, Yu Li, Jing Gong and Huanying Liu
56	<i>Analysis of Hydrogen Gas Injection at Various Compositions in an Existing Natural Gas Pipeline</i>
	Jingxuan Liu, Lin Teng, Bin Liu, Peng Han and Weidong Li
69	<i>Gas Discharge Resistance and Medium Damage Degree as Hydrate Dissociation at Different Ambient Conditions</i>
	Xueping Chen, Peng Zhang, Qingbai Wu, Lianhai Zhang, Shuaijun Li, Jing Zhan and Yingmei Wang
78	<i>Improved Analytical Method for Longitudinal Strain Analysis of Buried Pipelines Subjected to Thaw Slumping Load</i>
	Beilei Ji, Xiaoben Liu, Dinaer Bolati, Yue Yang, Jinxu Jiang, Yuqing Liu and Hong Zhang
92	<i>Study on Hydrate Phase Equilibrium Diagram of Methane Containing System Based on Thermodynamic Model</i>
	Hao Liang, Yonggang Duan, Jun Pei and Na Wei
104	<i>An Experiment on Flashing-Spray Jet Characteristics of Supercritical CO₂ From Various Orifice Geometries</i>
	Lin Teng, Jinbao Bai, Yuxing Li and Cailin Wang
114	<i>Simulation Study on the Development Process and Phase Interface Structure of Gas-Liquid Slug Flow in a Horizontal Pipe</i>
	Xiao Wu, Zhaoting Wang, Mei Dong, Quan Ge and Longfei Dong
127	<i>Optimization Design and Analysis of Single-Stage Mixed Refrigerant Liquefaction Process</i>
	Xiao Wu, Zhaoting Wang, Xiaodong Dai, Quan Ge and Fei Liu
137	<i>Transient Heat Transfer Characteristics of Twisted Structure Heated by Exponential Heat Flux</i>
	Li Wang and Qiusheng Liu
145	<i>Corrigendum: Transient Heat Transfer Characteristics of Twisted Structure Heated by Exponential Heat Flux</i>
	Li Wang and Qiusheng Liu

- 147 ***Study on Preparation of Oxygen Carrier Using Copper Slag as Precursor***
Yan Feng, Qianhui Yang, Zongliang Zuo, Siyi Luo, Dongdong Ren and Huan Lin
- 154 ***Numerical and Experimental Analysis of Influence of Impeller Structures on Slurry Pump Performance***
Guangjie Peng, Jialin Du, Hao Chang, Qiang Chen, Jiahu Li, Chengxiang Pan and Yongfei Yang
- 166 ***Mathematical Model of the Deaeration of Finely Dispersed Solid Media in a Spherical Matrix of a Roller-Type Apparatus***
Anna Kapranova, Mikhail Tarshis, Natalya Badaeva and Irina Sheronina
- 173 ***Effect of Fin Number and Position on Non-linear Characteristics of Natural Convection Heat Transfer in Internally Finned Horizontal Annulus***
Kun Zhang, Yu Zhang, Xiaoyu Wang and Liangbi Wang
- 184 ***Numerical Simulation of the Influence of CO₂ on the Combustion Characteristics and NO_x of Biogas***
Jinshuang Ma, Chuanjia Qi, Siyi Luo and Zongliang Zuo
- 191 ***A Semi-Analytical Mathematical Model for Off-Center Fractured Vertical Wells With Asymmetrical Fractures in Columnar Coalbed Methane***
Anzhao Ji, Zhanjun Chen, Yufeng Wang, Guangsheng Zhang, Zhenglin Mao and Fenjun Chen
- 204 ***Stress Analysis of the Effect of Additional Load on the Butt Weld of Suspended Pipeline With Variable Wall Thickness***
Fang Yingchao, Yu Dongliang, Wang Binbin, Xu Jian, Xuan Heng, Hou Hao and Wang lin
- 215 ***Coupled Heat and Flow Analysis Inside a Diversion-Type Gas Heater With Vertical Guide Plate Structure***
Yun Guo, Xuning Zhang and Zhongwei Zhou
- 223 ***Application of the Material Balance Equation Based on the BET Multimolecular Fractal Theory in a Shale Gas Reservoir***
Tingting Qiu, Shuyong Hu and Jiayi Zhang
- 232 ***Ignition Characteristics of Methane-Air Mixture at Low Initial Temperature***
Chao Yang, Qing Han, Haibo Liu, Yuanyuan Wang and Ran Cheng



Editorial: Cleaner Treatment Technologies and Productions in the Energy Industry

Jiang Bian^{1*}, Xuewen Cao¹ and Lin Teng²

¹College of Pipeline and Civil Engineering, China University of Petroleum (East China), Qingdao, China, ²College of Chemical Engineering, Fuzhou University, Fuzhou, China

Keywords: cleaner treatment technologies, energy industry, natural gas, hydrogen, cleaner production

Editorial on the Research Topic

Cleaner Treatment Technologies and Productions in Energy Industry

As the rapid development of world's economy brought serious environmental problems, the economy must accelerate the adjustment of industrial structure and the transformation of development mode in order to achieve sustainable development. Cleaner production mode based on cleaner technology is a crucial way to effectively solve the conflict between economic growth and environmental protection. In essence, cleaner production is a kind of production mode in which the environmental strategy of overall prevention is adopted for the production process to reduce or eliminate their possible harm to human beings and the environment, while fully meeting human needs and maximizing social and economic benefits.

Fossil energy and renewable energy have promoted the development of a large number of emerging industries, such as automobile industry, aerospace technology, modern production and processing, and modern transportation industry, and preventing the production of waste, while increasing efficiencies in the uses of energy is a very important issue. Specific measures include: using clean energy and raw materials; adopting advanced technology and equipment; comprehensive utilization; reducing pollution from the source; improving utilization efficiency; reducing or avoiding the generation and emission of pollutants in the process of production. This special issue aims to reports the most important and latest technological advances in cleaner treatment technologies of fossil energy (such as oil and natural gas) and renewable energy (such as hydrogen energy and geothermal energy), and serves as a platform for addressing and discussing theoretical and practical cleaner production.

How to develop the gas reservoir well is a main task for petroleum engineers. High-pressure abrasive water jet flushing is an effective method used to improve coal seam permeability. A coupled gas-rock model is established to investigate realistic failure processes by introducing equations for the evolution of mesoscopic element damage along with coal mass deformation. The gas pressure of the slotted soft coal seam is reduced and that the gas drainage volume is three times higher than that of a conventional borehole. The soft coal seam is significantly improved and that tunneling speed is nearly doubled (Zhang et al.). Considering the processing capacity, processing cost, floor area, construction cost of modular equipment, and the changes of market supply and demand, an optimization model is established, which can optimize the layout of modular equipment, make the modular equipment run efficiently and economically, reduce costs, and increase efficiency (Hong et al.). During shale gas reservoir development, BET multimolecular adsorption, considering the shale gas surface fractal dimension theory to describe the adsorption properties, can describe the adsorption surface as a multimolecular layer and regard adsorption using a fractal dimension,

OPEN ACCESS

Edited and reviewed by:

Xuezhong He,
Guangdong Technion-Israel Institute
of Technology (GTIIT), China

*Correspondence:

Jiang Bian
bj@s.upc.edu.cn

Specialty section:

This article was submitted to
Advanced Clean Fuel Technologies,
a section of the journal
Frontiers in Energy Research

Received: 24 May 2022

Accepted: 03 June 2022

Published: 23 June 2022

Citation:

Bian J, Cao X and Teng L (2022)
Editorial: Cleaner Treatment
Technologies and Productions in the
Energy Industry.
Front. Energy Res. 10:951477.
doi: 10.3389/fenrg.2022.951477

describing the adsorption property of shale gas more accurately (Qiu et al.). Coalbed methane (CBM) is one of the important unconventional oil and gas resources. It is meaningful to analyze the wellbore pressure response of the off-center fractured vertical wells with asymmetrical fracture. The wellbore pressure includes six flow regimes, which include bilinear flow, linear flow, elliptic flow, radial flow, arc boundary reflection, and boundary dominated flow regime (Ji et al.).

Carbon Capture and Storage (CCS) processes remove carbon dioxide (CO_2) that would otherwise be emitted from fossil fuel and other energy industrial processes and transport it for permanent underground storage. A comprehensive understanding of the effects of CO_2 dispersion pattern after release from CCS facilities is essential to allow the appropriate safety precautions to be taken. It was found that shrubbery affected the flow field near the ground, enhancing the lateral dispersion of CO_2 (Wang et al.). Supercritical CO_2 pipelines usually are used to link the CO_2 capture system to the geological storage. The flashing-spray jet structures of supercritical CO_2 from circular and rectangular orifices were recorded by a high-speed camera. The near-field structures of supercritical CO_2 jet from circular and rectangular orifices are totally different, which causes the different dispersion consequences (Teng et al.). The existence of inert gases such as N_2 and CO_2 in biogas will reduce the proportion of combustible components in syngas and affect the combustion and NOX formation characteristics. The effect of CO_2 concentration in biogas on NO_2 is complicated, when the combustion reaches the chemical equilibrium, the flame combustion temperature and flame propagation speed decrease with the increase of CO_2 concentration, and the flame propagation speed decreases even more slowly (Ma et al.).

Recently, several countries have conducted projects to explore and develop natural gas hydrate, which is one of the new alternative energy resources for the future. Methane hydrates formed inside porous media with different saturations were dissociated by depressurizations. These formed hydrates at higher temperature and pressure, and possess a higher saturation, and the nonuniformity of dissociation processes at different layer positions induced by depressurization is inhibited significantly (Chen et al.). The phase equilibrium curves of the methane containing systems are mainly related to the guest molecule type and the composition of gas. The evolution law of phase equilibrium pressure of different gases varies with composition and temperature, and the phase splitting of CO_2 at the quadruple point affects the phase equilibrium conditions (Liang et al.).

The safety and integrity of pipeline systems plays a crucial role in oil and gas transportation field. Variation in the thermo-physical properties of an H_2 -natural gas blend will impact the performance of pipeline appliances, thus, a one-dimensional pipeline model is proposed to predict the blended flow in a real existing pipeline, the influence of H_2 fractions on pipeline energy coefficient and the layout of pressurization stations are comprehensively analyzed (Liu et al.). Thawing landslide is a common geological disaster in permafrost regions, which seriously threatens the structural safety of oil and gas pipelines crossing permafrost regions. An improved analytical method is

introduced to accurately analyze the longitudinal strain characteristics of buried pipelines subjected to slope-thaw slumping load (Ji et al.). The fluctuation of pressure and flow caused by slug flow has an important impact on deep-sea oilfield and the design of production equipment. During the movement of the slug head, there is a throwing phenomenon and a wave-like motion of the liquid slug. In addition, the slug tail and body area have very similar velocity profiles, and the overall velocity field distribution becomes more uniform with the development of liquid slug (Wu et al.). ABAQUS software is used to establish a pipe-soil model of variable wall thickness butt welds of suspended pipelines. The axial stress distribution with different affected factors in the pipe, the change of curvature, and Mises stress change of the entire pipe along the axial direction are obtained by analyzing the internal pressure, wall thickness ratio, suspended length, weld position, and cone length (Fang et al.).

Heat and mass transfer theory and numeric calculation model are widely used in energy industry. The additional operation of deaeration (compaction) of powders affects the quality of many products of chemical industries. A plane-deformation model is described, neglecting the forces of interphase interaction and taking into account the compressibility of a solid-particle-gas mixture without elastoplastic deformations (Kapranova et al.). Flow separation commonly affects the stability of turbomachines, especially under low-flowrate conditions. The singularity characteristics of the blade surface separation are analyzed using a topological approach. The flow separation is explored in three-dimensional space using a topological-mapping method (Liang et al.). A novel impeller with splitter blade structure is proposed, and the impeller with splitter blades not only can reduce the energy loss of the slurry pump, but also enhance the wear characteristics of impeller under two-phase flow conditions (Peng et al.). High-pressure abrasive water jet flushing (HPAWJF) is an effective method used to improve coal seam permeability. A coupled gas-rock model is established to investigate realistic failure processes by introducing equations for the evolution of mesoscopic element damage along with coal mass deformation (Zhang et al.). To study the heat exchange rate between the heating medium water and the fire and gas tubes in the great-capacity cylinder, the discrete-ordinate model is utilized to build a 2-D combined natural convection and participating medium radiation heat transfer model, which is solved using the finite volume technique with unstructured body-fitted grids (Guo et al.). The response analysis for transient heat transfer at fluid-solid interface was conducted by applying the concept of penetration depth. It is considered that, when the penetration depth is smaller than the thermal boundary thickness, the heat transfer from the interface (wall surface) to the fluid domain is not fully developed during the disturbance (Wang and Liu). The copper slag modified through calcining in redox condition was proved to be a promising oxygen carrier in chemical looping process (Fang et al.). In the single-stage mixed refrigerant liquefaction process, reducing the feed gas temperature and increasing the feed gas pressure can reduce the total power consumption, exergy loss, freezing mixture circulation, and cooling water load, which can significantly improve liquefaction performance (Wu et al.).

AUTHOR CONTRIBUTIONS

JB is an associate editor of Frontiers in Energy Research and a guest associate editor of the Research Topic and wrote the paper. XC is a guest associate editor of the Research Topic and edited the paper. LT is a guest associate editor of the Research Topic and reviewed the paper.

FUNDING

JB is supported by the National Natural Science Foundation of China (Grants No. 52074341 and No. 52104071), the Natural Science Foundation of Shandong Province (Grant No. ZR2021QE030).

Conflict of Interest: The authors declare that the research was conducted in the absence of any commercial or financial relationships that could be construed as a potential conflict of interest.

Publisher's Note: All claims expressed in this article are solely those of the authors and do not necessarily represent those of their affiliated organizations, or those of the publisher, the editors and the reviewers. Any product that may be evaluated in this article, or claim that may be made by its manufacturer, is not guaranteed or endorsed by the publisher.

Copyright © 2022 Bian, Cao and Teng. This is an open-access article distributed under the terms of the Creative Commons Attribution License (CC BY). The use, distribution or reproduction in other forums is permitted, provided the original author(s) and the copyright owner(s) are credited and that the original publication in this journal is cited, in accordance with accepted academic practice. No use, distribution or reproduction is permitted which does not comply with these terms.



Permeability Enhancement Properties of High-Pressure Abrasive Water Jet Flushing and Its Application in a Soft Coal Seam

Xinzhe Zhang^{1,2}, Piotr Wiśniewski^{3*}, Sławomir Dykas³ and Guojie Zhang^{2*}

¹ School of Aeronautical Engineering, Zhengzhou University of Aeronautics, Zhengzhou, China, ² School of Mechanical and Power Engineering, Zhengzhou University, Zhengzhou, China, ³ Department of Power Engineering and Turbomachinery, Silesian University of Technology, Gliwice, Poland

OPEN ACCESS

Edited by:

Jiang Bian,
China University of Petroleum (East
China), China

Reviewed by:

Fengchao Wang,
China University of Mining
and Technology, China
Zhongning Zhou,
China University of Mining
and Technology, China

*Correspondence:

Piotr Wiśniewski
piotr.wisniewski@polsl.pl
Guojie Zhang
zhangguojie2018@zzu.edu.cn

Specialty section:

This article was submitted to
Advanced Clean Fuel Technologies,
a section of the journal
Frontiers in Energy Research

Received: 12 March 2021

Accepted: 06 April 2021

Published: 29 April 2021

Citation:

Zhang X, Wiśniewski P, Dykas S
and Zhang G (2021) Permeability
Enhancement Properties
of High-Pressure Abrasive Water Jet
Flushing and Its Application in a Soft
Coal Seam.
Front. Energy Res. 9:679623.
doi: 10.3389/fenrg.2021.679623

High-pressure abrasive water jet flushing (HPAWJF) is an effective method used to improve coal seam permeability. In this study, based on the theories of gas flow and coal deformation, a coupled gas-rock model is established to investigate realistic failure processes by introducing equations for the evolution of mesoscopic element damage along with coal mass deformation. Numerical simulation of the failure and pressure relief processes is carried out under different coal seam permeability and flushing length conditions. Distributions of the seepage and gas pressure fields of the realistic failure process are analyzed. The effects of flushing permeability enhancement in a soft coal seam on the gas drainage from boreholes are revealed by conducting a field experiment. Conclusions can be extracted that the gas pressure of the slotted soft coal seam is reduced and that the gas drainage volume is three times higher than that of a conventional borehole. Field tests demonstrate that the gas drainage effect of the soft coal seam is significantly improved and that tunneling speed is nearly doubled. The results obtained from this study can provide guidance to gas drainage in soft coal seams regarding the theory and practice application of the HPAWJF method.

Keywords: CFD, experimental study, permeability enhancement, numerical study, high-pressure abrasive water jet flushing

INTRODUCTION

Coal and gas outbursts have been widely studied because of their serious threat to safety in coal mine production (Frid, 1997; Li and Hua, 2006; Cao and Bian, 2019). High-pressure abrasive water jet flushing (HPAWJF) is a rapidly developing technology used to prevent coal and gas outbursts (Jiang et al., 2009, 2011). However, the geological conditions of soft coal seams, which are widely distributed in China, are relatively complex. Notably, the permeability of the soft coal seams of China is three to four orders of magnitude lower than those of Australia and North America (Aguado and Nicieza, 2007; Cheng et al., 2011). In recent years, with the increase in excavation depth of coal mining, the features of high gas content, high geostress, high geotemperature, and low permeability of soft coal seams have been significantly increasing (Jin et al., 2015), and the increasing number of coal and gas outbursts causes the risk of accidents to increase rapidly. Thus, it is of important practical and engineering significance to develop an efficient HPAWJF technology for soft coal seams.

Many researchers focus on the theory and practice of pressure relief and permeability enhancement of different coal seam geological conditions using the HPAWJF technology.

Originally applied for breaking rocks, Hood (1976) used a water jet technology to assist drag bits in drilling hard rocks. Yazici (1989) reported that a high-pressure abrasive water jet can be used as an independent cutting tool. Li et al. (2000) found that high-pressure abrasive water jets can significantly improve both the cutting capacity and the efficiency of hard coal rock flushing. Kim (2001) examined the relationship between the volume removal rate and the rotational speed of a nozzle by using a high-pressure abrasive injection and a suspension water jet for cutting tests in hard rock. Lin et al. (2011) used numerical simulation methods and found that the cutting depth of a high-pressure abrasive jet cutter is up to 700–800 mm. Momber et al. (2011) proposed a model for the cutting of reinforced concrete members using streamline cutting tools. Lu et al. (2013) showed that the depth of a borehole drilled using a pulsating jet flushing technology can be 2.7 times deeper than using traditional flushing technology.

As noted above, the HPAWJF technology and its devices have been efficiently used for different coal seams. However, many scholars concentrate on how to evaluate and analyze the performance of the flushing technology and devices in terms of their performance, investigating parameters such as pressure, velocity, confining pressure of a water jet, structure type, wear-resistant material, nozzle diameter and type, concentration, size of abrasive, flushing time, and rock strength, etc. Because the process of flushing a coal seam for gas drainage must be completed before exploiting the coal, the permeability enhancement properties after flushing will directly affect the efficiency and safety of coal mining operation. However, the research conducted on gas drainage efficiency after flushing is rare, especially for the soft coal seams of China. Therefore, in this study, theoretical, experimental, and numerical calculations are given more attention, which have an important significance for safe and efficient operation in the coal mines of China.

In this study, numerical calculation and field experimental validation methods are employed to analyze the permeability-enhancing properties of HPAWJF in soft coal seams. To investigate the realistic failure and pressure relief processes of coal rock, coupling of the permeability and damage evolution equations is established using the theories of gas flow and coal deformation. Additionally, the gas drainage volume, tunneling speed, and coal cutting quantity of a slotted soft coal seam are analyzed. The results of this study are expected to provide fundamental information for the application of the HPAWJF technology to improve soft coal seam gas drainage and production efficiency.

PERMEABILITY ENHANCEMENT MECHANISM OF HPAWJF

Pressure Relief Using HPAWJF

Coal seam permeability plays a major role in the process of gas drainage from boreholes (Connell, 2009; Liu et al., 2010). For this study, stress is normally divided into three mutually perpendicular directions, as coal mass is anisotropic (Yang et al., 2011). Therefore, the effect of stress on permeability is considered

to be a three-dimensional function, and the energy stored in the coal mass element is also closely related to three-dimensional stress. Moreover, according to the least energy principle (Zhao et al., 2003), the energy stored under the condition of one- or two-dimensional stress is smaller than that stored under the conditions of three-dimensional stress (Song et al., 2014).

At present, there are two major methods for flushing coal seams: horizontal radial slot and vertical circular slot (Lin and Shen, 2015). The pressure relief space is formed during water jet flushing of a borehole, which can effectively change original stress distribution and improve coal seam permeability (Shen et al., 2012). As shown in **Figure 1**, geostress acts on the three-dimensional space of the physical model, and the vertical circular slots are uniformly distributed in the cross section of the borehole. Three zones are formed in the area surrounding the borehole: the crushing, plastic, and elastic deformation zones (Shen et al., 2015).

The high-pressure abrasive water jet can cut a slot to a certain width and depth in a coal seam, which will reduce the three directions of force into two and lead to changes in the energy storage states of small coal mass elements surrounding the slot. As free space for the elastic recovery of the coal mass is created, the excess energy previously stored in the slotted coal mass is released (Song et al., 2014).

Under the condition of the Mohr–Coulomb criterion, the stress distribution of a circular slot (borehole) is shown in **Figure 2**. Here, r_0 is the radius of the circular slot; R is the radius of the limit equilibrium area (Wang et al., 2012), which is much larger than the diameter of the borehole; σ_t is the tangential stress; σ_r is the radial stress; γ is the average volume of the overlying strata; and H is the depth from the surface (Wang et al., 2012).

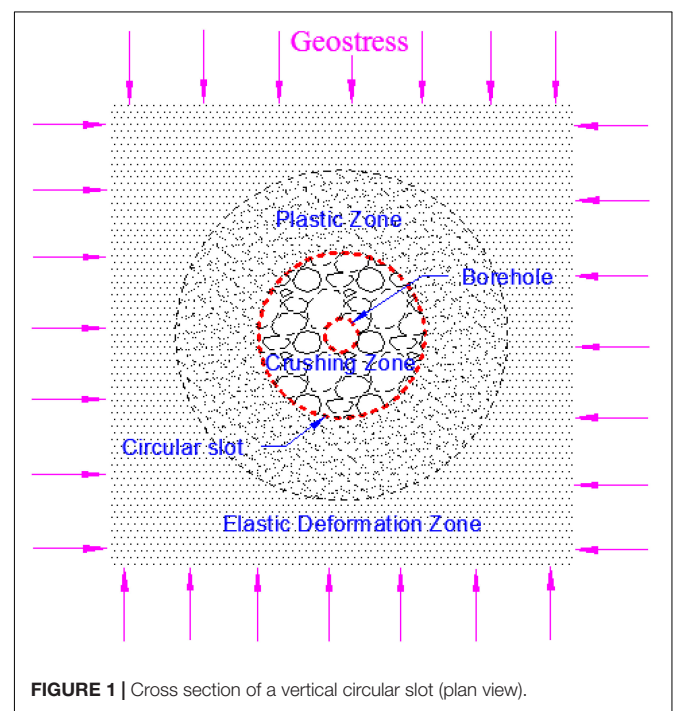


FIGURE 1 | Cross section of a vertical circular slot (plan view).

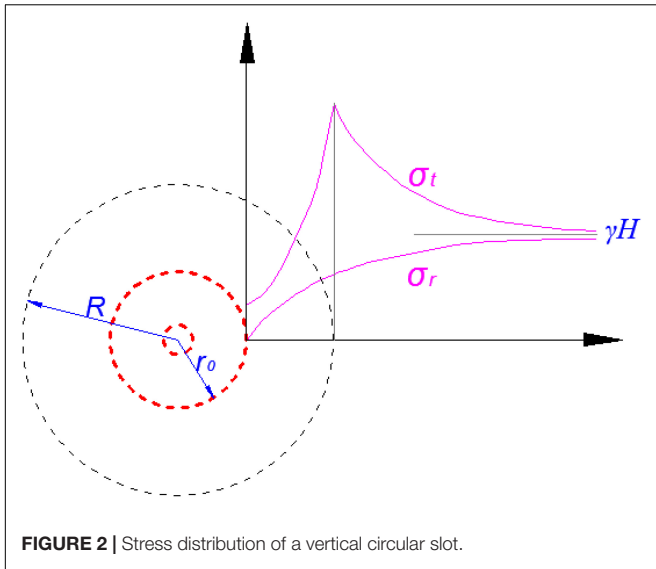


FIGURE 2 | Stress distribution of a vertical circular slot.

When the distance from the center of the circular slot is increased, the stress around the circular slot is also increased. At the same time, the stress at the same position is reduced, and the limit equilibrium area is extended (Shen et al., 2015).

Therefore, the use of a high-pressure abrasive water jet to cut slots in a coal seam is possible, which will change the stress state of the seam and induce the release of its internal energy. Additionally, the permeability of the slotted coal seam can be changed. In summary, mechanisms of permeability enhancement and pressure relief can be created, and the effect of HPAWJF on relief of pressure is much better than that of the conventional gas drainage method.

Coupling of Permeability and Damage Evolution in a Realistic Failure Process

Under the influence of mining, damage deformation in coal rock becomes increasingly apparent. When the stress in the mesoscopic element of a coal mass reaches a defined threshold, the element begins to deform. At the same time, the permeability of the element also changes. Based on the method of coupling of seepage and damage, coupled equations of permeability and damage evolution are established.

The elastic modulus of the damage element is defined by Formula (1):

$$E = (1 - D)E_0 \quad (1)$$

where D is the damage variable and E_0 is the elastic modulus of the non-damage element. These parameters are defined as scalar.

For uniaxial compression (Liu et al., 2015), the Mohr–Coulomb criterion is adopted in the process of element damage:

$$F = \sigma_1 - \sigma_3 \frac{1 + \sin \phi}{1 - \sin \phi} \geq f_c \quad (2)$$

where ϕ is the internal friction angle, ϕ is the uniaxial compressive strength, σ_1 is the maximum principal stress, and σ_3 is the minimum principal stress.

When the stress reaches the Mohr–Coulomb damage threshold, the damage variable D can be represented as Formula (3):

$$D = \begin{cases} 0 & \varepsilon < \varepsilon_{c0} \\ 1 - \frac{f_{cr}}{E_0 \varepsilon} & \varepsilon \geq \varepsilon_{c0} \end{cases} \quad (3)$$

where f_{cr} is the compressive residual strength, and ε_{c0} is the maximum compressive strain. Tang et al. (2002) demonstrated that permeability coefficient can increase rapidly in the process of damage, and the change in the permeability coefficient of the element can be represented as Formula (4):

$$\lambda = \begin{cases} \lambda_0 e^{-\beta(\sigma_1 - \alpha p)} & D = 0 \\ \xi \lambda_0 e^{-\beta(\sigma_1 - \alpha p)} & D > 0 \end{cases} \quad (4)$$

where λ_0 is the initial permeability coefficient; p is the pore pressure; and ξ , α , β are the ratios of the permeability coefficient, pore pressure coefficient, and coupling coefficient, respectively.

When the element reached the damage threshold of the uniaxial tensile strength f_t ,

$$\sigma_3 \leq -f_t \quad (5)$$

the damage variable D can be represented as Formula (6):

$$D = 1 - \begin{cases} 0 & \varepsilon \geq \varepsilon_{t0} \\ 1 - \frac{f_{tr}}{E_0 \varepsilon} & \varepsilon < \varepsilon_{t0} \\ 1 & \varepsilon \leq \varepsilon_{tu} \end{cases} \quad (6)$$

The change in the element permeability coefficient can be represented as Formula (7):

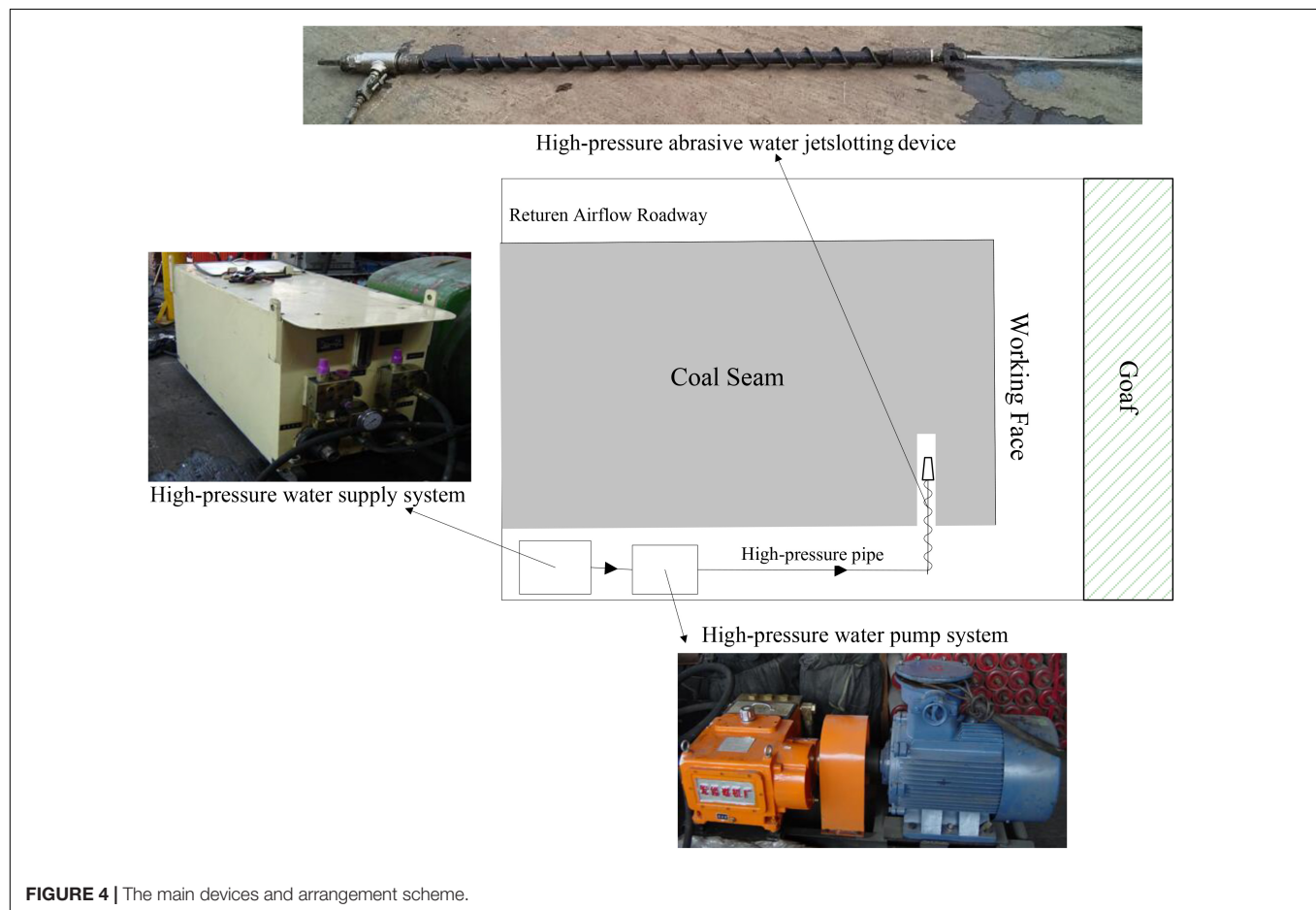
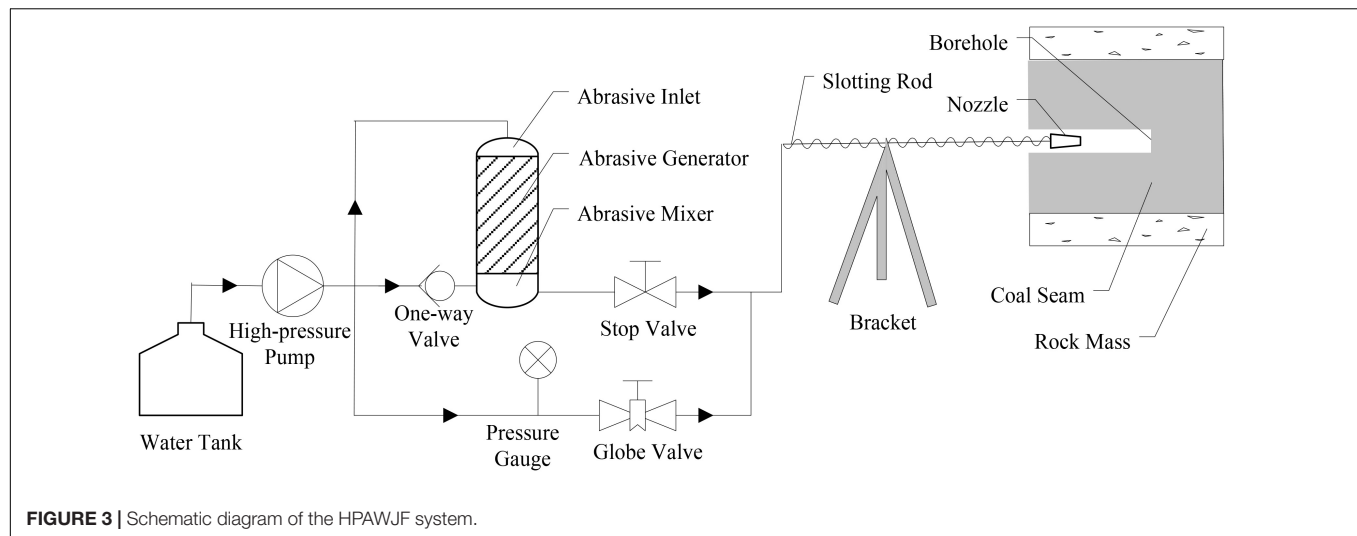
$$\lambda = \begin{cases} \lambda_0 e^{-\beta(\sigma_3 - \alpha p)} & D = 0 \\ \xi \lambda_0 e^{-\beta(\sigma_3 - \alpha p)} & 0 < D < 1 \\ \xi' \lambda_0 e^{-\beta(\sigma_3 - \alpha p)} & D = 1 \end{cases} \quad (7)$$

where f_{tr} is the tensile residual strength, and ξ' is the ratio of the permeability coefficient in the process of element damage.

EXPERIMENT AND MODELING

Field Experiment

The HPAWJF system consists of a water tank, a high-pressure pump, an abrasive generator, an abrasive mixer, a flushing rod, a nozzle, and some valves and pressure gauges (Figures 3, 4). Water is pressurized by the pump, and the outflow is divided into three flow paths. In order to drive the abrasive movement, the first high-pressure water flow reaches the top of the abrasive generator. To take the abrasive away, the second high-pressure water flow through the one-way valve reaches the abrasive mixer at the bottom of the abrasive generator. To obtain an ice mixing effect, the third high pressure water flow through the bypass is directly sent to the outlet of the abrasive mixer. Then, the high-pressure abrasive water jet flows through the flushing rod and nozzle, and it slots the coal seam.



The field experiment site is the 16,071 working face of the Daping Coalmine, which is located in the western region of Henan, China. The working face is in a typical “three-soft” (soft coal, soft roof, and soft floor) coal seam. The characteristics of the seam are as follows: depth is 880 m, thickness is 1.2–1.6 m, dip angle is 4–21°, consistent coefficient of the coal is 0.2–0.6, type

of coal damage is II–III, gas content of the coal seam is 15 ml/t, absolute volume of gas drainage is 1.43 ml/min, largest original gas pressure is up to 1.8 MPa, and soft coal seam thickness is 0.6 m. Before using the HPAWJF technology, the forecast indexes of outburst danger of the working face are often at the critical or above the critical state, the initial velocity of gas drainage from

the borehole (q value) is 8–20 L/min, and the drilling volume (s value) is 3–5 L/m.

As shown in **Figure 5**, Field experiment procedures include three parts: advance preparation, flushing procedures, and monitoring of gas drainage parameters. In addition, every step is strictly monitored to ensure that the experiment is safe. The R value comprehensive index method is used to evaluate the effect of the field experiment on the critical value indexes S , q , and R (3.3, 5, and 5.3 L/m, respectively). The R value is the key index used for judging the danger of coal and gas outbursts, and the S and q values are the reference values.

Model and Parameters

To investigate the distributions of seepage and gas pressure fields in the realistic failure process of HPAWJF, numerical simulation is carried out under different coal seam permeability and flushing length conditions. Based on the actual situation of the coal mine field experiment, the initial and boundary conditions of the simulation analysis are set. The basic computational mechanics parameters of the numerical simulation model are shown in **Table 1**. When the permeability coefficients are 0.1 and 1, we build three models with different flushing lengths (0, 3, and 7.5 m) for the simulation, and the diameter of the slots is 50 mm. The size of the numerical model is 15×5 m (length \times width), and the roof and floor of the model are impermeable rock.

To better protect the numerical simulation results, the mesh independence test for the model is verified using seven groups of different mesh numbers (Ding et al., 2021). In this study, a mesh number of 200,000 satisfies the requirements of computational accuracy and is selected for the model. For a satisfactory resolution in the vicinity of the interface, an H

TABLE 1 | Mechanical parameters of the numerical model.

Parameters	Coal seam	Roof and floor
Elastic modulus (GPa)	5	50
Compressive strength (MPa)	130	300
Poisson's ratio	0.25	0.20
Bulk density (10^{-5} N/mm ³)	1.33	2.67
Friction angle (°)	25	30
Ratio of compressive-tensile strength	20	10
Strength attenuation coefficient	0.1	0.3
Permeability coefficient [$\text{m}^2/(\text{MPa}^2 \cdot \text{d})$]	1/0.1	0.001
Gas content coefficient	1	0.01
Gas pore pressure coefficient	0.3	0.1
Coupling coefficient	0.1	0.2

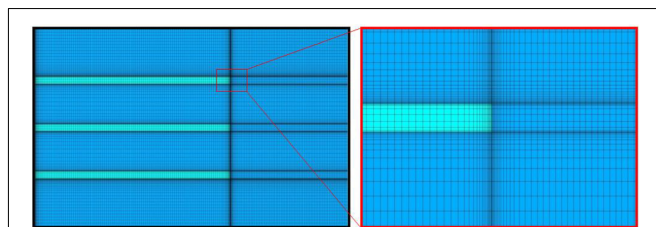


FIGURE 6 | The mesh for numerical calculation.

grid is constructed, and the value of y^+ is approximately 10 (**Figure 6**; Bian et al., 2020; Zhang et al., 2021). Therefore, the mesh resolution is acceptable. Gas pressure of the working face is 1 MPa, and internal gas pressure of the coal seam is 1.8 MPa. The numerical simulation implemented a transient process, and time step is 0.02 day.

RESULTS AND DISCUSSION

In this section, gas pressure and gas volume distribution will be discussed under different permeability coefficient (λ). Meanwhile, gas drainage efficiency will be investigated.

The Effect of Slot Distance Under $\lambda = 1$

As shown in **Figure 7A**, without HPAWJF, the gas pressure relief zone is approximately 2–6 m. With the increase in the inter-distance of the coal seam, the gas pressure increased sharply. Additionally, the gas pressure decreased slowly over time. When the inter-distance of the coal seam reached 1.2 m, all of the curves exceeded the critical pressure value (0.74 MPa). At a distance of 6 m, the gas pressure did not change, and the value of the internal gas pressure of the coal seam was 1.8 MPa. That demonstrated that the effect of gas pressure relief is very limited without HPAWJF.

To verify the effect of HPAWJF on gas pressure relief in a realistic failure process, numerical simulations using flushing lengths of 3 and 7.5 m are carried out. As shown in **Figure 7B**, in the slotted zone of the coal seam (0–3 m), the gas pressure changed smoothly. The maximum gas pressure relief zone increased to 6–7 m after 4 days. The curve of the gas pressure

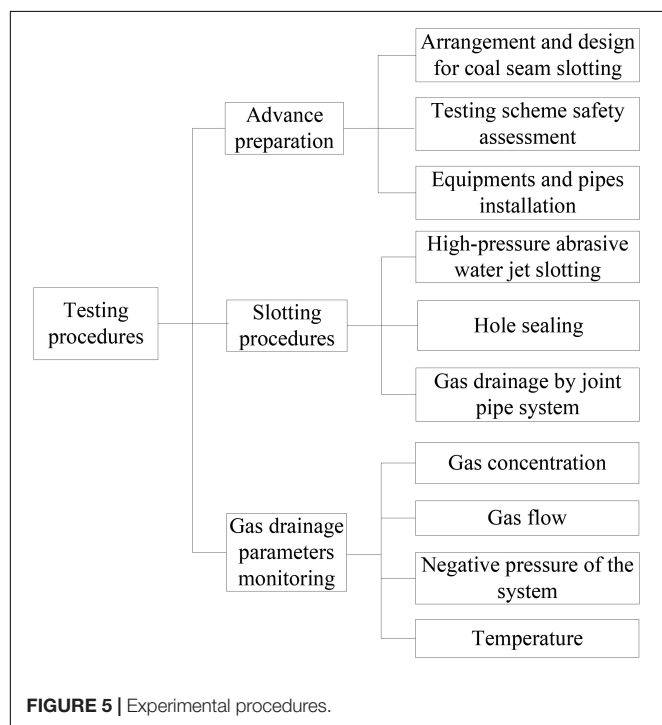


FIGURE 5 | Experimental procedures.

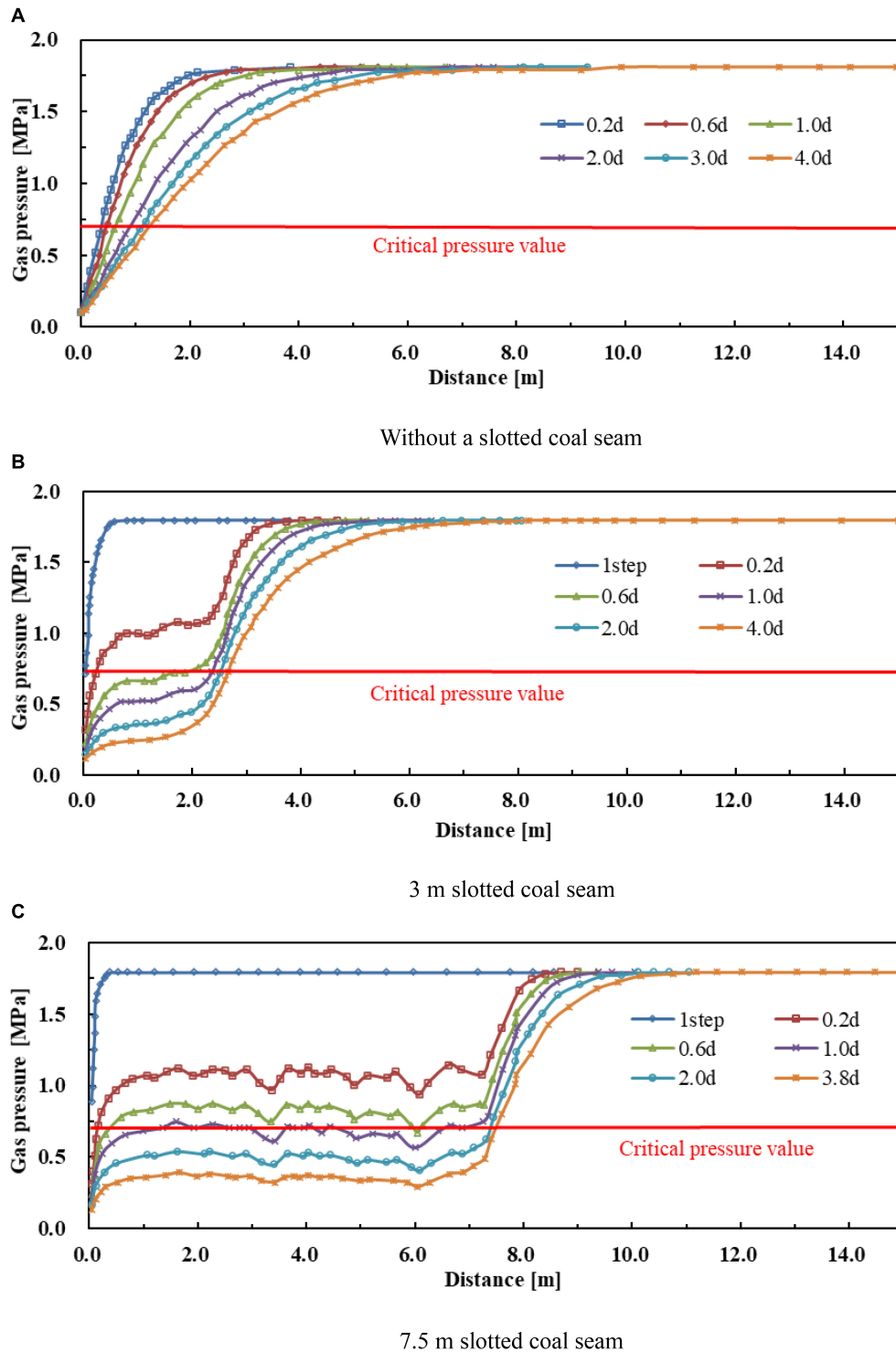


FIGURE 7 | Variation in gas pressure: (A) without a slotted coal seam, (B) 3-m slotted coal seam, and (C) 7.5-m slotted coal seam.

is below the critical pressure value (0.74 MPa) in the gas pressure relief zone after 0.6 day. Additionally, over time, the gas pressure decreased slowly. When the flushing length reached 2.5 m and the curve of the gas pressure increased rapidly, the internal gas

pressure of the coal seam was reached. At 6–7 m, the gas pressure had no change, and the value of the internal gas pressure of the coal seam is 1.8 MPa. In the slotted zone of the coal seam (0–7.5 m) (Figure 7C), the gas pressure had little change, and

the value is much lower than the others (**Figures 7A,B**). Over time, the gas pressure decreased. The curve of the gas pressure is below the critical pressure value (0.74 MPa) after 1 day. When the flushing length reached 7.5 m, the curve of gas pressure increased sharply and reached the internal gas pressure of the coal seam. At 10–11 m, the gas pressure had no change, and the value of the internal gas pressure of the coal seam is 1.8 MPa.

Figures 8, 9 show the gas volume fraction distributions of coal seams at different flushing lengths when the permeability coefficient is 1. In the early days of gas drainage, the gas volume fraction is very low in the slotted zones. The gas pressure relief zone increased significantly over time, and the gas volume fraction gradually became uniform in the gas drainage zone of the coal seam. Compared with the coal seam zones without flushing, the gas volume fraction decreased significantly. When the distance from the slot is increased, the gas volume fraction distribution in the coal seam is decreased, and the gas volume fraction is decreased slowly when the gas drainage time is decreased. Therefore, the desorption and diffusion of methane in the coal seam increased as a result of HPAWJF. This illustrates that the gas drainage from the coal is significantly impacted within the range of the gas pressure relief zone surrounding the center of the slot, which is consistent with the distribution of the flushing permeability enhancement function.

From **Figures 7–9**, it can also be observed that after 4 days of gas drainage with 3-m flushing, the average gas pressure in the zone of pressure relief is 0.319 MPa. Compared with the initial gas pressure of the coal seam it decreased by 82.3%. Similarly, after 4 days of gas drainage with 7.5-m flushing, the average gas pressure in the zone of pressure relief is 0.363 MPa, which is a 79.8% drop compared with the initial gas pressure of the coal seam. When the flushing length is increased from 3 to 7.5 m, the zone of gas pressure relief is increased synchronously.

The Effect of Slot Distance Under $\lambda = 0.1$

When the permeability coefficient is 0.1 and without HPAWJF, the gas pressure relief zone is only 2 m (**Figure 10A**). When the inter-distance of the coal seam is increased, the gas pressure is increased significantly. As the permeability coefficient is very low, the gas pressure of the same coal seam zone changed little over time. After 2 m, the gas pressure had no change, and the value of the internal gas pressure of the coal seam is 1.8 MPa.

As shown in **Figures 10B,C**, in the slotted zone of the coal seam, the gas pressure exhibited little change. The maximum gas pressure relief zone expanded to 3.5 and 8 m after 1.5 days. Additionally, over time, the gas pressure decreased slowly, and all of the curves exceeded the critical pressure value (0.74 MPa). The conclusions can be received from **Figures 11** and **12** that when the flushing length reached 3 m and 7 m respectively, the curves of gas pressure increased sharply toward the internal gas pressure of the coal seam. At 3.5 and 8 m, the gas pressure had no change, and the value of the internal gas pressure of the coal seam is 1.8 MPa. Regarding the curves of the gas pressure

(**Figures 7, 10**), although the effects of the HPAWJF permeability enhancement and pressure relief decreased significantly in lower-permeability coal seams, they are still much better than those of the conventional borehole.

Because the permeability coefficient of the coal seam is lower, the applied load provided by the coal mass elements of the slot walls is insufficient to form fractures. Thus, methane desorption and diffusion of the coal seam increased marginally when HPAWJF was used. For the coal seam with lower permeability coefficient, the method of increasing the flushing length is more effective than that of increasing the gas drainage time.

Analysis of Gas Drainage Efficiency

By combining the results of the field experiment and numerical simulation, the gas drainage efficiencies of the gas drainage volume, tunneling speed, and coal cutting quantity are analyzed.

The experimental working face is a coal and gas outburst coal seam. For the pre-drainage of the gas, the conventional method for releasing holes is adopted. The value of the effective index for judging the danger of coal and gas outburst is often greater than the critical value. Using the HPAWJF technology, the initial velocity of the gas drainage from the borehole (q value) is reduced from 20 to 3.4 L/min, which indicated that the coal seam structure is damaged, leading to further changes in the internal stress of the coal mass. Thus, the scalability of the coal seam fracture net is improved, and the increase in macroporosity is conducive to the movement of gas.

For the conventional method of releasing holes, the deformation is momentary. For flushing holes, the pressure relief in the coal seam around the borehole is remarkable. Under the condition of HPAWJF, the effective stress in the coal mass is appreciably reduced, and the pressure relief zone is much larger than that of the conventional method. This shows that, in the flushing procedure, the maximum gas concentration in the roadway is 0.79%. Before flushing, the average gas concentration in the roadway is 0.21% (**Figure 13**). This indicates that the gas drainage volume is enhanced more than three times compared with before flushing.

In the flushing procedure, the length of each flushing cycle is 4.2 m, and the corresponding excavation time is referred to as the single cycle excavation time. The field experiment results indicated that the single-cycle excavation times before and after the use of the HPAWJF technology are 3–4 and 1–2 days, respectively. For the conventional method of releasing holes, each drilling length is 2.7–6 m, and the maximum tunneling advance length is approximately 60 m. In contrast, for the flushing holes, each flushing length of the coal seam is 4.2 m, and the maximum tunneling advance length is approximately 120 m. This demonstrated that the tunneling speed is nearly doubled compared with before.

Without using the HPAWJF technology, the tunneling advance lengths of the working face for April, May, and June are 17, 35, and 24 m, respectively (**Figure 14**). The average tunneling speed is 25 m/month. Using the HPAWJF technology, the tunneling advance lengths of the working face for July, August, September, October, and November are 44, 42, 44, 40, and 74 m, respectively. The average tunneling speed is 49 m/month. From

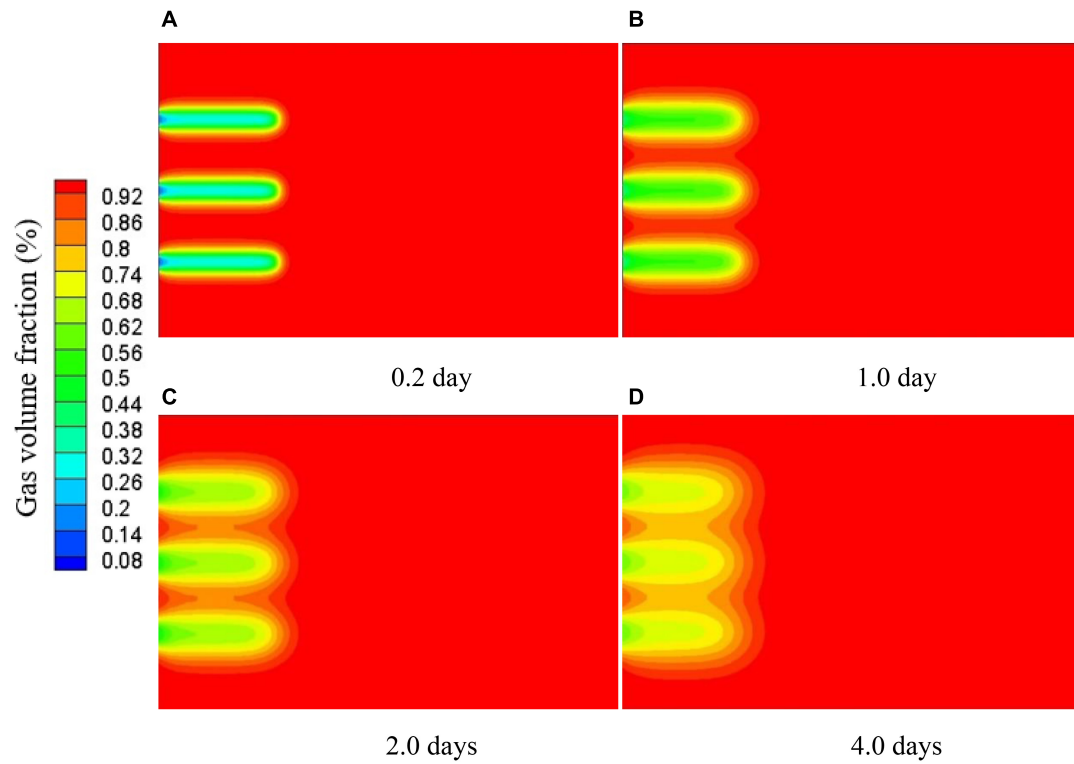


FIGURE 8 | Gas seepage fields of a 3-m slotted coal seam when $\lambda = 1$: (A) 0.2 day, (B) 1.0 day, (C) 2.0 days, and (D) 4.0 days.

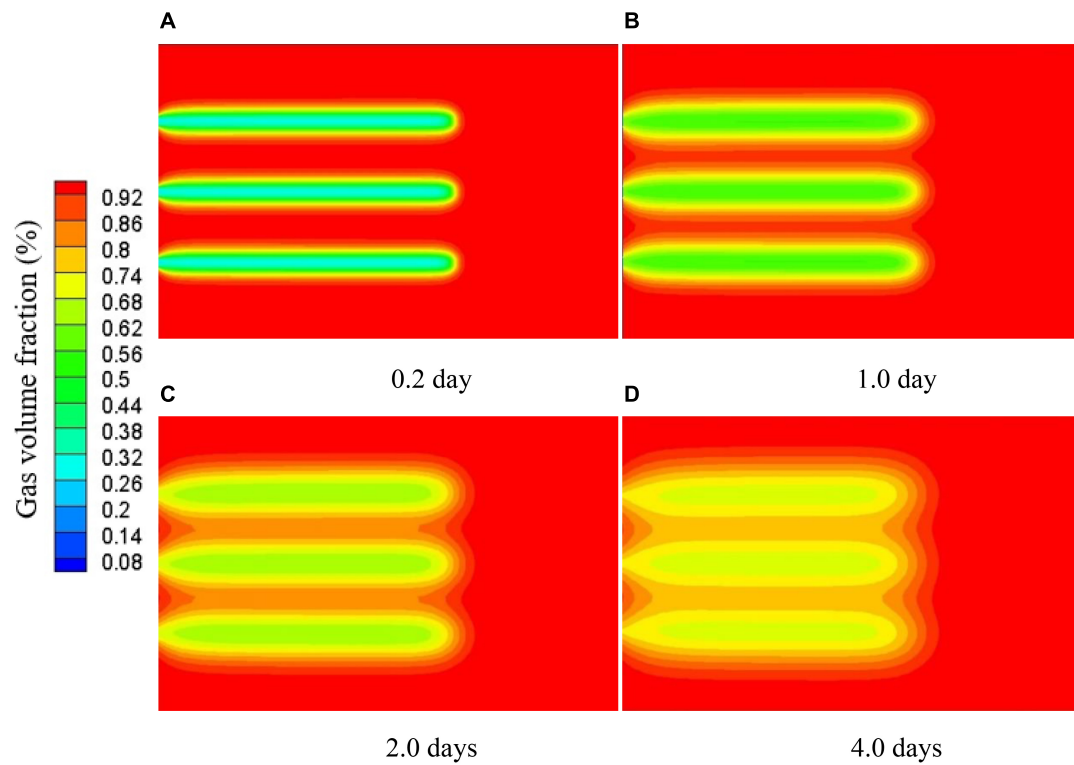


FIGURE 9 | Gas seepage fields of a 7.5-m slotted coal seam when $\lambda = 1$: (A) 0.2 day, (B) 1.0 day, (C) 2.0 days, and (D) 4.0 days.

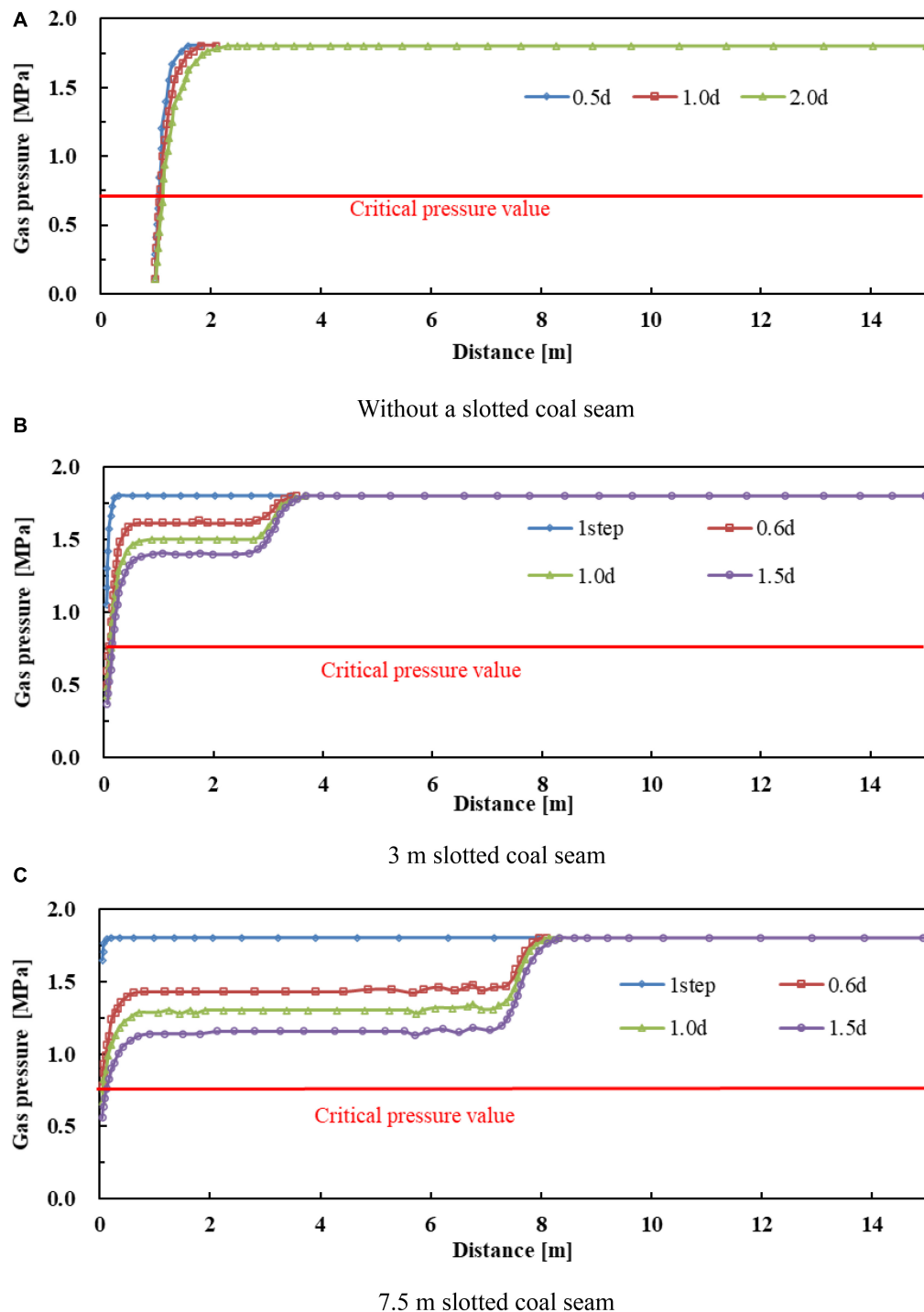


FIGURE 10 | Variation in gas pressure: (A) without a slotted coal seam, (B) 3-m slotted coal seam, and (C) 7.5-m slotted coal seam.

the results described above, it can be concluded that the average tunneling speed increased by 96%. The experimental test results are in good agreement with the theoretical analyses.

Figure 15 shows the coal cutting quantity of each flushing cycle in a month. In the flushing process, the maximum coal

cutting quantity of each flushing cycle is 6.5 t, the minimum coal cutting quantity of each flushing cycle is 3.4 t, and the average coal cutting quantity of each flushing cycle is 5.2 t. This illustrated that the abrasive water jet can directly break the coal rock and form free surfaces for the subsequent coal

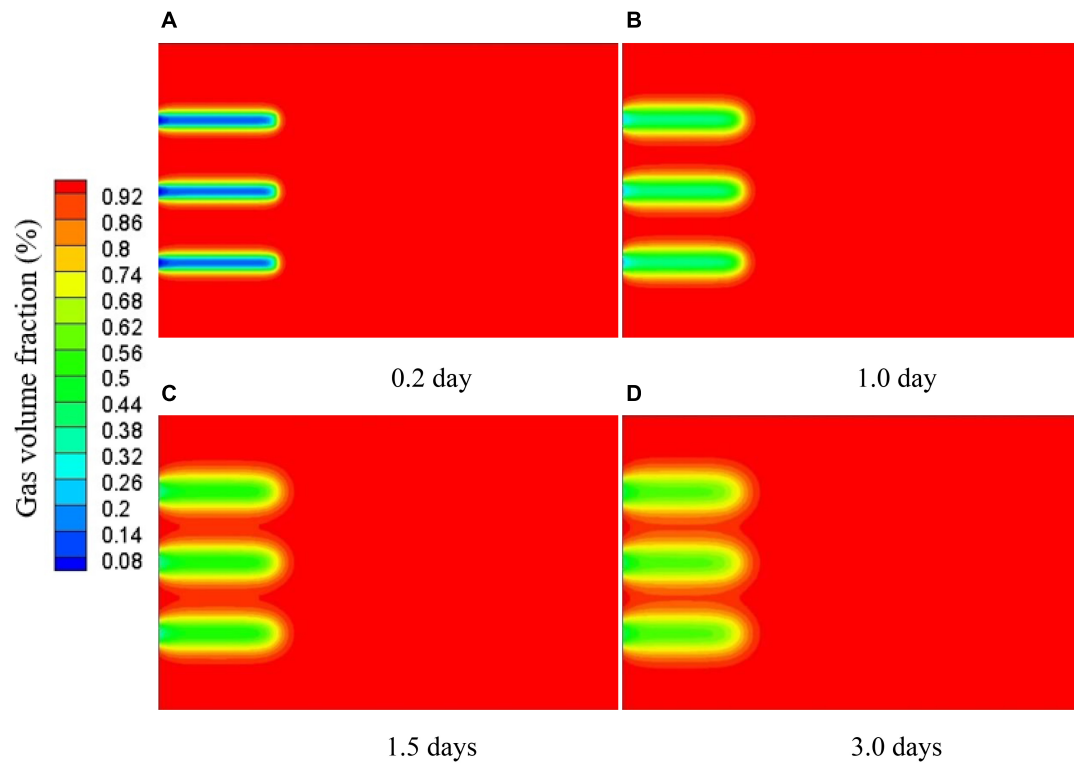


FIGURE 11 | Gas seepage fields of a 3-m slotted coal seam when $\lambda = 0.1$: (A) 2 day, (B) 1 day, (C) 1.5 days, and (D) 3 days.

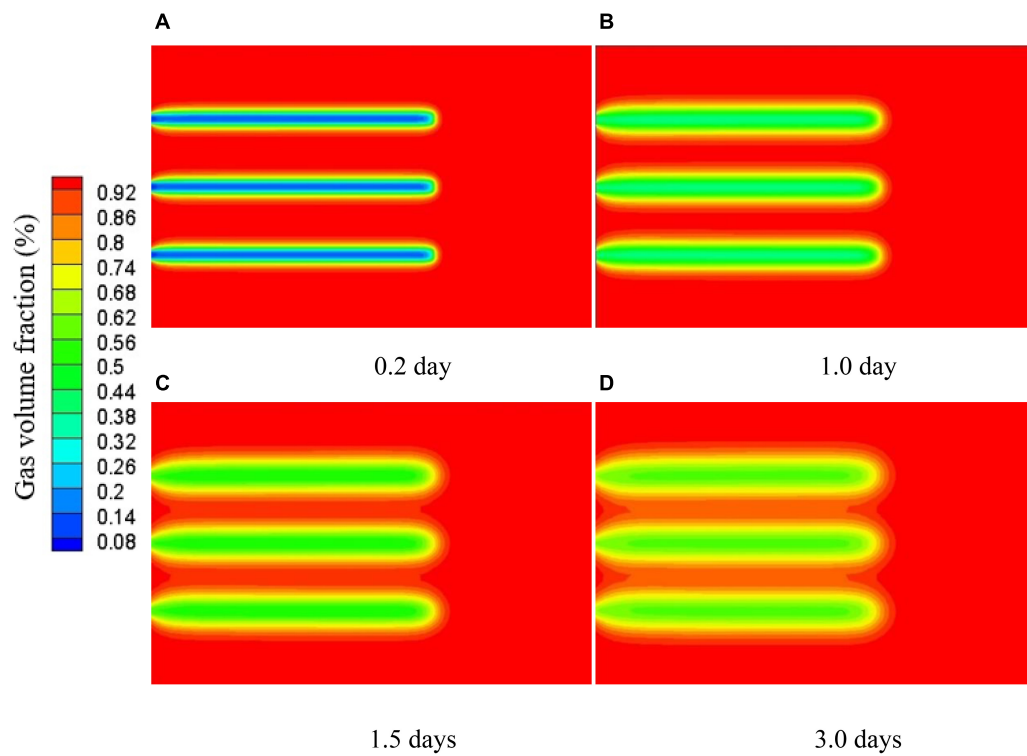
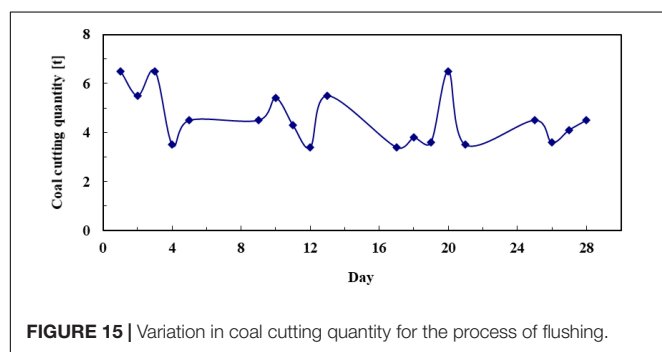
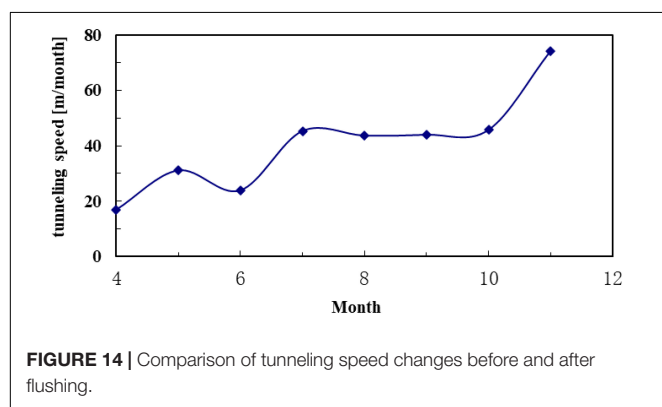
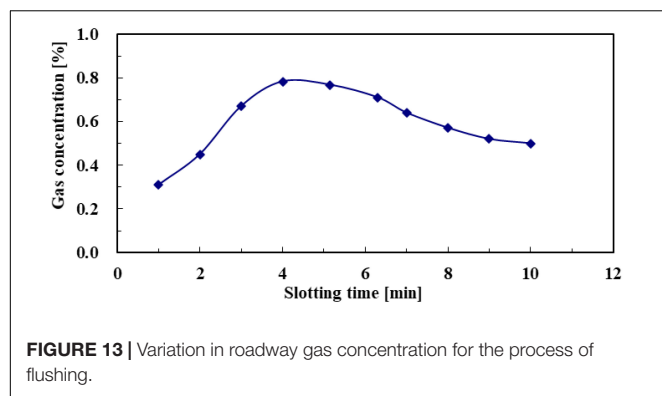


FIGURE 12 | Gas seepage fields of a 7.5-m slotted coal seam when $\lambda = 0.1$: (A) 2 day, (B) 1 day, (C) 1.5 days, and (D) 3 days.



rock breaking procedure (Lu et al., 2013). As the quantity of coal cutting increased, increased macroporosity improved the movement of gas. These results indicated that the permeability of the coal seam had increased.

CONCLUSION

In this study, the results of theoretical analysis and experimental verification of pressure relief and permeability enhancement resulting from HPAWJF are presented. Based on simulations and field experiments, the distribution characteristics of seepage fields and gas pressure fields in the realistic failure process are analyzed, and gas drainage efficiencies of gas drainage volume, tunneling speed, and coal cutting quantity are correspondingly summarized. The effect of the permeability enhancement of

soft coal seams is mutually verified by the results of the field experiment and numerical simulation. Conclusions from this study are as follows:

- (1) The stress and energy concentration state of the coal mass could be effectively destroyed by the application of HPAWJF. The force stress propagated to deeper zones and caused the release of gas pressure from the coal seam. Thus, the pressure relief zone increased significantly. After 1.2 days of gas drainage, when the flushing length was 7.5 m, the average gas pressure of the pressure relief zone decreased to the critical pressure value (0.74 MPa). At this point, the efficiency of the gas drainage was the highest. For the lower permeability coefficient, increasing the flushing length was more effective than increasing the gas drainage time.
- (2) The coal seam structure is damaged, leading to further changes in the internal stress of the coal mass. Thus, the net scalability of the coal seam fracture is improved, and the increase in macroporosity enhanced the movement of gas. The average coal cutting quantity of each flushing cycle increased to 5.2 t. The maximum gas concentration in the roadway is 0.79%. The gas drainage volume is three times higher than for conventional boreholes.
- (3) The abrasive water jet could directly break the coal rock and form free surfaces for the subsequent coal rock breaking procedure, which could also force the fracture to penetrate along with the coal rock texture and to extend continuously until coal fragments are formed. When HPAWJF was used, each flushing length of the coal seam reached 4.2 m. The theoretical maximum tunneling advance length is approximately 120 m, and the maximum tunneling advance length in the field experiment is 74 m. This demonstrates that the tunneling speed is nearly two times higher than before using HPAWJF.

DATA AVAILABILITY STATEMENT

The original contributions presented in the study are included in the article/supplementary material, further inquiries can be directed to the corresponding author/s.

AUTHOR CONTRIBUTIONS

XZ and SD provided the idea. PW designed the research. PW and SD developed the literature search. XZ and GZ drafted the manuscript. All authors contributed to the article and approved the submitted version.

ACKNOWLEDGMENTS

Thanks are due to the support by the Postdoctoral Foundation of Henan Province (Grant No: 19030014), the China Postdoctoral Science Foundation (2019M652575), and the Science and Technology R&D Program of Henan Province of China (192102210056).

REFERENCES

- Aguado, M. B. D., and Nicieza, C. G. (2007). Control and prevention of gas outbursts in coal mines, riosa-olloniego coalfield, Spain. *Int. J. Coal Geol.* 69, 253–266. doi: 10.1016/j.coal.2006.05.004
- Bian, J., Cao, X., Yang, W., Guo, D., and Xiang, C. (2020). Prediction of supersonic condensation process of methane gas considering real gas effects. *Appl. Therm. Eng.* 164:114508. doi: 10.1016/j.applthermaleng.2019.114508
- Cao, X. W., and Bian, J. (2019). Supersonic separation technology for natural gas processing: a review. *Chem. Eng. Process.* 136, 138–151. doi: 10.1016/j.cep.2019.01.007
- Cheng, Y. P., Wang, L., and Zhang, X. L. (2011). Environmental impact of coal mine methane emissions and responding strategies in China. *Int. J. Greenh. Gas Control* 5, 157–166. doi: 10.1016/j.ijggc.2010.07.007
- Connell, L. D. (2009). Coupled flow and geomechanical processes during gas production from coal seams. *Int. J. Coal Geol.* 79, 18–28. doi: 10.1016/j.coal.2009.03.008
- Ding, H., Tian, Y., Wen, C., Wang, C., and Sun, C. (2021). Polydispersed droplet spectrum and exergy analysis in wet steam flows using method of moments. *Appl. Therm. Eng.* 182:116148. doi: 10.1016/j.applthermaleng.2020.116148
- Frid, V. (1997). Electromagnetic radiation method for rock and gas outburst forecast. *J. Appl. Geophys.* 38, 97–104. doi: 10.1016/s0926-9851(97)00017-7
- Hood, M. (1976). Cutting strong rock with a drag bit assisted by high pressure water jets. *J. S. Afr. Institute Min. Metall.* 77, 79–90.
- Jiang, J. Y., Cheng, Y. P., Wang, L., and Li, W. (2011). Petrographic and geochemical effects of sill intrusions on coal and their implications for gas outbursts in the Wolonghu Mine, Huaibei Coalfield, China. *Int. J. Coal Geol.* 88, 55–66. doi: 10.1016/j.coal.2011.08.007
- Jiang, Y. D., Zhao, J. X., Liu, W. G., and Zhu, J. (2009). *Investigation on the Mechanism of Coal Bumps and Relating Experiments*. Beijing: Science Press.
- Jin, W. C., Gao, M. Z., Yu, B., Zhang, R., Xie, J., and Qiu, Z. Q. (2015). Elliptical fracture network modeling with validation in datong mine, China. *Environ. Earth Sci.* 73, 7089–7101. doi: 10.1007/s12665-015-4158-4
- Kim, D. I. (2001). *A Study on the Cutting of Rocks by Injection type Abrasive Water Jets*. M.S.Dissertation. Korea: University of Seoul National.
- Li, X. H., Wang, J. S., Lu, Y. Y., Yang, L., Kang, H. M., and Sun, J. J. (2000). Experimental investigation of hard rock cutting with collimated abrasive water jets. *Int. J. Rock Mech. Min. Sci.* 37, 1143–1148. doi: 10.1016/s1365-1609(00)00036-8
- Li, X. Z., and Hua, A. Z. (2006). Prediction and prevention of sandstone-gas outbursts in coal mines. *Int. J. Rock Mech. Min. Sci.* 43, 2–18. doi: 10.1016/j.ijrmms.2005.03.021
- Lin, B. Q., and Shen, C. M. (2015). Coal permeability-improving mechanism of multilevel slotting by water jet and application in coal mine gas extraction. *Environ. Earth Sci.* 73, 5975–5986. doi: 10.1007/s12665-015-4154-8
- Lin, B. Q., Meng, F. W., and Zhang, H. B. (2011). Regional gas control based on drilling-slotting-extracting integration technology. *J. China Coal Soc.* 36, 75–79.
- Liu, J. S., Chen, Z. W., Elsworth, D., Miao, X. X., and Mao, X. B. (2010). Linking gas-sorption induced changes in coal permeability to directional strains through a modulus reduction ratio. *Int. J. Coal Geol.* 83, 21–30. doi: 10.1016/j.coal.2010.04.006
- Liu, X. H., Dai, F., Zhang, R., and Liu, J. F. (2015). Static and dynamic uniaxial compression tests on coal rock considering the bedding directivity. *Environ. Earth Sci.* 73, 5933–5949. doi: 10.1007/s12665-015-4106-3
- Lu, Y. Y., Tang, J. R., Ge, Z. L., Xia, B. W., and Liu, Y. (2013). Hard rock drilling technique with abrasive water jet assistance. *Int. J. Rock Mech. Min. Sci.* 60, 47–56. doi: 10.1016/j.ijrmms.2012.12.021
- Momber, A. W., Budidharma, E., and Tjo, R. (2011). The separation of reinforced cementitious composites with a stream-line cutting tool. *Resour. Conserv. Recycl.* 55, 507–514. doi: 10.1016/j.resconrec.2010.12.014
- Shen, C. M., Lin, B. Q., Sun, C., Zhang, Q. Z., and Li, Q. Z. (2015). Analysis of the stress-permeability coupling property in water jet slotting coal and its impact on methane drainage. *J. Petrol. Sci. Eng.* 126, 231–241. doi: 10.1016/j.petrol.2014.11.035
- Shen, T., Wang, Y. B., Tang, D. Z., Xu, H., Lv, Y. M., He, W., et al. (2012). Dynamic variation effects of coal permeability during the coalbed methane development process in the Qinshui Basin, China. *Int. J. Coal Geol.* 93, 16–22. doi: 10.1016/j.coal.2012.01.006
- Song, D. Z., Wang, E. Y., Liu, Z. T., Liu, X. F., and Shen, R. X. (2014). Numerical simulation of rock-burst relief and prevention by water-jet cutting. *Int. J. Rock Mech. Min. Sci.* 70, 318–331. doi: 10.1016/j.ijrmms.2014.05.015
- Tang, C. A., Tham, L. G., Lee, P. K. K., Yang, T. H., and Li, L. C. (2002). Coupled analysis of flow, stress and damage (FSD) in rock failure. *Int. J. Rock Mech. Min. Sci.* 39, 477–489. doi: 10.1016/s1365-1609(02)00023-0
- Wang, F. T., Ren, T., Tu, S. H., Hungerford, F., and Aziz, N. (2012). Implementation of underground longhole directional drilling technology for greenhouse gas mitigation in Chinese coal mines. *Int. J. Greenh. Gas Control* 11, 290–303. doi: 10.1016/j.ijggc.2012.09.006
- Wang, S. L., Wu, Z. J., Guo, M. W., and Ge, X. R. (2012). Theoretical solutions of a circular tunnel with the influence of axial in situ stress in elastic-brittle-plastic rock. *Tunn. Undergr. Space Technol.* 30, 155–168. doi: 10.1016/j.tust.2012.02.016
- Yang, W., Lin, B. Q., Qu, Y. A., Li, Z. W., Zhai, C., Jia, L. L., et al. (2011). Stress evolution with time and space during mining of a coal seam. *Int. J. Rock Mech. Min. Sci.* 48, 1145–1152. doi: 10.1016/j.ijrmms.2011.07.006
- Yazici, S. (1989). *Abrasive Jet Cutting and Drilling of Rocks*. Ph.D. Dissertation. USA: University of Missouri-Rolla.
- Zhang, G., Dykas, S., Majkut, M., Smofka, K., and Cai, X. (2021). Experimental and numerical research on the effect of the inlet steam superheat degree on the spontaneous condensation in the IWSEP nozzle. *Int. J. Heat Mass Transf.* 165:120654. doi: 10.1016/j.ijheatmasstransfer.2020.120654
- Zhao, Y. S., Feng, Z. C., and Wan, Z. J. (2003). Least energy principle of dynamical failure of rock mass. *Chin. J. Rock Mech. Eng.* 22, 1781–1783.

Conflict of Interest: The authors declare that the research was conducted in the absence of any commercial or financial relationships that could be construed as a potential conflict of interest.

Copyright © 2021 Zhang, Wiśniewski, Dykas and Zhang. This is an open-access article distributed under the terms of the Creative Commons Attribution License (CC BY). The use, distribution or reproduction in other forums is permitted, provided the original author(s) and the copyright owner(s) are credited and that the original publication in this journal is cited, in accordance with accepted academic practice. No use, distribution or reproduction is permitted which does not comply with these terms.



Structure and Topology Analysis of Separated Vortex in Forward-Swept Blade

D. Liang¹, Y. Li¹, Z. Zhou^{1*}, P. Wiśniewski^{2*} and S. Dykas²

¹School of Electrical and Power Engineering, China University of Mining and Technology, Xuzhou, China, ²Department of Power Engineering and Turbomachinery, Silesian University of Technology, Gliwice, Poland

OPEN ACCESS

Edited by:

Lin Teng,
Fuzhou University, China

Reviewed by:

Hongbing Ding,
Tianjin University, China
Bin Liu,
Shijiazhuang Tiedao University, China
Xu Han,
North China Electric Power University,
China

*Correspondence:

Z. Zhou
zznwt@163.com
P. Wiśniewski
piotr.wisniewski@polsl.pl

Specialty section:

This article was submitted to
Advanced Clean Fuel Technologies,
a section of the journal
Frontiers in Energy Research

Received: 11 April 2021

Accepted: 06 May 2021

Published: 20 May 2021

Citation:

Liang D, Li Y, Zhou Z, Wiśniewski P and
Dykas S (2021) Structure and
Topology Analysis of Separated Vortex
in Forward-Swept Blade.
Front. Energy Res. 9:693596.
doi: 10.3389/fenrg.2021.693596

Flow separation commonly affects the stability of turbomachines, especially under low-flowrate conditions. Compared with conventional blades, a forward-swept blade is more efficient at high flowrates. However, experiments and numerical simulations show that a forward-swept blade produces an unstable region under low flowrate. In this paper, the topological analysis is used to analyze the structure and size of flow separation in forward swept blades. Three-dimensional structure and formation mechanism of vortices in forward-swept blades are analyzed using the cross-section flow pattern method. For forward-swept blades, flow separation mainly occurs at the blade tip and corner, accompanied by clear velocity fluctuations, the break-up of shed vortices, and diffusion. With decreasing flowrate, the shedding vortices move forward and the speed of vortex annihilation gradually decreases. In addition, the number of singularities in the rotor passage increases with the decrease of flow rate, and the region affected by shedding vortex increases. The rotating direction of internal vortex in turbomachinery is fixed. The pressure surface, passage vortex, and concentrated shedding vortex were found to rotate clockwise, whereas the suction surface, corner vortex, and shedding vortex rotate in a counterclockwise direction.

Keywords: flow separation, forward-swept blade, topological analysis, vortex structure, limit streamline

INTRODUCTION

With the development of manufacturing technology and numerical analysis software, three-dimensional blades are being increasingly used in axial turbomachines. Since the 1960s, the blade curve formation theory proposed by References (Filippov and Wang, 1962; Wang et al., 1981; Wang, 1999) has provided theoretical guidance for the design of three-dimensional blades. More recently, forward-swept blades have been mentioned (Wennerstrom and Puterbaugh, 1984; Wennerstrom, 1990) in the context of experimental transonic compressors. Experimental results show that forward-swept blades maintain high efficiency at the tip of the cascade at high speeds. Mohammed and Raj (1977) designed forward-swept blades for a low-speed compressor rotor, optimizing the flow separation at the tip of the suction surface and improving the characteristics of

Abbreviations: C_p , pressure coefficient $(P - P_0)/(1/2\rho U^2)$; f , blade frequency; F , focus points; L , chord length; n , rotational speed; N , node points; Q_v , Mass flowrates; S , saddle points; u , velocity component in the x direction; v , velocity component in the y direction; w , velocity component in the z direction; y^+ , wall function $(\rho u_\tau y/\mu)$; Z_Y , total number of blades; α , singular point integral angle; λ , eigenvalues; θ , installation angle; μ , dynamic viscosity; τ , shear stress; ω , angular velocity; η , fan efficiency $((P_{Total} \cdot Q_v/1,000 \cdot 3,600)/\pi \cdot \text{torque} \cdot n \cdot 360,000)$

the compressor. Vad et al. (2015) comprehensively described the characteristics of forward-swept blades. Combining straight blades and forward-swept blades can increase the efficiency of the fan by 2–3%, although for free-vortex rotors, there is little improvement in efficiency (He et al., 2018; Kaya et al., 2018).

Flow separation, which frequently occurs in the flow around various objects, is a complex flow phenomenon in fluid mechanics, and has been extensively studied along with its associated flow characteristics. Three-dimensional flow separation theory, first proposed by Maskell (1955) and Lighthill (1963), represents the cornerstone of such studies. Thereafter, bubble separation, free vortex separation, open separation, and closed separation configurations were investigated. References (Zhang and Deng, 1992; Zhang, 1994; Zhang, 1997) obtained the flow distributions of multiple cross-sections from experiments and calculations, and derived distribution rules for semi-singularities on cross-sectional contour lines and topological rules for determining the total number of different flows. Surana et al. (2006) developed a three-dimensional steady separation and reattachment theory using nonlinear dynamical systems, and obtained the separation point and separation line criteria under no-slip boundary conditions in a compressible flow. Gbadebo et al. (2005) adopted the limit streamline topology method and nonlinear dynamics to obtain the relationship between the inlet angle, boundary layer, and separation point. This method provided a new way of interpreting and researching flow separation theory.

The internal flow, boundary layer separation, and stall/instability conditions of turbomachines can be studied using experimental methods and numerical simulations. Karyakin et al. (2018); Zhang et al. (2018) used the tuft method and oil-flow method, respectively, to conduct experiments on flow separation control around isolated airfoils. However, few studies have applied these experimental methods to rotor flow separation. Taking the oil-flow method as an example, the uniform paint applied on the blade is subjected to two forces, namely the shear force from the airflow and the inertial centrifugal force $\omega^2 \vec{R}$ from the rotation of the blade itself. By using sophisticated numerical simulations, detailed flow field information can be revealed. Zhang et al. (2007) used the NUMECA numerical calculation software to analyze the separation characteristics and vortex structure of the front bending cascade of an axial compressor at different incidence angles. In addition, References (Chen et al., 2013; Ye et al., 2013; Jongwook et al., 2016; Pogorelov et al., 2016; Luo et al., 2017) have conducted detailed analyses of the flow field characteristics of axial flow turbomachines. Drózd (2021) from the view of boundary layer, the relationship between Reynolds number and flow separation is discussed. Cao (2019) studied the effect of flow rate on flow separation of last stage blade of steam turbine. The results show that the flow separation vortices appear near last stage blade at 30% of the rated volume flow. With the decrease of volume flow, the flow separation vortices gradually spread to the root of blade.

Numerical simulations and experimental methods cannot, however, fully explain the law of flow separation, especially for

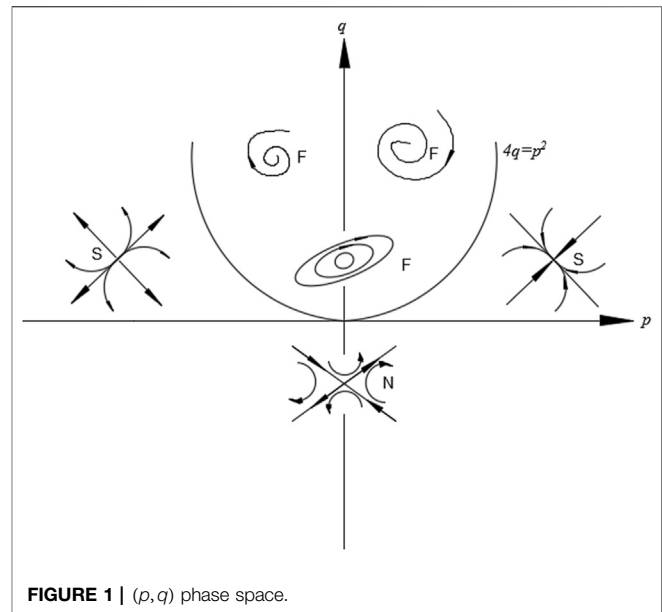


FIGURE 1 | (p, q) phase space.

forward-swept blade flow separation, which is still at the early stages of investigation. In this paper, the Navier–Stokes equations for internal flow in turbomachines are analyzed and the flow field on the blade surface of a forward-swept fan is investigated. The singularity characteristics of the blade surface separation are analyzed using a topological approach. The flow separation is explored in three-dimensional space using a topological-mapping method. The aim of this work is to determine the influence of forward-swept blades on the flow separation of axial flow turbomachines, and to provide a foundation for studying the control of flow separation.

MATHEMATICAL MODEL

In the study of Lighthill (1963), the limit streamline is equal to the friction line:

$$\frac{dy}{dx} = \frac{v}{u} = \frac{\tau_{wy}}{\tau_{wx}} \quad (1)$$

As can be seen from Eq. 1, the direction of the limit streamline is the same as that of the friction line. The limit streamline and the friction line are considered to be equivalent in most studies. In cascade experiments, the oil-flow method and the surface silk-line method can reveal the boundary layer flow state to an adequate degree of accuracy. The frictional line can be transformed into:

$$\begin{cases} \frac{dx}{dt} = \frac{\partial \tau_{xw}}{\partial x} x + \frac{\partial \tau_{xw}}{\partial y} y \\ \frac{dy}{dt} = \frac{\partial \tau_{yw}}{\partial x} x + \frac{\partial \tau_{yw}}{\partial y} y \end{cases} = \begin{bmatrix} \frac{\partial \tau_{xw}}{\partial x} & \frac{\partial \tau_{xw}}{\partial y} \\ \frac{\partial \tau_{yw}}{\partial x} & \frac{\partial \tau_{yw}}{\partial y} \end{bmatrix} \begin{bmatrix} x \\ y \end{bmatrix} \quad (2)$$

According to the theory of phase-plane analysis for ordinary differential equations, the shape and type of friction lines at critical points depend on the properties of the eigenvalues of the

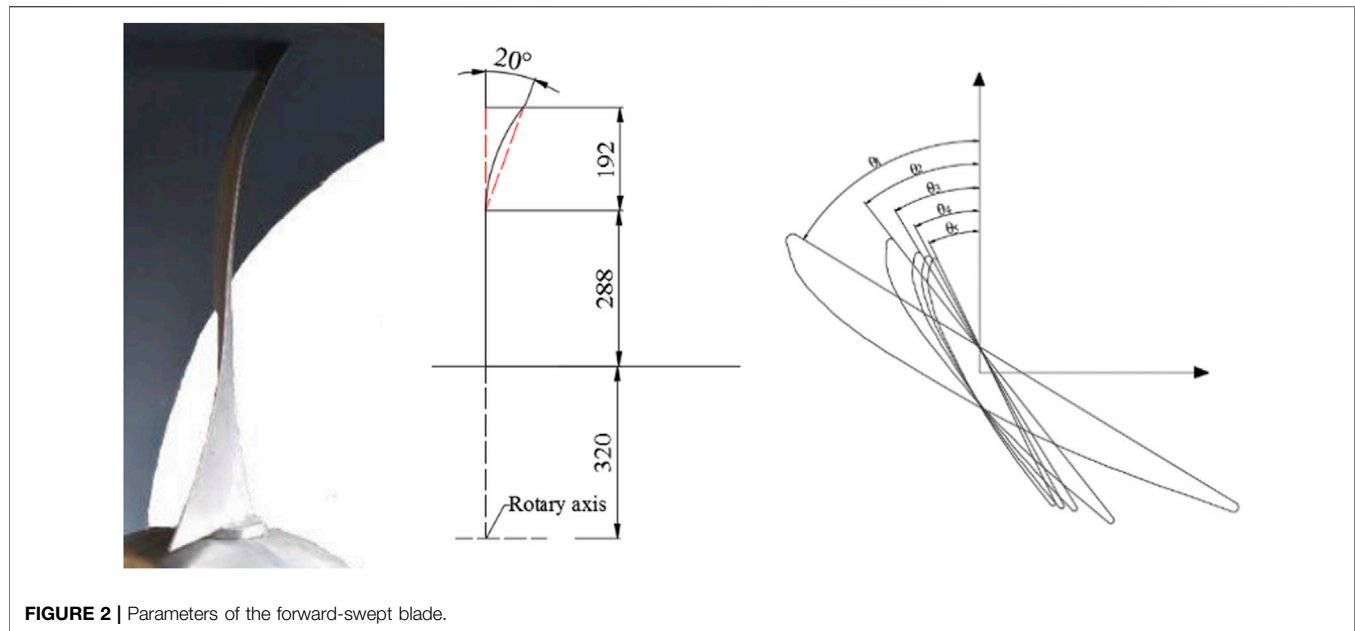


FIGURE 2 | Parameters of the forward-swept blade.

2×2 Jacobian matrix. The critical points can be classified by the surface streamlines nearby, which are determined by trace p and $\det q$ of the matrix. The characteristic roots $\lambda_{1,2}$ vary with position; in theory, all the critical points can occur. The singularities in the (p, q) phase space are mainly composed of saddle points (S), nodes (N), and focus points (F). A change in position causes a change in $\nabla \tau$ and, correspondingly, modifies the positive and negative distributions of the eigenvalues and the terms of the discriminant $\Delta = \sqrt{p^2 - 4q}$, leading to a different singularity distribution, as shown in **Figure 1**. The quantities p , q , and $\lambda_{1,2}$ are given by:

$$p = \frac{\partial \tau_{xw}}{\partial x} + \frac{\partial \tau_{yw}}{\partial y} \quad (3)$$

$$q = \frac{\partial \tau_{xw}}{\partial x} \frac{\partial \tau_{yw}}{\partial y} - \frac{\partial \tau_{xw}}{\partial y} \frac{\partial \tau_{yw}}{\partial x} \quad (4)$$

$$\lambda_{1,2} = \left(p \pm \sqrt{p^2 - 4q} \right) / 2 \quad (5)$$

Figure 1 shows an idealized linear phase space diagram with all of the patterns and distribution of limit streamlines that can appear on the object surface: when $q < 0$, the singularities are node points, when $q > 0$ and $p^2 - 4q > 0$, they are saddle points, and when $p^2 - 4q < 0$, they are focus points.

EXPERIMENTAL MODEL AND RESEARCH METHOD

Experimental Model

An experimental device is often used to evaluate the performance of axial flow fans. Pressure sensors are installed at the outlet of the collector and the entrance of the fan. A data collector is used to record pressure signals and motor parameters. The hub ratio of

TABLE 1 | Specific blade parameter values.

	Angle setting	Value	Chord length	Value
0 Span	θ_1	58°	L_1	236.11 mm
0.4 Span	θ_2	38°	L_2	161.63 mm
0.8 Span	θ_3	31°	L_3	135.50 mm
0.9 Span	θ_4	28°	L_4	128.14 mm
1 Span	θ_5	26°	L_5	122.83 mm

the fan is 0.4, the speed is 980–990 rpm, the outer diameter is 1,600 mm, the length of the intake duct is 4,000 mm, and the measuring length is 4,815 mm. We designed and manufactured the forward-swept blades ourselves, with the blade parameters shown in **Figure 2** and **Table 1**. The total height of blade is 480 mm, of which 60% is straight blade, 40% is swept forward blade, and forward swept angle is 20°.

Numerical model

ANSYS computational fluid dynamics X (ANSYS CFX) was used to simulate the whole flow passage at the fan. The physical model was divided into three areas: the inlet and outlet ducts and the experimental fan itself. The blade was meshed using Auto-Grid. An H-block was adopted for the inlet and outlet parts, with an O-block for the blade part, as shown in **Figure 3**. The quality of the grid is an important factor in the accuracy of the simulation results, and y^+ is an important parameter for measuring how well the grid and the turbulence model coordinate with each other. The thickness of the first layer grid was calculated to be $\Delta s = 0.6 \times 10^{-3}$ mm, ensuring that the y^+ value was less than 1. The boundary conditions, turbulence model, solution accuracy, and convergence criterion are presented in **Table 2**.

To eliminate the influence of the number of grid cells on the numerical results, four different grid resolutions were selected for

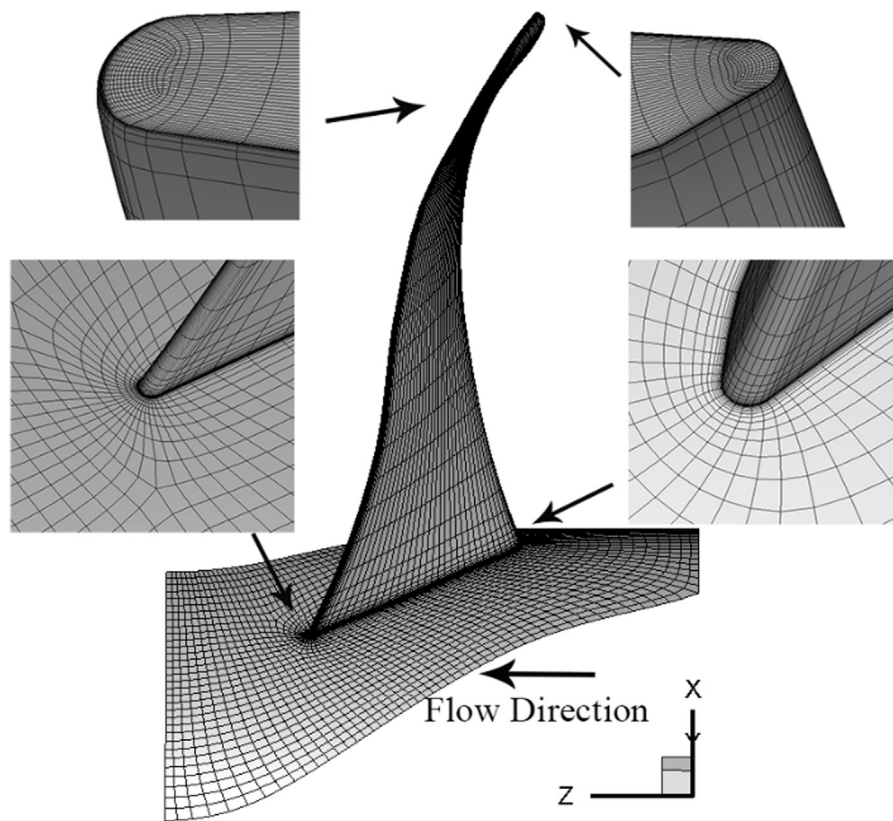


FIGURE 3 | Computational mesh of forward-swept fan.

TABLE 2 | Boundary conditions and convergence criteria for computation.

Inlet boundary	Mass flow inlet
Outlet boundary	Opening boundary condition
Rotational speed	980–990 rpm
Reference pressure	1 atm
Blade surface	No-slip wall
Turbulence model	SST $k - \omega$
Solver	Double precision
Convergence criterion	1×10^{-4}

calculation. The SST $k - \omega$ model includes a modified turbulent viscosity formula to simulate the transport effect caused by turbulent shear stress, and a reasonably accurate solution can be obtained for separated flow. Therefore, the SST $k - \omega$ model was selected as the basis of the flow separation calculations under low-flowrate conditions. For this grid independence verification, the shear-stress transport (SST) $k - \omega$ turbulence model was used and the $Q_v - P_{total}$ curves were plotted under different conditions. As shown in **Figure 4A**, as the number of grid cells increases, the calculated total pressure of the fan gradually increases. When the number of grid cells reaches 220,000, this upward trend is no longer obvious. This indicates that the number of grid cells no longer has an impact on the calculation results. Thus, the final number of grid cells was set to 220,000. As shown in **Figure 4B**,

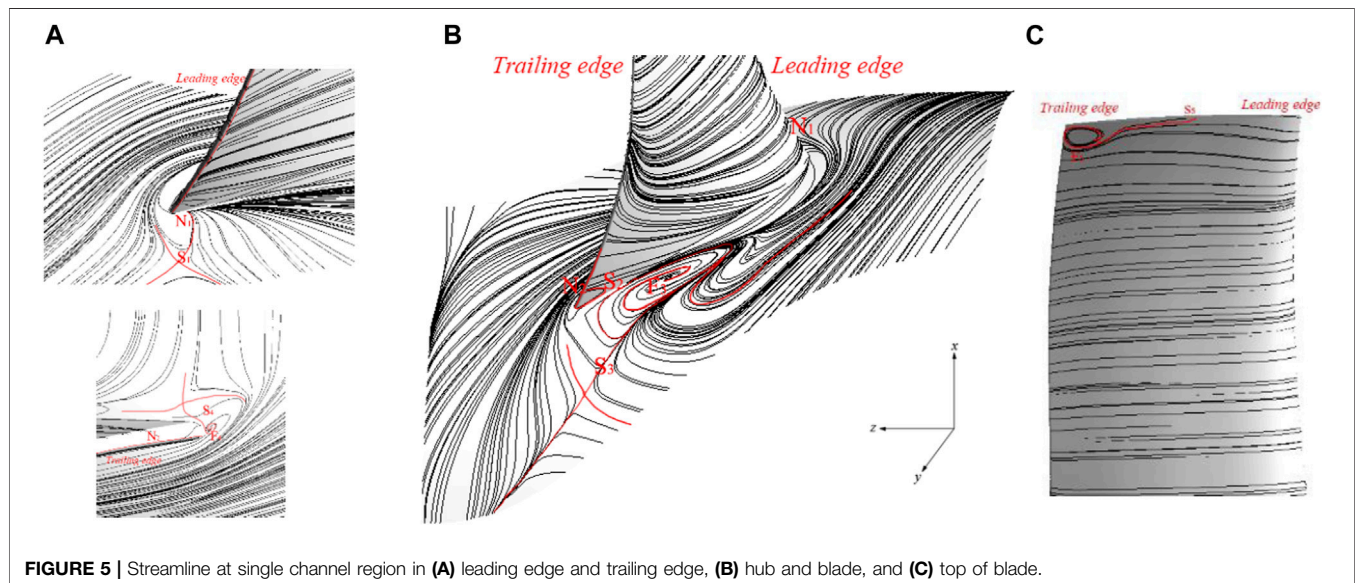
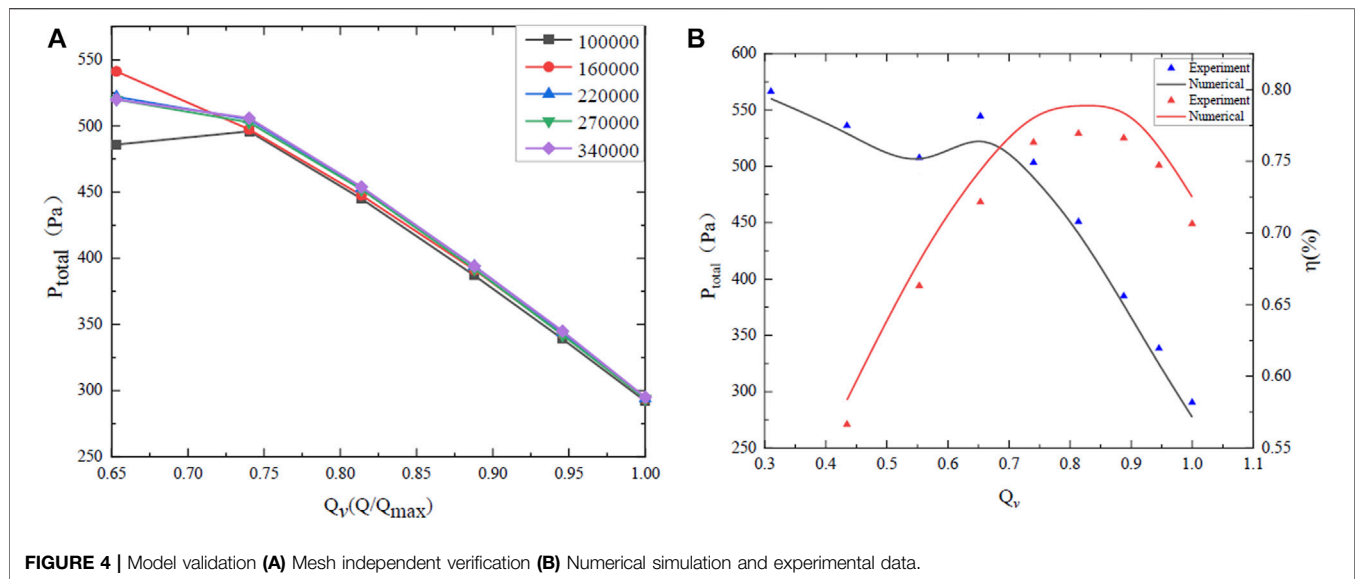
the maximum error between the experimental results and the numerical simulation results is less than 5%, which meets the requirements of model validation.

RESULTS AND ANALYSIS

Topological Analysis of Flow Separation

From **Figure 1**, it can be seen that the singularity type of the phase space diagram formed by the surface streamlines is independent of the time term, but is related to the eigenvalue (p, q) . Therefore, to study the distribution of the phase space diagram formed by the surface streamline equation, the streamline distribution is analyzed at a fixed time. **Figure 5** shows the numerical results for the forward-swept blade with a flowrate of $0.65 Q_v$ at $T = 0.165$ s.

Because of the relative motion between the blade and the flow field, the streamline aligns well with the wall and no flow separation occurs on the pressure surface of the blade. The streamline is significantly deflected by the suction surface of the blade; this is caused by the change of flow direction and the circumferential pressure gradient at the suction surface. According to the separation morphology, the separation starting point lies on the hub and cannot be seen, and closed separation occurs for the passage vortices. The starting point of the separation on the suction surface is a saddle point, and the subsequent separation is a free vortex separation, which is close to



open separation. The flow separates at a position 35% along the chord length and enters the mainstream before forming a vortex downstream; coupling of the hub and wall fluid boundary layers also occurs.

The hydrodynamic system in the rotor is nonlinear due to the unsteady working conditions. Many singularities appear on the hub and suction surface, and these influence the detailed fluid motion. Taking the local single passage in the rotor region as an example, the fluid enters from a large distance and no singularity appears on the separation line at the hub. The first group of singularities (saddle nodes) appears at the leading edge of the blade. There is a large corner separation coupling area between the suction surface and the hub, which affects the suction surface of the blade and the streamline at the hub. On the pressure surface, the streamline begins to shift upward from the middle

position, and saddle point S2 appears. The limit friction line terminates at the trailing edge of the blade, as shown in **Figure 5A**. The starting point of separation in this region is saddle point S2, and the separation terminates at tail edge node N2. As they are affected by the corner separation vortices, the larger separation vortices appear at the position where the suction surface streamline deviates, and the separation vortices form focus point F3 on the streamline at the hub.

The separation eddy line comes from two directions: the streamline near the suction leading edge of the blade and saddle point S3 at the hub on the trailing edge of the blade. During the analysis process, saddle point S4 was only found at the trailing edge of the blade and no matching singularity was found, which is inconsistent with the theoretical analysis. By encrypting the streamlines, a separate focus point F4 was found at the

junction of the pressure surface and suction surface on the trailing edge of the blade. Finally, the separation at the tip of the blade covers the region from the beginning of saddle point S5 in the middle of the blade to the end of focus point F5 near the trailing edge.

According to the principle of topological invariance, separated saddle points and attachment points (S1–N1) appear near the leading edge of the hub in a single passage near the blade. A saddle–node combination (S2–N2) is formed between saddle point S2 on the trailing edge and node N2 on the trailing edge. A saddle point–focus point pairing (S3–F3) occurs in the mainstream of the suction surface, and finally focus point F4 and saddle point S4 (S4–F4) combine near the root of the trailing edge of the blade. A separation saddle point S5 from the tip of the blade connects with focus point F5 at the trailing edge to form a saddle point–focus point pairing (S5–F5). Through analysis of the topological structure, it is found that the numbers of saddle and node pairs are the same in the single passage region, which is in good agreement with the theory of topological invariance.

Singularity Distribution on Forward-Swept Blade

When the limit streamline is a separation line, the distribution and coordination mode of the singularities on the separation line can be obtained by Taylor expansion. The frictional line equations can be expanded based on Taylor's formula at the origin of the object surface:

$$\begin{cases} (\partial u / \partial z) = xg + o^3 \\ (\partial v / \partial z) = xh + f + o^3 \end{cases} \quad (6)$$

$$\begin{cases} g = a_0 + a_1x + a_2y \\ f = b_0 + b_2y + b_3y^2 \\ h = b_1 + b_3x + b_4y \end{cases} \quad (7)$$

$$a_0 = \frac{\partial^2 u}{\partial x \partial z} \quad a_1 = \frac{1}{2} \frac{\partial^3 u}{\partial x^2 \partial z} \quad a_2 = \frac{\partial^3 u}{\partial x \partial y \partial z} \quad (8)$$

$$b_0 = \frac{\partial v}{\partial z} \quad b_1 = \frac{\partial^2 v}{\partial x \partial z} \quad b_2 = \frac{\partial^2 v}{\partial y \partial z} \quad (9)$$

$$b_3 = \frac{\partial^3 v}{\partial x^2 \partial z} \quad b_4 = \frac{\partial^3 v}{\partial x \partial y \partial z} \quad b_5 = \frac{\partial^3 v}{\partial y^2 \partial z}$$

$$\frac{dy}{dx} = \frac{xh + f}{xg} \quad (9)$$

The singularity of the solution to the surface friction line is given by:

$$\begin{cases} x = 0 \\ f = 0 \end{cases}, \quad \begin{cases} g = 0 \\ xh + f = 0 \end{cases} \quad (10)$$

$$\begin{cases} y_1 = C_1 = \frac{-b_2 + \sqrt{b_2^2 - 4b_0b_5}}{2b_5} \\ y_2 = C_2 = \frac{-b_2 - \sqrt{b_2^2 - 4b_0b_5}}{2b_5} \end{cases} \quad (11)$$

In Eq. 10, when $f = 0$, y has different combinations and distributions of solutions. Along the separation streamline, the phase space diagram of the singularities will change with position. By analyzing the changes in the discriminant and solution $C_{1,2}$, the solution distribution and spatial topological structure can be determined, as shown in Figure 6.

As shown in Figure 6A, the separation streamline has two singularities: $(0, C_1)$ and $(0, C_2)$. At this time, $b_5 = (\partial^2 f / \partial y^2) > 0$, $b_2^2 - 4b_0b_5 > 0$. Performing a coordinate transformation on points C_1 and C_2 on the separation streamline (move to the origin, Eq. 12) and substituting into Eq. 2 yields:

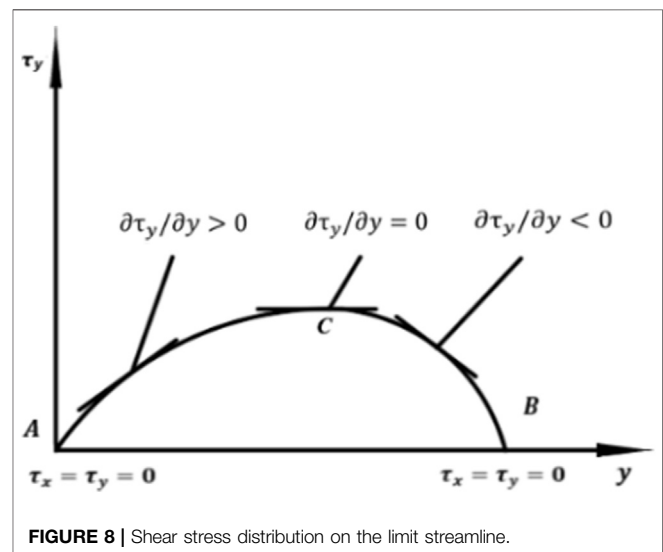
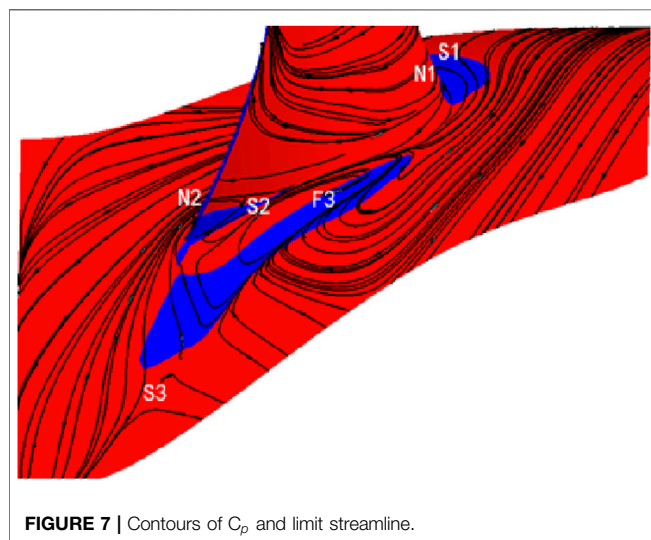
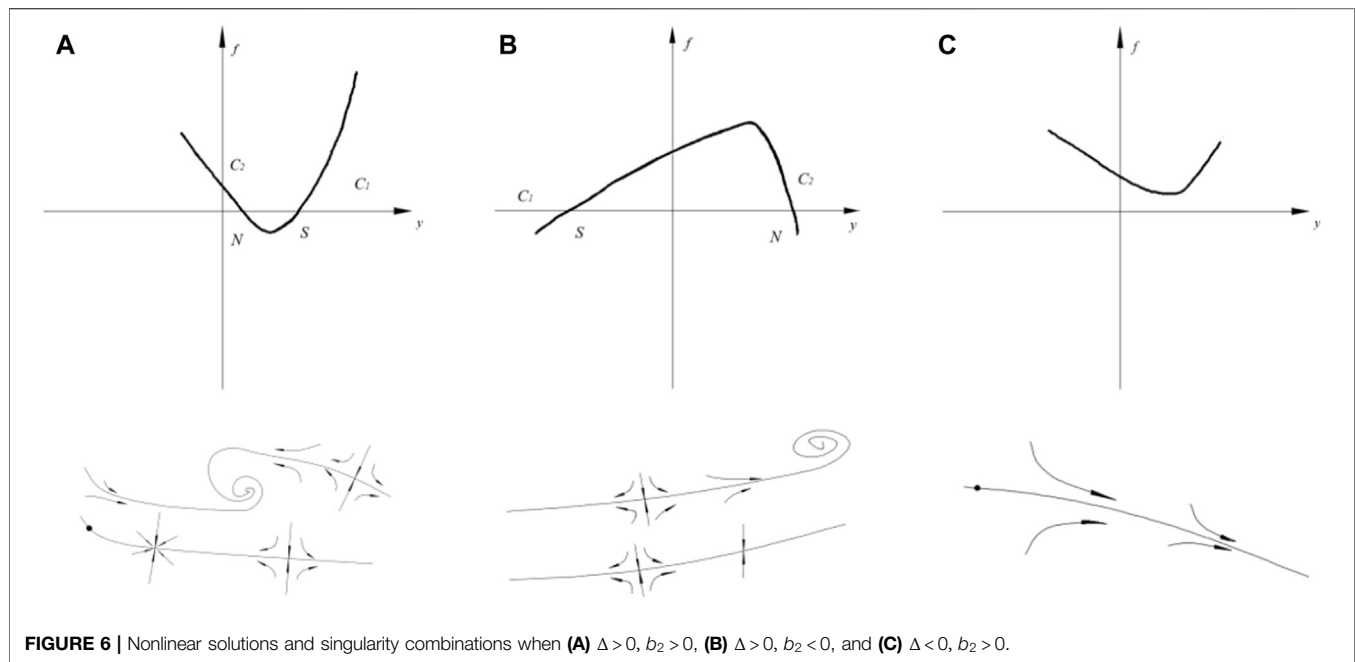
$$\begin{aligned} \zeta &= x \\ \eta_{1,2} &= y - C_1, y - C_2 \end{aligned} \quad (12)$$

$$\begin{aligned} \begin{bmatrix} \dot{\eta}_1 \\ \dot{\zeta} \end{bmatrix} &= \begin{bmatrix} k_{11} & k_{12} \\ k_{21} & 0 \end{bmatrix} \begin{bmatrix} \eta_1 \\ \zeta_1 \end{bmatrix} \\ \begin{bmatrix} \dot{\eta}_2 \\ \dot{\zeta} \end{bmatrix} &= \begin{bmatrix} k'_{11} & k'_{12} \\ k'_{21} & 0 \end{bmatrix} \begin{bmatrix} \eta_2 \\ \zeta_2 \end{bmatrix} \end{aligned} \quad (13)$$

where $k_{11} = b_1 + b_4C_1$, $k'_{11} = b_1 + b_4C_2$, $k_{12} = k'_{12} = b_2$, $k_{21} = a_0 + a_2C_1$, $k'_{21} = a_0 + a_2C_2$. For point C_1 , $k_{21} = a_0 + a_2C_1 < 0$ can be derived from the separation condition. The slope of the curve near point C_1 is greater than 0, so $b_2 > 0$. Substituting this into $q = k_{12} / k_{21} < 0$, it can be inferred that singularity C_1 is a saddle point. Figure 6B can be obtained in the same way. The separation line begins at the saddle point and ends at the node or focus point when $\Delta > 0$, $b_2 < 0$. When the equation has a featureless solution, the separation appears as a featureless critical situation. Figure 6C represents the normal limit friction line when $\Delta < 0$, $b_2 > 0$.

Flow separation occurs because the boundary layer leaves the blade and enters the mainstream, finally forming a free vortex surface. During the formation and development process, there is a change in the eigenvalues on the suction surface of the blade and hub due to, for example, changes in the wall reverse velocity gradient and the wall separation point. Figure 7 shows the topological structure and reverse flow (blue area) on the hub and blade surface at $0.65 Q_v$. The first and second groups of singularities start from a saddle point and end at a node point, which is consistent with the combination form of the singularity in Figure 6B. Combined with Figure 7, it can be seen that saddle points S1 and S2 flow from the blue area to the red area, which means that $\partial w / \partial x$ increases at the saddle point position along the streamline direction, and the saddle point is C_1 in Figure 6B. In the same way, we can determine that the node is C_2 . The third and fourth groups of singular points start from the focus point and move to the saddle point, and the matching mode is consistent with the singularity combination mode in Figure 6A. Combined with Figure 7, it can be observed that the area near point F3 changes from blue to red along the streamline direction—the focus point is C_2 in Figure 6A and the saddle point is C_1 .

Generally, the separation line is composed of a saddle point and the focus node. The location and type of the singularity can be quickly defined by the velocity gradient and streamline on the surface, as shown in Figure 8. There are three kinds of $\partial \tau / \partial y$ values on the separation line: when the limit streamline has an adverse velocity gradient, the sign of $\partial \tau / \partial y$ changes. Combining

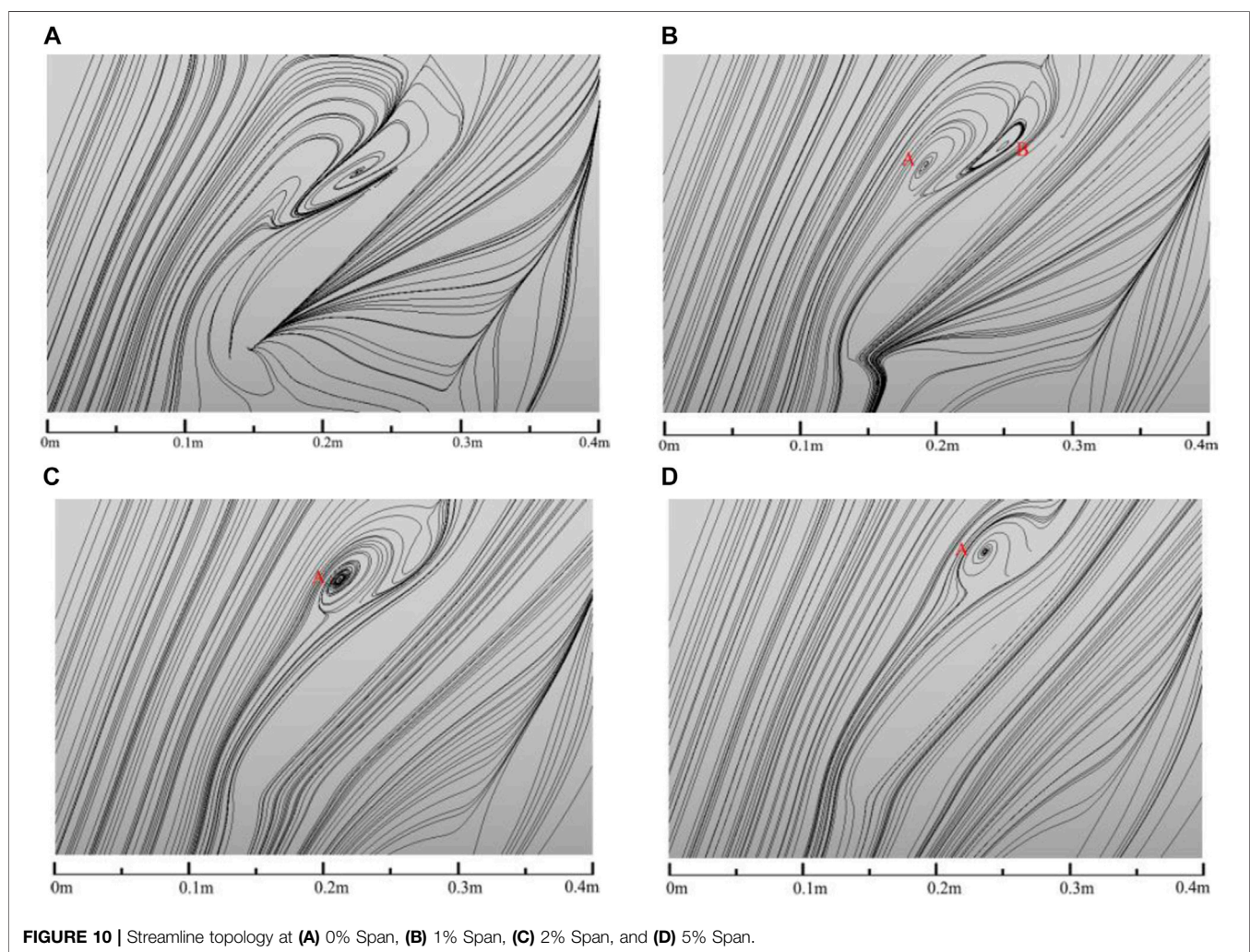
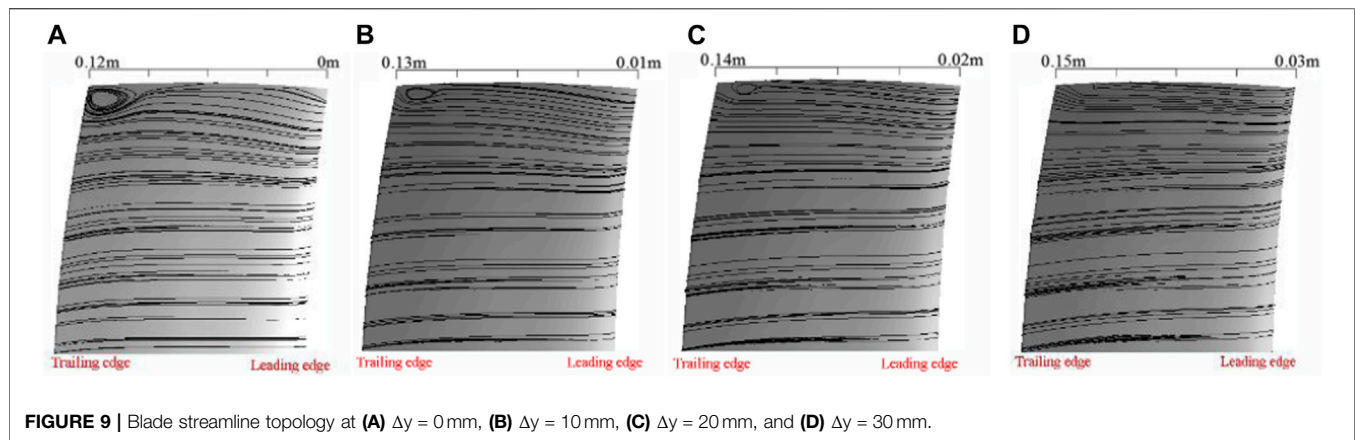


the types of separation points on the hub and suction surfaces with **Figure 7**, we find that the appearance of a reversed velocity gradient on the blade surface indicates the appearance of the singularity. Whether the fluid flows from A to B or from B to A, $\partial\tau/\partial y > 0$ indicates the saddle point and $\partial\tau/\partial y < 0$ indicates the node point. Therefore, the eigenvalues $\partial\tau/\partial y$ represent the characteristics in the fluid flow.

Spatial Evolution of Separation Vortex Structure

In the steady state, the streamline coincides with the path line. The structure and shape of the separation vortices can gradually

be revealed by taking successive cross-sections. Firstly, different planes are selected along the blade height, and the three-dimensional flow field information is obtained by plotting the streamline topology intercepted by each plane. When using the cross-section streamline method to analyze vortex structures away from the wall, the selected surface should be parallel to the surface of study. This paper selects the suction surface and performs a radial translation Δy [the y direction is given in **Figure 5B**]. The translated surface is input to CFD-Post to observe the surface streamlines. By comparing the dissipation process of the vortex on the hub and the vortex on the tip of the blade, it can be seen that the process of vortex dissipation at the tip of the blade is not accompanied by the rupturing of the vortex,



as shown in **Figure 9**. Note that the dissipation process of the vortex occurs along the mainstream direction.

The separation vortex structure on the hub surface can be analyzed by the same method (see **Figure 10**). On the plane at

the hub (0% Span), there is only one shedding vortex at the suction surface, and its core position is 0.23 m away from the fan rotor entrance. With an increase in height (1% Span), two separated vortices grow in the region, located 0.18 and 0.25 m

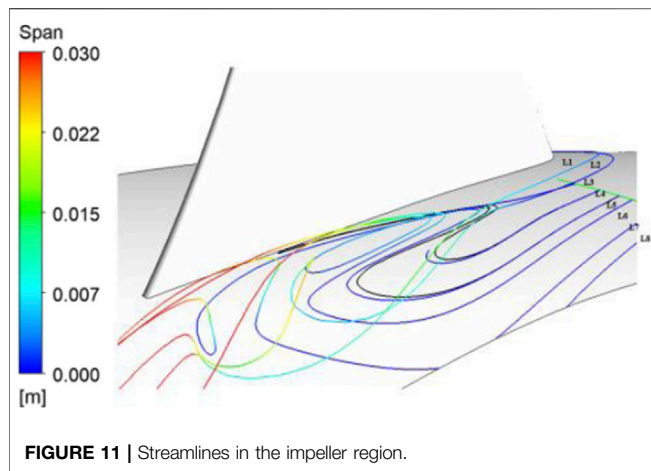


FIGURE 11 | Streamlines in the impeller region.

away from the rotor inlet of the fan. When the height reaches 2% Span, the shedding vortices at point B near the suction surface gradually shrink and diffuse into the mainstream. The core of the shedding vortices is at point A, 0.21 m from the rotor inlet, and finally appears at 5% Span; here, the shedding vortices at point B are completely annihilated in the mainstream, leaving only the shedding vortices at point A. The eddy is 0.24 m away from the fan entrance.

Figure 11 shows the streamlines in the impeller region at $0.625Q_v$. The black part is the streamline on the hub surface and the colored part is the three-dimensional streamline. Two vortices can be observed in the passage through the three-dimensional streamline, in which lines 1 and 2 come from the leading edge and lines 3–8 come from the hub surface. According to Figure 5, lines 1 and 2 are the extensions of a leading-edge horseshoe vortex, which leaves the hub surface near the leading edge and enters the region; lines 3–8 originate from the hub surface and leave the wall at the focus point to form a separation vortex.

According to Figures 10, 11, the shedding vortices formed on the hub surface disappear with the mainstream, and the positions of the vortex cores in different sections move along the streamline continuously. The shedding vortices break up and diffuse into the mainstream until they dissipate completely. As the flowrate decreases, the influence of the mainstream on the structure of the vortex gradually weakens, and the velocity and location of the vortex breakdown on the hub wall changes, as shown in Figure 12.

Variation of Separated Vortex Structure With Flow Rate

The topological structure of the rotor is not invariant under changes in flowrate, as shown in Figure 13. When the flowrate is $1 Q_v$, there are only two groups of singularities in the region (red line). When the flowrate decreases to $0.8 Q_v$, singularity F3–S3 grows on the hub and S2–N2 appears on the suction surface. When the flowrate is further reduced to $0.625 Q_v$, separation begins at the blade tip and a new singularity S5–F5

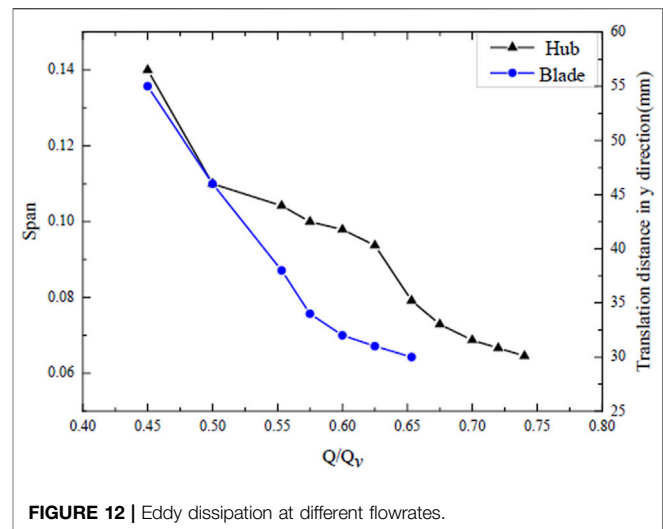


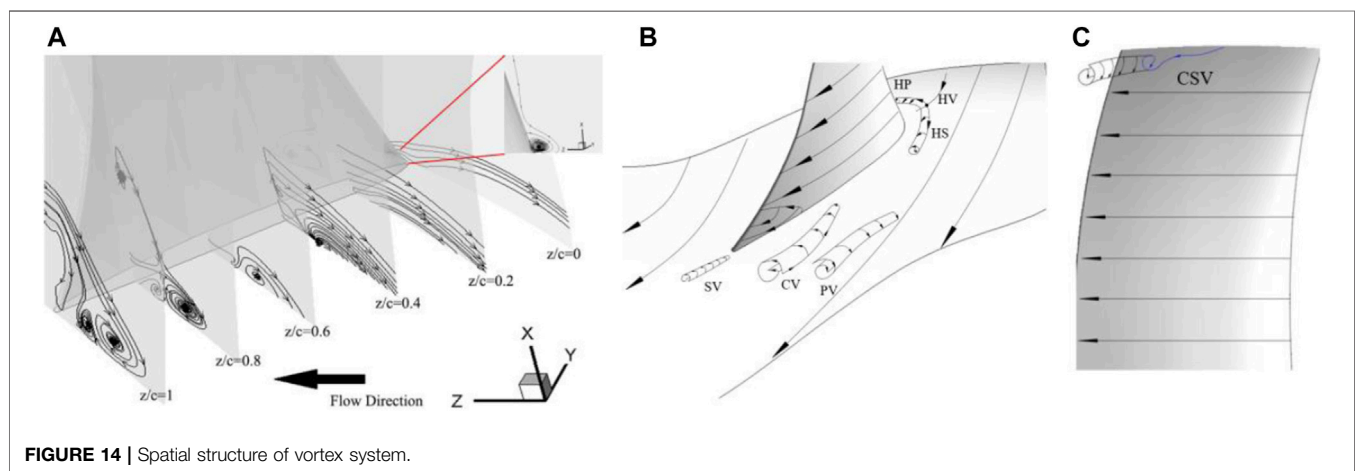
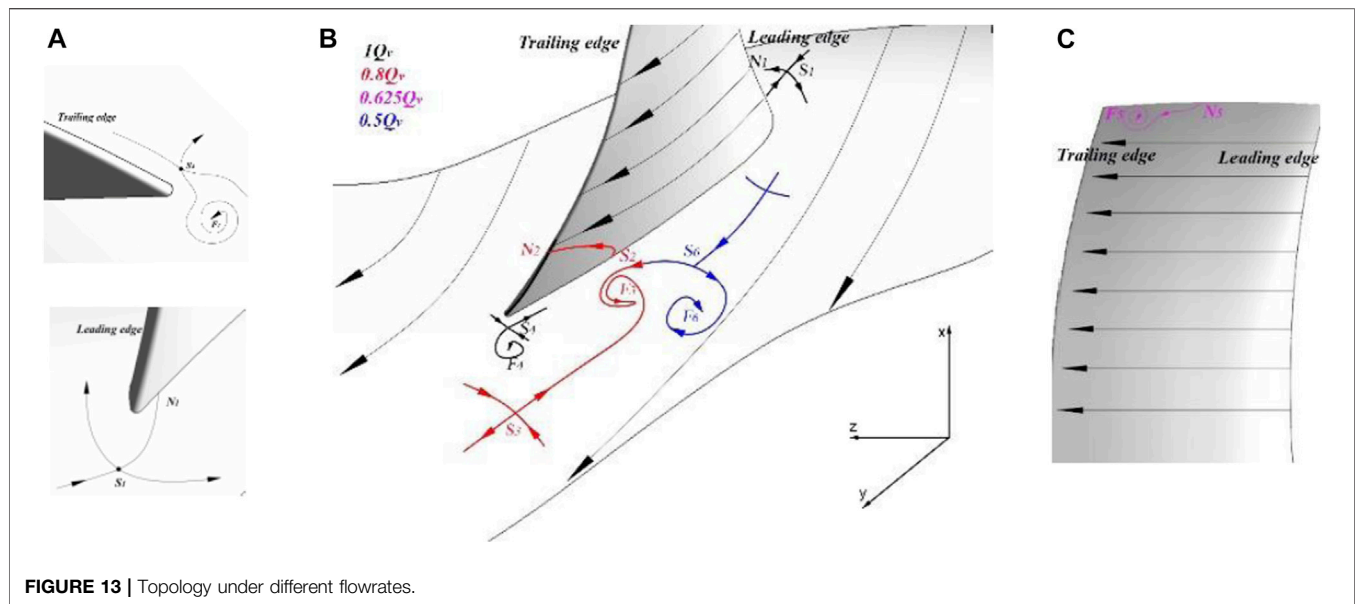
FIGURE 12 | Eddy dissipation at different flowrates.

appears. When the flowrate is $0.5 Q_v$, a new singularity S6–F6 appears on the hub.

The passage vortex structure can be inferred from the topological structure and cross-section flow pattern distribution, combined with the spatial streamline distribution, as shown in Figure 14B. Along the flow direction, the fluid forms a horseshoe vortex (HV) near the leading edge. According to Figure 9B, the horseshoe vortex is separated into two parts by the leading edge. The bifurcation of the passage vortex on the pressure surface (HP) rotates clockwise [as shown in Figure 14A, $Z/C = 0$], and finally converges with the passage vortex to form a single structure. Through local magnification, it can be observed that there is a counterclockwise-rotating vortex near the suction surface of the leading edge, which is the bifurcation of the passage vortex on the suction surface (HS). The passage vortex (PV) rotates clockwise and gradually approaches the suction surface as the flowrate decreases. In the vicinity of the suction surface, the corner vortex (CV) formed by the counter current in the region rotates counterclockwise. The shedding vortex (SV) near the trailing edge is caused by the pressure difference when the pressure surface meets the suction surface fluid. The direction of motion is from the pressure surface to the suction surface, and the rotation direction is counterclockwise. A clockwise-rotating concentrated shedding vortex (CSV) is formed by the boundary layer movement in the corner of the suction surface of the blade top.

CONCLUSION

- (1) The combinations of different singularities were obtained through a qualitative analysis of the limit friction line on the wall. The method accurately obtains the wake vortices formed by the convergence of the suction surface and pressure surface fluid at the trailing edge of the blade. The



flow on the forward-swept blade also follows the principle of topological invariance. The single blade and its adjacent flow passage can be regarded as a closed region. When there is no tip clearance, the Euler characteristic is 0. Through this method, five saddle points, two nodes, and three focus points were found by analyzing the singularities near the runner and the blade.

- (2) By taking the Taylor expansion of the governing equation of the limit streamline, the distribution of singular points along the separation line was obtained. Because the change in $f \approx \partial v / \partial z + \sigma^2$ along the y -axis is continuous, there are multiple intersections between f and the y -axis, and the slope $\partial \tau / \partial y$ at the adjacent intersection points must be positive and negative, which leads to changes between saddle points and nodes. When $\partial \tau / \partial y > 0$, a saddle point occurs, and

when $\partial \tau / \partial y < 0$, a node point occurs. In fluid flow, a change in sign represents the appearance of a countercurrent region. This type of singularity can be obtained by analyzing the intersection point of the countercurrent contour and the limit streamline.

- (3) The dynamical state of separation vortices on the hub was analyzed using cross-section streamline analysis. As the height increases, the separation vortices break up and are annihilated, and the position of the vortex core moves along the streamline. Changes in flowrate also affect the suction boundary.
- (4) With decreasing flowrate, the number of groups of singularities in the region increases, and the combinations of singularities are more abundant. In addition, the section flow pattern method can be used to infer the vortex structure and rotation direction. Numerical simulations show that larger PV and CV are

produced, while the CSV and HV are smaller. The HP, PV, and CSV were found to rotate clockwise, whereas the HS, CV, and SV rotate in a counterclockwise direction.

DATA AVAILABILITY STATEMENT

The original contributions presented in the study are included in the article/Supplementary Material, further inquiries can be directed to the corresponding authors.

REFERENCES

- Cao, L. (2019). Analysis on Flow Separation Characteristics of Last Stage Blade in Steam Turbine under Small Volume Flow Condition. *Therm. Sci.* 23, 25. doi:10.2298/tsci180904025c
- Chen, L., Liu, X. J., Yang, A. L., and Dai, R. (2013). Flow Performance of Highly Loaded Axial Fan with Bowed Rotor Blades. *IOP Conf. Ser. Mater. Sci. Eng.* 52, 042005. doi:10.1088/1757-899x/52/4/042005
- Dród, A. (2021). Effect of Reynolds Number on Turbulent Boundary Layer Approaching Separation. *Exp. Therm. Fluid Sci. (EXP THERM FLUID SCI)* 125, 110377. doi:10.1016/j.expthermflusci.2021.110377
- Filippov, G. A., and Wang, Z. Q. (1962). The Calculation of Axial Symmetric Flow in a Turbine Stage with Small Ratios of Diameter to Blade Length. *Teplenergetika* 8, 42.
- Gbadebo, S. A., Cumpsty, N. A., and Hynes, T. P. (2005). Three-dimensional Separations in Axial Compressors. *J. Turbomach.-Trans. ASME* 127, 331–339. doi:10.1115/1.1811093
- He, C., Ma, Y. F., Liu, X. H., Sun, D. K., and Sun, X. F. (2018). Aerodynamic Instabilities of Swept Airfoil Design in Transonic Axial-Flow Compressors. *AIAA J.* 56, 1. doi:10.2514/1.j056053
- Jongwook, J., Medic, G., and Sharma, O. (2016). "Large-eddy Simulation Investigation of Impact of Roughness on Flow in a Low-Pressure Turbine," ASME Turbo Expo. Turbomachinery Technical Conference & Exposition.
- Karyakin, O. M., Nalivaiko, A. G., Ustinov, M. V., and Flaxman, J. S. (2018). Separation Control on the wing by Jet Actuators. *AIP Conf. Proc.* 1959, 050014.
- Kaya, M. N., Kose, F., Ingham, D., Ma, L., and Pourkashanian, M. (2018). Aerodynamic Performance of a Horizontal axis Wind Turbine with Forward and Backward Swept Blades. *J. Wind Eng. Ind. Aerodynamics* 176, 166–173. doi:10.1016/j.jweia.2018.03.023
- Lighthill, M. J. (1963). "Attachment and Separation in Three-Dimensional Flows," in *Laminar Boundary Layers*. Editor L. Rosenhead (Oxford, UK: Oxford Univ. Press), 72–82.
- Luo, D., Huang, D., Sun, X., Chen, X., and Zheng, Z. (2017). A Computational Study on the Performance Improvement of Low-Speed Axial Flow Fans with Microplates. *Jafm* 10, 1537–1546. doi:10.29252/jafm.73.245.27492
- Maskell, E. C. (1955). "Flow Separation in Three Dimensions," Royal Aircraft Establishment. Report No.: Aero 2565.
- Mohammed, K. P., and Raj, D. P. (1977). Investigations on Axial Flow Fan Impellers with Forward Swept Blades. *ASME J. Fluid Eng.* 99, 543–547. doi:10.1115/1.3448839
- Pogorelov, A., Meinke, M., and Schröder, W. (2016). Effects of Tip-gap Width on the Flow Field in an Axial Fan. *Int. J. Heat Fluid Flow* 61, 466–481. doi:10.1016/j.ijheatfluidflow.2016.06.009
- Surana, A., Grunberg, O., and Haller, G. (2006). Exact Theory of Three-Dimensional Flow Separation. Part 1. Steady Separation. *J. Fluid Mech.* 564, 57. doi:10.1017/s0022112006001200
- Vad, J., Halász, G., and Benedek, T. (2015). Efficiency Gain of Low-Speed Axial Flow Rotors Due to Forward Sweep. *Proc. Inst. Mech. Eng. A: J. Power Eng.* 229, 16–23. doi:10.1177/0957650914552817
- Wang, Z. Q., Lai, S. K., and Xu, W. Y. (1981). "Aerodynamic Calculation of Turbine Stator Cascades with Curvilinear Leaned Blades and Some Experimental Results". Proceedings of the 5th ISABE. Bangalore
- Wang, Z. Q. (1999). *Three-dimensional Theory and Design Method of Bowed Twisted Blade and its Application to Turbomachines*. van Karman Institute for Fluid Dynamics, Vol. 2, D1–D41.
- Wennerstrom, A. J. (1990). Highly Loaded Axial Flow Compressors: History and Current Developments. *J. Turbomach.* 112, 567–578. doi:10.1115/1.2927695
- Wennerstrom, A. J., and Puterbaugh, S. L. (1984). A Three-Dimensional Model for the Prediction of Shock Losses in Compressor Blade Rows. *J. Eng. Gas Turbine Power* 106, 295–299. doi:10.1115/1.3239562
- Ye, Z., Zhao, H. Y., Yang, Y., Li, C., and Gao, W. (2013). Effect of Inlet Preshirl on Flow Field of Axial Flow Fan. *Amr* 732–733, 571–576. doi:10.4028/www.scientific.net/amr.732-733.571
- Zhang, H., Wang, S., and Wang, Z. (2007). Variation of Vortex Structure in a Compressor cascade at Different Incidences. *J. Propulsion Power* 23, 221–226. doi:10.2514/1.17245
- Zhang, H. X. (1994). Bifurcation of Vortex Motion along its axis. *Acta Aerodynamica Sinica* 3, 243, 1994. (in Chinese).
- Zhang, H. X. (1997). Crossflow Topology of Three-Dimensional Separated Flows and Vortex Motion. *Acta Aerodynamica Sinica* 1, 1, 1997. (in Chinese).
- Zhang, H. X., and Deng, X. (1992). Analytic Studies for Three-Dimensional Steady Separated Flows and Vortex Motion. *Acta Aerodynamica Sinica* 1, 8, 1992. (in Chinese).
- Zhang, Z. Y., Zhang, W. L., Chen, Z. H., Sun, X. H., and Xia, C. C. (2018). "Suction Control of Flow Separation of a Low-Aspect-Ratio wing at a Low Reynolds Number," *Fluid. Dyn. Res.* 50, 065504.

AUTHOR CONTRIBUTIONS

YL and ZZ provided experimental ideas and theoretical guidance. PW and SD provided language guidance and writing guidance.

FUNDING

This work was supported by the National Natural Science Foundation of China (Grant No. 51776217) and the China Scholarship Council (Grant No. 201806425052).

Conflict of Interest: The authors declare that the research was conducted in the absence of any commercial or financial relationships that could be construed as a potential conflict of interest.

Copyright © 2021 Liang, Li, Zhou, Wiśniewski and Dykas. This is an open-access article distributed under the terms of the Creative Commons Attribution License (CC BY). The use, distribution or reproduction in other forums is permitted, provided the original author(s) and the copyright owner(s) are credited and that the original publication in this journal is cited, in accordance with accepted academic practice. No use, distribution or reproduction is permitted which does not comply with these terms.



Study on Dispersion of Carbon Dioxide over the Shrubbery Region

Wang Huiru, You Zhanping*, Mo Fan, Liu Bin and Han Peng

School of Mechanical Engineering, Shijiazhuang Tiedao University, Shijiazhuang, China

OPEN ACCESS

Edited by:

Lin Teng,
Fuzhou University, China

Reviewed by:

Xiaolu Guo,
Hefei General Machinery Research
Institute Co., Ltd., China
Junlei Wang,
Zhengzhou University, China
Jiajia Deng,
Zhejiang Ocean University, China

*Correspondence:

You Zhanping
youzhanping@stdu.edu.cn

Specialty section:

This article was submitted to
Advanced Clean Fuel Technologies,
a section of the journal
Frontiers in Energy Research

Received: 14 April 2021

Accepted: 12 May 2021

Published: 14 June 2021

Citation:

Huiru W, Zhanping Y, Fan M, Bin L and
Peng H (2021) Study on Dispersion of
Carbon Dioxide over the
Shrubbery Region.
Front. Energy Res. 9:695224.
doi: 10.3389/fenrg.2021.695224

In the carbon capture and storage (CCS) infrastructure, the risk of a high-pressure buried pipeline rupture possibly leads to catastrophic accidents due to the release of tremendous amounts of carbon dioxide (CO₂). Therefore, a comprehensive understanding of the effects of CO₂ dispersion pattern after release from CCS facilities is essential to allow the appropriate safety precautions to be taken. Due to variations in topography above the pipeline, the pattern of CO₂ dispersion tends to be affected by the real terrain features, such as trees and hills. However, in most previous studies, the dynamic impact of trees on the wind field was often approximated to linear treatment or even ignored. In this article, a computational fluid dynamics (CFD) model was proposed to predict CO₂ dispersion over shrubbery areas. The shrubs were regarded as a kind of porous media, and the model was validated against the results from experiment. It was found that shrubbery affected the flow field near the ground, enhancing the lateral dispersion of CO₂. Compared with that of the shrub-free terrain, the coverage area of the three shrub terrains at 60 s increased by 8.1 times, 6.7 times, and 9.1 times, respectively. The influence of shrub height and porosity on CO₂ dispersion is nonlinear. This research provides reliable data for the risk assessment of CCS.

Keywords: carbon capture and storage, computational fluid dynamics modeling, porous medium, CO₂ pipeline, shrubbery areas

HIGHLIGHTS

CFD model of heavy gas dispersion considers shrubs under
Sensitive analysis on arrangement of shrubs on heavy gas dispersion
Influence of shrub height and porosity on CO₂ gas concentration is nonlinear

INTRODUCTION

Burning fossil fuels leads to the enormous amounts of emission of carbon dioxide (CO₂), which increases the concentration of CO₂ in the atmosphere inevitably and contributes to the “greenhouse effect” (Peters et al., 2013). Worldwide, due to continuous industrial development, fossil fuels are still in high demand (IEA 2018) in the foreseeable future; therefore, substantial attention has been paid to technologies that may reduce excessive concentrations of CO₂ in the atmosphere, and several technical methodologies need to be implemented. It is widely accepted that the deployment of carbon capture and storage (CCS) is one of the most promising and feasible methodologies for reducing artificial CO₂ emissions (Metz et al., 2005). CCS involves capturing CO₂ emitted by large-scale anthropogenic CO₂ sources (e.g., fossil fuel power plants) and transporting it to an isolated geological formation for storage, instead of being discharged into the atmosphere (Liu et al., 2015).

Furthermore, the renewable energy industry is developing rapidly currently; however, if no effective treatment is carried out correspondingly such as CCS, the final carbon emission in numerous new energy production processes may even exceed that of fossil fuel (hydrogen production from natural gas, etc.). Pressurized pipeline application constitutes a part of the CCS chain, which is regarded as the most practical and economical land transportation methodology for the subsequent storage of large amounts of CO₂ collected from CO₂ source such as coal-fired power plants. The delivery pressure of this type of pipeline usually ranges between 10 and 20 MPa and their length can be up to hundreds of kilometers.

However, CCS technology remains at the developing stage, and the safety issue is of paramount significance. Corrosion, material defects, operator errors, and earthquakes may affect the safety of CO₂ transportation pipelines, causing inevitable rupture and leakage (Gale and Davison 2004). Notably, CO₂ is heavier than air; thus, it is more likely to sink and accumulate in low-lying areas when the transport pipeline is broken, making its spread challenging. Also, CO₂ is an asphyxiant gas, and at high concentrations, excessive CO₂ inhalation may result in coma or even death for humans and animals, which poses a substantial danger to nearby organisms (Mazzoldi et al., 2008). In addition, the features of colorless and not flammable may bring about CO₂ leakage difficult to detect. Therefore, in order to protect humans and animals from the possible harmful effects caused by pipeline accidents, it is necessary to leave a sufficient safety distance between densely populated areas and high-pressure CO₂ pipelines (Lipponen et al., 2011; Liu et al., 2012). To predict such distance, it is necessary to develop a reliable CO₂ dispersion model after the event of accidental release.

Over the past few decades, various atmospheric dispersion models have been performed, such as Accident Damage Analysis Module (ADAM) (Fabbri et al., 2017; Fabbri and Wood 2019; Fabbri et al., 2020), ALOHA (NOAA/EPA 1992) [based on DEGADIS (Havens and Spicer 1990)], DRIFT (Gant et al., 2018; Gant et al., 2021), the ESCAPE model (Expert System for Consequence Analysis and Preparing for Emergencies) (Kukkonen et al., 2017), and the HPAC/SCIPUFF (Hazard Protection Assessment Capability/Second-Order Closure Puff) (Simpson et al., 2020). With improved computational resource availability, the computational fluid dynamics (CFD) models have gradually become the most popular model.

CFD models are based on the conservation principle of the Reynolds-averaged Navier–Stokes (RANS) equation to carry out complex mathematical descriptions, thus allowing the integration of complex geometrical or physical and chemical phenomena. They enabled to be established to solve the three-dimensional space and time of fluid mechanics equations and therefore can accurately and in detail describe the complex geometrical shape of the flow (Ahmed et al., 2016; Liu et al., 2016; Efthimiou et al., 2017; Liu et al., 2017) and is increasingly used in the study of hazardous gas dispersion over the complex terrain (Sklavounos and Rigas 2006; Luketa-Hanlin et al., 2007; Gavelli et al., 2008; Tauseef et al., 2011; Hsieh et al., 2013; Tan et al., 2018).

Typically, dispersion patterns over an isolated obstacle or a group of obstacles have been studied comprehensively conducted

by CFD modeling (Tominaga and Stathopoulos 2010; Takano and Moonen 2013; Kumar et al., 2015; Stabile et al., 2015; Bijad et al., 2016; Liu et al., 2016; Wingstedt et al., 2017; Liu J. et al., 2019; Ding et al., 2020; Ryan and Ripley 2020; Wang J. et al., 2021). These studies were usually designed to validate the performance of CFD in simulating the dispersion of pollutants around the obstacle/obstacles. In such terrains, pollutants may be trapped in the street “canyons” formed by buildings (obstacles) and also in the “wake” of buildings. The effects of pollutant transport models and inflow conditions, canyon structure and building size, were studied. Since the objective of the gas dispersion model is to predict the time-varying dispersion of pollutants in the real environment, it becomes necessary to consider geometrical variations within the area of interest because the wind field is inherently associating to the layout of buildings. Meroney (2010) used the CFD code ANSYS Fluent to simulate the dispersion of CO₂ in an urban environment with single or multiple building obstacles. Their study showed that a heavy gas cloud collapsed toward the ground rapidly and spread radially. Then, the cloud clusters were stratified due to the difference in density and preserved a pancake or flat appearance for a long-distance downwind. However, when the cloud was blocked by obstacles, the stratification was weakened and vertical movement was allowed. In the wake of a single obstacle or an array of buildings and owing to the low wind speed between the buildings, high concentrations of gas may continue to exist, delaying the dispersion time. Liu et al. (2016) developed a CFD model to study CO₂ dispersion over two types of terrain. It was found that the CFD model was able to produce relatively accurate concentration estimations. Also, terrain features and weather conditions had a great impact on the character of CO₂ dispersion. Hsieh et al. (2013) established a CFD model for dense gas dispersion based on the RANS method and analyzed the influence of buildings and complex terrain on the dispersion pattern. Based on the Boussinesq method, they derived the buoyancy term. This model can be used to provide the information needed for quantitative evaluation of the potential risks to the public caused by accidental or malicious release of CO₂ from CCS-related infrastructure.

From a modeling capability perspective, CFD models can simulate complex physical processes, such as heat and mass transfer, in a complex three-dimensional (3D) calculation domain. Moreover, CFD models allow the calculation of variable physical properties of the fluid, turbulence modeling, chemical reactions, creation of accurate descriptions of turbulent mixing, 3D plumes, and the geometric flow field required to disperse fluids. However, numerous previous CFD investigations have proven that the description of the turbulence model has a great influence on the predicted precision in reproducing heavy gas dispersion. This is especially true for real complex terrain. Thus, it is particularly important to select an appropriate turbulence model. Toja-Silva et al. (2017) compared differential column measurements (Chen et al., 2016) with CFD simulation. They used the RANS turbulence model based on the open-source CFD software package OpenFOAM. The accuracy of the model was validated by the comparison between the CO₂ prediction of column-averaged dry-air mole fraction

(XCO_2) and the experimental measurement results. Different turbulent Schmidt numbers were compared, and $\text{Sc}_t = 0.6$ was identified as the most adequate for being used in CFD simulations of CO_2 emissions from power plants in urban areas.

In recent years, a remarkable number of efforts have been implemented to improve the ecological environment and reduce the soil losses caused by floods using afforestation and the restoration of forest vegetation. Therefore, city suburbs now usually cover not only natural vegetation but also newly planted trees. The behavior of flows over or through tree areas has become a hot area of research in numerous fields. In what relates to the influence of plant canopies on atmospheric wind environment, the analysis has been carried out. Trees are known to reduce temperature, increase humidity, prevent wind and dust, cause particle deposition (Vos et al., 2013; Jeanjean et al., 2017; Buccolieri et al., 2018), as well as resuspension (Nowak et al., 2013; Hong et al., 2018), canopy transpiration (Hagishima et al., 2007), and create shadow effects (Sabatino et al., 2015). They also reduce energy consumption and alleviate air pollution notably (Gallagher et al., 2015; Gromke et al., 2016; Li et al., 2016). The deposition of particulate matter on plant surfaces helps remove pollutants from the atmosphere, reducing their concentration. However, trees themselves act as porous obstacles to reduce wind speed, airflow, decrease air exchange, and probably lead to higher pollutant concentrations primarily due to pressure and viscous drag forces. In the foundation of the understanding of the flow within and around trees, there was an extensive numerical CFD study on the effects of vegetation on the atmospheric wind environment, which were often carried out using large eddy simulation (LES) and RANS methods. Such CFD methods ensured a true representation of flow dynamics in complex environments (e.g., urban canopies covered by vegetation) and produced high-resolution flow fields. Buccolieri et al. (2009) studied the aerodynamic effects of tree-lined greening on the flow field in urban streets and canyons, through wind tunnel tests and numerical simulations. In addition, they analyzed the dispersion process of traffic source pollutants. The CFD code ANSYS Fluent was employed to achieve a 3D numerical simulation for the flow and dispersion of traffic exhaust gas in a tree-planted city street canyon with a width to building height aspect ratio of 2. It was deduced that street trees have a notable impact on pollutant concentrations in street canyons. Moonen et al. (2013) conducted CFD simulations with the LES model to quantitatively predict pollutant dispersion potential. The model performed better in predicting a leeward canyon than in a windward wall, and the system performance near the end of the street canyon was better than that in the center of the street canyon. The presence and density of trees in the street canyon hardly systematically affect the overall model performance. This model confirmed the applicability of the COST (COST Action 732, 2007a; COST Action 732, 2007b; COST Action 732, 2007c; COST Action 732, 2010) recommendation and supported the premise that it is necessary to combine qualitative and quantitative techniques to assess the applicability of a specific model for a specific purpose. Hefny Salim et al. (2015) employed three different methods to simplify the role of urban trees in the numerical simulation of wind

fields, emphasizing the impacts of trees on pollutant dispersion, air quality assessment, and wind environment comfort research. Compared with the case without trees on the streets, the results obtained by the explicit porous medium method demonstrated that trees reduced the wind speed in the street canyon. Barbano et al. (2020) used a simplified CFD tool (QUIC) to simulate and evaluate the average wind and turbulence fields of a vegetated urban neighborhood. By comparing the simulation results with and without trees, they found that trees could reduce airflow by restricting local circulation and reducing the intensity of turbulence. The results showed that the blocking effect of trees was dominant in both the average and turbulent flow fields. Both types of flow fields were sensitive to the density of obstacles (e.g., buildings and trees). Weakly unstable conditions and thermal stratification reduce the quality of the simulation results, not allowing the QUIC model to account for local airflow changes produced exclusively by trees; however, the model can capture the feature of near-neutral conditions and vertical wind directions well.

Shrubs are short woody plants with multiple trunks and are indispensable in many ecosystems. Shrubs tend to distribute more widely than trees (Myers-Smith et al., 2015). Although both trees and shrubs may exist in forest landscapes, most studies focus on tree species and their response to weather change (Morales et al., 2012; Götzmark et al., 2016). Previous studies have shown that shrubs have been more sensitive to weather change than trees (Morales et al., 2012; Pellizzari et al., 2017). The flow patterns through or around the shrubs are complicated by the presence of bleed flows and displaced flows. Dong et al. (2008) measured and analyzed the flow field around shrubs with different densities in the wind tunnel. The results showed that porosity was an important factor affecting the flow field structure around shrubs. When the density of the shrub was less than the critical density of 0.08, the airflow through the shrub was obviously strengthened, while the updraft on the windward side rapidly weakens, and the seepage flow was dominant; when the value of the shrub density was equal to or exceeded the critical density, the updraft was formed on the windward side and a large vortex structure rotating clockwise appears on the leeward side. Wu et al. (2015) simulated the flow field around the shrub windbreaks in the wind tunnel. The results show that the average velocity field around the shrub can be divided into the front deceleration zone, the upper acceleration zone, the rear vortex zone, and the recovery zone downwind of the vortex zone. The protection effect of shrub windbreak varied with the change of wind speed and was affected by its structure. The shrub windbreaks with more complex layout can reduce wind speed more effectively, extend sheltering distances, and have better protective effects than simple shrub windbreaks. However, there have been few studies linking the arrangement of shrubs and their impact on heavy gas dispersion patterns to date. To quantify the risks of heavy gas dispersion, it is essential to construct heavy gas dispersion models that consider the effects of shrubs on complex terrain.

The primary purpose of this study is to evaluate the influence of complex shrubland topography on the CO_2 dispersion characteristics. The CFD model was carried out to simulate CO_2 dispersion over shrubland, and shrubs were

regarded as porous media. Based on previous research, the correctness of the CFD model presented herein was verified by comparing its prediction with a full-scale blasting test data and the experimental measurement data of trees (Japan Architectural Society). The rest of this article is organized as follows: *Numerical Methods* introduces the numerical methods; *Computational Fluid Dynamics Model* explains the CFD model construction and model validation; and *Results and Discussion* present the influence of the location, height, and porosity of shrubs on the CO₂ dispersion characteristics. This research provides a reliable method for predicting heavy gas dispersion in case of the leakage of high-pressure CO₂ pipelines under complex shrubland terrain and the analysis procedures and results can be utilized for CCS risk assessment.

Numerical Methods

To predict the CO₂ dispersion characteristics released from high-pressure pipelines, we used CFD software ANSYS Fluent 15.0 (ANSYS 2011a) in current work. Considering the compromise between computational time and accuracy of the model, the RANS model was employed. The RANS model involves solving the conservation equations of mass, momentum, and energy. Apart from the conservation equations, turbulence and component transportation equations solve the complex problems of 3D turbulence field changes, time-varying rate of mass change of each component, and spatial distribution of concentration of different species. Shrubs were treated as kind of porous media, and their influence on the entire turbulent field was explored.

The equations used for continuity, energy conservation, and momentum were as follows:

Continuity equation

$$\frac{\partial \rho}{\partial t} + \nabla \cdot (\rho \vec{v}) = 0, \quad (1)$$

Energy equation

$$\frac{\partial (\rho E)}{\partial t} + \nabla \cdot [\vec{v} (\rho E + p)] = \nabla \cdot \left[k_{eff} \nabla T - \sum_i h_i \vec{J}_i + (\vec{\tau}_{eff} \cdot \vec{v}) \right], \quad (2)$$

Momentum equation (Navier–Stokes equation)

$$\frac{\partial (\rho \vec{v})}{\partial t} + \nabla \cdot (\rho \vec{v} \vec{v}) = -\nabla p + \nabla \cdot (\vec{\tau}) + \rho \vec{g} + F_d, \quad (3)$$

$$\vec{\tau} = \mu \left[(\nabla \vec{v} + \nabla \vec{v}^T) - \frac{2}{3} \nabla \cdot \vec{v} I \right], \quad (4)$$

where ρ , \vec{v} , and p are the density, velocity vector, and pressure, respectively; $\rho \vec{g}$ represents the gravitational force per unit volume; F_d is source term, and its specific content is shown in **Eq. 7**; $\vec{\tau}$ is the stress tensor (described in **Eq. 4**), where μ is the dynamic viscosity; E represents the total energy; and k_{eff} , T , h_i , and \vec{J}_i are the effective thermal conductivity, temperature, specific enthalpy of species i , and diffusion flux, respectively.

TABLE 1 | Dimensionless constants.

C_d	β_p	β_d	C_{e4}	C_{e5}
0.2	1	4	1.5	0.6

Turbulence Equations

An improved standard k – ε model characterized by a high Reynolds number was utilized for design selection, parameter study, and the initial iteration (Smagorinsky 1963; Launder, 1972). Turbulent kinetic energy k and its dissipation rate ε were obtained from the following transport equations:

$$\frac{\partial (\rho k)}{\partial t} + \frac{\partial}{\partial x_j} (\rho k u_j) = \frac{\partial}{\partial x_j} \left[\left(\mu + \frac{\mu_t}{\sigma_k} \right) \frac{\partial k}{\partial x_j} \right] + G_k + G_b - \rho \varepsilon - Y_M + S_k, \quad (5)$$

$$\frac{\partial (\rho \varepsilon)}{\partial t} + \frac{\partial}{\partial x_j} (\rho \varepsilon u_j) = \frac{\partial}{\partial x_j} \left[\left(\mu + \frac{\mu_t}{\sigma_\varepsilon} \right) \frac{\partial \varepsilon}{\partial x_j} \right] + C_{1\varepsilon} \frac{\varepsilon}{k} (G_k + C_{3\varepsilon} G_b) - C_{2\varepsilon} \rho \frac{\varepsilon^2}{k} + S_\varepsilon, \quad (6)$$

where G_k is the turbulent kinetic energy due to the average velocity gradient; G_b is the turbulent kinetic energy due to buoyancy; Y_M represents the contribution of wave expansion to the total dissipation rate in compressible turbulence; C_1 , C_2 , and C_3 are constants; σ_k and σ_ε are the turbulent Prandtl numbers for k and ε , respectively; and S_k and S_ε are the user-defined sources. The standard coefficient was used to build the turbulence model, and the Boussinesq approximation method was applied to model the buoyancy effect.

In the CFD simulation process, it is particularly important to select the appropriate geometric model and physical model. Liang et al. (2006) used three different canopy shapes: the pyramid crown model, the truncated body of the pyramid crown model, and the cuboid crown model to study the influence of shrub on atmospheric flow. The results showed that the canopy shapes affected the results distinctly and the cuboid canopy model provided the best consistency with the experiment data, also with less computational time. Therefore, in the current simulation, the cuboid canopy model is selected to describe the shrub's shape and treat it as a porous medium due to the complex microstructure of the shrub. The existence of shrubs increases the turbulence intensity around the shrub region. It reduces the wind speed downstream of the shrub region, so an additional momentum source term F_d was added to the momentum in **Eq. 3**:

$$F_d = -C_d a u_i |U|, \quad (7)$$

$$|U| = \left(\sum_{i=1}^2 u_i^2 \right)^{\frac{1}{2}}, \quad (8)$$

where C_d is the drag coefficient of shrubs (values are shown in **Table 1**); a is the leaf area density (m²/m³); u_i is the

velocity component (m/s); and $|U|$ is the average wind speed (m/s).

In the standard k - ε equation, owing to the influence of the shrub and wind shear in the airflow produces turbulence, and the turbulent energy of the surrounding flow field is attenuated. Therefore, additional source terms S_k and S_ε in Eqs. 9, 10 were defined as follows:

$$S_k = C_{da}(\beta_p|U|^2 - \beta_d|U|k), \quad (9)$$

$$S_\varepsilon = C_{da}\left(c_{\varepsilon 4}\beta_p|U|^2\frac{\varepsilon}{k} - c_{\varepsilon 5}\beta_d|U|\varepsilon\right). \quad (10)$$

The dimensionless constants β_p , β_d , $c_{\varepsilon 4}$, and $c_{\varepsilon 5}$ are shown in Table 1.

Species Transport Equation

The species transport equation of components was carried out to calculate the spatial distribution of concentration for each species. This equation is expressed as the time-varying change rate of a component mass in the system equal to the sum of the net diffusion flux through the system interface and the generation rate of the component by a chemical reaction. Two components were considered in the current study: CO₂ and air. As there is no chemical reaction between CO₂ and air, the mass change rate of CO₂ or air in the system is equal to its net diffusion flow flux. The mass fraction of each species was predicted by solving the convection-diffusion equation and using the species transport model (ANSYS 2011a):

$$\frac{\partial(\rho Y_i)}{\partial t} + \nabla \cdot (\rho \vec{v} Y_i) = \nabla \cdot \vec{J}_i + R_i + S_i, \quad (11)$$

where R_i is the net productivity of the species; ρ is the density of CO₂ or air in the system; Y_i is the mass fraction of species i , and the sum of fractions of all species equals 1; \vec{v} and \vec{J}_i are the gas diffusion velocity vector and diffusion flux, respectively; and R_i and S_i are the net production rate of species i and the additional production rate caused by the user-defined source term and discrete term, respectively. Since no chemical reaction occurs, both R_i and S_i were set to 0.

In the dispersion model, the viscosity and thermal conductivity of CO₂ were set to $1.37 \times 10^{-5} \text{ kg}\cdot\text{m}^{-1}\cdot\text{s}^{-1}$ and $0.013 \text{ W}\cdot\text{m}^{-1}\cdot\text{K}^{-1}$, respectively, and CO₂ was considered as an incompressible ideal gas and temperature T (K) as follows:

$$\rho = 5.3105 - 0.01432T. \quad (12)$$

Additionally, in heavy gas dispersion modeling, it is crucial to describe the wind speed precisely as it directly affects the air distribution. In the atmospheric boundary layer, the wind speed usually decreases with a reduction in height due to the friction effect of the ground. The wind inlet velocity is specified by a power-law correlation to express the atmospheric boundary layer. The velocity distribution defined by Peterson and Hennessey (1978) is most widely used to describe the vertical wind profile near the ground:

$$u = u_r \left(\frac{z}{z_r} \right)^\alpha, \quad (13)$$

where u is the wind velocity at altitude z ; u_r is the reference wind speed measured at reference altitude z_r ; and wind shear index α is related to atmospheric stability, geographical environment, and other factors. The parameters used in the current work are consistent with those used in previous studies (Wang H. et al., 2021).

COMPUTATIONAL FLUID DYNAMICS MODEL

Determination of Release Source and Computational Domain

In our previous study (Wang H. et al., 2021), we evaluated the performance of computed results of CO₂ dispersion over a flat terrain with the measures from the full-scale test carried out by the 2016 Australian CO₂ pipeline safe transportation project (Liu X. et al., 2019). Rather than the most of other “model” tests, this full-scale test provided the data represented a more realistic release scenario that CO₂ release from a buried high-pressure pipeline due to a crack induces a fracture propagating. As the test did not offer the information of all the terrain features, the influence of surrounding trees or shrubs on dispersion characteristics was ignored in the CFD model. However, trees or shrubs pattern, such as heights, porosities, and relative position from the CO₂ release source, may lead to a great impact on the surrounding flow field. This is probably the reason for the deviation between the measured and CFD resulted. Therefore, in current work, the CFD model was improved and the incorporated porous model represented the influence of trees or shrubs to provide a comprehensive view of the possible consequences of a full-scale pipeline fracture.

CO₂ dispersion over a flat featureless terrain was set as a reference case (case0), and the box-shaped computational domain was shown in Figure 1A. Figures 1B–D show the analogous computational domains with shrubs arranged in different relative positions. The domain enclosed with six boundaries, specifically the ground (in brown), wind inlet, left, right, outlet, and top. The strip shrub regions were shown in green. The size was 1,500 m (long) \times 800 m (wide) \times 400 m (height), and the wind inlet was located in 200 m upstream of CO₂ release source. The exit of the calculation domain (outlet) was located sufficiently far downstream from the release source; therefore, the backflow effect can be ignored. The size of the computational domain was sufficiently large and met the requirements for the dispersion simulation.

A vertical release perpendicular to the wind direction was considered. The environmental parameters of the wind parameters were consistent with the test conducted by the Architectural Society of Japan and were used for comparison (AIJ, 2020; Mochida et al., 2008). The specific parameters of the four simulated cases are listed in Table 2. Case0 is the basic topography of uncovered shrubs (Figure 1A); case1 is the topography of strip shrubs covered with release sources (Figure 1B) and strip shrubs are covering the release source.

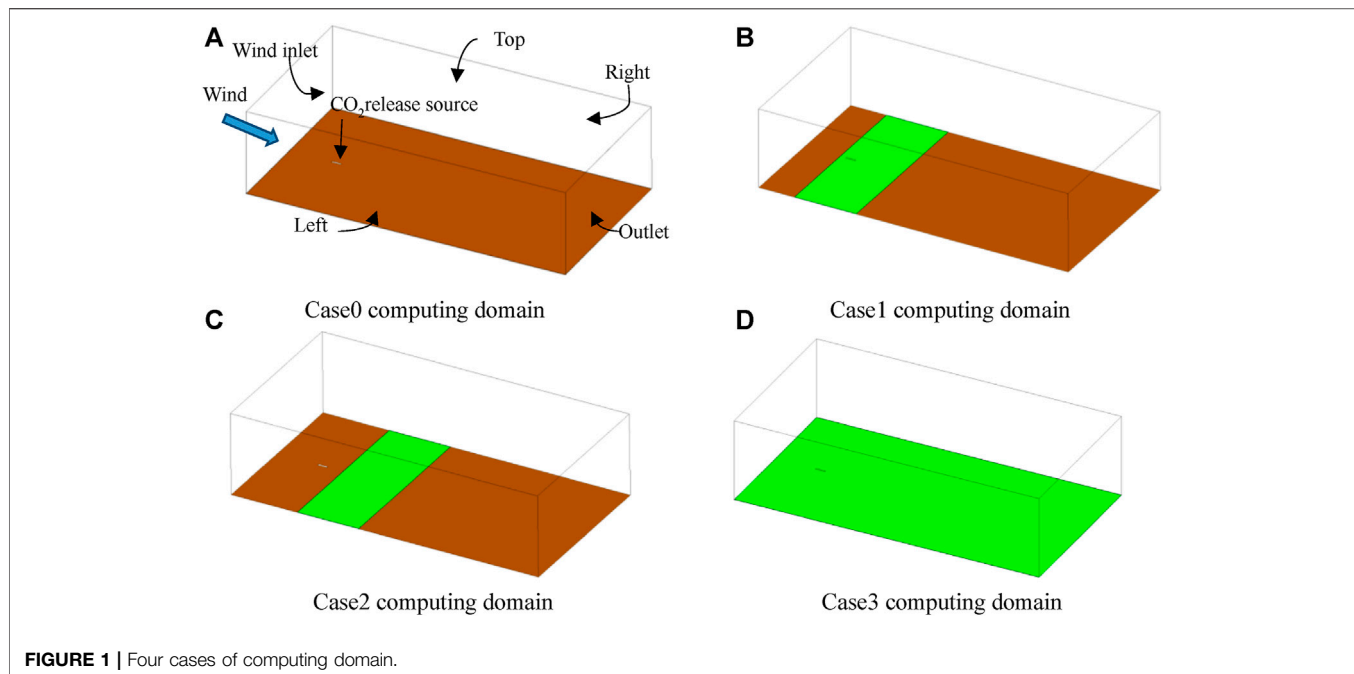


FIGURE 1 | Four cases of computing domain.

TABLE 2 | Specific parameters of the four computed cases.

	Shrub location (downstream of wind inlet)	Shrub size (m)	Porosity		
Case0	—	—	—	—	—
Case1_H_0.5 m	172.425 m	800 (L) × 300 (W) × 0.5 (H)	—	—	0.9
Case1_H_1 m	172.425 m	800 (L) × 300 (W) × 1 (H)	0.3	0.6	0.9
Case1_H_1.5 m	172.425 m	800 (L) × 300 (W) × 1.5 (H)	—	—	0.9
Case2	322.425 m	800 (L) × 300 (W) × 1 (H)	—	—	0.9
Case3	0	800 (L) × 1,500 (W) × 1 (H)	—	—	0.9

To analyze the impact of shrub height and porosity on gas dispersion, the heights of the shrubs in case1 are adjusted to 0.5, 1, and 1.5 m, respectively, and the porosities are 0.3, 0.6, and 0.9. The smaller the porosity, the greater the wind resistance. Case2 is also a strip shrub terrain. The strip shrub is located at 100 m behind the release source, which is different from case1. Case3 is a terrain that is covered entirely with shrubs. The heights of shrubs in case2 and case3 are both 1 m and the porosities are both 0.9.

ANSYS-ICEM is applied to reasonably generate the hexahedral structure mesh. The grid growth rate is fixed within a certain range according to previous research (Wang H. et al., 2021), and the numbers of grid for different terrains are between 3 and 4 million.

Boundary and Initial Conditions

The numerical simulation was divided into two stages: 1) steady-state simulation and 2) transient simulation. The initial wind flow field over the specified terrain was obtained using a steady-state simulation, without the emission of CO₂. The transient simulation was based on the steady-state initial flow field as

well as introducing CO₂ from the “source,” and CO₂ dispersion was simulated over time. Additionally, the simulation of case0 was based on a full-scale test (Liu X. et al., 2019), and the CFD models have been previously validated (Wang H. et al., 2021). In that case, CO₂ was simulated to dispersers over a flat featureless terrain. The numerical simulation used herein was based on the same time-varying release source inlet conditions as that in the previous study. Other cases were improved on this basis. The CFD simulation condition settings are presented in Table 3.

Porous Media Model Verification

To evaluate the performance of the proposed porous model, flow field data from the experiment carried out by the Architectural Society of Japan were used for comparison (AIJ, 2020; Mochida et al., 2008). All the parameters, including inlet conditions and monitoring point distribution were derived from and according to with the experiment. The settings for the porous media were based on Eqs. 8, 10, 11 to obtain the corresponding UDF (ANSYS 2011b).

Table 4 shows the comparison between the measured wind speed values (AIJ) and those from the numerical simulation. As

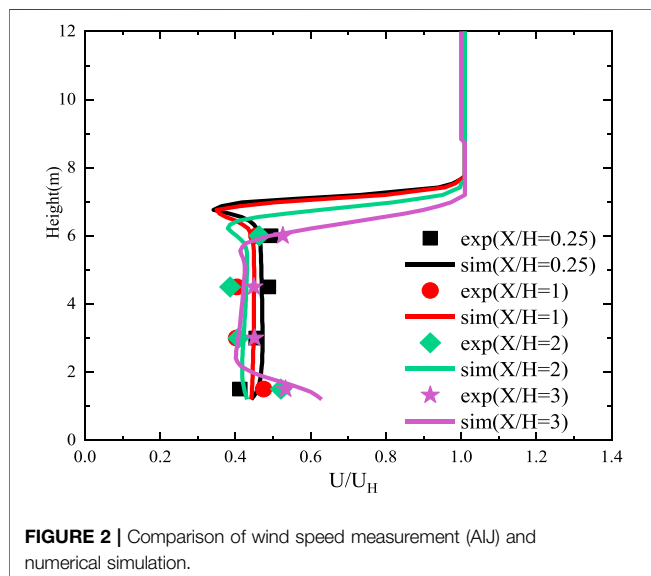
TABLE 3 | Boundary condition.

Variable	Boundary type	Specific parameters
Wind inlet	Velocity inlet	The temperature was set at 288 K and 100% air; the velocity distribution in the height direction was according to Eq. 13 and was incorporated using a user-defined function (UDF) ANSYS (2011b)
CO ₂ release source	Mass flow inlet	The release rate was consistent to previous study Wang et al. (2021a) and incorporated using UDF ANSYS (2011b). The pressure and temperature equalled the atmospheric pressure and 200 K (CO ₂ sublimation point under atmospheric pressure), respectively
Outlet	Pressure outlet	The gauge pressure was 0, and the temperature was set at 288 K
Ground	Nonslip wall	Nonslip wall. The temperature was equal to ambient air temperature
Top, left, and right	Symmetry	Impermeable symmetrical boundaries with zero normal velocity and zero gradient
Shrubs	Porous zone	The turbulence source term was based on Eq. 11 ; Eq. 12 and was incorporated using UDF ANSYS (2011b)

TABLE 4 | Comparison of wind speed measurement (AU) and numerical simulation.

	H	1.50 m	3.0 m	4.5 m	6.0 m
X/H _{TREE} = 0.25	<i>U</i> _{EXP}	1.4574	2.4055	2.8848	2.3664
	<i>U</i> _{SIM}	1.843	2.1682	2.3482	2.4623
	Relative error	0.2092	0.1095	0.2285	0.0389
X/H _{TREE} = 1	<i>U</i> _{EXP}	1.5556	2.0009	2.3463	2.5303
	<i>U</i> _{SIM}	1.7437	2.0668	2.2996	2.3726
	Relative error	0.1079	0.0319	0.0203	0.0665
X/H _{TREE} = 2	<i>U</i> _{EXP}	1.7934	1.7723	1.9424	2.3408
	<i>U</i> _{SIM}	1.6849	1.9624	2.1582	2.2722
	Relative error	0.0605	0.1073	0.1111	0.0293
X/H _{TREE} = 3	<i>U</i> _{EXP}	1.9671	1.7942	1.8559	2.3715
	<i>U</i> _{SIM}	1.6016	1.8631	2.0599	2.0658
	Relative error	0.1858	0.0384	0.1099	0.1289

*U*_{EXP} is the wind speed value measured in the experiment; *U*_{SIM} is the wind speed value simulated by CFD model; *X* is the horizontal distance between the monitoring point and the tree; and *H*_{TREE} is the tree height.



the monitoring point was located on the leeward side of the tree, the influence range and deceleration effect by the tree on the wind speed changed owing to the relative distance. Overall, the simulation results of the velocity profile were consistent with

that from the experimental values, especially when the value of *X/H* ranged between 0.5 and 3; the data were consistent, and the relative error was small. It is worth noting that when the value of *X/H* was 2, the data fit was slightly worse in **Figure 2**. This may attribute to the underestimation of the influence range and deceleration effect of the wind speed by trees. Generally speaking, the adopted porous model could accurately simulate the influence of trees on the flow field, thereby ensuring the accurate prediction of the entire model.

RESULTS AND DISCUSSION

Previous studies (Liu et al., 2016; Wang H. et al., 2021) indicated that the dispersion pattern of CO₂ under the condition of large-scale turbulence was dominated by convective diffusion, whereas molecular diffusion can be negligible. Initially, the effect of gravity was significant, and the gas collapsed to form a heavy gas cloud promptly. Then, the CO₂ cloud was gradually diluted by ambient air, resulting in decreased density and apparent lateral dispersion. With time, the heavy gas cloud was passively dispersed by the wind and was further diluted by air. Eventually, the effects of gravity and buoyancy achieved balance. The convection diffusion of heavy gases was affected by terrain features notably, such as obstacles, and other landscape aspects. The natural shrubs in the environment were mostly low. Since their heights quite differed from that of buildings or trees, the shrubs predominantly affected the flow field near the ground. When the location, height, porosity, and other profiles of the shrubs changed, the flow field, direction of CO₂ convection and dispersion, concentration at different locations, and consequence distance were all modified correspondingly.

Influence of Shrubland Relative Location

Figures 3A–D show the initial flow field covering the shrubs for cases 0–3 (a cross section parallel to the ground with a height of 1 m). The green region represents the zone covered by shrubs, whereas the yellow is the flat featureless region. When shrubbery cover the release source (case1), the flow field near the release source is prone to eddy currents (**Figure 3B**). The shrub coverage areas chosen for case1 and case3 differ substantially in terms of streamline distribution (as shown in **Figures 3B,D**). In terms of case2, the shrub region boundary is located 322.5 m downstream of the wind inlet and 100 m away from the center of the release

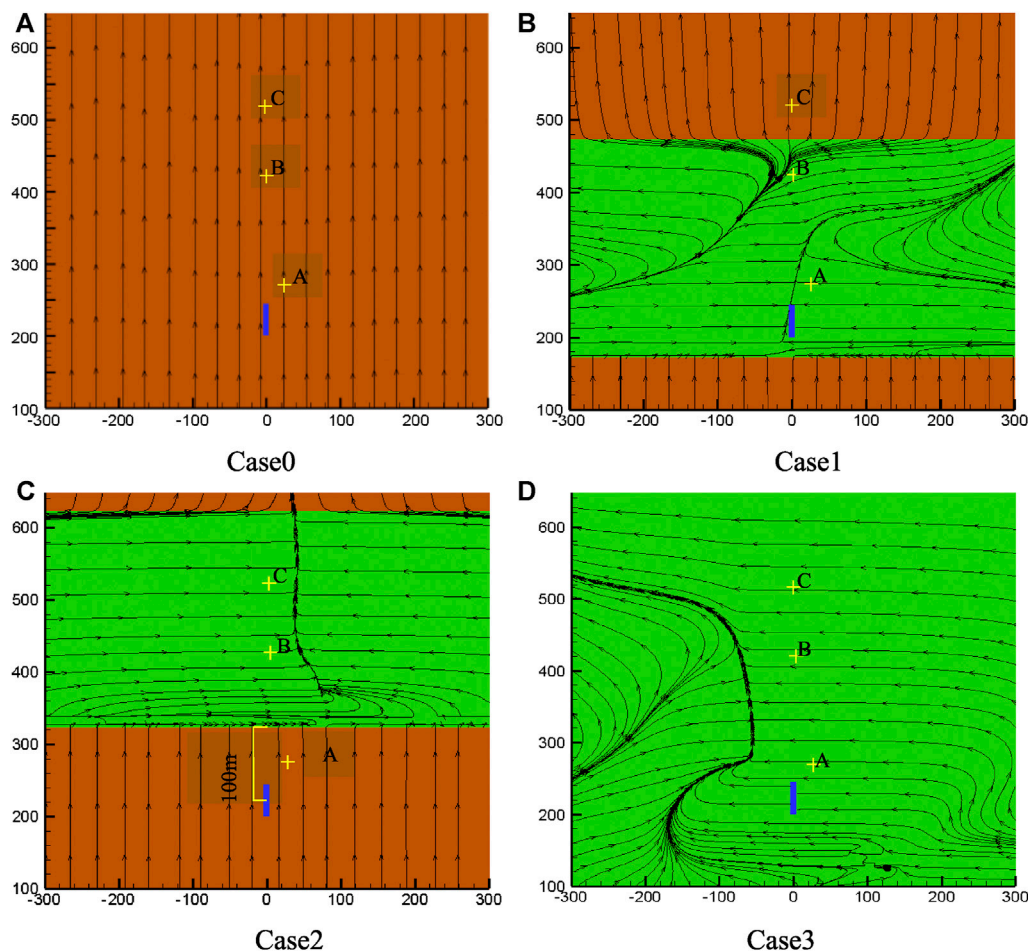


FIGURE 3 | Top view of the initial flow field created in the shrubbery for three different cases.

source. It should be noted that in a flat terrain without shrubs, the streamlines are mostly parallel to the wind direction and approximately perpendicular to the streamlines in the shrub area (especially at the wind inlet). Whereas in the shrubland-covered area, the streamlines are mostly perpendicular to the wind direction or have a clear angle with the wind direction. The turbulent flow around the porous medium area is enhanced, the wind speed is reduced, and obvious eddies could be observed. At the junction of flat terrain and shrubland terrain, the direction of the streamline changes suddenly, where the turbulence changes more obviously.

Figures 4A–C show the time-varying CO_2 concentration at 1 m elevation at points A (50 m), B (200 m), and C (400 m). The locations of the monitoring points of the three cases are the same; points A, B, and C are, respectively, located at 50, 200, and 400 m downwind from the center of the release source. At point A (**Figure 4A**), the CO_2 concentration varied rapidly under all three shrubbery-covered scenarios. Clearly, when the shrubbery covers the release source (case1), the CO_2 concentration peaked three times successively. The highest CO_2 concentration reaches 29.6% in terms of case1, 5.3% in case2, and only 2.1% in case3. Also, the CO_2 concentration in case1 covered by shrubbery is 4.5% higher

than that in case 0. There is no doubt that such a discrepancy is due to a significant change in the nearby flow field when a 1-m high shrub is located 100 m behind the release source (**Figure 4B**), thereby increasing the gas concentration. However, as for case2, unlike the other two cases where shrubs cover the release source (case1 and case3), shrubs represent porous media and substantially impact the wind environment around the release sources, diluting the CO_2 concentration and making it much lower at point A than that in a forest without shrubs (case0). It can be seen from **Figure 4B** that the CO_2 gas cloud in case2 disperses to point B at 39.5 s, and is the fastest case, whereas in case3 and case1, CO_2 disperses to point B at 59.2 and 65.3 s, respectively. It is observed that when the shrub region covers the release source (case1 and case3), the cloud dispersion speed slows down and the gas cloud reaches point B later. The results also show that from 104.6 s until 300 s, the concentration value at point B remained within the range between 0.5 and 1% (case1 and case3), and the overall CO_2 volume fraction vs. time curves fluctuate unobvious. Specifically, when CO_2 cloud in case2 disperses to point B, the first peak concentration of 2.3% appears at 47.6 s. Due to the existence of a certain distance between the shrub region and the release source,

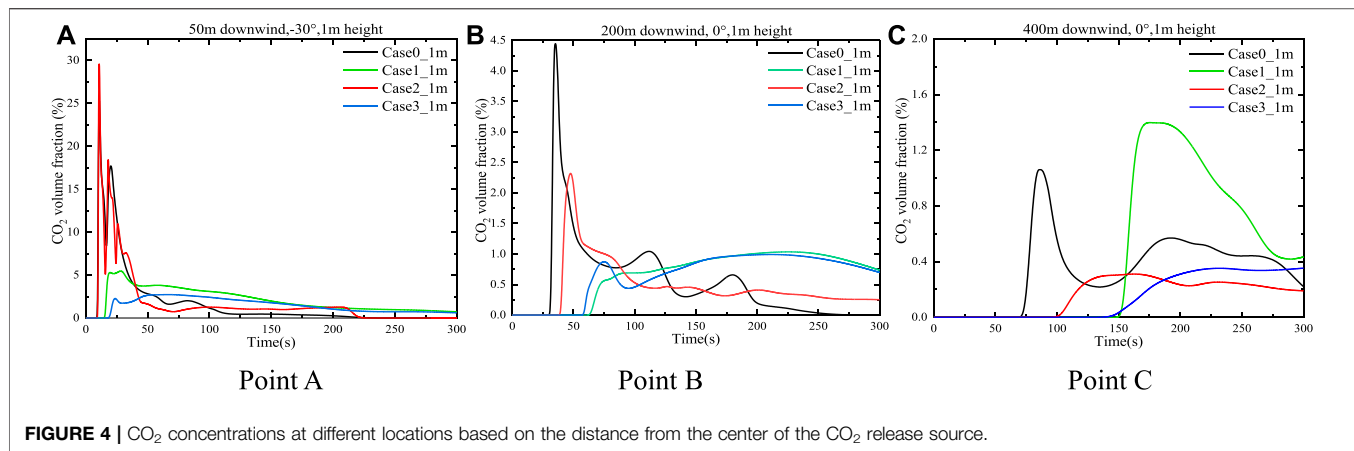


FIGURE 4 | CO₂ concentrations at different locations based on the distance from the center of the CO₂ release source.

the effect of shrub retardation on gas dispersion is not obvious. After reaching the first CO₂ concentration peak of 0.87% and appeared at 75.1 s in case3, the concentration first decreases and then increased to the second peak. It can be seen from this that for point B, there is little difference in the delaying effect of CO₂ gas between the whole ground cover shrub (case3) and the shrub cover at the center of the release source (case1). At point C (Figure 4C), the concentration of CO₂ in case1 raised more rapidly compared with those in case2 and case3, and the maximum concentration of 1.39% lasted for approximately 19 s.

Due to the strong Joule–Thomson effect during high-pressure CO₂ expansion, the temperature of CO₂ will drop sharply after leaking from a high-pressure pipe; therefore, dry ice is formed, which will sublimate quickly, thus forming a low-temperature area near the nozzle. After pipeline rupture, CO₂ leakage flow rate also changes significantly over time. The relationship between CO₂ flow rate and time measured in the real full-size blasting experiment is as follows:

$$m = C_1(e^{C_2t} - e^{C_3t}), \quad (14)$$

where t was time, and C_1 , C_2 , and C_3 are coefficients controlling the release rate. According to the data measured from the full-scale blasting experiment (Liu X. et al., 2019), the values of these three parameters were 75300 kg s⁻¹, -1 s⁻¹, and -10 s⁻¹, respectively.

The National Institute of Occupational Safety and Health (NIOSH) states that the long-term exposure to 0.5% (5,000 ppm) concentration of CO₂ will cause dizziness, restlessness, and helplessness. In addition, NIOSH pointed out that exposing people to a CO₂ concentration of 4% (40,000 ppm) will issue in very rapid breathing, confusion, and even coma (NIOSH 2005). Therefore, in the following analysis, the consequence distance was determined as the distance away from pipe rupture contained by the concentration envelope corresponding to this concentration level of 4% and it is called CD-4.

Figures 5–8 show the CD-4 obtained in four different terrains at different times. Under all terrain conditions, the CO₂ cloud clusters had a certain height at the initial stage of the release. As

CO₂ gas is released within 12 s [corresponding to the blasting experiment (Wang H. et al., 2021)], the cloud clusters begin to collapse because of the high cloud density. The release sources in case0 and case2 are not covered by shrubs, whereas there are different distances from release sources to the shrub covering boundary as for case1 and case3. Thus, in the initial stage, lateral dispersion of CO₂ for case0 and case2 is not as obvious as that for case1 and case3. Simultaneously, the coverage areas of the CD-4 for case0 and case2 are relatively smaller at 10 s (Table 5).

In the initial dispersion stage, compared with those in case0 and case0, the lateral consequence distances in case1 and case3 became more obvious. This is because the shrub had a strong blocking effect on the wind field around the release source and delayed the formation of heavy gas clouds. It is worth noting that the dispersion of clusters may make rescue operations more difficult, especially when the coverage area is extensive, and there are high CO₂ concentrations.

In general, regardless of the thermal gradient effect (related to the air stability level) on the generation or suppression of turbulence, shrubs have a substantial impact on the near-surface flow field and are more likely to produce mechanical turbulence than shrub-free terrain. When shrubs cover the release source, the lateral dispersion of heavy gas cloud clusters becomes more significant. It is indicated that the cloud cluster grows larger and the dispersion duration is prolonged.

Effect of Shrub Height

There are a series of types of shrubs, and their heights varied from 0.1–6 m, while the common shrub heights in suburban woodlands are 0.5–1.3 m (Zhang 2009). It is valuable to study the effect of shrub height on the dispersion pattern. The reference wind speed during the simulation of dispersion is 5 m s⁻¹. Three types of shrubs with heights of 0.5, 1, and 1.5 m are considered and termed Terrain I, Terrain II, and Terrain III, respectively. Figure 9 shows the predicted time-varying CO₂ concentrations at points A, B, and C with different shrub heights where the shrub region covered the release sources. As shown in Figure 9A, for point A, when the height of the shrub is 0.5 m (Terrain I), the maximum CO₂ concentration reached 14.2%, which is

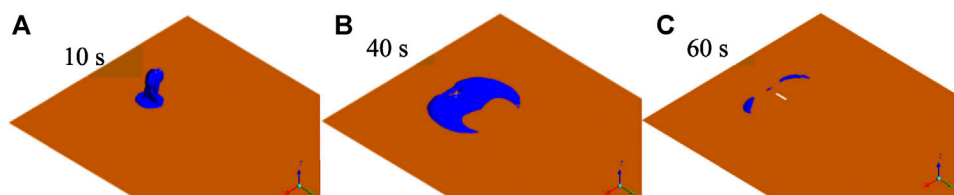


FIGURE 5 | CD-4 at different time (case0).

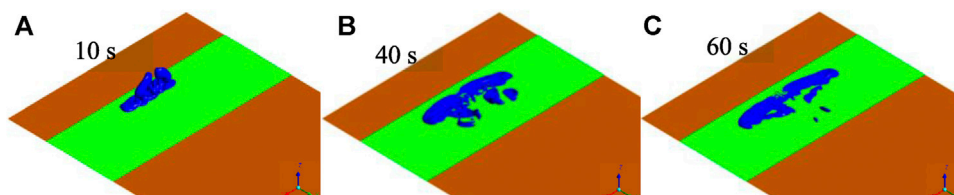


FIGURE 6 | CD-4 at different times (case1).

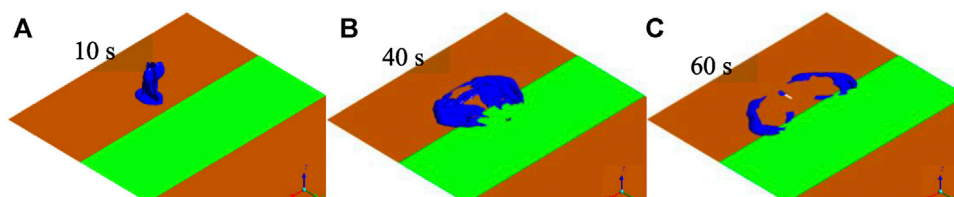


FIGURE 7 | CD-4 at different times (case2).

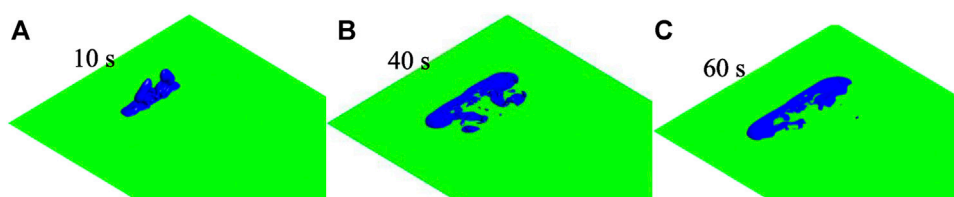


FIGURE 8 | CD-4 at different times (case3).

TABLE 5 | CD-4 calculated at different time points of four terrain types.

Time	10 s	20 s	40 s	60 s
Case0	25,794.3 m ²	34,990.7 m ²	47,160.4 m ²	5,127.5 m ²
Case1	51,880.4 m ²	65,800.3 m ²	66,950.6 m ²	46,753.1 m ²
Case2	32,726.4 m ²	49,999.4 m ²	69,708.4 m ²	39,396.7 m ²
Case3	47,061.8 m ²	65,107.8 m ²	70,156.6 m ²	51,726.7 m ²

TABLE 6 | Comparison of the CD-4 at different time points with shrubs of three different heights.

Time	10 s	20 s	40 s	60 s
Case1_0.5 m	42,495.2 m ²	49,214.4 m ²	58,005 m ²	52,360.3 m ²
Case1_1 m	51,880.4 m ²	65,800.3 m ²	66,950.6 m ²	46,753.1 m ²
Case1_1.5 m	43,117.9 m ²	62,459.9 m ²	69,257.1 m ²	42,879.2 m ²

approximately two times than those at the other monitoring points with shrub heights of 1 m (Terrain II) and 1.5 m (Terrain III). Such a discrepancy is supposed to be caused by the much

lower turbulent kinetic energy of the 0.5 m high shrubbery area (Terrain I) compared with the those of 1 m (Terrain II) and 1.5 m (Terrain III) high shrubbery areas (as shown in **Figure 10**). In

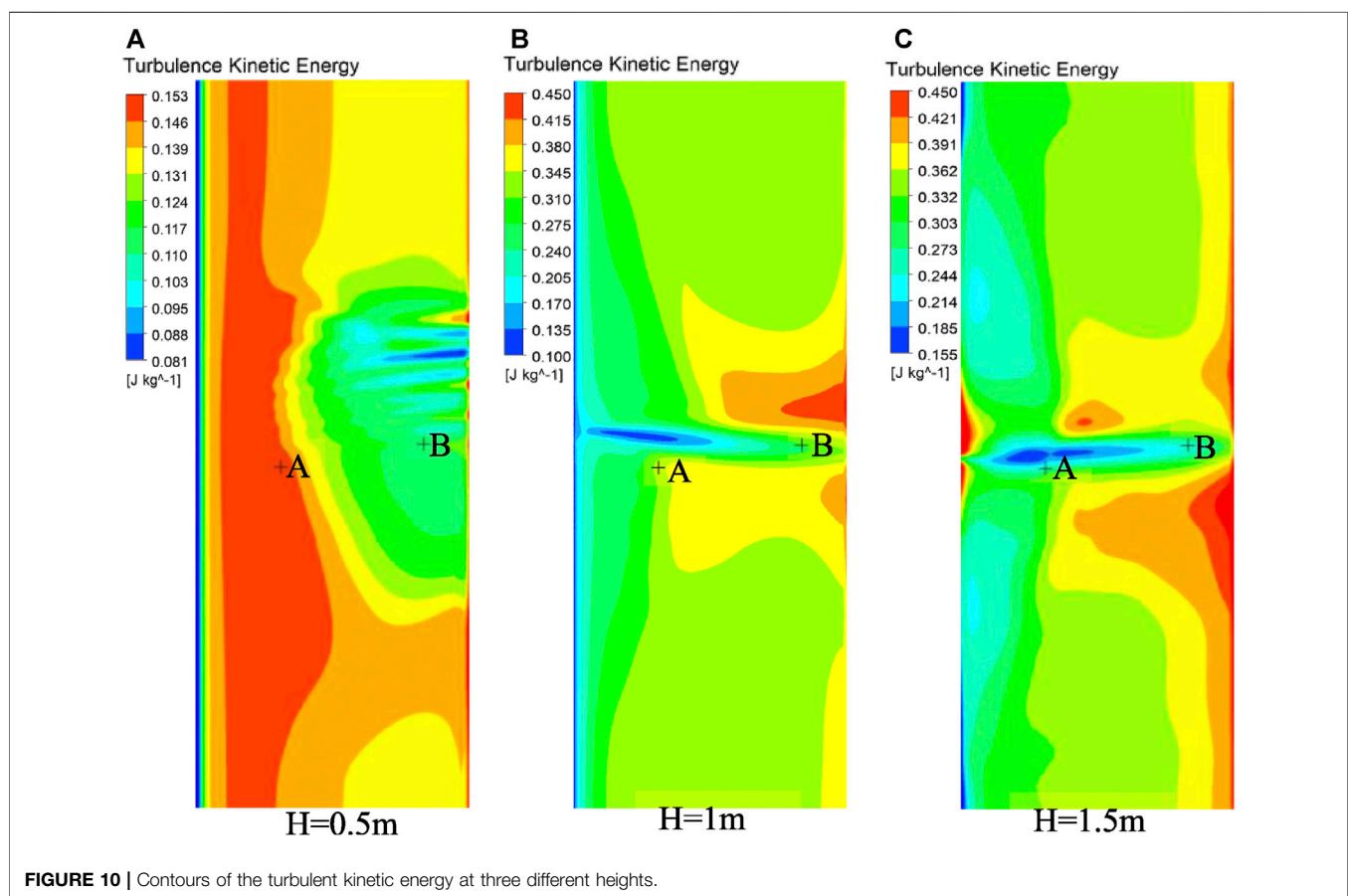
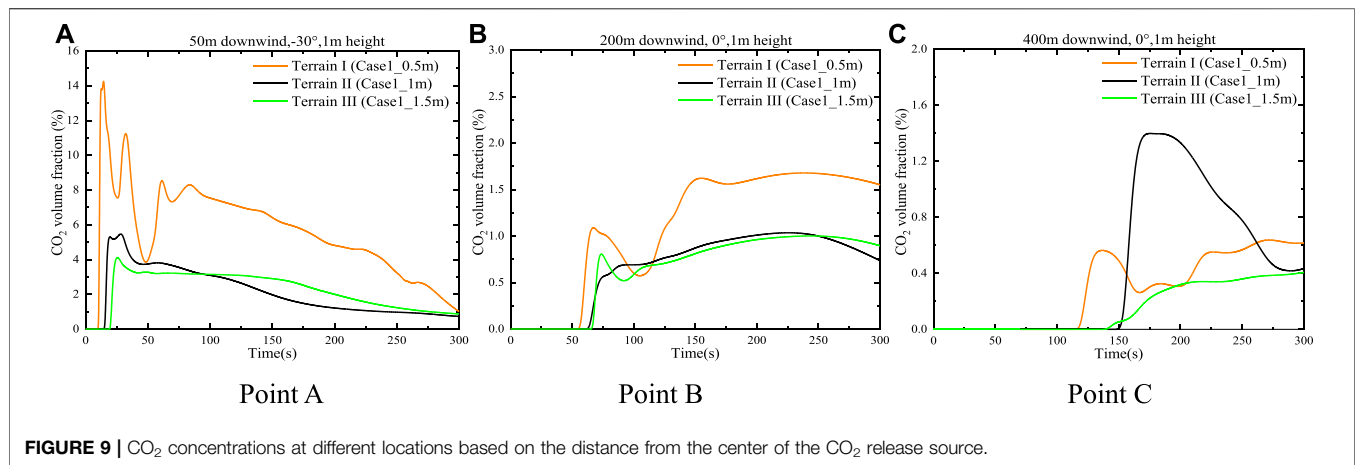


Figure 9B, when the height of shrubs is 0.5 m (Terrain I), the CO₂ concentration at point B presented two peaks, with the concentration at second peak being 0.5% higher than that at the first peak. This is due to the influences of the flow field in the area with the porous medium. When the heights of shrubs are 1 m (Terrain II) and 1.5 m (Terrain III), the CO₂ concentrations at point B are only with minor variations remaining stable within a range of 0.75–1.1% for a long time. As shown in **Figure 9B**, point

C was far away from the release source and is not located in the area of the porous medium. The gas concentration value is generally low in the three cases, but the gas concentration value at the monitoring point is higher when the height was 1 m. **Figures 10A–C** exhibit the turbulent energy cloud diagram of the shrubland area at three different heights. It is clear that when the height of the shrub was 0.5 m, the turbulent kinetic energy in the entire porous medium area is not high. When the

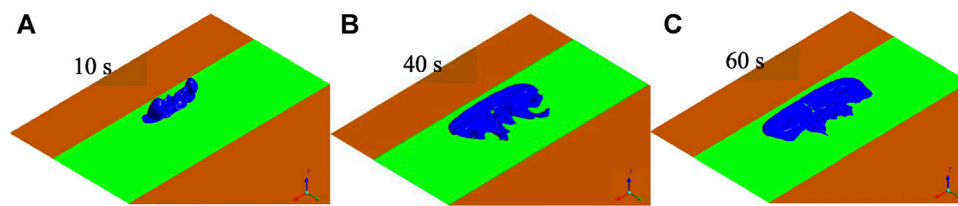


FIGURE 11 | CD-4 at different time points with 0.5-m high shrubs.

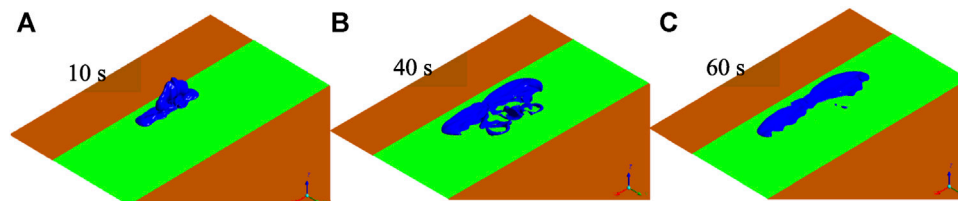


FIGURE 12 | CD-4 at different time points with 1.5-m high shrubs.

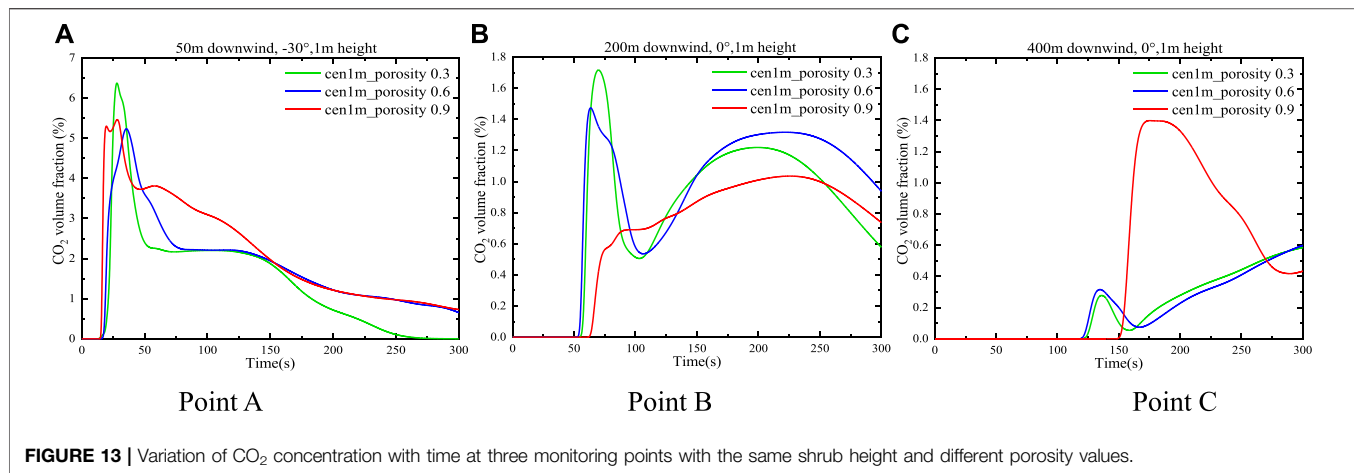
heights were 1 and 1.5 m, the turbulent kinetic energy distribution is close. This may be because the shrub was located 150 m behind the air inlet. Therefore, the flow field did not change correspondingly due to the linear increase in shrub height, which will be an important issue that is needed to explore in the future.

Figures 11, 12 demonstrate these CD-4s at different times when heights of the shrub are 0.5 and 1.5 m, respectively. Comparing with those in **Figure 6**, it is observed that in the initial release stage for the three height shrubs, the higher height gives rise to less degree of cloud collapse. The higher the shrub height is, the greater the thickness of the porous medium area is, and therefore, the flow field varies more obviously. Especially with the dispersion time goes on, the change is more significant. Clearly, the variation in the flow field became more remarkable (**Figure 12B**) at 40 s with a shrub height of 1.5 m. The CD-4 appeared as two vortex-like shapes located far from the release source. The coverage area of the isosurface also increased (**Table 6**). It is found by comparison that a greater shrub height led to more intense turbulent field changes in the porous medium area and more evident lateral dispersion. Generally, shrub height affects the range of cloud and the feature of CO₂ dispersion to a certain extent. Higher shrub height contributes to more complicated and noteworthy variations in the flow field, effectively delaying heavy gas dispersion and increasing lateral consequence distance.

Effect of Shrub Porosity on Heavy Gas Dispersion

The aforementioned contents mainly have focused on the assessment of the impact of shrub region relative position and shrub height on CO₂ dispersion. However, different shrub species have different densities of branches and leaves, and also the seasons will affect these densities remarkably as well. Canopy density

expressed as the porosity brings about significant variations in canopy turbulence. Therefore, it is of the great significance of investigating the effect of shrub porosity on the character of CO₂ dispersion. Nevertheless, there has a little discussion about the basic characteristics of this issue. In a sparse shrub canopy, the sparser branches and leaves result in higher porosity. As a result, the wind-blocking effect is weaker. As such, sparse canopies primarily cause variations in turbulence at the spatial level. **Figure 13** compares curves of CO₂ concentration vs. time between different porosities at the three monitoring points A, B, and C. The locations of the three monitoring points A, B, and C are shown in **Figure 3**. At point A, which located closer to the release source, time-varying concentration trends for three porosities are very similar. However, when the porosity is 0.3, the maximum CO₂ concentration is slightly higher than those in the other two cases. As the distance from the release source increased (i.e., point B in **Figure 13B**), the influence of porosity on the maximum gas concentration also increased. When the porosity is 0.9, the maximum CO₂ concentration at point B is significantly less than that with porosities of 0.3 and 0.6. In terms of point C located even farther away, it is observed that the gas concentration curve of porosity 0.9 increased significantly, and the maximum CO₂ concentration is more than three times higher than that of the gas concentration with the porosities of 0.3 and 0.6. The reason for this is that the gas release rate is relatively high in the initial jet state of the release, and point A is located near the release source, so the change in the porosity of the shrub had little effect on the wind speed at this point. With the continuous increase in the dispersion distance, the porous medium region has obvious differences in the wind field under different porosities. When the porosity is 0.9, the barrier effect on the wind is smaller, so it can be farther away from the release source and CO₂ is captured with a higher concentration value. For the porous medium regions with porosities of 0.3 and 0.6, when the height of the shrub is 1 m, the effect of resistance on wind field is similar.



CONCLUSION

This article developed a CFD model to explore the influence of the shrub region on the dispersion of CO₂ released from the ruptured high-pressure pipelines. Herein, shrubs were treated as a kind of porous media, and additional momentum source terms and turbulence source terms were applied to the entire porous medium area *via* UDF. The CFD model was validated using previous research and existing data.

The following conclusions are drawn:

1. Shrubs as porous media have a greater impact on the near-surface flow field than shrub-free terrains. As such, shrubs are more likely to produce mechanical turbulence. The lateral dispersion is of significance, and the gas dispersion time is prolonged. Compared with the shrub-free terrain, the CD-4 of the three shrub terrains at 60 s increased by 8.1 times, 6.7 times, and 9.1 times, respectively.
2. The relative position of the shrubbery and release source impact the surface flow field of the release source significantly. When shrubs cover the release source, at the initial stage of release and owing to the increased barrier effect of shrubs on the wind, the CO₂ gas cloud rapidly collapses. Due to the influence of the porous media on the flow field, the lateral dispersion distance increases. Specifically, at 10 s, the CD-4 of the strip shrubland without cover release source is reduced by 36.9% than that of the strip shrubland covered with the release source; while compared with the strip shrubland covered with the release source, the CD-4 of the terrain of the full-covered shrub is reduced by 9.2%.
3. When shrubs are located close to the wind inlet, the impacts of the 1- and 1.5-m high shrubs on the near-surface flow field are similar. The CD-4 is also alike for the two situations. However, 0.5-m high shrubs impact the near-surface flow field scarcely, and their ability to delay gas dispersion is much lower than that of taller shrubs. The height of shrubs does not correlate linearly with delays in gas dispersion.
4. Although porosity substantially affects the resistance of shrubs to the wind, they have different effects on various terrains. When the porosity of 1-m high shrubbery ranges between 0.3 and 0.6, its

impact on the flow field near the ground and the degree of gas dispersion are similar. When the porosity reaches 0.9, the impact of the multi-surface flow field of shrubs is considerably reduced, the blocking effect on the wind is weaker, and the CO₂ spreads faster.

This work supplements effective basis for understanding CO₂ dispersion over complex terrain. It also helps determine a sufficient protective distance for personnel working in resource mining and environmentally sensitive areas. Emergency plans developed based on this research can provide a reliable method for CCS-related risk assessment.

DATA AVAILABILITY STATEMENT

The original contributions presented in the study are included in the article/Supplementary Material, further inquiries can be directed to the corresponding author.

AUTHOR CONTRIBUTIONS

HW conducted experimental verification and CFD numerical simulation, analyzed the data, and wrote the manuscript. YZ made a significant contribution to the analysis and preparation of the manuscript, and he also reviewed and edited. MF helped the analysis through constructive discussions, and he also reviewed and edited. LB helped the analysis through constructive discussions. HP contributed to the research idea.

FUNDING

Natural Science Foundation of Hebei Province (E2019210036); Natural Science Foundation of Hebei Province (E2014210060); Fundamental research found for Hebei Province administrated Universities (ZCT202002).

REFERENCES

- Ahmed, I., Bengherbia, T., Zhvansky, R., Ferrara, G., Wen, J. X., and Stocks, N. G. (2016). Validation of Geometry Modelling Approaches for Offshore Gas Dispersion Simulations. *J. Loss Prev. Process Industries* 44, 594–600. doi:10.1016/j.jlp.2016.07.009
- AIJ (2020). AIJ Japanese Architectural Society (AIJ) Wind Tunnel Test and Field Measurement Data. Available at: https://www.aij.or.jp/jpn/publish/cfdguide/index_e.htm (Accessed February 15, 2020).
- ANSYS (2011a). *ANSYS FLUENT Theory Guide*. USA: ANSYS Inc.
- ANSYS (2011b). *ANSYS FLUENT UDF Manual*. USA: ANSYS Inc.
- Barbano, F., Di Sabatino, S., Stoll, R., and Pardyjak, E. R. (2020). A Numerical Study of the Impact of Vegetation on Mean and Turbulence fields in a European-city Neighbourhood. *Building Environ.* 186. doi:10.1016/j.buildenv.2020.107293
- Bijad, E., Delavar, M. A., and Sedighi, K. (2016). CFD Simulation of Effects of Dimension Changes of Buildings on Pollution Dispersion in the Built Environment. *Alexandria Eng. J.* 55, 3135–3144. doi:10.1016/j.aej.2016.08.024
- Buccolieri, R., Gromke, C., Di Sabatino, S., and Ruck, B. (2009). Aerodynamic Effects of Trees on Pollutant Concentration in Street Canyons. *Sci. Total Environ.* 407, 5247–5256. doi:10.1016/j.scitotenv.2009.06.016
- Buccolieri, R., Jeanjean, A. P. R., Gatto, E., and Leigh, R. J. (2018). The Impact of Trees on Street Ventilation, NOx and PM2.5 Concentrations across Heights in Marylebone Rd Street canyon. *Cent. Lond. Sustain. Cities Soc.* 41, 227–241. doi:10.1016/j.scs.2018.05.030
- Chen, J., Viatte, C., Hedelius, J. K., Jones, T., Franklin, J. E., Parker, H., et al. (2016). Differential Column Measurements Using Compact Solar-Tracking Spectrometers. *Atmos. Chem. Phys.* 16, 8479–8498. doi:10.5194/acp-16-8479-2016
- COST Action 732 (2007a). *Background and Justification Document to Support the Model Evaluation Guidance and Protocol*. Meteorological Inst.
- COST Action 732 (2007b). *Best Practise Guideline for the CFD Simulation of Flows in the Urban Environment*. Meteorological Inst.
- COST Action 732 (2007c). *Model Evaluation Guidance and Protocol Document*. Meteorological Inst.
- COST Action 732 (2010). *Model Evaluation Case Studies: Approach and Result*. Meteorological Inst.
- Ding, L., Mao, X., Yang, L., Yan, B., Wang, J., and Zhang, L. (2020). Effects of Installation Position of Fin-Shaped Rods on Wind-Induced Vibration and Energy Harvesting of Aeroelastic Energy Converter. *Smart Mater. Structures* 30. doi:10.1088/1361-665X/abd42b
- Dong, Z., Luo, W., Qian, G., and Lu, P. (2008). Wind Tunnel Simulation of the Three-Dimensional Airflow Patterns Around Shrubs. *J. Geophys. Res.* 113. doi:10.1029/2007jfo00880
- Efthimiou, G. C., Andronopoulos, S., Tavares, R., and Bartzis, J. G. (2017). CFD-RANS Prediction of the Dispersion of a Hazardous Airborne Material Released during a Real Accident in an Industrial Environment. *J. Loss Prev. Process Industries* 46, 23–36. doi:10.1016/j.jlp.2017.01.015
- Fabbri, L., Binda, M., and Bruin, Y. Bd. (2017). *Accident Damage Analysis Module (ADAM) – Technical Guidance*. Luxembourg, EUR 28732 EN: Publications Office of the European Union. doi:10.2760/719457
- Fabbri, L., and Wood, M. H. (2019). Accident Damage Analysis Module (ADAM): Novel European Commission Tool for Consequence Assessment—Scientific Evaluation of Performance. *Process Saf. Environ. Prot.* 129, 249–263. doi:10.1016/j.psep.2019.07.007
- Fabbri, L., Wood, M. H., Azzini, I., and Rosati, R. (2020). Global Sensitivity Analysis of the ADAM Dispersion Module: Jack Rabbit II Test Case. *Atmos. Environ.* 240, 117586. doi:10.1016/j.atmosenv.2020.117586
- Gale, J., and Davison, J. (2004). Transmission of CO₂—safety and Economic Considerations. *Energy* 29, 1319–1328. doi:10.1016/j.energy.2004.03.090
- Gallagher, J., Baldauf, R., Fuller, C. H., Kumar, P., Gill, L. W., and McNabola, A. (2015). Passive Methods for Improving Air Quality in the Built Environment: A Review of Porous and Solid Barriers. *Atmos. Environ.* 120, 61–70. doi:10.1016/j.atmosenv.2015.08.075
- Gant, S., Weil, J., Delle Monache, L., McKenna, B., Garcia, M. M., Tickle, G., et al. (2018). Dense Gas Dispersion Model Development and Testing for the Jack Rabbit II Phase 1 Chlorine Release Experiments. *Atmos. Environ.* 192, 218–240. doi:10.1016/j.atmosenv.2018.08.009
- Gant, S., Tickle, G., Kelsey, A., and Tucker, H. (2021). DRIFT Dispersion Model Predictions for the Jack Rabbit II Model Inter-comparison Exercise. *Atmos. Environ.* 244, 117717. doi:10.1016/j.atmosenv.2020.117717
- Gavelli, F., Bullister, E., and Kytomaa, H. (2008). Application of CFD (Fluent) to LNG Spills into Geometrically Complex Environments. *J. Hazard. Mater.* 159, 158–168. doi:10.1016/j.jhazmat.2008.02.037
- Götmarm, F., Götmarm, E., and Jensen, A. M. (2016). Why Be a Shrub? A Basic Model and Hypotheses for the Adaptive Values of a Common Growth Form. *Front. Plant Sci.* 7, 1–14. doi:10.3389/fpls.2016.01095
- Gromke, C., Jamarkattel, N., and Ruck, B. (2016). Influence of Roadside Hedgerows on Air Quality in Urban Street Canyons. *Atmos. Environ.* 139, 75–86. doi:10.1016/j.atmosenv.2016.05.014
- Hagishima, A., Narita, K-i., and Tanimoto, J. (2007). Field experiment on Transpiration from Isolated Urban Plants. *Hydrological Process.* 21, 1217–1222. doi:10.1002/hyp.6681
- Havens, J., and Spicer, T. O. (1990). “LNG Vapor Dispersion Prediction with the DEGADIS Dense Gas Dispersion Model,” Report GRI 89/0242 (United States: Gas Research Institute (GRI)).
- Hefny Salim, M., Heinke Schlünzen, K., and Grawe, D. (2015). Including Trees in the Numerical Simulations of the Wind Flow in Urban Areas: Should We Care? *J. Wind Eng. Ind. Aerodynamics* 144, 84–95. doi:10.1016/j.jweia.2015.05.004
- Hong, B., Qin, H., and Lin, B. (2018). Prediction of Wind Environment and Indoor/Outdoor Relationships for PM2.5 in Different Building–Tree Grouping Patterns. *Atmosphere* 9, 1–39. doi:10.3390/atmos9020039
- Hsieh, K-J., Lien, F-S., and Yee, E. (2013). Dense Gas Dispersion Modeling of CO₂ Released from Carbon Capture and Storage Infrastructure into a Complex Environment. *Int. J. Greenhouse Gas Control.* 17, 127–139. doi:10.1016/j.ijggc.2013.05.003
- IEA (2018). *World Energy Outlook 2018*. Paris: IEA. Available at: <https://www.iea.org/reports/world-energy-outlook-2018>.
- Jeanjean, A. P. R., Buccolieri, R., Eddy, J., Monks, P. S., and Leigh, R. J. (2017). Air Quality Affected by Trees in Real Street Canyons: The Case of Marylebone Neighbourhood in central London. *Urban Forestry & Urban Green.* 22, 41–53. doi:10.1016/j.ufug.2017.01.009
- Kukkonen, J., Nikmo, J., and Riikonen, K. (2017). An Improved Version of the Consequence Analysis Model for Chemical Emergencies. *ESCAPE Atmos. Environ.* 150, 198–209. doi:10.1016/j.atmosenv.2016.11.050
- Kumar, P., Feiz, A-A., Ngae, P., Singh, S. K., and Issartel, J-P. (2015). CFD Simulation of Short-Range Plume Dispersion from a point Release in an Urban like Environment. *Atmos. Environ.* 122, 645–656. doi:10.1016/j.atmosenv.2015.10.027
- Lauder, B. E., and Spalding, D. B. (1972). *Lectures in Mathematical Models of Turbulence*. (Waltham: Academic Press).
- Li, X-B., Lu, Q-C., Lu, S-J., He, H-D., Peng, Z-R., Gao, Y., et al. (2016). The Impacts of Roadside Vegetation Barriers on the Dispersion of Gaseous Traffic Pollution in Urban Street Canyons Urban. *For. Urban Green.* 17, 80–91. doi:10.1016/j.ufug.2016.03.006
- Liang, L., Xiaofeng, L., Borong, L., and Yingxin, Z. (2006). Simulation of Canopy Flows Using K-ε Two-Equation Turbulence Model Withsource/sink Terms. *Tsinghua Univ. (Sci. Tech.)* 46, 753–756. doi:10.16511/j.cnki.qhdxxb.2006.06.001
- Lipponen, J., Burnard, K., Beck, B., Gale, J., and Pegler, B. (2011). The IEA CCS Technology Roadmap. *One Year Energy. Proced.* 4, 5752–5761. doi:10.1016/j.egypro.2011.02.571
- Liu, B., Liu, X., Lu, C., Godbole, A., Michal, G., and Tieu, A. K. (2016). Computational Fluid Dynamics Simulation of Carbon Dioxide Dispersion in a Complex Environment. *J. Loss Prev. Process Industries* 40, 419–432. doi:10.1016/j.jlp.2016.01.017
- Liu, J., Zhang, X., Niu, J., and Tse, K. T. (2019a). Pedestrian-level Wind and Gust Around Buildings with a ‘lift-Up’ Design: Assessment of Influence from Surrounding Buildings by Adopting LES. *Building Simulation* 12, 1107–1118. doi:10.1007/s12273-019-0541-5
- Liu, X., Godbole, A., Lu, C., and Michal, G. (2017). Investigation of Terrain Effects on the Consequence Distance of CO₂ Released from High-Pressure Pipelines. *Int. J. Greenhouse Gas Control.* 66, 264–275. doi:10.1016/j.ijggc.2017.10.009
- Liu, X., Godbole, A., Lu, C., Michal, G., and Linton, V. (2019b). Investigation of the Consequence of High-Pressure CO₂ Pipeline Failure through Experimental and Numerical Studies. *Appl. Energy* 250, 32–47. doi:10.1016/j.apenergy.2019.05.017

- Liu, X., Godbole, A., Lu, C., Michal, G., and Venton, P. (2015). Optimisation of Dispersion Parameters of Gaussian Plume Model for CO₂ Dispersion. *Environ. Sci. Pollut. Res. Int.* 22, 18288–18299. doi:10.1007/s11356-015-5404-8
- Liu, Z., Zhou, Y., Huang, P., Sun, R., Wang, S., and Ma, X. (2012). Scaled Field Test for CO₂ Leakage and Dispersion from Pipelines. *J. Chem. Ind. Eng. (China)* 63, 1651–1659. doi:10.3969/j.issn.0438-1157.2012.05.046
- Luketa-Hanlin, A., Koopman, R. P., and Ermak, D. L. (2007). On the Application of Computational Fluid Dynamics Codes for Liquefied Natural Gas Dispersion. *J. Hazard. Mater.* 140, 504–517. doi:10.1016/j.jhazmat.2006.10.023
- Mazzoldi, A., Hill, T., and Colls, J. J. (2008). CFD and Gaussian Atmospheric Dispersion Models: A Comparison for Leak from Carbon Dioxide Transportation and Storage Facilities. *Atmos. Environ.* 42, 8046–8054. doi:10.1016/j.atmosenv.2008.06.038
- Meroney, R. N. (2010). *CFD Prediction of Dense Gas Clouds Spreading in a Mock Urban Environment, 5th International Symposium on Computational Wind Engineering (CWE2010)*. North Carolina, USA: Chapel Hill.
- Metz, B., Davidson, O., de Coninck, H., Loos, M., and Meyer, L. (2005). *IPCC Special Report on Carbon Dioxide Capture and Storage* United States. Available at <https://www.osti.gov/biblio/20740954>
- Mochida, A., Tabata, Y., Iwata, T., and Yoshino, H. (2008). Examining Tree Canopy Models for CFD Prediction of Wind Environment at Pedestrian Level. *J. Wind Eng. Ind. Aerodynamics* 96, 1667–1677. doi:10.1016/j.jweia.2008.02.055
- Moonen, P., Gromke, C., and Dorer, V. (2013). Performance Assessment of Large Eddy Simulation (LES) for Modeling Dispersion in an Urban Street canyon with Tree Planting. *Atmos. Environ.* 75, 66–76. doi:10.1016/j.atmosenv.2013.04.016
- Morales, A. I. G. C., Olano Mendoza, J. M., Eugenio Gozalbo, M., and Camarero Martínez, J. J. (2012). Arboreal and Prostrate Conifers Coexisting in Mediterranean High Mountains Differ in Their Climatic Responses. *Dendrochronologia* 30, 279–286. doi:10.1016/j.dendro.2012.02.004
- Myers-Smith, I. H., Elmendorf, S. C., Beck, P. S. A., Wilmsking, M., Hallinger, M., Blok, D., et al. (2015). Climate Sensitivity of Shrub Growth across the Tundra Biome. *Nat. Clim. Change* 5, 887–891. doi:10.1038/nclimate2697
- NIOSH (2005). *NIOSH Pocket Guide to Chemical Hazards, DHHS (NIOSH) Publication No. 2005-149* (Columbia Parkway: NIOSH Publications). Available at <https://www.cdc.gov/niosh/docs/2005-149/pdfs/2005-149.pdf>
- NOAA/EPA (1992). *ALOHA User's Manual and Theoretical Description*. Reports available from: NOAA/HMRAD, 7600 Sand Point Way NE, Seattle, WA 98115 and on CAMEO/ALOHA web site.
- Nowak, D. J., Hirabayashi, S., Bodine, A., and Hoehn, R. (2013). Modeled PM_{2.5} Removal by Trees in Ten U.S. Cities and Associated Health Effects. *Environ. Pollut.* 178, 395–402. doi:10.1016/j.envpol.2013.03.050
- Pellizzari, E., Camarero, J. J., Gazol, A., Granda, E., Shetti, R., Wilmsking, M., et al. (2017). Diverging Shrub and Tree Growth from the Polar to the Mediterranean Biomes across the European Continent. *Glob. Change Biol.* 23, 3169–3180. doi:10.1111/gcb.13577
- Peters, G. P., Andrew, R. M., Boden, T., Canadell, J. G., Ciais, P., Quere, C. L., et al. (2013). The challenge to Keep Global Warming below 2 °C. *Nat. Clim. Change* 3, 4–6. doi:10.1038/nclimate1783
- Peterson, E. W., and Hennessey, J. P. (1978). On the Use of Power Laws for Estimates of Wind Power Potential. *J. Appl. Meteorology* 17, 390–394. doi:10.1175/1520-0450(1978)017<0390:OTUOPL>2.0.CO;2
- Ryan, S. D., and Ripley, R. C. (2020). A Geometric Multigrid Treatment of Immersed Boundaries for Simulating Atmospheric Dispersion in Complex Urban Environments. *Atmos. Environ.* 237, 117685. doi:10.1016/j.atmosenv.2020.117685
- Sabatino, S. D., Buccolieri, R., Pappacogli, G., and Leo, L. S. (2015). The Effects of Trees on Micrometeorology in a Real Street canyon: Consequences for Local Air Quality. *Int. J. Environ. Pollut.* 58, 100–111. doi:10.1504/IJEP.2015.076587
- Simpson, S. M., Miner, S., Mazzola, T., and Meris, R. (2020). HPAC Model Studies of Selected Jack Rabbit II (JR II) Releases and Comparisons to Test Data. *Atmos. Environ.* 243, 117675. doi:10.1016/j.atmosenv.2020.117675
- Sklavounos, S., and Rigas, F. (2006). Simulation of Coyote Series Trials—Part I: CFD Estimation of Non-isothermal LNG Releases and Comparison with Box-Model Predictions. *Chem. Eng. Sci.* 61, 1434–1443. doi:10.1016/j.ces.2005.08.042
- Smagorinsky, J. (1963). GENERAL CIRCULATION EXPERIMENTS WITH THE PRIMITIVE EQUATIONS: I. THE BASIC EXPERIMENT*. *Monthly Weather Rev.* 91, 99–164. doi:10.1175/1520-0493(1963)091<0099:GCEWTP>2.3.CO;2
- Stabile, L., Arpino, F., Buonanno, G., Russi, A., and Frattolillo, A. (2015). A Simplified Benchmark of Ultrafine Particle Dispersion in Idealized Urban Street Canyons: A Wind Tunnel Study. *Building Environ.* 93, 186–198. doi:10.1016/j.buildenv.2015.05.045
- Takano, Y., and Moonen, P. (2013). On the Influence of Roof Shape on Flow and Dispersion in an Urban Street canyon. *J. Wind Eng. Ind. Aerodynamics* 123, 107–120. doi:10.1016/j.jweia.2013.10.006
- Tan, W., Wang, K., Li, C., Liu, L., Wang, Y., and Zhu, G. (2018). Experimental and Numerical Study on the Dispersion of Heavy Gases in Urban Environments. *Process Saf. Environ. Prot.* 116, 640–653. doi:10.1016/j.psep.2018.03.027
- Tauseef, S. M., Rashtchian, D., and Abbasi, S. A. (2011). CFD-based Simulation of Dense Gas Dispersion in Presence of Obstacles. *J. Loss Prev. Process Industries* 24, 371–376. doi:10.1016/j.jlp.2011.01.014
- Toja-Silva, F., Chen, J., Hachinger, S., and Hase, F. (2017). CFD Simulation of CO₂ Dispersion from Urban thermal Power Plant: Analysis of Turbulent Schmidt Number and Comparison with Gaussian Plume Model and Measurements. *J. Wind Eng. Ind. Aerodynamics* 169, 177–193. doi:10.1016/j.jweia.2017.07.015
- Tominaga, Y., and Stathopoulos, T. (2010). Numerical Simulation of Dispersion Around an Isolated Cubic Building: Model Evaluation of RANS and LES. *Building Environ.* 45, 2231–2239. doi:10.1016/j.buildenv.2010.04.004
- Vos, P. E. J., Maiheu, B., Vankerkom, J., and Janssen, S. (2013). Improving Local Air Quality in Cities: To Tree or Not to Tree? *Environ. Pollut.* 183, 113–122. doi:10.1016/j.envpol.2012.10.021
- Wang, H., Liu, B., Liu, X., Lu, C., Deng, J., and You, Z. (2021a). Dispersion of Carbon Dioxide Released from Buried High-Pressure Pipeline over Complex Terrain. *Environ. Sci. Pollut. Res.* 28, 1–14. doi:10.1007/s11356-020-11012-7
- Wang, J., Sun, S., Tang, L., Hu, G., and Liang, J. (2021b). On the Use of Metasurface for Vortex-Induced Vibration Suppression or Energy Harvesting. *Energ. Convers. Manage.* 235, 113991. doi:10.1016/j.enconman.2021.113991
- Wingstedt, E. M. M., Osnes, A. N., Åkervik, E., Eriksson, D., and Reif, B. A. P. (2017). Large-eddy Simulation of Dense Gas Dispersion over a Simplified Urban Area. *Atmos. Environ.* 152, 605–616. doi:10.1016/j.atmosenv.2016.12.039
- Wu, X., Zou, X., Zhou, N., Zhang, C., and Shi, S. (2015). Deceleration Efficiencies of Shrub Windbreaks in a Wind Tunnel. *Aeolian Res.* 16, 11–23. doi:10.1016/j.aeolia.2014.10.004
- Zhang, C. (2009). “Study on the Assessment and Remote Sensing Classification Technique of Shrub in Tibet.”. Doctoral dissertation.

Conflict of Interest: The authors declare that the research was conducted in the absence of any commercial or financial relationships that could be construed as a potential conflict of interest.

Copyright © 2021 Huiyu, Zhanping, Fan, Bin and Peng. This is an open-access article distributed under the terms of the Creative Commons Attribution License (CC BY). The use, distribution or reproduction in other forums is permitted, provided the original author(s) and the copyright owner(s) are credited and that the original publication in this journal is cited, in accordance with accepted academic practice. No use, distribution or reproduction is permitted which does not comply with these terms.



General Optimization Model of Modular Equipment Selection and Serialization for Shale Gas Field

Bingyuan Hong^{1*}, Xiaoping Li^{2*}, Xuemeng Cui², Jingjing Gao³, Yu Li⁴, Jing Gong² and Huanying Liu¹

¹School of Petrochemical Engineering and Environment, Zhejiang Ocean University, Zhoushan, China, ²National Engineering Laboratory for Pipeline Safety/ MOE Key Laboratory of Petroleum Engineering/ Beijing Key Laboratory of Urban Oil and Gas Distribution Technology, China University of Petroleum-Beijing, Beijing, China, ³Sinopec Qingdao Refining and Chemical CO. LTD, Qingdao, China, ⁴China National Oil and Gas Exploration and Development Corporation, Beijing, China

OPEN ACCESS

Edited by:

Jiang Bian,
China University of Petroleum, China

Reviewed by:

Yiming Zhao,
Dalian University of Technology, China
Dongxu Sun,
Liaoning Shihua University, China
Suyang Zhu,
Southwest Petroleum University,
China

*Correspondence:

Bingyuan Hong
hongby@zjou.edu.cn
Xiaoping Li
lxpmf@cup.edu.cn

Specialty section:

This article was submitted to
Advanced Clean Fuel Technologies,
a section of the journal
Frontiers in Energy Research

Received: 19 May 2021

Accepted: 15 June 2021

Published: 30 June 2021

Citation:

Hong B, Li X, Cui X, Gao J, Li Y, Gong J
and Liu H (2021) General Optimization
Model of Modular Equipment Selection
and Serialization for Shale Gas Field.
Front. Energy Res. 9:711974.
doi: 10.3389/fenrg.2021.711974

The potential technical and economic advantages and flexible operability of modular equipment make it increasingly widely used in gas field production and development. In addition to considering the manufacturing process, the selection and serialization of modular equipment should be made according to the productivity prediction of a gas well, so as to meet the field demand to the greatest extent and enhance the flexibility of gathering and transportation system. This article proposes a method to determine the use planning of modular equipment in shale gas field. Considering the processing capacity, processing cost, floor area, construction cost of modular equipment, and the changes of market supply and demand, an optimization model is established. On the basis of the abovementioned model, the method of serialization of modular equipment is proposed. The effectiveness of the model is verified by an actual case study. It is proved that the model can optimize the layout of modular equipment, make the modular equipment run efficiently and economically, reduce costs, and increase efficiency. This study provides a reference for optimizing the equipment management strategy and promoting green production practice of shale gas production.

Keywords: shale gas, MILP model, modular equipment, capacity selection, equipment serialization

INTRODUCTION

Shale gas revolution has greatly promoted the transformation of energy structure Gao and You (2017b), which is of great strategic significance to the goal of carbon neutrality and has been widely concerned (Fan et al., 2021; Shi et al., 2021). However, with the rapid decline of shale gas production capacity, the load rate and various operating conditions of the equipment are constantly changing (Hong et al., 2019; 2020a). Traditional fixed equipment is difficult to disassemble once installed, which makes it lack flexibility to adapt to the changes of production capacity, and it is difficult to work continuously in the efficient working area (Zhou et al., 2019). On the contrary, due to the characteristics of small floor area, convenient disassembly and assembly, being easy to move, and low development risk, modular equipment can better adapt to the changing production capacity (Gao and You, 2017a; Yang and You, 2018), showing great potential, and is expected to be widely used in all aspects of oil and gas development, production, and processing (Yin et al., 2018; Hong et al., 2020b).

Many scholars are committed to the economic research and process design of modular equipment. Baldea et al. (2017) summarized the status, challenges, and opportunities of modular

manufacturing processes and proposed the concept of value density to represent the geographical distribution of raw materials or markets absorbing products. The opportunity of modular manufacturing is related to value density, and it can reduce the scale of unit operation and improve efficiency by means of process strengthening. Tian et al. (2018) conducted a research on the most advanced method of process enhancement, process systems engineering, focusing on some recent advances in the modeling, design, and synthesis of enhanced systems, which can be used to develop larger-scale modularization equipment. Demirel et al. (2017) designed a process intensification method based on the basic components, which is opposite to the traditional flow chart. The method establishes a single mixed integer nonlinear optimization model to solve the problem for systematic process design and intensification. In addition, the economics and flexibility of a modular chemical plant is compared with traditional large-scale factories by investigating net present value (Lier and Grünewald, 2011). Palys et al. (2019) studied the economic benefits of traditional continuous and modular wind power ammonia production and proved the advantages of modular equipment from a quantitative perspective. Compared with continuous production, modular production leads to lower supply chain costs and more renewable energy integration. A new process obtaining input from the relatively old natural-gas-based process is specially designed for small-scale ammonia production and is combined with the recently developed dual fluidized bed technology for biomass feedstock. The results show that the small-scale ammonia plant based on biomass has more technical and economic advantages (Arora et al., 2016). Technical and economic analysis and environmental impact analysis were carried out on the four shale gas monetization schemes, and their economic and environmental benefits under the same conditions were systematically compared (Yang and You, 2018). The results show that modular methanol production is more economically competitive than traditional shale gas processing, although it will cause a higher environmental impact.

The above mentioned research shows that modular equipment has unique economic advantages and flexible operability, which provides a new perspective for the use of modular equipment. However, there is little research on the optimization methods of modular equipment selection and serialization in shale gas field. In the production of shale gas field, the layout combination and operation scheme of modular equipment can be optimized according to the change of gas field production, so as to realize efficient and economic operation. The serialization of the processing capacity of modular equipment refers to the scientific planning of the processing capacity sequence of the same modular equipment. The purpose is to optimize, simplify, and stereotype the bulk, common, and repetitive production and construction content, which is conducive to reducing engineering costs, improving the interoperability of equipment, and at the same time, facilitating production management. Therefore, a method to select and serialize modular equipment based on changes in gas well productivity needs to be further studied.

Therefore, this article proposes a method to determine the use planning of modular equipment in shale gas field. Considering

the processing capacity, processing cost, floor area, construction cost of modular equipment, and the changes of market supply and demand, an optimization model is established. On the basis of the abovementioned model, the method of serialization of modular equipment is proposed. The effectiveness of the model is verified by an actual case study. It is proved that the model can optimize the layout of modular equipment, make the modular equipment run efficiently and economically, reduce costs, and increase efficiency.

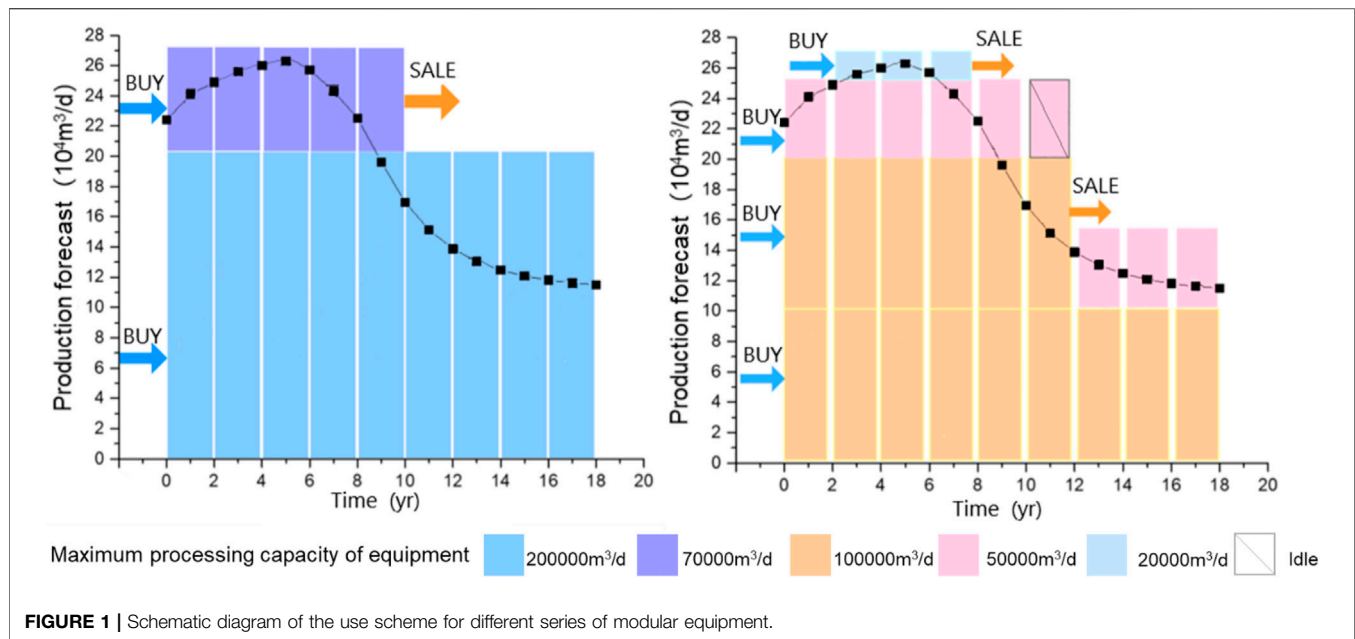
The structure of this article is as follows. In *Problem Description*, the optimization problem is explained in detail, including the basic parameters and decision variables. *Mathematical Model* shows the proposed optimization mathematical model. *Case Study* verifies the practicability of the proposed optimization model through case analysis and compares the modular and traditional methods. Finally, the conclusion and future research prospects are drawn.

PROBLEM DESCRIPTION

As mentioned above, modular equipment has more flexible processing capabilities and can achieve changes in processing scale. The production capacity of shale gas has changed drastically, with high production output in the initial stage and then rapidly declining. Therefore, modularization is more promising for the stable production of shale gas. The main purpose of this study is to propose an optimization model to determine the optimal selection and serialization of modular equipment for shale gas field. However, it should be noted that the productivity curve is considered in this model, which is applicable to all oil and gas fields and is universal, not limited to shale gas fields. The problems to be solved are stated as follows, taking the gas field as an example:

As mentioned above, modular equipment has potential technical and economic advantages and can be used in gas field development. As shown in **Figure 1**, for the same gas field, the gas reservoir engineering provides production capacity prediction, and there is a variety of different modular equipment usage plans throughout the life cycle of gas field development. Specifically, scheme 1 uses modular equipment with two processing capacity specifications of 70,000 m³/day and 200,000 m³/day, while scheme 2 uses modular equipment with three processing capacity specifications of 20,000 m³/day, 50,000 m³/day, and 100,000 m³/day. The adjustment of processing capacity is carried out through the purchase and sale of equipment in both schemes. Among many schemes, there must be one that can maximize the profit of the gas field. Decision makers need to decide how to replan and deploy modular equipment based on the time-varying production capacity forecast and market demand.

The processing capacity sequence of the modular equipment must be both economical and versatile. Different equipment have their own economic boundaries, so the capacity series of equipment should be made according to the changes of productivity curves of different gas fields, and the customization and universality of equipment should be chosen



to realize the economy and universality of equipment. For example, if a natural gas flow of $10,000 \text{ m}^3/\text{d}$ needs to be processed, it is more economical to choose equipment with a rated capacity of $10,000 \text{ m}^3/\text{d}$ than equipment with a rated capacity of $50,000 \text{ m}^3/\text{d}$. Universality means that a single piece of equipment in the serialized equipment should be more commonly used, and the serialized equipment as a whole means that, through a reasonable combination, it should be able to cover the needs of common capacity planning schemes. For example, the need to process a flow rate of $500,000 \text{ m}^3/\text{d}$ of natural gas can be achieved by two pieces of equipment with a rated capacity of $250,000 \text{ m}^3/\text{d}$ or by 50 pieces of equipment with a rated capacity of $10,000 \text{ m}^3/\text{d}$, while the latter will obviously cause maintenance problems for site personnel. Therefore, it is necessary to carry out research to seek the optimal selection and serialization of modular equipment in oil and gas field development, so as to improve the economic benefits of oil and gas field development.

In order to facilitate modeling and improve the efficiency of model solving, the following assumptions are proposed:

- ① The whole life cycle of gas field development is divided into a series of equal length discrete unit periods. It is assumed that the gas field production does not change in the unit period.
- ② The equipment is allowed to run beyond the scheduled life, but the equipment running beyond the scheduled life will incur additional operation and maintenance costs.
- ③ In this work, the purchase, sale, disassembly, and assembly of the equipment can be completed within a period of time. It is assumed that each equipment can be manufactured in the current period and no appointment is required in advance.
- ④ The variable operating cost depends on the gas processing capacity and unit processing cost, and it is considered that the unit processing cost of similar modular equipment is the same.

Given:

- ① Productivity information: the gas well production proposed by gas well production prediction
- ② Economic information: price of qualified natural gas in different periods
- ③ Equipment information: processing capacity, purchase, installation, disassembly, operation, and overdue maintenance cost of modular equipment with different processing capacities

Determine:

- ① Equipment usage planning: the equipment type, number, operation status (actual processing capacity) and installation, disassembly, and sale measures in different periods
- ② Economic cost: the net present value in different periods, the equipment purchase, sale, disassembly, operation, and over-term maintenance costs in different periods

MATHEMATICAL MODEL

All the known parameters involved in the proposed model are represented by symbols composed of lowercase letters, and variables are represented by symbols beginning with capital letters. $i \in (1, \dots, I)$ stands for the set of equipment specification types, $e \in (1, \dots, E)$ represents the number set of equipment, and $t, tb \in (1, \dots, T)$ is used to define the time periods over the given planning horizon.

Objective Function

Net present value is an important technical and economic index to evaluate the profitability of investment. Therefore, the

objective function is to maximize the net present value in the whole development cycle.

$$NPV = \sum_{t \in T} C_t \times (1+r)^{1-t}, \quad (1)$$

where NPV is the net present value, C_t is the cash flow in period t , and r is the discount rate.

Model Constraints

Economic Constraints

The cash flow (C_t) in period t consists of six parts: income from selling qualified products ($Igas_t$), income from selling used modular equipment ($Iequ_t$), expenses for purchasing modular equipment ($Ebuy_t$), expenses for installing modular equipment ($Eins_t$), expenses for dismantling modular equipment ($Edis_t$), expenses for operating modular equipment ($Eope_t$), and expenses for maintenance of overdue modular equipment ($Emai_t$).

$$C_t = Igas_t + Iequ_t - Ebuy_t - Eins_t - Edis_t - Eope_t - Emai_t \quad \forall t \in T. \quad (2)$$

The income from selling qualified products ($Igas_t$) is equal to the price ($pgas_t$) multiplied by the output. The output is equal to the total gas flow rate received by all equipment (q_t) multiplied by the ratio of the equipment outlet flow rate and the inlet flow rate (ra).

$$Igas_t = pgas_t \cdot q_t \cdot ra \quad \forall t \in T. \quad (3)$$

The income from selling used modular equipment ($Iequ_t$) is the sum of the selling income ($ELequ_{t,i,e}$) of each i -type e -numbered equipment. $eb_{i,e}$ is the origin purchase price of i -type e -numbered equipment. Service life affects equipment depreciation, and $deq_{t,tb}$ is employed to characterize the selling coefficient. The binary variable ($Bs_{t,i,e,tb}$) determines whether i -type e -numbered equipment is to be sold or not. If the i -type e -numbered equipment purchased in tb period is sold in t period, then $Bs_{t,i,e,tb} = 1$; otherwise, $Bs_{t,i,e,tb} = 0$.

$$Iequ_t = \sum_{i \in I} \sum_{e \in E} ELequ_{t,i,e} \quad \forall t \in T, \quad (4)$$

$$ELequ_{t,i,e} = \sum_{tb \leq t} eb_{i,e} \times Bs_{t,i,e,tb} \times deq_{t,tb} \quad \forall t \in T, i \in I, e \in E. \quad (5)$$

The expenses for purchasing modular equipment ($Ebuy_t$) are the sum of the purchase cost of each i -type e -numbered equipment ($EEbuy_t$). The binary variable ($Bb_{t,i,e}$) determines whether to buy i -type e -numbered equipment. If the i -type e -numbered equipment purchased is purchased in t period, then $Bb_{t,i,e} = 1$; otherwise, $Bb_{t,i,e} = 0$.

$$Ebuy_t = \sum_{i \in I} \sum_{e \in E} EEbuy_{t,i,e} \quad \forall t \in T, \quad (6)$$

$$EEbuy_{t,i,e} = eb_{i,e} \times Bb_{t,i,e} \quad \forall t \in T, i \in I, e \in E. \quad (7)$$

Installation is required when buying new equipment, and disassembly is required when selling used equipment. Similarly, the expenses for installing modular equipment

($Eins_t$) and the expenses for dismantling modular equipment ($Edis_t$) are the sum of according cost of each i -type e -numbered equipment. $eins_{i,e}$ is the cost of installation, and $edis_{i,e}$ is the cost of disassembly.

$$Eins_t = \sum_{i \in I} \sum_{e \in E} eins_{i,e} \times Bb_{t,i,e} \quad \forall t \in T, \quad (8)$$

$$Edis_t = \sum_{i \in I} \sum_{e \in E} \sum_{tb \leq t} edis_{i,e} \cdot Bs_{t,i,e,tb} \quad \forall t \in T. \quad (9)$$

The expenses for operating modular equipment ($Eope_t$) are the sum of ones of each i -type e -numbered equipment ($EEope_t$), which is related to the actual flow rate of the equipment ($Qa_{t,i,e}$). $\alpha_{i,e}$ is the processing cost per unit of original natural gas, and $\beta_{i,e}$ is the fixed cost of the equipment. $B_{t,i,e,tb}$ is a binary variable of the device state. If the i -type e -numbered equipment purchased in period tb still exists in period t , then $B_{t,i,e,tb} = 1$; otherwise, $B_{t,i,e,tb} = 0$.

$$Eope_t = \sum_{i \in I} \sum_{e \in E} EEope_{t,i,e} \quad \forall t \in T, \quad (10)$$

$$EEope_{t,i,e} = \alpha_{i,e} \times Qa_{t,i,e} + \beta_{i,e} \times \sum_{tb \leq t} B_{t,i,e,tb} \quad t \in T, i \in I, e \in E. \quad (11)$$

The expenses for maintenance of overdue modular equipment ($Emai_t$) depend on the amount of equipment that needs to be repaired and maintained. $emt_{i,e}$ is the base cost of equipment maintenance, and $meq_{t,tb}$ is employed to characterize the maintenance coefficient; the longer the service life, the higher the cost of equipment maintenance.

$$Emai_t = \sum_{i \in I} \sum_{e \in E} EEmai_{t,i,e} \quad \forall t \in T, \quad (12)$$

$$EEmai_{t,i,e} = \sum_{tb \leq t} emt_{i,e} \times B_{t,i,e,tb} \times meq_{t,tb} \quad t \in T, i \in I, e \in E. \quad (13)$$

Equipment Capacity Constraints

Each equipment has its own rated flow ($qecap_{i,e}$) and is allowed to work within a certain range of rated flow. aq_{max} and aq_{min} are flow coefficients used to represent the fluctuation range of relative rated capacity. $B_{t,i,e,tb}$ is a binary variable of the device state. If the i -type e -numbered equipment is purchased in period tb and is working in period t , then $Bu_{t,i,e,tb} = 1$; otherwise, $Bu_{t,i,e,tb} = 0$.

$$Qa_{t,i,e} \leq aq_{max} \cdot qecap_{i,e} \cdot \sum_{tb \leq t} Bu_{t,i,e,tb} \quad \forall t \in T, i \in I, e \in E, \quad (14)$$

$$Qa_{t,i,e} \geq aq_{min} \cdot qecap_{i,e} \cdot \sum_{tb \leq t} Bu_{t,i,e,tb} \quad \forall t \in T, i \in I, e \in E. \quad (15)$$

The sum of the actual processing capacity of each equipment is equal to the gas field production.

$$\sum_{i \in I} \sum_{e \in E} Qa_{t,i,e} = q_t \quad \forall w \in W, t \in T. \quad (16)$$

The total footprint of the equipment should be smaller than the available area of the gas field (sw_{max}).

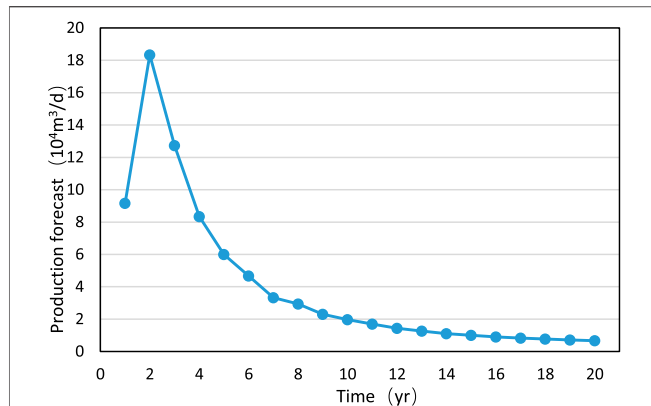


FIGURE 2 | The gas production forecast of the gas well.

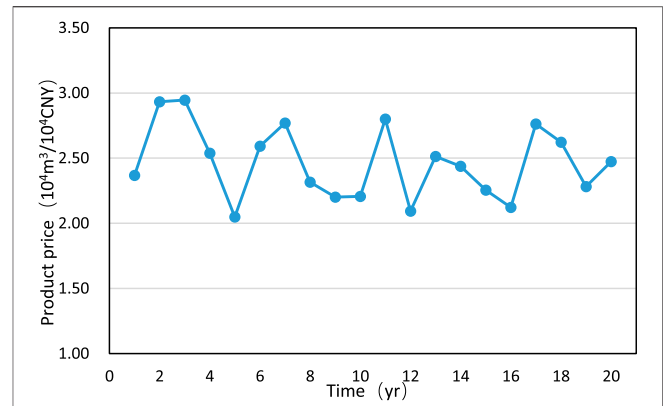


FIGURE 3 | The price of qualified natural gas.

$$\sum_{i \in I} \sum_{e \in E} \sum_{tb \leq t} B_{t,i,e,tb} \cdot es_{i,e} \leq sw_{max}. \quad (17)$$

Equipment Selection Constraints

Two subscripts are used to indicate the time state of the equipment; tb indicates the time the equipment was purchased, and t indicates the current time.

When $t < tb$, there is no equipment that has been purchased, so there is no equipment that can be sold.

$$B_{t,i,e,tb} = Bb_{t,i,e} \quad \forall t, tb \in T, i \in I, e \in E, \quad (18)$$

$$Bs_{t,i,e,tb} = 0 \quad \forall t, tb \in T, i \in I, e \in E. \quad (19)$$

When $t = tb$, the equipment is new at this time.

$$B_{t,i,e,tb} = Bb_{t,i,e} \quad \forall t, tb \in T, i \in I, e \in E. \quad (20)$$

When $t > tb$, the current number of equipment ($B_{t,i,e,tb}$) is equal to the equipment owned in the previous period ($b_{t-1,i,e,tb}$) minus the equipment sold at the moment ($Bs_{t,i,e,tb}$).

$$B_{t,i,e,tb} = B_{t-1,i,e,tb} - Bs_{t,i,e,tb} \quad \forall t, tb \in T, i \in I, e \in E. \quad (21)$$

Each device is purchased and sold at most once in the entire life cycle.

$$\sum_{t \in T} Bb_{t,i,e} \leq 1 \quad \forall i \in I, e \in E, \quad (22)$$

$$\sum_{t \in T} \sum_{tb \leq t} Bs_{t,i,e,tb} \leq 1 \quad \forall i \in I, e \in E. \quad (23)$$

When $t = t1$, no equipment is allowed to be sold in the first cycle.

$$Bs_{t,i,e,tb} = 0 \quad \forall t, tb \in T, i \in I, e \in E. \quad (24)$$

In addition, the sold equipment must be existing.

$$B_{t-1,i,e,tb} \geq Bs_{t,i,e,tb} \quad \forall t, tb \in T, i \in I, e \in E. \quad (25)$$

An existing equipment may be in use or may be out of service.

$$Bu_{t,i,e,tb} \leq B_{t,i,e,tb}. \quad (26)$$

CASE STUDY

Taking an actual gas field in Sichuan China as an example, equipment selection and serialization was carried out and compared with traditional methods to verify the effectiveness of the model. The program is written with gams software, and the commercial solver Gurobi is called to solve the problem, running on a 4-core 8-thread Intel CPU i7-6700 (2.6 GHz) and 16 GB memory computer. It is important to note that the optimization model proposed in this article has no special limitation on the type of production capacity prediction and equipment type, it is universal, and its application is not limited to any specific type of oil and gas fields.

Basic Parameters

The gas field is located in a certain place in Sichuan. According to the gas production forecast of the gas well, the gas production of the gas field changes with time, as shown in **Figure 2**. The output of the block reached its peak in the early stage of development and then declined rapidly. In addition, the price of qualified natural gas is shown in **Figure 3**.

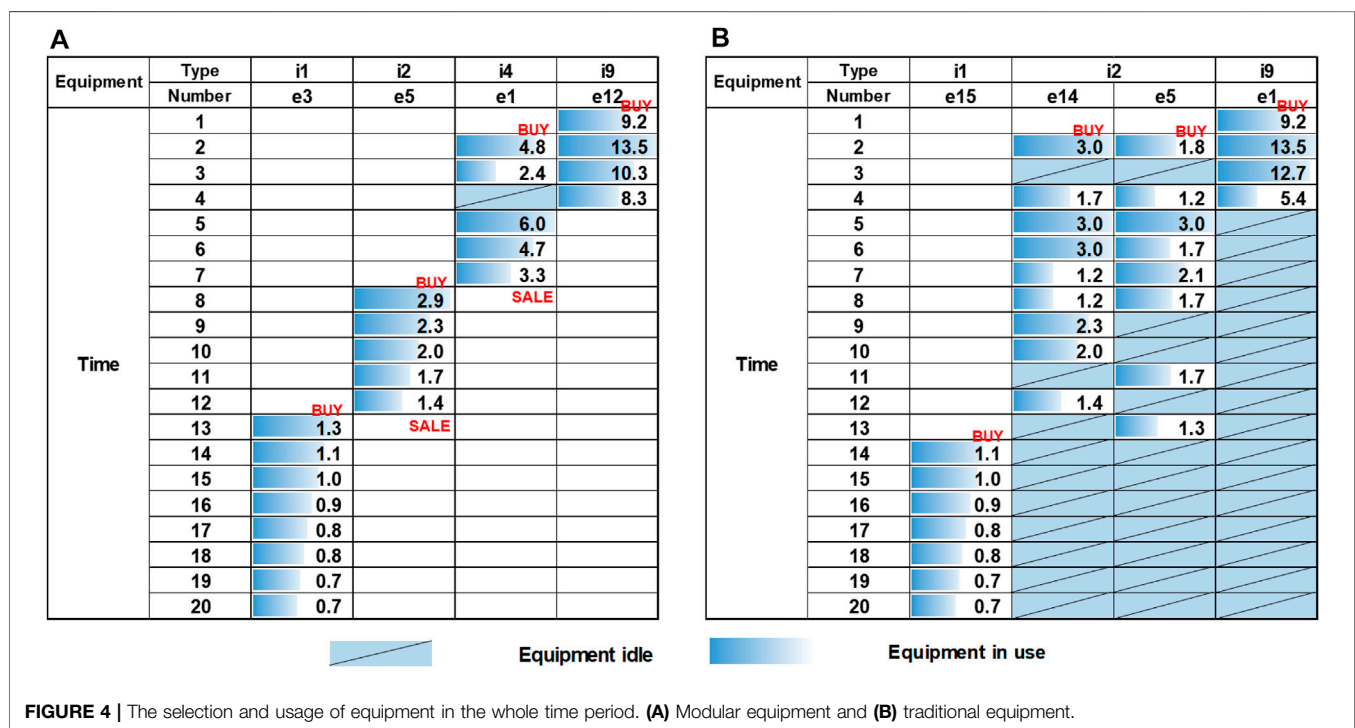
Modular TEG dehydration equipment is needed in the gas gathering station, and the annual fixed operating cost of each equipment is 2.5% of the purchase cost. The variable operating cost depends on the gas processing capacity and unit processing cost, and it is considered that the unit processing cost of similar modular equipment is the same. According to production practice, the purchase cost of 50,000 m³/d modular TEG dehydration equipment is 500,000 CNY, and the purchase cost of the same type of modular equipment of other scales is calculated according to the six-tenth rule widely used in the chemical industry (Hong et al., 2020b). In addition, based on data from gas field, the purchase cost of traditional fixed treatment equipment is 1.3 times that of modular equipment, and other cost parameters are the same as those for modular equipment. Therefore, equipment parameters are as shown in **Table 1**.

Equipment Selection

The results of the following equipment selection analysis show the optimized usage of the equipment. It can be seen that, among

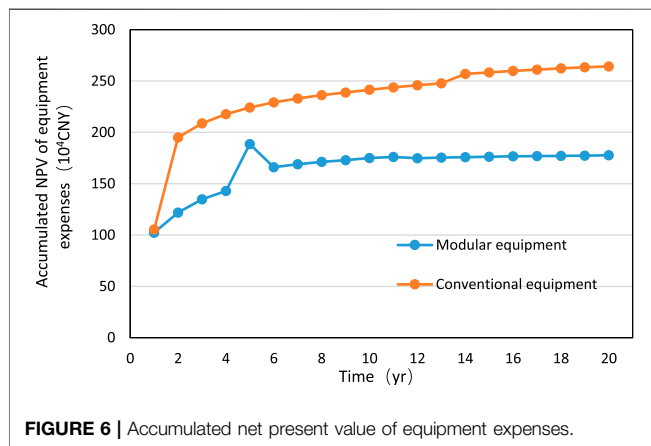
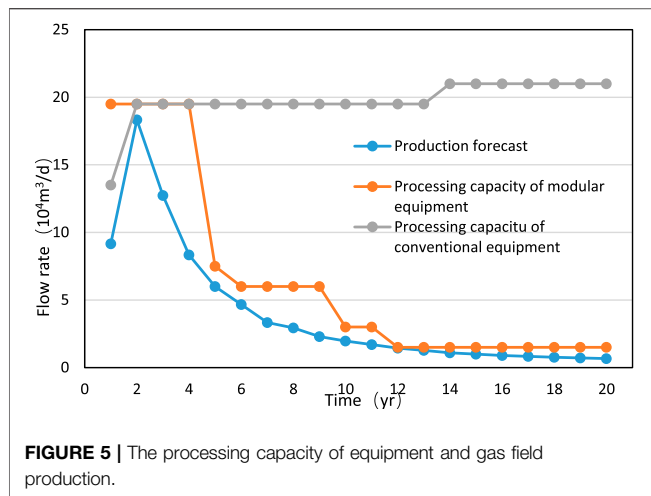
TABLE 1 | Equipment parameters.

Modular equipment type	Rated processing capacity ($q_{cap_{i,e}}$) [$10^4 \text{ m}^3/\text{d}$]	Equipment purchase cost ($ceb_{i,e}$) [10^4 CNY]	Variable operating cost ($a_{i,e}$) [$10^4 \text{ CNY}/10^4 \text{ m}^3$]	Fixed operating cost ($b_{i,e}$) [$10^4 \text{ CNY}/\text{yr}$]	Installation and disassembly expenses ($ceins_{i,e}$, $cedis_{i,e}$) [10^4 CNY]	Floor area ($es_{i,e}$) [m^2]
i1	1	19.04	0.003	0.05	0.38	12
i2	2	28.85	0.003	0.07	0.58	15
i3	3	36.80	0.003	0.09	0.74	21
i4	4	43.73	0.003	0.11	0.87	27
i5	5	50.00	0.003	0.13	1.00	34
i6	6	55.78	0.003	0.14	1.12	37
i7	7	61.19	0.003	0.15	1.22	41
i8	8	66.29	0.003	0.17	1.33	44
i9	9	71.14	0.003	0.18	1.42	49
i10	10	75.79	0.003	0.19	1.52	55
i11	11	80.25	0.003	0.20	1.60	58
i12	12	84.55	0.003	0.21	1.69	62
i13	13	88.71	0.003	0.22	1.77	66
i14	14	92.74	0.003	0.23	1.85	67
i15	15	96.66	0.003	0.24	1.93	72
i16	16	100.48	0.003	0.25	2.01	74
i17	17	104.20	0.003	0.26	2.08	77
i18	18	107.83	0.003	0.27	2.16	81
i19	19	111.39	0.003	0.28	2.23	83
i20	20	114.87	0.003	0.29	2.30	86

**FIGURE 4** | The selection and usage of equipment in the whole time period. **(A)** Modular equipment and **(B)** traditional equipment.

the 20 different processing capacity equipment, four modular equipment, (i1, e3), (i2, e5), (i4, e1), and (i9, e12), are selected. As shown in **Figure 4**, each number in the grid represents the actual processing flowrate of a modular equipment, and the shade intensity reflects the equipment load rate, that is, the ratio of the actual processing flowrate to the maximum processing

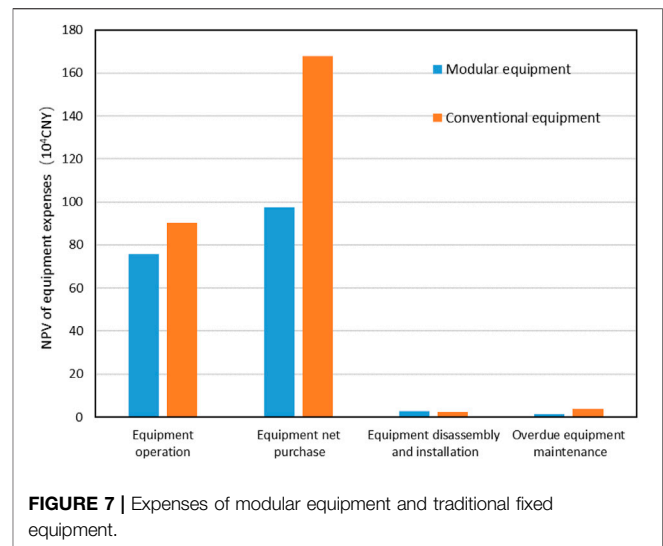
flowrate. For more information on the definition and calculation method of load rate, it is recommended to refer to our previous research (Hong et al., 2020b). The load rate of modular equipment is greatly improved from 0.20 to 0.62 compared with traditional fixed equipment. Each modular equipment is allocated to different locations according to



scheduling requirements. Among them, equipment (i2, e5), (i4, e1), and (i9, e12) are sold because they cannot be used, which can save investment. However, the traditional fixed equipment cannot be sold, so it can only stop operating, resulting in idle processing capacity.

The relationship of the equipment processing capacity and the gas field production in each block is shown in **Figure 5**. When the output of the gas source began to decline after the second period, the traditional fixed equipment has a lot of redundancy in processing capacity because it is not detachable. On the contrary, modular equipment can avoid this problem through the sale of equipment. The processing capacity of modular equipment changes throughout the life cycle of the gas field and is closely related to the change of gas production, so it is more flexible and has the ability to adapt to the fluctuation of gas field production. It is foreseeable that if there are multiple gas fields, equipment scheduling among multiple gas fields will help further increase the flexibility of production and reduce costs.

Figure 6 shows the accumulated net present value of equipment expenses using modular equipment and traditional fixed equipment, while the accumulated net present value of



equipment expenditure of modular equipment is less than that of conventional equipment.

The specific expenses of modular equipment and traditional fixed equipment are shown in **Figure 7**. The biggest expenditure is equipment operating cost and equipment purchase cost, while the proportion of equipment installation is very small. The economy of modular equipment is mainly reflected in the sharp reduction of equipment net purchase cost caused by the equipment resale.

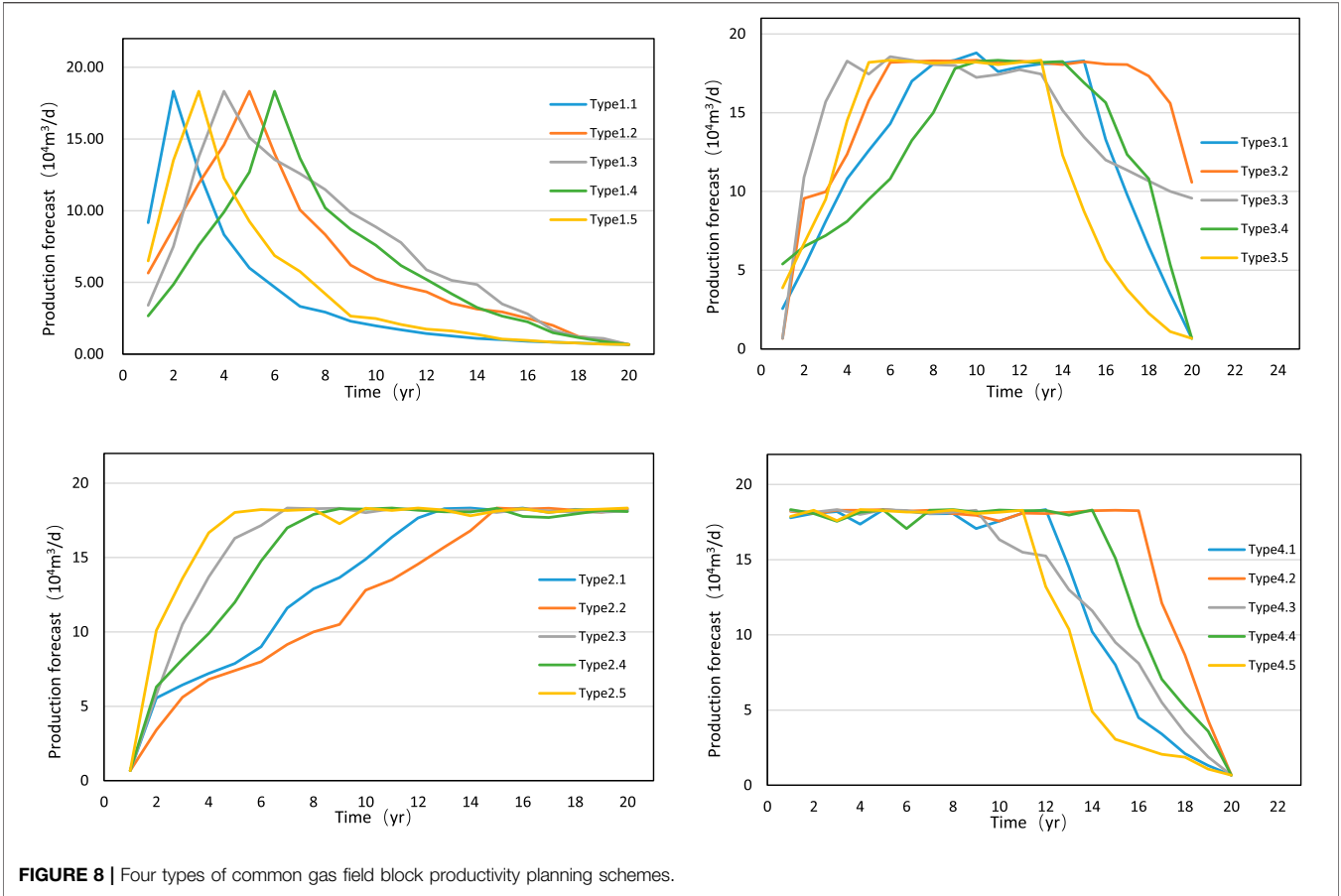
Equipment Serialization

The processing capacity sequence of the modular equipment must be both economical and universal. The optimization model of modular equipment capacity selection proposed in this article is precisely to determine the modular equipment arrangement and operation scheme with the best economic efficiency as the goal, but the universality of the equipment use scheme needs further analysis. In general, the serialization of capacity specifications should be balanced between universality and economy. An analysis method is proposed in the following.

Figure 8 shows four types of common gas field block productivity planning schemes, each with multiple production characteristics. Type 1, 2, 3, and 4 are the common productivity planning schemes in the early centralized development mode of unconventional gas field, in the early stage of long-term stable production development mode, in the whole cycle of long-term stable production development mode, and in the late stage of long-term stable production development mode, respectively.

Figure 9 shows the optimal serialization of modular equipment for the abovementioned four types of productivity planning schemes using the proposed optimization model. It can be seen that all serializations are a combination of several small-scale equipment and one medium processing capacity equipment or large-scale processing equipment.

In order to define the universality of the processing capacity sequence, the use frequency of modular equipment in the abovementioned optimal scheme is analyzed as shown in



Production forecast type	Number of equipment																				
	Small processing capacity						Medium processing capacity						Large processing capacity								
	i1	i2	i3	i4	i5	Total	Average	i6	i7	i8	i9	i10	Total	Average	i11	i12	i13	i14	Total	Average	
1.1	1	1		1		3	2.3				1		1	0.6					0	0.4	
1.2	2		1	1		4		1					1								0
1.3	2				1	3				1			1								0
1.4	2		1	1		4		1					1								0
1.5	1	1			1	3					1		1								0
2.1	1				1	2					1		1								0
2.2	1				1	2				1			1								0
2.3	1				1	2					1		1								0
2.4	3					3						1	1								0
2.5	1					1							0				1				1
3.1				1		1					1		1								0
3.2	1					1							0				1				1
3.3	1					1							0				1				1
3.4	1				1	2				1			1								0
3.5	2		1			3						1	1								0
4.1	1		1			2						0			1			1			
4.2	1	1				2						0				1		1			
4.3	2	1				3						0				1		1			
4.4	1				1	2						0					1	1			
4.5	1		1			2						0			1			1			

FIGURE 9 | Optimal serialization of modular equipment.

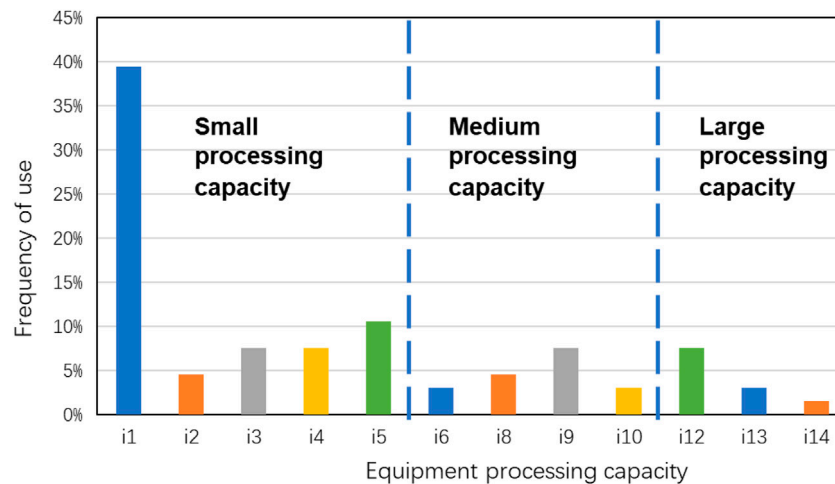


FIGURE 10 | Use frequency of modular equipment.

Figure 10. Because the small processing capacity equipment is used more frequently, the two types with the highest chosen frequency are selected, i1 and i5. For the medium processing capacity and the high-processing equipment, i9 and i12 are the two types with the highest chosen frequency.

Analyzing the selected equipment series, i1, i5, i9, and i12, the processing capacity corresponds to 10,000 m³/d, 50,000 m³/d, 90,000 m³/d, and 120,000 m³/d, respectively. The reasonable combination of these types of equipment can cover the demand of all the abovementioned capacity planning schemes, so the selected equipment series is universal enough. Therefore, under the conditions of the economic parameters and the production mode of the gas field described in this example, the processing capacities of the final selected specific type of modular TEG dehydration equipment are 10,000 m³/d, 50,000 m³/d, 90,000 m³/d, and 120,000 m³/d.

CONCLUSION

The main purpose of this study is to propose an optimization model to determine the optimal selection and serialization of modular equipment for shale gas field. Considering the processing capacity, processing cost, floor area, construction cost of modular equipment, and the changes of market supply and demand, a multiperiod optimization model is established, taking the maximum net present value as the objective function. In the modeling, the variable subscript couples the equipment type and number, which can realize the unique coding of the equipment, so as to track the use status of the specific equipment. It should be noted that the productivity curve is considered in this model, which is applicable to all oil and gas fields and is universal, not limited to shale gas fields.

An actual gas field in Sichuan, China, is employed to verify the practicability and effectiveness of the proposed model. Compared with traditional fixed equipment, modular equipment is allocated to different locations according to scheduling requirements and has the

ability to adapt to the fluctuation of gas field production. The accumulated net present value of equipment expenditure of modular equipment is less than that of conventional equipment, and the load rate of modular equipment is greatly improved from 0.20 to 0.62. On the basis of the abovementioned model, the method of serialization of modular equipment is proposed. Considering four types of common gas field block productivity planning schemes, the use frequency of different specifications modular equipment is analyzed to determine optimal equipment series; the processing capacities of the final selected specific type of modular TEG dehydration equipment are 10,000 m³/d, 50,000 m³/d, 90,000 m³/d, and 120,000 m³/d.

This study proves that the model can optimize the layout of modular equipment, make the modular equipment run efficiently and economically, and reduce costs and increase efficiency, providing a reference for optimizing the equipment management strategy and promoting green production practice of shale gas production. An interesting topic is to investigate modular equipment dynamic allocation among multiple gas fields. In the future, we will carry out new research to propose an MILP optimization model to make the dynamic scheduling of modular equipment in the whole life cycle of shale gas development.

DATA AVAILABILITY STATEMENT

The original contributions presented in the study are included in the article/supplementary material; further inquiries can be directed to the corresponding authors.

AUTHOR CONTRIBUTIONS

BH and XL provided the idea. BH, XC, and JGa designed the research. BH and JGo carried out the literature search. BH, YL, and HL drafted the manuscript. All authors contributed to the article and approved the submitted version.

FUNDING

This work was supported by the National Science and Technology Major Project of China (2016ZX05066005-001), National Natural Science Foundation of China

(51874323), Zhejiang Province Key Research and Development Plan (2021C03152), Zhoushan Science and Technology Project (2021C21011), and Science Foundation of Zhejiang Ocean University (11025090721), all of which are gratefully acknowledged.

REFERENCES

- Arora, P., Hoadley, A. F. A., Mahajani, S. M., and Ganesh, A. (2016). Small-Scale Ammonia Production from Biomass: A Techno-Enviro-Economic Perspective. *Ind. Eng. Chem. Res.* 55, 6422–6434. doi:10.1021/acs.iecr.5b04937
- Baldea, M., Edgar, T. F., Stanley, B. L., and Kiss, A. A. (2017). Modular Manufacturing Processes: Status, Challenges, and Opportunities. *Aiche J.* 63, 4262–4272. doi:10.1002/aic.15872
- Demirel, S. E., Li, J., and Hasan, M. M. F. (2017). Systematic Process Intensification Using Building Blocks. *Comput. Chem. Eng.* 105, 2–38. doi:10.1016/j.compchemeng.2017.01.044
- Fan, D., Gong, J., Zhang, S., Shi, G., Kang, Q., Xiao, Y., et al. (2021). A Transient Composition Tracking Method for Natural Gas Pipe Networks. *Energy* 215, 119131. doi:10.1016/j.energy.2020.119131
- Gao, J., and You, F. (2017a). Can Modular Manufacturing Be the Next Game-Changer in Shale Gas Supply Chain Design and Operations for Economic and Environmental Sustainability?. *ACS Sust. Chem. Eng.* 5, 10046–10071. doi:10.1021/acssuschemeng.7b02081
- Gao, J., and You, F. (2017b). Design and Optimization of Shale Gas Energy Systems: Overview, Research Challenges, and Future Directions. *Comput. Chem. Eng.* 106, 699–718. doi:10.1016/j.compchemeng.2017.01.032
- Hong, B., Li, X., Di, G., Li, Y., Liu, X., Chen, S., et al. (2019). An Integrated MILP Method for Gathering Pipeline Networks Considering Hydraulic Characteristics. *Chem. Eng. Res. Des.* 152, 320–335. doi:10.1016/j.cherd.2019.08.013
- Hong, B., Li, X., Di, G., Song, S., Yu, W., Chen, S., et al. (2020a). An Integrated MILP Model for Optimal Planning of Multi-Period Onshore Gas Field Gathering Pipeline System. *Comput. Ind. Eng.* 146, 106479. doi:10.1016/j.cie.2020.106479
- Hong, B., Li, X., Song, S., Chen, S., Zhao, C., and Gong, J. (2020b). Optimal Planning and Modular Infrastructure Dynamic Allocation for Shale Gas Production. *Appl. Energy* 261, 114439. doi:10.1016/j.apenergy.2019.114439
- Lier, S., and Grünewald, M. (2011). Net Present Value Analysis of Modular Chemical Production Plants. *Chem. Eng. Technol.* 34, 809–816. doi:10.1002/ceat.201000380
- Palys, M. J., Allman, A., and Daoutidis, P. (2019). Exploring the Benefits of Modular Renewable-Powered Ammonia Production: A Supply Chain Optimization Study. *Ind. Eng. Chem. Res.* 58, 5898–5908. doi:10.1021/acs.iecr.8b04189
- Shi, B., Song, S., Chen, Y., Duan, X., Liao, Q., Fu, S., et al. (2021). Status of Natural Gas Hydrate Flow Assurance Research in China: A Review. *Energy Fuels* 35, 3611–3658. doi:10.1021/acs.energyfuels.0c04209
- Tian, Y., Demirel, S. E., Hasan, M. M. F., and Pistikopoulos, E. N. (2018). An Overview of Process Systems Engineering Approaches for Process Intensification: State of the Art. *Chem. Eng. Process. - Process Intensification* 133, 160–210. doi:10.1016/j.ccep.2018.07.014
- Yang, M., and You, F. (2018). Modular Methanol Manufacturing from Shale Gas: Techno-economic and Environmental Analyses of Conventional Large-scale Production versus Small-scale Distributed, Modular Processing. *Aiche J.* 64, 495–510. doi:10.1002/aic.15958
- Yin, L., He, M.-L., Xie, W.-B., Yuan, F., Chen, D.-B., and Su, Y. (2018). A Quantitative Model of Universalization, Serialization and Modularization on Equipment Systems. *Physica A: Stat. Mech. its Appl.* 508, 359–366. doi:10.1016/j.physa.2018.05.120
- Zhou, J., Peng, J., Liang, G., and Deng, T. (2019). Layout Optimization of Tree-Tree Gas Pipeline Network. *J. Pet. Sci. Eng.* 173, 666–680. doi:10.1016/j.petrol.2018.10.067

Conflict of Interest: JG is employed by Sinopec Qingdao Refining and Chemical Co. Ltd. YL is employed by the China National Oil and Gas Exploration and Development Corporation.

The remaining authors declare that the research was conducted in the absence of any commercial or financial relationships that could be construed as a potential conflict of interest.

Copyright © 2021 Hong, Li, Cui, Gao, Li, Gong and Liu. This is an open-access article distributed under the terms of the Creative Commons Attribution License (CC BY). The use, distribution or reproduction in other forums is permitted, provided the original author(s) and the copyright owner(s) are credited and that the original publication in this journal is cited, in accordance with accepted academic practice. No use, distribution or reproduction is permitted which does not comply with these terms.



Analysis of Hydrogen Gas Injection at Various Compositions in an Existing Natural Gas Pipeline

Jingxuan Liu¹, Lin Teng^{2,3}, Bin Liu^{1*}, Peng Han¹ and Weidong Li²

¹School of Mechanical Engineering, Shijiazhuang Tiedao University, Shijiazhuang, Hebei, China, ²College of Chemical Engineering, Fuzhou University, Fuzhou, Fujian, China, ³Industrial Technology Research Institute, Chongqing University, Chongqing, China

OPEN ACCESS

Edited by:

Guojie Zhang,
Taiyuan University of Technology,
China

Reviewed by:

Zhen Wu,
Xi'an Jiaotong University, China
Peng Wang,
Beijing Institute of Petrochemical
Technology, China

*Correspondence:

Bin Liu
liubin@stdu.edu.cn

Specialty section:

This article was submitted to
Hydrogen Storage and Production,
a section of the journal
Frontiers in Energy Research

Received: 01 April 2021

Accepted: 28 June 2021

Published: 16 July 2021

Citation:

Liu J, Teng L, Liu B, Han P and Li W
(2021) Analysis of Hydrogen Gas
Injection at Various Compositions in an
Existing Natural Gas Pipeline.
Front. Energy Res. 9:685079.
doi: 10.3389/fenrg.2021.685079

The lack of hydrogen (H₂) transportation infrastructure restricts the development of the H₂ industry. Owing to the high investment of building specific facilities, using existing natural gas (NG) pipelines to transport a blend of H₂ and NG (H₂NG) is a viable means of transportation and approach for large-scale long-time storage. However, variation in the thermo-physical properties of an H₂NG blend will impact the performance of pipeline appliances. To address the gaps in H₂ transmission *via* an NG system in the context of energy consumption, in the present paper, a one-dimensional pipeline model is proposed to predict the blended flow in a real existing pipeline (Shan–Jing I, China). The data of NG components were derived from real gas fields. Furthermore, the influence of H₂ fractions on pipeline energy coefficient and the layout of pressurization stations are comprehensively analyzed. In addition, the case of intermediate gas injection is investigated, and the effects of injection positions are studied. This study serves as a useful reference for the design of an H₂NG pipeline system. The present study reveals that with the increasing in H₂ fraction, the distance between pressure stations increases. Furthermore, when the arrangement of original pressure stations is maintained, overpressure occur. Intermediate gas injection results in the inlet pressure of subsequent pressurization stations reducing. Using existing pipeline network to transport H₂NG, it is necessary to make appropriate adjustment.

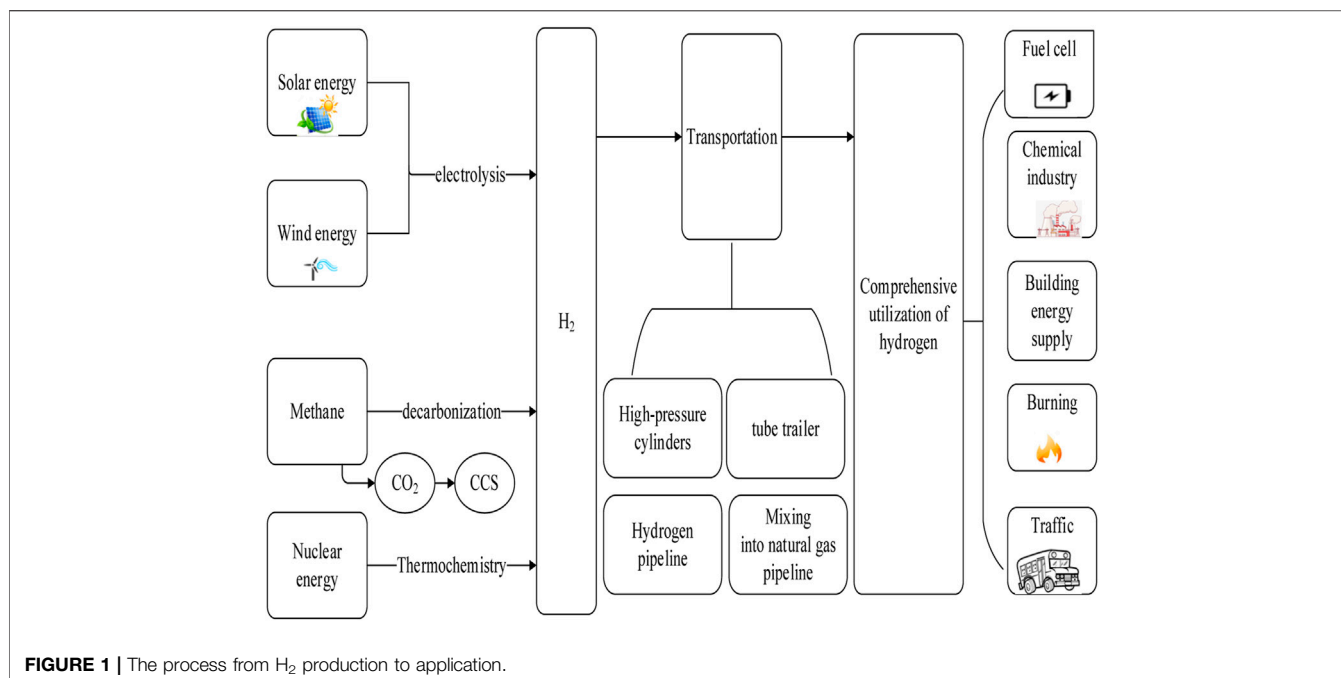
Keywords: hydrogen-natural gas mixture, pipeline, pressurization station, intermediate gas injection, hydrogen transport

HIGHLIGHTS

- A one-dimensional model for high-pressure hydrogen–natural gas (NG) mixture transportation.
- Studying the effects of hydrogen injection on the performance of an existing NG pipeline.
- Investigating the influence of intermediate gas injection.

INTRODUCTION

It is acknowledged that the large-scale use of fossil fuels directly causes global greenhouse gas (GHG) emissions and, as such, strategies are required to eliminate these emissions to meet carbon-neutral targets (Hengxuan et al., 2021; Mauricio et al., 2021). Although renewable energies such as solar, wind, and tidal energies may produce net-zero carbon emissions, their effectiveness is intermittent



and consequently cannot be used as dispatchable energy sources. Accordingly, the widespread use of such energies will require the development of energy carriers also without significant carbon production, such as batteries, compressed air, hydrogen (H₂) etc (Cherigui et al., 2008; Mah et al., 2019; Nadaleti et al., 2020). Among these energy carriers, H₂ is typically viewed as the most promising energy carrier due to its superior features, such as high energy density and low energy loss during its storage process. In addition to being an energy carrier, H₂ can also be applied as a clean, efficient, and versatile form of energy. Hence, using H₂ as an energy carrier is likely to flourish in the near future (Reuß et al., 2019).

Apart from viewed as an energy carrier, H₂ itself can also be applied as an energy source. H₂ is superior in terms of linking the characteristics in a range of application scenarios, such as electricity–gas conversion; it is also useful as a natural gas (NG) energy supplement, a heat supply, and for use in green transportation. The development of H₂ end-use products and the construction has become pivotal factors for improving the competitiveness and sustainable development of an H₂ industry (Chintala and Subramanian, 2017). A sketch of the process from H₂ production to its comprehensive application as an energy source is shown in **Figure 1** (Nadaleti et al., 2020). Currently, among various H₂ applications, H₂ fuel cell (HFC) technology represents the highest energy efficiency. This technology emits only water and warm air, producing no harmful tailpipe emissions, and is conducive to managing an H₂ society and improving the public acceptance of H₂ energy (Zhou et al., 2020). To date, HFC is mainly employed for vehicle powering systems following rapid development in the past decade. Hence, driven by policy and commercial interests, it is expected that in the next few years, the number of terminal H₂ users (e.g., hydrogenation stations) will increase sharply (Wang

et al., 2021). However, the popularization of hydrogenation stations requires significant investment (Kendall, 2018), and the current insufficient infrastructure restricts the promotional progress of HFC vehicles.

There are still several major issues that limit the popularization of H₂ technology, including H₂ transportation. The uneven distribution of H₂ between production sites and end-users leads to the inevitable need for long-distance transportation. At present, H₂ itself is primarily stored in large vessels and high-pressure tanks and conveyed by trucks or other vehicles (Cerniauskas et al., 2020). However, these approaches are far from adequate for transporting large quantities of H₂ over long distances in the future. Although the initial investment is higher, pipeline transmission rates as the most efficient and economical way for large quantities of fluid transportation over long distances, and can also be applied for high-pressure pipeline H₂ transportation (Qingmei et al., 2019). However, the long construction period required for new H₂ pipelines may restrict the proliferation of the H₂ energy industry to some extent. Ogden et al. (2018) proposed a transitional method using existing NG pipeline networks to transport blends of H₂ and NG (H₂NG), rather than constructing specific pipelines for H₂ delivery. Research related to H₂NG systems has attracted increasing attention in recent years. Quarton et al. (Quarton and Samsatli, 2020) evaluated the opportunities and challenges of H₂ injection into NG distribution systems and found that the system was able to support a share of the H₂ injection. The researchers stated that H₂NG could make use of the inherent flexibility provided by the NG network in the low-carbon future, which also presents a feasible strategy for maintaining and serving decarbonization of the NG grid. Timmerberg et al. (Timmerberg and Kaltschmitt, 2019) analyzed the economy of H₂ production from wind and solar power in North Africa and employed an

existing pipeline to transport H₂NG. They found that using the pipeline to convey H₂ presented an economically competitive option. The current distribution grid of NG pipelines is reasonably mature. It is, however, necessary to improve and enhance pipeline safety management systems, standards, regulations, and technical expertise for transporting H₂ using existing NG pipelines (Chen et al., 2021).

The existence of H₂ in blended form increases the critical pressure and decreases the critical temperature of the mixture (Ali et al., 2020). The specific energy per volume of H₂ is significantly lower compared with the main component of NG (i.e., methane (CH₄)) at a given pressure. Accordingly, when transporting an equal amount of burning energy (typically using a calorific value), an H₂NG pipeline will need to manage a higher pressure. Following H₂ injection, the physical properties of a mix can vary greatly, which will influence the hydraulic and thermal characteristics of the pipeline. Elaoud et al. (2017) pointed out that injection of H₂ into NG had a significant influence on the transient pressure of the gas mixture, accordingly affected the flow characteristics of existing NG pipeline significantly. Therefore, the variation in flow characteristics inside the pipeline caused by changes in thermophysical properties requires further study. However, the effects of an H₂NG-blend's properties on pipeline transportation and, therefore, on gas network operation and management, have to date not been studied in detail. There may be numerous unforeseen issues when using an existing pipeline to directly transport an H₂NG blend. It is thus necessary to comprehensively study and evaluate the flow in the pipeline before such a system is practically applied (Lu, 2011).

Pressure drop is an important index for evaluating the flow characteristics of a gas pipeline. Pressure drop is a function of the density and the average velocity of the gas in the pipe. Therefore, when a gas mixture composition varies from that of NG, the volume flow rate (velocity) will vary. Additionally, with H₂ injection, the energy consumption of pipeline transportation will increase; accordingly, safety may be reduced. Hence, the combined effect of more than one gas should be evaluated when considering the injection of H₂ in different parts of a pipeline (Quarton and Samsatli, 2020). Several researchers have studied the effect of H₂ injection on parameters related to existing pipelines. The results of (Chang, 2018) illustrated that with an increase in H₂ fraction and gas consumption, the pressure drop increased compared with flow comprising NG only. Witkowski et al. (2017) created a one-dimensional model to analyze H₂NG-blended gas flow in a high-pressure pipeline. The results revealed that with an increase in H₂ volume fraction, the density and velocity of gas mixture decreased and the pressure loss also decreased.

Because pressure along the pipeline will decrease gradually, pressurization stations are required to compensate for the distance-related pressure drop in the transportation process; these stations are responsible for the separation, measurement, and pressure regulation of gas flow. Therefore, whether the existing pressurization equipment and pressurization station distribution can meet the transportation requirements of H₂NG must be reviewed. Deymi-Dashtebayaz et al. (2019) stated that

the H₂ injection improved the upper and lower flammability limits and compressibility factor of gas mixture, along with the relative density decrease with hydrogen concentration increase. Accordingly, new requirements were put forward for the adaptability and safety of equipment such as pipelines, compressors, and valves, which require additional study. Sherif et al. (2005) stated that the distance between the pressurization stations required adjustment for H₂ injection, the maximum distance may be double that of the original. Uilhoorn (2009) studied the non-isothermal transient flow in the Yamal–European NG pipeline with H₂ injection in Poland. The study found that the presence of H₂ reduced the pressure and temperature gradient of the pipeline, and the compressor power of H₂NG decreased under the same energy demand compared with only NG. Haeseldonckx et al. (Haeseldonckx and D'haeseleer, 2006) studied the application of existing NG pipeline infrastructures to transport H₂ and found that H₂ injection would have adverse effects on the use and short-term supply safety of original NG centrifugal compressors, owing to the variation in thermodynamic properties of fluid in pipe.

Previous studies on assessing the impact of H₂ injection on existing gas networks focused on the integrity and safety aspects. H₂ injection may cause hydrogen embrittlement and lead to a loss of structural integrity in steel (Singh et al., 2018). An increase in H₂ partial pressure will raise the possibility of hydrogen embrittlement (Kouchachvili and Entchev, 2018). Meliani et al. (2011) analyzed the effect of H₂ on the failure curve of APL 5 L gas pipeline steel from the perspective of notch fracture mechanics. The study results indicated that there existed a critical H₂ concentration beyond which the local fracture resistance of the steel decreased considerably. Hafsi et al. (2018) followed the phenomena involved in the dissolution, penetration, and diffusion of H₂ molecules into the lattice structure of pipeline materials and showed that preventive measures had to be taken to prevent the risk of explosion caused by hydrogen embrittlement, as well as other effects that may lead to changes in the safety conditions of gas conduction. Li et al. (2020) showed that realization of the hydrogen embrittlement effect in metallic materials was largely assisted by the boundary disruption and local stress state concentrated through the plasticity process. Bouledroua et al. (Omar et al., 2020) pointed out that the hydrogen embrittlement of steel pipelines in contact with an H₂ environment, together with the transient gas flow and significantly increased transient pressure values, also increased the probability of failure of a cracked pipeline. Hafsi et al. (2019) simulated the transient flow of H₂NG in a loop network using the finite element software COMSOL Multiphysics. The transient overpressure was found to be proportional to the H₂ fraction in the blend, and the overpressure promoted circumferential stress and the internal load on the pipe wall. Furthermore, the risk of hydrogen embrittlement observably increased with an increase in overpressure; hence, safety factors have to be guaranteed to ensure the safety of the H₂NG transmission process (Pluvineau, 2021). Liu et al. (2019a) considered that the effect of H₂ fraction on the decompression wave speed in an H₂NG mixture depended on

whether the thermodynamic trajectory intersected with the corresponding phase envelope.

In the actual long-distance pipeline transportation process, complex terrains will inevitably be encountered; furthermore, terrain fluctuation will also have a significant impact on the transportation process. It is important to extract data related to pipeline diameter, length, and corresponding elevation for gas pipeline flow simulation. Geographic information system (GIS) technology can efficiently collect large-scale terrain information data from different areas within a short time, extract geographic elements and pipeline facilities, obtain accurate terrain information and elevation changes along a pipeline, and combine data with computer information technology to establish database management systems, thereby realizing the creation of a parameter database including gas stations and other tools; this will improve the information quality and accuracy of decision-making and monitoring efficiency (Tikhonova et al., 2019). At present, GIS technology plays an increasingly important role in pipeline integrity management, which can solve a series of problems in long-distance pipeline construction and operation, and facilitate the rapid update of pipeline management data (Shay et al., 2016).

When gas is transported through pipelines, energy conversion is inevitable, including heat transfers between the system and the environment, as well as energy dissipation within the system. Generally, the energy consumption of a long-distance pipeline system is represented by the pressure loss of the transported gas. A lower pressure drop means a higher gas transmission efficiency (Zhao et al., 2019). Mitigating energy consumption is of significance for reducing the operating costs of gas transmission systems and improving economic benefits. To analyze the energy consumption of a gas transmission system, the energy loss rate (the energy consumed per unit mass per unit length of the pipeline) is selected as the energy consumption evaluation index of a gas transmission pipeline system.

However, analysis on the transportation characteristics of an H₂NG-blend pipeline network has to date been limited; furthermore, there is a lack of research on the distribution of pressurization stations. To address this lack, ASPEN HYSYS was used to establish a one-dimensional pipe flow model in the present study. The Peng–Robinson (PR) equation of state (EOS) is introduced in this model to provide an accurate prediction of the thermophysical properties of H₂NG. Additionally, GIS is used to provide pipeline data and topographic information. According to the design specifications of a gas transmission pipeline, stations are arranged at appropriate positions to analyze the influence of transporting gas mixture with different H₂ fractions and injecting gas at the middle of the pipeline network system. Furthermore, the pipeline transportation process and exergy analysis are presented in this paper. This study may provide theoretical guidance for the subsequent use of existing NG pipeline networks to transport H₂, simultaneously, it also has a positive reference for the subsequent layout design of pressurization station.

MODELING APPROACH

Gas Component

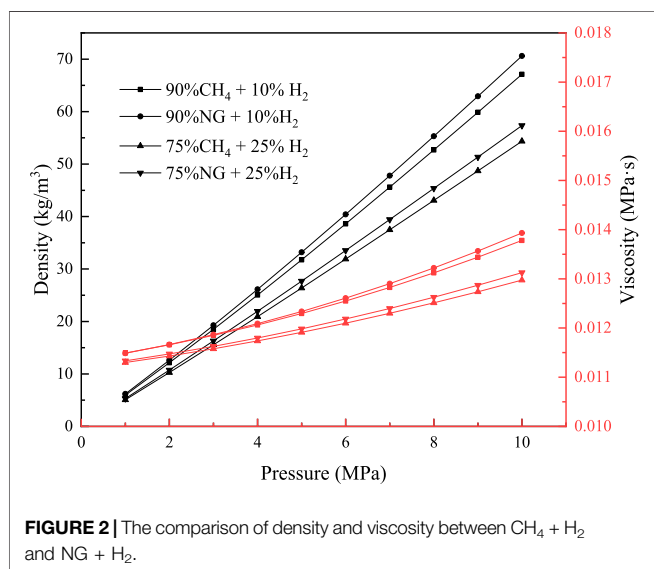
Thermophysical property discrepancies between CH₄ and H₂ give rise to different features in pipeline transportation and also affect flow and heat transfer characteristics. Additionally, the selection of equipment parameters is also affected by gas composition. Hence, when using an existing NG pipeline to transport an H₂NG blend, it is necessary to study the influence of an H₂ fraction on the transportation process to ensure the feasibility, safety, and economy of such a system. Although several previous simulations have been conducted on H₂NG flow in a pipeline, most of these simulations considered NG comprised entirely of CH₄. However, in reality, NG includes a variety of gases such as CH₄, ethane (C₂H₆), propane (C₃H₈), and others. Its composition varies according to available gas sources. The influence of an H₂ fraction may be related to the actual gas composition of a specific pipeline network. Therefore, simulations should be based on the actual situation in terms of modeling the pipe flow and reviewing the impact on H₂ injection. The thermodynamic properties of H₂NG must be accurately predicted. The foundation of modeling requires an accurate description of the thermophysical properties of H₂NG, rather than of a CH₄–H₂ mixture. The NG pipeline of Shan–Jing I (Jingbian, Shanxi to Shijingshan, Beijing, China) is considered in the present study. The Jingbian gas field is the main gas source of this pipeline. Approximately 85% of the NG in the Jingbian gas field derives from Upper Paleozoic coal measures. The gas composition at this field was obtained by chromatography as shown in **Table 1** (as original NG types) (MI et al., 2012). **Figure 2** compares the thermophysical properties between CH₄ and NG. It can be seen that there is a great difference between the actual NG and CH₄. Consequently, when simulating the flow characteristics in the pipeline, the actual composites must be considered to ensure the accuracy prediction of properties, which influence the pipe flow significantly. It can be inferred that the impurities in NG enhance the pressure drop due to increased density and viscosity. Because the volume fraction of CH₄ in NG is as high as 96.77%, for the sake of simplicity, in this study, it was considered that other component fractions were kept constant, except H₂ and CH₄ as shown in **Table 1**.

Thermophysical Property Model

A precise description of thermodynamic properties is the basis for establishing an accurate pipeline flow model. It is commonly acknowledged that prediction errors in ideal gas EOS are unacceptable at high pressure. This is because the ideal gas EOS ignores intermolecular force; additionally, the isobaric specific heat capacity and sound speed are assumed to be constant at a given temperature. Accordingly, real gas EOS is introduced herein. In this context, EOS is mainly divided into two categories: 1) cubic equations with simple structures, such as the PR equation (Peng and Robinson, 1976); 2) equations with complex structures, such as Groupe Europeen de Recherches Gazieres (GERG) (Varzandeh et al., 2017). Despite the simple

TABLE 1 | Components of H2NG.

Component mole fraction type	Methane (CH ₄)	Ethane (C ₂ H ₆)	Propane (C ₃ H ₈)	Isobutane (C ₄ H ₁₀)	N-butane (N-C ₄ H ₁₀)	Ethylene (C ₂ H ₄)	Hydrogen (H ₂)
1 (original NG)	0.9677	0.025	0.0038	0.0006	0.0009	0.002	0
2 (10% H2NG)	0.8677	0.025	0.0038	0.0006	0.0009	0.002	0.1
3 (20% H2NG)	0.7677	0.025	0.0038	0.0006	0.0009	0.002	0.2
4 (30% H2NG)	0.6677	0.025	0.0038	0.0006	0.0009	0.002	0.3
5 (40% H2NG)	0.5677	0.025	0.0038	0.0006	0.0009	0.002	0.4
6 (50% H2NG)	0.4677	0.025	0.0038	0.0006	0.0009	0.002	0.5
7 (60% H2NG)	0.3677	0.025	0.0038	0.0006	0.0009	0.002	0.6

**FIGURE 2** | The comparison of density and viscosity between CH₄ + H₂ and NG + H₂.

nature of a cubic EOS, it is capable of deriving reasonable results. An EOS with a more complex structure may yield better estimations for selected properties but they tend to be extremely difficult to apply due to their complicated calculation procedures. In the present work, the PR EOS is employed based on its proven accuracy in modeling the behavior of H2NG, is relatively simple, and presents computational efficiency. The PR EOS is expressed as follows (Dall'Acqua et al., 2017; Liu et al., 2014):

$$P = \frac{RT}{V-b} - \frac{a}{V^2 + 2bV - b^2} \quad (1)$$

$$Z^3 - (1-B)Z^2 + (A-2B-3B^2)Z - (AB-B^2-B^3) = 0 \quad (2)$$

where P is the absolute pressure, T is the absolute temperature, V is the molar specific volume, R is the universal gas constant, and Z is the compressibility factor of the gas expressed as below Eq. 3; a and b are empirical parameters accounting for the intermolecular attraction forces and the molecular volume, expressed as below Eq. 6, Eq. 9 respectively.

$$Z = PV/RT \quad (3)$$

$$A = aP/(RT)^2 \quad (4)$$

$$B = bP/RT \quad (5)$$

$$a = \sum_{i=1}^N \sum_{j=1}^N x_i x_j \left[\left(0.45723553 \frac{R^2 T_{ci}^2}{P_{ci}} \right) \alpha_i \left(0.45723553 \frac{R^2 T_{cj}^2}{P_{cj}} \right) \alpha_j \right] \times (1 - k_{ij}) \quad (6)$$

$$\alpha_i = \left[1 + m_i \left(1 - \sqrt{\frac{T_i}{T_{ci}}} \right) \right]^2 \quad (7)$$

$$m_i = 0.37464 + 1.54226\omega_i - 0.26992\omega_i^2 \quad (8)$$

$$b = \sum_{i=1}^N x_i 0.077796074 \frac{RT_{ci}}{P_{ci}} \quad (9)$$

where T_c is the critical temperature, P_c is the critical pressure, and ω is the Pitzer acentric factor; x is the mole fraction of components, i and j identify the i and j -elements of the fluid mixture, k_{ij} represents the binary interaction parameter between components i and j , assuming a value of 0 for $i = j$.

Governing Equations

In terms of full, long pipelines, the velocity can be regarded as only along the pipe direction, and the radial velocity can be ignored. Thus, it is feasible to create a one-dimensional flow model. The finite element method is used to make difference for the pipe model, and the fluid micro element flow in the pipe is shown in Figure 3.

The governing equations proposed by the one-dimensional model are expressed as:

Continue equation.

$$\frac{\partial \rho}{\partial t} + \frac{\partial(\rho u)}{\partial x} = 0, \quad (10)$$

Momentum equation.

$$\frac{\partial(\rho u)}{\partial t} + \frac{\partial(\rho u^2 + P)}{\partial x} = -\rho g \sin \theta - f \frac{\rho u |u|}{2D}, \quad (11)$$

Energy equation.

$$\rho C_V \left(\frac{\partial T}{\partial t} + u \frac{\partial T}{\partial x} \right) + T \left(\frac{\partial P}{\partial T} \right)_p \frac{\partial u}{\partial x} = f \frac{\rho u^3}{2D} - \frac{4U}{T} (T - T_a). \quad (12)$$

where D is the inner diameter of the pipe, f is the friction factor, g is the acceleration of gravity, P is the pressure, t is the time (this

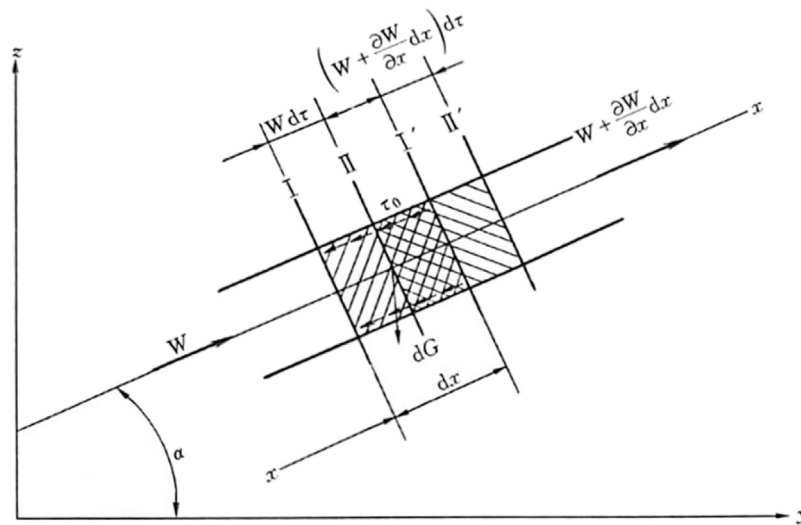


FIGURE 3 | Schematic diagram of fluid micro element in pipe.

paper presents a steady-state condition study and, as such, a time term is not involved), T_a is the ambient temperature, u is the velocity, x is the distance, θ is the pipe inclination angle ρ is the density, and U is the total heat transfer coefficient.

Total heat-transfer coefficient U represents the heat transfer intensity between the gas and environment. Neglecting the heat accumulation of the soil, U can be expressed as follows (Witkowski et al., 2017):

$$U = \frac{1}{\frac{D}{\lambda_g} \ln \frac{D_2}{D} + \frac{D}{\lambda_b} \ln \frac{D_b}{D_2} + \frac{D}{\lambda_s} \ln \frac{2z}{D_b} + \frac{D}{z} \frac{1}{\alpha}} \quad (13)$$

where D is the inner diameter of the pipe, D_2 is the outer diameter of the pipe, D_b is the outer diameter after adding an insulating layer, z is the buried depth of the pipeline, λ is the thermal conductivity, and g, b , and s indicate the thermal conductivity of the pipe wall, insulation, and anti-corrosion materials and soil, respectively; α is the air convective heat transfer coefficient, which depends on the unpredictable wind velocity. The thermal resistance of the convective heat transfer between the air and the pipe outer wall tends to be much smaller than that of the heat conduction, hence, the heat resistance of convection heat transfer on the air side can be ignored.

The friction coefficient of pipeline flow is determined by the flow pattern, the roughness of the inner wall, the pipe diameter, the flow rate, and the properties of the gas. The Darcy–Weisbach formula is generally employed to calculate the friction between the fluid and a pipe wall. The losses due to friction and potential energy variation are considered in the formula. The formula can be given as follows:

$$\frac{dP}{dx} = f \frac{\rho}{2} \frac{u^2}{D} \quad (14)$$

where dP/dx denotes the pressure gradient caused by friction, f is the Darcy friction factor for wall of pipe, and ρ is the density of the fluid.

According to the actual operating parameters of an NG pipeline, the Reynolds number (Re) tends to be as high as 10^6 – 10^7 , the Colebrook–White formula was employed to the predict friction coefficient f in the Darcy–Weisbach formula because its calculation reflects the influence of Re in a low Re region and the influence of internal roughness in a high Re region (Helgaker et al., 2014). Eq. 15 shows the Colebrook–White equation as follows:

$$\frac{1}{\sqrt{f}} = -2 \log \left(\frac{\varepsilon}{3.71D} + \frac{2.51}{Re\sqrt{f}} \right) \quad (15)$$

where ε is the equivalent sand grain roughness.

Methodology

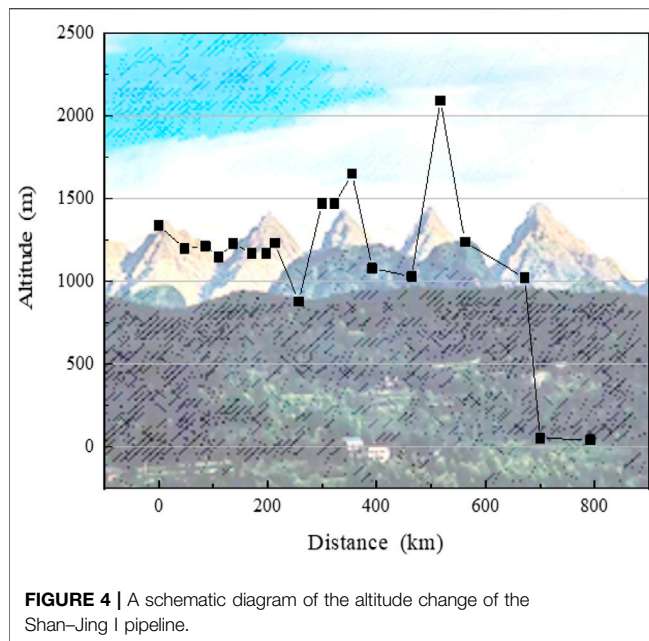
Energy Conversion Analysis

The relationship between energy entering and leaving the system is analyzed based on the first law of thermodynamics. In a steady state, the energy carried by gas in a straight pipe primarily comprises internal energy and pressure energy. Internal energy will be lost due to heat exchange between the pipeline and the environment, and pressure energy will be lost owing to friction. The energy carried by gas can be represented as specific enthalpy ($h = pv + u$). Enthalpy flux is introduced in the present study, where it is expressed by H_f as follows:

$$H_f = PV + MC(T - 273.15) \quad (16)$$

where H_f is the enthalpy flux, V is the volume flow rate, M is the mass flow rate, and C is the mass heat capacity of the fluid. The first term on the right represents the pressure energy, and the second term is internal energy.

The pipeline gathering efficiency is a key index for evaluating the network system (Qingqing, 2015). Generally, in this evaluation, the entire pipeline network system is simplified as follows: 1) it is assumed that the pipeline network comprises only



primary and branch pipelines; 2) the influence of dynamic and thermal equipment is ignored. The pipeline efficiency of a gas transmission pipeline between pressurization stations is the ratio of outlet H_{f2i} and inlet H_{f1j} . The efficiency of the gathering and transportation network is the ratio of the total H_{fi} at the outlets of all pipelines to the H_{fj} at the inlets in the entire transportation process. The formula for this is as follows:

$$\eta = \frac{\sum_{i=1}^n H_{f2i}}{\sum_{j=1}^n H_{f1j}} = \frac{\sum_{i=1}^n [P_{2i} V_{2i} + M_{2i} C_{2i} (T_{2i} - 273.15)]}{\sum_{j=1}^n [P_{1j} V_{1j} + M_{1j} C_{1j} (T_{1j} - 273.15)]} \quad (17)$$

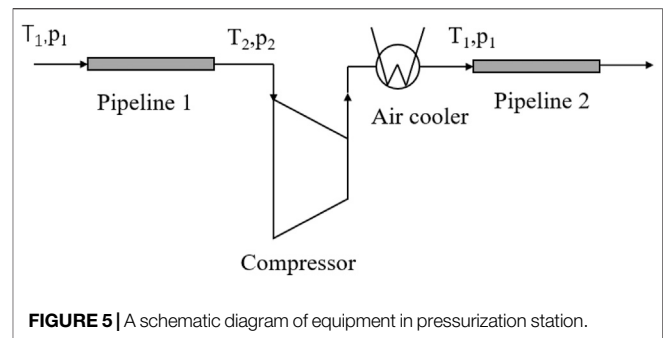
where H_f is the enthalpy flux (kJ/h), V is the volume flow rate (m^3/h), M is the mass flow (kg/h), C is the mass heat capacity [$\text{kJ}/(\text{kg}/\text{K})$], T is the thermodynamic temperature (K), and P is the pressure (kPa). The variables that include $_{2i}$ are the data of the i -th outlets, and the variables that include $_{1j}$ are the data of the j -th inlets.

Exergy Analysis

“Exergy” refers to the maximum work that can be produced when a system experiences a reversible process from its current state to equilibrium with its surrounding environment under the condition of only environmental action. The purpose of exergy analysis is to detect the irreversible loss according to an imbalance in the system and to provide a comprehensive evaluation of the system’s energy use (Aihua, 2011). An exergy analysis effectively supplements an energy analysis. Herein, exergy is expressed as

$$E_x = T\Delta S - \Delta H \quad (18)$$

where E_x is the exergy of the fluid, ΔS is the entropy difference between a fluid and environmental reference state, and ΔH is the enthalpy difference between the fluid state and the environmental reference state.



During the exergy analysis, the first step is to define a reference state, where Ex is considered to be 0. Generally, the average ambient temperature and pressure of the area Shan-Jing I pipeline passed through are 25°C (298 K) and 1 atm (101.325 kPa), respectively (Liu et al., 2019b). The present study also adopted this as the reference state. We used the model to calculate the energy loss of each link in the transportation process to analyze the exergy loss and distribution in the system. The exergy carried by gas includes primarily pressure exergy (Exp) and heat exergy (Ex_T); the latter is based on the environmental temperature according to the following formula:

$$E_{xT} = T\Delta S - \Delta H = \int_{T_0}^T \left(1 - \frac{T_0}{T}\right) C_p dT \quad (19)$$

where Exp refers to the work capacity delivered by the pressure difference between the gas system and the environment, expressed as Eq. 20:

$$E_{xp} = \int_{P_0}^P \left[V - (T - T_0) \left(\frac{\partial V}{\partial T} \right) \right] p dp \quad (20)$$

Description of the Pipeline

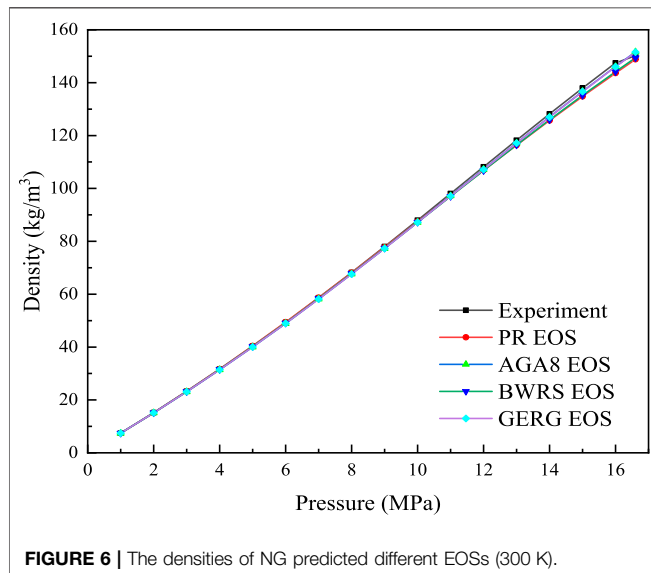
The Shan-Jing I pipeline employs X60 pipe steel with an outer diameter of 660 mm, an inner diameter of 648 mm, a design working pressure of 6.4 MPa, and has a total length of 792 km (Natural gas in China, 1997). The elevation variation information along the pipeline was obtained using GIS technology as shown in Figure 4. In the region with the most dramatic height change, the pipeline climbs 890 m with a horizontal length of 30 km.

Pressure stations are required to compensate for pressure losses. According to Specification for Gas Transmission Pipeline Engineering Design GB50251-2015 (Gas Transmission System, 2015), the ratio of inlet and outlet pressure of pressurization station is recommended to be 1.5. Accordingly, this pressure ratio was selected for analyzing the distribution of pressure stations. The equipment in the pressurization station is shown in Figure 5, the compressor in the station adopts centrifugal compressor with pressure ratio of 1.5 and adiabatic efficiency of 85%, an air cooler is set behind the compressor to cool the mixed gas to the operating temperature and pressure.

The original distances between NG pressurization stations and the pipeline’s starting point are shown in Table 2.

TABLE 2 | The original distances between pressurization stations and the pipeline's starting point.

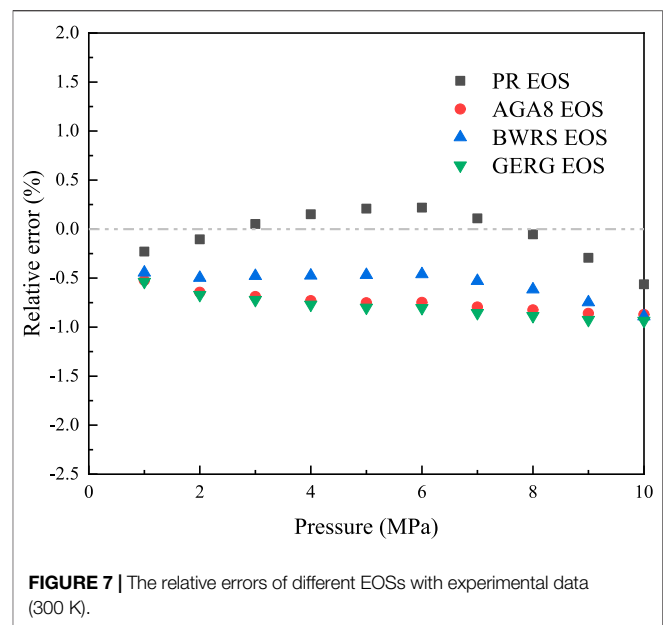
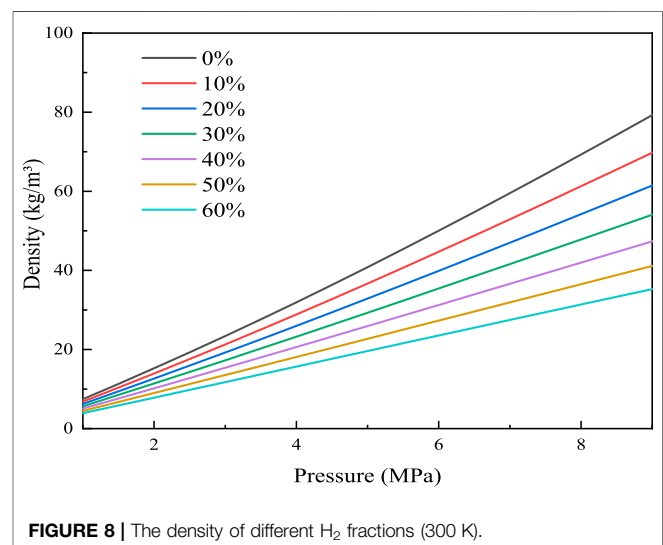
Station number	Distance/km	Station number	Distance/km
1	40	11	444
2	80	12	484
3	120	13	519
4	159	14	565
5	199	15	605
6	240	16	649
7	280	17	694
8	320	18	734
9	358	19	776
10	404	—	—

**FIGURE 6 |** The densities of NG predicted different EOSs (300 K).

RESULTS AND DISCUSSION

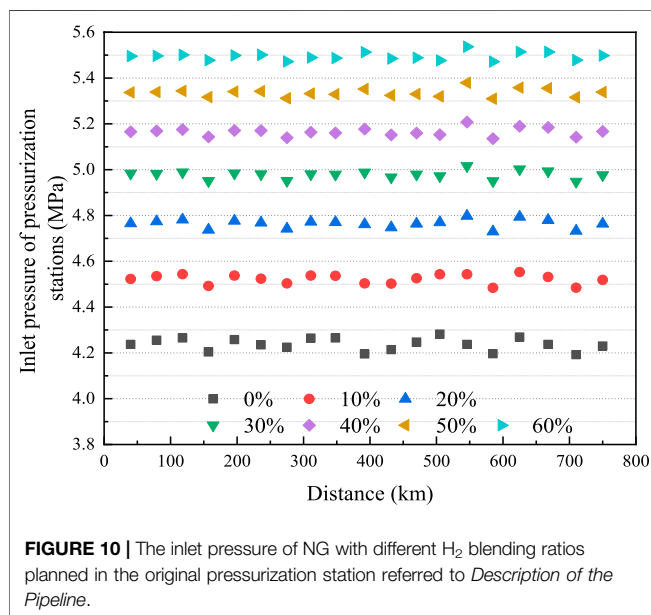
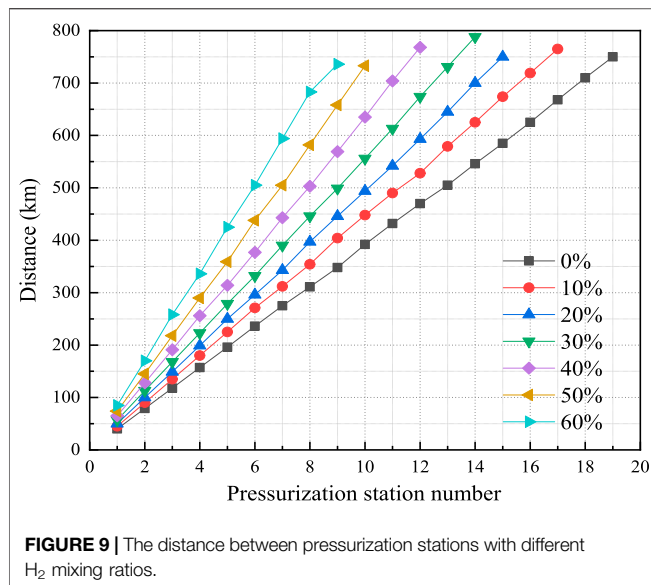
Model Validation

In order to evaluate the accuracy of the PR EOS, the mixture density predicted by four EOSs—namely—PR EOS, AGA8 EOS, BWRS EOS and GERG EOS are compared with the experimental data prepared by the Federal Institute for materials research and testing in Berlin, Germany [51]. The mole fractions of the mixture are 0.8845 for CH₄, 0.005 for O₂, 0.04 for N₂, 0.015 for CO₂, 0.04 for C₂H₆, 0.01 for C₃H₈, 0.002 for n-C₄H₁₀, 0.002 for i-C₄H₁₀, and 0.0005 for i-C₅H₁₂, C₅H₁₂, and i-C₆H₁₄, respectively (Chemical analysis, 2015). **Figure 6** shows the comparison between the predicted densities and the experimental results, and **Figure 7** exhibits the relative errors. Clearly, all of the four EOSs are agreement with measured well. The average absolute deviation of PR EOS is less than 2%, and it is closer to the experimental data when the pressure is lower than 10 MPa. Therefore, PR EOS can provide a satisfactory prediction of thermophysical properties, which guarantee an accurate simulation of the pipe flow.

**FIGURE 7 |** The relative errors of different EOSs with experimental data (300 K).**FIGURE 8 |** The density of different H₂ fractions (300 K).

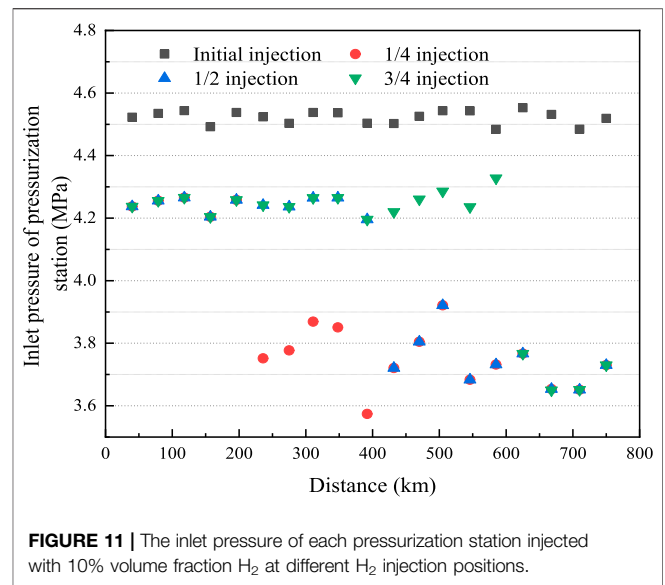
The Effect of Hydrogen Fraction on the Layout of Pressurization Stations

As noted above in *Description of the Pipeline*, it is suggested that the station pressure compression ratio be 1.5 when a centrifugal compressor is used. Under a full load situation, the average outlet pressure of the first station and each pressurization station in the Shan–Jing I pipeline is 6.4 MPa, the average inlet pressure of the pressurization station tends to be 4.3 MPa, and the pressure drop between the two stations is approximately 2.1 MPa. It is assumed that the velocity and volume flow rate of the blend or NG at the inlet of the pipe is constant in all cases. As shown in **Figure 8**, due to the relatively lower density of H₂, with an increase in H₂ fraction, the blend density decreases, which results in both the mass flow rate and the pressure loss decreasing at the same



distance. Consequently, the injection of H₂ prolongs the distance between pressurization stations. **Figure 9** shows the distances between every station and the first station when the pressurization stations are relocated according to the recommended pipeline pressure drop. Observably, the distance increased with an increase in H₂ fraction. The distance between stations for the original NG was approximately 40 km/station and approximately 45 km/station for 10% H₂, indicating an increase of 12.5%. With a 60% H₂ injection, the distance was extended to 85 km/station, an increase of 112.5% compared with the original.

The construction cost and time were, however, increased by changing the layout of the pressurization stations. Therefore, the effect of H₂ injection on the pipeline was also studied without changing the layout of the pressurization stations. Under the



condition of keeping the original layout of pressurization stations, when transporting an H₂NG blend with different H₂ fractions, the inlet pressure of each pressurization station was no longer 4.3 MPa as calculated by the recommended pressure ratio of 1.5. The inlet pressure of each pressurization station is shown in **Figure 10**. The figure shows that the higher the H₂ fraction, the smaller the pressure drop at the same distance, and consequently, the higher the inlet pressure. At this time, if the original pressurization and cooling equipment was used and had not been adjusted properly, accordingly, the phenomenon of overpressure arose, which will also add new challenges to the safety and economy of the equipment. Therefore, it is suggested that the original pressure station equipment be adjusted to ensure safe and stable operation on the premise of reducing energy consumption.

The Effect of Intermediate Gas Injection on Pressurization Stations

In reality, large-scale H₂ production sites may not be closely situated to an NG field; hence, H₂ may be injected at different pressurization stations. In this case, the H₂NG composition and volume flow rate will change following H₂ injection, affecting the transportation process after the H₂ injection point. To study the influence of the injection point on the flow, H₂ injection points were set at 1/4, 1/2, and 3/4 of the entire length of the original pipeline, and 1/9 or 1/4 of the original volume flow of H₂ was injected into the pipeline network. As a result, the volume fraction of H₂ in the H₂NG blend was 10 or 20%, respectively. The influence of H₂ injection on station inlet pressure is shown in **Figure 11**. For the convenience of comparison, the comparison group in **Figure 12** show groups injected with NG with the same composition as the original.

When H₂ was injected directly at the starting point, the average inlet pressure of the subsequent pressurization station was 4.53 MPa. However, when injecting H₂ at 1/4 of the total length, the flow rate and the pressure drop increased, resulting in

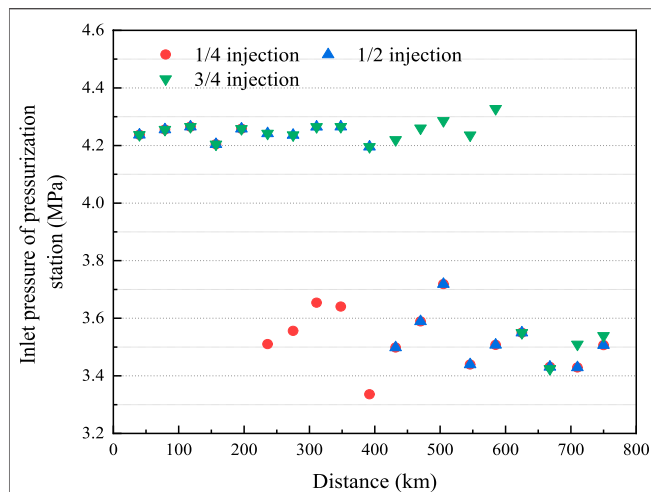


FIGURE 12 | Inlet pressure of each pressurization station injected with 10% volume fraction NG at different H₂ injection positions.

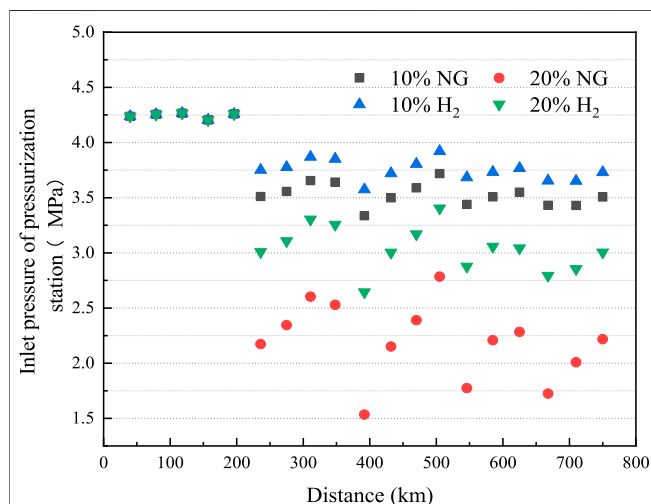


FIGURE 13 | The inlet pressure of a pressurization station after injecting different gases at 1/4 of the entire distance of the pipeline.

a decrease in the inlet pressure of the downstream pressurization stations. The lowest inlet pressure was as low as 3.57 MPa, and the average was 3.75 MPa. In the case of 1/2 and 3/4 of the total length injection, the influence trend was consistent with that of 1/4 injection. Although the injecting positions were different, the average inlet pressures were all approximately 3.75 MPa, which was 10.7% lower than that of the original pipe network. Compared with the influence of NG injection, the inlet pressure of pressurization stations decreased and the change tendency was essentially the same. The reason for this was because the NG density was much higher than that of H₂; consequently, the mass flow rate was larger under the same volume flow rate. This also caused a pressure drop higher than that of H₂ injection, and the inlet pressure was lower than that of H₂ injection with the same volume flow rate. The average inlet pressure was

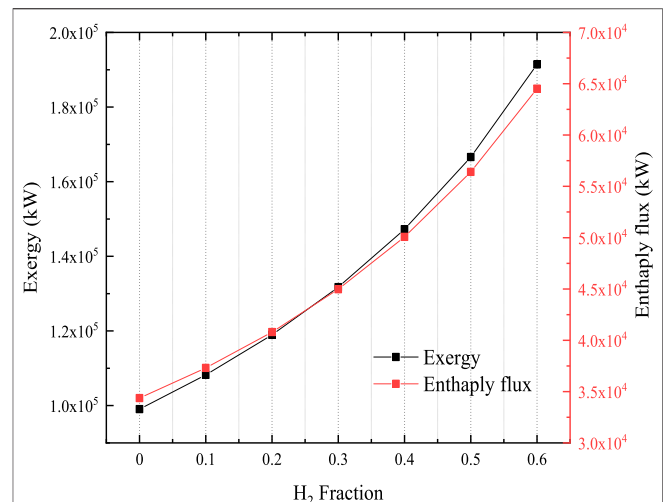


FIGURE 14 | The exergy and enthalpy flux at various H₂ fractions.

approximately 3.55 MPa, which was 15.5% lower than that of the original pipeline.

Figure 13 compares the effect of different gas injections at 1/4 of the entire pipeline length on the inlet pressure. When the same gas was injected, with an increase in gas injection, the mass flow rate of the subsequent transportation process and the pressure drop were larger but the inlet pressure was smaller. Compared with CH₄ injecting with the same volume flow rate, H₂ injection reduced the pressure loss on the subsequent transportation process, and the inlet pressure of the subsequent pressurization station was larger due to its significantly lower density. Intermediate gas injection thus imposes new challenges on original pipeline network equipment, which requires comprehensive review and consideration.

Analysis of Enthalpy Flux, Exergy, and Pipeline Efficiency

Figure 14 shows the exergy and enthalpy flux at various H₂ fractions. The enthalpy flux and exergy were found to increase with an increase in H₂ fraction. The original NG exergy component value was 99,057 kW; however, this value reached 108,214 kW with 10% H₂ injection (an increase of 9.24%), and this value reached 191,402 kW with 60% H₂ injection (an increase of 93.22%). Similarly, H₂ injection also led to an increase in enthalpy flux. According to **Eq. 16**, when the volume flow rate and initial pressure of the blend are the same, the pressure energy (PV in **Eq. 16**) carried by the blend is the same, and the specific heat capacity of the blend after H₂ injection is greater than that of NG (As shown in **Figure 15**, compared with the original NG at 300 K and 6.4 MPa, the mass heat capacities of H₂NG with 10 and 60% H₂ fractions increased by 3.5 and 41%, respectively.)

Therefore, the internal energy increases and the H_f also increases correspondingly when H₂ is injected. According to **Eq. 19**, **Eq. 20** after H₂ injection, although the value of Exp was the same, the Ext was affected by the C_p of the blend. Accordingly, the high H₂ fraction also led to a rise in Ex .

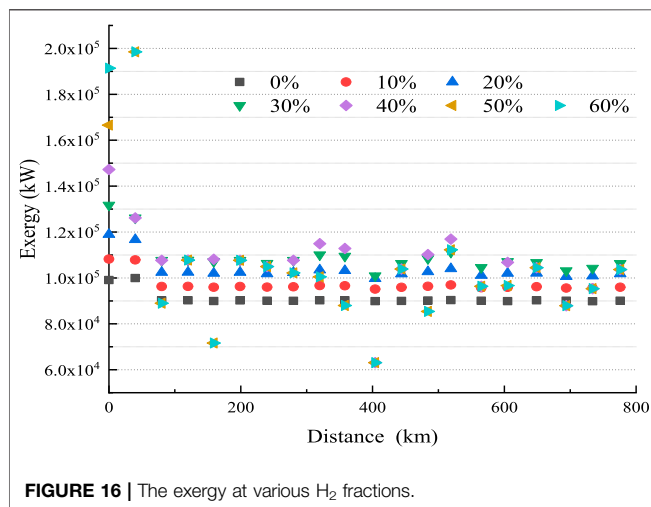
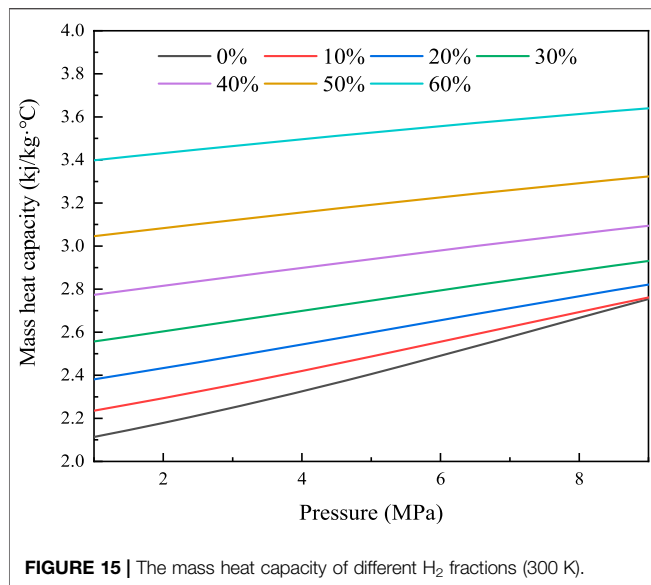
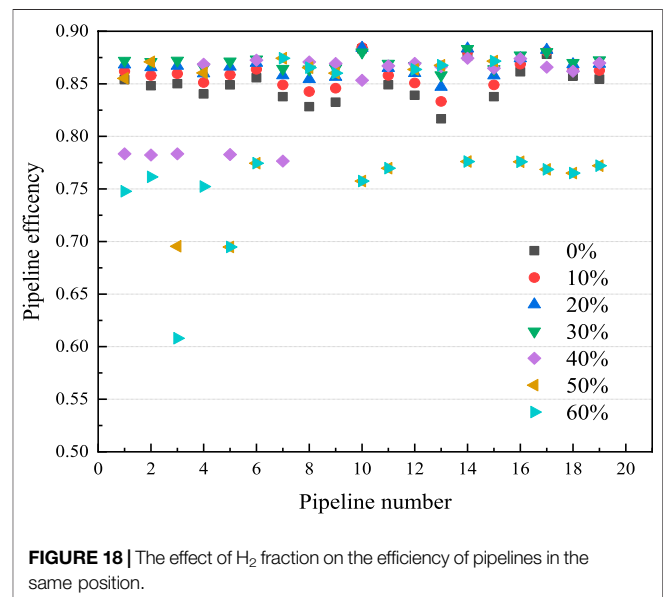
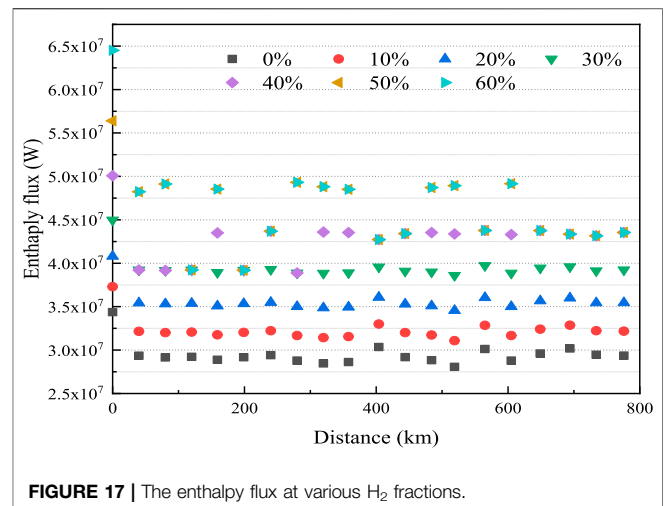


Figure 16, Figure 17 show the Ex and H_f at the original pressurization station after using the NG gas pipeline network to transport the gas blend with different H₂ fractions. The Exp was determined only by pressure and volume flow, whereas the Ext and H_f were also influenced by specific heat capacity at a given pressure and temperature. With an increase in H₂ fraction, the specific heat capacity of the blend increased, the corresponding Ex and H_f increased. A high H₂ fraction increased pressure and temperature at the inlets of the pressure stations, and the corresponding inlets Ex and H_f . When the H₂ fraction was less than 30%, the Ex and H_f at the inlet of the pressure station essentially remained stable; when the H₂ fraction was more than 30%, the fluctuations were considerable. The enthalpy and enthalpy flow of the nodes of the pressurization station fluctuate greatly during the pipeline transportation, which is not conducive to the safety of the gas transportation process. Therefore, the existing pipeline and pressure station equipment requires modification to ensure the smooth operation of the



existing pipeline network when the volume fraction of H₂ is higher than 30%.

In the pipeline transportation process, enhancing the value of η to reduce energy loss in the pipeline network is anticipated. The efficiency of the pipeline network pressurization stations under different H₂ fractions is compared in Figure 18. The main factors affecting pipeline efficiency were volume flow, specific heat capacity, inlet and outlet pressure, and temperature. The length of the pipeline between each two pressurization stations was roughly the same, and the inlet and outlet pressure were almost the same as the pressure stations. As a result, although the pipeline efficiency of each pipe section at the same distance was different, it reached an average of 85%. When the H₂ fraction was less than 30%, with an increase in the H₂ fraction, the pipeline efficiency improved slightly (85.7 for 10%, 86.5 for 20%, and 87.2 for 30% injection). However, when the H₂ fraction exceeded 30%, the pipeline's efficiency was no longer stable and decreased

significantly, and transportation became unstable with an increase in the H₂ fraction. The lowest pipeline efficiency was 60.8% (when the H₂ fraction was 60%). In the actual pipeline transportation process, although a pressure drop at the same distance decreases with an increase in the H₂ fraction, a high H₂ fraction will boost the possibility of H₂ permeation and H₂ embrittlement, which will not only affect transportation safety but may also lead to inefficient transportation. That is not conducive to the improvement of gas transmission efficiency. Therefore, it is suggested that the distribution of pressurization stations be adjusted and the operating pressure properly increased when the H₂ fraction is higher than 30% to ensure gas transmission efficiency and pipeline safety.

CONCLUSION

The objective of the present study was to analyze the effect of H₂ injection on the flow characteristics of an NG pipeline. Based on the Shan–Jing I gas pipeline, this paper used GIS technology to extract terrain information and pipeline data to propose a transportation model for an H₂NG-blend pipeline under the conditions of undulating terrain. To produce quantitative data for evaluating the influence of H₂ injection on pipe flow character, a parametric study was performed by changing H₂ fraction amounts. The primary conclusions of the study are as follows.

- 1) With an increase in the H₂ fraction, the distance between pressure stations increased. When the arrangement of original pressure stations were maintained, overpressure occurred.
- 2) Intermediate gas injection reduced the inlet pressure of subsequent pressurization stations to gas injection point.
- 3) When the H₂ fraction was less than 30%, the increase in the H₂ fraction led to a decrease in the pressure drop and an increase in pipeline efficiency. However, when the H₂ fraction exceeded 30%, the transportation process was unstable and the pipeline efficiency decreased.

REFERENCES

- Aihua, J. (2011). *pan Exergy Analysis Method and its Application*. Central South University.
- Ali, A. A., Naji, S. Z., Thian, T. C., and Othman, M. R. (2020). Evaluation of Hydrogen Concentration Effect on the Natural Gas Properties and Flow Performance. *Int. J. Hydrogen Energ.*
- Cerniauskas, S., Jose Chavez Junco, A., Grube, T., Robinius, M., and Stolten, D. (2020). Options of Natural Gas Pipeline Reassignment for Hydrogen: Cost Assessment for a Germany Case Study. *Int. J. Hydrogen Energ.* 45 (21), 12095–12107. doi:10.1016/j.ijhydene.2020.02.121
- Chang, W. (2018). *Feasibility Study of Natural Gas Mixed with Hydrogen*. Chongqing University.
- Chemical analysis (2015). *Gas Analysis e preparation of calibration gas mixtures e Part 1: gravimetric method for Class I mixtures*. Geneva: International Organization for Standardization.
- Chen, C., Li, C., Reniers, G., and Yang, F. (2021). Safety and Security of Oil and Gas Pipeline Transportation: A Systematic Analysis of Research Trends and Future Needs Using WoS. *J. Clean. Prod.* 279, 123583. doi:10.1016/j.jclepro.2020.123583
- 4) Appropriate H₂ addition can improve the economy of pipeline transportation, increase pipeline efficiency and pipeline efficiency. When using existing pipeline network to transport H₂NG, it is necessary to make appropriate adjustment to the pipeline network and infrastructure.
- Overall, this study show that the proposed transportation model can predict the transportation of H₂NG well. This will help the layout design and equipment selection for the subsequent transportation of H₂NG, to ensure the safety and efficiency of transportation. Further studies will be carried out to the operation analysis and optimization of the equipment in the pressurization station. This will enable more accurate modeling of an H₂NG pipeline transportation.
- ## DATA AVAILABILITY STATEMENT
- The original contributions presented in the study are included in the article/Supplementary Material, further inquiries can be directed to the corresponding author.
- ## AUTHOR CONTRIBUTIONS
- JL and LT designed the model and simulated it; BL and PH analyzed the simulation results and data; JL draft papers; PH and WL make important revisions to the paper.
- ## FUNDING
- This work was supported by the the Natural Science Foundation of Hebei Province (E2019210036), the Chongqing Natural Science Foundation (Grant No. CYY202010102001) and the Fundamental research found for Hebei Province administrated Universities (ZCT202002).
- Cherigui, A.-N., Mahmah, B., Harouadi, F., Belhamel, M., Chader, S., M'Raoui, A., et al. (2008). Solar Hydrogen Energy: The European–Maghreb Connection. A New Way of Excellence for a Sustainable Energy Development. *Int. J. Hydrogen Energ.* 34 (11).
- Chintala, V., and Subramanian, K. A. (2017). A Comprehensive Review on Utilization of Hydrogen in a Compression Ignition Engine under Dual Fuel Mode. *Renew. Sust. Energ. Rev.* 70. doi:10.1016/j.rser.2016.11.247
- Dall'Acqua, D., Terenzi, A., Leporini, M., D'Alessandro, V., Giacchetta, G., and Marchetti, B. (2017). A New Tool for Modelling the Decompression Behaviour of CO₂ with Impurities Using the Peng–Robinson Equation of State. *Appl. Energ.*, 206.
- Deymi-Dashtebayaz, M., Moghadam, A. E., Pishbin, S. I., and Pourramezan, M. (2019). Investigating the Effect of Hydrogen Injection on Natural Gas Thermo-Physical Properties with Various Compositions. *Energy*, 167.
- Elaoud, S., Hafsi, Z., and Hadj-Taieb, L. (2017). Numerical Modelling of Hydrogen–Natural Gas Mixtures Flows in Looped Networks. *J. Pet. Sci. Eng.* 159. doi:10.1016/j.petrol.2017.09.063
- Gas Transmission System (2015). *Specification for Gas Transmission Pipeline Engineering Design[S]*. Beijing: China Planning Perss.
- Haeseldonckx, D., and D'haeseleer, W. (2006). The Use of the Natural-Gas Pipeline Infrastructure for Hydrogen Transport in a Changing Market Structure. *Int. J. Hydrogen Energ.* 32 (10).

- Hafsi, Z., Elaoud, S., and Mishra, M. (2019). A Computational Modelling of Natural Gas Flow in Looped Network: Effect of Upstream Hydrogen Injection on the Structural Integrity of Gas Pipelines. *J. Nat. Gas Sci. Eng.* 64, 107–117. doi:10.1016/j.jngse.2019.01.021
- Hafsi, Z., Mishra, M., and Elaoud, S. (2018). Hydrogen Embrittlement of Steel Pipelines during Transients. *Proced. Struct. Integrity* 13. doi:10.1016/j.prostr.2018.12.035
- Helgaker, J. F., Oosterkamp, A., Langelandsvik, L. I., and Ytrehus, T. (2014). Validation of 1D Flow Model for High Pressure Offshore Natural Gas Pipelines. *J. Nat. Gas Sci. Eng.* 16. doi:10.1016/j.jngse.2013.11.001
- Hengxuan, C. O., Gregory, D., and Dogan, G. (2021). Interactive Effects of Message Framing and Information Content on Carbon Offsetting Behaviors. *Tourism Manag.*, 83.
- Kendall, M. (2018). Fuel Cell Development for New Energy Vehicles (NEVs) and Clean Air in China. *Prog. Nat. Sci. Mater. Int.* 28 (2). doi:10.1016/j.pnsc.2018.03.001
- Kouchachvili, L., and Entchev, E. (2018). Power to Gas and H₂/NG Blend in SMART Energy Networks Concept. *Renew. Energ.*, 125.
- Li, J., Lu, C., Pei, L., Zhang, C., and Wang, R. (2020). Atomistic Investigation of Hydrogen Induced Decohesion of Ni Grain Boundaries. *Mech. Mater.*, 150.
- Liu, B., Liu, X., Lu, C., Godbole, A., Michal, G., and Teng, L. (2019). Decompression of Hydrogen–Natural Gas Mixtures in High-Pressure Pipelines: CFD Modelling Using Different Equations of State. *Int. J. Hydrogen Energ.* 44 (14). doi:10.1016/j.ijhydene.2019.01.221
- Liu, X., Godbole, A., Lu, C., Michal, G., and Venton, P. (2014). Source Strength and Dispersion of CO₂ Releases from High-Pressure Pipelines: CFD Model Using Real Gas Equation of State. *Appl. Energ.* 126. doi:10.1016/j.apenergy.2014.03.073
- Liu, Y., Cheng, Q., Gan, Y., Wang, Y., Li, Z., and Zhao, J. (2019). Multi-objective Optimization of Energy Consumption in Crude Oil Pipeline Transportation System Operation Based on Exergy Loss Analysis. *Neurocomputing* 332, 100–110. doi:10.1016/j.neucom.2018.12.022
- Lu, L. (2011). Database Design Base on GIS Gas Management Network. *Proced. Eng.* 15, 3954–3958. doi:10.1016/j.proeng.2011.08.740
- Mah, A. X. Y., Ho, W. S., Bong, C. P. C., Hassim, M. H., Liew, P. Y., Asli, U. A., et al. (2019). Review of Hydrogen Economy in Malaysia and its Way Forward. *Int. J. Hydrogen Energ.* 44 (12). doi:10.1016/j.ijhydene.2019.01.077
- Mauricio, L., Lára, J., and Brynhildur, D. (2021). The Energy Company of the Future: Drivers and Characteristics for a Responsible Business Framework. *J. Clean. Prod.*, 288.
- Meliani, M. H., Azari, Z., Matvienkoc, Y. G., and Pluvinae, G. (2011). The Effect of Hydrogen on the Master Failure Curve of APL 5L Gas Pipe Steels. *Proced. Eng.* 10. doi:10.1016/j.proeng.2011.04.155
- Mi, J., Wang, X., and Zhu, G. (2012). Origin Determination of Gas from Jingbian Gas Field in Ordos basin Collective through the Geochemistry of Gas from Inclusions and Source Rock Pyrolysis[J]. *Acta Petrologica Sinica*.
- Nadaleti, W. C., Santos, G. B. d., and Lourenço, V. A. (2020). Integration of Renewable Energies Using the Surplus Capacity of Wind Farms to Generate H₂ and Electricity in Brazil and in the Rio Grande Do Sul State: Energy Planning and Avoided Emissions within a Circular Economy. *Int. J. Hydrogen Energ.* 45 (46). doi:10.1016/j.ijhydene.2020.06.226
- Natural gas in China (1997). The Shaanxi-Beijing Natural Gas Pipeline Is Put into Operation[J]. *Oil & Gas Storage and Transportation* (09), 28.
- Ogden, J., Jaffe, A. M., Scheitrum, D., McDonald, Z., and Miller, M. (2018). Natural Gas as a Bridge to Hydrogen Transportation Fuel: Insights from the Literature. *Energy Policy* 115. doi:10.1016/j.enpol.2017.12.049
- Omar, B., Hafsi, Z., Djukic, M. B., and Elaoud, S. (2020). The Synergistic Effects of Hydrogen Embrittlement and Transient Gas Flow Conditions on Integrity Assessment of a Precracked Steel Pipeline. *Int. J. Hydrogen Energ.*
- Peng, D.-Y., and Robinson, D. B. (1976). A New Two-Constant Equation of State. *Ind. Eng. Chem. Fund.* 15 (1), 59–64. doi:10.1021/i160057a011
- Pluvinae, G. (2021). Mechanical Properties of a Wide Range of Pipe Steels under Influence of Pure Hydrogen or Hydrogen Blended with Natural Gas. *Int. J. Press. Vessels Piping* 190, 104293. doi:10.1016/j.ijpvp.2020.104293
- Qingmei, J., Qin, W., Ping, X., and Xiangjun, Q. (2019). Development Status and Analysis of Long Distance Hydrogen Pipeline at home and Abroad [J]. *oil gas fields Surf. Eng.* 38 (12), 6–8.
- Qingqing, G. (2015). *Analysis and Research on Energy Saving and Consumption Reduction Evaluation of Gathering and Transportation System in Old Oilfields*. China University of Petroleum (East China).
- Quarton, C. J., and Samsatli, S. (2020). Should We Inject Hydrogen into Gas Grids? Practicalities and Whole-System Value Chain Optimisation. *Appl. Energ.*, 275.
- Reuß, M., Welder, L., Thürauf, J., Linßen, J., Grube, T., Schewe, L., et al. (2019). Modeling Hydrogen Networks for Future Energy Systems: A Comparison of Linear and Nonlinear Approaches. *Int. J. Hydrogen Energ.*
- Shay, E., Combs, T. S., Findley, D., Kolosna, C., Madeley, M., and Salvesen, D. (2016). Identifying Transportation Disadvantage: Mixed-Methods Analysis Combining GIS Mapping with Qualitative Data. *Transport Policy* 48, 129–138. doi:10.1016/j.tranpol.2016.03.002
- Sherif, S. A., Barbir, F., and Veziroglu, T. N. (2005). Wind Energy and the Hydrogen Economy — Review of the Technology. *Fuel Energ. Abstr.* 46 (6).
- Singh, V., Singh, R., Singh, A., and Mahajan, D. K. (2018). Tracking Hydrogen Embrittlement Using Short Fatigue Crack Behavior of Metals. *Proced. Struct. Integrity* 13. doi:10.1016/j.prostr.2018.12.296
- Tikhonova, S. A., Kapitonova, T. A., and Struchkova, G. P. (2019). Safety Assessment of Oil and Gas Pipelines Using Satellite Information. *Proced. Struct. Integrity* 20, 230–235. doi:10.1016/j.prostr.2019.12.144
- Timmerberg, S., and Kaltschmitt, M. (2019). Hydrogen from Renewables: Supply from North Africa to Central Europe as Blend in Existing Pipelines – Potentials and Costs. *Appl. Energ.*, 237.
- Uilhoorn, F. E. (2009). Dynamic Behaviour of Non-isothermal Compressible Natural Gases Mixed with Hydrogen in Pipelines. *Int. J. Hydrogen Energ.* 34 (16), 6722–6729. doi:10.1016/j.ijhydene.2009.06.062
- Varzandeh, F., Stenby, E. H., and Yan, W. (2017). Comparison of GERG-2008 and Simpler EoS Models in Calculation of Phase Equilibrium and Physical Properties of Natural Gas Related Systems. *Fluid Phase Equilibria*, 434.
- Wang, Y., Yuan, H., Martinez, A., Hong, P., Xu, H., and Bockmiller, F. R. (2021). Polymer Electrolyte Membrane Fuel Cell and Hydrogen Station Networks for Automobiles: Status, Technology, and Perspectives. *Adv. Appl. Energ.* 2, 100011. doi:10.1016/j.adapen.2021.100011
- Witkowski, A., Rusin, A., Majkut, M., and Stolecka, K. (2017). Comprehensive Analysis of Hydrogen Compression and Pipeline Transportation from Thermodynamics and Safety Aspects. *Energy*, 141.
- Zhao, Y., Yao, L., Liu, L., and Xu, Y. (2019). Optimization of Energy Saving Gathering and Transportation Mode in a Block of Tahe Oilfield. *Case Stud. Therm. Eng.* 13, 100378. doi:10.1016/j.csite.2018.100378
- Zhou, J., Wu, Y., Dong, H., Tao, Y., and Xu, C. (2020). Proposal and Comprehensive Analysis of Gas-Wind-Photovoltaic-Hydrogen Integrated Energy System Considering Multi-Participant Interest Preference. *J. Clean. Prod.* 265, 121679. doi:10.1016/j.jclepro.2020.121679

Conflict of Interest: The authors declare that the research was conducted in the absence of any commercial or financial relationships that could be construed as a potential conflict of interest.

Copyright © 2021 Liu, Teng, Liu, Han and Li. This is an open-access article distributed under the terms of the Creative Commons Attribution License (CC BY). The use, distribution or reproduction in other forums is permitted, provided the original author(s) and the copyright owner(s) are credited and that the original publication in this journal is cited, in accordance with accepted academic practice. No use, distribution or reproduction is permitted which does not comply with these terms.



Gas Discharge Resistance and Medium Damage Degree as Hydrate Dissociation at Different Ambient Conditions

Xueping Chen¹, Peng Zhang^{1*}, Qingbai Wu^{1*}, Lianhai Zhang¹, Shuaijun Li^{1,2}, Jing Zhan^{1,2} and Yingmei Wang³

¹State Key Laboratory of Frozen Soil Engineering, Northwest Institute of Eco-Environment and Resources, Chinese Academy of Sciences, Lanzhou, China, ²University of Chinese Academy of Sciences, Beijing, China, ³Western China Energy and Environment Research Center, Lanzhou University of Technology, Lanzhou, China

OPEN ACCESS

Edited by:

Jiang Bian,
China University of Petroleum, China

Reviewed by:

Chungang Xu,
Guangzhou Institute of Energy
Conversion (CAS), China
Ahmet Ansoy,
Istanbul Technical University, Turkey

*Correspondence:

Peng Zhang
Zhangpeng@lzb.ac.cn
Qingbai Wu
qbwu@lzb.ac.cn

Specialty section:

This article was submitted to
Advanced Clean Fuel Technologies,
a section of the journal
Frontiers in Energy Research

Received: 20 May 2021

Accepted: 08 July 2021

Published: 13 August 2021

Citation:

Chen X, Zhang P, Wu Q, Zhang L, Li S,
Zhan J and Wang Y (2021) Gas
Discharge Resistance and Medium
Damage Degree as Hydrate
Dissociation at Different
Ambient Conditions.
Front. Energy Res. 9:712156.
doi: 10.3389/fenrg.2021.712156

For the investigation on some hydrate dissociation behaviors at different ambient conditions, methane hydrates formed inside porous media with different saturations were dissociated by depressurizations. Plots of the instantaneous flow rate of gas as dissociation *versus* production pressure as well as deformation of experimental sample *versus* accumulative amount of released gas were drawn. These two lines slopes are, respectively, characterized as gas discharge resistance and reciprocal of the latter one as damage degree of experimental samples. The results show that these formed hydrates at higher ambient conditions, that is, temperature and pressure, and possess a higher saturation, which is beneficial to discharge gas and to keep experimental samples undamaged. And the nonuniformity of dissociation processes at different layer positions induced by depressurization is inhibited significantly, especially while combining extra heating. Hydrate saturation dominates the total volume loss of these samples under loadings. These conclusions can provide reference for the prediction in gas discharge capability and media damage degree as hydrate dissociation at different experimental and natural ambient conditions.

Keywords: methane hydrate, discharge resistance, damage degree, porous medium, depressurization, ambient condition

INTRODUCTION

Natural gas hydrates are one kind of ice-like crystalline solids composed of water and gas molecules (Sloan and Koh, 2008). Under high pressure and low temperature, water molecules form polyhedral cavities through hydrogen bonds and gas molecules are engaged inside (Koh, 2002). Various species of gas, ranging from light hydrocarbons like methane, ethane, and carbon dioxide to heavy isobutane and noble gases, can be enclathrated within the water lattices (Reed and Westacott, 2008). Explorations *via* bore holes in marine sediments confirmed that natural gas hydrates occur widely in nature (Max and Lowri, 1996; Makogon et al., 2007). These reservoirs mainly exist within marine and freshwater sediments at depths greater than 300 m (Khlystov et al., 2013; Naudts et al., 2012). Natural gas hydrate is also called methane hydrate (Kvenvolden and Rogers, 2005) because the main gas component is methane. As estimated, the amount of carbon stored in natural gas hydrate is about twice the total amount of exploitable hydrocarbon reserves stored in the form of fossil fuels (Kvenvolden, 1988; Milkov, 2004; Wallmann et al., 2012).

Initially, owing to considerable amounts of plugs formed within the pipelines, natural gas hydrates attracted a great deal of attention. These plugs caused severe economic losses such as the production and transportation of natural gas and oil (Sloan, 2005; Gbaruko et al., 2007; Mokhtab et al., 2007; Gao, 2008). Methane hydrate has subsequently ignited great interest of enormous amount of research groups around the world as one of the most potential substitutes for the traditional fuels. For the high efficiency exploitation, many research studies have been done to develop the production methods of gas and investigate the production behaviors as hydrate dissociation. The most common methods to dissociate hydrate are 1) thermal stimulation, in which the hydrate reservoirs are heated above the temperature of equilibrium decomposition, and 2) depressurization, the pressure of reservoir is reduced below that of equilibrium decomposition (Wang et al., 2016). Under these two methods, the local P–T conditions remaining hydrate stable are altered and then hydrate is dissociated into water and gas.

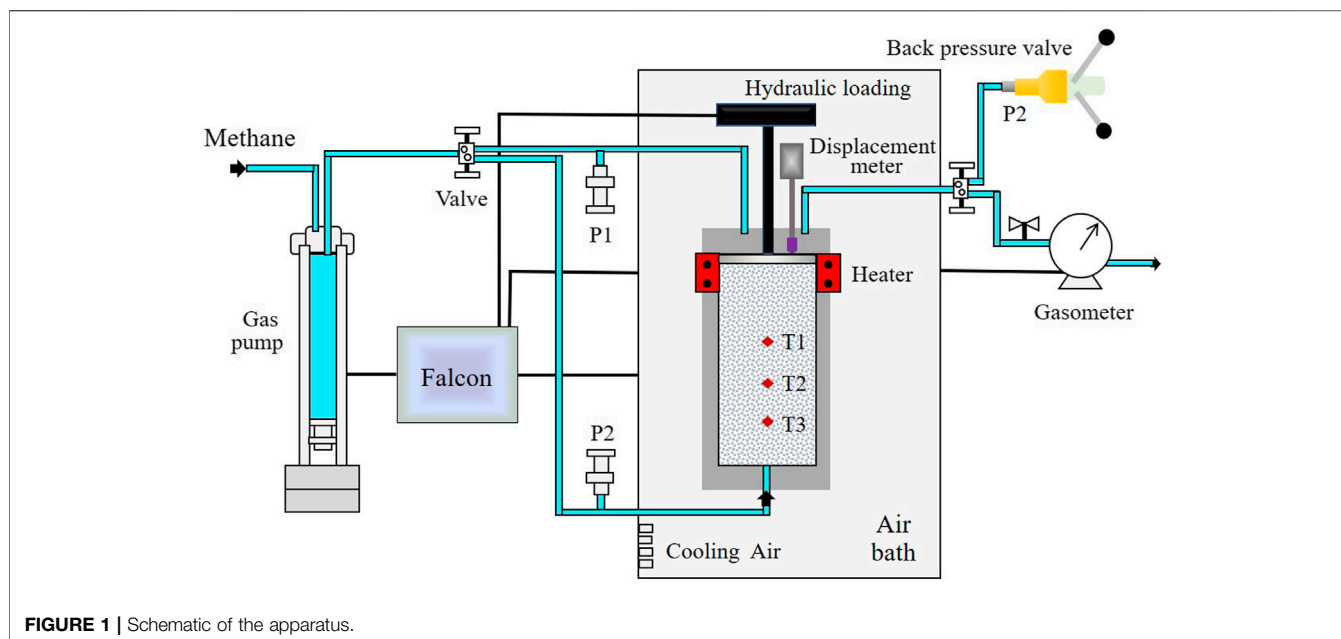
At a laboratory scale, hydrate dissociation behaviors have been widely investigated by the controlled thermal stimulation and depressurization (Chong et al., 2016). In general, thermal stimulation includes change in environmental temperature by water or air bath heating (Pang et al., 2009; Linga et al., 2009; Mekala et al., 2014; Zhao et al., 2012), hot fluid injection into the hydrate sample (Tang et al., 2005), and heat supplying through point sources (Fitzgerald and Castaldi, 2005). Of these, water or air bath heating is just a research method used in the laboratory but not feasible in the field (Chong et al., 2016). However, these methods can be used to simulate the ambient temperature changes under which methane hydrate is exploited in the laboratory. And the depressurization can be performed in different temperature ranges. For example, at 273–275 K, the dissociation behaviors of methane hydrate when being depressurized to three different pressures, that is, 0.1, 0.93, and 1.93 MPa, were compared (Tang et al., 2007), which showed that the dissociation rate at the lowest pressure 0.1 MPa was the fastest. With production pressure ranging from 4.5 to 5.6 MPa, the gas production behavior from methane hydrate in a porous sediment was also investigated at 281.15 K (Li X. S. et al., 2012). Further research shows that the gas production process was mainly influenced by the depressurization rate, heat from ambient environment, and free gas saturation in hydrate deposits (Li et al., 2014). In a range between 272 and 289 K, a significant thermal buffering phenomenon, that is, the temperature decreased to and maintained below 272.7 K until above 95% of the dissociation process was completed, was observed in the middle section of the samples during methane hydrate dissociation by rapid depressurization to 0.1 MPa (Circone et al., 2000). The authors highlighted that for the depressurization method, heating is required. A combination of these two methods is finally widely deemed as an effective technique to enhance the gas production efficiency significantly. Effectiveness of the combined method, named the huff and puff, in enhancing the production of gas has been investigated by some groups (Li et al., 2011; Li B. et al., 2012; Wang et al., 2014). By comparing the

energy efficiency difference among the single-well depressurization, five-spot thermal stimulation, and the combination of them, under similar saturation and environment conditions, it was found that efficiency of the combination was enhanced by 15 times comparing with the sole thermal stimulation (Wang et al., 2013).

In nature, methane hydrate is generally deemed to exist within marine and freshwater sediments below water depths more than 600 m and in intermediate water depths 1,000–3,000 m (Kvenvolden, 1993). Some exceptions have, however, also been found, for example, one location in the Arctic Ocean where hydrate occurs at depths of only 250 m and the ambient temperature is -1.5°C (Buffett and Archer, 2004). The ambient temperature in sediments under the sea or lake floor changes as a function of the geothermal and hydrothermal gradients of specific natural environment. These gradients have location or seasonality properties (Milkov et al., 2000; Buffett and Archer, 2004). The influence of specific ambient conditions on the dissociation behaviors of methane hydrate should therefore be taken into account during actual exploitation. Besides, the enhancement on gas production efficiency is the most important research target of methane hydrate dissociation in general. The flow behaviors of gas and liquid through porous sediments also have significant importance to the hydrate reservoir exploitation. As pointed out by Chong et al. (2016), the change patterns of them at different pressure conditions and hydrate saturation should also be well understood. Along with changes in measured resistivity, Li B. et al. (2012); Li X. S. et al. (2012) analyzed the water flow property in the porous sediment during dissociation processes of methane hydrate. Chen et al. (2019) pointed out that depressurization decreases the flow resistance of the water phase and optimizes the water flow environment during the hydrate dissociation. By comparison, change patterns of gas flow resistance in media as dissociation have rarely been reported, and damage situation of media following continuous gas discharge has rarely been mentioned.

For the thorough understanding on gas discharge law and medium damage as a hydrate dissociation process, methane hydrate was formed within porous media using an air-cooling method at different temperatures. The ambient temperature of the experimental sample was then regulated through an electric heating board on top, and the as-formed hydrate was dissociated through different production pressures. The change patterns of gas, the flow resistance, and the sample deformation were investigated during the entire hydrate dissociation. Possible influence of the hydrate dissociation process on its sediment skeleton was analyzed through gas discharge resistance and sample deformation. This study provides some guidance for the safe gas extraction from methane hydrates formed in porous structures. The main conclusions of this article can be summarized as follows:

- 1) Hydrates formed at high temperatures and pressures possess high saturations;
- 2) higher condition (i.e., high pressure and temperature) is beneficial to discharge gas and keep the sample undamaged as hydrate dissociation; and
- 3) the gas discharge resistance is mainly controlled by the viscosity of dissociation product—water, and the total loss of



sample volume under some loading is dominated by hydrate saturation.

EXPERIMENTS

Experimental Apparatus and Materials

The apparatus used in this work has been employed to investigate the influence of temperature on methane hydrate formation in porous media (Zhang et al., 2017). As shown in **Figure 1**, the apparatus involves a high-pressure reactor, a digitally controlled gas pump, a back pressure valve and a digital gasometer. The reactor has a diameter of 6.2 cm and a height of 19 cm, and is fixed in an air bath with a size of 80 cm × 50 cm × 80 cm, which is made of 316 stainless steels. The top cover of the reactor is unfixed, and a mechanical load ranging 0–50 MPa can be exerted with a digital hydraulic pump. A digital displacement meter is mounted on the top, ranging 0–100 mm with a resolution of 0.01 mm. Three pin-type temperature sensors, labeled T1, T2, and T3 in **Figure 1**, are vertically mounted on the reactor, ranging –20–50°C, the resolution is 0.01°C, and the heights are 7.0, 5.1, and 3.1 cm, respectively. An electric heater is mounted on the top of the reactor. Two pressure sensors, P1 and P2, connect to the top and bottom ends through a stainless steel conduit, respectively, with a range of 0–50 MPa and a precision of 0.001 MPa. The reactor is pressurized through a digital gas pump. Through the software Falcon, the pumps and heater are controlled, and all the parameters are logged and stored at intervals of 5 s.

Silica gel powder with an average particle size of 25–58 μm was chosen as the experimental medium. The density is 0.35 g/cm³ and the porosity is 77.44%. Being water saturated, the mass ratio of water to silica gel ($W_{\text{water}}/W_{\text{media}}$) is 2.2:1. A fixed ratio of 1.5:1 was used in the all experiments, that is, 68% water saturation.

Specific used amounts of water are exhibited in **Table 1**. The methane gas purity is 99.99%.

Experimental Procedure

Three predetermined pressures, that is, 5, 10, and 12 MPa, were chosen, and the corresponding equilibrium temperatures were calculated as 6.49, 12.91, and 14.48°C by the software CSMGem (Gas Hydrate Center, Colorado School of Mines). Before hydrate formation, the mixed medium was charged into the reactor until the height reached 14 cm. The whole experimental system was then slowly purged for about 5 min with the methane gas at atmospheric pressure, removing the residual air. A mechanical load of 3 MPa higher than the predetermined pressure was exerted on the sample top to compact through the hydraulic pump (**Figure 1**). The temperature of the reactor was rapidly reduced to the initial preparatory value with the air bath. After the sample was slowly pressurized to the predetermined pressure, the pump volume was maintained at a constant volume of 450 ml. The whole system was left undisturbed overnight to make the gas dissolve sufficiently. Subsequently, the temperature was uniformly reduced by 3.5°C at a fixed cooling rate of 1°C/h and maintained constant for more than 36 h to form hydrates completely. Hence, the final temperatures at which the formed hydrates were dissociated were 2.99, 9.41°C, and 10.98°C, corresponding to the predetermined pressure 5 MPa, 10 MPa, and 12 MPa, respectively.

Before hydrate dissociation, the valve between the gas pump and reactor was closed. Two methods, that is, sole depressurization and a combination with top heating, were employed to dissociate the as-formed hydrates at different ambient conditions. Three production pressures, that is, 0.5, 1.5, and 2.5 MPa, were manually set by a back pressure valve. Two combinations were performed as follows: the reactor top was heated by 2 and 4°C under a constant production pressure

TABLE 1 | Specific dissociation conditions of experimental media containing hydrate.

Experiment number	Production pressure (MPa)	Dissociation temperature (°C)	Amount of water (g)	Dissociation temperature (°C)	Amount of water (g)	Dissociation temperature (°C)	Amount of water (g)
1	0.5	2.99	224.83	9.41	224.12	10.98	224.75
2	1.5	2.99	224.79	9.41	224.82	10.98	224.61
3	2.5	2.99	224.76	9.41	224.30	10.98	224.65
4	1.5	4.99	224.86	11.41	224.08	12.98	224.99
5	1.5	6.99	224.74	13.41	225.16	14.98	224.71
6 (1 ^{re})	0.5	2.99	224.72	9.41	224.31	10.98	224.58
7 (2 ^{re})	1.5	2.99	225.11	9.41	225.79	10.98	224.57
8 (3 ^{re})	2.5	2.99	225.26	9.41	224.50	10.98	224.92
9 (4 ^{re})	1.5	4.99	224.61	11.41	224.96	12.98	224.77
10 (5 ^{re})	1.5	6.99	224.65	13.41	224.66	14.98	224.80

The abbreviation "re" means the repeat of the corresponding experiment number.

1.5 MPa. The gasometer measured the instantaneous flow rate of released gas during the dissociation, at atmospheric pressure and room temperature. To ensure the results reliability, all the dissociation experiments were repeated, and the detailed conditions are exhibited in **Table 1**.

Calculation Methods

The unit of data measured by the gasometer was in L/min. The amount of gas was calculated through the following gas equation:

$$PV = nZRT. \quad (1)$$

Through calculation, the compressibility factor Z of methane gas at atmospheric pressure and room temperature is 0.9982. At standard temperature and pressure conditions, the per unit volume of hydrate releases 164 volumes of methane gas after dissociation. The conversion ratio of water was then calculated with the accumulative volumes of released gas. The saturation of hydrates formed in the medium was calculated with the following equation:

$$S_h = V_w \cdot \eta / 0.99 \cdot V \cdot \phi, \quad (2)$$

where S_h is the hydrate saturation, V_w is the volume of liquid water in the sample, η is the calculated conversion ratio of water to hydrate, V is the volume of the experimental sample, and ϕ is the porosity, which is 77.44%. The coefficient 0.99 expresses the volume difference between solid hydrate and liquid water.

Using Darcy's law (**Eq. 3**) for reference, the permeability capability of gas during the dissociation processes of hydrate can be expressed with the permeability coefficient of medium K . The expression of Darcy's law is as follows:

$$Q = K\omega h/L, \quad (3)$$

where Q is the amount of liquid flowed out in unit time, K is the permeability coefficient, ω is the wetted cross section, h is the water head loss, and L is the permeability path. In this work, the water contents (**Table 1**) and heights of the media are almost similar. The cross section of the reactor is fixed (**Figure 1**). Hence, the permeability of gas during dissociation is expressed as follows:

$$K = Q/h, \quad (4)$$

where Q is the measured instantaneous flow rate of gas (L/min) and h is the set production pressure (MPa). Because the measured

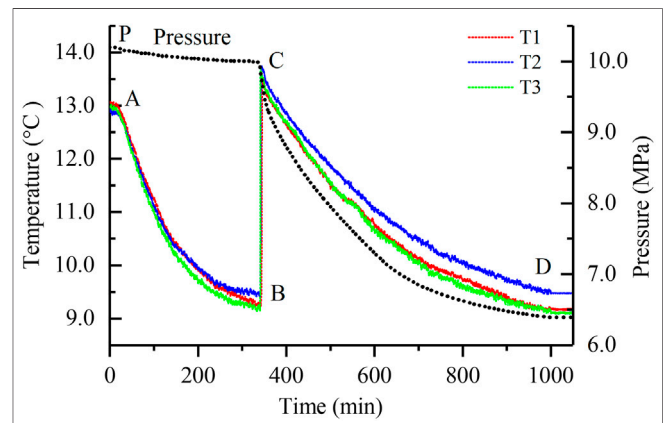


FIGURE 2 | Changes in temperature and pressure inside the reactor during the hydrate formation at the predetermined pressure 10 Mpa.

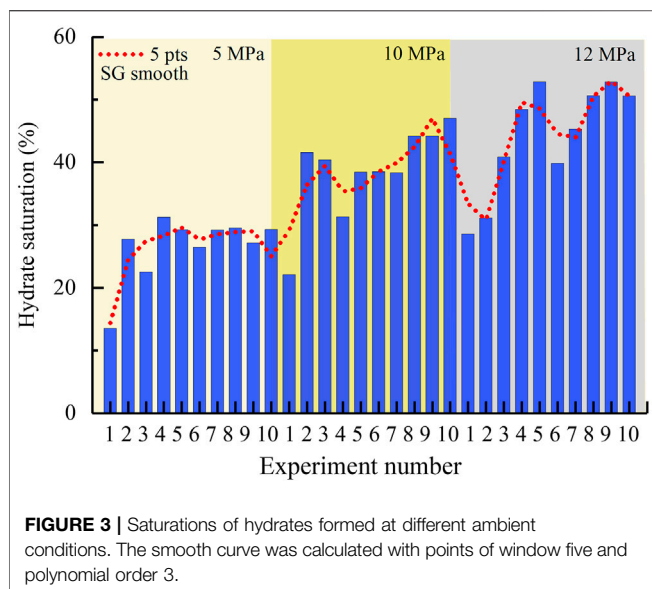
parameter during dissociation is the gas flow rate, the reciprocal of permeability coefficient K , that is, $1/K$ ((min·MPa)/L), characterizes the gas discharge resistance.

While dissociating into gas and water, the hydrate volume shrinks by 1%. Hence, the change pattern of the experimental sample volume along with the released gas amount was also investigated. Because the cross section of the reactor is fixed (**Figure 1**), the volume can be expressed with the sample length. The change pattern is hence expressed as follows:

$$V_c = D/V_g, \quad (5)$$

where V_c is the change degree of the experimental sample volume (mm/L), D is the deformation of the sample (mm), and V_g is the accumulative amount of the released gas (L). V_c also characterizes the sample damage degree while discharging unit volume of gas.

By plotting Q versus h and D versus V_g using Excel, the gas discharge resistance and damage degree of the sample along with hydrate dissociation processes were calculated and discussed. For simplicity, the specific ambient condition while dissociating was symbolized with the predetermined pressure value to form hydrates, that is, 5, 10, or 12 MPa, in the following sections.

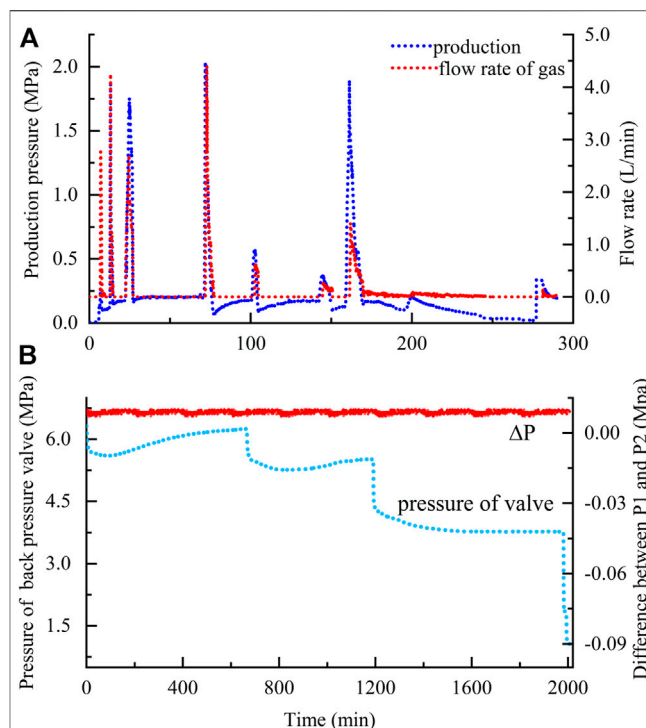


RESULTS AND DISCUSSION

Influence of Different Conditions on the Hydrate Formation Process

Using a semi-batch cooling method, methane hydrate was formed in porous media. As shown in **Figure 2**, the hydrate formation process shows two distinct stages (AB and CD). After undergoing an induction period (denoted by sections AB and PC) of rapid temperature reduction, hydrate begins nucleating, and the temperatures at three different layer positions rise suddenly (BC section). Then, the temperatures slowly decrease along with a significant pressure drop (CD section). All the parameters finally tend to remain stable (after point D) when the hydrates are thoroughly formed. Because the change patterns of pressure and temperatures at other formation conditions are similar, the representative formation process at the predetermined pressure 10 MPa with a dissociation production pressure 2.5 MPa was only exhibited in **Figure 2**. The sudden temperatures rise from B to C is caused by the rapid heat releasing while nucleating. After that, hydrate crystals slowly grow, and methane gas is fiercely consumed. The curves of pressure and temperatures remain stable after the formation process is finally completed. The high similarity between the three temperature curves indicates that hydrates were uniformly formed at the different layer positions inside the porous medium.

The experimental results show that formation conditions at which hydrate was formed have a significant influence on saturation. As shown in **Figure 3**, the saturations tend to gradually increase along with pressure rise. The average value of saturation is 26.7% at 5 MPa, 38.6% at 10 MPa, and 44.1% at 12 MPa, that is, when pressure increases by 5 and 7 MPa, the hydrate saturation increased to 1.45 and 1.65 times of the original, respectively. Studies have shown that lower temperatures lead to the easier generation of such hydrate clathrate structures including some unstable pseudocages (defective structures) that are empty, or occupied by water molecules; while at



higher temperature, these defective structures are efficiently inhibited (Guo and Rodger, 2013). As stated above, these symbolized pressures in **Figure 3** correspond to the dissociation temperatures 2.99, 9.41°C, and 10.98°C (**Table 1**), from low to high. In this work, a fixed cooling magnitude of 3.5°C and a cooling rate of 1°C/h were employed to form hydrates. These hydrates formed at higher temperatures hence have the higher saturations and less structure defects.

Gas Discharge Resistance and Medium Damage Degree as Dissociation

With a back-pressure valve, different production pressures were regulated to dissociate the as-formed hydrates. As shown in **Figure 4**, for one complete hydrate dissociation, several times of depressurization performances are required. During each one, the change patterns of production pressure show obvious synchronism with that of gas releasing, showing that the stability of hydrates is significantly affected by the pressure decline (**Figure 4A**). A fixed production pressure corresponding to the pressure inside reactor was provided to dissociate hydrate (**Figure 4B**). Because the valve was manually regulated, some slight differences occur between the two different performances (**Figures 4A,B**). But, the pressure difference between the top and bottom of the reactor (P1 and P2 in

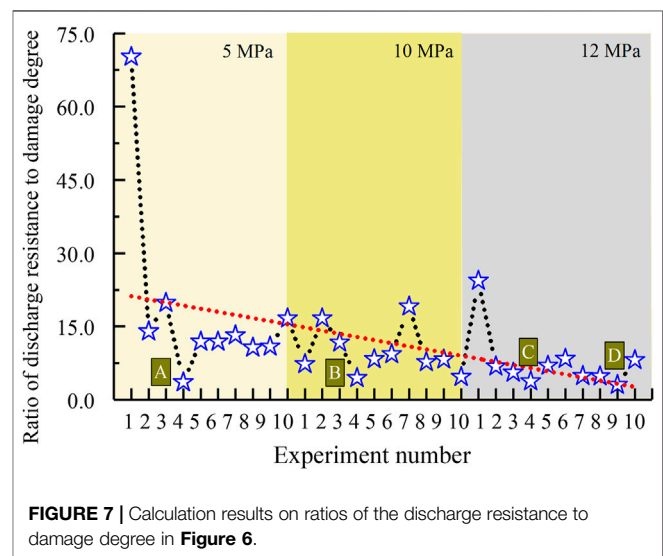
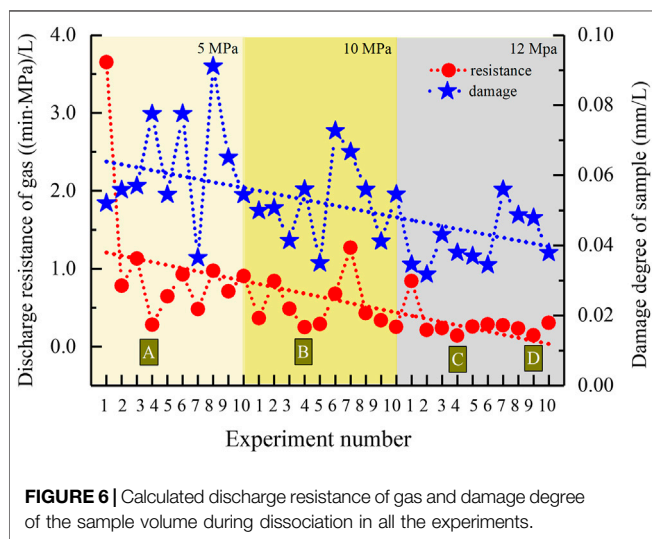
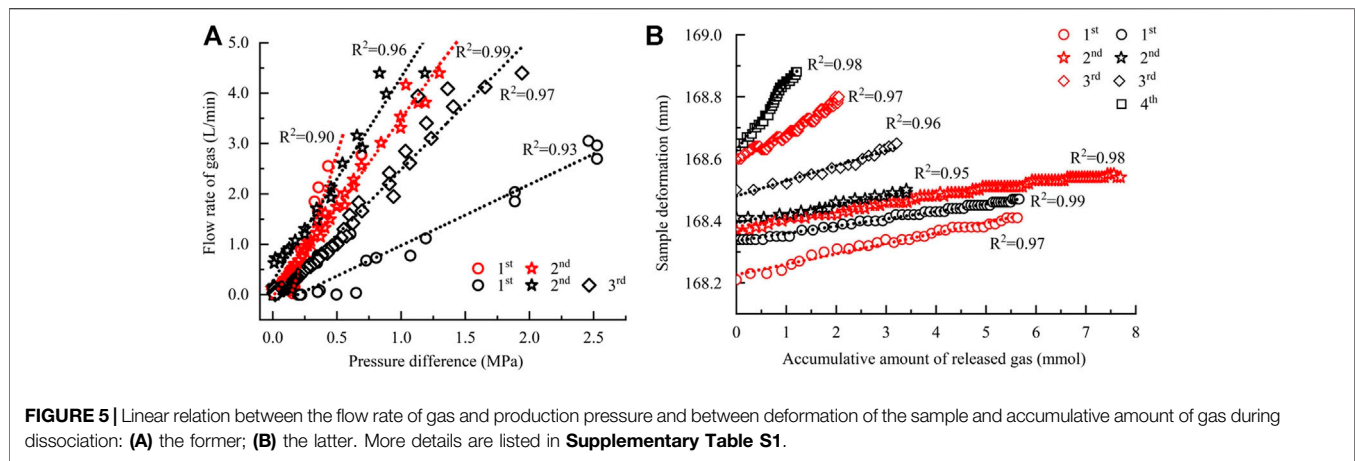
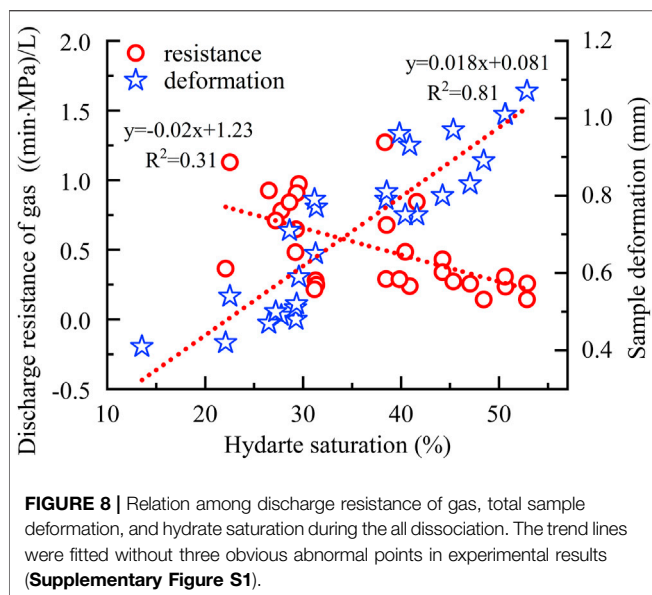


Figure 1) remains less than 0.01 MPa constantly (Figure 4B) over the entire dissociation process. Based on the synchronism between the gas releasing and production pressure, the releasing rates (Q , L/min) were then plotted against the corresponding production pressures (h , MPa). As shown in Figure 5A, there is a significant linear relationship between them during each depressurization (Figure 4A) as well as between the sample deformation (D , mm) and accumulative amount of released gas (V_g , L) (Figure 5B). The slopes of these two types of lines were then calculated to characterize the gas permeability capability (K , L/(min·MPa)) and the sample damage degree caused by gas discharge (V_c , mm/L), respectively. Among them, the gas discharge resistance as dissociation was characterized by the reciprocal of K . Because one complete hydrate dissociation requires several depressurizations (Figure 5), the calculated values were averaged at each experimental condition.

As shown in Figure 6, along with pressure rise, both the gas discharge resistance ($1/K$) and sample damage degree (V_c) decrease gradually. The average values are, respectively, 1.05 (min·MPa)/L, 0.062 mm/L at 5 MPa, 0.52 (min·MPa)/L,

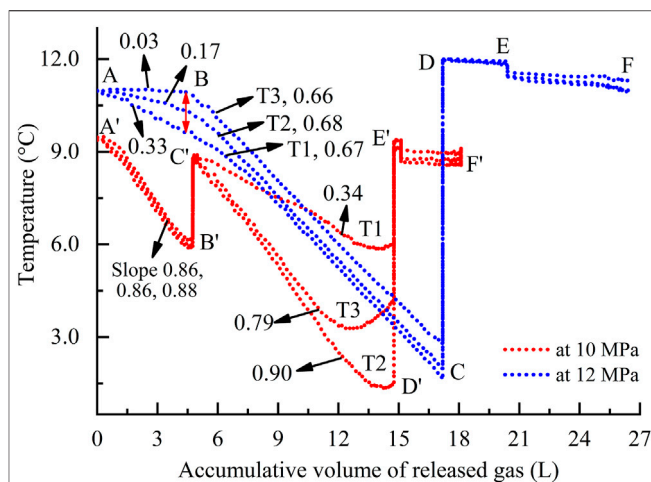
0.052 mm/L at 10 MPa, 0.30 (min·MPa)/L, and 0.041 mm/L at 12 MPa. Besides, among all the dissociation methods, the combination of 1.5 MPa production pressure and top heating by 2.0°C is the most favorable for hydrate dissociation, according to the minimum value of gas discharge resistance at each condition in Figure 6, that is, 0.28 (min·MPa)/L at 5 MPa (Point A), 0.25 (min·MPa)/L at 10 MPa (Point B), and 0.144 and 0.145 (min·MPa)/L at 10 MPa (Points C and D). They are all generated by this combined method. By comparison, the performances corresponding to the minimum of the sample damage degree do not have obvious regularity. Basing the similarity between two trend lines in Figure 6, the ratios of discharge resistances to damage degrees were calculated. As shown in Figure 7, both the change pattern and minimum values of ratios are similar with those of the discharge resistances in Figure 6. The ratio gradually decreased along with the rise in pressure condition with an average value 18.30 at 5 MPa, 9.76 at 10 MPa, and 7.68 at 12 MPa, reduced by about 1.8 and 2.4 times, respectively. Due to the significant hydrate saturation difference in all experiments (Figure 3), the



relationships among gas discharge resistance, total sample deformation, and hydrate saturation were additionally considered. As shown in **Figure 8**, along with the rise in saturation, the gas discharge resistance tends to decrease gradually as dissociation, while the total sample deformation shows an obvious increase, with R^2 equals to 0.81.

During each depressurization, the excellent linear relationships in **Figure 5** imply the reliability of statistic results in **Figure 6**. It can be found that the higher ambient condition is beneficial to discharge gas and keep the experimental sample undamaged as hydrate dissociation. The main reason is that higher formation conditions lead to higher hydrate saturations (**Figure 3**), thus less total pore volume that gas needs to pass inside the sample remains. In accordance with the relation between hydrate saturation and specific ambient condition (**Figure 3**), the gas discharge resistance logically presents a reverse correlation with hydrate saturation (**Figure 8**). However, the constant pressure difference between P1 and P2 (**Figure 4**) in fact means that the released gas can disperse instantly in entire space inside the sample once hydrate dissociates, suggesting that the gas discharge resistance is actually not predominated by the remaining pore spaces after deducting these occupied by solid hydrate. In addition, comparing **Figures 6** and **7**, it can be found that the change pattern of the ratio during all experiments is similar to that of single gas discharge resistance, especially the four minimum points A to D. Conclusively, the gas discharge resistance is not dominated by the sample damages as hydrate dissociation but the specific dissociation process.

Because the gas discharge resistance has no direct relation with these physical properties of experimental samples to contain hydrate, we infer that the above conclusion is mainly induced by the product properties from dissociation, for example, liquid water and gas released during dissociation of hydrates. Because when the temperature is lowered, the flow activation energy of water molecules reduces significantly, and the molecular collisions and other motions inside the water become more



moderate, which enhances the viscosity of liquid water significantly. Relevant measurements showed that when the temperature drops from 10 to 0°C, the viscosity of water increases by 37%, from 1.3069 to 1.7916 (Korson et al., 1969). In addition, a decrease in temperature results in a reduction in the distance between molecules, and the chemical bonds of gas–water and water–medium will be strengthened, leading to a further increase in the viscosity of water. Moreover, because the hydrates were all formed above 0°C, the liquid water existing in the media could not be converted into hydrate absolutely (**Figure 3**). As a consequence, the lower the temperature is, the more residual liquid water remains in the pores of samples after hydrate formations. It is then more difficult for the released gas to escape from the liquid water at the lower ambient temperature. And the samples will be damaged more seriously by these dissociations with a longer discharging process, that is, greater skeleton deformation of hydrate sediments. Additionally, the loss of the total sample length exhibits a significant positive correlation with hydrate saturation (**Figure 8**), implying that in all experiments, the total loss of the sample volume under some mechanical loadings after dissociation is dominated by the hydrate saturation.

Influence of Different Dissociation Methods on Each Layer

Using the three pin-type temperature sensors mounted in the reactor vertically, changes in temperature at different layers inside one sample were measured during dissociation. Owing to the similarity with the change patterns of temperatures at other ambient conditions, only two representatives at 10 and 12 MPa are exhibited in **Figure 9**. As shown, the change patterns are significantly influenced by the dissociation

methods. Like the pressure curves in **Figure 4**, the change patterns of temperature curves also show that several times of depressurizations are required to dissociate the as-formed hydrate completely, that is, the sections AB, BC, DE, and EF at 12 MPa and A'B', C'D', and E'F' at 10 MPa. During the first depressurization (A'B'), the extremely approximation between the slopes of three curves, 0.86 (T1), 0.86 (T2), and 0.88 (T3), suggests that the hydrate formed at the predetermined pressure 10 MPa is uniformly dissociated at three different layer positions. In contrast, the change patterns of the three curves show a high diversity during the second depressurization (C'D'). The curves slopes are, respectively, 0.79 and 0.90 of T3 and T2, being 2.3 and 2.6 times higher than those of T1, 0.34. During the final performance (E'F'), the temperatures almost remain stable even if the accumulative volumes of gas continue to increase. By comparison, at 12 MPa, the change patterns of curves in the two former periods are contrary to those at 10 MPa. During the first depressurization, the smallest slope among the three layers is T3, 0.03, and then the immediate T2, 0.17, which are 11 and 1.9 times smaller than that of the biggest one T1, 0.33, respectively. During the second performance, the three curves tend to converge, with the almost similar slopes of T1, 0.67; T2, 0.68; and T3, 0.66. The latter sections DE and EF are similar to the final E'F' at 10 MPa.

The gas source for hydrate formation is a digital gas pump (**Figure 1**); all the experimental samples had been compacted with a loading by 3 MPa higher than the predetermined pressure before formation. Before dissociation, the valve between the gas pump and reactor was closed; as a result, only a very small amount of free gas in the system is released during the first depressurization period. The significant temperature reduction inside the reactor in **Figure 9** is mainly attributed to the endothermic hydrate dissociation but not the free gas releasing (Li X. S. et al., 2012). Hence, these slopes in fact denote the hydrate dissociation efficiency at the different layer positions inside the sample. Because the average saturation at predetermined pressure 10 MPa is lower than that at 12 MPa (**Figure 3**), the hydrate with lower saturation is uniformly dissociated during first depressurization. The thermal buffering effect induced by depressurization (Circone et al., 2000) subsequently lowers the dissociation efficiency significantly, and the first depressurization is then forced to end. During the second depressurization, the hydrate with lower saturation at layer positions T2 and T3 dissociates much faster than that at T1. By comparison, the hydrate with higher saturation at 12 MPa is dissociated in a layer sequence T1 to T3 during the first depressurization and with lower dissociation efficiencies, that is, the three slopes less than 0.33. The thermal buffering effect (Circone et al., 2000) is significantly weakened by the combined dissociation method of 1.5 MPa production pressure and top heating by 4°C, as shown by the red double head arrow at Point B in **Figure 9**. In the subsequent second depressurization, the nonuniformity of dissociation processes at different layer positions is also inhibited significantly. This means that during methane hydrate dissociation by depressurization at the higher ambient condition, the nonuniformity of dissociation processes appearing at different layer positions can be inhibited

significantly, especially when combining an extra energy source (Holder et al., 1982).

CONCLUSION

Methane hydrates formed inside porous media with different saturations were dissociated through different depressurization methods at different ambient conditions. During dissociation, the instantaneous gas flow rate was plotted *versus* production pressure and the experimental sample deformation *versus* accumulative amount of released gas to investigate some new dissociation behaviors. The plotted relationships exhibit excellent linear properties, and the lines slopes are then used to characterize the gas discharge resistance, that is, the reciprocal of slope, and the damage degree of the sample volume during dissociation. The results show that under higher ambient condition, that is, higher temperature and pressure, the hydrates formed have higher saturation. The higher condition is beneficial to discharge gas and keep the sample undamaged during dissociation. The main reason is that the viscosity of the dissociation product, that is, liquid water, is significantly decreased at that condition. And the nonuniformity of dissociation processes by depressurization at different layer positions can be inhibited significantly, especially if combining extra heating.

DATA AVAILABILITY STATEMENT

The raw data supporting the conclusion of this article will be made available by the authors, without undue reservation.

AUTHOR CONTRIBUTIONS

XC carried out most of the experiments and prepared all of the figures. Manuscripts were prepared by XC and PZ. PZ and QW conceived the research. PZ directed specific experiments. LZ and SL provided constructive suggestions for the English translation. JZ and YW did some data analysis. All authors reviewed and approved the final manuscript.

FUNDING

The authors thank the National Key R&D Program of China (Grant No. 2017YFC0307303) and the National Natural Science Foundation of China (41571072, 41601079, and 41661103) for their financial support.

SUPPLEMENTARY MATERIAL

The Supplementary Material for this article can be found online at: <https://www.frontiersin.org/articles/10.3389/fenrg.2021.712156/full#supplementary-material>

REFERENCES

- Buffett, B., and Archer, D. (2004). Global Inventory of Methane Clathrate: Sensitivity to Changes in the Deep Ocean. *Earth Planet. Sci. Lett.* 227, 185–199. doi:10.1016/j.epsl.2004.09.005
- Chen, B., Sun, H., Li, K., Wang, D., and Yang, M. (2019). Experimental Investigation of Natural Gas Hydrate Production Characteristics via Novel Combination Modes of Depressurization With Water Flow Erosion. *Fuel* 252, 295–303. doi:10.1016/j.fuel.2019.04.120
- Chong, Z. R., Yang, S. H. B., Babu, P., Linga, P., and Li, X.-S. (2016). Review of Natural Gas Hydrates as an Energy Resource: Prospects and Challenges. *Appl. Energy* 162, 1633–1652. doi:10.1016/j.apenergy.2014.12.061
- Circone, S., Stern, L. A., Kirby, S. H., Pinkston, J. C., and Durham, W. B. (2000). Methane Hydrate Dissociation Rates at 0.1 MPa and Temperatures above 272 K. *Ann. N. Y. Acad. Sci.* 912, 544–555. doi:10.1111/j.1749-6632.2000.tb06809.x
- Fitzgerald, G. C., and Castaldi, M. J. (2013). Thermal Stimulation Based Methane Production From Hydrate Bearing Quartz Sediment. *Ind. Eng. Chem. Res.* 52, 6571–6581. doi:10.1021/ie400025f
- Gao, S. (2008). Investigation of Interactions Between Gas Hydrates and Several Other Flow Assurance Elements. *Energy Fuels* 22, 3150–3153. doi:10.1021/ef800189k
- Gbaruko, B. C., Igwe, J. C., Gbaruko, P. N., and Nwokeoma, R. C. (2007). Gas Hydrates and Clathrates: Flow Assurance, Environmental and Economic Perspectives and the Nigerian Liquefied Natural Gas Project. *J. Pet. Sci. Eng.* 56, 192–198. doi:10.1016/j.petrol.2005.12.011
- Guo, G.-J., and Rodger, P. M. (2013). Solubility of Aqueous Methane Under Metastable Conditions: Implications for Gas Hydrate Nucleation. *J. Phys. Chem. B* 117, 6498–6504. doi:10.1021/jp3117215
- Holder, G. D., Angert, P. F., John, V. T., and Yen, S. (1982). A Thermodynamic Evaluation of Thermal Recovery of Gas from Hydrates in the Earth (Includes Associated Papers 11863 and 11924). *J. Pet. Technol.* 34, 1127–1132. doi:10.2118/8929-PA
- Khlystov, O., Batist, M. D., Shoji, H., Hachikubo, A., Nishio, S., Naudts, L., et al. (2013). Gas Hydrate of Lake Baikal: Discovery and Varieties. *J. Asian Earth Sci.* 62, 162–166. doi:10.1016/j.jseae.2012.03.009
- Koh, C. A. (2002). Towards a Fundamental Understanding of Natural Gas Hydrates. *Chem. Soc. Rev.* 31, 157–167. doi:10.1039/b008672j
- Korson, L., Drost-Hansen, W., and Millero, F. J. (1969). Viscosity of Water at Various Temperatures. *J. Phys. Chem.* 73 (1), 34–39. doi:10.1021/j100721a006
- Kvenvolden, K. A., and Rogers, B. W. (2005). Gaia's Breath-Global Methane Exhalations. *Mar. Pet. Geology* 22, 579–590. doi:10.1016/j.marpetgeo.2004.08.004
- Kvenvolden, K. A. (1988). Methane Hydrate - A Major Reservoir of Carbon in the Shallow Geosphere? *Chem. Geology* 71, 41–51. doi:10.1016/0009-2541(88)90104-0
- Kvenvolden, K. A. (1993). Gas Hydrates-Geological Perspective and Global Change. *Rev. Geophys.* 31 (2), 173–187. doi:10.1029/93RG00268
- Li, B., Li, G., Li, X.-S., Li, Q.-P., Yang, B., Zhang, Y., et al. (2012). Gas Production from Methane Hydrate in a Pilot-Scale Hydrate Simulator Using the Huff and Puff Method by Experimental and Numerical Studies. *Energy Fuels* 26, 7183–7194. doi:10.1021/ef301258w
- Li, X.-S., Zhang, Y., Li, G., Chen, Z.-Y., and Wu, H.-J. (2011). Experimental Investigation into the Production Behavior of Methane Hydrate in Porous Sediment by Depressurization With a Novel Three-Dimensional Cubic Hydrate Simulator. *Energy Fuels* 25, 4497–4505. doi:10.1021/ef200757g
- Li, B., Li, X.-S., Li, G., Feng, J.-C., and Wang, Y. (2014). Depressurization Induced Gas Production From Hydrate Deposits With Low Gas Saturation in a Pilot-Scale Hydrate Simulator. *Appl. Energy* 129, 274–286. doi:10.1016/j.apenergy.2014.05.018
- Li, X.-S., Yang, B., Li, G., Li, B., Zhang, Y., and Chen, Z.-Y. (2012). Experimental Study on Gas Production from Methane Hydrate in Porous Media by Huff and Puff Method in Pilot-Scale Hydrate Simulator. *Fuel* 94, 486–494. doi:10.1016/j.fuel.2011.11.011
- Linga, P., Haligva, C., Nam, S. C., Ripmeester, J. A., and Englezos, P. (2009). Recovery of Methane from Hydrate Formed in a Variable Volume Bed of Silica Sand Particles. *Energy Fuels* 23, 5508–5516. doi:10.1021/ef900543v
- Makogon, Y. F., Holditch, S. A., and Makogon, T. Y. (2007). Natural Gas-Hydrates - A Potential Energy Source for the 21st Century. *J. Pet. Sci. Eng.* 56, 14–31. doi:10.1016/j.petrol.2005.10.009
- Max, M. D., and Lowrie, A. (1996). Oceanic Methane Hydrates: a "Frontier" Gas Resource. *J. Pet. Geol.* 19, 41–56. doi:10.1111/j.1747-5457.1996.tb00512.x
- Mekala, P., Babu, P., Sangwai, J. S., and Linga, P. (2014). Formation and Dissociation Kinetics of Methane Hydrates in Seawater and Silica Sand. *Energy Fuels* 28, 2708–2716. doi:10.1021/ef402445k
- Milkov, A. V., Sassen, R., Novikova, I., and Mikhailov, E. (2000). Gas Hydrates at Minimum Stability Water Depths in the Gulf of Mexico: Significance to Geohazard Assessment 2000. *Gcags Trans.* 3, 217–224. doi:10.2307/1936103
- Milkov, A. V. (2004). Global Estimates of Hydrate-Bound Gas in marine Sediments: How Much Is Really Out There?. *Earth-Sci. Rev.* 66, 183–197. doi:10.1016/j.earscirev.2003.11.002
- Mokhtab, S., Wilkens, R. J., and Leontaritis, K. J. (2007). A Review of Strategies for Solving Gas-Hydrate Problems in Subsea Pipelines. *Energy Sour. A: Recovery, Util. Environ. Effects* 29, 39–45. doi:10.1080/009083190933988
- Naudts, L., Khlystov, O., Granin, N., Chensky, A., Poort, J., and De Batist, M. (2012). Stratigraphic and Structural Control on the Distribution of Gas Hydrates and Active Gas Seeps on the Posolsky Bank, Lake Baikal. *Geo-mar Lett.* 32, 395–406. doi:10.1007/s00367-012-0286-y
- Pang, W. X., Xu, W. Y., Sun, C. Y., Zhang, C. L., and Chen, G. J. (2009). Methane Hydrate Dissociation experiment in a Middle-Sized Quiescent Reactor Using Thermal Method. *Fuel* 88, 497–503. doi:10.1016/j.fuel.2008.11.002
- Reed, S. K., and Westacott, R. E. (2008). The Interface Between Water and a Hydrophobic Gas. *Phys. Chem. Chem. Phys.* 10, 4614–4622. doi:10.1039/b801220b
- Sloan, E. D., and Koh, C. A. (2008). *Clathrate Hydrates of Natural Gases*. 3rd Edition. New York: Taylor & Francis Group, 1.
- Sloan, E. D. (2005). A Changing Hydrate Paradigm-From Apprehension to Avoidance to Risk Management. *Fluid Phase Equilib.* 228–229, 67–74. doi:10.1016/j.fluid.2004.08.009
- Tang, L. G., Xiao, R., Huang, C., Feng, Z. P., and Fan, S. S. (2005). Experimental Investigation of Production Behavior of Gas Hydrate under thermal Stimulation in Unconsolidated Sediment. *Energy Fuels* 19, 2402–2407. doi:10.1021/ef050223g
- Tang, L.-G., Li, X.-S., Feng, Z.-P., Li, G., and Fan, S.-S. (2007). Control Mechanisms for Gas Hydrate Production by Depressurization in Different Scale Hydrate Reservoirs. *Energy Fuels* 21, 227–233. doi:10.1021/ef0601869
- Wallmann, K., Pinero, E., Burwicz, E., Haeckel, M., Hensen, C., Dale, A., et al. (2012). The Global Inventory of Methane Hydrate in marine Sediments: A Theoretical Approach. *Energies* 5, 2449–2498. doi:10.3390/en5072449
- Wang, Y., Li, X.-S., Li, G., Zhang, Y., Li, B., and Feng, J.-C. (2013). A Three-Dimensional Study on Methane Hydrate Decomposition With Different Methods Using Five-Spot Well. *Appl. Energy* 112, 83–92. doi:10.1016/j.apenergy.2013.05.079
- Wang, Y., Li, X., Li, G., Huang, N., and Feng, J. (2014). Experimental Study on the Hydrate Dissociation in Porous Media by Five-Spot Thermal Huff and Puff Method. *Fuel* 117, 688–696. doi:10.1016/j.fuel.2013.09.088
- Wang, Y., Feng, J.-C., Li, X.-S., Zhang, Y., and Li, G. (2016). Large Scale Experimental Evaluation to Methane Hydrate Dissociation Below Quadruple Point in Sandy Sediment. *Appl. Energy* 162, 372–381. doi:10.1016/j.apenergy.2015.10.099
- Zhang, P., Wu, Q., and Mu, C. (2017). Influence of Temperature on Methane Hydrate Formation. *Sci. Rep.* 7, 7904. doi:10.1038/s41598-017-08430-y
- Zhao, J., Cheng, C., Song, Y., Liu, W., Liu, Y., Xue, K., et al. (2012). Heat Transfer Analysis of Methane Hydrate Sediment Dissociation in a Closed Reactor by a Thermal Method. *Energies* 5, 1292–1308. doi:10.3390/en5051292

Conflict of Interest: The authors declare that the research was conducted in the absence of any commercial or financial relationships that could be construed as a potential conflict of interest.

Publisher's Note: All claims expressed in this article are solely those of the authors and do not necessarily represent those of their affiliated organizations, or those of the publisher, the editors and the reviewers. Any product that may be evaluated in this article, or claim that may be made by its manufacturer, is not guaranteed or endorsed by the publisher.

Copyright © 2021 Chen, Zhang, Wu, Zhang, Li, Zhan and Wang. This is an open-access article distributed under the terms of the Creative Commons Attribution License (CC BY). The use, distribution or reproduction in other forums is permitted, provided the original author(s) and the copyright owner(s) are credited and that the original publication in this journal is cited, in accordance with accepted academic practice. No use, distribution or reproduction is permitted which does not comply with these terms.



Improved Analytical Method for Longitudinal Strain Analysis of Buried Pipelines Subjected to Thaw Slumping Load

Beilei Ji¹, Xiaoben Liu^{1,2*}, Dinaer Bolati^{1,3}, Yue Yang¹, Jinxu Jiang¹, Yuqing Liu⁴ and Hong Zhang¹

¹National Engineering Laboratory for Pipeline Safety, MOE Key Laboratory of Petroleum Engineering, Beijing Key Laboratory of Urban Oil and Gas Distribution Technology, China University of Petroleum-Beijing, Beijing, China, ²China University of Petroleum (Beijing) Karamay Campus, Karamay, China, ³Western Pipeline Co. Ltd of PipeChina, Urumqi, China, ⁴China Petroleum Pipeline Engineering Corporation, Langfang, China

OPEN ACCESS

Edited by:

Jiang Bian,
China University of Petroleum (East
China), China

Reviewed by:

Lingzhen Kong,
Southwest Petroleum University,
China
Zhanfeng Chen,
Hangzhou Dianzi University, China

*Correspondence:

Xiaoben Liu
xiaobenliu@cup.edu.cn

Specialty section:

This article was submitted to
Advanced Clean Fuel Technologies,
a section of the journal
Frontiers in Energy Research

Received: 16 July 2021

Accepted: 09 August 2021

Published: 01 September 2021

Citation:

Ji B, Liu X, Bolati D, Yang Y, Jiang J,
Liu Y and Zhang H (2021) Improved
Analytical Method for Longitudinal
Strain Analysis of Buried Pipelines
Subjected to Thaw Slumping Load.
Front. Energy Res. 9:742348.
doi: 10.3389/fenrg.2021.742348

Thawing landslide is a common geological disaster in permafrost regions, which seriously threatens the structural safety of oil and gas pipelines crossing permafrost regions. Most of the analytical methods have been used to calculate the longitudinal stress of buried pipelines. These analytical methods are subjected to slope-thaw slumping load, and the elastic characteristic of the soil in a nonlinear interaction behavior is ignored. Also, these methods have not considered the real boundary at both ends of the slope. This study set out to introduce an improved analytical method to accurately analyze the longitudinal strain characteristics of buried pipelines subjected to slope-thaw slumping load. In this regard, an iterative algorithm was based on an ideal elastoplastic model in the pipeline-soil interaction. Based on field monitoring and previous finite element results, the accuracy of the proposed method was validated. Besides, a parametric analysis was conducted to study the effects of wall thickness, internal pressure, ultimate soil resistance, and slope angle on the maximum longitudinal strain of the pipeline. The results from the compression section showed that the pipeline is more likely to yield, indicating an actual situation in engineering. Moreover, the maximum longitudinal tensile and compression strain of pipelines decrease with increasing the wall thickness, internal pressure, ultimate resistance of soil, and slope angle. Finally, based on the pipeline limit state equations in CSA Z662-2007 and CRES which considered the critical compression factor comprehensively, the critical slumping displacements for both tensile and compressive strain failures were derived for reference. The research results attach great significance to the safety of pipeline under slope.

Keywords: thawing landslide, buried pipelines, longitudinal strain, analytical method, critical slumping displacement

INTRODUCTION

Permafrost regions in China account for 22.4% of the total land area, mainly distributed in the Qinghai-Tibet Plateau and the Great and Small Xing'an Mountains (Xu et al., 2010). As a link between oil and gas resources and markets, pipelines are exposed to different geological conditions. Among the several oil and gas pipelines that have been crossed, e.g., the Gela pipeline unavoidably traverses the permafrost regions. In China, the Mo-Da line is the first long-distance pipeline that passes through the permafrost regions. According to incomplete statistics by PipeChina North Pipeline Company, more than 40

slopes are greater than 10° along the northern area, and the maximum slope is greater than 60° (Chen, 2012). The length of slopes is mostly over 200 m, and the most extended slope reaches more than 3,000 m. It faces the risk of thawing landslides during pipelines implementation. The stability of slopes is one of the severe problems faced by pipelines in frozen soil areas (McRoberts and Morgenstern, 1974). Slope-thaw slumping often occurs along with frozen soil melting (FSM). The FSM in the trench attaches complex force loadings to the buried pipelines, which is also vulnerable to changes in operating temperature, vegetation damage on the pipeline route, climate warming, and other factors.

Frozen soil areas are commonly faced with thawing landslides, as one of the common geological disasters (**Supplementary Figure S1**). In this regard, the permafrost regions accelerate their degradation effect on the oil and gas pipelines and the surrounding areas (Vasseghi et al., 2020). For instance, the Norman Wells pipeline in Canada has been bent and wrinkled six times due to landslides successively, bringing significant risks to pipeline management. The pipe under the slope of 84# was yielded and bent because of the thermal melt landslide. As a degradation effect on the Norman Wells pipeline, a new pipe with a length of 110 m was replaced and implemented in winter.

Recently, research analyzing the mechanical response of pipelines under the thermal melt slip has been categorized into numerical and analytical methods. One of the crucial discussions in the numerical method is an interaction model between pipe and soil. Tsatsis and Ocampo et al. introduced the pipe-soil model with nonlinear contact and used the Mohr-Coulomb nonlinear constitutive model to describe the material properties (Tsatsis, 2015; Andrés et al., 2017). Ho and Eichhorn applied the nonlinear soil spring model (Ho et al., 2014; Eichhorn and Haigh, 2018). In the finite element model established by Ho, the thermal stress of the pipeline was considered, and the stress and strain distribution of the pipeline was analyzed under the action of the longitudinal landslide. Eichhorn made an in-depth analysis on the pipe-soil interaction model of the longitudinal landslide with a horizontal foundation. In the model introduced by Eichhorn, it is assumed that the soil-spring model is not necessarily applicable to the problem of large ground deformation. The soil springs in all directions are interdependent and influenced by each other, and need to be verified according to an actual situation. Furthermore, Chen et al., Huang et al. considered the interaction between pipes and soil as simple forces such as thrust and friction, without considering the elasticity characteristics of soil (Chen and Hu, 2014; Huang et al., 2015). Besides, Li and Chen et al. adopted the pipe-soil model of nonlinear contact, adding contact units at the interface of pipe-soil, so the nonlinear contact problem between pipes and soil has been solved, and further considering the elasticity of soil (Li et al., 2016; Chen et al., 2017). However, these studies abridge the frictional action between the pipe and the soil as linear, and have not profoundly investigated the nonlinearity of the soil. In doing so, Wang, Zhang et al. implemented a nonlinearity-based soil spring model to evaluate a large deformation in soil and pipeline geometry (Wang et al., 2014; Zhang et al., 2017). However, this model could not simulate the contact nonlinearity between pipe and soil, and the simulation effect of nonlinear friction between pipe and soil is not perfect. Besides, the numerical method can accurately

provide the approaches to the mechanical response of pipelines under thermal-thawing slip. However, there are some issues such as costly evaluation process and standardization by applying the numerical methods.

On the other hand, the analytical method is mostly used for pipeline mechanics calculation, which is simple and easy to standardize (Zhang and Liu, 2017). A considerable amount of literature has simplified the analytical method of pipelines to a bilinear elastoplastic model. These studies have focused on the interaction between the pipelines and the soil (as an ideal elastoplastic material) in an elastic foundation beam model following Winkler's hypothesis. Yuan established a Z-shaped pipeline model where in the middle part of pipeline is horizontally located in the landslide section at both ends (Yuan, 1993). In this study, it is considered that the surface of the slope pipe is subjected to constant shear stress, and the pipes at both ends of the slope are regarded as beams buried horizontally in the elastic soil model. The formulas for calculating the displacement and axial stress are discussed in the case of different resistance coefficients at both ends of the soil. However, elastic-plastic characteristics of soil are not considered in the landslide section of Yuan's study, namely no attention to the relative soil displacement caused by the different pipe shearing stress. Also, Rajani et al. considered the pipe as an elastic beam buried in the elastoplastic soil, and the landslide section was semi-infinite in length with no bending at both ends (Rajani et al., 1995). In their model, the relationship between soil displacement and its resistance is linear in an elastic state. When the soil displacement increases to a certain extent, the soil will deform to a plastic state, and the resistance remains unchanged. The model introduced by Rajani et al. is classified as a bilinear elastoplastic model; however, the Poisson's ratio and the temperature effect are not considered in this model. Moreover, Yoosef-Ghods et al. remarked the Poisson's ratio and the temperature effect on the strain caused in the pipelines and believed that the initial strain of the pipeline is not zero (Yoosefghods et al., 2008). O'Rourke et al. used the nonlinear model of Ramberg-Osgood power exponential hardening to describe the constitutive relationship of pipes, assumed the soil displacement of various forms of permanent ground deformation and considered the relative displacements between pipes and soil (O'Rourke et al., 1995). He believed that the strain in the slope of middle pipeline section is zero. Based on the above considerations, the distribution of the strain in the pipelines is obtained under the action of the longitudinal landslide. However, O'Rourke et al. assumed that the amount of soil displacement is perfect and may not be consistent with the actual situation. Chan also adopted O'Rourke's infinite slope model and idealized soil displacement model but denied the boundary condition (i.e., the strain is zero) from O'Rourke et al.'s model in the slope of middle pipeline section (Chan, 2000). Chan assumed that the pipeline is always in a linear elastic state with a displacement of soil along the pipeline axes. Thus, the discontinuity of pipelines strain is solved by a relative displacement of soil and pipeline in an elastoplastic state.

Above all, although the finite element numerical simulation can obtain accurate results, the calculation cost is expensive. The existing analytical methods ignore the elastic characteristics of soil spring and do not consider the actual situation of the boundary at both ends of the slope. Therefore, given the above

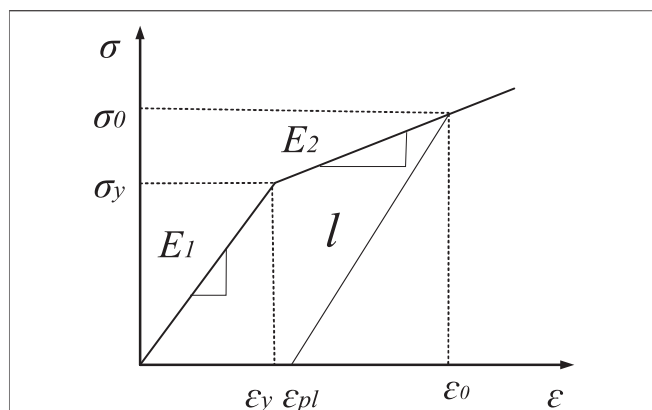


FIGURE 1 | Stress and strain curves of the steel pipeline.

deficiencies, this paper provides an improved analytical method for the longitudinal strain of buried pipelines under the thawing landslide, which considers elastoplastic characteristics of the axial nonlinear pipe soil interaction behaviors. Moreover, it is suitable for the pipeline under the large slope.

A BILINEAR STRESS-STRAIN MODEL FOR BURIED STEEL PIPELINES

The bilinear stress-strain model was considered for pipeline material. Figure 1 shows a stress-strain relationship in where the elastic and plastic modulus of pipe material are E_1 and E_2 , respectively. σ_y denotes the material yield strength, and the corresponding strain is the elastic limit strain ε_y . ε_{pl} denotes the plastic strain.

In case the longitudinal stress was less than the yield strength, the material characterizations were analyzed through a linear elasticity model. The maximum plastic strain of the analyzed material was considered 0.2%. The pipe will be failure when the material strain exceeds this value. Eq. 1 describes the stress-strain relationship of steel pipelines in an elastic-linear strain hardening model.

$$\begin{cases} \sigma = E_1 \varepsilon & (\varepsilon \leq \varepsilon_y) \\ \sigma = \sigma_y + E_2 (\varepsilon - \varepsilon_y) & (\varepsilon > \varepsilon_y) \end{cases} \quad (1)$$

Where σ is the real stress in MPa. ε is the real strain. σ_y is the yield strength of the analyzed material in MPa. E_1 and E_2 are the elastic and plastic modulus of the pipeline, respectively, in MPa.

THE PIPE-SOIL INTERACTION MODEL FOR BURIED PIPELINES

Eq. 2 describes the pipe-soil interaction as an ideal elastic-plastic model (Rajani et al., 1995).

$$\begin{cases} f = \pi D k_x u & (|u| \leq u_x) \\ f = \pi D k_x u_x = F_x & (|u| \geq u_x) \end{cases} \quad (2)$$

Where f is the soil friction of pipes per unit length, u is the relative longitudinal displacement between pipe and soil, F_x is the

ultimate soil resistance of pipes per unit length, and u_x is the longitudinal subgrade modulus of soil.

From Figure 2, the value of f was assumed to increase linearly with increasing the value of u when the relative longitudinal displacement value is smaller than the maximum elastic displacement. While the value of u reaches the maximum elastic displacement (i.e., u_x), the elastic stage of the soil enters the plastic state, and the value of f reaches the ultimate resistance and remains unchanged (i.e., F_x).

ANALYTICAL METHOD FOR THE LONGITUDINAL STRAIN OF PIPELINES

Mechanical Model

Figure 3 shows a side view of the pipeline sections subjected to the thawing landslide of soil. The section of BC was located in an unstable soil. Both sections of AB and CD were in stabilized soils. The length of the BC pipe section is L , and the slope angle is θ .

The pipeline was mainly subjected to the axial force by soil slippage and friction force between pipeline and soil. As shown in Figure 3, the BC section of the pipeline was also subjected to gravity, which was expressed as $q \sin \theta$ alongside the axial direction. As found by the previous investigation results, the axial force of the pipeline in the slope section almost equals its horizontal section (Zhou, 2010). The axial displacement of the BC and AB sections at point B was u_{0t1} and u_{0t2} , respectively, due to the axial tension p_{0t} . While the axial displacement of BC and CD sections at point C was u_{0t1} and u_{0t2} , respectively, due to the axial compression p_{0c} .

According to the engineering, there is no relative displacement between the pipe and the soil when a pipe section is located in the unstable soil. Thus, the soil friction does not affect the pipeline. As shown in Figure 4, the axial force of the pipe reaches its maximum value at points B and C, and it gradually decreases to zero as it moves away from points B and C.

Considering the soil landslide, the axial force, P_0 (P_{0t} , P_{0c}), of the pipeline was calculated from Eq. 3.

$$P_0 = A(\sigma_1^{total} - \sigma_1^{init}) \quad (3)$$

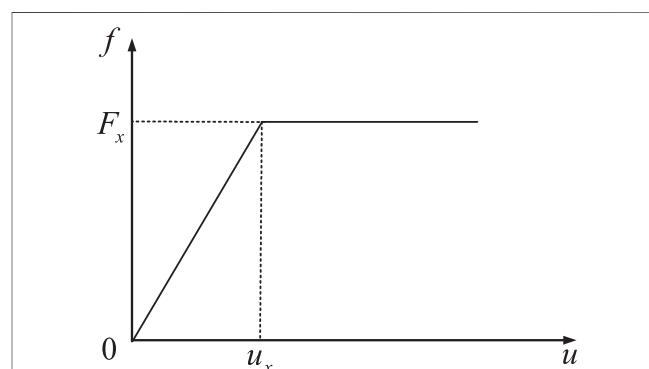


FIGURE 2 | The pipe-soil interaction model (f : the soil friction of pipes per unit length; u : the relative longitudinal displacement between pipe and soil; F_x : the ultimate soil resistance of pipes per unit length; k_x : the longitudinal subgrade modulus of soil).

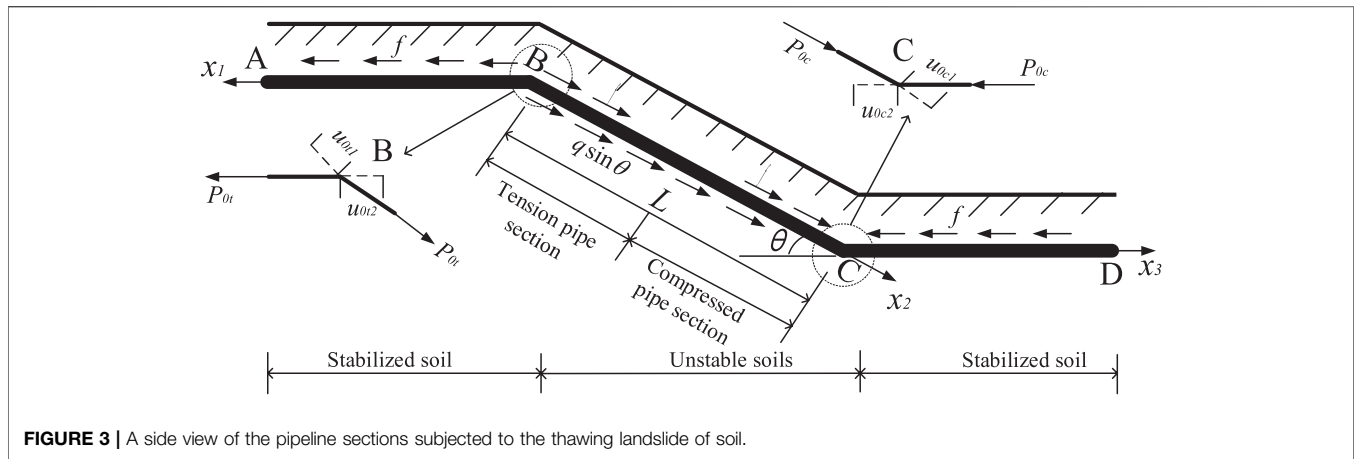


FIGURE 3 | A side view of the pipeline sections subjected to the thawing landslide of soil.

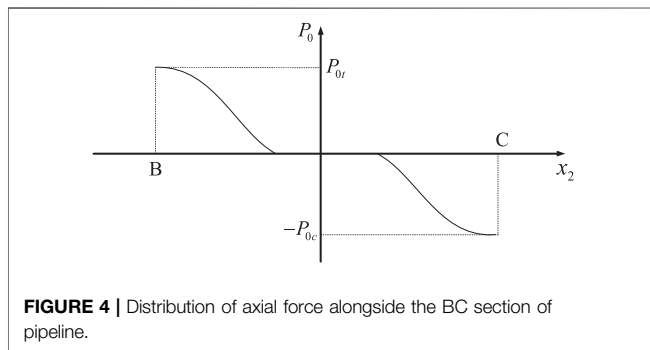


FIGURE 4 | Distribution of axial force alongside the BC section of pipeline.

A is the cross-sectional area of pipeline in mm^2 . σ_1^{total} is the total longitudinal stress of the pipe in MPa. σ_1^{init} is the initial axial force of pipeline in MPa due to the Poisson's ratio and temperature effect, which was obtained from eq. (5) and (6).

$$\sigma_1^{\text{init}} = \nu \sigma_h - E_1 \alpha \Delta T \quad (4)$$

$$\sigma_{\text{Mises}} = \sqrt{\frac{1}{2} [(\sigma_1 - \sigma_2)^2 + (\sigma_2 - \sigma_3)^2 + (\sigma_3 - \sigma_1)^2]} \quad (5)$$

From eq. (9) and (10), σ_{Mises} is the Mises stress of pipeline. σ_1 , σ_2 and σ_3 are the maximum, intermediate, and minimum principal stresses of pipeline, respectively, in MPa. In this regard, the σ_1 of the pipeline is subjected to internal pressure, and the axial tensile load is the axial tensile stress. The σ_2 is the hoop stress σ_h , while the σ_3 is 0. When the Mises stress value of the pipeline achieves the yield stress, it is considered to be yielded. The axial tensile stress σ_{1y}^t was calculated from eq. (11) and (12) by considering the yield strength of the pipeline.

$$\sigma_{1y}^t = \frac{1}{2} \left(\sigma_h + \sqrt{4\sigma_y^2 - 3\sigma_h^2} \right) \quad (6)$$

$$\sigma_h = \frac{p(D - 2t)}{2t} \quad (7)$$

Similar to eq. (15) and (16), the σ_1 of the pipeline is subjected to the internal pressure, and the axial compression load is the

hoop stress σ_h . The σ_2 is 0, and the σ_3 is the axial compression stress of the pipeline. The axial compression stress σ_{1y}^c was calculated from eq. (17) by considering the yield strength of the pipeline.

$$\sigma_{1y}^c = \frac{1}{2} \left(\sigma_h - \sqrt{4\sigma_y^2 - 3\sigma_h^2} \right) \quad (8)$$

Thus, the ultimate axial force of the pipeline was obtained from eq. (19) and (20) subjected to the tension and compression loads.

$$P_{yt} = A(\sigma_{1y}^t - \sigma_1^{\text{init}}) \quad (9)$$

$$P_{yc} = A(\sigma_{1y}^c - \sigma_1^{\text{init}}) \quad (10)$$

A vertical view of the pipeline crossing the slope is shown in **Figure 5**. The displacement of points A and D at the infinite far end of the horizontal pipeline is 0. The displacement at points B and C in the horizontal direction is converted into the slope direction. It was assumed that the displacement of the slope u_{total} is equal to the geometric elongation of the pipe under a tension in the slope direction. It is also equal to the geometric compression of the pipe being compressed in the slope direction (eq. 23).

$$\begin{cases} u_{\text{total}}(P_{0t}) = u_{0t1}(P_{0t}) + u_{0t2}(P_{0t}) \cos \theta \\ u_{\text{total}}(P_{0c}) = u_{0c1}(P_{0t}) + u_{0c2}(P_{0t}) \cos \theta \end{cases} \quad (11)$$

Governing Equations for a Pipe Segment in the Slope Section

As shown in **Figure 5**, the crossing pipeline in the slope was divided into three parts: AB ($-\infty < x_1 \leq 0$), BC ($0 \leq x_2 \leq L$), and CD ($0 \leq x_3 \leq +\infty$) pipe sections. A micro-unit was selected from the section of BC in the pipeline. dx (x_1 , x_2 , and x_3) the length changes of the micro-unit, and N is the total axial force of the pipeline (**Figure 6**, eq. 25).

$$N + (f + q \sin \theta) \cdot dx = N + dN \quad (12)$$

The density ($\rho_{\text{soil}} = 7.85 \times 10^{-6} \text{ kg/mm}$) and gravity ($q = \rho_{\text{soil}} D \pi t g_{\text{gra}}$) of the steel pipe are 2.49 kN/m and 77 kN/m,

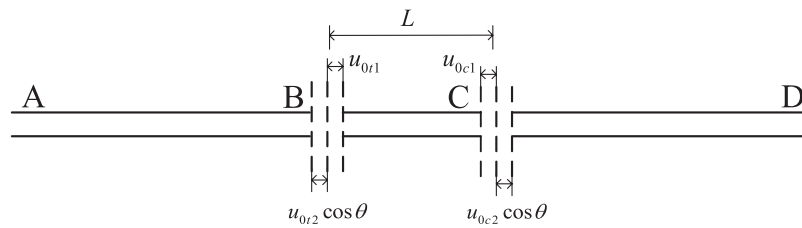


FIGURE 5 | A vertical view of a pipeline longitudinally crossing a thawing landslide slope.

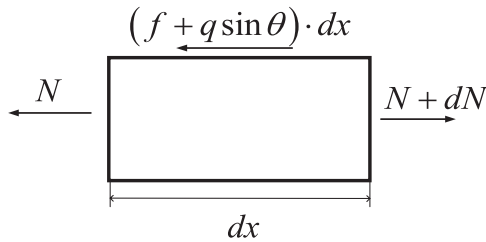


FIGURE 6 | A schematic diagram of the total axial force in the pipeline segments.

respectively. In this study, the friction force of the steel pipe is much greater than its gravity value; thus, the effect of gravity on the results was ignored (Eq. 13)-(15).

$$N + f \cdot dx = N + dN \quad (13)$$

$$\frac{dN}{dx} = \begin{cases} k_x \pi D u & \text{When the soil is elastic} \\ F_x & \text{When the soil is plastic} \end{cases} \quad (14)$$

$$\begin{cases} N = E_1 A \varepsilon = E_1 A \frac{d}{dx} u & (\varepsilon \leq \varepsilon_y) \\ N = A \sigma_y + A E_2 \left(\varepsilon - \varepsilon_y \right) = A \sigma_y + A E_2 \left(\frac{d}{dx} u - \varepsilon_y \right) & (\varepsilon > \varepsilon_y) \end{cases} \quad (15)$$

Eq. (30) and (31) were obtained through substituting the geometric eq. (32) and (33).

$$\begin{cases} \frac{d^2 u}{dx^2} - \frac{k_x u \pi D}{EA} = 0 & \text{When the soil is elastic} \\ \frac{d^2 u}{dx^2} - \frac{F_x}{EA} = 0 & \text{When the soil is plastic} \end{cases} \quad (16)$$

$$\begin{cases} u = k_1 e^{\lambda x_2} + k_2 e^{-\lambda x_2} & \text{When the soil is elastic} \\ u = \frac{1}{2EA} F_x x^2 + k_3 x + k_4 & \text{When the soil is plastic} \end{cases} \quad (17)$$

Where $\lambda = \sqrt{k_x \pi D / EA}$, k_1 , k_2 , k_3 , k_4 are undetermined coefficients.

The Distribution Function of the Longitudinal Strain in Pipelines

Pipelines in unstable and stabilized soils are semi-infinite (Xi and Wen, 2019), the tension section of the pipeline in the uphill stabilized and unsteady slope soils is symmetrical. Meanwhile, the compression section of the pipeline in the downhill stabilized and unsteady slope soils is symmetrical. The distribution function of the longitudinal strain in pipelines were divided into three stages I, II, and III.

At the stage I, the pipeline and soil represent an elastic state. As shown in Figure 7, the coordinate value of point B is 0. The soil on the left and right sides of point B is defined as stabilized and unstable types, respectively.

The displacement and strain functions of the uphill pipeline section were determined as follows:

$$u_1 = a_1 e^{\lambda x_2} + a_2 e^{-\lambda x_2} \quad (18)$$

$$\varepsilon_1 = a_1 \lambda e^{\lambda x_2} - a_2 \lambda e^{-\lambda x_2} \quad (19)$$

Where boundary conditions are $u_1(x=\infty) = 0$ and $\varepsilon_1(x=0) = \frac{P_{0t}}{E_1 A}$. Thus,

$$u_1 = \frac{P_{0t}}{E_1 A \lambda} e^{-\lambda x} \quad (20)$$

$$\varepsilon_1 = \frac{P_{0t}}{E_1 A} e^{-\lambda x} \quad (21)$$

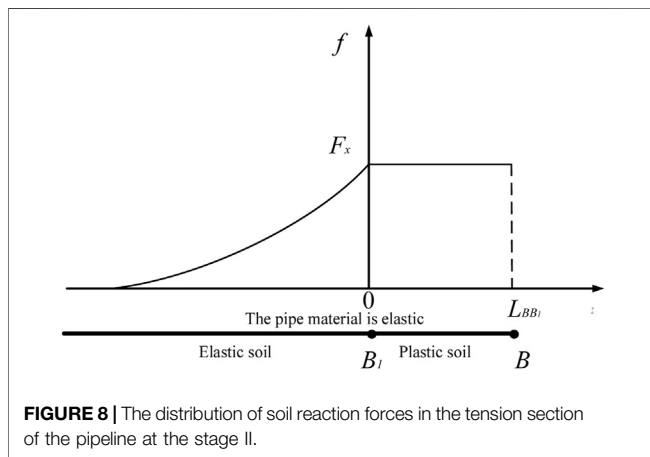
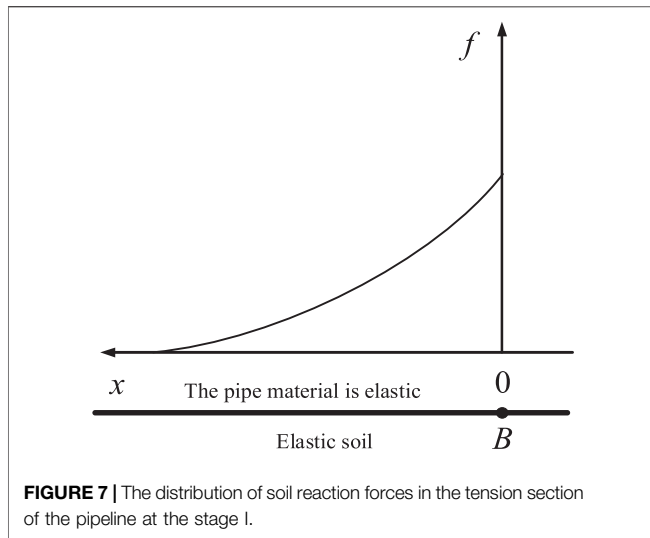
In eq. (40) and (41), the displacement of the horizontal section in the pipeline at point B is $u_{0r2} = \frac{P_{0t}}{E_1 A \lambda}$. The displacement of the horizontal section in the pipeline at point C is $u_{0c2} = \frac{P_{0t}}{E_1 A \lambda}$.

At the stage II, the soil is in a plastic state, and the pipeline is in an elastic state. As shown in Figure 8, the coordinate value of point B₁ is 0. When $x \leq 0$, the soil is in an elastic state. When $0 < x \leq L_{BB1}$, the soil is in a plastic state.

The displacement and strain functions of the uphill section of pipeline are as follows:

$$\begin{cases} u_1 = a_3 e^{\lambda x} + a_4 e^{-\lambda x} & (-\infty < x \leq 0) \\ u_1 = \frac{1}{2EA} F_x x^2 + a_5 x + a_6 & (0 \leq x \leq L_{BB1}) \end{cases} \quad (22)$$

$$\begin{cases} \varepsilon_1 = a_3 \lambda e^{\lambda x} - a_4 \lambda e^{-\lambda x} & (-\infty < x \leq 0) \\ \varepsilon_1 = \frac{1}{EA} F_x x + a_5 & (0 \leq x \leq L_{BB1}) \end{cases} \quad (23)$$



Where boundary conditions are $u_1(x=-\infty) = 0$, $u_1(x=0) = u_x$, and $\varepsilon_1(x=L_{BB1}) = \frac{P_{0t}}{E_1 A}$.

$$\begin{cases} u_1 = u_x e^{\lambda x} & (-\infty < x \leq 0) \\ u_1 = \frac{1}{2E_1 A} F_x x^2 + \frac{P_{0t} - F_x L_{BB1}}{E_1 A} x + u_x & (0 \leq x \leq L_{BB1}) \end{cases} \quad (24)$$

$$\begin{cases} \varepsilon_1 = u_x \lambda e^{\lambda x} & (-\infty < x \leq 0) \\ \varepsilon_1 = \frac{1}{E_1 A} F_x x + \frac{P_{0t} - F_x L_{BB1}}{E_1 A} & (0 \leq x \leq L_{BB1}) \end{cases} \quad (25)$$

Eq. (46) represents the displacement function of the horizontal section in the pipeline at point B.

$$u_{0t2} = -\frac{1}{2E_1 A} F_x L_{BB1}^2 + \frac{P_{0t}}{E_1 A} L_{BB1} + u_x \quad (26)$$

$$u_{0t2} = \frac{1}{2E_1 A F_x} \left(P_{0t}^2 - (P_{0t}^{cri1})^2 \right) + u_x \quad (27)$$

Also, the critical axial force and the displacement function at point C are formulated as eq. (49) and (50), respectively.

$$P_{0c}^{cri1} = |-E_1 S \lambda u_x| \quad (28)$$

$$u_{0c2} = \frac{1}{2E_1 A F_x} \left(P_{0c}^2 - (P_{0c}^{cri1})^2 \right) + u_x \quad (29)$$

At the stage III, both the pipeline and soil are in a plastic state. As shown in **Figure 9**, the coordinate value of points B, B₂, and B₃ are L_{BB3} , L_{B2B3} , and 0, respectively. When $x \leq -L_{B2B3}$, the soil is in an elastic state. When $-L_{B2B3} < x \leq -L_{BB3}$, the soil is in a plastic state. Considering $x \leq 0$ and $0 < x \leq -L_{BB3}$, the pipeline is in an elastic and a plastic state, respectively. As the pipeline reaches $P_{0t}^{cri2} = P_{yt}$ at point B, the elastoplastic boundary is $P_{0t} = P_{yt}$. Also, the critical axial force of the pipeline is P_{0t}^{cri2} at point B. When $P_{0t} > P_{yt}$ the pipeline enters a plastic state at point B. The length of the elastic section in the pipeline (L_{B2B3}) was calculated from eq. (53) in the plastic soil.

$$L_{B2B3} = \frac{1}{F_x} (P_{0t}^{cri2} - P_{0t}^{cri1}) \quad (30)$$

At point B₃, the displacement function of the pipeline is:

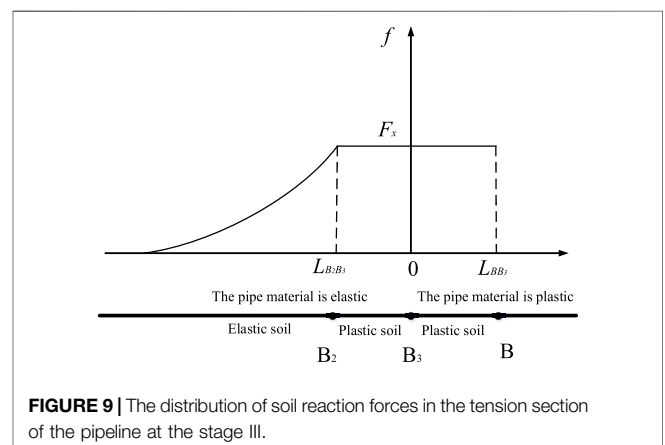
$$u_{0t3} = -\frac{F_x}{2E_1 A} L_{B2B3}^2 + \frac{P_{0t}^{cri2}}{E_1 A} L_{B2B3} + u_x \quad (31)$$

Also, the length of the plastic section in the pipeline (L_{BB3}) from eq. (56) in the plastic soil.

$$L_{BB3} = \frac{1}{F_x} (P_{0t} - P_{yt}) \quad (32)$$

Thus, the displacement and strain functions of the uphill horizontal section in the pipeline were calculated from eq. (58) and (59).

$$\begin{cases} u_1 = a_7 e^{\lambda x} + a_8 e^{-\lambda x} & (-\infty < x \leq -L_{B2B3}) \\ u_1 = \frac{1}{2E_1 A} F_x x^2 + a_9 x + a_{10} & (-L_{B2B3} < x \leq 0) \\ u_1 = \frac{1}{2E_2 A} F_x x^2 + a_{11} x + a_{12} & (0 < x \leq L_{BB3}) \end{cases} \quad (33)$$



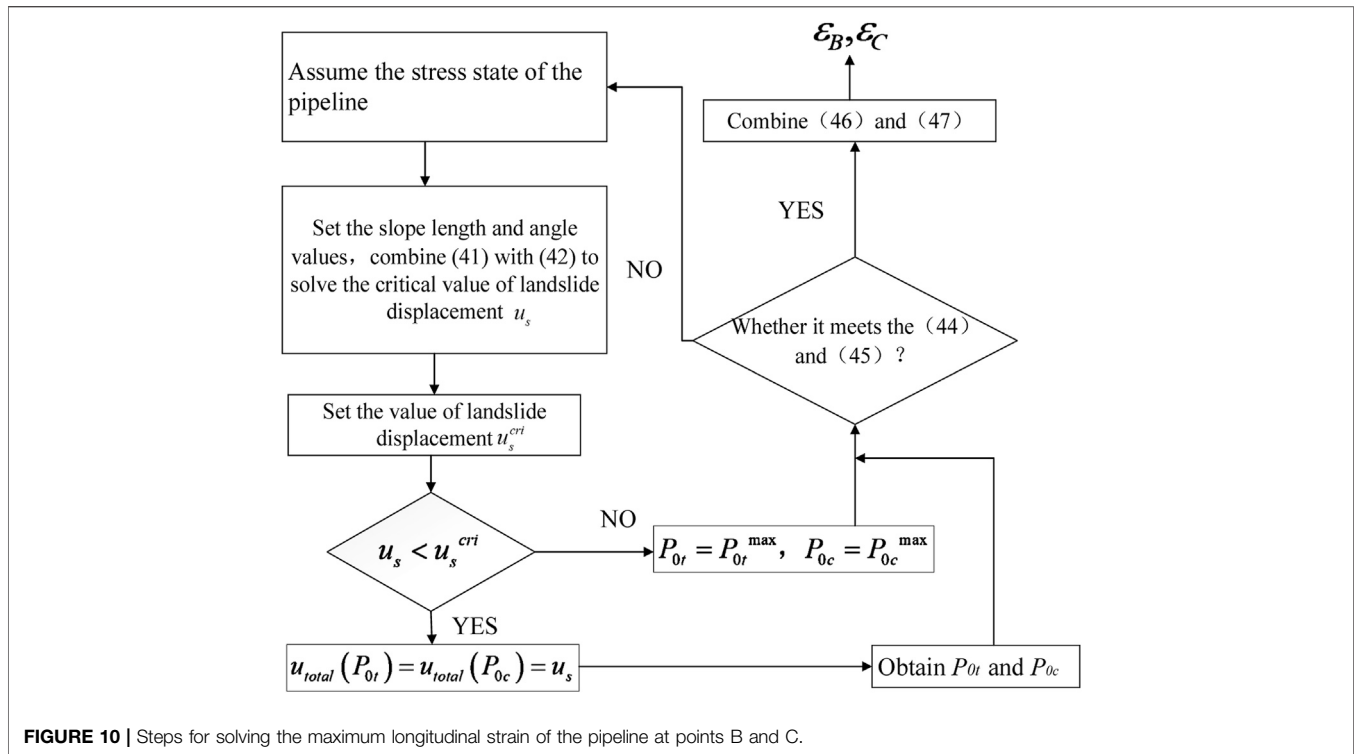


FIGURE 10 | Steps for solving the maximum longitudinal strain of the pipeline at points B and C.

$$\begin{cases} \epsilon_1 = a_7 \lambda e^{\lambda x} - a_8 \lambda e^{-\lambda x} & (-\infty < x \leq -L_{B_2 B_3}) \\ \epsilon_1 = \frac{1}{E_1 A} F_x x + a_9 & (-L_{B_2 B_3} \leq x \leq 0) \\ \epsilon_1 = \frac{1}{E_2 A} F_x x + a_{11} & (0 \leq x \leq L_{B B_3}) \end{cases} \quad (34)$$

At the stage III, boundary conditions are $\epsilon_1(x=L_{B B_3}) = \frac{P_{0t}}{E_2 A} + \frac{P_{yt}}{E_1 A} - \frac{P_{yt}}{E_2 A}$, $u_1(x=-\infty) = 0$, $u_1(x=-L_{B_2 B_3}) = u_x$, and $u_1(x=0) = u_{0t3}$.

$$\begin{cases} u_1 = u_x e^{\lambda L_{B_2 B_3}} e^{\lambda x} & (-\infty < x \leq -L_{B_2 B_3}) \\ u_1 = \frac{1}{2E_1 A} F_x x^2 + \left(\frac{u_{0t3} - u_x}{L_{B_2 B_3}} + \frac{F_x L_{B_2 B_3}}{2E_1 A} \right) x + u_{0t3} & (-L_{B_2 B_3} \leq x \leq 0) \\ u_1 = \frac{1}{2E_2 A} F_x x^2 + \left(\frac{P_{yt}}{E_1 A} - \frac{P_{yt}}{E_2 A} \right) x + \frac{1}{E_2 A} (P_{0t} - F_x L_{B B_3}) x + u_{0t3} & (0 \leq x \leq L_{B B_3}) \end{cases} \quad (35)$$

$$\begin{cases} \epsilon_1 = u_x e^{\lambda L_{B_2 B_3}} \lambda e^{\lambda x} & (-\infty < x \leq -L_{B_2 B_3}) \\ \epsilon_1 = \frac{1}{E_1 A} F_x x + \frac{u_{0t3} - u_x}{L_{B_2 B_3}} + \frac{F_x L_{B_2 B_3}}{2E_1 A} & (-L_{B_2 B_3} \leq x \leq 0) \\ \epsilon_1 = \frac{1}{E_2 A} F_x x + \frac{P_{yt}}{E_1 A} - \frac{P_{yt}}{E_2 A} + \frac{1}{E_2 A} (P_{0t} - F_x L_{B B_3}) & (0 \leq x \leq L_{B B_3}) \end{cases} \quad (36)$$

At point B, the displacement of the uphill horizontal section in the pipeline is:

$$u_{0t2} = \frac{1}{2E_2 A} F_x L_{B B_3}^2 + \left(\frac{P_{yt}}{E_1 A} - \frac{P_{yt}}{E_2 A} \right) L_{B B_3} + \frac{1}{E_2 A} (P_{0t} - F_x L_{B B_3}) L_{B B_3} + u_{0t3} \quad (37)$$

$$u_{0t2} = \frac{P_{0t}^2}{2E_2 A F_x} + \left(\frac{1}{E_2} - \frac{1}{E_1} \right) \frac{(P_{0t}^{cri2} - 2P_{0t}) P_{0t}^{cri2}}{2A F_x} + \frac{u_x}{2} \quad (38)$$

At point C, the critical axial force ($P_{0c}^{cri2} = P_{yc}$) and the displacement function of the pipeline were calculated by the following equations.

$$u_{0c2} = \frac{P_{0c}^2}{2E_2 A F_x} + \left(\frac{1}{E_2} - \frac{1}{E_1} \right) \frac{(P_{0c}^{cri2} - 2P_{0c}) P_{0c}^{cri2}}{2A F_x} + \frac{u_x}{2} \quad (39)$$

$$u_{0t1} = u_{0t2}; u_{0c1} = u_{0c2} \quad (40)$$

A Solution for the Maximum Longitudinal Strain of the Pipeline

The maximum longitudinal tensile strain of the pipeline is at point B, and the maximum longitudinal compressive strain is at point C. When the soil on the slope is in a plastic state, the friction force of the pipeline per unit length is F_x . The axial force of the pipeline at points B and C is $P_{0t} = P_{0t}^{max}$ and $P_{0c} = P_{0c}^{max}$, respectively. The equilibrium equation of axial force for the pipeline on the slope can be expressed as follows:

$$P_{0t}^{max} + P_{0c}^{max} = F_x L \quad (41)$$

The amount of thawing landslide is the same on the uphill and downhill slopes. Thus, the maximum axial force of the pipeline and critical value of thawing landslide u_s^{crit} is calculated using eq. (69) when the soil is in a plastic state.

$$u_{total}(P_{0t}^{max}) = u_{total}(P_{0c}^{max}) \quad (42)$$

For a specific value of thawing landslide u_s , when $u_s < u_s^{crit}$, the soil is in an elastic state. Eq. (71) was used to calculate the axial force of the slope pipeline at points B and C.

$$u_{total}(P_{0t}) = u_{total}(P_{0c}) = u_s \quad (43)$$

When $u_s \geq u_s^{crit}$, the soil is in a plastic state. The axial force of the slope pipeline at points B and C reaches the maximum value $P_{0t} = P_{0t}^{max}$ and $P_{0c} = P_{0c}^{max}$, respectively.

$$\begin{cases} 0 < P_{0t}^{crit1} & \text{(the first stage)} \\ P_{0t}^{crit1} \leq P_{0t} \leq P_{0t}^{crit2} & \text{(the second stage)} \\ P_{0t} \geq P_{0t}^{crit2} & \text{(the third stage)} \end{cases} \quad (44)$$

$$\begin{cases} 0 < P_{0c}^{crit1} & \text{(the first stage)} \\ P_{0c}^{crit1} \leq P_{0c} \leq P_{0c}^{crit2} & \text{(the second stage)} \\ P_{0c} \geq P_{0c}^{crit2} & \text{(the third stage)} \end{cases} \quad (45)$$

$$\begin{cases} P_{0t} = E_1 A \varepsilon_B & \text{(the first stage and second stage)} \\ P_{0t} = A \sigma_{yt} + A E_2^t (\varepsilon_B - \varepsilon_{yt}) & \text{(the third stage)} \end{cases} \quad (46)$$

$$\begin{cases} P_{0c} = E_1 A \varepsilon_C & \text{(the first stage and second stage)} \\ P_{0c} = A \sigma_{yc} + A E_2^c (\varepsilon_C - \varepsilon_{yc}) & \text{(the third stage)} \end{cases} \quad (47)$$

The specific process is shown in **Figure 10**. The strain of the pipeline at points B and C are ε_B and ε_C , respectively. Thus, the maximum longitudinal tensile and compressive strains of the pipeline can be expressed as eq. (77), respectively.

$$\begin{cases} \varepsilon_t^{max} = \varepsilon_B + \varepsilon_1^{init} & (a) \\ \varepsilon_c^{max} = \varepsilon_C + \varepsilon_1^{init} & (b) \end{cases} \quad (48)$$

VALIDATION OF THE ANALYTICAL METHOD

Verification of Strain Results Using Field Monitoring

To validate the developed analytical model, combined with the actual situation of an X65 pipeline in China, the analytical calculated results were compared with monitoring data. As shown in **Supplementary Figure S2**, the length of the slope is 1,000 m, and the slope angle is about 30°. The soil types mainly include silty clay, gravelly silty clay, gravel, and gravel sand. The value of a thawing landslide is about 10 mm. **Table 1** represents the effective parameters of the pipeline subjected to the thawing landslide. The diameter (D) and the wall thickness (t) are 813 mm, 12.7 mm, respectively. Also, the design factor (f_p) is 0.4. Besides, the operating internal pressure (p) is 5.80 MPa, the yield strength of pipeline (σ_y), and the tensile strength (F_y) are 5.8,

TABLE 1 | Critical displacements of the thawing landslide of soil under an ultimate strain.

Wall thickness t (mm)	12.7	10.3	8.7	7.9
Tensile failure (%)	1.07	0.83	0.55	0.38
Compressive buckling failure (%)	1.05	0.79	0.63	0.56
Critical displacements u_s (mm)				
Tensile	784	543	393	335
Compression	495	308	225	190

450, and 535 MPa, respectively. The yield ratio ($R_{Y/T}$) and the Poisson's ratio (ν) are 0.84 and 0.3, respectively. Moreover, the elastic modulus (E_1) is 205 GPa, the plastic modulus (E_2^t, E_2^c) is 6,150 MPa. Furthermore, the temperature difference between the pipe installation and operation (ΔT) is 20°C. The ultimate resistance of soil (F_x) is 77kN/m.

The stress value of the pipeline was obtained by a fiber grating sensing technology. The monitoring results revealed that the maximum longitudinal tensile stress at position 1 is 50 MPa, and the maximum longitudinal compressive stress at position 2 is 30 MPa. Theoretical calculation results showed that the maximum longitudinal tensile stress of the pipeline is 59.90 MPa, and the maximum longitudinal compressive stress is 35.55 MPa. The relative error between the analytical and monitoring results is less than 20%.

Verification via Previous Landslide FEM Results

To further validate the developed analytical model, a comparative analysis was performed between results from theoretical analysis of the maximum longitudinal strain and numerical simulation in the pipeline subjected to the thawing landslide of soil. **Supplementary Table S1** represents the effective parameters of the pipeline subjected to the thawing landslide. Also, **Figure 11** shows that the maximum longitudinal strain of the pipeline derived by the proposed analytical model agrees well with documented FE results.

PARAMETRIC ANALYSIS OF PIPES' MAXIMUM LONGITUDINAL STRAIN

The maximum longitudinal strain subjected to thawing landslide was calculated by coding the program of the maximum longitudinal strain with numerical calculation software MATLAB. The size and operation related parameters, soil properties, and slope angle impact on the maximum axial strain of the pipeline subjected to thaw slumping load. In this section, the effects of wall thickness, internal pressure, ultimate resistance of soil, and slope angle are researched on the longitudinal strain of the pipeline.

Baseline Condition

Supplementary Table S2 shows basic parameters of the pipeline, which mainly come from the X65 pipeline in China. The slope

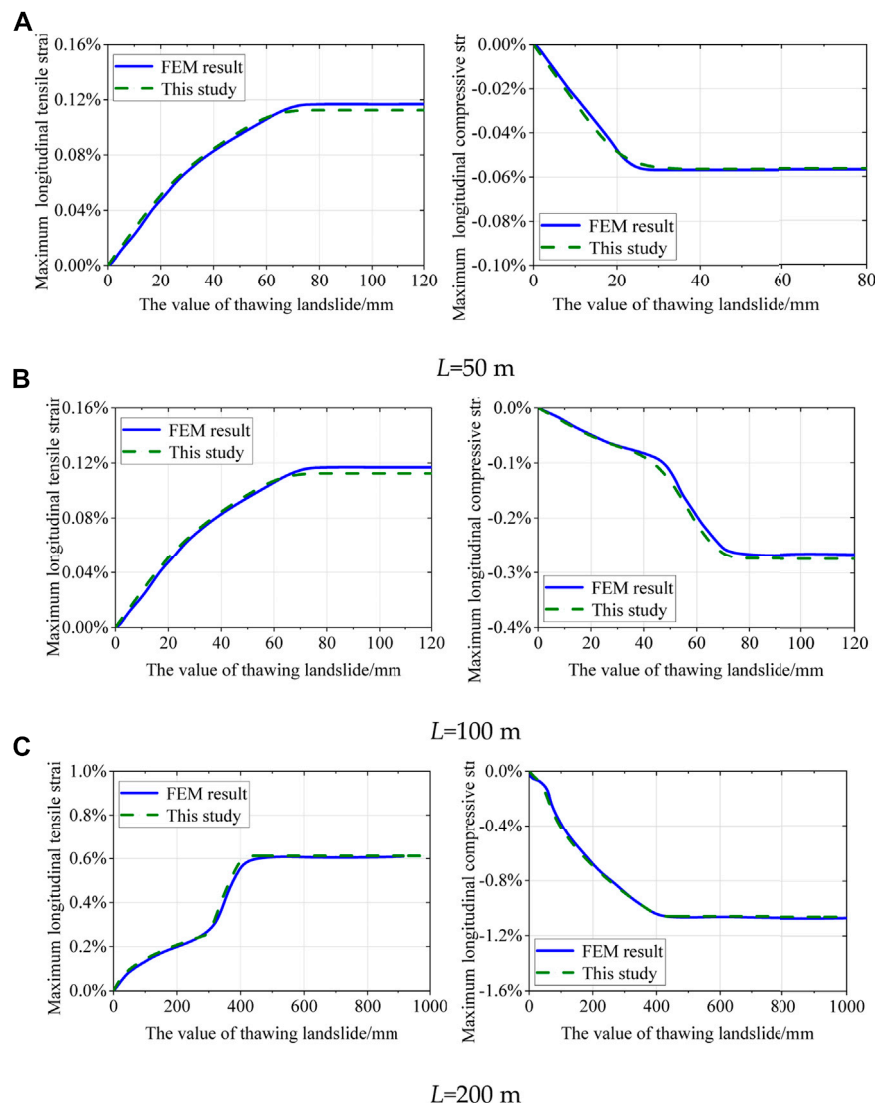


FIGURE 11 | The result verification of the maximum longitudinal strain in the pipeline with (A) $L = 50$ m, (B) $L = 100$ m, and (C) $L = 200$ m.

length was ranged at 200, 300, 400, and 500 m, respectively. The calculated longitudinal tensile and compressive strains of the pipeline under the basic conditions are shown in **Figure 12**.

From **Figure 12**, when the thermal melt slip of the soil reaches the critical value (u_s^{cri}), the frictional force between the pipeline and the soil reaches an ultimate resistance. It means the soil enters the plastic state, and the longitudinal strain of the pipeline also reaches the maximum value. As a result, the continuous increase of the slip will not cause the increase of the longitudinal strain.

The Ultimate Strain of the Pipeline

The tensile failure and compression buckling of the pipeline are related to each other. When the maximum longitudinal tensile strain reaches the ultimate tensile strain, the pipeline undergoes a tensile failure. While the maximum longitudinal compressive

strain reaches the ultimate compressive strain, the compression buckling occurs in the pipeline. In this paper, the weld defect was assumed to be a surface type, and the strain-based design of CSA Z662-2007 guideline was used to calculate the ultimate tensile strain of the pipeline (eq. 49).

$$\epsilon_t^{cri} = \delta^{(2.36-1.58R_{Y/T}-0.101\xi\eta)} (1 + 16.1R_{Y/T}^{-4.45}) (-0.157 + 0.239\xi^{-0.241}\eta^{-0.315}) \quad (49)$$

Also, a model proposed by CRES (Liu et al., 2017) which considered the critical compression factor comprehensively was adopted to calculate the ultimate compressive strain. This model accurately considers the geometrical imperfections and the pipeline properties (eqs. 50-58).

$$F_{LD} = 1 \quad (50)$$

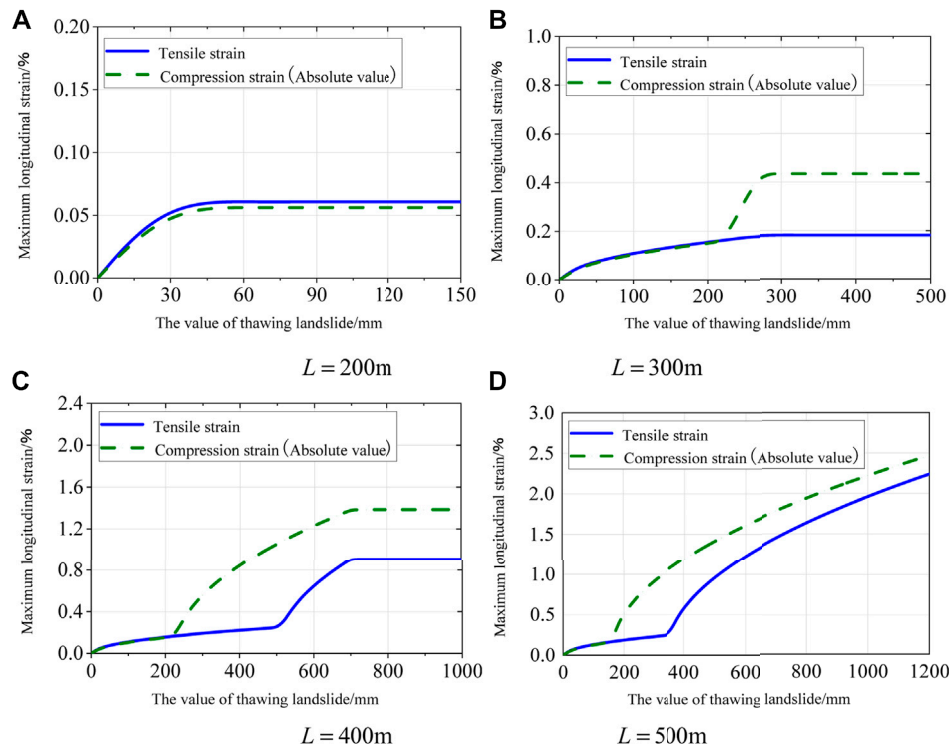


FIGURE 12 | The maximum longitudinal strain of the pipeline under the reference condition with (A) $L = 200$ m, (B) $L = 300$ m, (C) $L = 400$ m and (D) $L = 500$ m.

$$\varepsilon_r = F_{DP} \cdot F_{YT} \cdot F_{G1} \cdot F_{NF} \quad (51)$$

$$f_{pc} = 1.8 \times 10^{-4} \times \left(\frac{D}{\delta}\right)^{1.6} \quad (52)$$

$$f_p = \frac{PD}{2\delta\sigma_y} \quad (53)$$

$$\begin{cases} F_{DP} = 980 \times \left[0.5 \left(\frac{D}{\delta}\right)^{-1.6} + 1.9 \times 10^{-4} \right] & f_p < f_{pc} \\ F_{DP} = 980 \times \left(1.06 f_p + 0.5 \right) \left(\frac{D}{\delta}\right)^{-1.6} & f_p \geq f_{pc} \end{cases} \quad (54)$$

$$f_g = \frac{h_g}{\delta} \quad (55)$$

$$f_n = \frac{\sigma_a^c}{\sigma_y} \quad (56)$$

$$\begin{cases} F_{NF} = 1.2 f_n^2 + 1 & f_n \geq 0 \\ F_{NF} = 1 & f_n < 0 \end{cases} \quad (57)$$

$$\varepsilon_c^{\text{crit}} = \min(\varepsilon_u, F_{LD} \times \varepsilon_r) \quad (58)$$

Supplementary Table S3 represents the results from the ultimate tensile strain parameters. The buckling strength ratio of the

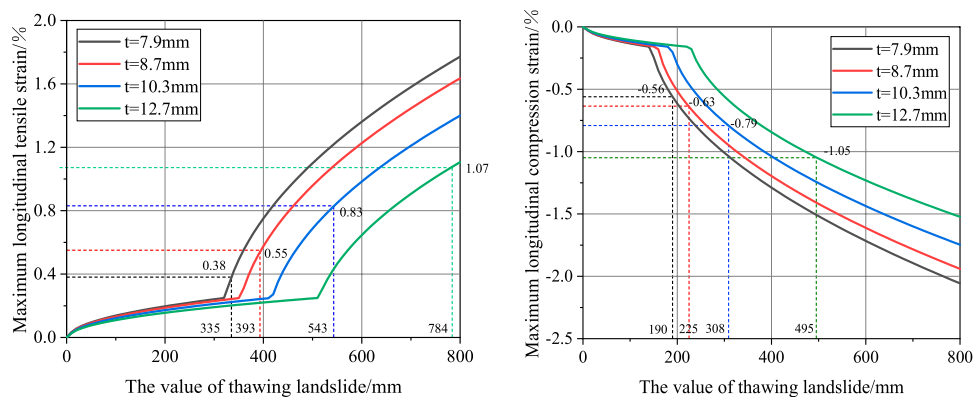


FIGURE 13 | Influence of wall thickness on the maximum longitudinal strain.

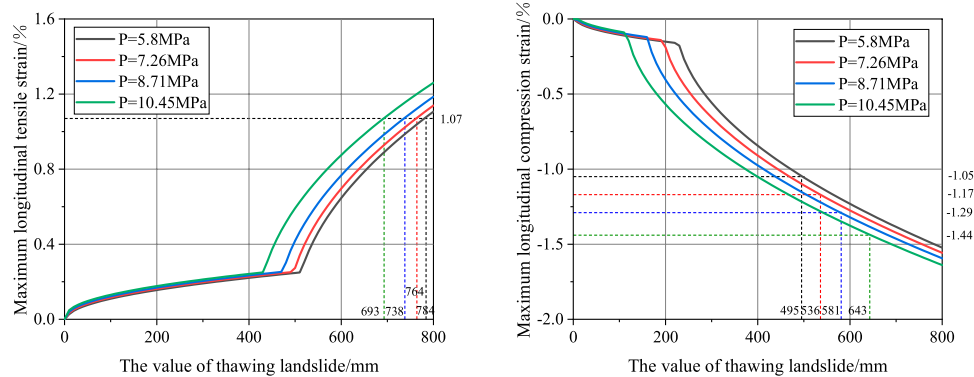


FIGURE 14 | The effect of operating internal pressure on the maximum longitudinal strain.

TABLE 2 | The results of critical displacements in the thawing landslide of soil under an ultimate strain.

Internal pressure p (MPa)	5.80	7.26	8.71	10.45
Tensile failure (%)	1.07			
Compression buckling failure (%)	1.05	1.17	1.29	1.44
Critical displacements u_s (mm)				
Tensile	784	764	738	693
Compression	495	536	581	643

pipeline (R_y) is 0.84, and the apparent toughness (δ_T) is 0.267 mm. By analyzing the factors affecting the tensile failure, the weld defect size is 50×5 mm. From analyzing the factors affecting the compression buckling, the peak wave of the weld defect from the height to bottom of the outer surface (h_g) is the maximum value of $0.13\%D$ and $8\%\delta$.

The Effect of Wall Thickness

Due to different design factors of four regional levels, the wall thickness alongside the gas pipeline was different under the same design pressure. **Figure 13** shows the effect of wall thickness on the pipeline's maximum longitudinal tensile and

compression strains. In **Figure 13**, the length of the slope is 500 m. The design factors are 0.4, 0.5, 0.6, and 0.72, and the internal pressure of the pipeline is set at 5.8 MPa. According to the specification of API standard steel pipe, the pipeline's wall thickness is 12.7, 10.3, 8.7 and 7.9 mm, respectively. The values of other parameters are the same as shown in **Supplementary Table S2**.

As shown in **Figure 13**, the compression section of the pipeline is more likely to yield. As analyzed in *Mechanical Model*, the absolute value of the longitudinal compressive stress is less than the longitudinal tensile stress when the pipeline is yielding so that the stress of the pipeline is more likely to reach the yield stress under the compressional conditions. The pipeline is prone to a buckling damage at the bottom slope. These results are consistent with the actual situation in engineering (Randolph et al., 2010).

Both the maximum longitudinal tensile and compression strains increase with decreasing the pipe's wall thickness. As indicated in **Table 1**, the smaller the pipe's wall thickness leads to the smaller the critical displacement of soil. This is due to the fact that the smaller the wall thickness, the greater the hoop stress and the longitudinal strain of the pipeline. Moreover, a decrease in the ultimate tensile stress is due to the smaller of wall thickness.

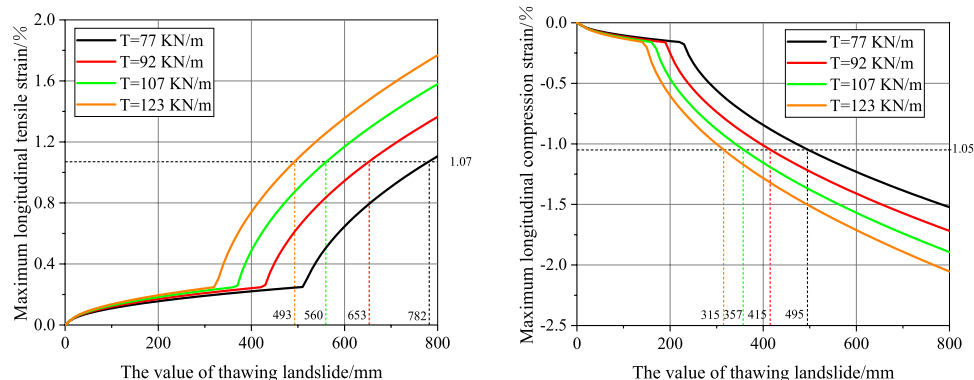


FIGURE 15 | The effect of the maximum resistance of soil on the maximum longitudinal strain.

TABLE 3 | The results of critical displacements of the thawing landslide of the soil under an ultimate strain.

The maximum resistance of soil F_x (kN/m)		77	92	107	123
Tensile failure (%)		1.07			
Compression buckling failure (%)		1.05			
Critical displacements u_s (mm)	Tensile	782	653	560	493
	Compression	495	415	357	315

Therefore, the smaller the pipe's wall thickness easily enters to the plastic state.

When the pipeline is in an elastic state, the wall thickness has little effect on the maximum longitudinal tensile and compression strains. In the pipe's bilinear stress-strain model, the pipe's elastic modulus is larger than the plastic modulus. Therefore, the fluctuation of longitudinal stress in the pipeline produces a larger strain change in the plastic state than the elastic state.

The Effect of Internal Pressure

The operating pressure alongside the pipeline was affected by seasonality and design factors. **Figure 14** shows the effect of internal pressure on the maximum longitudinal tensile and compression strains of the pipeline. In **Figure 14**, the slope length and the wall thickness of the pipeline are 500 m and 12.7 mm, respectively. The design factor is 0.4, 0.5, 0.6, and 0.72. The internal pressure of the pipeline corresponds to 5.80, 7.26, 8.71, and 10.45 MPa, respectively. The values of other parameters are the same as shown in **Supplementary Table S2**.

As shown in **Figure 14**, both the maximum longitudinal tensile and compression strains of the pipeline increase with the internal pressure. **Table 2** also represents the results of the critical displacement in the pipeline under various working conditions. The results show that the greater the internal

pressure, the smaller the critical displacement of tensile failure. Due to the higher operating pressure of the pipeline, the hoop stress will be a larger value so that the longitudinal conduit of the strain increases. Pipes with larger internal pressure are more likely to achieve the yield strength under the same ultimate tensile strain. However, for compressive buckling case, the critical displacement increases with the internal pressure oppositely, caused by the increase of ultimate tensile strain.

The Effect of the Maximum Resistance of Soil

The field investigation shows that the yielding soil displacement is between 5 and 8 mm; therefore, the ultimate resistance of the axial soil spring in the pipeline is between 77 kN/m and 122 kN/m. **Figure 15** shows the effect of soil's ultimate resistance on the maximum longitudinal tensile and compression strains in the pipeline. From **Figure 15**, the length of the slope is 500 m, the yielding soil displacement is between 5 and 8 mm, and the ultimate resistance of the soil per unit length is 77 kN/m, 92 kN/m, 107 kN/m, and 123 kN/m, respectively. The values of other parameters are the same as presented in **Supplementary Table S2**.

As shown in **Figure 15**, both the maximum longitudinal tensile and compression strains of the pipeline increase with the ultimate resistance of the soil. **Table 3** also represents the results of the critical displacement in the pipeline under various working conditions. The results show that the greater the ultimate resistance of soil, the smaller the critical displacement of soil. Due to the greater the ultimate resistance of soil, the axial friction of the pipeline will be greater so that the greater the longitudinal strain is the easier the pipeline to achieve the yield strength.

The Effect of Slope Angle

The field investigation shows that most of the slope angles are between 20° and 60°. **Figure 16** illustrates the effect of slope angle

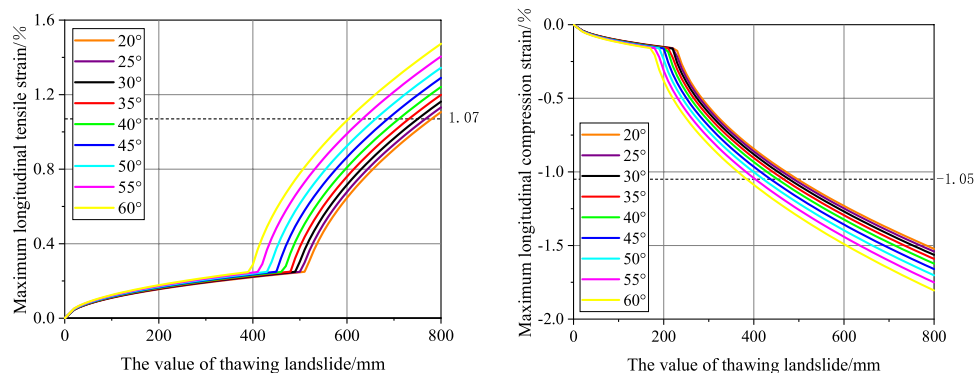
**FIGURE 16** | Influence of slope angle on the maximum longitudinal strain.

TABLE 4 | The results of critical displacements of thawing landslide of soil under ultimate strain.

Slope of angle (°)		20	25	30	35	40
Tensile failure (%)				1.07		
Compression buckling failure (%)				1.05		
Critical displacements u_s (mm)	Tensile	784	768	751	732	711
	Compression	495	486	476	464	451
Slope of angle (°)		45	50	55	60	
Tensile failure (%)				1.07		
Compression buckling failure (%)				1.05		
Critical displacements u_s (mm)	Tensile	687	661	633	605	
	Compression	435	419	401	382	

on the maximum longitudinal tensile and compression strains in the pipeline. From **Figure 16**, the length of the slope is 500 m, and the slope angle is between 20° and 60° with an equal interval of 5°. The values of other parameters are the same as presented in **Supplementary Table S2**.

According to **Figure 16**, both the maximum longitudinal tensile and compression strains of the pipeline increase with the slope angle. **Table 4** also represents the results of the critical displacement in the pipeline under various working conditions. The results show that the greater the slope angle, the smaller the critical displacement of soil. According to **Figure 3**, and Eq. (11), by increasing the slope angle (θ), the value of $\cos \theta$ is smaller, and the axial force and the maximum axial strain are greater in the slope of pipeline, leading to easily achieve the yield strength.

CONCLUSION

The purpose of the current study was to introduce an improved analytical method for the longitudinal strain analysis of buried pipelines subjected to the thaw slumping load. In the analytical calculations, a bilinear stress-strain model was adopted to the pipe material, and the pipe-soil interaction was assumed to be an ideal elastoplastic model. According to the elastoplastic change process of the pipeline-soil, the derivation was divided into three stages. First, the pipelines are all in the elastic state. Second, parts of the soil enter the plastic state, but the pipeline is still in the elastic state. Third, the pipeline and parts of the soil enter the plastic state. Based on these stages, the calculation method of the maximum longitudinal stress of the pipeline subjected to the thaw slumping load was given, and the rapid calculation of the maximum longitudinal strain of the pipeline was realized by numerical calculation software MATLAB. This research provides important insights into the improved analytical method is consistent with the calculated results of the nonlinear finite element model and is inconsistent with the real monitoring data of one X65 pipeline. Some conclusions can be drawn as follows:

- 1) In comparison with the tensile section, the compression section of the pipeline is more likely to yield. Since the absolute value of the longitudinal compressive stress is less than the longitudinal tensile stress, the pipeline is yielding so that the stress of the pipeline is more likely to reach the yield stress under a compressive condition. This result which discussed above is also consistent with the actual situation that the pipeline is prone to buckling damage at the bottom slope under pressure.
- 2) The maximum longitudinal tensile and compression strains decrease with the increase of wall thickness and increase with the internal pressure, the ultimate resistance of soil, and the slope angle. The soil's ultimate resistance has the most significant influence on the maximum longitudinal strain, while the slope of angle has the most negligible impact.
- 3) The critical displacement of tensile failure in the pipeline increases with increasing the pipe's wall thickness and decreases with increasing the internal pressure, the ultimate resistance of soil, and the slope angle. The main reason is that the hoop stress of the pipeline is closely related to the pipe's wall thickness and operating internal pressure. The hoop stress increases as the pipe's wall thickness decreases and the internal pressure increases, leading to increase the maximum longitudinal tensile strain. If the pipe's wall thickness is smaller, the internal pressure is larger and the pipeline easily yields. While the ultimate resistance of soil increases and the slope angle decreases, the longitudinal tensile force and the maximum longitudinal tensile strain increases in the pipeline. It can be concluded that the larger ultimate resistance of soil leads to the smaller of slope angle and the pipeline easily yields.
- 4) The critical displacement of compressive buckling in the pipeline increases with increasing the pipe's wall thickness and internal pressure; however, it decreases with increasing the ultimate resistance of soil and slope angle. The effect of the pipe's wall thickness, the ultimate resistance of soil, and the slope angle on the critical displacement of compression buckling is the same as tensile failure effect on the pipeline. The ultimate compression stress increases with increasing the internal pressure, leading to an increase in the critical displacement of pipelines.

DATA AVAILABILITY STATEMENT

The original contributions presented in the study are included in the article/**Supplementary Material**, further inquiries can be directed to the corresponding author.

AUTHOR CONTRIBUTIONS

BJ: Research the method and wrote the first draft of the manuscript XL: Methodological and theoretical guidance of the study DB: verify the method and data analysis YY and JJ: wrote sections of the manuscript YL: acquisition of data HZ:

revising the manuscript critically for important intellectual content.

FUNDING

This research has been co-financed by National Science Foundation of China (Grant No. 52004314), Tianshan Youth Program (Grant No. 2019Q088), the Open Project Program of Beijing Key

Laboratory of Pipeline Critical Technology and Equipment for Deepwater Oil and Gas Development (Grant No. BIPT2020005).

SUPPLEMENTARY MATERIAL

The Supplementary Material for this article can be found online at: <https://www.frontiersin.org/articles/10.3389/fenrg.2021.742348/full#supplementary-material>

REFERENCES

- Andrés, O., Hernandez, J., and Mauricio, P. O. (2017). Analysis and Mitigation Techniques for Axial Landslides to Pipeline: Case Study KM 35+690 Orensa. ASME 2017 International Pipeline Geotechnical Conference, Lima, Peru, July 25–26, 2017.
- Chan, P. (2000). *Soil-Pipeline Interaction in Slopes*. Canada: Doctoral dissertation, University of Calgary.
- Chen, L. Q., Song, L. Q., Wu, X. D., Qiu, X. D., Liu, Q., Xia, Y., et al. (2017). Fem-based Stress Analysis of Gas Pipelines in Landslide Areas. *Nat. Gas Industry*.
- Chen, P. C. (2012). *Risk Analysis and Management Solution in Permafrost Regions of Mohe-Daqing Pipeline*. *Pipeline Technique and Equipment*. doi:10.3969/j.issn.1004-9614.2012.01.001
- Chen, Q. Q., and Hu, M. L. (2014). *Stress Analysis of Product Oil Pipeline Crossing Landslide Area*. *Pipeline Technique and Equipment*. doi:10.3969/j.issn.1004-9614.2014.05.005
- Eichhorn, G. N., and Haigh, S. K. (2018). "Landslide Pipe-Soil Interaction: State of the Practice," in *Pipeline Safety Management Systems; Project Management, Design, Construction, and Environmental Issues; Strain Based Design; Risk and Reliability; Northern Offshore and Production Pipelines*, 2. doi:10.1115/ipc2018-78434
- Ho, D., Wilbourn, N., Vega, A., and Tache, J. (2014). Safeguarding a Buried Pipeline in a Landslide Region. *Pipelines*. 2014, 1162–1174. doi:10.1061/9780784413692.105
- Huang, K., Lu, H., Wu, S., Han, X., and Jiang, Y. (2015). The Stress Analysis of Buried Gas Pipeline Crossing the Landslide. *Chin. J. Appl. Mech.* 4, 689–693. doi:10.11776/cjam.32.04.D023
- Li, C., Ma, G., Cai, S., Yang, D., Xia, K., and Cui, H. (2016). Effect of Thawing Landslide on Stress of Buried Pipelines in Permafrost Regions. *J. Liaoning Shihua Univ.* 36, 30–33. doi:10.3969/j.issn.1672-6952.2016.03.007
- Liu, M., Zhou, H. G., and Wang, B. (2017). *Strain-based Design and Assessment in Critical Areas of Pipeline Systems With Realistic Anomalies*. TRB 2017 Meeting, Washington, DC.
- Mcroberts, E. C., and Morgenstern, N. R. (1974). The Stability of Thawing Slopes. *Can. Geotech. J.* 11 (4), 447–469. doi:10.1139/t74-052
- O'Rourke, M. J., Liu, X., and Flores-Berrones, R. (1995). Steel Pipe Wrinkling Due to Longitudinal Permanent Ground Deformation. *J. Transportation Eng.* 121 (5), 443–451. doi:10.1061/(ASCE)0733-947x(1995)121:5(443)
- Rajani, B. B., Robertson, P. K., and Morgenstern, N. R. (1995). Simplified Design Methods for Pipelines Subject to Transverse and Longitudinal Soil Movements: Reply. *Can. Geotechnical J.* 32, 783. doi:10.1139/t95-111
- Randolph, M. F., Seo, D., and White, D. J. (2010). Parametric Solutions for Slide Impact on Pipelines. *J. Geotech. Geoenviron. Eng.* 136 (7), 940–949. doi:10.1061/(ASCE)gt.1943-5606.0000314
- Tsatsis, A., Kourkoulis, R., and Gazetas, G. (2015). Buried Pipelines Subjected to Ground Deformation Caused by Landslide Triggering, 5th ECCOMAS Thematic Conference. *Comput. Methods Struct. Dyn. Earthquake Eng.* 3, 25–27. doi:10.7712/120115.3524.1405
- Vasseghi, A., Haghshenas, E., Soroushian, A., and Rakhshandeh, M. (2021). Failure Analysis of a Natural Gas Pipeline Subjected to Landslide. *Eng. Fail. Anal.* 119, 105009. doi:10.1016/j.engfailanal.2020.105009
- Wang, L. W., Zhang, L., Dong, S. H., and Lu, M. X. (2014). Analysis of Mechanical Influencing Factors of Pipeline Landslide Based on Soil spring Model. *Oil & Gas Storage Transport.* 33, 380–390. doi:10.6047/j.issn.1000-8241.2014.04.008
- Xi, S., and Wen, B. P. (2019). Mechanical Response of Polygonal-Shape Transverse Buried Gas Pipeline Under the Action of Landslide. *Oil & Gas Storage Transport.* 38, 1350–1358. doi:10.6047/j.issn.1000-8241.2019.12.005
- Xu, X. Z., Wang, J. C., and Zhang, L. X. (2010). *Frozen Soil Physics*. Beijing: Science Press.
- Yoosefghodsi, N., Zhou, J., and Murray, D. W. (2008). A Simplified Model for Evaluating Strain Demand in a Pipeline Subjected to Longitudinal Ground Movement. International Pipeline Conference, Calgary, September 29–October 3, 2008.
- Yuan, Z. M. (1993). The Axial Force Caused by Landsliding Along the Axial Direction of Pipeline. *Pet. Plann. Eng.* 4, 35–38. doi:10.3969/j.issn.1004-2970.1993.06.006
- Zhang, H., and Liu, X. B. (2017). Design Strain Calculation Model for Oil and Gas Pipelines Subject to Geological Hazards. *Oil & Gas Storage Transport.* 36, 91–97. doi:10.6047/j.issn.1000-8241.2017.01.012
- Zhang, S. Z., Li, S. Y., Chen, S. N., Wu, Z. Z., Wang, R. J., and Duo, Y. Q. (2017). Stress Analysis on Large-Diameter Buried Gas Pipelines under Catastrophic Landslides. *Pet. Sci.* 14, 1–7. doi:10.1007/s12182-017-0177-y
- Zhou, W. (2010). Reliability of Pressurised Pipelines Subjected to Longitudinal Ground Movement. *Struct. Infrastructure Eng.* 8, 1–13. doi:10.1080/15732479.2010.505244

Conflict of Interest: Author DB was employed by company Western Pipeline Co. Ltd of PipeChina. Author YL was employed by company China Petroleum Pipeline Engineering Corporation.

The remaining authors declare that the research was conducted in the absence of any commercial or financial relationships that could be construed as a potential conflict of interest.

Publisher's Note: All claims expressed in this article are solely those of the authors and do not necessarily represent those of their affiliated organizations, or those of the publisher, the editors and the reviewers. Any product that may be evaluated in this article, or claim that may be made by its manufacturer, is not guaranteed or endorsed by the publisher.

Copyright © 2021 Ji, Liu, Bolati, Yang, Jiang, Liu and Zhang. This is an open-access article distributed under the terms of the Creative Commons Attribution License (CC BY). The use, distribution or reproduction in other forums is permitted, provided the original author(s) and the copyright owner(s) are credited and that the original publication in this journal is cited, in accordance with accepted academic practice. No use, distribution or reproduction is permitted which does not comply with these terms.



Study on Hydrate Phase Equilibrium Diagram of Methane Containing System Based on Thermodynamic Model

Hao Liang^{1,2}, Yonggang Duan¹, Jun Pei^{1*} and Na Wei^{1,3}

¹State Key Laboratory of Oil and Gas Reservoir Geology and Exploitation, Southwest Petroleum University, Chengdu, China, ²CNOOC (China) Co., Ltd. Hainan, Haikou, China, ³State Key Laboratory of Natural Gas Hydrate, Beijing, China

OPEN ACCESS

Edited by:

Bamidele Victor Ayodele,
Universiti Tenaga Nasional, Malaysia

Reviewed by:

Chang-Yu Sun,
China University of Petroleum, China
May Ali Alsaffar,
University of Technology, Iraq

*Correspondence:

Jun Pei
asharey@yeah.net

Specialty section:

This article was submitted to
Advanced Clean Fuel Technologies,
a section of the journal
Frontiers in Energy Research

Received: 18 July 2021

Accepted: 21 September 2021

Published: 06 October 2021

Citation:

Liang H, Duan Y, Pei J and Wei N
(2021) Study on Hydrate Phase
Equilibrium Diagram of Methane
Containing System Based on
Thermodynamic Model.
Front. Energy Res. 9:743296.
doi: 10.3389/fenrg.2021.743296

Natural gas hydrate is a potential energy source in the future, which widely occurs in nature and industrial activities, and its formation and decomposition are identified by phase equilibrium. The calculation of multicomponent gas phase equilibrium is more complex than that of single component gas, which depends on the accurate model characterized by enthalpy and free energy. Based on the Kvamme-Tanaka statistical thermodynamic model, theoretical and experimental methods were used to predict and verify the phase equilibrium of pure methane hydrate and carbon dioxide hydrate in the temperature range of 273.17–289.05 K. The phase equilibrium curves of methane-containing gases such as CH_4+CO_2 , $\text{CH}_4+\text{C}_2\text{H}_6$, $\text{CH}_4+\text{H}_2\text{S}$ and $\text{CH}_4+\text{CO}_2+\text{H}_2\text{S}$ under different mole fractions were drawn and analyzed, and the decomposition or formation enthalpy and free energy of hydrate were calculated. The results show that, the phase equilibrium curves of the methane containing systems is mainly related to the guest molecule type and the composition of gas. The evolution law of phase equilibrium pressure of different gases varies with composition and temperature, and the phase splitting of CO_2 at the quadruple point affects the phase equilibrium conditions. Due to the consideration of the interaction between the motion of guest molecules and the vibration of crystal lattice, the model exhibits a good performance, which is quantified in terms of mean square error (MSE) with respect to the experimental data. The magnitudes of MSE percent are respectively 1.2, 4.8, 15.12 and 9.20 MPa^2 for CH_4+CO_2 , $\text{CH}_4+\text{C}_2\text{H}_6$, $\text{CH}_4+\text{H}_2\text{S}$ and $\text{CH}_4+\text{CO}_2+\text{H}_2\text{S}$ systems, and the values are as low as 3.57 and 1.32 MPa^2 for pure methane and carbon dioxide, respectively. This study provides engineers and researchers who want to consult the diagrams at any time with some new and accurate experimental data, calculated results and phase equilibrium curves. The research results are of great significance to the development and utilization of gas hydrate and the flow safety prediction of gas gathering and transportation.

Keywords: hydrate, methane, thermodynamics, phase equilibrium, enthalpy, free energy

INTRODUCTION

Natural gas hydrate (NGH) is a solid clathrate crystal material composed of water cages, which contain molecules such as hydrocarbons, carbon dioxide, hydrogen sulfide and other molecules, in which methane is the dominant gas (Vedachalam et al., 2015). Different structures of NGH can be formed by the reaction of water and gas molecules under certain conditions such as temperature, pressure, gas saturation, water salinity and pH value, etc (Makogon, 1997; Darbouret et al., 2005; Makogon, 2010; Babu et al., 2013; Babu et al., 2014; Veluswamy et al., 2016; Anwar et al., 2018). NGH is a potential alternative energy with tremendous reserves, which occurs in permafrost and marine sediments. Collett et al. estimate that the amount of natural gas stored in hydrate reservoirs in the world is between 2.8×10^5 and $8 \times 10^8 \text{ m}^3$ at standard conditions, which is a fairly high value (Collett, 2009). Therefore, it has attracted great attention in Japan, China, South Korea, India and other countries with relatively scarce resources, where researchers are more interested in hydrates than in the United States, Canada and Europe in recent years (Zhao et al., 2019). Although some hydrate production tests have been carried out all over the world, there is no efficient and safe exploitation method at present, and the exploitation of NGH still faces many basic research problems (Liu et al., 2019; Ye et al., 2020). The academia pay close attention to the phase equilibrium research of NGH, and the related work has been applied in many fields such as energy, chemical industry, bioengineering and environmental protection (Qorbani, 2017).

NGH widely occurs in the natural environment or in the process of oil and gas production and transportation, and its formation and decomposition are identified by phase equilibrium. How to describe all the complex phases and components quantitatively in a model is a question that people have been trying to answer for many years. Since the first hydrate phase equilibrium model was established based on statistical thermodynamic (van der Waals and Platteeuw, 1959), other scholars have proposed more accurate prediction models, most of which are based on van der Waals and Platteeuw's theory (vdW-P model). For instance, Parrish and Prausnitz used an empirical correlation to calculate the Langmuir constant, which greatly simplified the application of van der Waals- Platteeuw model (Parrish and Prausnitz, 1972). To overcome the disadvantage of Parrish-Prausnitz model in predicting the pressure of asymmetric mixtures, Ng and Robinson modified the chemical potential of water in hydrate phase, which improved the prediction results (Ng and Robinson, 1976). John et al. noticed the effects of the non-spherical and outer water molecules of the guest molecules on the total potential energy of the cavity (John et al., 1985). They used the three-layer sphere model to describe the interaction between the guest molecules in the hydrate cavity and the water molecules around the cavity, and introduced a correction factor Q^* to correct the non-spherical characteristics of the molecules. Du and Guo improved the model of John et al., and predicted the hydrate formation conditions of methanol-containing system, and finally obtained satisfactory results (Chen and Guo, 1996). Chen and Guo thought that the similarity between the process of gas molecules wrapped by water

molecules and the Langmuir isothermal adsorption process is not as great as van der Waals and Platteeuw thought, so they proposed a new model (Du and Guo, 1990). In 1995, Kvamme and Tanaka extended the theory of van der Waals and Platteeuw to study the thermodynamic stability of C_2H_4 , C_2H_6 and CO_2 (Kvamme and Tanaka, 1995). As we know, the simplest calculation of hydrate phase equilibrium starts from pure gas hydrate. Using the phase equilibrium relationship of pure methane to predict the hydrate formation and decomposition of multicomponent gases was a common phenomenon in oil and gas field production in the past, and even many gas fields over the world adopt this simple method currently. However, this practice can no longer meet the needs of current industrial development, because natural gas contains not only methane, but also hydrocarbon gases such as ethane and propane, as well as non-hydrocarbon gases such as carbon dioxide and hydrogen sulfide. Hence, the models of multicomponent gas hydrate were established by researchers to predict the phase equilibrium boundary of NGH with complex gas components and experiments were carried out to verify the accuracy of these model. Subramanian et al. measured the transformation of sI hydrate and sII hydrate in $\text{CH}_4\text{-C}_2\text{H}_6$ binary system and studied the phase equilibrium (Subramanian et al., 2000a). Anderson et al. studied the phase equilibrium of $\text{CH}_4\text{-CO}_2$ binary system and found that the phase equilibrium pressure of CO_2 hydrate is lower than that of CH_4 hydrate when the temperature is lower than 283 K (Anderson et al., 2003). Huang and Sun measured the hydrate formation data of $\text{CH}_4\text{+CO}_2\text{+H}_2\text{S}$ system at 274.2–299.7K and 0.58–8.68 MPa, and calculated the phase equilibrium data using Chen-Guo model (Huang et al., 2005). Moradi et al. studied the phase equilibrium of CH_4 , C_2H_6 , C_3H_8 , CO_2 , N_2 and their two-component gas hydrates (Moradi and Khosravani, 2012). To predict the phase equilibrium data of pure CO_2 , H_2S and multicomponent acid gas hydrates, Bahman and Mohammad proposed a CPA/Electrolyte/Chen–Guo model, which took into account the effects of hydrolysis and hydrogen bond association (ZareNezhad and Ziaee, 2013). In summary, different thermodynamic models have been used to study the multi-component system hydrate, and some conclusions have reached a consensus.

In addition to the pressure and temperature conditions along the equilibrium curve, other thermodynamic properties such as enthalpy and free energy are crucial to studies related to the aforementioned applications. However, it is found that the hydrate formation mechanism of multi-component system is complex, and there are many research models with different precision. Most of these models increase the prediction accuracy by improving Langmuir constant or potential energy function, and the vdW-P model and Chen-Guo model are most widely used in thermodynamic calculation. Nevertheless, there are few studies on the systematic image description of hydrate phase equilibrium for multi-component system containing methane so far, and there is a lack of phase equilibrium research based on the modified Kvamme-Tanaka model. Beyond that, to our knowledge, the phase transition with rapid change in CO_2 density is rarely mentioned in the literature, and the misunderstanding of CO_2 hydrate is more stable than CH_4

hydrate over a limited range of pressures and temperatures is widely recognized. Therefore, to fill the abovementioned gap, the phase equilibrium and thermodynamic parameters of gas hydrate in methane containing system were studied and analyzed by Kvamme-Tanaka statistical thermodynamic model (Kvamme and Tanaka, 1995) in this manuscript. Based on the experimental data and calculation results, we compared the phase equilibrium curves of methane hydrate, carbon dioxide hydrate and some methane containing multi-component hydrate, and calculated the enthalpy change and free energy of them. This study complements the new data for mixed gas phase equilibrium and gives some hydrate phase equilibrium diagrams of methane containing system, which can provide a basis for the development and utilization of NGH, and the prediction of gas gathering and transportation flow safety.

METHODOLOGY

Thermodynamic Model of Hydrate

There are many theoretical models to predict the phase equilibrium of gas hydrate, among which the statistical mechanical model based on Langmuir adsorption isotherm theory by van der Waals and Platteeuw plays an important role (van der Waals and Platteeuw, 1959). The four main assumptions of the model include that the guest molecules do not deform the cavity, that there is no interaction between the guest molecules, that each cavity can accommodate only one guest molecule, and that the cavity is spherically symmetric. In theory, the thermodynamic calculation of gas hydrate can be carried out by using the properties of single component gas. However, the vdW-P model does not consider the interaction between the motion of guest molecules and the vibration of crystal lattice, which has some limitations in application. When the guest molecule is a small nonpolar molecule, the interaction between the motion of the guest molecule and the vibration of the crystal lattice is small, and the assumption of vdW-P model is comparatively reasonable. However, the reasonableness of this assumption is weakened for large molecules or small polar molecules because they distort the water lattice and have a very significant interaction, resulting in the inaccuracy of the classical calculation method of Langmuir constant. So Kvamme and Tanaka proposed an improved model, which can calculate the phase equilibrium of multi-component hydrates of large or micro polar molecules such as CO₂ and H₂S (Kvamme and Tanaka, 1995). In this work, it is assumed that the chemical potentials of guest molecules in large and small cavities are equal and the ideal liquid is chosen as a reference state in fugacity coefficient calculation. The chemical potential of the water inside the hydrate can be expressed as (Kvamme and Tanaka, 1995; Kvamme, 2019; Kvamme et al., 2019):

$$\mu_{H_2O}^H = \mu_{H_2O}^{O,H} - \sum_{j=1,2} RT v_j \ln \left(1 + \sum_i h_{ij} \right), \quad (1)$$

in which the superscript *H* denotes hydrate phase, the superscript *O* denotes empty clathrate. *v_j* is *j*-type cavity number of per water

molecule in hydrate structure. In sI hydrate, small cavity *v_S* = 1/23, large cavity *v_L* = 3/23. *R* is universal gas constant and *T* is temperature. *h_{ij}* is canonical partition function of *i* guest molecule in *j* cavity, which is given by the following equation:

$$h_{ij} = e^{\beta(\mu_{ij}^H - \Delta g_{ij}^{inc})} = C_{ij} f_i, \quad (2)$$

where β is the inverse of the general gas constant times the temperature. In thermodynamic equilibrium, the chemical potential μ_{ij}^H of guest molecule *i* in *j* cavity is equal to its chemical potential in the original phase (gas, liquid or fluid). *C_{ij}* is the Langmuir constant and *f_i* is the fugacity of guest molecule *i*, which is obtained from SRK equation of state (Soave, 1972). Δg_{ij}^{inc} is the free energy of guest molecule *i* in the *j* cavity of hydrate, which can be expressed as:

$$\Delta g_{ij}^{inc} = \sum_{i=0}^5 k_i \frac{T_c^i}{T^i}, \quad (3)$$

where *T_c* is the critical temperature of the guest molecule. The reference values of *k_i* for different guest molecules are shown in the relevant literature (Kvamme and Tanaka, 1995; Qorbani, 2017). The form of Eq. 3 is also used for empty clathrates. To calculate the chemical potential, it is necessary to associate the cavity partition function with the composition and express the occupancy of guest molecule *i* in *j* cavity with the filling fraction θ_{ij} .

$$\theta_{ij} = \frac{C_{ij} f_i}{1 + \sum_i C_{ij} f_i}, \quad (4)$$

Substituting Eq. 4 into Eq. 2, the relationship between the filling fraction, mole fraction and cavity partition function of the guest molecules can be obtained, which is expressed as follows:

$$\theta_{ij} = \frac{h_{ij}}{1 + \sum_i h_{ij}} = \frac{x_{ij}^H}{v_j (1 - x_T)}, \quad (5)$$

where *x_T* represents the total mole fraction of all guest molecules in the hydrate and *x_{ij}^H* represents the mole fraction of guest molecule *i* in the *j* cavity; The corresponding mole fraction of water is:

$$x_{H_2O}^H = 1 - \sum_i x_{ij}^H, \quad (6)$$

in which the subscript *H₂O* refers to the water transformed into hydrate. The water phase is usually liquid or ice, but only liquid water is considered in this study. The chemical potential of liquid water is as follows:

$$\mu_{H_2O} \left(T, P, \vec{x} \right) = \mu_{H_2O}^{pure, H_2O} (T, P) + RT \ln x_{H_2O}, \quad (7)$$

Thermodynamic equilibrium is reached when the temperature, pressure, and chemical potential of all the co-existing phases are equal at the phase boundary. To ensure that the reference state of free energy of each phase is the same, the chemical potential calculation of each phase and

each component takes the ideal state as the reference and is expressed as:

$$\mu_i(T, P, \vec{y}) = \mu_i^{ig}(T, P, \vec{y}) + RT \cdot \ln \phi_i(T, P, \vec{y}), \quad (8)$$

$$\mu_i(T, P, \vec{x}) = \mu_i^{il}(T, P, \vec{x}) + RT \cdot \ln \gamma_i(T, P, \vec{x}), \quad (9)$$

$$\mu_i(T, P, \vec{x}) = \mu_i^{\infty}(T, P, \vec{x}) + RT \cdot \ln \gamma_i^{\infty}(T, P, \vec{x}), \quad (10)$$

where the superscript *ig* and *il* denote ideal gas and ideal liquid respectively, and the superscript ∞ denotes infinite dilution. T is temperature and P is pressure. ϕ_i is fugacity coefficient and the fugacity coefficient of ideal gas is 1. \vec{x} and \vec{y} are the mole fraction vectors of guest molecule i in liquid mixtures. When $x_i \rightarrow 1$, $\gamma_i = 1$, and when $x_i \rightarrow 0$, $\gamma_i^{\infty} = 1$. The hydrate content of all gas components can be estimated by calculating their chemical potential when dissolved in the methane phase using the above formulae, where Eq. 8 calculates the chemical potential required by the partition function in Eq. 2. According to Eqs 1, 9, typical equilibrium approximate equations used in many hydrate reservoir simulators are obtained, which can be expressed as:

$$\begin{aligned} \mu_{H_2O}^{O,H} - \sum_{j=1,2} RT v_j \ln \left(1 + \sum_i h_{ij} \right) \\ = \mu_{i,H_2O}^{pure,H_2O}(T, P) + RT \ln \left[x_{i,H_2O} \gamma_i(T, P, \vec{x}) \right], \end{aligned} \quad (11)$$

The Gibbs free energy of the hydrate phase is written as the sum of the chemical potentials of each component and given by:

$$G_H = x_{H_2O}^H \mu_{H_2O}^H + \sum_i x_i \mu_i^H, \quad (12)$$

The free energy gradient of all independent thermodynamic variables must cause the change of free energy to be negative. The following eq. 13 is used to calculate the phase transition free energy.

$$\begin{aligned} \Delta G^H = \delta x_{H_2O}^H \left[\mu_{H_2O}^H(T, P, \vec{x}^H) - \mu_{H_2O}^{water}(T, P, \vec{x}) \right] \\ + \delta \sum_i x_i^H \left[\mu_i^H(T, P, \vec{x}^H) - \mu_i^{gas}(T, P, \vec{y}^{gas}) \right], \end{aligned} \quad (13)$$

where δ is a constant coefficient, when it is equal to 1 means hydrate generation, while it is equal to -1 means hydrate decomposition. x represents the mole fraction of liquid, or the mole fraction of water or guest molecule in the hydrate. i denotes guest molecule. Superscript *water* denotes water phase. μ denotes chemical potential. The vector notation represents the mole fraction of all the components in the real phase. The summation symbol covers all the components in the hydrate phase. The calculation of Eq. 13 is based on a full understanding of hydrate composition.

To produce natural gas from large amounts of *in-situ* methane hydrates scattered around the world and control the hydrate formation and decomposition in low temperature or high pressure pipelines, information about the heat of hydrate formation and dissociation is of vital important. The

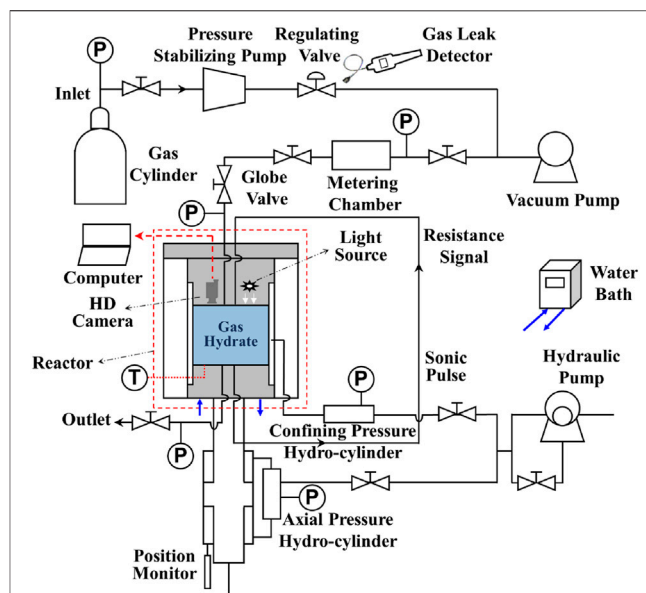


FIGURE 1 | Schematic diagram of experimental apparatus for hydrate reaction. Hydrate cores were not used in this manuscript, and the confining pressure regulation system and axial pressure regulation system for core deformation test was not used.

enthalpies of hydrate formation or decomposition can usually be estimated by Clausius-Clapeyron or Clapeyron methods (Tsimpanogiannis et al., 2019), however, these two methods may be too simplistic. The residual thermodynamic can provide more reliable data and extend the calculation to non-equilibrium conditions. The heat (enthalpy) formed in the hydrate phase transition process must be transported from the reaction system. The absolute value of the heat to be transferred is given by eq. 14, which is solved by numerical method. The enthalpy of pure guest molecular is calculated by residual thermodynamics, as shown in eq. 15.

$$\Delta H = -RT^2 \frac{\partial \left[\frac{\Delta G^{Total}}{RT} \right]_{P,N}}{\partial T}, \quad (14)$$

$$H_i^R = -RT^2 \sum_i y_i \left[\frac{\partial \ln \phi_i^{gas}}{\partial T} \right]_{P, y_j \neq i}, \quad (15)$$

where N is the number of moles of hydrate formed. The total free energy change ΔG^{Total} is the sum of the phase transition free energy ΔG^H and the energy to push away the original phase of the guest molecule.

Experiments

The main purpose of the experiments is to determine the phase equilibrium temperature and pressure of hydrate formation under different gas components, so as to analyze and verify the accuracy of the phase equilibrium diagram. The experiments were completed by SHW-III hydrate electroacoustic testing device (as illustrated in Figure 1), which can meet the requirements of image observation,

temperature and pressure measurement. In these experiments, the temperature regulation system, pressure regulation system, fluid control system and data acquisition system of the device are mainly involved (Wei et al., 2021). The main body of the setup is the NGH reactor, where gas hydrate is generated and decomposed. The side wall of the reactor encloses the inside of the reactor into a cylindrical space, and the upper and lower parts of the reactor vessel are sealed by the steel cover of the pressure regulation system. The working pressure range of 0–30 MPa and the temperature range of -6°C – 25°C in the reactor are considered acceptable. To keep the temperature constant, the hydrate reaction vessel is submerged into the water bath temperature regulation system, to a closed system where the reactor enclosed by a customized cylindrical cooling jacket. Industrial alcohol and water are mixed in a certain proportion and added to the water bath device. The temperature in the reaction kettle is adjusted by the water bath, and monitored by thermocouples (accuracy 0.05% of reading). Continuous commissioning of the water bath temperature regulation system is required according to the experimental conditions to ensure that the temperature meets the requirements. The pressure regulation system is composed of confining pressure regulation system, axial pressure regulation system and gas pressure regulation system. The experiments in this manuscript only need to adjust the gas pressure regulation system to provide the necessary pressure conditions for the phase equilibria measurement of NGH. The fluid control system mainly consists of a vacuum pump, a pressure stabilizing pump and a gas cylinder. The gas flow rate and pressure in the system can be adjusted by using pressure stabilizing pump and gas cylinder after the air in the reactor is vacuumed by vacuum pump. The data acquisition system controls the setting of axial pressure and confining pressure by computer, and automatically records the parameters in the process of experiments. The purity of the gas used in the experiment is 99.9%, which was provided by Huate Gas Co., Ltd. and the distilled water was self-made in the laboratory.

The phase equilibrium temperature of hydrate was determined by decomposition method, and the specific method was carried out according to the following steps.

- 1) Prepare the experimental system. Clean the reactor with deionized water, then wipe and clean the unit with a wet alcohol cotton to ensure that there are no impurities in the reactor. Calibrate the pressure and temperature sensors, and check the airtightness of valves, pipes and reactors with gas leak detector and soapy water. Vacuum after connecting the re-actor to the line, check and ensure the integrity of the device.
- 2) Hydrate preparation. After preliminary checking the device, an appropriate amount of distilled water is added into the reactor (about 5 ml water for acid gas reaction and 30 ml water for general gas reaction). Thereafter, the valves of the inlet pipeline are opened and the single or multi-component gas is injected into the pump. To keep the pressure in the reactor constant, the fluid control system is set to adjust the pressure automatically with the change of the pressure in the reactor.

Gas leak detector is used to check the tightness of the device at the line interface. After all the preliminary, the refrigeration device is turned on to reduce the temperature, and the hydrate began to form after reaching the appropriate setting temperature.

- 3) Hydrate decomposition and phase equilibrium temperature measurement. When the gas hydrate is formed, the temperature in the reactor is controlled to be constant, and the pressure is reduced to the level when only a small amount of hydrate does not decomposed (stage 1). When the hydrate does not decompose in 3–4 h under stable temperature and pressure, the pressure in the reactor was reduced by a micro pressure gradient (0.1 MPa) to find the temperature and pressure where the hydrate can decompose completely (stage 2). This process needs to be repeated many times, and the obtained temperature and pressure are phase equilibrium points.
- 4) Data measurement and recording. The temperature in the reactor, the pressure 1 on the inlet side of the reactor, the pressure 2 on the outlet side of the core are automatically measured and stored. The equilibrium pressure is the average of the above two pressures.

To achieve the experimental purpose, the reaction experiments of two kinds of pure gases and four kinds of mixed gases were designed according to the experimental method, and the phase equilibrium tests of 6 different gas components were carried out under different experimental pressure and temperature, and totally 24 groups of experiments were completed. Repeated tests were carried out to avoid accidental errors in the measurement of phase equilibrium pressure. Nevertheless, some systematic errors are unavoidable. For examples, the pressure difference between the pressure sensors at the inlet and outlet of the reactor is about 0.02–0.05 MPa due their performance differences. Moreover, the pressure in the reactor changes slightly during the experiments because the gas expands with the decrease of pressure and the hydrate decomposes into gas. The pressure stabilizing pump minimizes this effect, and it is found that this error is acceptable. From the point view of experimental temperature, studies have shown that the actual marine hydrates are mostly distributed in the water depth of 300–2000 m and exist in the reservoir within 300 m below the seabed (Sun et al., 2021a; Sun et al., 2021b). In submarine pipeline at cold climates or offshore production, the pressure and temperature ranges are also in line with the actual conditions. So it is believed that the temperature range is reasonable and sufficient in this study.

RESULTS AND DISCUSSION

Thermodynamic Calculation of Pure Gas Hydrate

Taking CH_4 and CO_2 as examples, the phase equilibria of sl hydrate formed by pure gas were calculated by using the thermodynamic model mentioned above. The thermodynamic calculations carried out in this paper are obtained from

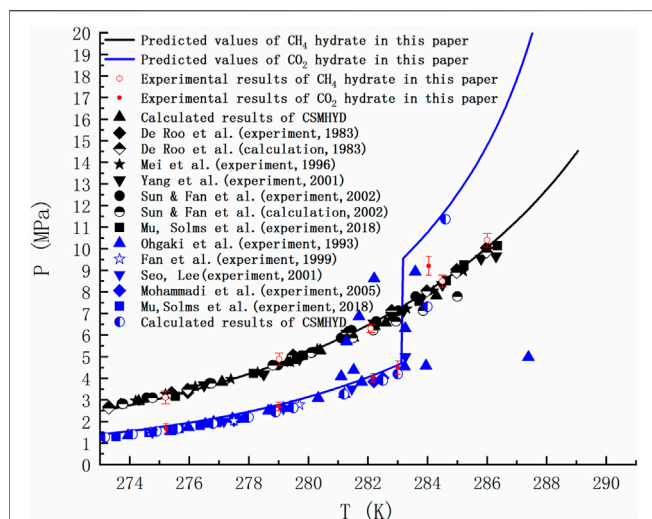


FIGURE 2 | Comparison of predicted phase equilibrium curves of pure CH₄ hydrate and CO₂ hydrate with literature values (De Roo et al., 1983; Ohgaki et al., 1993; Mei et al., 1996; Fan and Guo, 1999; Seo et al., 2001; Yang et al., 2001; Sun et al., 2002; Mohammadi et al., 2005; Mu and von Solms, 2018a).

FORTRAN code, in which the results of dynamic simulation are used (Kvamme and Tanaka, 1995; Kvamme et al., 2019; Kvamme, 2019). As seen in **Figure 2**, the equilibrium curve in the temperature range of 273.17–289.05 K is shown. Note that the black and blue lines respectively represent the equilibrium curves of CH₄ hydrate and CO₂ hydrate predicted in this paper, and the black and blue dots are the reference values of the phase equilibrium of CH₄ hydrate and CO₂ hydrate respectively (De Roo et al., 1983; Ohgaki et al., 1993; Mei et al., 1996; Fan and Guo, 1999; Seo et al., 2001; Yang et al., 2001; Sun et al., 2002; Mohammadi et al., 2005; Mu and von Solms, 2018a). The figure shows 10 groups of phase equilibrium temperature and pressure measured in the formation and decomposition experiments of CH₄ hydrate and CO₂ hydrate in the high-pressure reactor. The standard deviation of experimental data is represented by error bars. Notably, the blue line shows a sudden change at 283.15 K, which is due to the increased density of guest molecules as part of CO₂ turns to liquid at higher pressures. The point at which hydrates, liquid water, liquid carbon dioxide and gaseous carbon dioxide coexist is known as the quadruple point, beyond which the pressure to hydrate increases. The temperature and pressure corresponding to the quadruple point have been straightened out in many literatures. Ohgaki et al. (Ohgaki et al., 1993) found this phenomenon and thought it is caused by liquid carbon dioxide. **Figure 2** shows some of his experimental data. However, more studies lack the data and explanation on the right side of the quadruple point when calculating the phase equilibrium, and even ignore it.

Figure 2 is of guiding significance to the exploitation of NGH by CO₂ replacement method. Injecting CO₂ into the hydrate layer can not only seal it in the hydrate cage, but also replace CH₄. Many research groups around the world has been tempted by the possibility of this win-win situation. However, if only the

temperature and pressure at equilibrium are observed, it is easy to form the misconception that the equilibrium curve of CO₂ hydrate is discontinuous and that CO₂ hydrate is only more stable than CH₄ hydrate in a limited range of temperature and pressure. In fact, due to the Gibbs phase rule ($F = C - P + 2$) and the limitation of heat and mass transfer, the hydrate in natural sediments can never reach the thermodynamic equilibrium. Taking the hydrate formed by the mixtures of methane, ethane and propane containing water as an example, the number of active components C is 4 and the actively coexisting phases P is 3 (water, alkane gas and hydrate) when the adsorption phase is ignored. Then the degree of freedom F is equal to 3, and the system still cannot reach equilibrium at a given temperature and pressure. For a system as simple as the reaction of methane and water to form hydrate ($F = 2 - 3 + 2 = 1$), even if we specify a thermodynamic variable, the nucleation of hydrates may be blocked due to heat and mass transfer restrictions, thus resulting in slow growth of hydrate. Therefore, the equilibrium curve is the limit of hydrate stability. Decomposition of hydrate occurs either below phase equilibrium pressure or above phase equilibrium temperature. There is a competitive phase transition in the formation and dissociation of hydrate. The formation of hydrate can only occur when the free energy of hydrate is lower than that of guest molecule and water, because the thermodynamic process strives to minimize the free energy. According to the data in **Figure 3**, the free energy of CO₂ hydrate is about 2 kJ/mol lower than that of CH₄ hydrate on the left side of the quadruple point, and about 1.83 kJ/mol lower than that of CH₄ hydrate on the right side of the quadruple point. This indicates that CO₂ hydrate is more stable than CH₄ hydrate in a wide range of temperature and pressure.

Table 1 and **Table 2** show the calculated phase transition data of pure CH₄ hydrate and CO₂ hydrate, where ΔH_w and ΔH_i respectively represent the contribution of water and guest molecules to the enthalpy change, and G is the Gibbs free energy. **Table 3** is the decomposition enthalpy of methane

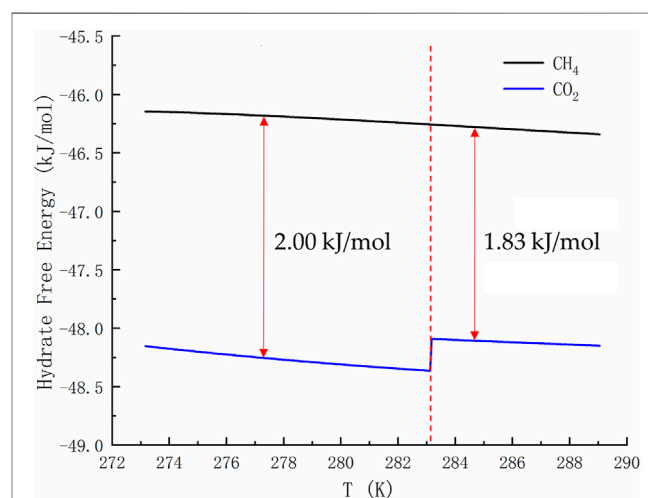


FIGURE 3 | Free energy of pure CH₄ hydrate and CO₂ hydrate. The temperature range shown in the curve is 273.17–289.05 K.

TABLE 1 | Data of methane hydrate phase transition (partial).

T (K)	P (MPa)	ΔH_w (kJ/mol)	ΔH_f (kJ/mol)	ΔH (kJ/mol)	G (kJ/mol)
273.17	2.52	38.68	18.38	57.06	-46.14
275.50	3.23	37.81	18.21	56.02	-46.16
277.26	3.89	37.23	18.04	55.27	-46.18
279.37	4.87	36.57	17.79	54.36	-46.21
281.87	6.37	35.85	17.40	53.25	-46.24
283.29	7.43	35.45	17.13	52.58	-46.26
285.05	9.04	34.97	16.73	51.70	-46.28
285.81	9.84	34.77	16.54	51.34	-46.29
286.45	10.59	34.60	16.36	50.96	-46.30
287.35	11.77	34.36	16.08	50.44	-46.32
288.84	14.14	33.97	15.57	49.54	-46.34

TABLE 2 | Data of carbon dioxide hydrate phase transition (partial).

T (K)	P (MPa)	ΔH_w (kJ/mol)	ΔH_f (kJ/mol)	ΔH (kJ/mol)	G (kJ/mol)
273.17	1.42	45.43	22.36	67.79	-48.15
275.50	1.83	44.10	22.35	66.45	-48.21
277.26	2.25	43.10	22.33	65.43	-48.25
279.37	2.90	41.91	22.31	64.22	-48.30
281.87	3.98	40.50	22.27	62.77	-48.34
283.29	9.70	39.43	22.02	61.45	-48.09
285.05	12.63	38.50	21.96	60.46	-48.11
285.81	14.30	38.11	21.94	60.05	-48.12
286.45	16.02	37.78	21.94	59.72	-48.12
287.35	19.25	37.32	21.97	59.29	-48.13
288.84	28.45	36.55	22.20	58.75	-48.15

TABLE 3 | Reported values of decomposition enthalpy of methane hydrate (Handa, 1986; Lievois et al., 1990; Sloan and Fleyfel, 1992; Kang et al., 2001; Anderson, 2004; Rydzy et al., 2007; Gupta et al., 2008; Nakagawa et al., 2008; Mu and von Solms, 2018b).

Source	T (K)	P (MPa)	ΔH (kJ/mol)
Handa	273.15	0.10	54.19
Lievois et al	273.15	—	54.77
Sloan et al	273.15	0.10	56.90
Kang et al	273.15	0.10	56.84
Rydzy et al	271.00	15.00	51.60
Nakagawa et al	279.00–282.00	5.00	55.30
Gupta et al	280.60–291.65	5.50–19.30	54.44
Mu et al	275.54–286.35	3.163–10.143	55.01
Anderson	274.00–318.00	2.85–311.12	53.50
Experimental data	273.17–289.05	2.52–14.15	53.32

hydrate reported by relevant scholars. The enthalpy of hydrate formation (or decomposition) is calculated by calculating the enthalpy change of structural water and guest molecules respectively. The enthalpy change value is negative, indicating formation, and positive, indicating decomposition. According to **Table 1**, the average enthalpy of decomposition (or formation) of methane hydrate is 53.32 kJ/mol and the average value of Gibbs energy is -46.26 kJ/mol within the range of 273.17–289.05 K. Similarly, as shown in **Table 2**, the average enthalpy of decomposition (or formation) of carbon dioxide hydrate is 63.48 kJ/mol, and the average value of Gibbs energy is

-48.18 kJ/mol. **Table 3** is the decomposition enthalpy of methane hydrate reported by relevant scholars. The enthalpy of hydrate formation (or decomposition) is calculated by calculating the enthalpy change of structural water and guest molecules respectively. The enthalpy change value is negative, indicating formation, and positive, indicating decomposition. According to **Table 1**, the average enthalpy of decomposition (or formation) of methane hydrate is 53.32 kJ/mol and the average value of Gibbs energy is -46.26 kJ/mol within the range of 273.17–289.05 K. Similarly, as shown in **Table 2**, the average enthalpy of decomposition (or formation) of carbon dioxide hydrate is 63.48 kJ/mol, and the average value of Gibbs energy is -48.18 kJ/mol.

Eq. 16 is used to calculate the mean square error (MSE). The smaller the MSE, the higher the accuracy of the prediction model to describe the real data. The results show that the MSE of 5 methane hydrate phase equilibrium pressure points is 3.57% MPa² and that of carbon dioxide hydrate phase equilibrium pressure on the left side of the quadruple point is 1.32% MPa², which is lower than 5% MPa². On the other hand, the relative error between the average decomposition enthalpy of methane hydrate calculated in this paper and the 9 average enthalpy data values reported in **Table 3** is only 2.6% (Handa, 1986; Lievois et al., 1990; Sloan and Fleyfel, 1992; Kang et al., 2001; Anderson, 2004; Rydzy et al., 2007; Gupta et al., 2008; Nakagawa et al., 2008; Mu and von Solms, 2018b). It can be seen that the modified model by Kvamme and Tanaka is of high

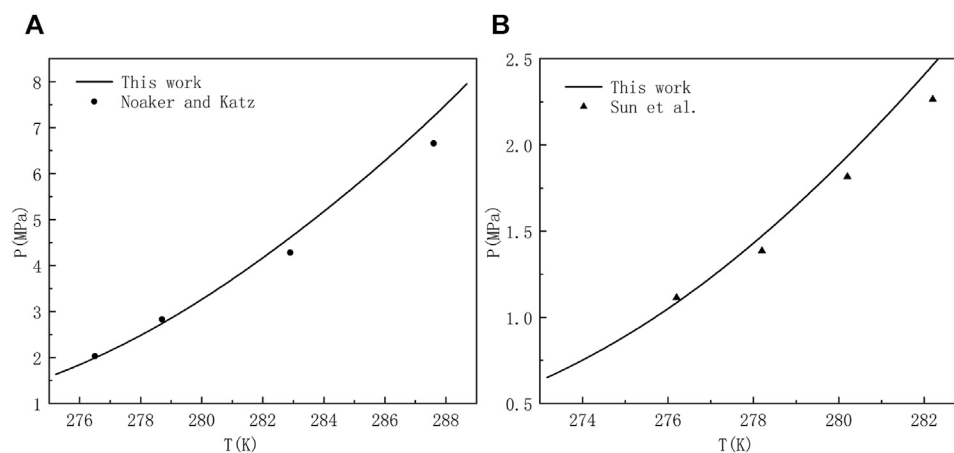


FIGURE 4 | Estimated and experimental hydrate equilibrium pressures for a system of **(A)** 96.89 mol% methane and 3.11 mol% hydrogen sulfide (Noaker and Katz, 1954), and **(B)** 82.45 mol% methane, 10.77 mol% carbon dioxide, and 6.78 mol% hydrogen sulfide (Sun and Chen, 2005).

reliability, which can accurately predict the phase equilibrium of methane hydrate and carbon dioxide hydrate within a wide range of temperature and pressure.

$$\text{MSE} = \frac{1}{n} \sum_{i=1}^n (x_i^c - x_i^e)^2, \quad (16)$$

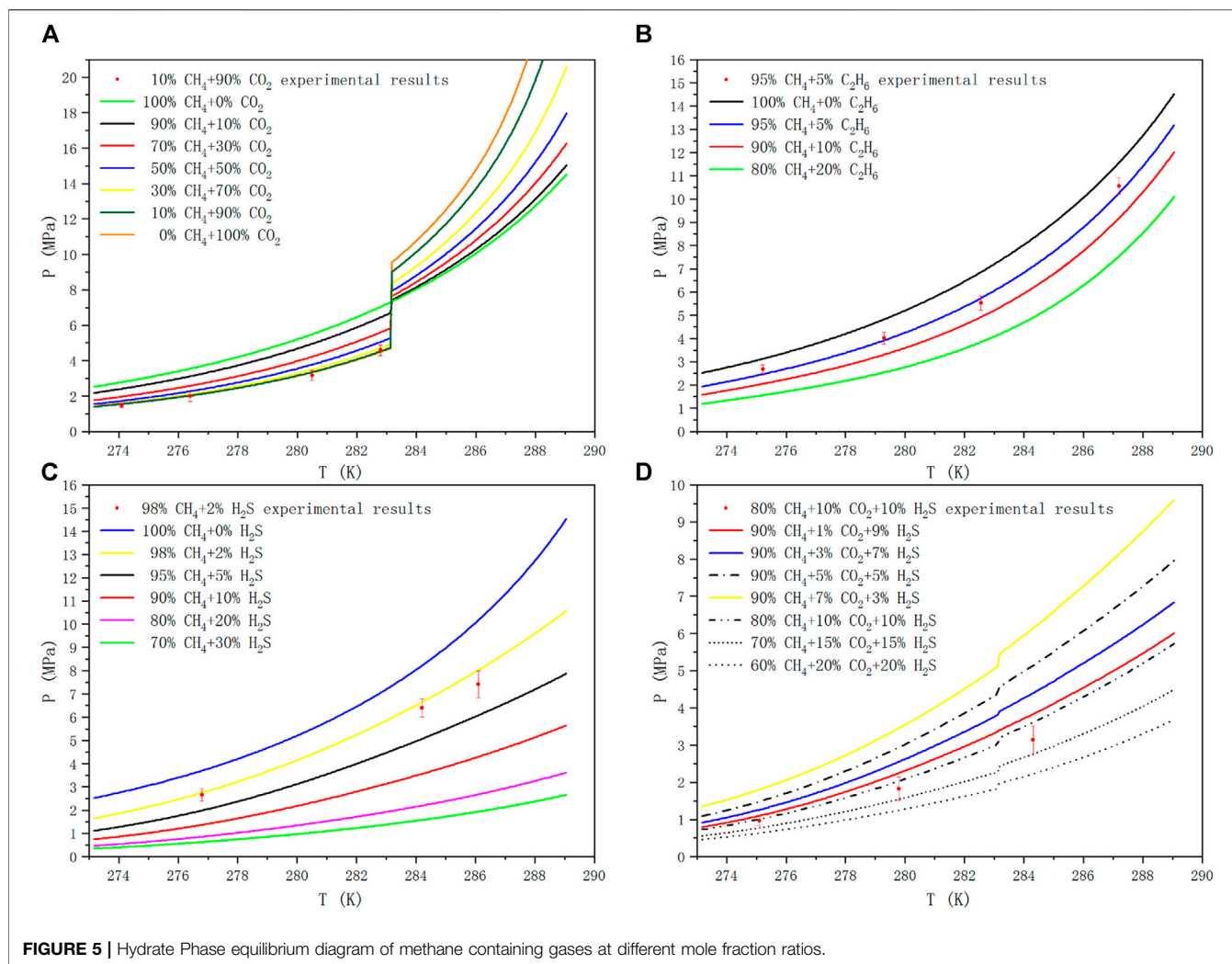
where x_i^c and x_i^e represent the calculated and measured values of the model, respectively.

Phase Equilibrium Diagram of Methane Containing Gas Hydrate

CH_4 and common gases, such as C_2H_6 , C_3H_8 , N_2 , H_2S , CO_2 , etc. are mixed to form multi-component gases which can react with water to form hydrate under low temperature and high pressure. The type of hydrate formed depends on gas composition, concentration and temperature and pressure conditions. Compared with pure gas hydrate, the formation mechanism of multi-component gas hydrates is more complex and there may be structural transformation of sI hydrate and sII hydrate. The main components of natural gas, such as CH_4 , C_2H_6 , CO_2 and H_2S , are usually the object molecules of interest in the industrial field (Jamaluddin et al., 1991). The existence of CO_2 and H_2S , which are the strong hydrate forming components, is the key problem in flow assurance. Some gas fields in China, such as Puguang gas field and Yuanba gas field, have a high content of H_2S and CO_2 in the produced gas, and hydrate can be formed under relatively low pressure and relatively high temperature, which is easy to cause hydrate blockage in the production system. Consequently, there is a need to predict and draw the phase equilibrium curves of multi-component gases at different mole fraction ratio for engineers and researchers who want to consult the diagrams at any time. But before that happens, the validation of the theoretical model is very necessary. In **Figure 4**, we use the proposed method to compare the results with those obtained by classical techniques used in industry or academia, and some experimental data for

hydrate equilibria involving multicomponent gas mixtures with CH_4 in literature (Noaker and Katz, 1954; Sun and Chen, 2005). When comparing literature data and predictions, the perfect matching of our work with experimental data is not the ultimate goal. Because anyone who wants to use this model can make the prediction more accurate by adjusting the Langmuir constant and associated interaction parameters. To our delight, the comparison between the equilibrium pressures of methane containing gas mixture and the measured experimental data in **Figure 4** shows good consistency and stability. Accordingly, it can be confirmed that the model systems is considered to be accurate enough within the scope of this work.

In this paper, taking CH_4+CO_2 , $\text{CH}_4+\text{C}_2\text{H}_6$, $\text{CH}_4+\text{H}_2\text{S}$, $\text{CH}_4+\text{CO}_2+\text{H}_2\text{S}$ as examples, the phase equilibria of methane mixed with CO_2 , C_2H_6 and H_2S in different molar ratios were analyzed in the temperature range of 273.17–289.05 K. When calculating the phase equilibria of the methane containing system, the mole fraction of the gas component meets the normalization condition. As shown in **Figure 5**, the phase equilibrium curves of methane containing multicomponent gases at different mole fraction ratios were predicted. The uncertainty of the measurement is marked with error bars, and the pressure at the same temperature was tested twice to ensure that the measurement error is within an acceptable range. The curves of different line-types and colors show the phase equilibrium curves of different gas ratios, and the red dots are the experimental value. In the low temperature and high pressure environment, the molecules with the lowest free energy and the lowest pressure needed to fill the cavity participate in the nucleation to form a stable hydrate structure firstly based on the law of thermodynamics, and then other metastable gas molecules fill the cavity to continue to grow. CO_2 molecules in sI hydrate mainly enter large cavities. Although it has been found that it can exist in small cavities, the conditions required are rather harsh. It is still unclear whether the structure of small cavity filled with CO_2 molecule will be formed at the temperature above 0°C , which is beneficial to the structural stability of hydrate.



Therefore, in this paper, CH_4 mainly fills the small cavity of sI hydrate structure, C_2H_6 and CO_2 fill the large cavity, while H_2S can not only fill the large cavity, but also exist stably in the small cavity.

One would have to investigate mixed hydrates with certain CO_2 contents in order to determine what is stable and what is not. From only investigating pure methane and pure CO_2 hydrates one cannot simply say that under certain conditions only methane or only CO_2 would go into the hydrate structure, as always mixed hydrates would form if CO_2 and CH_4 are together in a mixture with water. **Figure 5A** is the phase equilibrium diagram of the hydrate formed by the mixtures of CH_4 and CO_2 at different mole fraction ratios. In the sI hydrate formed by CH_4 - CO_2 binary gas, CH_4 mainly occupies the small cavity, while CO_2 occupies the large cavity, which is more stable than pure gas hydrate. The phase equilibrium pressure of gas mixture changes differently before and after the quadrupole point of CO_2 , and the phase splitting at the quadrupole affects the phase equilibrium conditions. It can be seen that when the temperature is lower than 283.15 K, with the increase of CO_2 proportion in CH_4 gas, the corresponding phase equilibrium

pressure at the same temperature decreases, and with the accumulation of CO_2 concentration in the mixtures, the pressure drop caused by increasing the same CO_2 proportion becomes smaller and smaller. On the contrary, when the temperature is higher than 283.15 K, with the increase of CO_2 ratio, the corresponding phase equilibrium pressure increases at the same temperature, and the increase of CO_2 ratio leads to the increase of pressurization amplitude.

The hydrate formation mechanism of CH_4 - C_2H_6 system is different from that of CH_4 - H_2S , but it shows similar trends in phase equilibrium curve. CH_4 and C_2H_6 form sI hydrate with their pure gas, but their mixed gas can be transformed into sII structure when the composition of CH_4 is in the range of 75–99 mol% (Kwon et al., 2014). The unit cell is composed of 16 12-hedral and 8 16-hedral cages of water molecules in sII hydrate, which is more stable than sI structure. More detailed studies related to structural transformation can be found in (Subramanian et al., 2000a; Subramanian et al., 2000b). Unlike ethane, hydrogen sulfide hydrolyzes in the presence of water, producing HS^- , trace amounts of S^{2-} , and positively charged hydrogen atoms. And under appropriate temperature and

TABLE 4 | Calculated results of free energy of hydrate in 90 mol% CH₄+10 mol% C₂H₆/CO₂/H₂S system. G in the table represents Gibbs free energy.

T (K)	G _{C1} (kJ/mol)	G _{C1+H2S} (kJ/mol)	G _{C1+ C2} (kJ/mol)	G _{C1+CO2} (kJ/mol)
273.17	-46.14	-47.12	-46.52	-46.45
275.50	-46.16	-47.02	-46.49	-46.46
277.26	-46.18	-46.92	-46.49	-46.47
279.37	-46.21	-46.87	-46.50	-46.48
281.87	-46.24	-46.85	-46.50	-46.49
283.29	-46.26	-46.86	-46.49	-46.36
285.05	-46.28	-46.89	-46.48	-46.38
285.81	-46.29	-46.90	-46.48	-46.39
286.45	-46.30	-46.91	-46.48	-46.40
287.35	-46.32	-46.93	-46.47	-46.41
288.84	-46.34	-46.97	-46.46	-46.42

pressure, the stability of cage structure can be ensured by the action of dipole moment and Coulomb force. **Figure 5B** and **Figure 5C** are the phase equilibrium diagrams of sl hydrate formed by CH₄+C₂H₆ binary gas system and CH₄+H₂S binary gas system at different mole fraction ratios, respectively. We can see from the figures that, compared with hydrate phase equilibrium of pure CH₄, with the increase of C₂H₆ or H₂S ratio in binary gas mixtures, the corresponding phase equilibrium pressure at the same temperature decreases, and with the accumulation of C₂H₆ or H₂S in the mixtures, the pressure drop caused by increasing the same C₂H₆ or H₂S ratio becomes smaller and smaller.

Figure 5D shows the phase equilibrium diagrams of hydrate formation from CH₄, CO₂ and H₂S ternary mixtures at different mole fraction ratios. It can be seen from **Figure 5D** that in the temperature range of 273.17–289.05 K, if the CH₄ content in the mixtures remains unchanged (90 mol%), the higher the CO₂ content is, the lower the average value of Gibbs energy is, and the corresponding phase equilibrium pressure is higher at the same temperature. If the ratio of CO₂ and H₂S remains unchanged, the lower the content of CH₄, the lower the mean free energy and the lower the corresponding phase equilibrium pressure at the same temperature. Compared with the CH₄+CO₂ binary mixtures system, H₂S not only reduces the equilibrium pressure, but also reduces the influence of liquid CO₂ on the equilibrium system to some extent. Therefore, the pressure mutation in the CH₄+CO₂+H₂S ternary mixtures system is relatively moderate. The deviation of the predicted results may be due to the underestimated effect of small molecule gas adsorption into small pores on the reduction of the formation pressure of hydrogen sulfide hydrate. Our calculations show that the magnitudes of MSE are respectively 1.2, 4.8, 15.12 and 9.20% MPa² for CH₄+CO₂, CH₄+C₂H₆, CH₄+H₂S and CH₄+CO₂+H₂S systems, in which 14 hydrate phase equilibrium pressure data are used. Even though remarkable deviations occur for the higher temperature regions in the presence of hydrogen sulfide, the agreement is sufficiently fair for analysis of hydrate formation and decomposition in reservoirs and pipelines.

H₂S can enter both large and small cavities simultaneously. When it enters the cavity of the hydrate, the positive hydrogen atom and the negative oxygen atom in the inner wall of the cavity attract each other by Coulomb force, which increases the stability

of the hydrate. Thus, the hydrate equilibrium conditions are shifted to areas where it is more likely to be generated or decomposed. Therefore, the phase equilibrium data of hydrate in the system of 90% CH₄+10% C₂H₆ (also CO₂ and H₂S) were compared in this paper, and the free energy was calculated. The results are shown in **Table 4**. It can be seen from the table that the hydrate free energy of the binary system under the same conditions is CH₄+H₂S system < CH₄+C₂H₆ system < CH₄+CO₂ system. These three values have little difference in within the uncertainties of their determination, so they are just a simple description of a small change here.

CONCLUSION

In the present study, the effects of different mole fractions of CO₂, C₂H₆ and H₂S on the phase equilibrium of methane hydrate by the hydrate electroacoustic testing device were mainly investigated, and the thermodynamic parameters such as decomposition or formation enthalpy and free energy of hydrate were calculated and analyzed by using the modified Kvamme-Tanaka thermodynamic model. The thermodynamic process of hydrate decomposition and formation in methane containing system was analyzed and some new and accurate experimental data, calculated results and phase equilibrium curves of methane containing system have been obtained. Due to the consideration of the interaction between the motion of guest molecules and the vibration of crystal lattice, the model exhibits a good performance. The magnitudes of MSE percent are respectively 1.2, 4.8, 15.12 and 9.20 MPa² for CH₄+CO₂, CH₄+C₂H₆, CH₄+H₂S and CH₄+CO₂+H₂S systems, and the values are as low as 3.57 and 1.32 MPa² for pure methane and carbon dioxide, respectively. Accordingly, the model systems is considered to be accurate enough within the scope of this work. The results are discussed from three aspects: theoretical analysis, numerical calculation and laboratory experiment. In the range of 273.17–289.05 K, the average decomposition enthalpies of CH₄ hydrate and CO₂ hydrate are 53.32 kJ/mol and 63.48 kJ/mol, respectively, and the average value of Gibbs free energy is -46.26 kJ/mol and -48.18 kJ/mol, respectively. The free energy of CO₂ hydrate is 2 kJ/mol lower than that of CH₄ hydrate on the left side of the quadruple point, and 1.83 kJ/mol lower than that of

CH₄ hydrate after the quadruple point. CO₂ hydrate is more stable than CH₄ hydrate in a wide range of temperature and pressure. Additionally, with the increase of the mole ratio of C₂H₆ or H₂S in the binary system containing methane, the equilibrium pressure of hydrate decreases at the same temperature. When the temperature is lower than 283.15 K, the corresponding phase equilibrium pressure decreases with the increase of the molar ratio of CO₂ in CH₄+CO₂ binary system, but the reverse trend appears when the temperature is higher than 283.15 K. In the ternary system of CH₄+CO₂+H₂S mixtures, the higher the CO₂ content is, the lower the average value of Gibbs energy is, and the higher the phase equilibrium pressure is at the same temperature. The lower the CH₄ content, the lower the average value of Gibbs energy and the lower the phase equilibrium pressure at the same temperature. This study is helpful for engineers and technicians to accurately and conveniently estimate the thermodynamic parameters of hydrate, which is of great significance to the safe production and efficient development of hydrate.

DATA AVAILABILITY STATEMENT

The original contributions presented in the study are included in the article/Supplementary Material, further inquiries can be directed to the corresponding author.

REFERENCES

- Anderson, G. K. (2004). Enthalpy of Dissociation and Hydration Number of Methane Hydrate from the Clapeyron Equation. *The J. Chem. Thermodynamics* 36, 1119–1127. doi:10.1016/j.jct.2004.07.005
- Anderson, R., Llamado, M., Tohidi, B., and Burgass, R. W. (2003). Experimental Measurement of Methane and Carbon Dioxide Clathrate Hydrate Equilibria in Mesoporous Silica. *J. Phys. Chem. B* 107, 3507–3514. doi:10.1021/jp0263370
- Anwar, M. N., Fayyaz, A., Sohail, N. F., Khokhar, M. F., Baqar, M., Khan, W. D., et al. (2018). CO₂ Capture and Storage: A Way Forward for Sustainable Environment. *J. Environ. Manage.* 226, 131–144. doi:10.1016/j.jenvman.2018.08.009
- Babu, P., Kumar, R., and Linga, P. (2013). Medium Pressure Hydrate Based Gas Separation (HBGS) Process for Pre-combustion Capture of Carbon Dioxide Employing a Novel Fixed Bed Reactor. *Int. J. Greenhouse Gas Control* 17, 206–214. doi:10.1016/j.ijggc.2013.05.010
- Babu, P., Kumar, R., and Linga, P. (2014). Unusual Behavior of Propane as a Co-guest during Hydrate Formation in Silica Sand: Potential Application to Seawater Desalination and Carbon Dioxide Capture. *Chem. Eng. Sci.* 117, 342–351. doi:10.1016/j.ces.2014.06.044
- Chen, G., and Guo, T. (1996). Thermodynamic Modeling of Hydrate Formation Based on New Concepts. *Fluid Phase Equilibria* 122 (1–2), 43–65. doi:10.1016/0378-3812(96)03032-4
- Collett, T. S. (2009). *Natural Gas Hydrates: Energy Resource Potential and Associated Geologic Hazards*. Tulsa, U.S.A: American Association of Petroleum Geologists.
- Darbouret, M., Cournil, M., and Herri, J. M. (2005). Rheological Study of TBAB Hydrate Slurries as Secondary Two-phase Refrigerants. *Int. J. Refrig.* 28, 63–671. doi:10.1016/j.ijrefrig.2005.01.002
- De Roo, J. L., Peters, C. J., Lichtenthaler, R. N., and Diepen, G. A. M. (1983). Occurrence of Methane Hydrate in Saturated and Unsaturated Solutions of Sodium Chloride and Water in Dependence of Temperature and Pressure. *AIChE J.* 29, 651–657. doi:10.1002/aic.690290420
- Du, Y., and Guo, T.-M. (1990). Prediction of Hydrate Formation for Systems Containing Methanol. *Chem. Eng. Sci.* 45 (4), 893–900. doi:10.1016/0009-2509(90)85011-2
- Fan, S.-S., and Guo, T.-M. (1999). Hydrate Formation of CO₂-Rich Binary and Quaternary Gas Mixtures in Aqueous Sodium Chloride Solutions. *J. Chem. Eng. Data* 44, 829–832. doi:10.1021/jc990011b
- Gupta, A., Lachance, J., Sloan, E. D., and Koh, C. A. (2008). Measurements of Methane Hydrate Heat of Dissociation Using High Pressure Differential Scanning Calorimetry. *Chem. Eng. Sci.* 63, 5848–5853. doi:10.1016/j.ces.2008.09.002
- Handa, Y. P. (1986). Compositions, Enthalpies of Dissociation, and Heat Capacities in the Range 85 to 270 K for Clathrate Hydrates of Methane, Ethane, and Propane, and Enthalpy of Dissociation of Isobutane Hydrate, as Determined by a Heat-Flow Calorimeter. *J. Chem. Thermodynamics* 18, 915–921. doi:10.1016/0021-9614(86)90149-7
- Huang, Q., Sun, C., Chen, G., and Yang, L. (2005). Experiment and Calculation of Hydrate Formation Conditions of Sour Natural Gas Containing Methane, Carbon Dioxide and Hydrogen Sulfide (In Chinese). *J. Chem. Eng.* 07, 1159–1163.
- Jamaluddin, A. K. M., Kalogerakis, N., and Bishnoi, P. R. (1991). Hydrate Plugging Problems in Undersea Natural Gas Pipelines under Shutdown Conditions. *J. Pet. Sci. Eng.* 5, 323–335. doi:10.1016/0920-4105(91)90051-n
- John, V. T., Papadopoulos, K. D., and Holder, G. D. (1985). A Generalized Model for Predicting Equilibrium Conditions for Gas Hydrates. *AIChE J.* 31 (2), 252–259. doi:10.1002/aic.690310212
- Kang, S.-P., Lee, H., and Ryu, B.-J. (2001). Enthalpies of Dissociation of Clathrate Hydrates of Carbon Dioxide, Nitrogen, (Carbon Dioxide+ Nitrogen), and (Carbon Dioxide + Nitrogen+ Tetrahydrofuran). *J. Chem. Thermodynamics* 33, 513–521. doi:10.1006/jcht.2000.0765
- Kvamme, B., Coffin, R. B., Zhao, J., Wei, N., Zhou, S., Li, Q., et al. (2019). Stages in the Dynamics of Hydrate Formation and Consequences for Design of Experiments for Hydrate Formation in Sediments. *Energies* 12, 3399. doi:10.3390/en12173399

AUTHOR CONTRIBUTIONS

HL performed the experiments, simulations, thermodynamic calculations and wrote the manuscript. YD designed the study and revised the whole manuscript. JP organized the database, assisted in research design, manuscript writing and review. NW contributed in project management, experimental design and manuscript review process. All authors contributed to the article and approved the submitted version.

FUNDING

The research is supported by the 111 Project (D21025), National Key Research and Development Program (2019YFC0312300), National Natural Science Foundation Item of China (U20B6005-05, 51874252) and Open Fund of State Key Laboratory Of Oil and Gas Reservoir Geology and Exploitation (Southwest Petroleum University) (PLN 2021–02, PLN 2021–03, PLN201816).

ACKNOWLEDGMENTS

The authors would like to express their gratitude to the researchers of Southwest Petroleum University, especially professor Kvamme and his colleagues for their guidance.

- Kvamme, B. (2019). Environmentally Friendly Production of Methane from Natural Gas Hydrate Using Carbon Dioxide. *Sustainability* 11 (7), 1964. doi:10.3390/su11071964
- Kvamme, B., and Tanaka, H. (1995). Thermodynamic Stability of Hydrates for Ethane, Ethylene, and Carbon Dioxide. *J. Phys. Chem.* 99, 7114–7119. doi:10.1021/j100018a052
- Kwon, M., Lee, J.-W., and Lee, H. (2014). Temperature-Dependent Structural Transitions in Methane-Ethane Mixed Gas Hydrates. *J. Phys. Chem. C* 118 (49), 28906–28913. doi:10.1021/jp5102219
- Liegeois, J. S., Perkins, R., Martin, R. J., and Kobayashi, R. (1990). Development of an Automated, High Pressure Heat Flux Calorimeter and its Application to Measure the Heat of Dissociation and Hydrate Numbers of Methane Hydrate. *Fluid Phase Equilibria* 59, 73–97. doi:10.1016/0378-3812(90)85147-3
- Liu, L., Sun, Z., Zhang, L., Wu, N., Qin, Y., Jiang, Z., et al. (2019). Progress in Global Gas Hydrate Development and Production as a New Energy Resource. *Acta Geologica Sinica* 93 (03), 731–755. doi:10.1111/1755-6724.13876
- Makogon, Y. F. (1997). *Hydrates of Hydrocarbons*. Tulsa, U.S.A: Penn Well Publishing Company.
- Makogon, Y. F. (2010). Natural Gas Hydrates - A Promising Source of Energy. *J. Nat. Gas Sci. Eng.* 2, 49–59. doi:10.1016/j.jngse.2009.12.004
- Mei, D.-H., Liao, J., Yang, J.-T., and Guo, T.-M. (1996). Experimental and Modeling Studies on the Hydrate Formation of a Methane + Nitrogen Gas Mixture in the Presence of Aqueous Electrolyte Solutions. *Ind. Eng. Chem. Res.* 35, 4342–4347. doi:10.1021/ie9601662
- Mohammadi, A. H., Anderson, R., and Tohidi, B. (2005). Carbon Monoxide Clathrate Hydrates: Equilibrium Data and Thermodynamic Modeling. *AIChE J.* 51 (10), 2825–2833. doi:10.1002/aic.10526
- Moradi, G., and Khosravi, E. (2012). Application of PRSV2 Equation of State to Predict Hydrate Formation Temperature in the Presence of Inhibitors. *Fluid Phase Equilibria* 333, 18–26. doi:10.1016/j.fluid.2012.07.019
- Mu, L., and von Solms, N. (2018). Hydrate thermal Dissociation Behavior and Dissociation Enthalpies in Methane-Carbon Dioxide Swapping Process. *J. Chem. Thermodynamics* 117, 33–42. doi:10.1016/j.jct.2017.08.018
- Mu, L., and von Solms, N. (2018). Hydrate thermal Dissociation Behavior and Dissociation Enthalpies in Methane-Carbon Dioxide Swapping Process. *J. Chem. Thermodynamics* 117, 33–42. doi:10.1016/j.jct.2017.08.018
- Nakagawa, R., Hachikubo, A., and Shoji, H. (2008). “Dissociation and Specific Heats of Gas Hydrates under Submarine and Sublacustrine Environments,” in The 6th International Conference on Gas Hydrates (ICGH 2008), July 6–10, 2008, Vancouver, Canada.
- Ng, H.-J., and Robinson, D. B. (1976). The Measurement and Prediction of Hydrate Formation in Liquid Hydrocarbon-Water Systems. *Ind. Eng. Chem. Fund.* 15 (4), 293–298. doi:10.1021/i160060a012
- Noaker, L. J., and Katz, D. L. (1954). Gas Hydrates of Hydrogen Sulfide-Methane Mixtures. *J. Petrol. Technol.* 6, 135–137. doi:10.2118/367-g
- Ohgaki, K., Makihara, Y., and Takano, K. (1993). Formation of CO₂ Hydrate in Pure and Sea Waters. *J. Chem. Eng. Jpn.* 26, 558–564. doi:10.1252/jcej.26.558
- Parrish, W. R., and Prausnitz, J. M. (1972). Dissociation Pressures of Gas Hydrates Formed by Gas Mixtures. *Ind. Eng. Chem. Proc. Des. Dev.* 11 (1), 26–35. doi:10.1021/i260041a006
- Qorbani, K. (2017). “Non-equilibrium Modelling of Hydrate Phase Transition Kinetics in Sediments,” (Bergen: University of Bergen). Doctoral Dissertation.
- Rydz, M. B., Schicks, J. M., Naumann, R., and Erzinger, J. (2007). Dissociation Enthalpies of Synthesized Multicomponent Gas Hydrates with Respect to the Guest Composition and Cage Occupancy. *J. Phys. Chem. B* 111, 9539–9545. doi:10.1021/jp0712755
- Seo, Y.-T., Lee, H., and Yoon, J.-H. (2001). Hydrate Phase Equilibria of the Carbon Dioxide, Methane, and Water System. *J. Chem. Eng. Data* 46, 381–384. doi:10.1021/je000237a
- Sloan, E. D., and Fleyfel, F. (1992). Hydrate Dissociation Enthalpy and Guest Size. *Fluid Phase Equilibria* 76, 123–140. doi:10.1016/0378-3812(92)85082-j
- Soave, G. (1972). Equilibrium Constants from a Modified Redlich-Kwong Equation of State. *Chem. Eng. Sci.* 27, 1197–1203. doi:10.1016/0009-2509(72)80096-4
- Subramanian, S., Ballard, A. L., Kini, R. A., Dec, S. F., and Sloan, E. D. (2000). Structural Transitions in Methane+ethane Gas Hydrates - Part I: Upper Transition point and Applications. *Chem. Eng. Sci.* 55 (23), 5763–5771. doi:10.1016/s0009-2509(00)00162-7
- Subramanian, S., Kini, R. A., Dec, S. F., and Sloan, E. D. (2000). Evidence of Structure II Hydrate Formation from Methane+ethane Mixtures. *Chem. Eng. Sci.* 55, 1981–1999. doi:10.1016/s0009-2509(99)00389-9
- Sun, C.-Y., and Chen, G.-J. (2005). Modelling the Hydrate Formation Condition for Sour Gas and Mixtures. *Chem. Eng. Sci.* 60 (17), 4879–4885. doi:10.1016/j.ces.2005.04.013
- Sun, W., Wei, N., Zhao, J., Kvamme, B., Zhou, S., Zhang, L., et al. (2021). Imitating Possible Consequences of Drilling through marine Hydrate Reservoir. *Energy* 239, 121802. doi:10.1016/j.energy.2021.121802
- Sun, W., Wei, N., Zhao, J., Zhou, S., Zhang, L., Li, Q., et al. (2021). Wellbore Temperature and Pressure Field in Deep-Water Drilling and the Applications in Prediction of Hydrate Formation Region. *Front. Energy Res.* 9, 696392. doi:10.3389/fenrg.2021.696392
- Sun, Z., Fan, S., Guo, K., Shi, L., and Wang, R. (2002). Experimental Study and Theoretical Prediction on the Formation Conditions of Natural Gas Hydrate (In Chinese). *J. Xi'an Jiaotong Univ.* 01, 16–19.
- Tsimpanogiannis, I. N., Michalis, V. K., and Economou, I. G. (2019). Enthalpy of Dissociation of Methane Hydrates at a Wide Pressure and Temperature Range. *Fluid Phase Equilibria* 489, 30–40. doi:10.1016/j.fluid.2019.01.024
- van der Waals, J. H., and Platteeuw, J. C. (1959). Clathrate Solutions. *Adv. Chem. Phys.* 2 (1), 1–57.
- Vedachalam, N., Srinivasulu, S., Rajendran, G., Ramadass, G. A., and Atmanand, M. A. (2015). Review of Unconventional Hydrocarbon Resources in Major Energy Consuming Countries and Efforts in Realizing Natural Gas Hydrates as a Future Source of Energy. *J. Nat. Gas Sci. Eng.* 26, 163–175. doi:10.1016/j.jngse.2015.06.008
- Veluswamy, H. P., Wong, A. J. H., Babu, P., Kumar, R., Kulprathipanja, S., Rangsunvigit, P., et al. (2016). Rapid Methane Hydrate Formation to Develop a Cost Effective Large Scale Energy Storage System. *Chem. Eng. J.* 290, 161–173. doi:10.1016/j.ccej.2016.01.026
- Wei, N., Zhao, J., Liu, A., Zhou, S., Zhang, L., and Jiang, L. (2021). Evaluation of Physical Parameters and Construction of the Classification System of Natural Gas Hydrate in the Northern South China Sea. *Energy Fuels* 35, 7637–7645. doi:10.1021/acs.energyfuels.0c04043
- Yang, S. O., Cho, S. H., Lee, H., and Lee, C. S. (2001). Measurement and Prediction of Phase Equilibria for Water + Methane in Hydrate Forming Conditions. *Fluid Phase Equilibria* 185, 53–63. doi:10.1016/s0378-3812(01)00456-3
- Ye, J., Qin, X., Xie, W., Ma, B., Qiu, H., Liang, J., et al. (2020). The Second Natural Gas Hydrate Production Test in the South China Sea. *China Geology* 3 (2), 197–209.
- ZareNezhad, B., and Ziaee, M. (2013). Accurate Prediction of H₂S and CO₂ Containing Sour Gas Hydrates Formation Conditions Considering Hydrolytic and Hydrogen Bonding Association Effects. *Fluid Phase Equilibria* 356, 321–328. doi:10.1016/j.fluid.2013.07.055
- Zhao, J., Zhang, L., Wei, N., Zhou, S., and Li, Q. (2019). “New Development of Gas Hydrate Exploitation in the World—China Has Led the Test Production Level of Other Countries,” in Proceedings of the International Field Exploration and Development Conference 2019, Xi'an, China, October 16–18, 2020, Springer Nature Singapore Pte Ltd.

Conflict of Interest: Author HL is employed by CNOOC (China) Co., Ltd. Hainan, Haikou.

The remaining authors declare that the research was conducted in the absence of any commercial or financial relationships that could be construed as a potential conflict of interest.

Publisher's Note: All claims expressed in this article are solely those of the authors and do not necessarily represent those of their affiliated organizations, or those of the publisher, the editors and the reviewers. Any product that may be evaluated in this article, or claim that may be made by its manufacturer, is not guaranteed or endorsed by the publisher.

Copyright © 2021 Liang, Duan, Pei and Wei. This is an open-access article distributed under the terms of the Creative Commons Attribution License (CC BY). The use, distribution or reproduction in other forums is permitted, provided the original author(s) and the copyright owner(s) are credited and that the original publication in this journal is cited, in accordance with accepted academic practice. No use, distribution or reproduction is permitted which does not comply with these terms.



An Experiment on Flashing-Spray Jet Characteristics of Supercritical CO₂ from Various Orifice Geometries

Lin Teng^{1,2*}, Jinbao Bai¹, Yuxing Li³ and Cailin Wang³

¹College of Chemical Engineering, Fuzhou University, Fuzhou, China, ²Chongqing University Industrial Technology Research Institute, Chongqing University, Chongqing, China, ³Shandong Provincial Key Laboratory of Oil and Gas Storage and Transportation Security, China University of Petroleum (East China), Qingdao, China

OPEN ACCESS

Edited by:

Michelle K Kidder,
Oak Ridge National Laboratory (DOE),
United States

Reviewed by:

Muhammad Farooq,
University of Engineering and
Technology, Pakistan
Sohaib Mohammed,
Cornell University, United States

*Correspondence:

Lin Teng
tengl@fzu.edu.cn

Specialty section:

This article was submitted to
Carbon Capture, Utilization and
Storage,
a section of the journal
Frontiers in Energy Research

Received: 12 May 2021

Accepted: 24 August 2021

Published: 08 October 2021

Citation:

Teng L, Bai J, Li Y and Wang C (2021)
An Experiment on Flashing-Spray Jet
Characteristics of Supercritical CO₂
from Various Orifice Geometries.
Front. Energy Res. 9:697031.
doi: 10.3389/fenrg.2021.697031

Supercritical CO₂ pipelines usually are used to link the CO₂ capture system to the geological storage. There are severe hazards once the asphyxiating gas leaks from the long-distance pipeline. The uncertainty of near-field jet characteristics results in imprecise consequences assessment of accidental release of supercritical CO₂. To improve the prediction of consequences of accidental release accuracy, the near-field mechanisms of flashing-spray jet was investigated. In this work, an experimental setup with multiple measurement instruments was developed to impose controllable CO₂ release from a high-pressure vessel. The flashing-spray jet structures of supercritical CO₂ from circular and rectangular orifices were recorded by a high-speed camera. Results indicate that the near-field structures of supercritical CO₂ jet from circular and rectangular orifices are totally different, which causes the different dispersion consequences. The jet angle and shock waves were analyzed quantitatively. Lastly, the models of flashing-spray based on the two different phenomena from rectangular and circular orifices were discussed. The combination of macroscopic and microscopic data in the jet can help to understand the complex physics and improve discharge and dispersion model. This work provides a fundamental data to consequences assessment of accidental release of supercritical CO₂.

Keywords: supercritical CO₂, release, near-field structure, flashing-spray model, Mach disc

INTRODUCTION

Carbon dioxide (CO₂) as a major greenhouse gas (GHG) has increased significantly impacts on the earth owing to human activities such as burning of oil and gas and the discharge of exhaust gases. The Intergovernmental Panel on Climate Change (IPCC) reported that Carbon Dioxide Capture and Storage (CCS) can eliminate 20–40% of global carbon emissions (Metz et al., 2005). Carbon dioxide usually would be captured at a large point emission source (e.g., power plants) and be transported via long pipelines to another spot for use [e.g., oil field for enhanced oil recovery (EOR)] (Ziabakhsh-Ganji and Kooi, 2014). Currently more than 50 million tons of CO₂ is transported by over 6,400 km of pipelines in the United States (Metz et al., 2005). And the most pipelines are under supercritical/

Abbreviations: A, orifice area; d, diameter of the nozzle; d_e, equivalent diameter of the nozzle; ΔG^* , free energy barrier; J, nucleation rate; k_B, Boltzmann constant; m, single molecular mass; P_e, static pressure; P_{co}, atmosphere pressure; r_c, critical radius; R, universal gas constant, 8.31451 J/(mol·K); T, temperature; u, velocity; v, specific volume; X_m, location of the Mach disc; Greek letters; ρ, density (kg/m³); σ, surface tension (N/m); γ, heat capacity ratio; θ, jet angle (degree); Subscript/superscript; gas, phase; l, liquid phase; m, multiphase fluid; s, saturation state.

dense state which is considered as the most efficient way. Under stricter environmental policies, up to 200,000–360,000 km by 2050 could be built and operated in the United States, China, and Europe (John and John, 2004). This would require more attention to CO₂ transportation safety.

Potential leakage can happen with the development of pipeline corrosion and other outside forces, such as construction defects, solid movement, etc. The discharge and dispersion of high-pressure CO₂ pipeline different from the hydrocarbons pipeline involve complex physics including cool temperature, phase transition, sonic multiphase flow, and heavy gas dispersion. As an asphyxiant at high concentrations and heavier than air, the leaked CO₂ would accumulate in low-lying land and harm safety of living creature nearby (Wang et al., 2020). For safety issues related to CO₂ transportation, it is necessary to determine how CO₂ is released in the case of failure. More importantly, there exists little quantitative information on the source terms including near-field characteristics, which are useful for establishing appropriate models in release and dispersion.

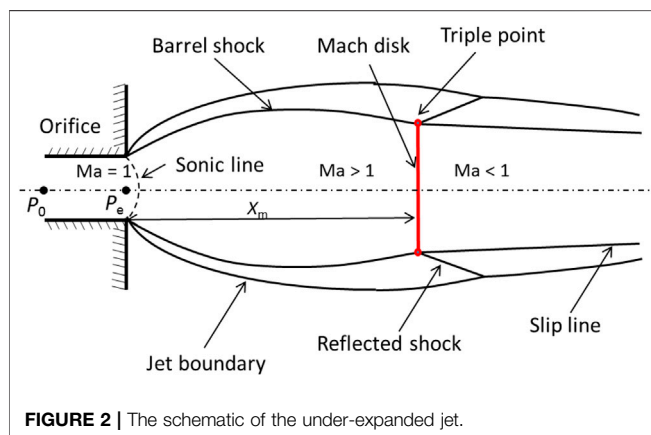
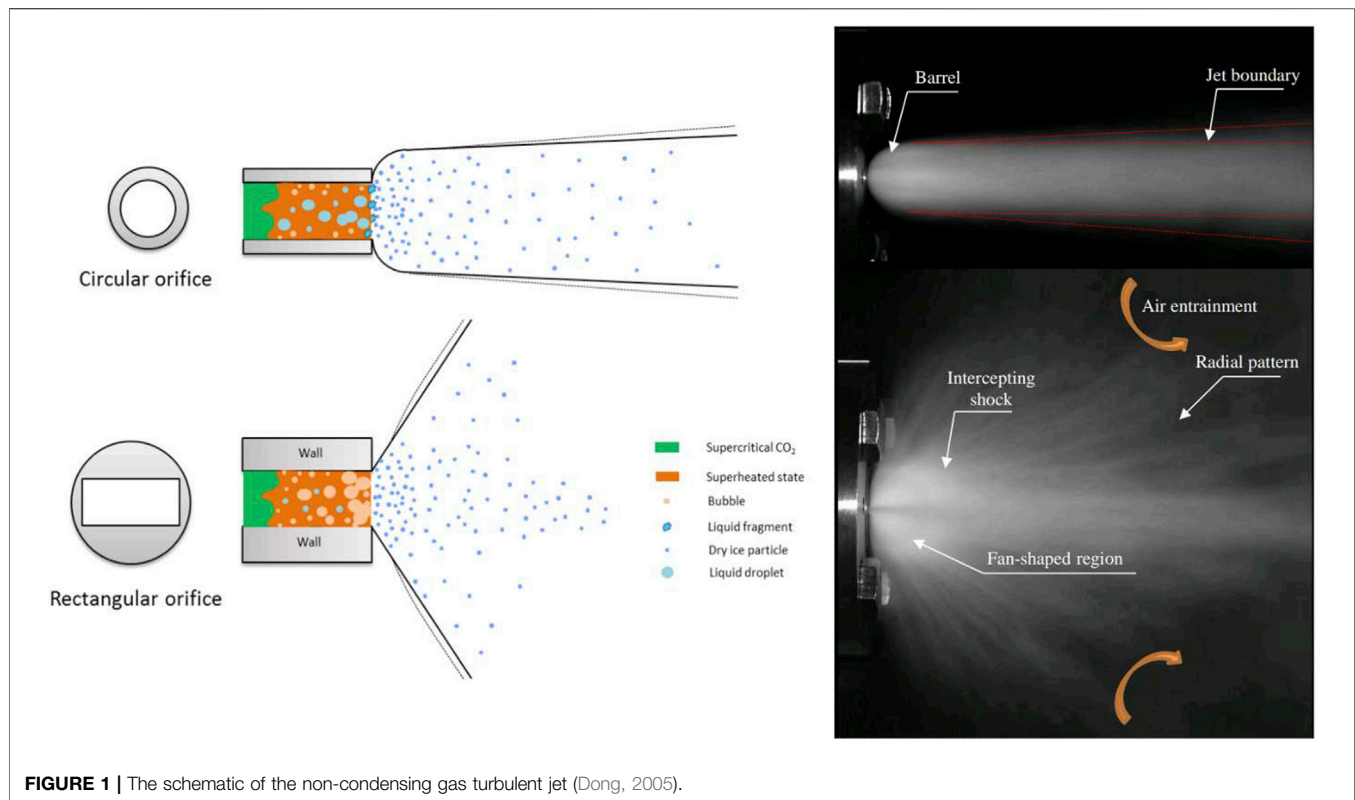
In recent years, many researchers have made a lot of achievements in the numerical simulation of CO₂ release and diffusion. (Webber, 2011) developed the two-phase flow model for flashing jet of CO₂. It revealed that two-phase homogeneous equilibrium flow models may be generalized to cover such a release. (Liu et al., 2016) simulated the CO₂ dispersion over two hypothetical topographies. This study provides a viable method for assessment of risks associated with CCS. (Wareing et al., 2013a) present a composite equation of state accounting for the three-phase CO₂ in the modeling of liquid CO₂ release. The paper predicted the near-field structure of the jet and the fraction of solid CO₂. (Liu et al., 2014) simulated the highly under-expanded single-phase CO₂ jets using CFD software Fluent implanted with Peng–Robinson (PR) equation of state (EoS) for accounting for real gas behavior. The two-stages simulation approach was used and resulted in heavy computational workloads. A consequence model with a pseudo source is employed to predict the dispersion of supercritical CO₂ from a high-pressure pipeline (Joshi et al., 2016). They assumed that the pseudo source plane is in the plane that is approximately 3.5 times the diameter of the orifice away from the exit plane. And in this plane, it is homogenous flow. (Woolley et al., 2014) designed an effective multiphase jet expansion model to predict the leakage of CO₂ after accidental damage to the high-pressure casing. The evolution of dry ice has been considered in some research. The behavior of CO₂ particles during the release of high-pressure liquids has been studied using a CFD, combined with a Reynolds stress turbulence model, Lagrangian particle tracker, particle distribution function, and turbulent shear agglomeration model for the particle evolution (Wareing et al., 2013b). The heavy gas dispersion models were developed based on the study of discharge models. In order to predict the dispersion consequences more accurately, the complex physics in near-field such as the structure and shock waves should be figured out. Unfortunately, due to a lack of experimental data in supercritical CO₂ releases focusing on near-field characteristics, currently the development of more complex models is limited.

Some experiments related to the supercritical CO₂ release almost focused on the macroscopic parameters, such as pressure, temperature, concentration, and velocity. However, few studies focused on microscopic parameters, such as the structure of shock waves, the evolution of solid CO₂, and the expanded angle. (Ahmad et al., 2013) carried out a controlled CO₂ release experiment from various circular orifices to obtain the thermo-hydraulic data of CO₂. A superheated jet was founded during the releases. In our previous work (Wang et al., 2019), effects of impurity concentration, initial inner pressure, and temperature on dispersion behavior were studied. (Guo et al., 2016) designed and built a large-scale supercritical experimental pipeline with a total length of 258 m and an inner diameter of 233 mm. The under-expanded jet flow structure and phase transitions in the near-field were studied for supercritical CO₂ released through different orifice diameters. Relating to the small-scale experiments focused on the near-field jet of CO₂. (Wareing et al., 2014) measured dry ice particles distribution along the jets in liquid CO₂ release and found that the sizes of particles are around 0.1–100 μm. And the study presented Mach disc in these releases is at a distance of around seven nozzle diameters along the centerline from the nozzle and the particles are likely to be close to equilibrium after Mach disc. The effect of superheat on flashing atomization characteristics and on the snow formation of liquid CO₂ has been investigated (Lin et al., 2013). Results show that the spray pattern transfers from jet spray to cone spray, and then to a bowl spray configuration with the increase of superheat. As mentioned above, a lack of near-field experiments data limits the development of models of discharge and dispersion of CO₂. In addition, CO₂ was released from a circular orifice or nozzle in almost current release experiments of CO₂ pipeline. However, the cracks in the damaged pipeline usually are not circular. The difference in orifice pattern may result in different consequence in an accident release.

In this paper, an experimental setup with a high-speed camera system was designed and constructed to study the near-field characteristics of flashing-spray jet of supercritical CO₂ from various orifice geometries. The work focused on (1) the near-field structures during CO₂ released from different orifice geometries; (2) the evolution of jet angle which can affect the dispersion region; (3) the shock waves system in the release from orifices with different geometries; (4) finally models of the flashing-spray jet of supercritical CO₂.

BACKGROUND OF HIGHLY UNDER-EXPANDED JET

The jet from a high-pressure CO₂ vessel is different from general gas jet due to the phase transition and multiphase flow and must be considered. In view of general gas jet, the jet zone is divided into three sub-zones: flow establishment zone, transition zone, and established flow zone, as shown in **Figure 1**. The fluid jet from the orifice to the ambient, which causes discontinuous velocity,



further causes turbulence. As shown in **Figure 1**, extending the upper and lower boundaries of the jet to intersect at one point (Point O), and O is the virtual origin of the jet. And then θ is the jet angle.

A schematic of the highly under-expanded jet is shown in **Figure 2**. An expansion fan generates at the nozzle lip as the flow expands into the atmosphere. The pressure ratio P_0/P_∞ is an important parameter to describe the expansion level, where P_0 is a stagnation pressure in the vessel and P_∞ is the ambient pressure. When $P_0/P_\infty > 15$, the complicated shock waves system will forms. Except for the intercepting shock in the interior of the jet, the Mack disc normal to the flow is unique for under-expanded

jet. The flow front the Mach disc is supersonic, whereas the flow behind the Mach disc is obviously subsonic. The temperature will rise sharply near the Mach disc. However, the shock-wave structure in these jets also depends on a geometry of the nozzle and the property of gas (Velikorodny and Kudriakov, 2012). Some researchers also reported that the Mack disc cannot be observed when the flow jets from a elliptic nozzle (Menon and Skews, 2010).

For non-condensing gas jet, a theoretical analysis has been developed to predict the Mach disc location,

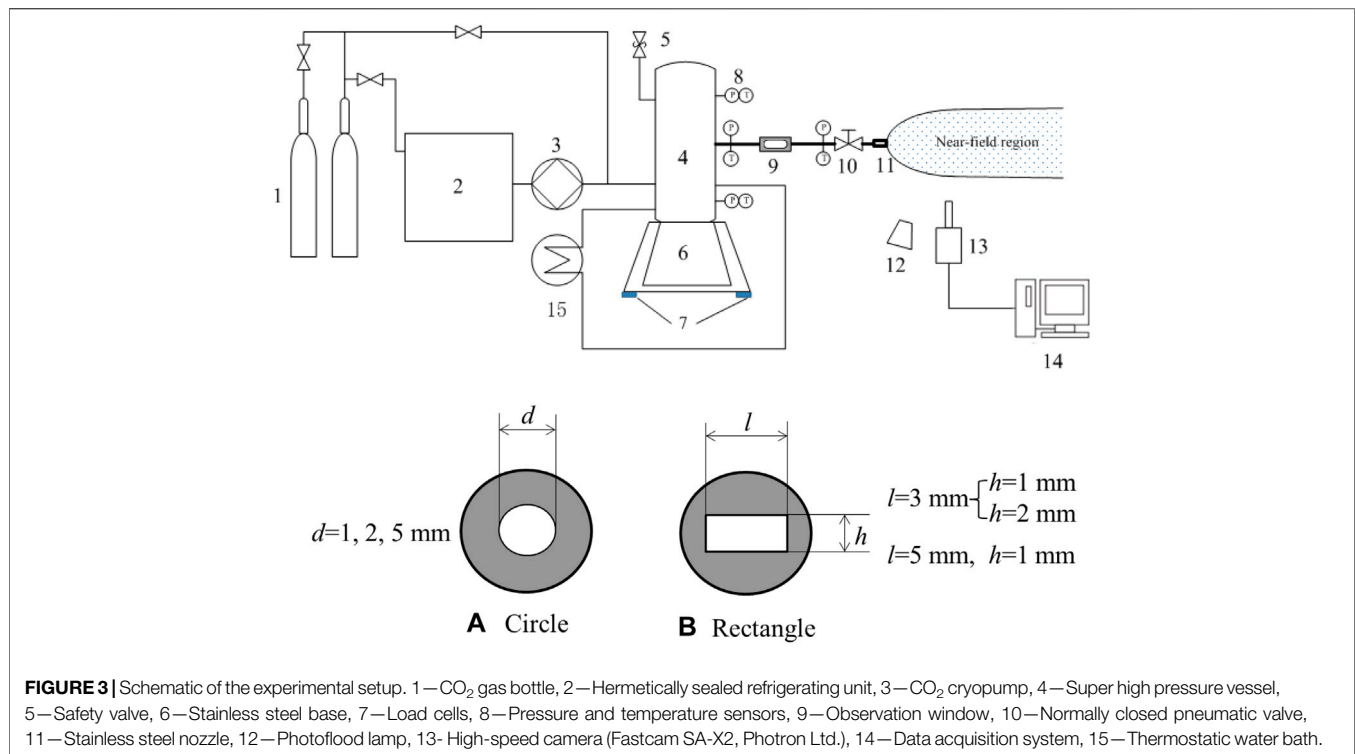
$$\frac{X_m}{d_e} = 0.5 \sqrt{\gamma} \sqrt{\frac{P_e}{P_\infty}} \times \left(\frac{\gamma + 1}{\gamma - 1} \right)^{0.25} \quad (1)$$

where X_m is location of the Mach disc, P_e is the static pressure at the exit section. It should be noted that in the fact the Mach disc location weakly depends on γ , and it can be approximated by a commonly used experimental correlation of (Ashkenas and Sherman, 1966):

$$\frac{X_m}{d_e} = 0.67 \times \sqrt{\frac{P_0}{P_\infty}} \quad (2)$$

EXPERIMENTAL DETAILS

In order to study the near-field structure of supercritical CO₂ released from the pressure pipe, a new experimental device was



designed and built, as shown in **Figure 3**. The experimental apparatus consists of high-pressure vessel, gas source, CO₂ pump, refrigerating unit, thermostatic water bath, nozzle, and high-speed camera system. The rated pressure of the vessel with a volume 6 L is 15.0 MPa, and the material is 316L stainless steel. The container is filled with liquid CO₂ cooled by a refrigeration unit and controlled by a constant temperature water bath. To study the influence of different orifice diameters and orifice patterns (circular and rectangular) on near-field structure and dispersion of supercritical CO₂, six different orifices were used, as shown in **Figure 3**. The supercritical CO₂ near-field jet structure was observed with a single-lens reflector camera with a maximum frame rate of 200,000 FPS (frames per second). In this experiment, the frame rate of the high-speed camera is set at 3000 FPS.

It is very necessary to carry out the experiment under the premise of ensuring the safety of the experiment. In the process of supercritical CO₂ injection, steel frame is adopted to prevent the generation of reaction force, and the noise level is controlled in an acceptable range. To ensure the stable experimental conditions, the experiments were carried out indoor to avoid the impact of atmospheric turbulence. According to the actual transportation conditions of CO₂ pipeline, most of the initial conditions in the experiment are in the supercritical region. The main steps list as follows: (1) Before work, check whether the connection of the experimental device is loose and whether the container is damaged to ensure the normal operation of the equipment; (2) Open the cleaning mode to empty the air in the container to remove impurities; (3) The liquid carbon dioxide cooled by the refrigerator is fed into the container by means of a CO₂ pump; (4)

When the appropriate amount of CO₂ is injected into the container, all valves are closed and a water bath heating sleeve is used to control the temperature in the container; (5) When the experimental conditions in the container reach the design conditions, the pneumatic valve in the pipeline will be opened quickly; (6) Record the experimental process with high speed camera.

RESULTS AND DISCUSSIONS

The Near-Field Structure of the Supercritical Jet

Figure 4 presents that the near-field structure of the supercritical jet from a circular orifice and a rectangular orifice, and the experimental conditions are also presented. Same as the non-condensing gas jet, the jet region of supercritical CO₂ is divided into three zones. As shown in **Figure 4**, in core zone, the concentration of CO₂ is 100% and the constituent is gas-solid CO₂ (Teng et al., 2018). With increase of jet distance, the air entrainment caused by turbulence resulted in the decrease of CO₂ concentration. There is a difference between circular orifice and rectangular orifice. It can be obviously seen that the jet angle of rectangular orifice is much larger than that of circular orifice. But the jet distance of circular orifice is further than that of rectangular orifice. The jet structure in near-field caused the difference. **Figure 4A** shows that the release from circular hole was typical highly under-expanded jet. The shape of jet is a barrel configuration. The Mack disc appeared in this process. When supercritical CO₂ is released from the rectangular orifice, the

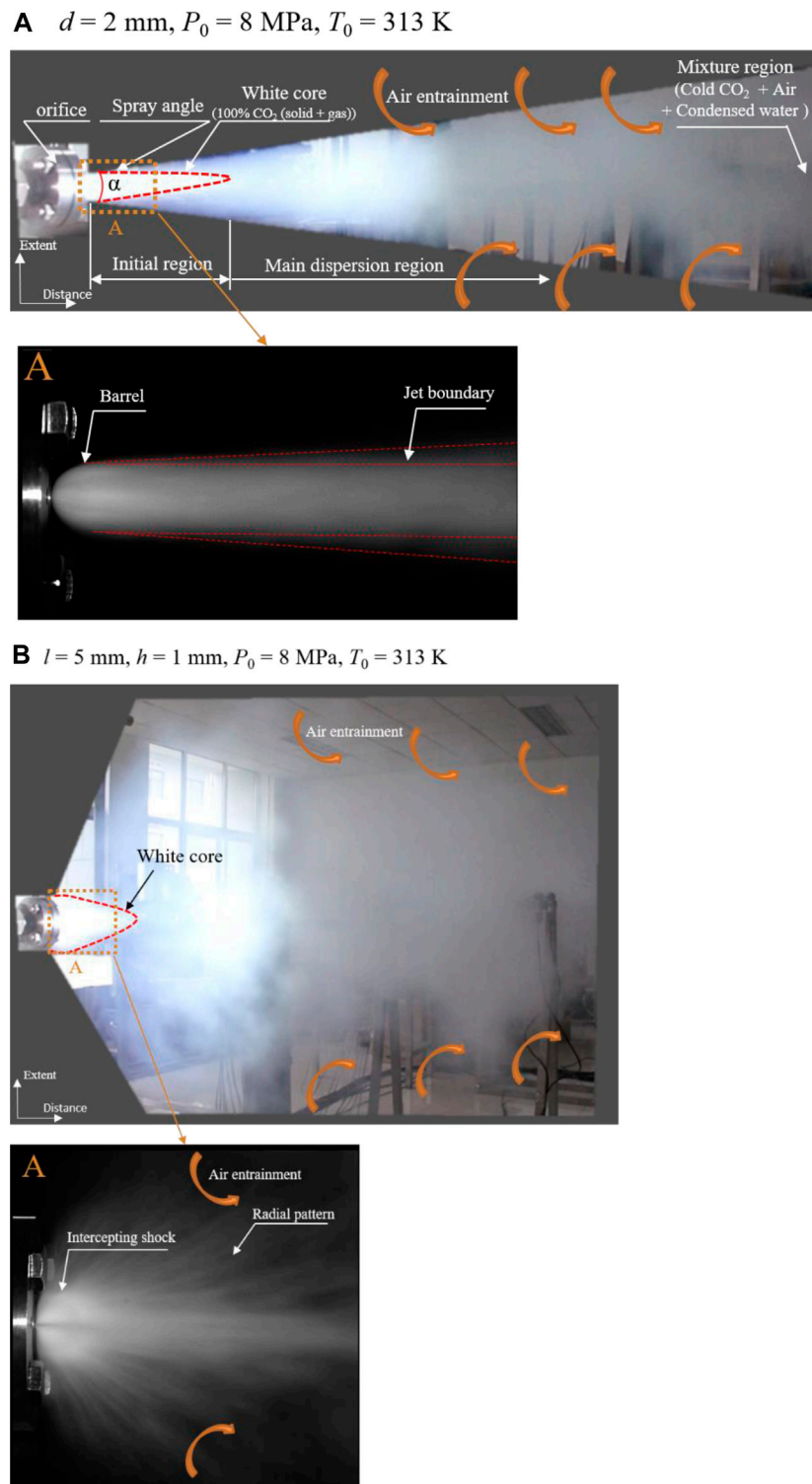


FIGURE 4 | The patterns of jet of supercritical CO₂ for circular **(A)** and rectangular **(B)** orifices.

shockwave system has a fan-shaped structure, as shown in **Figure 4B**. In addition, the fan-shaped region in near field was brighter than other regions, because a greater

concentration of solid CO₂ caused a stronger reflex of light. The Mach disc was unobserved and the intercepting shock can be observed. The CO₂ jet flows radially after shock wave.

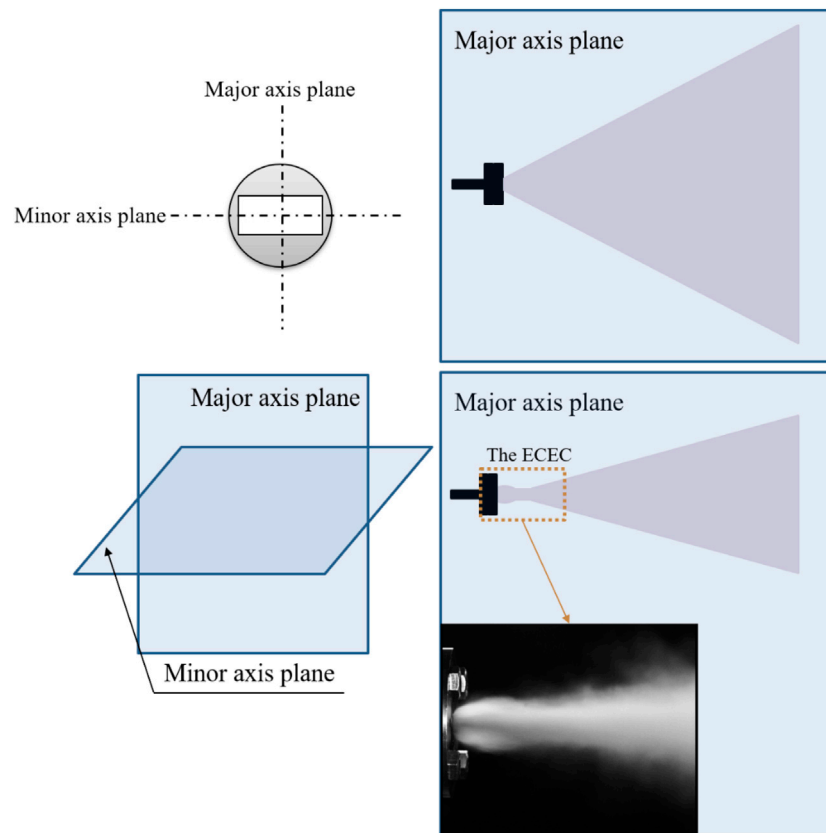


FIGURE 5 | The configuration of the supercritical CO₂ jet from a rectangular orifice.

In the process of release, the air entrainment occurred in a broader region when supercritical CO₂ released from a rectangular orifice. This phenomenon may affect the component of heavy gas cloud in the dispersion.

Some researchers show that the Mach disc may not be observed in rectangular jet, even though the pressure ratio is ca. 5.60 (Li et al., 2017). In our research, the Mach disc cannot be observed for rectangular jet. However, the change process of the intercepting shock was recorded by high-speed camera, as shown in **Supplementary Video S1**. The pressure ratios in the experiments are 70–100. It can be seen from **Figure 4** that the brighter region where plenty of micron-level dry ice particles generated has stronger reflectivity. Across the shock system, lots of dry ice particles sublimate due the temperature rose sharply. Thus, lower concentration of dry ice cause weaker reflectivity.

To understand the overall supercritical CO₂ jet, the configuration of jet of supercritical CO₂ released from a rectangular orifice (5 × 1 mm) was analyzed, as shown in **Figure 5**. Overall, the shape in the major axis plane is fan-shaped, and the photo from the high-speed camera was presented in **Figure 4B**. The shape in the minor axis plane is conical and the photo from the high-speed camera was presented in **Figure 5**. It may be interesting to note that the results show in the minor axis plane, the fluid expands firstly and then shrinks,

and finally appears core-shaped. It can be called “Expansion-Contraction-Expansion Configuration (ECEC).” It can be obviously seen from **Figure 4**; **Figure 5** that the shape of jet of supercritical CO₂ released from a rectangular orifice is very different from that release from a circular orifice, which may cause the difference of dispersion region.

The Characteristics of the Jet Angle and Shock Waves

Expanded Angle

The jet angle and shock waves have important impact on the near-field characteristics, which is related to the accuracy of source term model. In order to investigate the effect of orifice pattern on jet angle, a characteristic model of crack was developed to analyze the angle evolution. We assumed that the crack of the pipeline is elliptic. The rectangular orifice was used to characterize the crack. As shown in **Figure 6**, the length of rectangular orifice is the major axis (a) of the ellipse and the width of rectangular orifice is the minor axis (b) of the ellipse. Thus, the elliptic equation is $\frac{x^2}{a^2} + \frac{y^2}{b^2} = 1$.

If $a \neq b$, the variation of the jet angle with b/a was presented, and if $a = b$, the variation of the jet angle with diameter was presented in **Figure 6**.

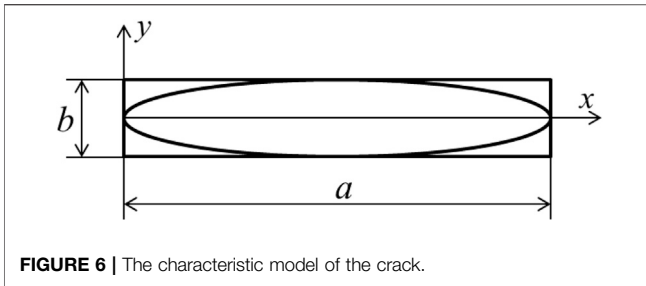


FIGURE 6 | The characteristic model of the crack.

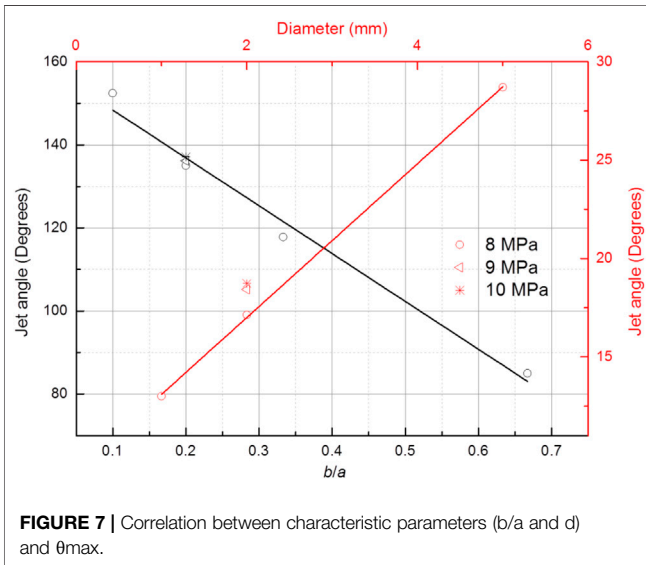


FIGURE 7 | Correlation between characteristic parameters (b/a and d) and θ_{\max} .

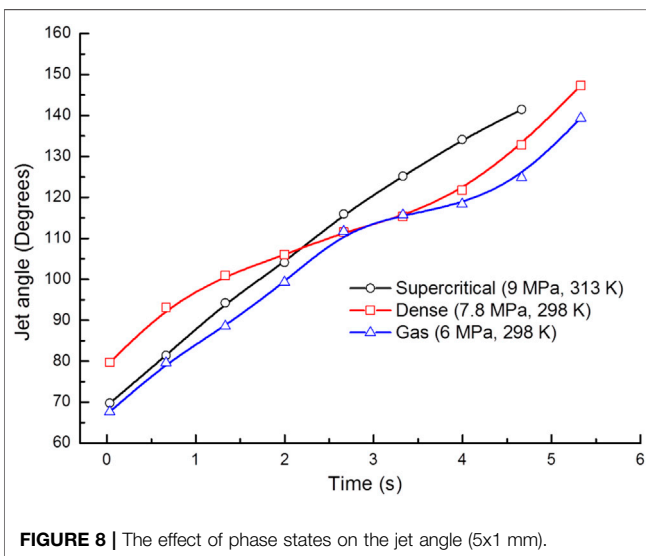


FIGURE 8 | The effect of phase states on the jet angle (5x1 mm).

Figure 7 presents the correlation between the peak value of θ ($=\theta_{\max}$) and the characteristic parameters (b/a and d) for different pressure. **Figure 7** shows the jet angle increases linearly with increased diameter of leakage orifice in circular

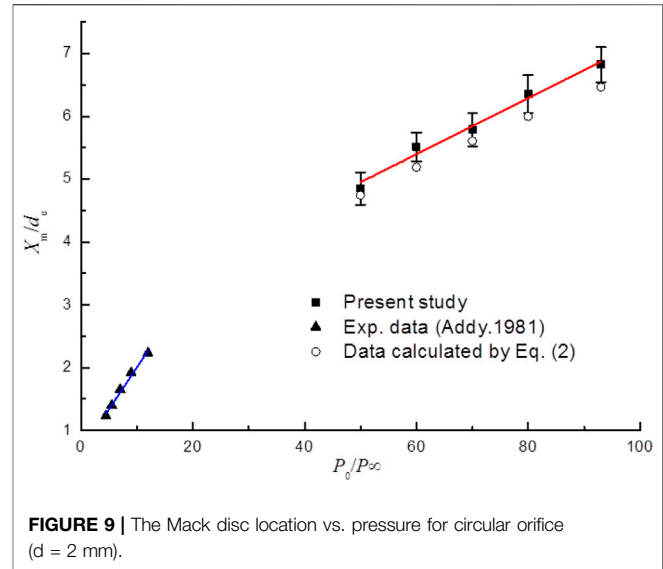


FIGURE 9 | The Mack disc location vs. pressure for circular orifice ($d = 2$ mm).

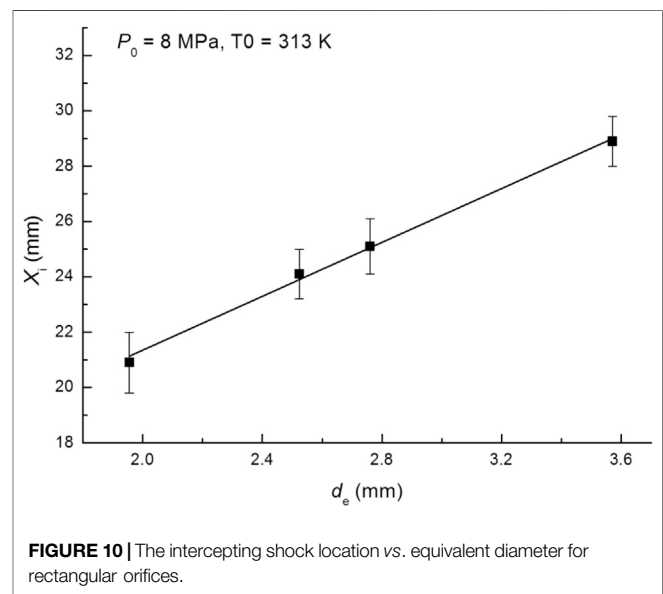


FIGURE 10 | The intercepting shock location vs. equivalent diameter for rectangular orifices.

release. And the jet angle decreases with increase of b/a . It indicates that the longer and narrower crack may cause broader dispersion region. Generally, the maximum jet angle can reach to 180°.

Comparing with the circular release with the similar area ($d = 2$ mm), the jet angle of the rectangular release (3×1 mm) is six times larger than that. **Figure 7** also indicates that the transportation pressure has a relatively small impact on the jet angle during supercritical CO₂ release. Thus, the peak jet angle (θ) can be given as an empirical equation,

$$\theta = -115.18 \left(\frac{b}{a} \right) + 159.89 \quad R^2 = 0.98, \quad b/a \neq 1 \quad (3)$$

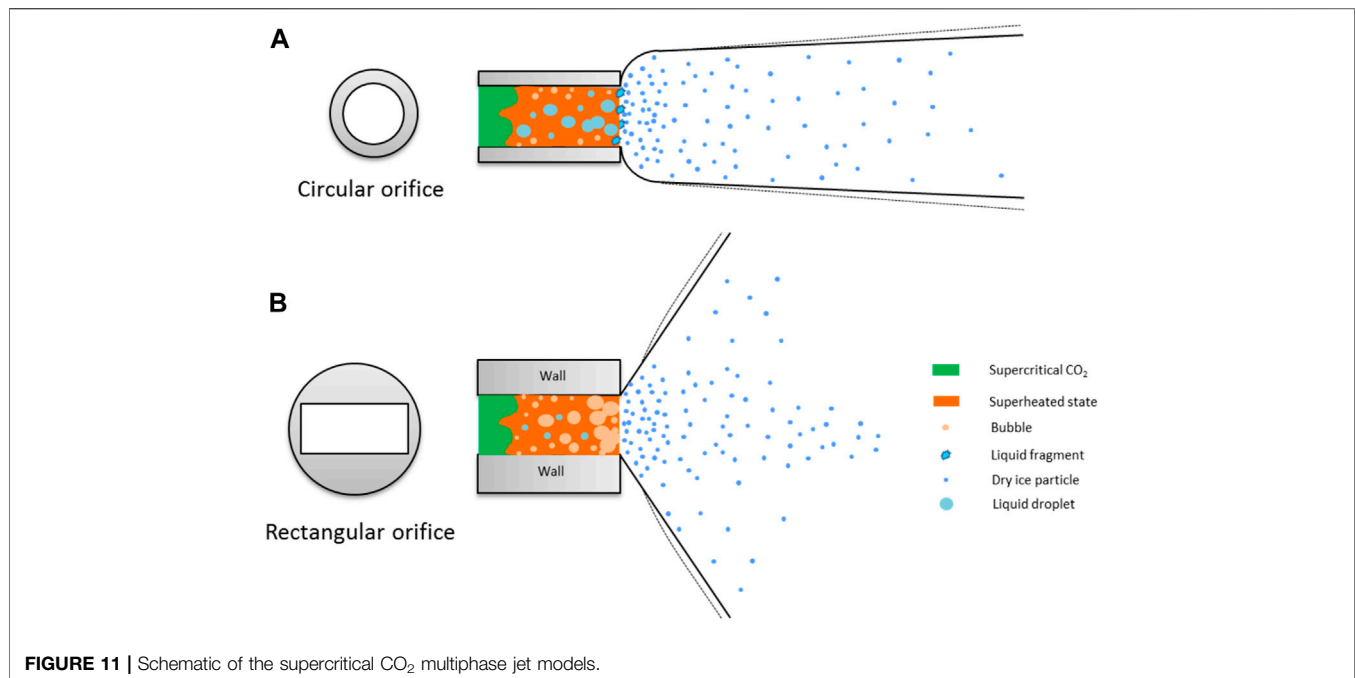


FIGURE 11 | Schematic of the supercritical CO₂ multiphase jet models.

$$\theta = 3.91d + 9.19R^2 = 0.99, b/a = 1 \quad (4)$$

Generally, the current CO₂ transportation is under supercritical or dense state (Teng et al., 2016a). But some short-distance CO₂ pipeline is under gas state (Teng et al., 2016b). To evaluate the effect of phase states on jet angle, the discharge experiments from a rectangular orifice (5 × 1 mm) for supercritical, dense and gas CO₂ were carried out. **Figure 8** shows the variation of jet angle with time for three phase states. It can be seen that the effects of different phase states on jet angle are different. The rate of change of jet angle for supercritical CO₂ release is nearly constant. In other words, the jet angle increases linearly with time. However, the rate of change of jet angle for dense and gas CO₂ release is constant firstly and then increasing. And the peak jet angle of dense CO₂ is slightly bigger than that of gas CO₂. Overall, it can infer that the jet angles are affected by expanded process and phase transition process inside the nozzles.

Shock Waves

The data points and the error bars denote the averaged value of experimental data and the standard deviations, respectively, as shown in **Figure 9**. The Mach disc is a feature of under-expanded jet and the temperature changes dramatically across the Mach disc. Many researchers investigated the Mach disc (Abbett, 1971; Vesper et al., 2011; Mitchell et al., 2013; Zhou et al., 2018). The pressure ratio in most of the studies is below 20 and the multiphase flow and phase transition was not involved (Otoibe et al., 2008). Generally, the location of Mach disc away from the orifice is increasing with the pressure ratio. The condition is a supercritical state in our research, which indicates that the pressure ratio can be over 70. **Figure 9** shows the variation of the Mach disc location with pressure ratio when supercritical CO₂

released from a circular orifice. It reveals that the Mach disc location X_m increases linearly with the pressure ratio.

It can be seen from **Figure 9** that **Eq. 2** tends to under-predict the Mach disc location. It indicates that the theoretical equation may be not applicable to the jet of supercritical CO₂ because the phase transition and multiphase flow appear in this process. **Figure 10** shows the peak intercepting shock locations in different size rectangular orifices. It indicates that the intercepting shock location increases approximately linearly with the equivalent diameter d_e . And the aspect ratio has little impact on the intercepting shock location.

Modeling the Flashing-Spray of Supercritical CO₂

Note that it is difficult to observe or measure directly the internal situation of multiphase jet in such a supercritical release because of the complex phase transition and multiphase flow. The mechanisms of multiphase jet of supercritical CO₂ can be drawn from the present experimental results including the near-field jet structure, expanded angle, and shock waves. **Figure 11** presents the schematic of the model of multiphase jet of supercritical CO₂ released from different pattern orifices. Overall, the multiphase jet appears due to the joint effect of internal and external transition. The supercritical CO₂ in the chamber is transformed to metastable state (supersaturated state) due to the rapid pressure drop. The extremely rapid nucleation of vapor bubble in superheated state would occur with further pressure drop. This process can be supposed to homogeneous nucleation. Meanwhile, the droplets appear in the process of homogeneous nucleation. The classical nucleation theory (CNT) (Zel'dovich, 1961) for the spontaneous nucleation is

$$J = (\rho_g^2/\rho_l) \sqrt{2\sigma/\pi m^3} \cdot e^{-\Delta G^*/(k_B T)} \quad (5)$$

where J is nucleation rate, k_B is Boltzmann constant, m is single molecular mass, ΔG is the free energy barrier, ρ is density, σ is surface tension, and T is temperature. Subsequently, the radius of bubbles grows extremely. The critical radius for CO₂ bubbles derived from Young-Laplace Equation (Nagayama et al., 2006) can be expressed as

$$r_c = \frac{2\sigma v_l}{RT \ln \frac{p}{p_g}} \quad (6)$$

Where r_c is the critical radius, v is specific volume, R is universal gas constant, and p is pressure.

Outside the chamber, the temperature reduces below triple point, which caused by Joule-Thomson effect, and then plenty of dry ice particles jet fast. As shown in near-field structure, the biggest difference between circular and rectangular jet is the different of jet angle. In earlier work (Wu et al., 1983), in the atomization regime for liquid, the jet angle was found to follow the relationship

$$\tan \frac{\theta}{2} = \frac{C}{A} 4\pi \sqrt{\left(\frac{\rho_g}{\rho_m}\right)} \quad (7)$$

where θ is the jet angle, ρ_g is the density of the gas outside the chamber, ρ_m is the density of the multiphase fluid in the chamber, A is a constant for a given nozzle geometry and C is also a constant, and $c = \frac{\sqrt{3}}{6}$. Thus, θ is proportional to $\sqrt{\rho_g}$ and is inversely proportional to A and $\sqrt{\rho_m}$. It indicated that the density of fluid in the chamber is heavy for circular jet of supercritical CO₂. It also appears that the droplets growth and coalescence transform the supersaturated fluid to the liquid flow with separate bubbles, as shown in **Figure 11A**. For the rectangular jet of supercritical CO₂, a vapor flow with separate droplets can be inferred by the larger-angle jet, as shown in **Figure 11B**. It can be explained that the low-density mixture with gas domain has a stronger ability to expand than heavy mixture.

CONCLUSION

This paper presents the experimental results of near-field structure when supercritical CO₂ releases from the orifices with different sizes and patterns. The main conclusions are summarized as follows:

- 1) The shape of supercritical CO₂ jet from a circular orifice is a near-cylinder structure and the process is a highly under-expanded jet marked with the Mach disc. However, when

supercritical CO₂ is released from the rectangular orifice, the shock wave system has a fan-shaped structure, and the dispersion region perpendicular to the jet is wide.

- 2) According to the characteristic model of the crack, the peak jet angle increases linearly with increased diameter of leakage orifice in a circular jet. And the peak jet angle decreases with increase of b/a in a rectangular jet.
- 3) The traditional equation tends to under-predict the Mach disc location. The intercepting shock location in a rectangular jet increases approximately linearly with the equivalent diameter d_e .
- 4) The supercritical CO₂ in the chamber is transformed to metastable state firstly, and then the droplets growth and coalescence transforms the supersaturated fluid to the liquid-domain two-phase flow for the circular jet; however, the bubble nucleation and growth transforms the flow to gas-domain two-phase flow for the rectangular jet. In the outside, the solidification process causes CO₂ gas-particle flow.

DATA AVAILABILITY STATEMENT

The original contributions presented in the study are included in the article/**Supplementary Material**, further inquiries can be directed to the corresponding author.

AUTHOR CONTRIBUTIONS

LT and JB contributed to conception and design of the study. LT wrote sections of the manuscript. LT, JB, YL, and CW wrote sections of the manuscript. All authors contributed to manuscript revision, read, and approved the submitted version.

FUNDING

The present work is supported by the Research Foundation of Fuzhou University (Grant No. GXRC-20041) and the Natural Science Foundation of Chongqing (Grant No. CYY202010102001).

SUPPLEMENTARY MATERIAL

The Supplementary Material for this article can be found online at: <https://www.frontiersin.org/articles/10.3389/fenrg.2021.697031/full#supplementary-material>

REFERENCES

- Abbett, M. (1971). Mach disk in underexpanded exhaust plumes. *AIAA J.* 9, 512–514. doi:10.2514/3.6212
- Ahmad, M., Osch, M. B.-v., Buit, L., Florisson, O., Hulsbosch-Dam, C., Spruijt, M., et al. (2013). Study of the thermohydraulics

of CO₂ discharge from a high pressure reservoir. *Int. J. Greenhouse Gas Control.* 19, 63–73. doi:10.1016/j.ijggc.2013.08.004

Ashkenas, H., and Sherman, F. S. (1966). *Experimental methods in rarefied gas dynamics: Jet Propulsion Laboratory*. California: California Institute of Technology.

Dong, Z. (2005). *The mechanics of jet flow*. Lloyd: Chinese Science Press.

- Guo, X., Yan, X., Yu, J., Zhang, Y., Chen, S., Mahgerefteh, H., et al. (2016). Under-expanded jets and dispersion in supercritical CO₂ releases from a large-scale pipeline. *Appl. Energ.* 183, 1279–1291. doi:10.1016/j.apenergy.2016.09.088
- John, G., and John, D. (2004). Transmission of CO₂—safety and economic considerations, IEA Greenhouse Gas R&D Programme. *Energy* 29, 1319–1328.
- Joshi, P., Bikkina, P., and Wang, Q. (2016). Consequence analysis of accidental release of supercritical carbon dioxide from high pressure pipelines. *Int. J. Greenhouse Gas Control.* 55, 166–176. doi:10.1016/j.ijggc.2016.10.010
- Li, X., Zhou, R., Yao, W., and Fan, X. (2017). Flow characteristic of highly underexpanded jets from various nozzle geometries. *Appl. Therm. Eng.* 125, 240–253. doi:10.1016/j.applthermaleng.2017.07.002
- Lin, T.-C., Shen, Y.-J., and Wang, M.-R. (2013). Effects of superheat on characteristics of flashing spray and snow particles produced by expanding liquid carbon dioxide. *J. Aerosol Sci.* 61, 27–35. doi:10.1016/j.jaerosci.2013.03.005
- Liu, B., Liu, X., Lu, C., Godbole, A., Michal, G., and Tieu, A. K. (2016). Computational fluid dynamics simulation of carbon dioxide dispersion in a complex environment. *J. Loss Prev. process industries* 40, 419–432. doi:10.1016/j.jlp.2016.01.017
- Liu, X., Godbole, A., Lu, C., Michal, G., and Venton, P. (2014). Source strength and dispersion of CO₂ releases from high-pressure pipelines: CFD model using real gas equation of state. *Appl. Energ.* 126, 56–68. doi:10.1016/j.apenergy.2014.03.073
- Menon, N., and Skews, B. W. (2010). Shock wave configurations and flow structures in non-axisymmetric underexpanded sonic jets. *Shock Waves* 20, 175–190. doi:10.1007/s00193-010-0257-z
- Metz, B., Davidson, O., De Coninck, H., Loos, M., and Meyer, L. (2005). “IPCC special report on carbon dioxide capture and storage,” in *Prepared by Working Group III of the Intergovernmental Panel on Climate Change* (Cambridge, United Kingdom and New York, USA: IPCC, Cambridge University Press), 4.
- Mitchell, D. M., Honnery, D. R., and Soria, J. (2013). Near-field structure of underexpanded elliptic jets. *Exp. Fluids* 54, 1578. doi:10.1007/s00348-013-1578-3
- Nagayama, G., Tsuruta, T., and Cheng, P. (2006). Molecular dynamics simulation on bubble formation in a nanochannel. *Int. J. Heat Mass Transfer* 49, 4437–4443. doi:10.1016/j.ijheatmasstransfer.2006.04.030
- Otobe, Y., Kashimura, H., Matsuo, S., Setoguchi, T., and Kim, H.-D. (2008). Influence of nozzle geometry on the near-field structure of a highly underexpanded sonic jet. *J. Fluids Structures* 24, 281–293. doi:10.1016/j.jfluidstructs.2007.07.003
- Teng, L., Li, Y., Zhang, D., Ye, X., Gu, S., Wang, C., et al. (2018). Evolution and Size Distribution of Solid CO₂ Particles in Supercritical CO₂ Releases. *Ind. Eng. Chem. Res.* 57, 7655–7663. doi:10.1021/acs.iecr.8b00178
- Teng, L., Li, Y., Zhao, Q., Wang, W., Hu, Q., Ye, X., et al. (2016). Decompression characteristics of CO₂ pipelines following rupture. *J. Nat. Gas Sci. Eng.* 36, 213–223. doi:10.1016/j.jngse.2016.10.026
- Teng, L., Zhang, D., Li, Y., Wang, W., Wang, L., Hu, Q., et al. (2016). Multiphase mixture model to predict temperature drop in highly choked conditions in CO₂ enhanced oil recovery. *Appl. Therm. Eng.* 108, 670–679. doi:10.1016/j.applthermaleng.2016.07.156
- Velikorodny, A., and Kudriakov, S. (2012). Numerical study of the near-field of highly underexpanded turbulent gas jets. *Int. J. Hydrogen Energ.* 37, 17390–17399. doi:10.1016/j.ijhydene.2012.05.142
- Veser, A., Kuznetsov, M., Fast, G., Friedrich, A., Kotchourko, N., Stern, G., et al. (2011). The structure and flame propagation regimes in turbulent hydrogen jets. *Int. J. Hydrogen Energ.* 36, 2351–2359. doi:10.1016/j.ijhydene.2010.03.123
- Wang, C., Li, Y., Teng, L., Gu, S., Hu, Q., Zhang, D., et al. (2019). Experimental study on dispersion behavior during the leakage of high pressure CO₂ pipelines. *Exp. Therm. Fluid Sci.* 105, 77–84. doi:10.1016/j.expthermflusci.2019.03.014
- Wang, H., Liu, B., Liu, X., Lu, C., Deng, J., and You, Z. (2020). Dispersion of carbon dioxide released from buried high-pressure pipeline over complex terrain. *Environ. Sci. Pollut. Res.* doi:10.1007/s11356-020-11012-7
- Wareing, C., Fairweather, M., Peakall, J., Keevil, G., Falle, S., and Woolley, R. (2013). Numerical modelling of particle-laden sonic CO₂ jets with experimental validation. *AIP Conf. Proc. AIP Publishing LLC*, 98–102.
- Wareing, C. J., Fairweather, M., Falle, S. A. E. G., and Woolley, R. M. (2014). Validation of a model of gas and dense phase CO₂ jet releases for carbon capture and storage application. *Int. J. Greenhouse Gas Control.* 20, 254–271. doi:10.1016/j.ijggc.2013.11.012
- Wareing, C. J., Woolley, R. M., Fairweather, M., and Falle, S. A. E. G. (2013). A composite equation of state for the modeling of sonic carbon dioxide jets in carbon capture and storage scenarios. *Aiche J.* 59, 3928–3942. doi:10.1002/aic.14102
- Webber, D. M. (2011). Generalising two-phase homogeneous equilibrium pipeline and jet models to the case of carbon dioxide. *J. Loss Prev. Process Industries* 24, 356–360. doi:10.1016/j.jlp.2011.01.010
- Woolley, R. M., Fairweather, M., Wareing, C. J., Proust, C., Hebrard, J., Jamois, D., et al. (2014). An integrated, multi-scale modelling approach for the simulation of multiphase dispersion from accidental CO₂ pipeline releases in realistic terrain. *Int. J. Greenhouse Gas Control.* 27, 221–238. doi:10.1016/j.ijggc.2014.06.001
- Wu, K.-J., Su, C.-C., Steinberger, R. L., Santavica, D. A., and Bracco, F. V. (1983). Measurements of the spray angle of atomizing jets. *J. Fluids Eng.* 105, 406–413. doi:10.1115/1.3241019
- Zel'dovich, I. Ak. B. (1961). *Theory of formation of a new phase cavitation*. USA: US Joint Publications Research Service.
- Zhou, Z., Yanfei, L., Xiao, M., Haichun, D., Hongming, X., Zhi, W., et al. (2018). Characteristics of trans-critical propane spray discharged from multi-hole GDI injector. *Exp. Therm. Fluid Sci.* 99, 446–457.
- Ziabakhsh-Ganji, Z., and Kooi, H. (2014). Sensitivity of Joule-Thomson cooling to impure CO₂ injection in depleted gas reservoirs. *Appl. Energ.* 113, 434–451. doi:10.1016/j.apenergy.2013.07.059

Conflict of Interest: The authors declare that the research was conducted in the absence of any commercial or financial relationships that could be construed as a potential conflict of interest.

Publisher's Note: All claims expressed in this article are solely those of the authors and do not necessarily represent those of their affiliated organizations, or those of the publisher, the editors and the reviewers. Any product that may be evaluated in this article, or claim that may be made by its manufacturer, is not guaranteed or endorsed by the publisher.

Copyright © 2021 Teng, Bai, Li and Wang. This is an open-access article distributed under the terms of the Creative Commons Attribution License (CC BY). The use, distribution or reproduction in other forums is permitted, provided the original author(s) and the copyright owner(s) are credited and that the original publication in this journal is cited, in accordance with accepted academic practice. No use, distribution or reproduction is permitted which does not comply with these terms.



Simulation Study on the Development Process and Phase Interface Structure of Gas-Liquid Slug Flow in a Horizontal Pipe

Xiao Wu¹, Zhaoting Wang^{1*}, Mei Dong², Quan Ge¹ and Longfei Dong¹

¹College of Oil and Gas Engineering, Shengli College China University of Petroleum, Dongying, China, ²Safety Consulting Division, Qingdao Nuocheng Chemical Safety Technology Co., Ltd., Qingdao, China

OPEN ACCESS

Edited by:

Jiang Bian,
China University of Petroleum (East
China), China

Reviewed by:

Junbing Xiao,
Changsha University of Science and
Technology, China
Lin Wang,
Southwest Petroleum University,
China

*Correspondence:

Zhaoting Wang
slxywuxiao@163.com

Specialty section:

This article was submitted to
Advanced Clean Fuel Technologies,
a section of the journal
Frontiers in Energy Research

Received: 22 August 2021

Accepted: 28 September 2021

Published: 18 October 2021

Citation:

Wu X, Wang Z, Dong M, Ge Q and
Dong L (2021) Simulation Study on the
Development Process and Phase
Interface Structure of Gas-Liquid Slug
Flow in a Horizontal Pipe.
Front. Energy Res. 9:762471.
doi: 10.3389/fenrg.2021.762471

Here, a unified 3D numerical model of gas-liquid two-phase flow in a horizontal pipe was established using the interface capture method based on the open source software package OpenFOAM. Through numerical simulation of the natural slugging and development process of slug flow under different working conditions, the motion, phase interface structure, pressure and velocity field distributions of the liquid slug were fully developed and analyzed. The simulation results are consistent with the experiment. The results showed that during the movement of the slug head, there is a throwing phenomenon and a wave-like motion of the liquid slug. In addition, the slug tail and body area have very similar velocity profiles, and the overall velocity field distribution becomes more uniform with the development of liquid slug. Moreover, there are sudden pressure fluctuations at the head and tail of the liquid slug.

Keywords: slug flow, phase interface structure, flow characteristics, numerical simulation, 3D numerical model

INTRODUCTION

The mixed transmission pipelines on the seabed laid along the seabed terrain are mainly horizontal and near horizontal. Slug flow is the most common flow pattern in the mixed transmission of oil and gas in horizontal and near horizontal pipelines, and the production parameters of most oil wells are within the parameter range of this flow pattern (Bonizzi, 2003). Due to the randomness, complexity and intermittence of slug flow, the understanding of its flow characteristics and phase interface structure is not thorough. The fluctuation of pressure and flow caused by slug flow has an important impact on deep-sea oilfield and the design of production equipment. In the beginning macroscopic studies are focused on average length and holding capacity of liquid slugs, but now researchers have gradually turned to the more complex study of the natural development process and transient gas-liquid interface structures of liquid slugs.

Taitel's study (Taitel et al., 2000) showed that the steady-state model often presents non-physics profiles when calculating the slug flow in a downcast pipe. According to the characteristics of gas-liquid distribution and pressure drop fluctuation, Yin et al. (2022) divided intermittent flow and segregated flow into various sub-flow patterns. The distribution of the flow patterns was summarized under different working conditions. The experimental results enhance the understanding of the morphology and evolution process of gas-liquid flow. Ishii (Ishii, 2006) established a 1D two-fluid model, but the governing and constitutive equations of different flow patterns were quite different. Lu (2015) used six commercial finite volume codes to simulate the slug flow in horizontal pipe sections by 1D two-fluid model, and compared the results with experimental data, finding that the

simulated slug flow characteristics were quite different from the experimental ones. Ekambara et al. (2008) used the VOF (volume of fluid) model to simulate the internal phase distribution of the slug flow in a horizontal pipeline with an inner diameter of 50.3 mm. The results indicated that the volume fraction had a maximum near the upper pipe wall, and the profiles tended to flatten with increasing liquid flow rate. It was found that increasing the gas flow rate at fixed liquid flow rate would increase the local volume fraction. Abdulkadir et al. (2013) used VOF model and RANS (Reynolds-averaged Navier-Stokes) turbulence model to simulate the air silicone oil slug flow in 90° vertical elbow and compared it with the experimental results. It was found that the flow pattern before and after turning was consistent with the one captured by high-speed camera, and the model could predict the gas phase distribution at turning. Glatzel et al. (2008) used VOF model to simulate the liquid-liquid and gas-liquid two-phase flow in T-shaped microchannel, and analyzed the bubble shape in gas-liquid two-phase flow, micro droplet volume and separation time in liquid-liquid two-phase flow. There was a gap between the simulated phase interface structure and the experimental results. Ratkovich et al. (2009) established a 2D vertical pipe model with inner diameter of 190.5 mm and length of 3.4 m by using VOF model to analyze the void fraction of gas-liquid two-phase slug flow of Newtonian fluid and non-Newtonian fluid. The simulation results of void fraction were in good agreement with the experimental results. Deendarlianto et al. (2016) used VOF model to simulate gas-liquid two-phase flow in horizontal pipe. The results showed that there was a quantitative consistency between the calculated results and the experimental data for the changes of long bubble length and liquid holdup. A slug tracking model was proposed by Zheng et al. (1994), although it was found that this model cannot fundamentally simulate the natural evolution process of the slug, and the resulting calculations of high gas-liquid velocity are yet to be verified. Vallée et al. (2008), Vallée et al. (2010) used CFX software in conjunction with the Euler two-phase flow and SST Turbulence models to establish a 2D numerical model of slug flow; however, due to the restriction of inlet conditions in the model, the gas-liquid interface structure of the slug flow was quite different from that observed in experiments. Ramdin and Henkes (2011), Ramdin and Henkes (2012) established 2D and 3D models using FLUENT software. They simulated Benjamin bubbles in a horizontal tube and Taylor bubbles in a vertical tube and analyzed the influence of viscosity and surface tension on the bubbles. For the most part, the simulation results were consistent with the experimental results; however, when the surface tension was high, the 2D Benjamin bubble model greatly deviated from the experimental results. De Schepper et al. (2008) used VOF model and piecewise linear interface calculation (PLIC) interface recombination method to build a 3D horizontal pipe model. The simulation results for the air-water two-phase flow pattern at different gas-liquid velocities were consistent with the baker flow pattern, but the gas-liquid interface structures of each flow pattern were quite different from experiments.

From the aforementioned studies, it is found that the idea of establishing these transient models is to divide the slug flow into

liquid slug region and bubble slug region, and simulate the transient characteristics of gas-liquid slug flow with the help of experimental empirical relationship on the basis of assumption. Slug flow simulation currently mostly relies on 1D and 2D models, which cannot reflect the actual phase interface structures and transient flow characteristics of slug flow. Moreover, these models cannot satisfactorily simulate the natural evolution process of the slug from starting to full development, and the local structures, transient flow characteristics, velocities and pressure distributions of the slug obtained by such model show large discrepancies with experimental data. To address these issues, the present study uses an interface capture method, implemented using the open source software package OpenFOAM (2019), to establish a unified 3D numerical model of two-phase flow in a horizontal pipe. This method allows the development of slug flow under different working conditions to be simulated, and the motion, phase interface structure, pressure, and velocity field distributions of the developing and fully-developed slug to be obtained.

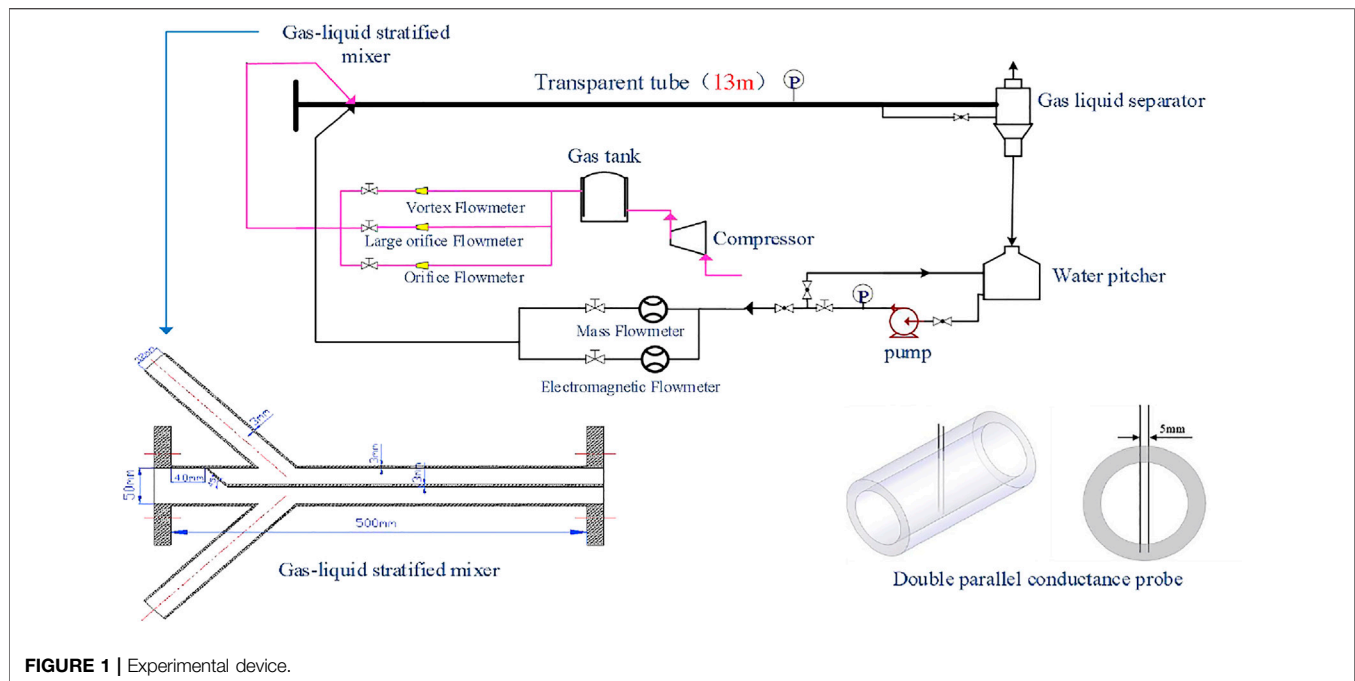
EXPERIMENT

In order to verify the accuracy of the simulation, an experimental device for two-phase flow in horizontal pipe is built. The experimental system includes three parts: gas phase circulation system, liquid phase circulation system and gas-liquid mixing experimental system. As shown in **Figure 1**.

The gas-phase circulation system mainly includes gas-phase supply system, metering system and gas-phase pipeline. The gas tank is used to reduce the fluctuation of gas volume and pressure, provide stable flow for the downstream and prevent accidental slugging caused by pressure and flow fluctuation. The metering system includes large orifice Flowmeter, orifice Flowmeter, vortex Flowmeter and precision regulating valve. Combined with the measurement accuracy range of the three Flowmeters, it can cover the flow range required for the experiment in all aspects and meet the experimental measurement requirements. The precision regulating valve is respectively connected with three kinds of flow meters to form a large, medium and small three-way metering system to realize the precise control of gas volume.

The liquid phase circulation system consists of water pitcher, pressure gauge, centrifugal pump, frequency converter, mass Flowmeter, electromagnetic Flowmeter, precision regulating valve and relevant pipelines. Mass Flowmeter, electromagnetic Flowmeter and precision regulating valve constitute the metering system of liquid phase circulation. The two metering systems are selected in real time according to the experimental conditions.

The gas-liquid mixing experimental system mainly includes gas-liquid layered mixer, transparent tube test observation section and gas-liquid separation system. In order to provide stable gas-liquid two-phase flow as much as possible, a Gas-Liquid Stratified mixer was designed in this experiment. The transparent tube is the main pipe section for experimental test and observation, with a total length of 13 m. It is composed of PMMA pipe with an inner diameter of 50 mm and a wall thickness of 5 mm, which is convenient for video capture of the development process of liquid slug.



In the experiment, 20 groups of double parallel conductance probes are arranged from the inlet to the outlet. The cross-correlation method is used to measure the flow characteristic parameters such as liquid slug frequency and velocity during the development of liquid slug. HD (high definition) camera is used to determine the flow pattern and position of slug flow.

TWO-PHASE FLOW NUMERICAL MODEL

Governing Equations

The model gas and liquid share a set of mass and momentum equations and form a closed equation along with the volume fraction transfer equation, as follows:

$$\nabla \cdot u = 0 \quad (1)$$

$$\frac{\partial}{\partial t}(\rho u) + \nabla \cdot (\rho u u) = -\nabla P + \nabla \cdot \tau + \rho g + \delta \kappa \nabla \alpha \quad (2)$$

$$\frac{\partial \alpha}{\partial t} + \nabla \cdot (\alpha u) + \nabla \cdot [u_r \alpha (1 - \alpha)] = 0 \quad (3)$$

Where u is the velocity, p is the pressure, δ is the surface tension coefficient, τ is the viscous force, α is the volume fraction of water in two-phase flow, κ is the interface curvature, V_{sg} is the apparent gas phase velocity, V_{sl} is the apparent velocity of liquid phase, u_r is the relative velocity of gas and liquid phase.

Calculation Model and Boundary Initial Conditions

The geometric model uses a Cartesian coordinate system to simulate a 3D horizontal cylindrical tube with an inner diameter of 50 mm and a length of 13 m (260D). The

geometric model is shown in **Figure 2**. The gas-liquid inlet and outlet are at $x = 0$ and $x = 13$ m, respectively, and the direction of g is along the negative z -axis.

The height ratio of the inlet layer is 0.5. Air and water enter the horizontal pipeline through the blue and red inlet cross-sections (as indicated in **Figure 1**), respectively, at constant flow rates. The outlet is at standard atmospheric pressure. The model used the Newtonian fluid viscosity and Brackbill (Brackbill et al., 1992) continuous interface force (CFS) models. The phase interfacial tension per unit length was defined as 0.07 N/m with reference to Wang Xin's fluid slug tracking model (Wang, 2006). The model uses OpenFOAM's unique PIMPLE algorithm (Robertson et al., 2015), that is, the SIMPLE algorithm was used to solve the Navier-Stokes equations, and each time step was regarded as steady-state flow and was solved using the pressure implicit split operator (PISO) algorithm.

Turbulence Model

Choosing a reasonable turbulence model is the key to obtaining numerical simulation results which are consistent with the experimental results. Of the available turbulence models, the Direct Numerical Simulation model and Large Eddy Simulation model have low calculation efficiencies. The turbulence models commonly used in two-phase flow simulations include standard $k-\varepsilon$ models, RNG $k-\varepsilon$ models, realizable $k-\varepsilon$ models, and $k-\varepsilon$ SST models. Here, $V_{sg} = 3 \text{ m/s}$ and $V_{sl} = 1 \text{ m/s}$ were used as input parameter values to evaluate the four turbulence models under the same grid number and time step. The models were used to simulate slug flow in the horizontal pipe section, and the results for slug formation distance and liquid slug frequency along the flow direction were compared with experimental data, as shown in **Figures 3**.

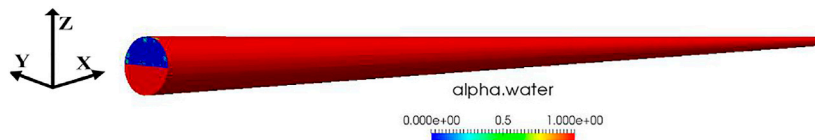


FIGURE 2 | Geometric model of 3D horizontal pipe.

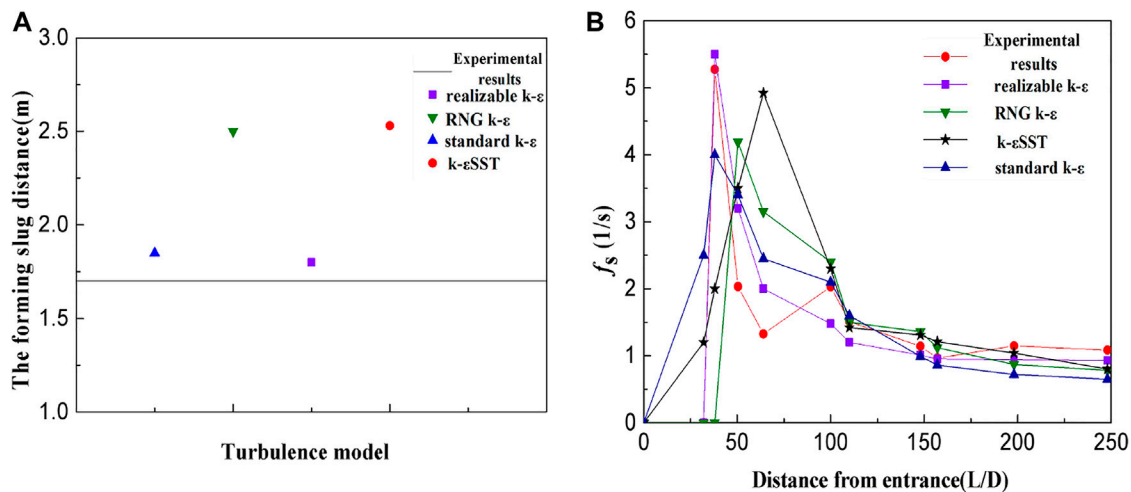


FIGURE 3 | Comparison between simulated and experimental values of (A) slug formation position and (B) slug frequency by different turbulence models.

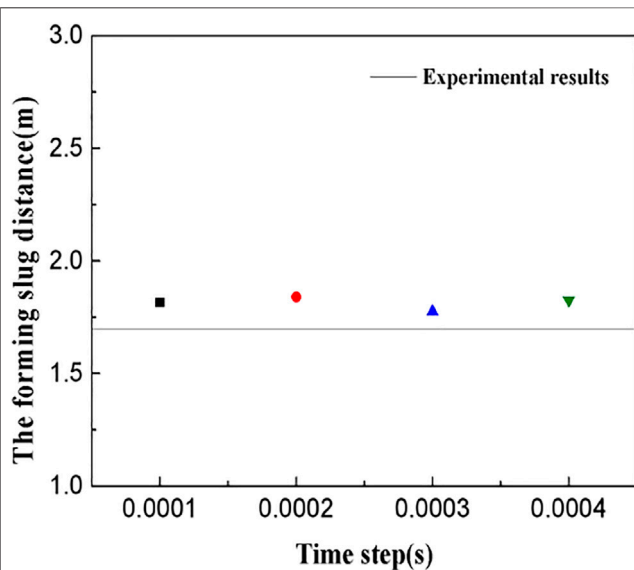


FIGURE 4 | Variation of slug formation position with time step.

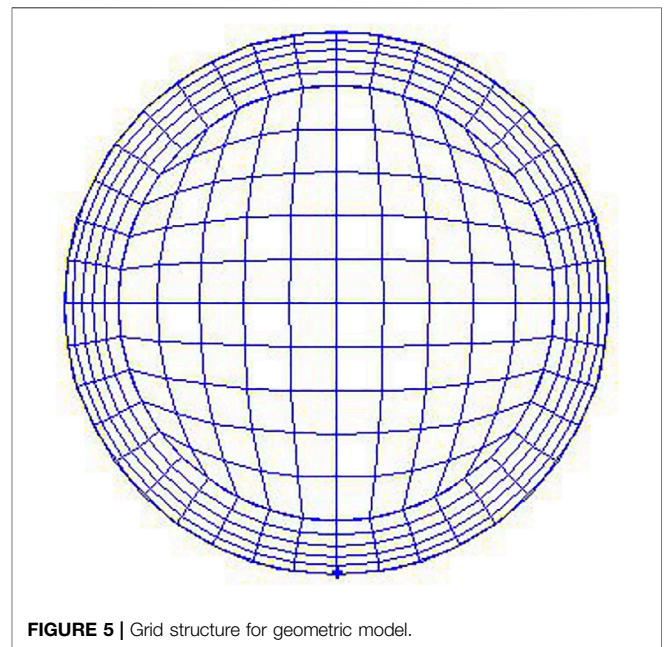


FIGURE 5 | Grid structure for geometric model.

whence it can be seen that the calculation examples from the realizable $k-\epsilon$ model were the closest to the experimental results and have a good degree of consistency. Therefore, the realizable $k-\epsilon$ model was selected as the turbulence model.

Grid, Time Step Independence Analysis

In order to capture the transient characteristics of the gas-liquid interface in the calculations, the Courant number was set at < 0.5 . The value of the spatial step size Δx was fixed, and the time step

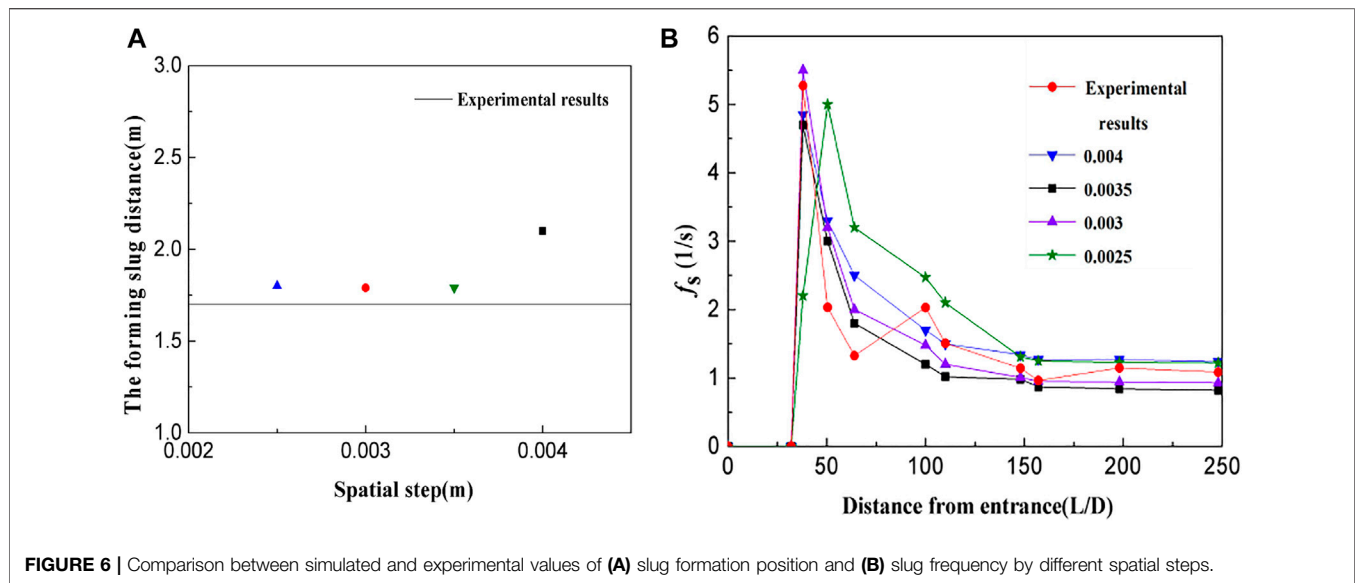


FIGURE 6 | Comparison between simulated and experimental values of (A) slug formation position and (B) slug frequency by different spatial steps.

size Δt was automatically adjusted according to the maximum phase velocity, U_{\max} , obtained in each calculation time layer.

$$Co = \frac{|U_{\max}|\Delta t}{\Delta x} \leq 0.5 \quad (4)$$

As in the previous section, $V_{sg} = 3$ m/s and $V_{sl} = 1$ m/s were taken as input values, and Courant numbers were simulated at the same spatial steps of 0.125, 0.25, 0.375, and 0.5, as shown in **Figure 4**, whence it can be seen that the time step has little effect on the simulation results. Hence, in order to improve the calculation efficiency, the time step at a Courant number of 0.5 was selected.

Here, a boundary layer encrypted hexahedral mesh was used to divide the geometric model, as shown in **Figure 5**. In order to eliminate the influence of grid sparsity on the results, simulations were conducted using spatial steps of 0.0025 m, 0.003 m, 0.0035 m, and 0.004 m (with the same V_{sg} and V_{sl} values as previously). The results are shown in **Figure 6**, whence it can be seen that the smaller the grid size, the closer the slug formation distance is to the experimental value. Simultaneously, the consistency of the simulated liquid slug frequency with the experimental value at different positions along the flow direction improves initially, before deteriorating as the number of grids becomes smaller. But when the spatial step is too small, the simulation accuracy is not accurate. This may be due to the fact that when the grid size is small, the frequent transmission of information between the grids leads to increased errors, which makes the simulations inconsistent with real slug flow. Therefore, a smaller spatial step size is not clearly better, and hence a spatial step size of 0.003 m was ultimately chosen.

Model Validation

The numerical model was validated by simulating the two-phase flow of gas and water under different velocity conditions for a pipe with an inner diameter of 50 mm. **Figure 7** shows a

comparison between the five different flow patterns generated by the simulation and the corresponding experimental data, whence it can be seen that the simulated flow pattern is consistent with the experiments and appears to qualitatively reflect the characteristics of the phase interface structure of the two-phase flow at different gas-liquid speeds.

The validated 3D model was then used to simulate the two-phase flow in the pipe geometry shown in **Figure 2** at different gas and liquid velocities. The apparent velocity range of the gas phase was 0.1–6.5 m/s, and that of the liquid phase was 0.05–2 m/s, with a total of 148 data points chosen. A logarithmic coordinate system was used, whereby the abscissa and the ordinate represent the apparent velocities of the gas and liquid phases, respectively. The simulated operating conditions were drawn superimposed on a Mandhane flow pattern diagram according to the type of flow pattern, as shown in **Figure 8**. The red, blue, purple, and green points represent the operating points where the flow pattern simulation results are Bubble flow, Slug flow, Smooth Stratified flow and Stratified Wavy flow. The simulated operating points of Bubbly flow, Slug flow, and Smooth Stratified flow are consistent with the Mandhane flow pattern diagram. Taking slug flow as an example, the simulation result shows that among 57 operating points of the slug flow, 56 operating points are located in the slug flow area of the Mandhane flow pattern, and the accuracy rate is 98.2%. The Stratified Wavy flow has poor consistency with the Mandhane flow pattern diagram. This is because the Stratified Wavy flow area is small and the simulated operating points are few. In general, the simulation results are consistent with the Mandhane flow pattern diagram, which indicates the reliability of the model for two-phase flow simulations.

Figure 9 shows the comparison between simulation value and experimental value of slug frequency under different working conditions ($L/D = 258$). It can be seen that the simulation value under high gas velocity are consistent with the experiment, and the simulation value under low gas velocity have a certain gap

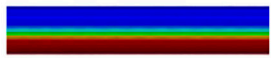

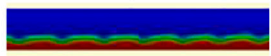

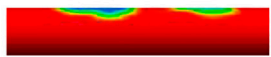

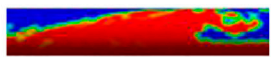



Simulation	Experiment	Flow pattern	V_{sg} (m/s)	V_{sl} (m/s)
		Smooth Stratified	0.5	0.1
		Stratified Wavy	2.5	0.1
		Bubble flow	0.1	3
		Slug flow	5	1
		Bubble flow	0.3	1

FIGURE 7 | Comparison of simulation and experiments for five kinds of flow patterns.

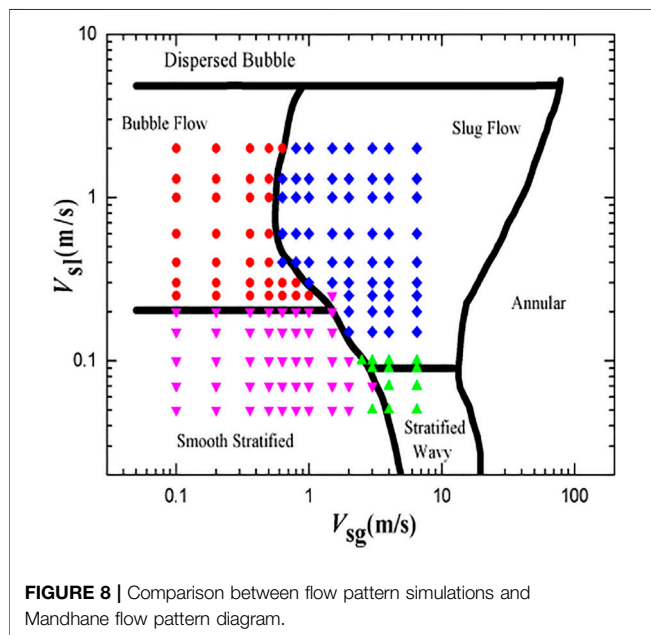


FIGURE 8 | Comparison between flow pattern simulations and Mandhane flow pattern diagram.

with the experimental value. When the gas velocity is constant, the slug frequency increases as the liquid velocity increases.

Figure 10 shows a comparison between the simulated and experimental liquid slug frequency changes along the flow direction for $V_{sg} = 3$ m/s and $V_{sl} = 1$ m/s. From the figure, it can be seen that the simulated slug frequency closer to the inlet slightly overpredicts the experimental result. This is because the model assumes that the gas is incompressible, and that the change in inlet pressure, which is an important contributor to slug formation but has little effect on fully developed liquid slugs, will be directly transmitted to the downstream pipeline. The model results are quantitatively consistent with the experiments, and seem to reflect the natural development process of liquid slug formation, merger, and disappearance, thereby demonstrating the effectiveness of the model for slug flow simulation.

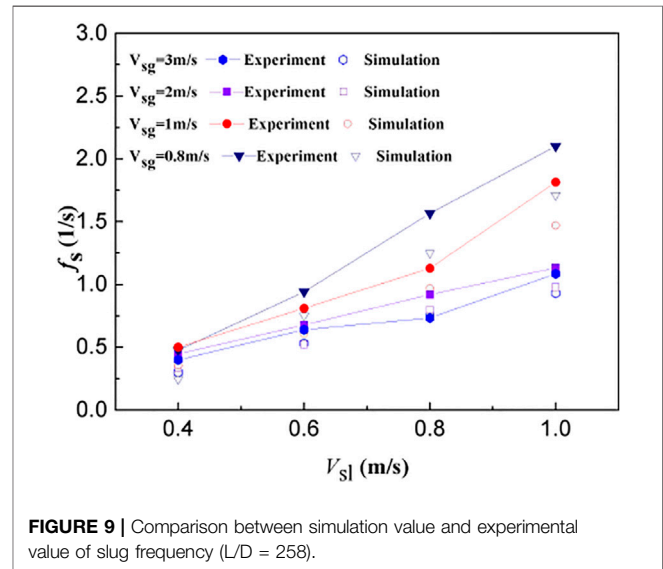
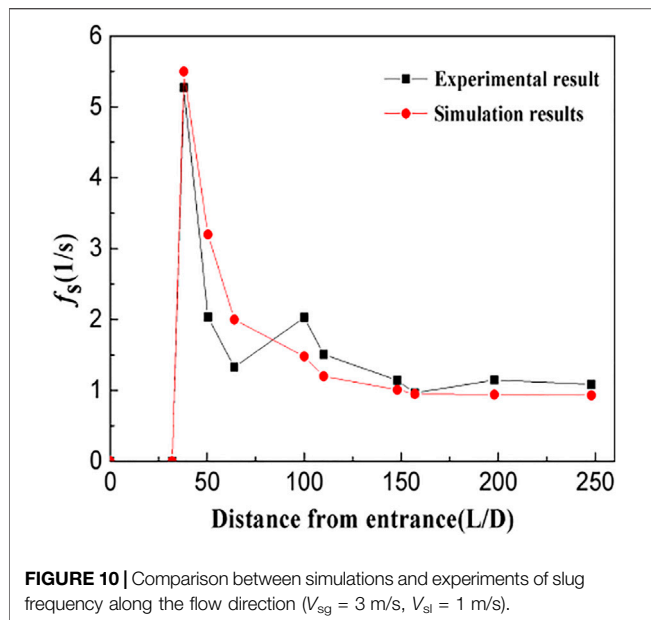


FIGURE 9 | Comparison between simulation value and experimental value of slug frequency ($L/D = 258$).

SIMULATION RESULTS AND DISCUSSION

Characteristics of Slug Formation

Figure 11 shows a comparison of 2D simulation and experimental data of the slug formation process at the pipe entrance for $V_{sg} = 2$ m/s and $V_{sl} = 0.2$ m/s. It can be seen from the figure that a series of interface waves with high frequency and small amplitude are formed under the flowing gas. The momentum transfer between the gas and liquid causes the interface to become unstable, and the interface waves merge with each other, reducing the interface wave frequency and increasing the amplitude. When the cross-sectional area of the upper gas flow becomes smaller, the gas accelerates through the highest point of the interface wave. Due to the Bernoulli effect, the pressure of the gas above the interface wave decreases. When the pressure difference between the phases overcomes the interfacial tension and gravity, the interface wave is elevated. The slug formation phenomenon occurs when the crest of the interface



wave blocks the pipeline. In both the experimental data and the simulations, the top of the interface wave is thrown forward by the gas velocity, forming the head of the thrown liquid slug.

Characteristics of Liquid Slug Motion

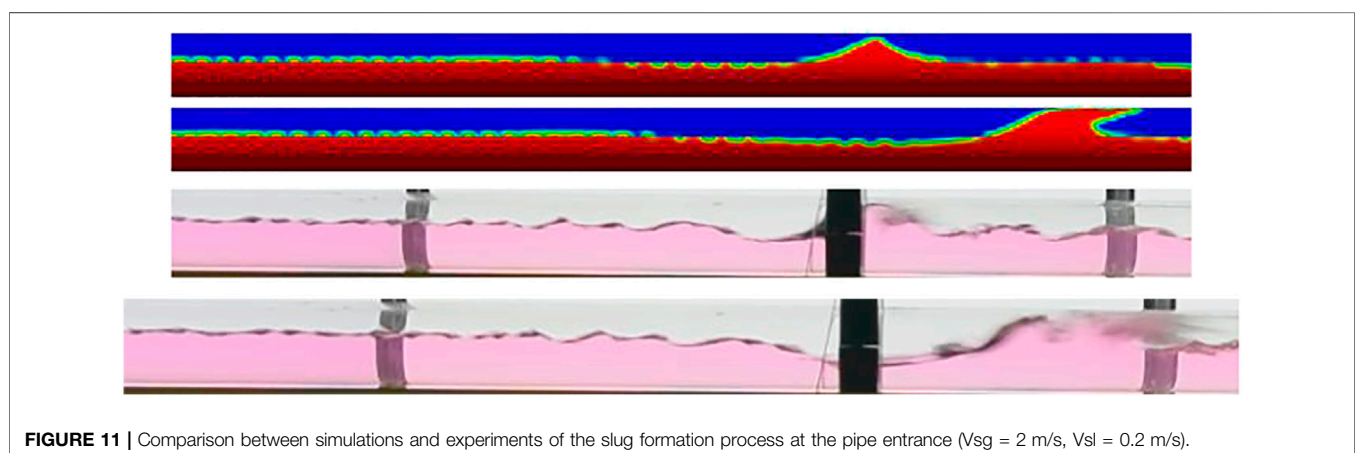
Figure 12 shows a distribution diagram of the retention rate of a developing liquid slug for $V_{sg} = 2$ m/s and $V_{sl} = 1$ m/s, with a time interval of 0.05 s between each graph. For graphs (1)–(7) it can be seen that during the development of the liquid slug, the head of the slug is thrown forward and falls under the action of gravity. As a result, it sucks up the upstream liquid film, causing the slug length to increase. Simultaneously, the head of the liquid slug draws liquid into the bubbles with larger volume, causing these bubbles to gradually become smaller with the liquid slug motion and move to the tail of the slug, where they are finally discharged, before the next cycle of circulation, as shown in graphs (8)–(16). As the figure shows, it is due to this development process that the liquid slug head contains a much greater gas content than that in the tail.

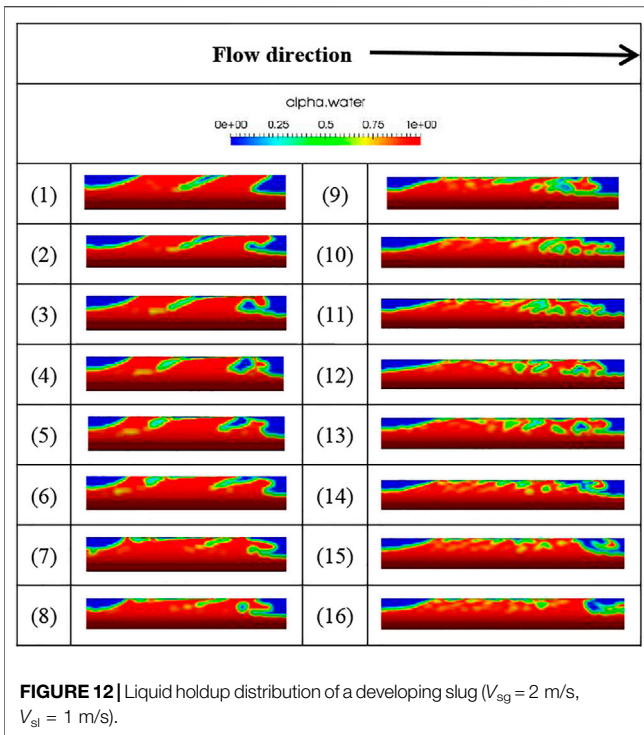
Figure 13 shows the displacement of a liquid slug changing with time for a constant V_{sl} of 1 m/s and V_{sg} values of 1, 2, and 3 m/s. It can be seen from the figure that increasing V_{sg} causes the liquid slug holding rate and the length of the liquid slug to decrease significantly, while the degree of ‘head throwing’ of the liquid slug increases. When the gas-liquid speed difference is small, the liquid level is high; hence, the liquid slug body is long and the throwing phenomenon of the liquid slug head is not obvious. Here, the liquid slug is moved forward by the gas in a balanced manner, absorbing the liquid film in front. When the gas-liquid speed difference is large, however, the throwing phenomenon is clearly evident, with the liquid slug advancing the liquid film through the periodic throwing and falling motion. This is because when the gas and liquid velocity difference is large, the liquid level is low and the amount of liquid slug is small. At high air flow speeds, the head of the liquid slug is thrown forward, causing a gap to form between the liquid and the upper part of the tube, and the gas accelerates through. The resulting pressure difference causes the liquid to be lifted and thrown forward, and the developing liquid slug circulates and moves forward in this way.

Figure 14 shows the displacement of a fully developed liquid slug changing with time for a constant V_{sl} of 1 m/s, and V_{sg} values of 1 and 3 m/s. The figure shows that as V_{sg} increases, the liquid slug gas content increases significantly and degree of throwing of the liquid slug head increases. Compared to Table 2, it is evident that the characteristics of the fully-developed liquid slug motion are very different from that of the developing liquid slug, with fully-developed liquid slug head not displaying any periodic throwing and falling. Further, it appears that the difference in gas-liquid speed has no obvious effect on the fully-developed liquid slug’s movement and that the volume of liquid entrained by the liquid slug head is equal to the discharge volume of the tail. Hence, the length is kept stable, and the liquid slug moves forward evenly with its head thrown forward.

Transient Characteristics of the Liquid Slug Interface

In the simulations, the phenomenon of the head of the liquid slug being thrown forward and sucking in gas was observed, which is consistent with the structure of the actual liquid slug head from the





high-definition photographs. **Figure 15C** shows that after the liquid slug is formed, the pressure behind it rises sharply, as evidenced by the effect of the pressure difference between the front and back of the slug. As a result, the liquid at the top of the slug is pushed out quickly, causing the head of the slug to be thrown forward, as the kinetic energy of the slug body is greater than that of the front liquid film area, as shown by the color of the vector arrows in **Figure 15A**. When the slug absorbs liquid from the film, this liquid is accelerated

to the speed of the slug, thus forming a vortex zone at the slug's front end. Due to the existence of the vortex, the liquid slug will entrain part of the gas, eventually forming a gas-liquid mixing zone with high kinetic energy at the head of the slug. This is consistent with the physical model of the shortest liquid slug length proposed by Dukler et al. (1985) in that the liquid slug speed is greater than the liquid film speed. Assuming that the slug is stationary, it is equivalent to the front liquid film jet entering the slug and forming a vortex in the area between the liquid film separation point and the return point, accompanied by a large number of air bubbles. This area is the liquid slug mixing area.

Figure 16 shows the velocity distribution curves at different positions along a liquid slug during and after full development for $V_{sg} = 1$ m/s and $V_{sl} = 1$ m/s. For the developing liquid slug, the velocity of the upper part of the liquid gradually increases from the tail to the head of the slug, while the velocity of the lower part of the liquid gradually decreases. **Figure 16A** shows that the velocity distribution of the liquid slug during development is uneven, with the velocity in the upper half being greater than that in the lower half, particularly at $x = 7.22$ m, which is the liquid slug head. For fully developed liquid slugs, the velocity distribution is more uniform. The difference in the local maximum velocity between the slug tail and slug head area is 25.1%. Comparing **Figures 16A,B**, both the developing and fully-developed liquid slug heads are thrown forward, which is consistent with the analyses from **Figures 13, 14**.

It can be seen from the velocity distribution curves that the velocity values near the bottom wall of the pipeline are similar. As the liquid slugs move downstream, the slug tail and body area have very similar velocity profiles, especially in the lower half region of the pipe regardless of the location.

Figure 17 shows the velocity distribution curves at different positions along a liquid slug during and after full development for $V_{sg} = 2$ m/s and $V_{sl} = 1$ m/s, which are consistent with those in

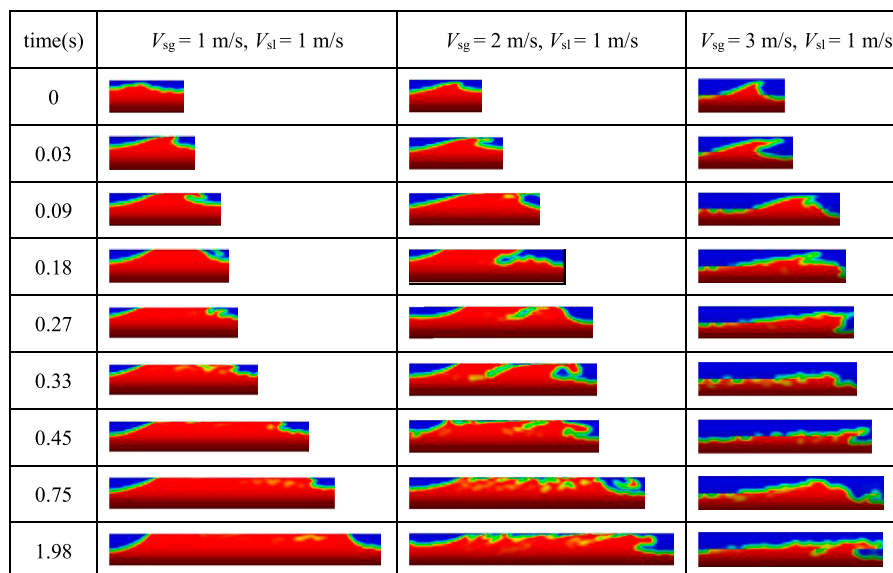


FIGURE 13 | Variation of a developing slug with time with increasing gas-liquid speed difference.

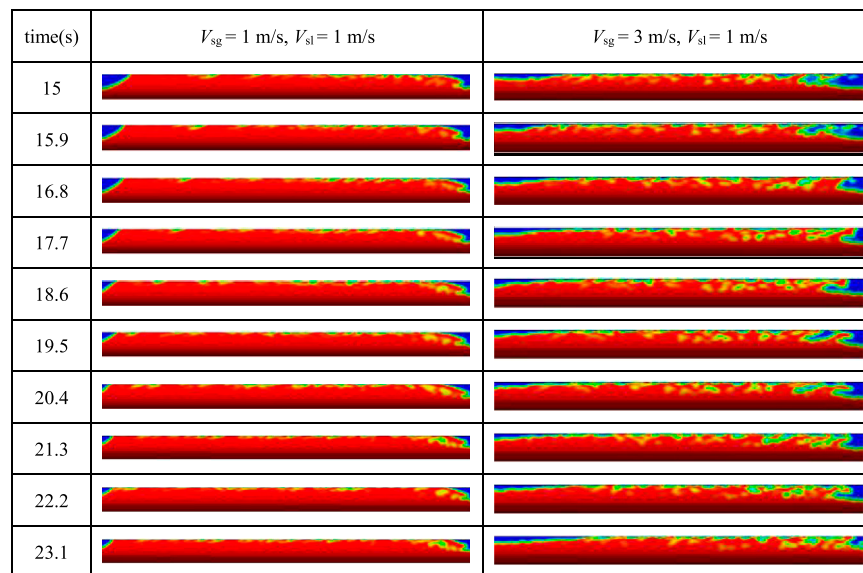


FIGURE 14 | Variation of a fully-developed slug with time with increasing gas-liquid speed difference.

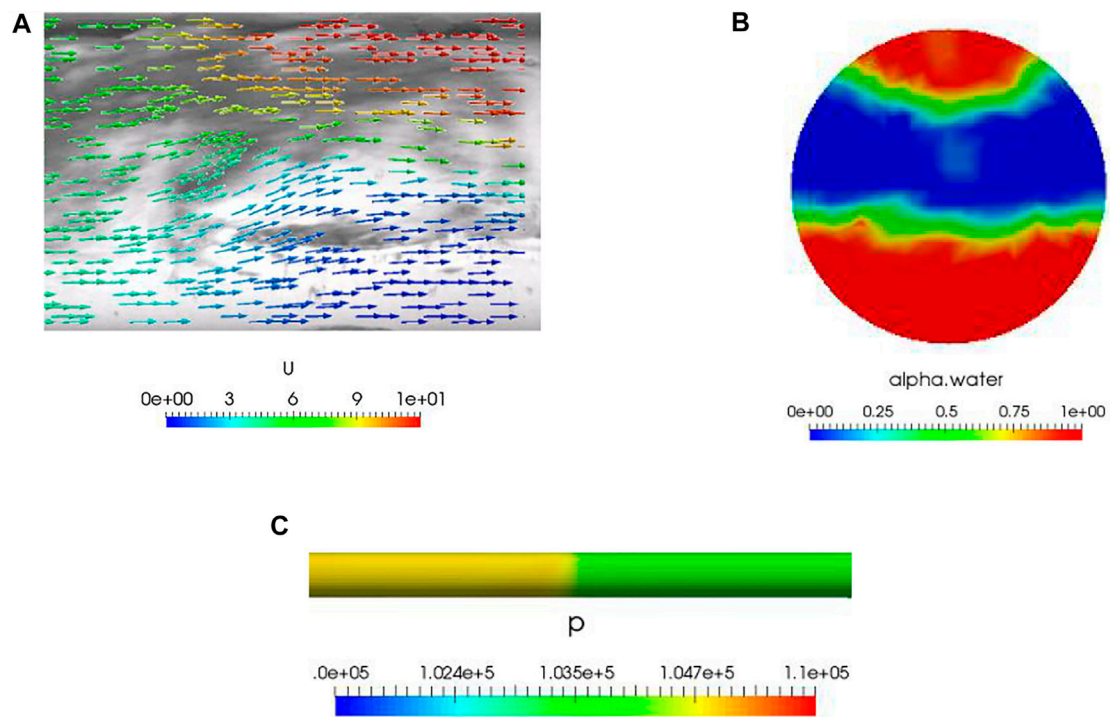


FIGURE 15 | (A) Comparison between experimentally obtained slug head image and simulated velocity vectors. (B) Distribution of liquid holdup in the pipe cross-section. (C) Pressure distribution in the pipe before and after the slug.

Figure 16; however, compared to **Figure 16**, the increase in gas velocity makes the difference between the upper and lower speeds of the developing and the fully-developed slug increase significantly. The speed change of the slug head is particularly

significant, and the difference in the local maximum velocity between the slug tail and slug head area is 33.5%. The result shows that the gas velocity has a significant effect on the liquid slug velocity distribution, i.e., the greater the gas velocity, the greater

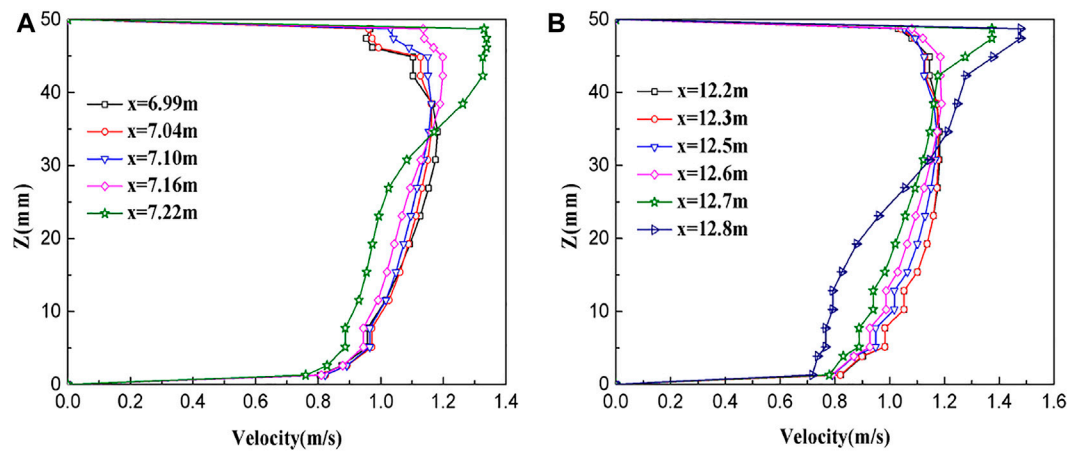


FIGURE 16 | Velocity distribution curves of (A) developing and (B) developed slugs ($V_{sg} = 1$ m/s, $V_{sl} = 1$ m/s).

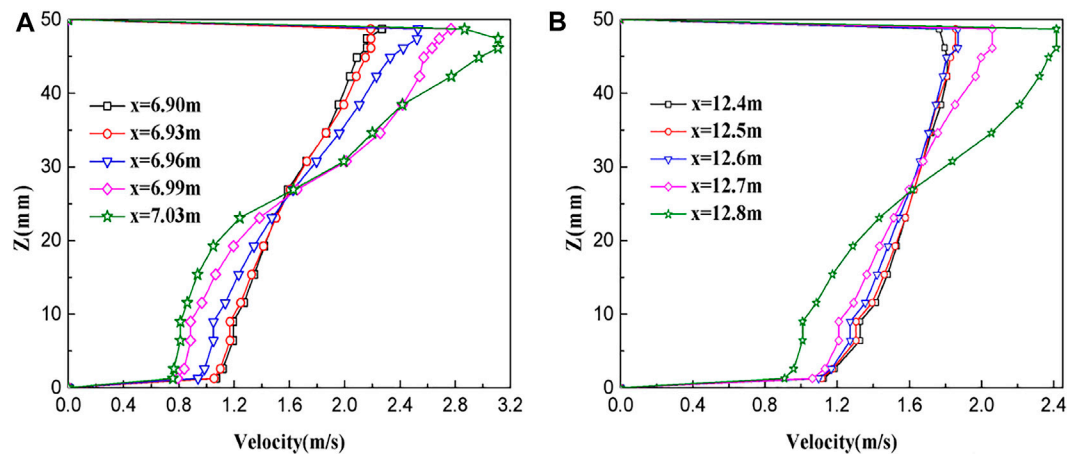


FIGURE 17 | Velocity distribution curve of (A) developing and (B) developed slugs ($V_{sg} = 2$ m/s, $V_{sl} = 1$ m/s).

the velocity difference between the upper and lower of the liquid slug and the head and tail of the liquid slug.

Figure 18 shows a cloud diagram of the cross-sectional velocity distribution of a developing and a fully-developed liquid slug for $V_{sg} = 2$ m/s and $V_{sl} = 1$ m/s. The position of the cross section is determined by dividing the liquid slug into equal parts along the flow direction. As the table shows, the velocity distribution of the fully-developed slug is more uniform, which is consistent with **Figure 17**. For the developing liquid slug, however, the velocity distribution is much more uneven, with the liquid velocity in the upper part of the slug being greater than that in the lower part. The velocity of the liquid from the tail to the upper part of the head of the slug gradually increases until it approaches the mixing speed of the gas and liquid phases. The velocity of the lower liquid gradually decreases to slightly lower than the velocity of the liquid film, which is the result of the combined action of pushing by the gas and the shear forces between the gas-liquid phase and the wall surface. Therefore, the

speed of the liquid slug during development is mainly determined by the liquid velocity in its upper half. The formation and development of the liquid slug can be described as follows: the disturbance caused by the difference in the gas-liquid velocity at the pipeline inlet forms an interface wave, which merges and grows. Due to the limitations of the enclosed space in the pipeline, the bridge slug eventually forms a liquid slug, which moves forward in a way similar to interface wave.

Figure 19 shows the relative pressure distribution curves of the central axis of the pipeline from the inlet to the outlet at a certain moment under different working conditions, with corresponding pressure distribution cloud diagrams shown in **Figure 20**. These data show that the pressure decreased from the inlet to the outlet of the pipeline, and the convex shape in **Figure 19** represents the liquid slug. As the gas pushes the liquid slug, the pressure from the liquid film area to the liquid slug tail shows a sudden increase. The energy loss of the viscous fluid in the flow process causes the pressure from the liquid slug tail to head gradually decrease. From the liquid slug head to the

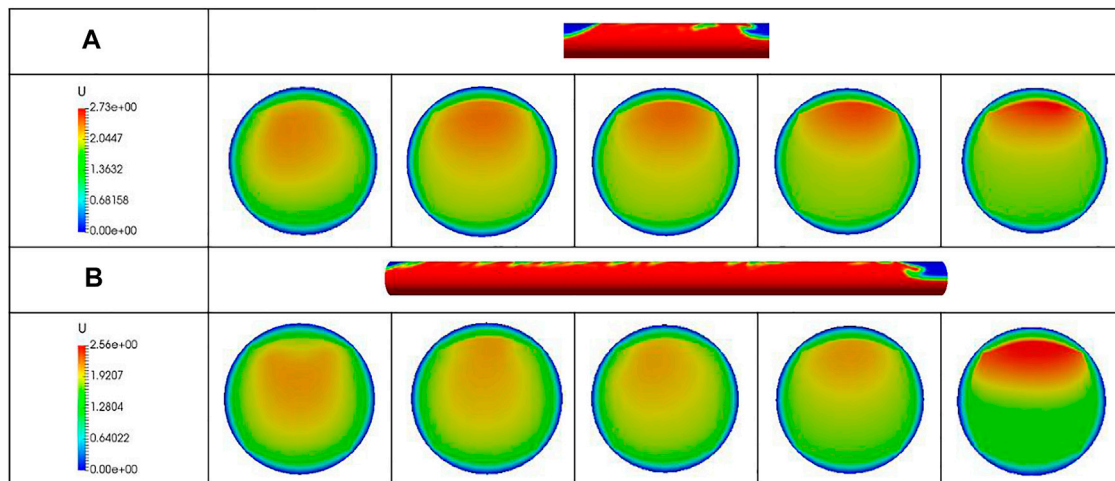


FIGURE 18 | Cross-sectional flow distributions in **(A)** a developing and **(B)** a fully-developed slug ($V_{sg} = 2$ m/s, $V_{sl} = 1$ m/s).

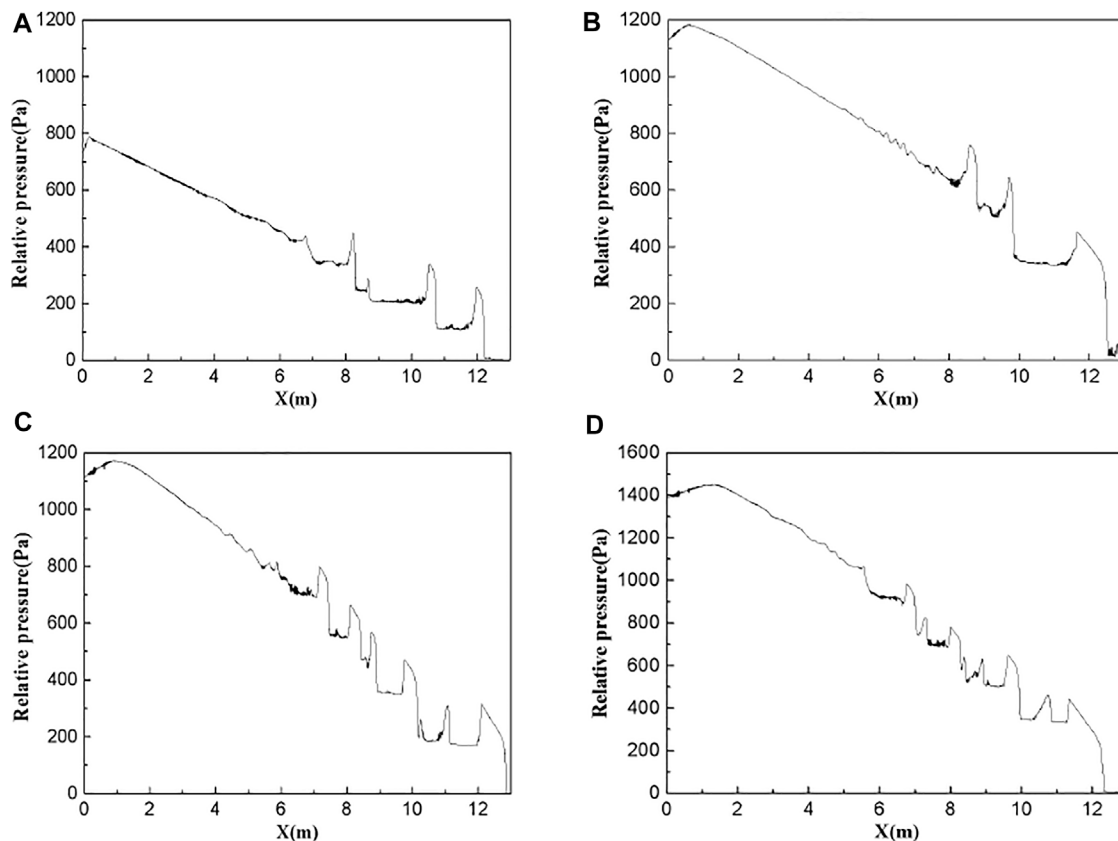


FIGURE 19 | Relative pressure distribution curves of the central axis of the pipeline at a certain moment under the following flow conditions: **(A)** $V_{sg} = 1$ m/s, $V_{sl} = 0.6$ m/s, **(B)** $V_{sg} = 1$ m/s, $V_{sl} = 0.8$ m/s, and **(C)** $V_{sg} = 1$ m/s, $V_{sl} = 1$ m/s. **(D)** $V_{sg} = 1$ m/s, $V_{sl} = 1.2$ m/s.

downstream liquid film area, a sudden drop in pressure occurs, due to the head of the liquid slug accelerating the front liquid film. Subsequently, the pressure in the liquid film does not change

much. Therefore, it may be inferred that the pressure surge at the tail of the liquid slug is the main reason for the pressure fluctuations and vibrations in the pipeline. Through the quantitative analysis of

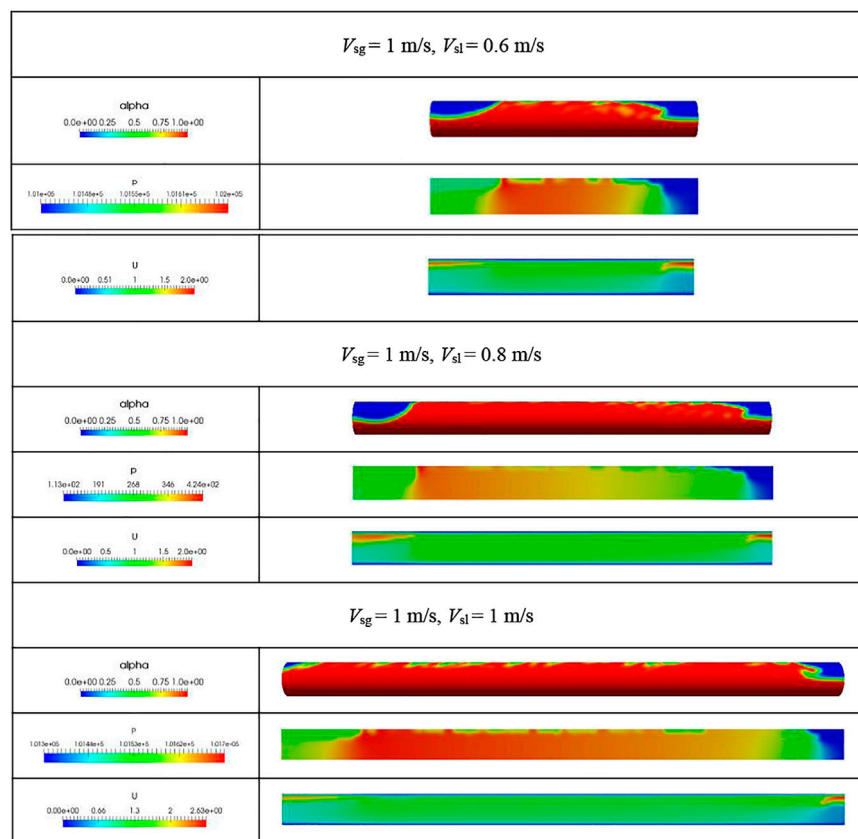


FIGURE 20 | Pressure distribution of a fully-developed slug at different liquid velocities.

Figure 20, it is found that as the liquid velocity increases, the pressure rise value from the upstream liquid film area to the liquid slug tail will increase, and the pressure drop value from the liquid slug head to the downstream liquid film area will increase accordingly, the pressure drop value caused by the liquid slug is about twice the pressure rise value at the tail of the slug, and it is mainly caused by the pressure drop at the head of the liquid slug, which is much higher than the normal hydraulic gradient. Therefore, the generation of slugs will increase the pressure energy loss of the entire pipeline.

CONCLUSION

- 1) Driven by the gas, a series of interface waves with high frequency and small amplitude are formed at the entrance of the pipeline. The instability of the interface causes the interface waves to merge with each other, reducing the interface wave frequency and increasing the wavelength and amplitude. When the crest of the interface wave blocks the pipeline, a slugging phenomenon occurs. Under the impulse of gas, the speed of the liquid slug head is greater than the speed of the front liquid film. The liquid slug head is thrown forward, forming a vortex at the junction of the liquid slug head and the front liquid film, and entraining a large amount of gas to form a liquid slug mixing area.
- 2) In the development of the liquid slug, when the gas-liquid speed difference is small, the liquid slug does not have a pronounced head, and it moves forward in a balanced manner under the force of the gas. When the gas-liquid speed difference is large, the head of the liquid slug is clearly thrown out, and it is pushed forward by the periodic throwing and falling motion. However, the fully-developed liquid slug head does not exhibit this periodic throwing and falling. Additionally, the difference in gas-liquid speed has no obvious effect on the form of the liquid slug, which moves forward evenly by throwing its head forward. With the increase in the superficial velocity of the gas phase, the gas content of the developing and fully-developed liquid slugs increase significantly, which causes the degree of head ejection of the liquid slug as well as the difference between its upper and lower speeds to increase.
- 3) The velocity distribution of the liquid slug during development is uneven, and the slug continuously moves forward through entraining liquid in the head and discharging it in the tail. The overall velocity field distribution becomes more uniform after fully-developed. The slug tail and body area have very similar velocity profiles, especially in the lower half region of the pipe regardless of the location.
- 4) The pressure from the upstream liquid membrane area to the end of the slug suddenly increases, while that from the end of the slug to its head gradually decreases, and the pressure from the slug head

to the downstream liquid membrane area suddenly drops. The pressure drop value caused by the liquid slug is about twice the pressure rise value at the tail of the slug, and it is mainly caused by the pressure drop at the head of the liquid slug, which is much higher than the normal hydraulic gradient. The sudden pressure rise in the slug tail is the main cause of pipeline pressure fluctuations and pipeline vibration.

DATA AVAILABILITY STATEMENT

The original contributions presented in the study are included in the article/Supplementary Material, further inquiries can be directed to the corresponding author.

AUTHOR CONTRIBUTIONS

XW put forward research ideas and formulated or formed overall research objectives; ZW provided experimental

data and led research activities; MD integrated literature and data; LD reviewed and modified the article; QG received financial support for the publication project.

FUNDING

This work was supported by Science Development Funding Program of Dongying, Grant No. DJ2020009. Qingdao Nuocheng Chemical Safety Technology Co., Ltd. is jointly funded by the chemical registration center of emergency management department and China Chemical Safety Association. The company mainly provides enterprises with “one-stop solutions” in the fields of safety consulting, environmental protection management, emergency and fire protection technology, chemical management and so on, and creates a comprehensive HSSE product and technical service model.

REFERENCES

- Abdulkadir, M., Hernandez-Perez, V., Lo, S., Lowndes, I. S., and Azzopardi, B. J. (2013). Comparison of Experimental and Computational Fluid Dynamics (CFD) Studies of Slug Flow in a Vertical 90° Bend. *The J. Comput. Multiphase Flows* 5 (4), 265–281. doi:10.1260/1757-482x.5.4.265
- Bonizzi, M. (2003). *Transient One-Dimensional Modeling of Multiphase Slug Flows*. London: Imperial College London. Doc.S.Dissertation.
- Brackbill, J. U., Kothe, D. B., and Zemach, C. (1992). A Continuum Method for Modeling Surface Tension. *J. Comput. Phys.* 100 (2), 335–354. doi:10.1016/0021-9991(92)90240-Y
- De Schepper, S. C. K., Heynderickx, G. J., and Marin, G. B. (2008). CFD Modeling of All Gas-Liquid and Vapor-Liquid Flow Regimes Predicted by the Baker Chart. *Chem. Eng. J.* 138 (1), 349–357. doi:10.1016/j.cej.2007.06.007
- Deendarlianto, Andrianto, M., Widyaparaga, A., Dinaryanto, O., Khasani, F., and Indarto, C. (2016). CFD Studies on the Gas-Liquid Plug Two-phase Flow in a Horizontal Pipe. *J. Pet. Sci. Eng.* 147, 779–787. doi:10.1016/j.petrol.2016.09.019
- Dukler, A. E., Moalem Maron, D., and Brauner, N. (1985). A Physical Model for Predicting the Minimum Stable Slug Length. *Chem. Eng. Sci.* 40 (8), 1379–1385. doi:10.1016/0009-2509(85)80077-4
- Ekambara, K., Sanders, R. S., Nandakumar, K., and Masliyah, J. H. (2008). CFD Simulation of Bubbly Two-phase Flow in Horizontal Pipes. *Chem. Eng. J.* 144 (2), 277–288. doi:10.1016/j.cej.2008.06.008
- Glatzel, T., Litterst, C., Cupelli, C., Lindemann, T., Moosmann, C., Niekrawietz, R., et al. (2008). Computational Fluid Dynamics (CFD) Software Tools for Microfluidic Applications - A Case Study. *Comput. Fluids* 37 (3), 218–235. doi:10.1016/j.compfluid.2007.07.014
- Ishii, M. (2006). *Thermo-fluid Dynamic Theory of Two-phase Flows*. Springer New York Press.
- Lu, M. (2015). *Experimental and Computational Study of Two-phase Slug Flow*. UK: Imperial College London. Doc.S.Dissertation.
- OpenFOAM (2019). *OpenFOAM User Guide*, V6. London, United Kingdom: Henry Weller.
- Ramdin, M., and Henkes, R. A. W. M. (2011). “CFD for Multiphase Flow Transport in Pipelines,” in ASME International Conference on Ocean, Offshore and Arctic Engineering, 377–387. doi:10.1115/omae2011-49514
- Ramdin, M., and Henkes, R. (2012). Computational Fluid Dynamics Modeling of Benjamin and Taylor Bubbles in Two-phase Flow in Pipes. *J. Fluid Eng-t. ASME*. 134 (4), 041303. doi:10.1115/1.4006405
- Ratkovich, N., Chan, C. C. V., Berube, P. R., and Nopens, I. (2009). Experimental Study and CFD Modelling of a Two-phase Slug Flow for an Airlift Tubular Membrane. *Chem. Eng. Sci.* 64 (16), 3576–3584. doi:10.1016/j.ces.2009.04.048
- Robertson, E., Choudhury, V., Bhushan, S., and Walters, D. K. (2015). Validation of OpenFOAM Numerical Methods and Turbulence Models for Incompressible bluff Body Flows. *Comput. Fluids* 123, 122–145. doi:10.1016/j.compfluid.2015.09.010
- Taitel, Y., Sarica, C., and Brill, J. P. (2000). Slug Flow Modeling for Downward Inclined Pipe Flow: Theoretical Considerations. *Int. J. Multiphase Flow* 26 (5), 833–844. doi:10.1016/S0301-9322(99)00053-1
- Vallée, C., Höhne, T., Prasser, H.-M., and Sühnel, T. (2008). Experimental Investigation and CFD Simulation of Horizontal Stratified Two-phase Flow Phenomena. *Nucl. Eng. Des.* 238 (3), 637–646. doi:10.1016/j.nucengdes.2007.02.051
- Vallée, C., Lucas, D., Beyer, M., Pietruske, H., Schütz, P., and Carl, H. (2010). Experimental CFD Grade Data for Stratified Two-phase Flows. *Nucl. Eng. Des.* 240 (9), 2347–2356. doi:10.1016/j.nucengdes.2009.11.011
- Wang, X. (2006). *Investigation of Two-Phase and Multiphase Slug Flow in Horizontal Pipe and Multiphase Slug Flow and Ascending Pipe System*. China: Xi'an Jiaotong University. Doc.S.Dissertation.
- Yin, P., Zhang, P., Cao, X., Li, X., Li, Y., and Bian, J. (2022). Effect of SDBS Surfactant on Gas-Liquid Flow Pattern and Pressure Drop in Upward-Inclined Pipelines. *Exp. Therm. Fluid Sci.* 130, 110507. doi:10.1016/j.expthermflusci.2021.110507
- Zheng, G., Brill, J. P., and Taitel, Y. (1994). Slug Flow Behavior in a Hilly Terrain Pipeline. *Int. J. Multiphase Flow* 20 (1), 63–79. doi:10.1016/0301-9322(94)90006-X

Conflict of Interest: MD was employed by Qingdao Nuocheng Chemical Safety Technology Co., Ltd.

The remaining authors declare that the research was conducted in the absence of any commercial or financial relationships that could be construed as a potential conflict of interest.

Publisher's Note: All claims expressed in this article are solely those of the authors and do not necessarily represent those of their affiliated organizations, or those of the publisher, the editors and the reviewers. Any product that may be evaluated in this article, or claim that may be made by its manufacturer, is not guaranteed or endorsed by the publisher.

Copyright © 2021 Wu, Wang, Dong, Ge and Dong. This is an open-access article distributed under the terms of the Creative Commons Attribution License (CC BY). The use, distribution or reproduction in other forums is permitted, provided the original author(s) and the copyright owner(s) are credited and that the original publication in this journal is cited, in accordance with accepted academic practice. No use, distribution or reproduction is permitted which does not comply with these terms.



Optimization Design and Analysis of Single-Stage Mixed Refrigerant Liquefaction Process

Xiao Wu, Zhaoting Wang*, Xiaodong Dai, Quan Ge and Fei Liu

College of Oil and Gas Engineering, Shengli College China University of Petroleum, Dongying, China

OPEN ACCESS

Edited by:

Zheng Li,

Vanderbilt University, United States

Reviewed by:

Guojie Zhang,

Zhengzhou University, China

Yuan Sun,

Changzhou University, China

*Correspondence:

Zhaoting Wang

slxywuxiao@163.com

Specialty section:

This article was submitted to
Advanced Clean Fuel Technologies,
a section of the journal
Frontiers in Energy Research

Received: 29 August 2021

Accepted: 23 September 2021

Published: 29 October 2021

Citation:

Wu X, Wang Z, Dai X, Ge Q and Liu F
(2021) Optimization Design and
Analysis of Single-Stage Mixed
Refrigerant Liquefaction Process.
Front. Energy Res. 9:766588.
doi: 10.3389/fenrg.2021.766588

Small-scale natural gas liquefaction processes have several clear advantages, particularly in the exploitation of ‘unconventional’ natural gas (NG) from sources such as difficult-to-access and offshore gas fields. Moreover, conventional liquefaction processes have a number of disadvantages such as high energy consumption, large cooling loads required in the refrigeration cycle, and non-uniform matching of cold and hot flows in liquified natural gas (LNG) heat exchanger (HE). The main objective of this study was to optimize the most commonly used mixed refrigerant process. The liquefaction performance of the optimized process was analyzed and the influence of gas parameters on the power consumption, exergy loss, freezing mixture circulation, and cooling water load were investigated. The results show that compressor power consumption can be reduced by 29.8%, the cooling water load can be reduced by 21.3%, and the system exergy efficiency can be increased by 41% with the optimized process. Furthermore, throttling and compression of the freezing mixture were increased during the refrigeration stage. It can be concluded that reducing the feed gas temperature and increasing the feed gas pressure can reduce the total power consumption, exergy loss, freezing mixture circulation, and cooling water load, which can significantly improve liquefaction performance.

Keywords: liquefaction process, single-stage mixed refrigerant, process optimization, power consumption, exergy loss

INTRODUCTION

Global energy demand has rapidly increased over the past few decades and is expected to increase further in the coming years. Global energy consumption statistics show that the demand for oil is declining, and the search for alternative sources of energy is ushering in a golden age of natural gas (NG) (Wang Z. et al., 2020; Li et al., 2021). While natural gas is typically used in densely populated, economically developed areas, natural gas reserves are often located in remote areas, creating a regional imbalance between production and consumption regions. It is also worth noting that there are many operational challenges in transporting offshore natural gas to land (Cao and Bian, 2019; Zaitsev et al., 2020).

The specific volume of liquefied natural gas (LNG) is about 1/625 that of gaseous natural gas, which presents a considerable advantage in terms of the transportation, storage, and utilization of natural gas (He et al., 2019; Uwitonze et al., 2020). The LNG industry has developed rapidly around the world recently. Accordingly, the design and development of liquefaction processes are of significant importance, particularly small-scale NG liquefaction processes, which could offer significant value in the development of shale gas and coalbed methane, peak shaving of natural gas, and remote gas fields (Ikealumba and Wu, 2014). Various processes have been proposed for

natural gas liquefaction. Conventional processes include mixed refrigerant (MR) process (Lee and Moon, 2017; Ghorbani et al., 2018; Brodal et al., 2019; Primabudi et al., 2019), cascade process (Eiksund et al., 2018), and expander-based process (Song et al., 2017; Zhang et al., 2020). Among these, the MR process is the most commonly used (He et al., 2018). Recently, Bian et al. (Bian et al., 2018; Bian et al., 2019) investigated the feasibility of using supersonic separation technology in the field of natural gas liquefaction, which provides the possibility of save space and simplifying the liquefaction process, and applied this technology (Bian et al., 2020a; Bian et al., 2020b; Liu et al., 2021).

Thermodynamic parameters of the natural gas liquefaction process can be obtained through numerical simulations, then the process can be thermodynamically analyzed using appropriate evaluation methods and indicators. Mafi et al. (2009) established a thermodynamic model of the liquefaction process and adopted the coefficient of performance (COP) and exergy efficiency as evaluation indicators. To improve the efficiency of the proposed liquefaction process, Kanoglu et al. (2008) established an exergy balance equation for the equipment and calculated the exergy loss of the cascade liquefaction process. Moreover, Kanoglu et al. (Remelje and Hoadley, 2006) simulated various small-to medium-scale natural gas liquefaction processes and showed that the single-stage mixed refrigerant (SMR) process is a simple and efficient process and can be considered as an appropriate choice for small-to medium-sized liquefaction plants. Shukri and Barclay (2007) analyzed the characteristics of SMR and demonstrated that the SMR process is suitable for onshore and offshore liquefaction plants with capacities of less than 1.5×10^6 t/y and 1.2×10^6 t/y, respectively. Barclay and Denton (2005) compared offshore and onshore liquefaction plants and found that expansion refrigeration is an appropriate option for floating liquefaction plants.

Further investigations have revealed that there many significant parameters involved in natural gas liquefaction and the performances of liquefaction systems vary greatly with these parameters. Moreover, the freezing mixture composition and structure of the freezing mixture circulation system will affect the performance of the system. Accordingly, an optimization algorithm should be used to find the optimal process parameters and improve the performance of the liquefaction process. To address this, Angira and Santosh (2007) and Shah and Hoadley (2007) used numerical calculation methods to optimize the compression ratio. Nogal et al. (2008) and Lee et al. (2002) optimized the freezing mixture circulation process and compared liquefaction efficiencies and energy losses before and after optimization under different working conditions. Kamath et al. (2012) combined the internal equation of state code with a general algebraic modeling system (GAMS) and adopted nonlinear programming to optimize the SMR process. Wahl and Løvseth (2015) applied the sequential quadratic programming method to investigate the influence of the model formula on the SMR process optimization. Various aspects of the formula, including the optimization variables and their boundaries, internal node numbers, starting points, and derivative estimates, were studied. Tak et al. (2015) used a continuous reduced-order algorithm to optimize the SMR process and compared optimized

compression system structures. Pattison and Baldea (2015) proposed an equation-based pseudo-transient method for LNG process optimization to solve the problem of numerical failures that often occur with equation-oriented frameworks. Furthermore, Tak et al. (2018) used the enthalpy feasibility method to improve convergence of the enthalpy-temperature calculation. Watson et al. (2018) proposed a non-differentiable model based on the interior point algorithm for optimizing the SMR system. Wang X. et al. (2020) designed a new type of pre-cooled MR process for small-scale skid-mounted LNG equipment to reduce energy consumption and increase exergy efficiency.

Small-scale natural gas liquefaction processes have remarkable advantages such as high efficiency, excellent flexibility, and good adaptability (Primabudi et al., 2019). Meanwhile, they are easy to operate. Based on the distribution of natural gas resources in the world, small-scale LNG plants have broad development prospects (Ghorbani et al., 2018). Unconventional natural gas from remote gas fields, offshore gas fields, and shale gas can provide gas sources for small-to medium-sized liquefaction plants. These plants can be used as a basis for continuous production and natural gas peak shaving. However, existing small-to medium-scale liquefaction processes for natural gas have a number of limitations, including high energy consumption, large cooling loads of freezing mixture circulation devices, and so on (Lee and Moon, 2017). To solve these problems, in the present study, small-to medium-sized liquefaction processes were optimized with the aim of designing and optimizing the SMR liquefaction process to improve the overall performance of the liquefaction system. The influence of natural gas parameters on the total power consumption, total exergy loss, refrigerant circulation, and cooling water load were considered and the liquefaction performance of the optimized process was analyzed.

THERMODYNAMIC ANALYSIS MODEL

Energy Analysis Model

The performance of the optimized process was evaluated using steady-state models in Aspen HYSYS V10 software designed to serve many processing industries including natural gas liquefaction (AspenTech (2011). Aspen H, 2011). The system was thermodynamically analyzed in terms of energy conversion, transfer, and utilization considering the quantitative correlation of energy, including liquefaction rate, cooling capacity, power consumption, and specific power consumption calculation, which are described as follows.

(1) Liquefaction rate.

Liquefaction rate is the ratio of LNG produced by the liquefaction system to feed gas entering the system, and can be mathematically expressed as:

$$\varepsilon = \frac{n_{\text{LNG}}}{n} \times 100\% \quad (1)$$

where, ε , n_{LNG} , and n denote the liquefaction rate of the system, molar flow rate of LNG produced by the system, and molar flow rate of inlet feed gas, respectively.

(2) Cooling capacity.

In the natural gas liquefaction system, the refrigeration capacity is equal to the sum of heat from natural gas absorbed by the freezing mixture circulating in the heat exchanger (HE), regardless of the heat loss. Accordingly, the theoretical cooling capacity can be expressed in the following form:

$$Q_0 = H_{NG} - H_{LNG} \quad (2)$$

(3) Power consumption (W).

The power consumption is concentrated in the freezing mixture circulation unit and pressurization by the compressor and pump require an external source of energy. For liquefaction with an expander, the output power of the expander can be recycled during pressurization by the compressor. Therefore, when the power consumption of the compressor and pump (W_c) is greater than the output power of the expander (W_s), the total power consumption of the system is the difference between W_c and W_s . When $W_c < W_s$, the total power consumption of the system is 0.

The power consumption of the throttling refrigeration liquefaction process is equal to that of the compressor and pump:

$$W = W_c \quad (3)$$

Specific power consumption (W_n) is defined as the energy consumed to obtain 1 mole of LNG, which can be expressed as:

$$W_n = \frac{W}{n} \quad (4)$$

Exergy Analysis Model

Exergy refers to the maximum theoretical power that an entire system, composed of both the system and surroundings, can obtain when the system and the surroundings are in equilibrium (Moran et al., 2011). The specific exergy can be calculated using the following formula:

$$e_x = h - h_0 - T_0(s - s_0) \quad (5)$$

where, e_x is the unit mass exergy, h is the unit mass enthalpy, T is temperature, and s is entropy.

During the liquefaction process, sources of exergy loss include the expansion, heat exchange and power equipment. The specific exergy loss can be written as:

$$\Delta e_{x,loss} = (h - T_{0s})state2 - (h - T_{0s})state1 \quad (6)$$

The exergy utilization rate is used to measure the amount of exergy utilization in an open system, defined as the ratio of exergy utilization to total exergy. The amount of exergy utilization (E_u) is given by

$$E_u = E_{x,in} - E_{x,out} - \Delta E_{x,loss} \quad (7)$$

The total amount of exergy is:

$$E_{x,in} = \dot{m}_{in} e_{in} \quad (8)$$

where, m is the mass flow rate.

The outlet exergy of the liquefaction process is:

$$E_{x,out} = \dot{m}_{out} e_{out} + \dot{m}_{out} e_{out} \quad (9)$$

The exergy loss during the liquefaction process is:

$$\Delta E_{x,loss} = \sum m_i \Delta e_{x,loss} \quad (10)$$

The exergy utilization rate is:

$$\eta_e = E_u / E_{x,in} \quad (11)$$

where, η_e is the exergy utilization rate.

Equation of State

The EOS is the basis for calculating the thermal parameters. Here, the Peng-Robinson (P-R) EOS is selected (Robinson et al., 1985), given by:

$$p = RTv - b - av(v + b) + b(v - b) \quad (12)$$

where, p is pressure, R is the universal gas constant, v is molar volume, a is the attractive parameter, and b is effective molecular volume. Parameters a and b can be expressed in the following forms:

$$a = \sum \sum z_i z_j (a_i a_j) 0.5(1 - k_{ij}) \quad (13)$$

$$b = \sum z_i b_i \quad (14)$$

where, z is mole fraction for the component and k_{ij} is the binary interaction coefficient.

DESIGN AND OPTIMIZATION OF LIQUEFACTION PROCESS

Conventional SMR Liquefaction Process

The SMR liquefaction process consists of three units: a natural gas liquefaction unit, MRC unit, and LNG storage unit. A SMR model, including an LNG HE, throttle valve, freezing mixture compressor, and cooler, was established in HYSYS, as shown in **Figure 1**. In the NG liquefaction unit, purified natural gas (4.5 MPa, 30°C) initially enters the cryogenic HE to obtain liquefied natural gas. During this process, the temperature reaches -165°C, the pressure is reduced to 0.1 MPa through the throttle, and the product is sent to the LNG storage tank. **Table 1** shows that the freezing mixture in the cycle is composed of methane, ethane, propane, isobutane, and nitrogen. After pressurized cooling (4.3 MPa, 38°C), the freezing mixture enters the LNG HE, where it is cooled and liquefies. It is worth noting that freezing mixture flowing out of the LNG HE is in the pure liquid phase. The liquid freezing mixture is throttled to 0.5 MPa through throttle valve VLV-2, then flows back to the HE to provide the required cooling capacity. The freezing mixture absorbs heat and evaporates continuously in the HE. Finally, the freezing mixture flows out of the HE in the pure gas phase and goes back to the inlet of the compressor to complete the cycle.



Composition	CH ₄	C ₂ H ₆	C ₃ H ₈	i-C ₄ H ₁₀	N ₂
Mole fraction	0.29	0.19	0.21	0.15	0.16

Figure 2 shows the liquefaction process after optimization. Compared with the original liquefaction process, the optimized process presents as follows:

- (1) The pressurization system of the freezing mixture circulation is changed from one stage to three stages, and an intercooler is installed to reduce the energy loss of the compressor.
- (2) The one stage throttling refrigeration is replaced by two stages. Two sets of LNG HE are set up. Then the MR streams is divided into two parts. The heavy liquid phase provides the cooling capacity of the pre-cooling HE, while the light gas phase provides the cooling capacity of the main HE. This modification increases the degree of



TABLE 2 | Molar composition of the freezing mixture.

Composition	CH ₄	C ₂ H ₆	C ₃ H ₈	i-C ₄ H ₁₀	N ₂
Mole fraction	0.31	0.3	0.21	0.08	0.10

matching of flows with different temperature and ensures a uniform temperature difference in the HE.

- (3) The recombined freezing mixture is returned to the second-stage compressor to reduce the energy loss of the first-stage compressor.

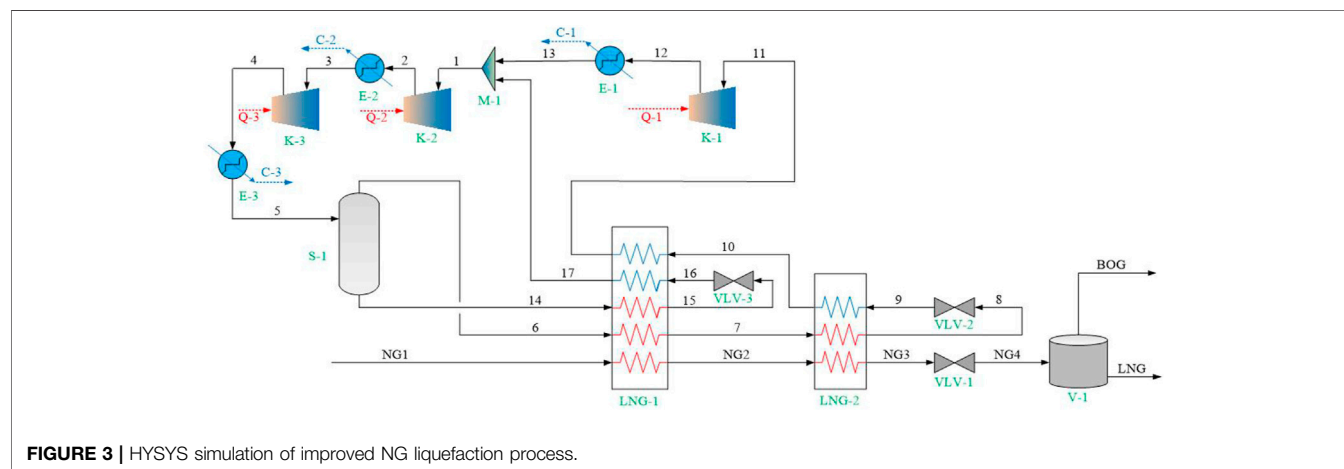
The parameters of the natural gas inlet and LNG storage are the same as those presented in *Conventional SMR Liquefaction Process*. For the single-cycle refrigeration system, the refrigeration temperature range of the freezing mixture is -165°C – -30°C . Moreover, a freezing mixture composed of nitrogen and light hydrocarbon components was selected in the simulation. **Table 2** presents the chemical composition of the freezing mixture.

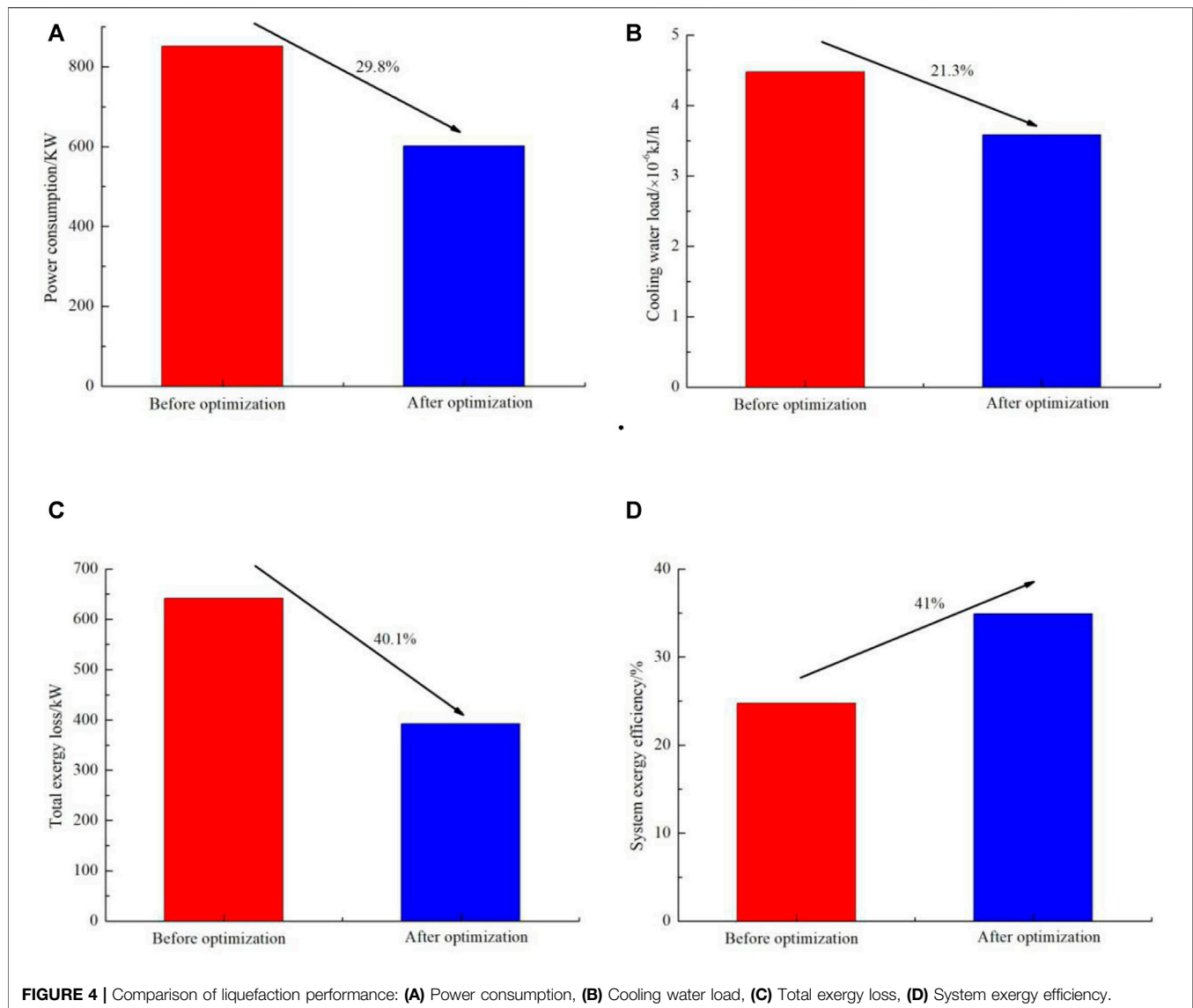
Figure 3 shows the established liquefaction process model in HYSYS. Two LNG HEs and three freezing mixture compressors were set up in the liquefaction process. Before entering the HE, the high-pressure freezing mixture was divided into two gas-liquid phases for cooling the pre-cooling HE and the main HE. Some of the freezing mixture from the pre-cooling HE flows back to the secondary compressor to reduce the pressurization load of the primary compressor. The P-R equation is used to calculate the physical properties of the natural gas and freezing mixture. In all calculations, the adiabatic efficiency of the compressor was set to 80% (Kwak et al., 2018). It is assumed that the material flow can achieve complete heat exchange in the LNG HE, the minimum heat exchange temperature difference is 2°C , and the outlet temperatures of the hot and cold flows are equal. Assuming that the heat loss of the HE is negligible and the pressure loss of the natural gas and freezing mixture in the HE was set to 20 kPa (Kochunni and Chowdhury, 2020). Moreover, it is assumed that there is no pressure loss in the equipment and pipelines except for the throttle valve (Abdul Qyyum et al., 2018). And the conversion

between electrical energy and mechanical energy is 100% (Ferreira et al., 2017).

In the natural gas liquefaction unit, pretreated natural gas (4.5 MPa , 30°C) enters the HE and flows through pre-cooling HE, where the gas temperature drops to -30°C after heat exchange with the freezing mixture. Then, the natural gas flows into the main HE for further cooling and liquefaction. After passing through the two-stage HE, the LNG temperature drops to -156.5°C and the LNG is in the supercooled state. Finally, the LNG is depressurized by throttle valve VLV-3 to maintain a certain supercooling degree and sent to the LNG storage tank.

The freezing mixture cycle unit can be divided into two parts: the freezing mixture heat exchange process and freezing mixture pressurization process. In the freezing mixture heat exchange process, after pressure cooling, high-pressure freezing mixture (5.2 MPa , 30°C) passes through the gas-liquid separator to form liquid-phase freezing mixture flow (17) and gas-phase freezing mixture flow (4). The liquid phase flow (17) is cooled to -30°C by the HE, then throttled by the throttle valve to reduce the temperature and pressure. Then, the freezing mixture flows back to the HE to provide the cooling capacity for precooling of the natural gas and freezing mixture, before finally returning to the secondary compressor. Gas-phase flow (4) is cooled by HE to realize liquefaction, then throttled by throttle valve to reduce its temperature and pressure and flows back to HE to provide the cooling capacity for liquefaction of the natural gas and freezing mixture, and finally returns to primary compressor. The pressurization process of freezing mixture includes three stages. In the first stage, low-pressure freezing mixture (stream 9) flows back to compressor at 0.4 MPa , then its pressure increases to 1.3 MPa after the first pressurization stage. The inter-stage cooler is downstream from the compressor and cool the freezing mixture (stream 10) to 35°C . Stream 10 and the medium pressure freezing mixture return stream 20 are fully mixed and then the mixture enters the second-stage compressor for pressurization. After two-stage compression, the freezing mixture pressure is increased to 2.6 MPa and the high-pressure freezing mixture is cooled to 30°C and enters the freezing mixture heat exchange process.

**FIGURE 3** | HYSYS simulation of improved NG liquefaction process.



PERFORMANCE OF IMPROVED LIQUEFACTION PROCESS

Energy Consumption Analysis

Figure 4 shows the system performance parameters of the optimized NG liquefaction process. The freezing mixture circulation capacity of the improved liquefaction system and the total power consumption are 320.8 kmol/h and 602.0 kW, respectively. Moreover, the specific power consumption and cooling water load are 21.92 kJ/h and 3.59×10^6 kJ/h, respectively. Compared with the conventional SMR liquefaction process, the compressor power consumption decreased by 29.8%, the cooling water load decreased by 21.3%, and the system exergy efficiency increased by 41% when the throttling stage and compression stage were adopted. Based on the analysis, it can be concluded that the performance of the optimized liquefaction system was significantly improved.

Influence of Gas Source Temperature on System Performance

The enthalpy value at the inlet of the liquefaction system varies with the gas source temperature, cooling load in the HE, and freezing mixture circulation rate. The influence of gas source temperature, varying from 5°C to 50°C, on the total power consumption, total exergy loss, freezing mixture circulation capacity, and cooling water load of the process with a source pressure of 4.5 MPa, LNG storage pressure of 0.1 MPa, and temperature of -163.3°C was studied. The results are presented in Figures 5, 6.

As the gas source temperature increases, the total power consumption, total power loss, freezing mixture circulation capacity, and cooling water load of the system increase. When the gas source temperature increases from 5°C to 50°C, the total power consumption of the system increases from 563.2 to 601.8 kW, the total power loss increases from 360.44 to 394.26 kW, the freezing mixture circulation capacity increases

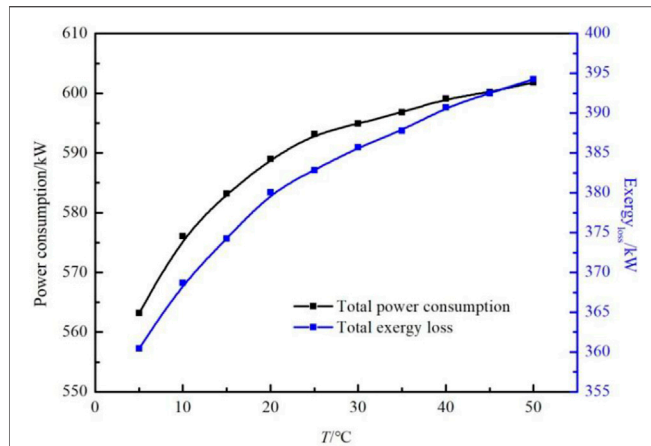


FIGURE 5 | Influence of natural gas pressure on power consumption and exergy loss of the system.

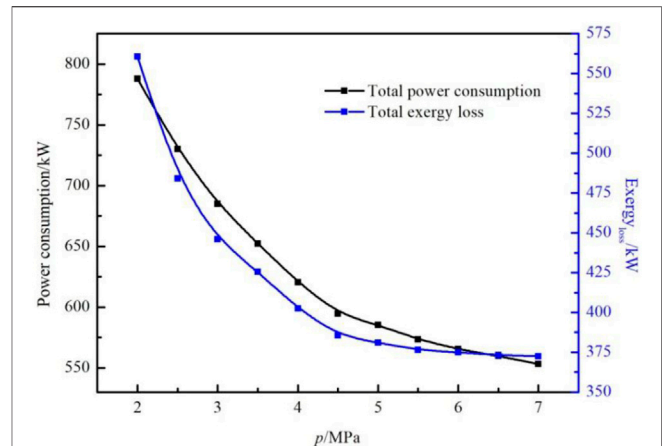


FIGURE 7 | Influence of natural gas pressure on power consumption and exergy loss of the system.

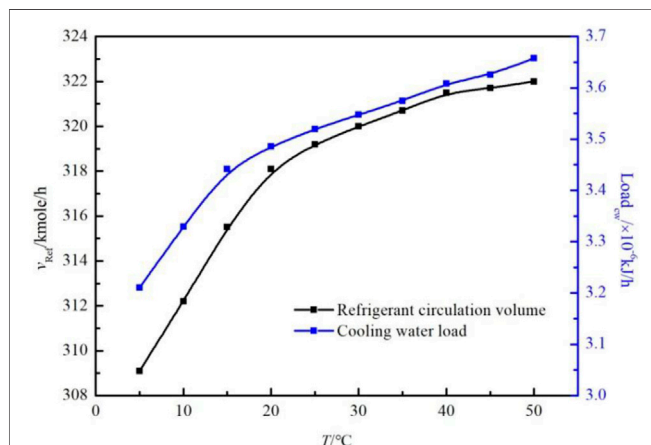


FIGURE 6 | Influence of natural gas pressure on freezing mixture circulation capacity and cooling water load of the system.

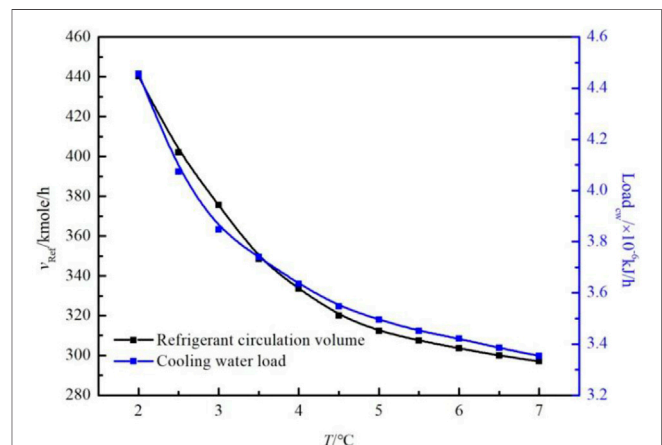


FIGURE 8 | Influence of natural gas pressure on freezing mixture circulation rate and cooling water load of the system.

from 309.1 kmol/h to 322.5 kmol/h, and the cooling water load increases from 3.21 kJ/h to 3.66 kJ/h. This is because when the inlet gas temperature increases, the enthalpy of the inlet gas increases, resulting in an increase in the enthalpy difference between the inlet and outlet gas in the liquefaction process, thereby increasing the required cooling capacity for liquefaction. The required cooling capacity is provided by the freezing mixture circulation. Assuming that the product of heat transfer area and heat transfer coefficient (UA) remains constant, the increase in refrigeration capacity will increase the freezing mixture circulation capacity, leading to an increase in compressor power consumption and cooling water load, and irreversibility of the system. Under these conditions, the total power consumption and total exergy loss increase.

Influence of Gas Source Pressure on System Performance

The effects of gas source pressure, varying from 2.0 to 7.0 MPa, on the total power consumption, total exergy loss, freezing mixture

circulation, and cooling water load of the process with a gas source temperature of 30°C, LNG storage pressure of 0.1 MPa, and temperature of −163.3°C was studied. The results are presented in **Figures 7, 8**.

As the gas source pressure increases, the total power consumption, total exergy loss, freezing mixture circulation, and cooling water load decrease. The rate of decrease is high when the pressure varies from 2.0 to 4.5 MPa, whereas the rate of variation is gentle when the pressure varies from 4.5 to 7.0 MPa. As the gas source pressure increases from 2.0 to 7.0 MPa, the total power consumption of the system decreases from 788.7 to 553.2 kW, the total exergy loss decreases from 560.58 to 372.54 kW, the freezing mixture circulation quantity decreases from 440.2 kmol/h to 297.1 kmol/h, and the cooling water load decreases from 4.46 kJ/h to 3.25 kJ/h. This is because when the inlet gas pressure increases, the enthalpy of the natural gas decreases, while the state parameters of the produced LNG almost remain constant such that the enthalpy does not change. Therefore, a higher gas source pressure decreases the enthalpy difference in

natural gas at the inlet and outlet of the liquefaction system (H_{NG} - H_{LNG}). Accordingly, the required cooling capacity of the natural gas liquefaction decreases. Based on this analysis, it can be concluded that the heat load of the refrigeration cycle decreases as the source gas pressure increases since the UA value of the HE remains constant while cooling capacity decreases. Consequently, the freezing mixture circulation capacity is reduced, thereby reducing the power consumption of the compressor and the cooling water load. Accordingly, the total power consumption and total exergy loss decrease.

CONCLUSION

In the present study, a steady-state model of the SMR liquefaction process was established. Mathematical modeling and numerical simulations were carried out in HYSYS and the thermodynamic performance of the system was analyzed. Furthermore, the structure of the conventional liquefaction process was optimized by setting the throttling stage of the freezing mixture and the compression stage of the refrigeration cycle. The freezing mixture circulation capacity of the improved liquefaction system and the total power consumption were 320.8 kmol/h and 602.0 kW, respectively. Moreover, the specific power consumption and the cooling water load were 21.92 kJ/h and 3.59×10^6 kJ/h, respectively. Compared with the conventional SMR liquefaction process, the compressor power consumption was reduced by 29.8%, the cooling water load decreased by 21.3%, and the system exergy efficiency increased by 41% in the optimized process.

The effects of gas source parameters on the total power consumption, total exergy loss, freezing mixture circulation, and cooling water load of the improved liquefaction process were analyzed. The feed gas temperature was found to be positively correlated with total power consumption, freezing

mixture circulation, and cooling water load. In contrast, feed gas pressure is negatively correlated with these parameters. Therefore, decreasing the feed gas temperature and increasing the feed gas pressure within a reasonable range can improve the performance of the liquefaction system.

In the next research, The liquefaction process will continue to be optimized for the purpose of saving land occupation, and the unit energy consumption, exergy efficiency and performance coefficient of the process will be calculated and compared, and the adaptability of the process at offshore will be analyzed].

DATA AVAILABILITY STATEMENT

The original contributions presented in the study are included in the article/supplementary material, further inquiries can be directed to the corresponding author.

AUTHOR CONTRIBUTIONS

XW designed the research scheme and wrote the paper; ZW proposed the topic of the article and designed the framework of the paper; XD is responsible for sorting out documents and revising papers; QG provided research funds; FL conducted the final review of the paper.

FUNDING

This work was supported by the Youth Innovation Team Science and Technology Development Program of Shandong Province Higher Educational Institutions (2019KJA024) and Science Development Funding Program of Dongying of China (DJ2020009).

REFERENCES

- Abdul Qyum, M., Qadeer, K., and Lee, M. (2018). Closed-Loop Self-Cooling Recuperative N₂ Expander Cycle for the Energy Efficient and Ecological Natural Gas Liquefaction Process. *ACS Sust. Chem. Eng.* 6, 5021–5033. doi:10.1016/10.1021/acssuschemeng.7b04679
- Angira, R., and Santosh, A. (2007). Optimization of Dynamic Systems: A Trigonometric Differential Evolution Approach. *Comput. Chem. Eng.* 31, 1055–1063. doi:10.1016/j.compchemeng.2006.09.015
- AspenTech (2011). *Aspen HYSYS User Guides*. V7. 3 edition. Burlington (MA, USA).
- Barclay, M., and Denton, N. (2005). Selecting Offshore LNG Processes. *LNG J.* 10, 34–36.
- Bian, J., Cao, X., Yang, W., Edem, M. A., Yin, P., and Jiang, W. (2018). Supersonic Liquefaction Properties of Natural Gas in the Laval Nozzle. *Energy* 159, 706–715. doi:10.1016/j.energy.2018.06.196
- Bian, J., Cao, X., Yang, W., Gao, S., and Xiang, C. (2020). A New Liquefaction Method for Natural Gas by Utilizing Cold Energy and Separating Power of Swirl Nozzle. *Aiche J.* 66, 16811. doi:10.1002/aic.16811
- Bian, J., Cao, X., Yang, W., Guo, D., and Xiang, C. (2020). Prediction of Supersonic Condensation Process of Methane Gas Considering Real Gas Effects. *Appl. Therm. Eng.* 164, 114508. doi:10.1016/j.applthermaleng.2019.114508
- Bian, J., Cao, X., Yang, W., Song, X., Xiang, C., and Gao, S. (2019). Condensation Characteristics of Natural Gas in the Supersonic Liquefaction Process. *Energy* 168, 99–110. doi:10.1016/j.energy.2018.11.102
- Brodal, E., Jackson, S., and Eiksund, O. (2019). Performance and Design Study of Optimized LNG Mixed Fluid Cascade Processes. *Energy* 189, 116207. doi:10.1016/j.energy.2019.116207
- Cao, X., and Bian, J. (2019). Supersonic Separation Technology for Natural Gas Processing: A Review. *Chem. Eng. Process. - Process Intensification* 136, 138–151. doi:10.1016/j.cep.2019.01.007
- Eiksund, O., Brodal, E., and Jackson, S. (2018). Optimization of Pure-Component LNG cascade Processes with Heat Integration. *Energies* 11, 202. doi:10.3390/en11010202
- Ferreira, P. A., Catarino, I., and Vaz, D. (2017). Thermodynamic Analysis for Working Fluids Comparison in Rankine-type Cycles Exploiting the Cryogenic Exergy in Liquefied Natural Gas (LNG) Regasification. *Appl. Therm. Eng.* 121, 887–896. doi:10.1016/j.applthermaleng.2017.04.082
- Ghorbani, B., Shirmohammadi, R., Mehrpooya, M., and Hamed, M.-H. (2018). Structural, Operational and Economic Optimization of Cryogenic Natural Gas Plant Using NSGAII Two-Objective Genetic Algorithm. *Energy* 159, 410–428. doi:10.1016/j.energy.2018.06.078
- He, T., Chong, Z. R., Zheng, J., Ju, Y., and Ling, P. (2019). LNG Cold Energy Utilization: Prospects and Challenges. *Energy* 170, 557–568. doi:10.1016/j.energy.2018.12.170

- He, T., Karimi, I. A., and Ju, Y. (2018). Review on the Design and Optimization of Natural Gas Liquefaction Processes for Onshore and Offshore Applications. *Chem. Eng. Res. Des.* 132, 89–114. doi:10.1016/j.cherd.2018.01.002
- Ikealumba, W. C., and Wu, H. (2014). Some Recent Advances in Liquefied Natural Gas (LNG) Production, Spill, Dispersion, and Safety. *Energy Fuels* 28, 3556–3586. doi:10.1021/ef500626u
- Kamath, R. S., Biegler, L. T., and Grossmann, I. E. (2012). Modeling Multistream Heat Exchangers with and without Phase Changes for Simultaneous Optimization and Heat Integration. *Aiche J.* 58, 190–204. doi:10.1002/aic.12565
- Kanoglu, M., Dincer, I., and Rosen, M. A. (2008). Performance Analysis of Gas Liquefaction Cycles. *Int. J. Energ. Res.* 32, 35–43. doi:10.1002/er.1333
- Kochunni, S. K., and Chowdhury, K. (2020). Zero Methane Loss in Reliquefaction of Boil-Off Gas in Liquefied Natural Gas Carrier Ships by Using Packed Bed Distillation in Reverse Brayton System. *J. Clean. Prod.* 260, 121037. doi:10.1016/j.jclepro.2020.121037
- Kwak, D.-H., Heo, J.-H., Park, S.-H., Seo, S.-J., and Kim, J.-K. (2018). Energy-efficient Design and Optimization of Boil-Off Gas (BOG) Re-liquefaction Process for Liquefied Natural Gas (LNG)-fuelled Ship. *Energy* 148, 915–929. doi:10.1016/j.energy.2018.01.154
- Lee, G. C., Smith, R., and Zhu, X. X. (2002). Optimal Synthesis of Mixed-Refrigerant Systems for Low-Temperature Processes. *Ind. Eng. Chem. Res.* 41, 5016–5028. doi:10.1021/ie020057p
- Lee, I., and Moon, I. (2017). Economic Optimization of Dual Mixed Refrigerant Liquefied Natural Gas Plant Considering Natural Gas Extraction Rate. *Ind. Eng. Chem. Res.* 56, 2804–2814. doi:10.1021/acs.iecr.6b04124
- Li, Y., Wang, Y., Wang, Q., Liu, Z., Tang, L., Liang, L., et al. (2021). Achieving the Super Gas-Wetting Alteration by Functionalized Nano-Silica for Improving Fluid Flowing Capacity in Gas Condensate Reservoirs. *ACS Appl. Mater. Inter.* 13, 10996–11006. doi:10.1021/acsami.0c22831
- Liu, Y., Cao, X., Yang, J., Li, Y., and Bian, J. (2021). Energy Separation and Condensation Effects in Pressure Energy Recovery Process of Natural Gas Supersonic Dehydration. *Energ. Convers. Manag.* 245, 114557. doi:10.1016/j.enconman.2021.114557
- Mafi, M., Amidpour, M., and Mousavi Naeynian, S. M. (2009). Comparison of Low Temperature Mixed Refrigerant Cycles for Separation Systems. *Int. J. Energ. Res.* 33, 358–377. doi:10.1002/er.1480
- Moran, M. J., Shapiro, H. N., Boettner, D. D., and Bailey, M. B. (2011). *Fundamentals of Engineering Thermodynamics*. Seventh ed. NJ: John Wiley & Sons.
- Nogal, F. D., Kim, J.-K., Perry, S., and Smith, R. (2008). Optimal Design of Mixed Refrigerant Cycles. *Ind. Eng. Chem. Res.* 47, 8724–8740. doi:10.1021/ie800515u
- Pattison, R. C., and Baldea, M. (2015). Multistream Heat Exchangers: Equation-Oriented Modeling and Flowsheet Optimization. *Aiche J.* 61, 1856–1866. doi:10.1002/aic.14766
- Primabudi, E., Morosuk, T., and Tsatsaronis, G. (2019). Multi-objective Optimization of Propane Pre-cooled Mixed Refrigerant (C3MR) LNG Process. *Energy* 185, 492–504. doi:10.1016/j.energy.2019.07.035
- Remelje, C., and Hoadley, A. (2006). An Exergy Analysis of Small-Scale Liquefied Natural Gas (LNG) Liquefaction Processes. *Energy* 31, 2005–2019. doi:10.1016/j.energy.2005.09.005
- Robinson, D. B., Peng, D.-Y., and Chung, S. Y.-K. (1985). The Development of the Peng - Robinson Equation and its Application to Phase Equilibrium in a System Containing Methanol. *Fluid Phase Equilibria* 24, 25–41. doi:10.1016/0378-3812(85)87035-7
- Shah, N. M., and Hoadley, A. F. A. (2007). A Targeting Methodology for Multistage Gas-phase Auto Refrigeration Processes. *Ind. Eng. Chem. Res.* 46, 4497–4505. doi:10.1021/ie060868j
- Shukri, T., and Barclay, M. (2007). Single Mixed Refrigerant Process Has Appeal for Growing Offshore Market. *LNG J.* 7, 35–37.
- Song, R., Cui, M., and Liu, J. (2017). Single and Multiple Objective Optimization of a Natural Gas Liquefaction Process. *Energy* 124, 19–28. doi:10.1016/j.energy.2017.02.073
- Tak, K., Kwon, H., Park, J., Cho, J. H., and Moon, I. (2018). A Multistream Heat Exchanger Model with Enthalpy Feasibility. *Comput. Chem. Eng.* 115, 81–88. doi:10.1016/j.compchemeng.2018.03.023
- Tak, K., Lee, I., Kwon, H., Kim, J., Ko, D., and Moon, I. (2015). Comparison of Multistage Compression Configurations for Single Mixed Refrigerant Processes. *Ind. Eng. Chem. Res.* 54, 9992–10000. doi:10.1021/acs.iecr.5b00936
- Uwitonze, H., Hwang, K. S., and Lee, I. (2020). Improving NGL Recovery Process with Dividing-wall Column for Offshore Applications. *Chem. Eng. Process. - Process Intensification* 147, 107747. doi:10.1016/j.ccep.2019.107747
- Wahl, P. E., and Løvseth, S. W. (2015). Formulating the Optimization Problem when Using Sequential Quadratic Programming Applied to a Simple LNG Process. *Comput. Chem. Eng.* 82, 1–12. doi:10.1016/j.compchemeng.2015.06.003
- Wang, X., Li, M., Cai, L., and Li, Y. (2020). Propane and Iso-Butane Pre-cooled Mixed Refrigerant Liquefaction Process for Small-Scale Skid-Mounted Natural Gas Liquefaction. *Appl. Energy* 275, 115333. doi:10.1016/j.apenergy.2020.115333
- Wang, Z., Han, F., Ji, Y., and Li, W. (2020). Analysis on Feasibility of a Novel Cryogenic Heat Exchange Network with Liquid Nitrogen Regeneration Process for Onboard Liquefied Natural Gas Reliquefaction. *Case Stud. Therm. Eng.* 22, 100760. doi:10.1016/j.csite.2020.100760
- Watson, H. A. J., Vikse, M., Gundersen, T., and Barton, P. I. (2018). Optimization of Single Mixed-Refrigerant Natural Gas Liquefaction Processes Described by Nondifferentiable Models. *Energy* 150, 860–876. doi:10.1016/j.energy.2018.03.013
- Zaitsev, A., Mehrpooya, M., Ghorbani, B., Sanavbarov, R., Naumov, F., and Shermatova, F. (2020). Novel Integrated Helium Extraction and Natural Gas Liquefaction Process Configurations Using Absorption Refrigeration and Waste Heat. *Int. J. Energ. Res.* 44, 6430–6451. doi:10.1002/er.5377
- Zhang, J., Meerman, H., Benders, R., and Faaij, A. (2020). Technical and Economic Optimization of Expander-Based Small-Scale Natural Gas Liquefaction Processes with Absorption Precooling Cycle. *Energy* 191, 116592. doi:10.1016/j.energy.2019.116592

Conflict of Interest: The authors declare that the research was conducted in the absence of any commercial or financial relationships that could be construed as a potential conflict of interest.

Publisher's Note: All claims expressed in this article are solely those of the authors and do not necessarily represent those of their affiliated organizations, or those of the publisher, the editors and the reviewers. Any product that may be evaluated in this article, or claim that may be made by its manufacturer, is not guaranteed or endorsed by the publisher.

Copyright © 2021 Wu, Wang, Dai, Ge and Liu. This is an open-access article distributed under the terms of the Creative Commons Attribution License (CC BY). The use, distribution or reproduction in other forums is permitted, provided the original author(s) and the copyright owner(s) are credited and that the original publication in this journal is cited, in accordance with accepted academic practice. No use, distribution or reproduction is permitted which does not comply with these terms.

NOMENCLATURE

a attractive parameter
 b effective molecular volume
 E_u amount of exergy utilization
 E_x total amount of exergy
 e_x unit mass exergy
 h unit mass enthalpy
 k_{ij} binary interaction coefficient
 n molar flow rate of inlet feed gas
 n_{LNG} molar flow rate of LNG produced by the system
 p pressure
 R universal gas constant
 s entropy
 T temperature
 v molar volume
 W power consumption

W_c power consumption of the compressor and pump
 W_n Specific power consumption
 W_s output power of the expander
 z mole fraction for the component

Greek Characters

ε liquefaction rate of the system
 η_e exergy utilization rate

Abbreviation

COP coefficient of performance
 GAMS general algebraic modeling system
 HE heat exchanger
 LNG liquified natural gas
 MR mixed refrigerant
 NG natural gas
 SMR single-stage mixed refrigerant
 UA heat transfer area and heat transfer coefficient



Transient Heat Transfer Characteristics of Twisted Structure Heated by Exponential Heat Flux

Li Wang* and Qiusheng Liu

School of Mechanical Engineering, Nantong University, Nantong, China

OPEN ACCESS

Edited by:

Xuwen Cao,
China University of Petroleum (East
China), China

Reviewed by:

Qunqing Lin,
Nanjing University of Science and
Technology, China
Wenlei Lian,
Nanjing University of Aeronautics and
Astronautics, China
Yantao Li,
Dalian Maritime University, China

*Correspondence:

Li Wang
wang1988@ntu.edu.cn

Specialty section:

This article was submitted to
Advanced Clean Fuel Technologies,
a section of the journal
Frontiers in Energy Research

Received: 07 September 2021

Accepted: 05 October 2021

Published: 15 November 2021

Citation:

Wang L and Liu Q (2021) Transient
Heat Transfer Characteristics of
Twisted Structure Heated by
Exponential Heat Flux.
Front. Energy Res. 9:771900.
doi: 10.3389/fenrg.2021.771900

This study was conducted to investigate the transient heat transfer characteristics of a twisted structure. The twisted structure was heated according to exponential function ($Q = Q_0 \times \exp(t/\tau)$, where Q_0 is the initial heat generation rate, W/m^3 ; t is time, s; and τ is the period of heat generation rate). A wide range of τ from 37 ms to 14 s was applied for the experimental study. A platinum plate with five pitches (each was 180° twisted with 20 mm in length) was used in the experiment. Helium gas with inlet temperature of 298 K under 500 kPa was used as the coolant. The heat transfer coefficient is found to increase with the decrease of τ , and the transition point was estimated to be at $\tau \approx 1$ s, which means that, when the increasing ratio of heat generation rate satisfies $\frac{dQ}{dt} \geq Q_0 \cdot e^t$, the heat transfer enhancement phenomenon will be observed. The response analysis for transient heat transfer at fluid-solid interface was conducted by applying the concept of penetration depth. It is considered that, when the penetration depth is smaller than the thermal boundary thickness, the heat transfer from the interface (wall surface) to the fluid domain is not fully developed during the disturbance.

Keywords: exponential heat flux, twisted plate, transient heat transfer, forced convection, heat transfer enhancement

1 INTRODUCTION

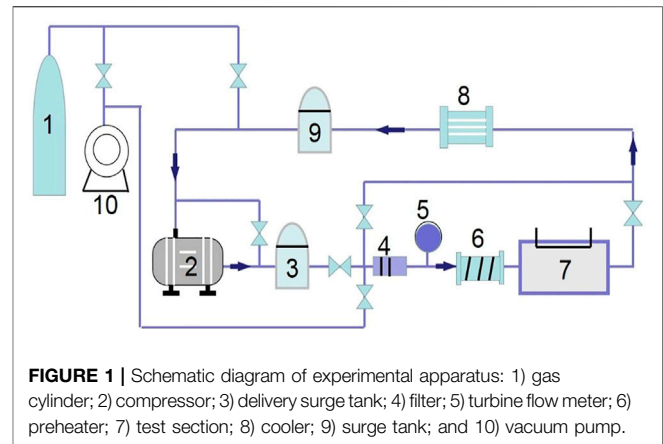
Heat transfer enhancement technology is of great importance in industries, such as power generation industry, chemical industry, and automotive. Researchers have been committed to increase heat transfer coefficients in all types of heat exchange equipment. Detailed surveys of enhancement techniques have been made by Patil and Farkade (2016), Menni et al. (2019), Suri et al. (2018), etc. Among all these techniques, twisted tape can change the flow pattern in a channel, reduce thickness of the boundary layer, and increase the heat transfer area. Thus, many research studies focused on the flow, and heat transfer characteristics for tube with twisted inserts have been carried out.

Abbreviations: c_p , specific heat of test heater [$J/(kg \cdot K)$]; c_p , specific heat of helium gas [$J/(kg \cdot K)$]; D , diameter of the circular channel [m]; g , gravitational acceleration [m/s^2]; h , heat transfer coefficient [$W/(m^2 \cdot K)$]; k , thermal conductivity [$W/(m \cdot K)$]; p , static pressure [Pa]; Pr , Prantl number; Q , heat generation rate per unit volume [W/m^3]; Q_0 , initial heat generation rate [W/m^3]; q , heat flux [W/m^2]; T , temperature [K]; T_a , average temperature of the heater [K]; T_f , fluid temperature at point F [K]; T_s , temperature of the solid tape at point S [K]; T_{wa} , average temperature of wall surface [K]; ΔT , temperature difference, $\Delta T = T_{wa} - T_\infty$ [K]; t , time [s]; U , inlet velocity [m/s]; X , coordinate along the axis of the plate [m]; Y , coordinate along the width of the plate [m]; Z , coordinate along the thickness of the plate [m]; δ , plate (heater) thickness [m]; δ_p , penetration depth [m]; δ_t , the time period of the disturbance [s]; μ , molecular viscosity [$kg/(m \cdot s)$]; ρ , density of helium gas [kg/m^3]; τ , period of heat generation rate or e-fold time [s]; τ_T , period of surface temperature curve or e-fold time [s].

Manglik and Bergles (1993a) and Manglik and Bergles (1993b) obtained empirical correlations from wide experimental conditions for isothermal tubes with twisted tape as inserts. Saha et al. (2001) conducted experimental study for regularly spaced twisted tape-induced laminar tube flow with uniform heat flux (UHF), and the effect of tape width was discussed. Man et al. (2017) experimentally studied the heat transfer and friction characteristics of dual-pipe heat exchanger with alternation of clockwise and counterclockwise twisted tape. They suggest that this shape of twisted tape has an advantage in heat transfer enhancement over the typical twisted tapes. Kumar and Layek. (2018) studied the effect of twisted rib over the absorber plate of solar air heater with a maximum enhancement for heat propagation and friction factor to be 2.58 and 1.78 times that of smooth surface, respectively. Ponnada et al. (2019) compared the thermal performance of a circular tube with twisted tapes, perforated twisted tapes, and perforated twisted tapes with alternate axis. Most of the works deal with tubes or ducts with twisted tape as inserts and study the heat transfer enhancement effect with uniform wall temperature (UWT) or UHF boundary conditions. Few studies have focused on the twisted plate itself.

Forced convection process with transient heating boundary is much more complex than the UWT or UHF boundary conditions due to the thermal response behavior in the thermal boundary layer. Cess (1961), Riley (1963), and Cotta and Özişik (1986) analytically studied the thermal response of an unsteady laminar boundary layer on a flat plate due to step changes in wall temperature and wall heat flux. These studies have been made for the case in which the velocity field is independent of time. The solution of energy equation generally adopts the energy integral equation or use similarity variables to reduce the mathematical difficulties. Khaled (2012) compared the heat transfer enhancement in laminar channel flow with four kinds of heat flux distributions: periodic step, periodic sinusoidal, linear, and exponential distribution. It was found that the maximum heating source excess temperature for the case with exponential heat flux is at most of about 22.4% lower than that with UHF over the boundary. This work proves that, with a proper heat flux distribution, additional heat can be transferred under same maximum temperatures. Hata and Masuzaki (2011) studied the tube flow with twisted tape as inserts. Exponentially increasing heat generation rate was added to the tube, and the transient heat transfer coefficient of the tube was analyzed. In our previous research, Liu et al. (2008), Liu et al. (2014), and Liu et al. (2017) experimentally studied the transient heat transfer process for parallel flow of helium gas over a horizontal cylinder and a flat plate. An exponential increasing heat generation rate was applied for the transient heating condition. The flow and heat transfer parameters on transient heat transfer were investigated under wide experimental conditions.

This study is aimed to investigate the transient heat transfer phenomena of a twisted plate. Exponentially increasing heat generation rate ($Q = Q_0 \cdot \exp(t/\tau)$, where Q_0 is the initial heat generation rate, W/m^2 ; t is time, s; and τ is the period of heat generation rate) with different increasing rates (represented by τ , a smaller τ means a higher increasing rate) was applied for the



twisted plate. The time-dependent heat flux, surface temperature, and heat transfer coefficient were measured for the twisted plate. The effect of the increasing rate of heat flux on transient heat transfer was obtained with Reynolds number ranged from 8,000 to 30,000. Effect of the twisted structure on heat transfer enhancement was discussed by comparing the experimental results with published empirical correlations for tubes, plates, and tubes with twisted inserts.

2 EXPERIMENTAL STUDY

2.1 Experimental Apparatus

The experimental apparatus consisted of gas cylinder (1), compressor (2), surge tanks (3) (9), preheater (6), cooler (8), vacuum pump (10), and the test section (7), as shown in **Figure 1** (Liu et al., 2014). The flow direction of the coolant (helium gas) is shown by arrows. A vacuum pump was used to degas the main flow loop and other branches. Helium gas was circulated by a compressor, and the fluctuations of gas flowing and pressure caused by compressor were removed with the high-capacity surge tanks that are set at both inlet and outlet of the compressor. The helium gas inside the loop was cooled by a cooler after the exit of the test section. A preheater was set before the gas flows into the test section to ensure the inlet temperature. The flow rate in the test section was measured with the turbine meter, and the system pressure was measured with a pressure transducer. The temperature of the gas at the exit of turbine flow meter and in the test section was measured by K-type thermocouples with a precision of ± 1 K.

The test heater was mounted horizontally along the center axis of the circular test channel, which is made of stainless steel with inside diameter of 20 mm, as shown in **Figure 2** (Liu et al., 2014). A twisted tape with five pitches (each was 180° twisted with 20 mm in length) was used in the experiment. It was made from a platinum plate with thickness of 0.1 mm and width of 4 mm. The ends of twisted tape were connected to two copper plates and then connected to two copper electrodes. Two fine platinum wires (50 μm in diameter) were spot welded to the end parts of the twisted plate as potential conductors. The length between the potential taps is defined as the effective length on which transient heat transfer was measured.

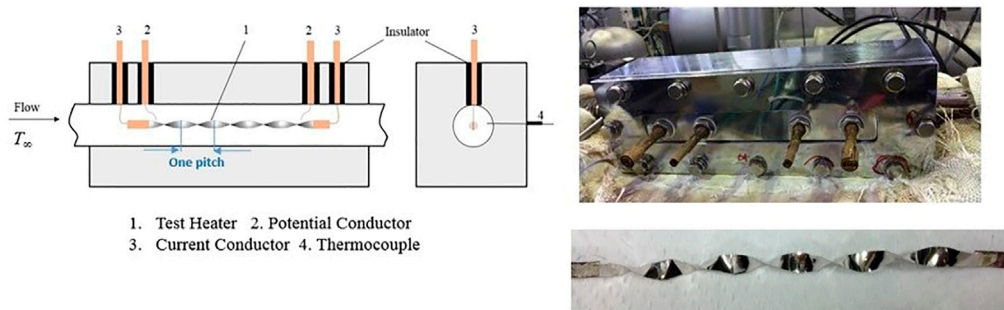


FIGURE 2 | The test section: 1) test heater; 2) potential conductor; 3) current conductor; 4) thermocouple.

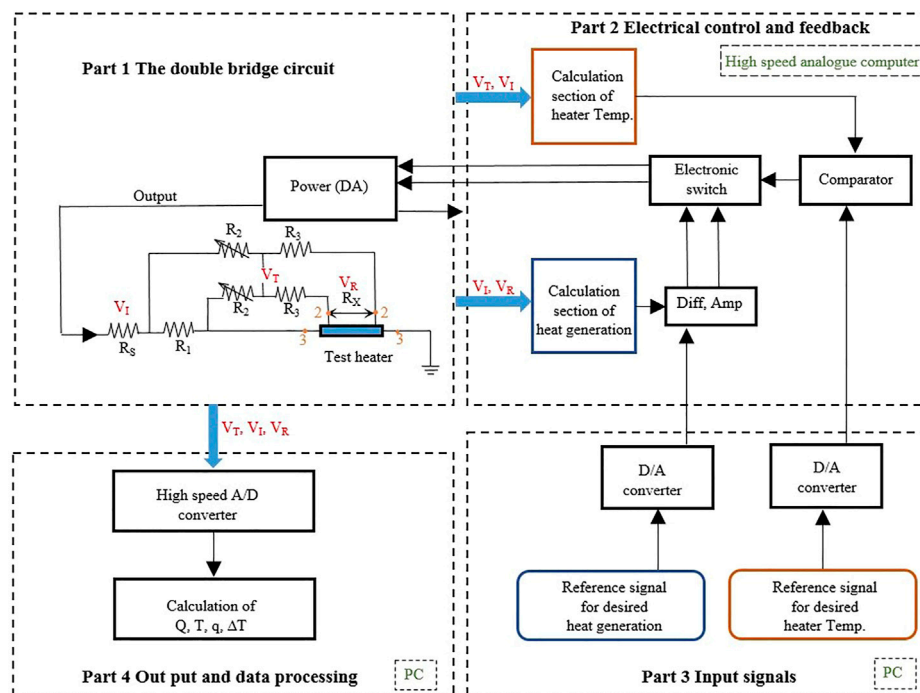


FIGURE 3 | Electrical control and measurement circuit.

The twisted plate was heated by the direct current from a power source. The heat generation rate of the plate was controlled and measured by electrical control and measurement circuit. A total of four parts, namely, the double bridge circuit, the electrical control and feedback part, the signal input part, and the output data processing part, were built with connections. The double bridge circuit (also called Kelvin bridge or Kelvin double bridge) was applied to measure the resistance of the test heater to obtain the average temperature of the test heater on the basis of a calibrated temperature-resistance correlation. A high-speed analog computer was applied in part 2 to support a rapid and precise calculation-feedback process for the heat generation and heater temperature control. While the signal input and output data processing were fulfilled with a personal computer (PC) (Figure 3) (Liu et al., 2014).

2.2 Experimental Method and Procedure

The experiment was conducted with the following procedure.

Before the twisted plate was installed into the test section, a calibration for temperature-resistance correlation was completed in a thermostat, with the calibration range for room temperature of up to 150°C. A calibrated correlation for the test heater was obtained.

Next, the test heater was installed horizontally along the axis of the test section with both ends connected to two copper plates and then connected to the double bridge branch. Two fine platinum wires (50 μm in diameter) were spot welded close to the end parts of the twisted plate as potential conductors and then connected to the double bridge branch.

Then, the helium gas (99.9% purity) was filled to the test loop and maintained at a certain pressure after the test loop being

TABLE 1 | Experimental conditions.

Test fluid	Helium gas
Helical pitch (H)	20 mm
Pitch numbers	5
Total length	106.4 mm
Plate width (W)	4 mm
Gas temperature	298 K
System pressure	500 kPa
Period of heat generation rate	37 ms~14 s
Flow velocity	4~10 m/s
Reynolds number	8,000~25,000

degassed by a vacuum pump. A piston compressor was used to circulate the flow in the test loop. There are two bypass branches for the test loop: one is parallel to the test section and the other goes side by side with the compressor. By adjusting the two bypass valves in the bypass branches, the flow rate could be sequentially lowered from the maximum flow rate to the desired values.

After the pressure and flow rate were confirmed to be stable at desired value in the loop, the electric current was supplied to the test heater with exponentially increasing heat generation rate controlled by the electrical control circuit. Meanwhile, the heat flux and the heater surface temperature were measured.

The uncertainties of the measurements of the heat generation rate, the heat flux of the test heater, and the heater surface temperature are estimated to be $\pm 1\%$, $\pm 2\%$, and ± 1 K, respectively (Liu et al., 2008).

The heat flux of the heater is calculated by the following equation:

$$q = \frac{\delta}{2} \left(Q - \rho_h c_h \frac{dT_a}{dt} \right) \quad (1)$$

where ρ_h , c_h , and δ are the density, specific heat, and thickness of the test heater, respectively.

The instantaneous surface temperature of test heater was calculated by the following equation assuming that the surface temperature of test heater is uniform:

$$\alpha \frac{\partial^2 T}{\partial Z^2} + \frac{Q}{\rho_h c_h} = \frac{\partial T}{\partial t} \quad (2)$$

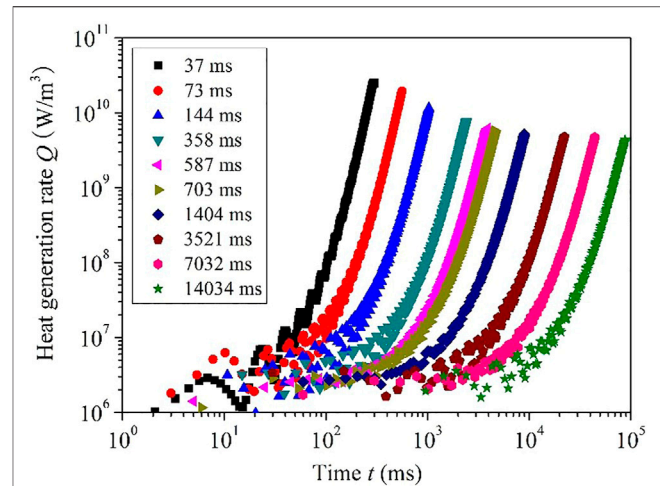
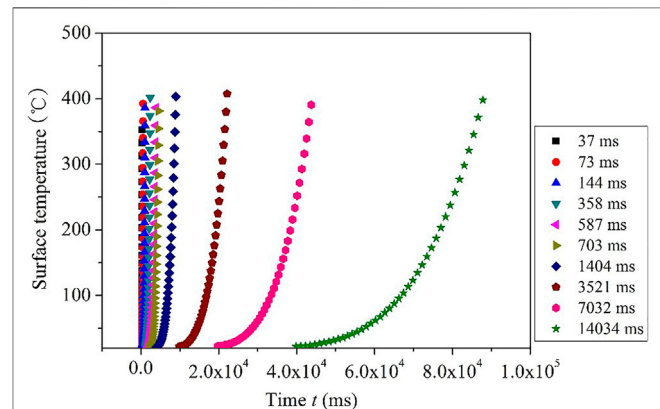
Equation 2 is an unsteady heat conduction equation, which was used to calculate instantaneous surface temperature of the test heater by assuming the surface temperature around the test heater to be uniform. Boundary conditions are as follows:

$$\left. \frac{\partial T}{\partial Z} \right|_{Z=0} = 0, \quad -\lambda \left. \frac{\partial T}{\partial Z} \right|_{Z=\frac{\delta}{2}} = q \quad (3)$$

$$T_a = \frac{\int_0^{\delta/2} T dZ}{\int_0^{\delta/2} dZ} = \frac{2}{\delta} \int_0^{\delta/2} T dZ \quad (4)$$

where α and λ are the thermal diffusivity and thermal conductivity, respectively. T_a is average temperature of the heater.

Experimental conditions are shown in **Table 1**. The twist tape has five pitches (each pitch is 180° twisted with 20 mm in length). The actual length of the twist tape is 106.4 mm, which is used in the

**FIGURE 4** | The exponential heat generation rate for the twisted plate with various heat generation periods.**FIGURE 5** | The average surface temperature of the twisted plate at various heat generation periods.

experiment test due to manufacturing error. The inlet temperature of coolant gas (helium) is 298 K under a system pressure of 500 kPa. The flow velocity ranged from 4 to 10 m/s, and the corresponding Reynolds numbers ranged from 8×10^3 to 2.5×10^4 . The heat generation rate was raised with exponential function. $Q = Q_0 \cdot \exp(t/\tau)$, where Q is heat generation rate, W/m^3 ; Q_0 is initial heat generation rate, W/m^3 ; t is time, s; and τ is period of heat generation rate, s. The period of heat generation rate ranged from 37 ms to 14 s. A smaller period means a higher increasing rate of heat generation.

3 EXPERIMENTAL RESULTS

Figure 4 shows the experimental data of heat generation rate applied to the twisted plate. A total of 10 periods of heat generation rate τ were adopted ranging from 37 to 14,034 ms. As can be seen from the figure, the heat generation rate increases exponentially although some fluctuations occur at the beginning of the transient heating process. This is due to the inevitable oscillating

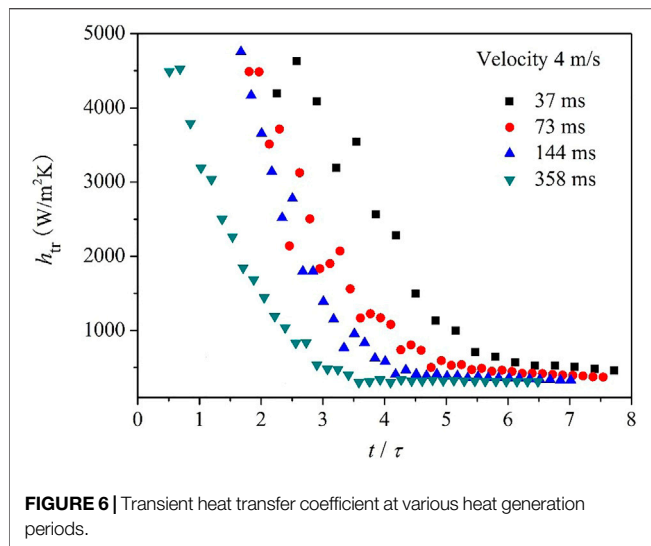


FIGURE 6 | Transient heat transfer coefficient at various heat generation periods.

of the electrical control circuit. For this reason, we used the data after the heat generation curve is stable in this research.

As can be seen in **Figure 5**, the average surface temperature increases exponentially as the heat generation rate increases in exponential function. By fitting the curves with an exponential function, C is a coefficient to be fitted, τ_T is the period of the surface temperature curve, and it is observed that the period τ_T is almost the same value with each τ for heat generation rate, respectively, which means that a similar exponential increasing surface temperature was generated as the heat generation rate increases in exponential function.

The surface heat transfer coefficient of the twisted plate, h , is defined as follows:

$$h = \frac{q}{\Delta T} \quad (5)$$

where q is the heat flux of the heater, which can be calculated according to **Eq. 1**; ΔT is the surface temperature difference of the twisted plate, which is defined as the difference between the average surface temperature of the twisted plate (T_{wa} , T_{sa} , T_{sa}) and the inlet gas temperature (T_{∞}), expressed as follows:

$$\Delta T = T_{wa} - T_{\infty} \quad (6)$$

Transient heat transfer coefficient at various heat generation periods of 37, 73, 144, and 358 ms is shown in **Figure 6**. The flow velocity of helium gas is 4 m/s. Transient heat transfer coefficient decreases to quasi-steady value after several t/τ . With a smaller τ , the transient heat transfer coefficient is larger in both the initial decreasing region and the quasi-steady region. The quasi-steady value of transient heat transfer coefficient is defined as h_{qs} .

The quasi-steady heat transfer coefficients at various heat generation periods and flow velocities are shown in **Figure 7**. As can be found in the figure, h_{qs} increases with the increase of flow velocity. The increasing rate at lower velocities is higher than that at higher velocities. The main reason for this is that, for higher velocities, the convective heat transfer plays a dominant role and the effect of heat conduction is of less importance than that for

lower velocities. The quasi-steady heat transfer coefficient approaches asymptotic value at each velocity when τ is longer than about 1 s. On the other hand, when the period τ is shorter than about 1 s, h_{qs} increases as τ shortens. When the period is relatively short, it means that the increasing rate of the heat generation rate and the surface temperature is relatively high. With fast increasing boundary temperature, the temperature gradient of the fluid in the near-wall region becomes larger compared to steady state heat transfer process, which results in a larger heat transfer coefficient. Therefore, during the transient process, temperature distribution in the thermal boundary is different compared to UWT or UHF boundary conditions. When period τ is larger than about 1 s, the instantaneous changes in the thermal boundary become less prominent. The heat transfer process is similar to normal UWT or UHF conditions.

The Nusselt number of the twisted plate at steady state (periods ranging from 1.4 to 14 s) with flow velocity ranging from 4 to 10 m/s was compared with published empirical correlations, as the laminar analytical solution for plate (Holman, 2010), the Manglik and Bergles (1993a) correlation for tube flow with twisted tape insert, and the Dittus-Boelter correlation for tube flow (Faghri et al., 2010).

$$Nu_L = 0.664 Re_L^{0.5} Pr^{1/3} \text{ Plate (Laminar)} \quad (7)$$

$$Nu_L = 0.106$$

$$\times \left\{ y^{-0.5} \left[1 + \left(\frac{\pi}{2y} \right)^{0.5} \right] Re \right\}^{0.767} Pr^{0.3} \text{ Manglik and Bergles} \quad (8)$$

$$Nu = 0.023 Re^{0.8} Pr^{0.4} \text{ Dettus - Boelter} \quad (9)$$

As shown in **Figure 8**, by comparing the Nu for the twisted plate with flat plate, it is about 3.2 times higher at Reynolds number of 15,000. With the increase of Re , the twisted plate shows even better performance. For tube flows without any inserts as the Dittus-Boelter correlation shows, the Nu is the lowest. The experimental data for twisted plate is about 5.2 times of the tube flow at Reynolds

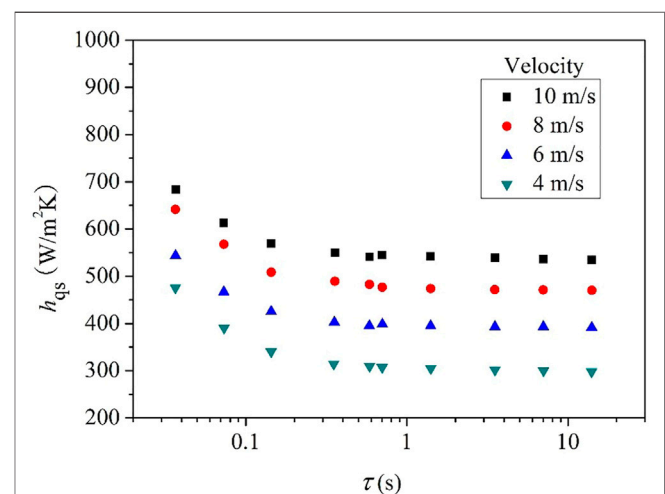


FIGURE 7 | Quasi-steady heat transfer coefficient at various heat generation periods and velocities.

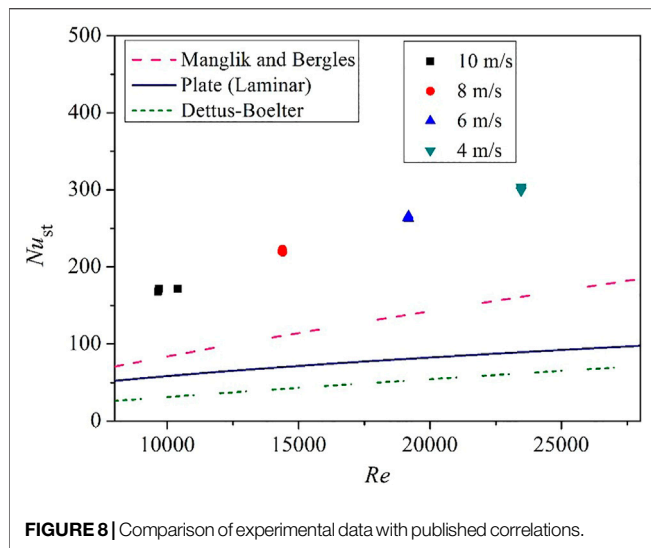


FIGURE 8 | Comparison of experimental data with published correlations.

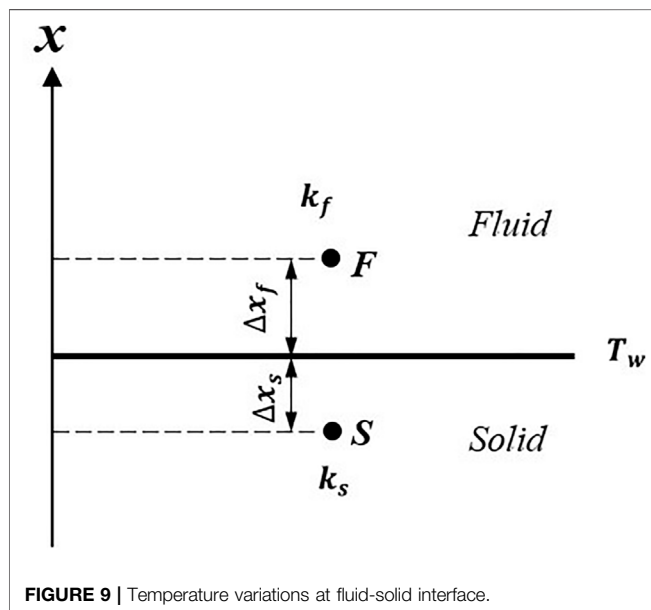


FIGURE 9 | Temperature variations at fluid-solid interface.

number of 15,000. When we compare the experimental data with Manglik and Bergles correlation, the Nusselt number is about twice the value. This is because the experimental result for Nu in this study is for the twisted plate itself, whereas in the Manglik and Bergles correlation, the Nu is for the tube with twisted plate as inserts. The Manglik and Bergles correlation was obtained for Re ranged from 300 to 30,000. The twist ratio y ($y = H/W$, where H is 180° twist pitch and W is width) is 3–6.

4 RESPONSE ANALYSIS FOR HEAT TRANSFER INTERFACE OF SOLID AND FLUID AREA

To help understand the heat transfer response for transient heat transfer process, we now carry out a simple analysis for

fluid-solid coupled transient heat transfer procedure. A near-wall point in the fluid domain is set as point F, and a near-wall point in the solid domain is set as point S, as shown in Figure 9. During the transient process, physical parameters such as temperature and conductivity vary with time, so as the variables at the interface (wall surface). Taking a simple finite difference to approximate the heat fluxes for both sides, we then have a discrete form of the physical heat flux and temperature continuity across the interface.

$$k_f \left(\frac{T_f - T_w}{\Delta x_f} \right) = k_s \left(\frac{T_w - T_s}{\Delta x_s} \right) \quad (10)$$

The wall temperature can thus be represented in terms of updated T_f and T_s .

$$T_w = \frac{T_f k_f / \Delta x_f + T_s k_s / \Delta x_s}{k_f / \Delta x_f + k_s / \Delta x_s} \quad (12)$$

A linear correlation will be obtained for T_w , when assuming the thermal conductivities for fluid (k_f) and solid (k_s) as constant. Instantaneous wall temperature can be expressed as follows:

$$T_w = T_{w0} + \Delta T_w \quad (13)$$

where ΔT_w is the fluctuation.

The key to the accuracy and consistency of the wall temperature fluctuation value T_w is how fast the temperature disturbance can propagate in the near-wall boundary layer of fluid. For one-dimensional semi-infinite domain, penetration depth was suggested by Faghri et al. (2010).

$$\delta_p = \sqrt{8\alpha\delta_t} \quad (14)$$

The time scale δ_t is given by the time period of the disturbance. Take the diffusivity α for helium gas and suppose δ_t as 1 ms, the penetration depth is about 0.57 mm, which might be smaller than the thermal boundary thickness. When the penetration depth is smaller than the thermal boundary thickness, heat transfer from solid domain to fluid domain is not fully developed during the disturbance. The wall temperature is lower due to the lower T_f and thus results in higher heat transfer coefficient.

For this research with exponential increasing heat input, it is considered that, with a fixed Pr , the increasing rate of heat generation rate is the main effect that affects the quasi-steady heat transfer coefficient. On the basis of all these research studies, we would like to take $\tau \approx 1$ s as the transition point, which means that, when the increasing rate of heat generation rate is large enough ($(dQ/dt) \geq Q_0 \cdot e^t$), the heat transfer enhancement phenomenon will be observed.

According to our early research, it is observed that the transition point of period τ for heat transfer coefficient does not show much dependence on velocity because we have rose up the flow velocity to 150 m/s in a narrow channel (Liu et al., 2017). Besides, the effects of gas pressure, initial gas temperature, initial heat generation rate, and structure of the heating surface on transition point are not obvious according to this research and our wide range experiments (Liu et al., 2008; Liu et al., 2014; Liu et al., 2017). Early research by Chao and Cheema (1967) indicated

that the response time of the thermal layer due to a step change in wall flux varies directly as $Pr^{1/3}$ with Pr ranged from 0.72 to 100. The research by Khaled (2012) also suggested that the monotonic heat flux increase effect tends to increase the heat transfer coefficient due to the associated increase in the temperature difference near boundary. However, the heat flux discussed in this research is spatial dependent, not time dependent.

5 CONCLUSION

Forced convection transient heat transfer for helium gas flowing over a twisted plate with exponential increasing heat input was experimentally studied. The following conclusions were obtained.

- 1) Surface temperature difference increases exponentially with the same period as the heat generation rate increases with exponential function.
- 2) The heat transfer coefficient approaches the quasi-steady state one after a large enough heat generation period of about 1 s, and it becomes higher for a small period less than about 1 s.
- 3) It is estimated that, when the increasing rate of heat generation rate is high enough ($(dQ/dt) \geq Q_0 \cdot e^t$), the heat transfer enhancement effect will be observed.
- 4) The heat transfer enhancement characteristics were discussed with penetration depth.

REFERENCES

- Cess, R. D. (1961). Heat Transfer to Laminar Flow across a Flat Plate with a Nonsteady Surface Temperature. *Trans. ASME* 83 (3), 274–279. doi:10.1115/1.3682256
- Chao, B. T., and Cheema, L. S. (1967). Unsteady Heat Transfer in Laminar Boundary Layer over a Flat Plate. *Int. J. Heat Mass Transfer* 11, 1311–1324. doi:10.1016/0017-9310(68)90177-4
- Cotta, R. M., and Özişik, M. N. (1986). Transient Forced Convection in Laminar Channel Flow with Stepwise Variations of wall Temperature. *Can. J. Chem. Eng.* 64, 734–742. doi:10.1002/cjce.5450640504
- Dittus, F. W., and Boelter, L. M. K. (1985). Heat Transfer in Automobile Radiators of the Tubular Type. *Int. Commun. Heat Mass Transfer* 12, 3–22. doi:10.1016/0735-1933(85)90003-x
- Faghri, A., Zhang, Y., and Howell, J. (2010). *Advanced Heat and Mass Transfer*. Columbia, United States: Global Digital Press. 978-0-9842760-0-4.
- Hata, K., and Masuzaki, S. (2011). Twisted-tape-induced Swirl Flow Heat Transfer and Pressure Drop in a Short Circular Tube under Velocities Controlled. *Nucl. Eng. Des.* 241 (No.11), 4434–4444. doi:10.1016/j.nucengdes.2010.09.023
- Holman, J. P. (2010). *Heat Transfer*. 10th Edition. The McGraw-Hill Companies, Inc., 187–194.
- Khaled, A. (2012). Heat Transfer Enhancement Due to Properly Managing the Distribution of the Heat Flux: Exact Solutions. *Energ. Convers. Manag.* 53 (1), 247–258. doi:10.1016/j.enconman.2011.09.004
- Kumar, A., and Layek, A. (2018). Thermo-hydraulic Performance of Solar Air Heater Having Twisted Rib over the Absorber Plate. *Int. J. Therm. Sci.* 133, 181–195. doi:10.1016/j.jthermalsci.2018.07.026
- Liu, Q. S., Shibahara, M., and Fukuda, K. (2008). Transient Heat Transfer for Forced Convection Flow of Helium Gas over a Horizontal Plate. *Exp. Heat Transfer* 21, 206–219. doi:10.1080/08916150802072859

DATA AVAILABILITY STATEMENT

The original contributions presented in the study are included in the article/supplementary material; further inquiries can be directed to the corresponding author.

AUTHOR CONTRIBUTIONS

LW contributed to the conception of the study, collected the experiment data, performed the analysis, and wrote the manuscript. QL has contributed to experimental apparatus and paper instructions.

FUNDING

This research work is supported by Nantong Science and Technology Plan Project (JC2020145).

ACKNOWLEDGMENTS

The experiment work in this paper was done in Graduate School of Marine Engineering, Kobe University, Japan. We would like to thank for the support by the Japan Society for the Promotion of Science (JSPS) (Grant-in Aid for Scientific Research (C), KAKENHI, No. 15K05829).

- Liu, Q., Wang, L., Mitsuishi, A., Shibahara, M., and Fukuda, K. (2017). Transient Heat Transfer for Helium Gas Flowing over a Horizontal cylinder in a Narrow Channel. *Exp. Heat transfer* 30 (4), 341–354. doi:10.1080/08916152.2017.1283373
- Liu, Q., Zhao, Z., and Fukuda, K. (2014). Transient Heat Transfer for Forced Flow of Helium Gas along a Horizontal Plate with Different Widths. *Int. J. Heat Mass Transfer* 75, 433–441. doi:10.1016/j.jheatmasstransfer.2014.03.077
- Man, C., Lv, X., Hu, J., Sun, P., and Tang, Y. (2017). Experimental Study on Effect of Heat Transfer Enhancement for Single-phase Forced Convective Flow with Twisted Tape Inserts. *Int. J. Heat Mass Transfer* 106, 877–883. doi:10.1016/j.jheatmasstransfer.2016.10.026
- Manglik, R. M., and Bergles, A. E. (1993). Heat Transfer and Pressure Drop Correlations for Twisted-Tape Inserts in Isothermal Tubes: Part I-Laminar Flows. *J. Heat Transfer* 115, 881–889. doi:10.1115/1.2911383
- Manglik, R. M., and Bergles, A. E. (1993). Heat Transfer and Pressure Drop Correlations for Twisted-Tape Inserts in Isothermal Tubes: Part II-Transition and Turbulent Flows. *J. Heat Transfer* 115, 890–896. doi:10.1115/1.2911384
- Menni, Y., Azzi, A., and Chamkha, A. (2019). Enhancement of Convective Heat Transfer in Smooth Air Channels with wall-mounted Obstacles in the Flow Path. *J. Therm. Anal. Calorim.* 135, 1951–1976. doi:10.1007/s10973-018-7268-x
- Patil, M. R., and Farkade, H. S. (2016). Review of Heat Transfer Enhancement Techniques in Circular Tube. *Discov. Eng.* 4 (12), 1–7. doi:10.1155/2014/250354
- Ponnada, S., Subrahmanyam, T., and Naidu, S. V. (2019). A Comparative Study on the thermal Performance of Water in a Circular Tube with Twisted tapes, Perforated Twisted tapes and Perforated Twisted tapes with Alternate axis. *Int. J. Therm. Sci.* 136, 530–538. doi:10.1016/j.jthermalsci.2018.11.008
- Riley, N. (1963). Unsteady Heat Transfer for Flow over a Flat Plate. *J. Fluid Mech.* 17 (1), 97–104. doi:10.1017/s0022112063001130
- Saha, S. K., Dutta, A., and Dhal, S. K. (2001). Friction and Heat Transfer Characteristics of Laminar Swirl Flow through a Circular Tube Fitted with Regularly Spaced Twisted-Tape Elements. *Int. J. Heat Mass Transfer* 44, 4211–4223. doi:10.1016/s0017-9310(01)00077-1

Suri, A. R. S., Kumar, A., and Maithani, R. (2018). Convective Heat Transfer Enhancement Techniques of Heat Exchanger Tubes: A Review. *Int. J. Ambient Energ.* 39 (7), 649–670. doi:10.1080/01430750.2017.1324816

Conflict of Interest: The author declares that the research was conducted in the absence of any commercial or financial relationships that could be construed as a potential conflict of interest.

Publisher's Note: All claims expressed in this article are solely those of the authors and do not necessarily represent those of their affiliated organizations or those of

the publisher, the editors, and the reviewers. Any product that may be evaluated in this article, or claim that may be made by its manufacturer, is not guaranteed or endorsed by the publisher.

Copyright © 2021 Wang and Liu. This is an open-access article distributed under the terms of the Creative Commons Attribution License (CC BY). The use, distribution or reproduction in other forums is permitted, provided the original author(s) and the copyright owner(s) are credited and that the original publication in this journal is cited, in accordance with accepted academic practice. No use, distribution or reproduction is permitted which does not comply with these terms.



Corrigendum: Transient Heat Transfer Characteristics of Twisted Structure Heated by Exponential Heat Flux

Li Wang^{1*} and Qiusheng Liu²

¹School of Mechanical Engineering, Nantong University, Nantong, China, ²Department of Marine Engineering, Kobe University, Kobe, Japan

Keywords: exponential heat flux, twisted plate, transient heat transfer, forced convection, heat transfer enhancement

A Corrigendum on

Transient Heat Transfer Characteristics of Twisted Structure Heated by Exponential Heat Flux by Wang, L. (2021). *Front. Energy Res.* 9:771900. doi: 10.3389/fenrg.2021.771900

The author Qiusheng Liu was not initially included as an author in the published article despite their contribution. The corrected **Author Contributions** statement appears below.

AUTHOR CONTRIBUTIONS

LW contributed to the conception of the study, collected the experiment data, performed the analysis, and wrote the manuscript. QL has contributed to experimental apparatus and paper instructions.

Further, in the original article, we neglected to include an acknowledgement. The updated **Acknowledgments** statement appears below.

ACKNOWLEDGMENTS

The experiment work in this paper was done in Graduate School of Marine Engineering, Kobe University, Japan. We would like to thank for the support by the Japan Society for the Promotion of Science (JSPS) (Grant-in Aid for Scientific Research (C), KAKENHI, No. 15K05829).

In the original article **Figure 1**, **Figure 2**, and **Figure 3** were not cited in the article. The citation has now been inserted in section 2 ‘**EXPERIMENTAL STUDY**’, sub-section 2.1 ‘**Experimental Apparatus**’, and should read:

“The experimental apparatus consisted of gas cylinder (1), compressor (2), surge tanks (3) (9), preheater (6), cooler (8), vacuum pump (10), and the test section (7), as shown in **Figure 1** (Liu et al., 2014).”

“The test heater was mounted horizontally along the center axis of the circular test channel, which is made of stainless steel with inside diameter of 20 mm, as shown in **Figure 2** (Liu et al. 2014). A twisted tape with five pitches (each was 180° twisted with 20 mm in length) was used in the experiment.”

“A high-speed analog computer was applied in part 2 to support a rapid and precise calculation-feedback process for the heat generation and heater temperature control. While the signal input and output data processing were fulfilled with a personal computer (PC) (**Figure 3**) (Liu et al., 2014).”

The authors apologize for these errors and state that this does not change the scientific conclusions of the article in any way. The original article has been updated.

OPEN ACCESS

Edited and reviewed by:

Xuewen Cao,
China University of Petroleum (East
China), China

*Correspondence:

Li Wang
wang1988@ntu.edu.cn

Specialty section:

This article was submitted to
Advanced Clean Fuel Technologies,
a section of the journal
Frontiers in Energy Research

Received: 20 December 2021

Accepted: 13 January 2022

Published: 08 February 2022

Citation:

Wang L and Liu Q (2022)
Corrigendum: Transient Heat Transfer
Characteristics of Twisted Structure
Heated by Exponential Heat Flux.
Front. Energy Res. 10:839701.
doi: 10.3389/fenrg.2022.839701

REFERENCES

Liu, Q., Zhao, Z., and Fukuda, K. (2014). Transient Heat Transfer for Forced Flow of Helium Gas along a Horizontal Plate with Different Widths. *Int. J. Heat Mass Transfer* 75, 433–441. doi:10.1016/j.ijheatmasstransfer.2014.03.077

Publisher's Note: All claims expressed in this article are solely those of the authors and do not necessarily represent those of their affiliated organizations, or those of

the publisher, the editors and the reviewers. Any product that may be evaluated in this article, or claim that may be made by its manufacturer, is not guaranteed or endorsed by the publisher.

Copyright © 2022 Wang and Liu. This is an open-access article distributed under the terms of the Creative Commons Attribution License (CC BY). The use, distribution or reproduction in other forums is permitted, provided the original author(s) and the copyright owner(s) are credited and that the original publication in this journal is cited, in accordance with accepted academic practice. No use, distribution or reproduction is permitted which does not comply with these terms.



Study on Preparation of Oxygen Carrier Using Copper Slag as Precursor

Yan Feng, Qianhui Yang, Zongliang Zuo*, Siyi Luo*, Dongdong Ren and Huan Lin

Energy and Power Engineering, School of Environment and Municipal Engineering, Qingdao University of Technology, Qingdao, China

OPEN ACCESS

Edited by:

Chuang Wen,
University of Exeter, United Kingdom

Reviewed by:

Roman Jaskulski,
Warsaw University of Technology,
Poland

Duygu Yilmaz,
Chalmers University of Technology,
Sweden

*Correspondence:

Zongliang Zuo
zuozongliangneu@163.com
Siyi Luo
luosiyi666@126.com

Specialty section:

This article was submitted to
Advanced Clean Fuel Technologies,
a section of the journal
Frontiers in Energy Research

Received: 23 September 2021

Accepted: 22 October 2021

Published: 22 November 2021

Citation:

Feng Y, Yang Q, Zuo Z, Luo S, Ren D
and Lin H (2021) Study on Preparation
of Oxygen Carrier Using Copper Slag
as Precursor.
Front. Energy Res. 9:781914.
doi: 10.3389/fenrg.2021.781914

Copper slag, an important by-product of the copper smelting process, is mainly composed of $2\text{FeO} \cdot \text{SiO}_2$, Fe_3O_4 , and SiO_2 . Due to the sufficient metal oxides, copper slag is regarded as a potential oxygen carrier (OC), which can be applied in chemical looping technology. This research proposed to use the granulated copper slag particles as precursor to produce oxygen carrier. Through this method, waste heat of the high-temperature slag can be fully recovered, eliminating the complicated copper slag pretreatment process. In this paper, the reactivity of granulated copper slag after redox calcination was studied by X-ray diffractometer (XRD) and Scanning Electron Microscope (SEM), the highest reactivity occurred at $1,000^\circ\text{C}$. In addition, the oxygen release and absorption performance of OC were tested in thermal-gravimetric (TG). According to theoretical calculations, the mass loss caused by oxygen release accounts for 70.57% of the total loss and the mass reached by 4.2% at $1,000^\circ\text{C}$ in oxygen absorption experiment. The copper slag modified through calcining in redox condition was proved to be a promising oxygen carrier in chemical looping process. Furthermore, the performance research on OC also provided theoretical references for the operating parameters of OC circulating between air reactor and fuel reactor in practical chemical looping processes.

Keywords: copper slag, granulation, oxygen carrier, calcination, redox

INTRODUCTION

Chemical looping technology is an emerging combustion technology which expected to achieve 100% CO_2 capture efficiency with a low energy consumption (Abuelgasim et al., 2021). Oxygen carrier (OC) is used to transfer lattice oxygen between air and fuel reactors and plays an essential role in chemical looping processes. The high oxygen carrying capacity, redox activity, gas selectivity, mechanical strength as well as sintering resistance of OC determine the speed and efficiency of reactors in chemical looping conversions (Li et al., 2009). Therefore, a suitable OC has received particular interest in recent years.

There have been significant advances in metal oxide OC such as Fe, Ni, Cu, and Mn for chemical looping applications (Kang et al., 2010; Gu et al., 2015; Jiang et al., 2017). Among these materials, Fe-based OC has attracted increasing attention because of its high oxygen release capacity (Cheng et al., 2018), cost benefits (He et al., 2013; Mayer et al., 2018) as well as environmental compatibility (Luo et al., 2014; Chen et al., 2021). In addition, due to their sulfur tolerance, Fe-based oxygen carriers can react with acid gases or even solid sulfur fuels without

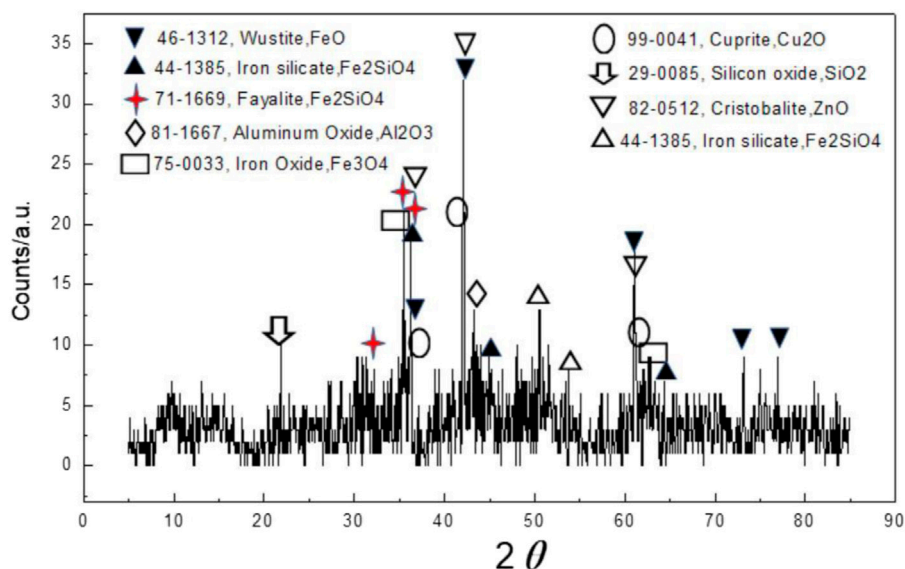


FIGURE 1 | XRD analyzed results of initial copper slag.

affecting its reactivity and phase (Garcia-Labiano et al., 2014; Garcia-Labiano et al., 2016). In general, the application of Fe-based oxygen carriers is a promising research direction in the field of chemical looping technology.

Tones of oxygen carriers will be used in a commercial chemical looping process, and in this case, the cost of materials should be considered. Therefore, the low-cost Fe-based materials such as copper slag, a solid by-product from copper smelting plants, will be an attractive OC to further reduce costs. It has been estimated that about 2–3 tons of slag generated for every ton of copper produced (Alp et al., 2008). Copper slag contains large amount of heat and some valuable metals, in which the content of iron could reach to 45% (Shi et al., 2008) along with other trace elements like Cu, Ni, and Zn. From this aspect, copper slag may be regarded as a source of costless Fe-based oxygen carrier. At the same time, Cu in the copper slag may lead to a synergistic improvement in the reactivity, and SiO₂, the second most abundant compound, could improve the mechanical strength as a support material (Durmaz et al., 2020). It is found the copper slag increases the content of CO₂ and the carbon conversion rate in the chemical looping gasification of sewage sludge process (Fang et al., 2021). Copper slag, doped with K metal, exhibits the highest carbon conversion efficiency (Yonghao et al., 2020). In summary, copper slag is a candidate for OC in chemical looping technology.

Copper slag used as a precursor for OC preparation generally has a relatively uniform particle size distribution. However, the initial copper slags from copper smelting plants are lumpy, needing pretreatment processes like crushing and screening before being made into a precursor. In order to eliminate the complicated pretreatment process, this paper put forward to using granulated copper slags as precursor, which fully utilizes the waste heat of the high-temperature slag and provides a new idea to recover thermal energy from copper slag. In previous

work, the dry granulation method has been proved to be a feasible way to produce copper slag particles with uniform particle diameter distribution (Zuo et al., 2020b; Zuo et al., 2021a).

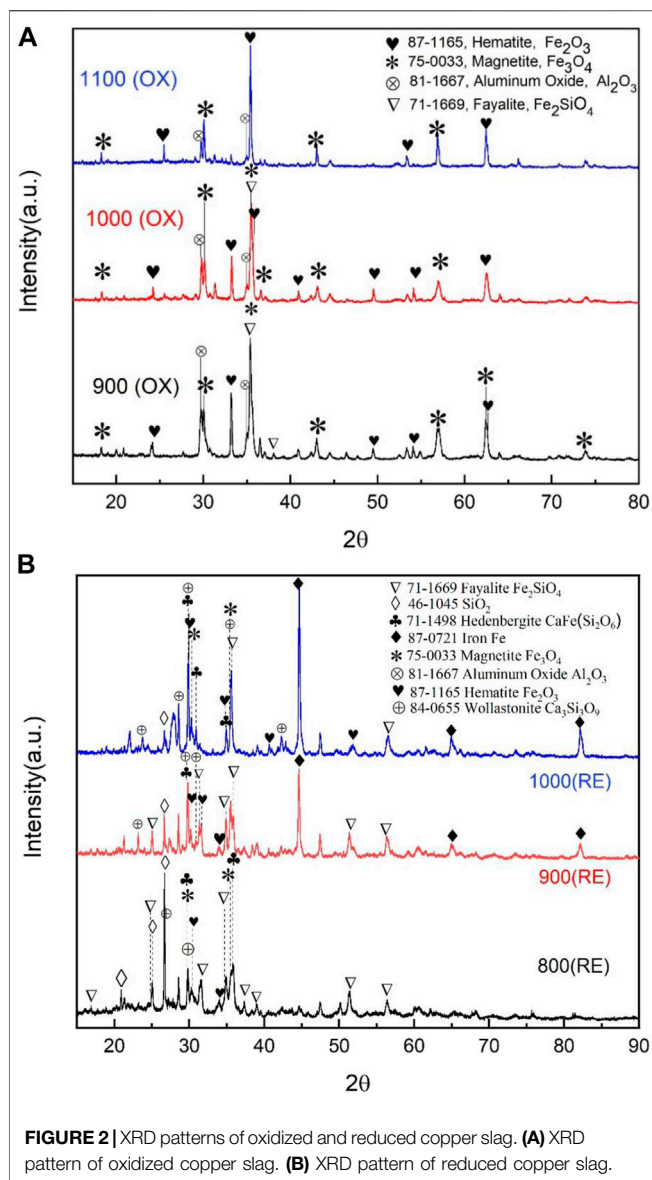
In general, the original copper slag has a little redox activity. Modifying is necessary to improve the reactivity of OC. At present, most of studies have proposed to modify the OC by doping alkali metals (Bao et al., 2013) or metal (Gu et al., 2012; Dong et al., 2021) and have indeed improved the surface reactivity of OC. However, these modification progresses are usually cumbersome. In order to solve above issues, this paper proposed to calcinate the copper slag to modify OC. There are some studies demonstrate that calcination is a promising method to further improve the redox reactivity and mechanical properties (Gorai et al., 2003).

This work aims to study the characteristics of OC using granulated copper slag as precursor. In this paper, oxidation and reduction calcination of copper slag both took place in a pipe-typed furnace at different temperatures. Then the phase characterization and element detection of OC were measured by X-ray diffractometer (XRD). Multiple experiments were conducted to find the optimal redox calcination temperature. Additionally, in order to verify the oxygen release and absorption performance of OC, experiments were conducted by thermal-gravimetric (TG) method.

METHODS

Materials

Copper slag was obtained from Jinchuan Company from Gansu province, China. The mineral phase of initial copper slag was analyzed by X-ray Diffractometry (XRD) with a scanning rate of 4°/min from range of $2\theta = 10^\circ$ – 90° and the elements composition was tested by X-ray Fluorescence (XRF). The XRD results are



shown in **Figure 1**, the main mineral phases of initial copper slag are fayalite, magnetite and silicon oxide. Fayalite is $2\text{FeO} \cdot \text{SiO}_2$ in copper slag composed of net-like tetrahedrons. The XRF analysis are as follows: 37.3% of Fe_2O_3 , 12.9% of SiO_2 , 12.2% of CaO , 6.6% of Al_2O_3 , 12.1% of ZnO as well as some minor elements like K, Cu, Pb, and Co.

Coal is a kind of lignite from Fuxin City, Liaoning Province, China. The compositions are as follows: 35.1% of moisture, 25% of ash, 20.5% of volatile, and 19.4% of fixed carbon. Coal samples were dried at 105°C in a constant temperature oven for 2 h, then sieved into powder with a size of 0.15 mm. The coal powder was used as a reducer for the next experiments.

Copper Slag Calcination

$\text{Fe}_3\text{O}_4/\text{Fe}_2\text{O}_3$ species decomposed from calcinated copper slag can provide the lattice oxygen for chemical looping process (Gorai

et al., 2003; Deng et al., 2019). There also were some results have indicated the redox reactivity and the initial oxygen transport capacity of calcined ilmenite were better than fresh ilmenite (Adnez et al., 2010). Therefore, calcination is a promising method to improve the lattice oxygen transfer ability and the reaction activity of copper slag. Hence, in this study, to improve the lattice oxygen transport capacity, granulated copper slag was calcinated at different temperature under redox conditions. Furthermore, the performance research on OC can provide theoretical references for the operating characteristics and parameters of OC circulating between air reactor and fuel reactor in practical chemical looping processes.

The oxidation calcination process is as follows: copper slag particles heated in a tube furnace (SHKGL-1200 horizontal high temperature furnace) in an air atmosphere at a heating rate of $10^\circ\text{C}/\text{min}$ before 600°C then changed the rate to $5^\circ\text{C}/\text{min}$ until the temperature reaches 900, 1,000, and $1,100^\circ\text{C}$. The above samples are marked as 900 (OX), 1,000 (OX), and 1,100 (OX), respectively.

The reduction modification process is as follows: the mixture of copper slag, coal and CaO at a mass ratio of 1:1:1 was made into 4 g pellet by a hydraulic pelletizer. CaO not only played the role of an adhesive, but also played the role of a slagging agent and had a promotion influence on the reduction reactions of copper slag by a large margin (Zuo et al., 2020b). Then heated to $800\text{--}1,000^\circ\text{C}$ in N_2 atmosphere with the heating rate same as the oxidation conditions to obtain 800 (RE), 900 (RE), and 1,000 (RE). Finally, the modified copper slag magnetically separated was selected as OC. Coal is a reducer of copper slag with the main contents of fixed carbon, which reduction temperature is lower than gaseous reducers H_2 (Zuo et al., 2020b), and thus it decreases the heat consumption of reduction process.

Thermo Gravimetric Experiments

In order to verify the oxygen release and absorption characteristics of OC, experiments were conducted using thermo gravimetric (TG). It was turned out 1,000 (OX) and 1,000 (RE) were the most suitable oxygen carriers according to XRD analysis. With respect to the oxygen release experiment, 20 mg mixture of 1,000 (OX) and coal powder heated to $1,000^\circ\text{C}$ at a heating rate of $10^\circ\text{C}/\text{min}$ and kept 1 h under a N_2 flow of 30 ml/min. As for oxygen absorption test, 20 mg 1,000 (RE) heated to $1,000^\circ\text{C}$ at a heating rate of $10^\circ\text{C}/\text{min}$ in N_2 atmosphere, then N_2 was switched to air and kept 2 h. As a blank control experiment, 10 mg coal was heated under the same condition. In this experiment, the degree of mass reduction can reflect the degree of oxygen release capacity of OC.

RESULTS AND DISCUSSION

Phase Transformation of Copper Slag by Oxidation

As shown in **Figure 2**, fayalite was decomposed into main phases (Fe_3O_4 , Fe_2O_3 , and SiO_2) in the air (Gyurov et al., 2011), the intensity of Fe_2O_3 in the calcined sample gradually increased and Fe_3O_4 phase decreased as the calcined temperature increased

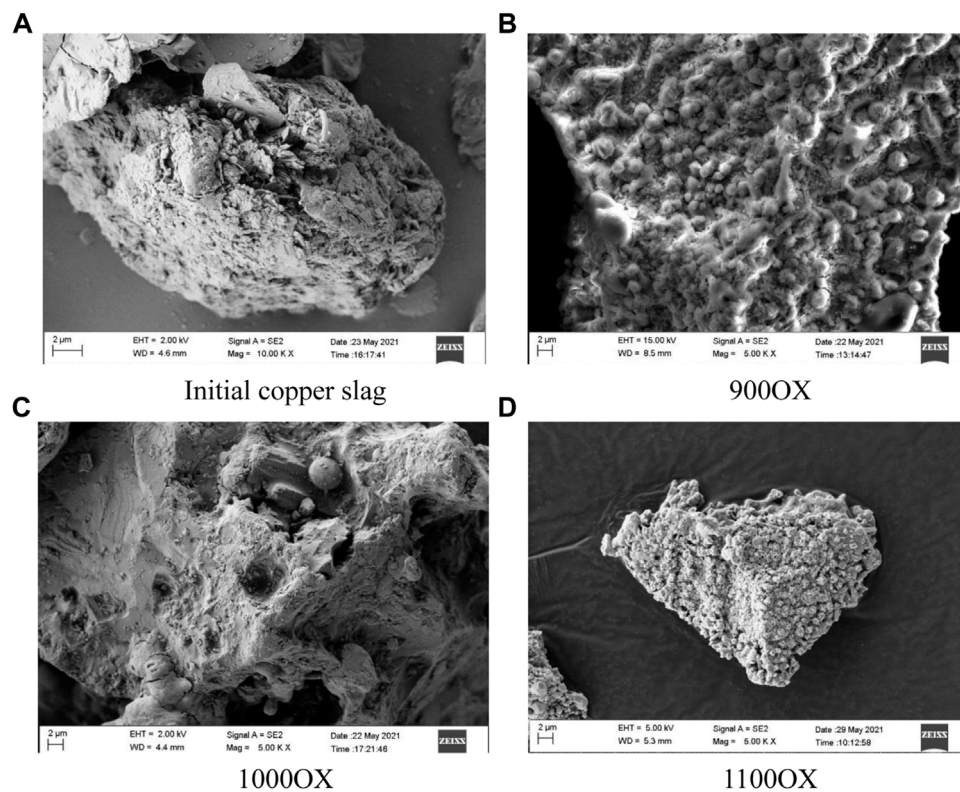
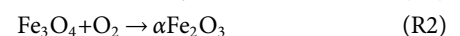
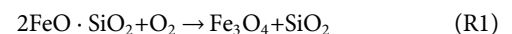


FIGURE 3 | SEM diagrams of copper slag. **(A)** Initial copper slag. **(B)** 900°C. **(C)** 1000°C. **(D)** 1100°C.

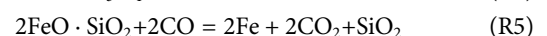
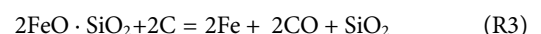
from 900°C to 1,100°C. It indicates that the transformation rule of iron phase in copper slag during calcination process is “ $2\text{FeO} \cdot \text{SiO}_2 \rightarrow \text{Fe}_3\text{O}_4 \rightarrow \alpha\text{Fe}_2\text{O}_3$ ” shown in R1-R2 (Gorai et al., 2003). At a relatively low temperature (900°C), the calcined reaction R1 dominated and more fayalite was decomposed into Fe_3O_4 and Fe_2O_3 (Deng et al., 2019). At 900°C, the XRD pattern shows characteristic peaks of magnetite, accompanied by weak characteristic peaks of hematite. Most of fayalite (Fe^{2+}) was decomposed into magnetite ($\text{Fe}^{8/3+}$), indicating that the oxygen carrier has a poor oxidability under this circumstance. With the increase of temperature, the proportions of the characteristic peaks of Fe_3O_4 and Fe_2O_3 at 1,000°C are almost same because most of the Fe_3O_4 has been oxidized to Fe_2O_3 as R2 describes. At 1,100°C, although the Fe_3O_4 phase becomes weaker, it did not completely disappear, revealing that the copper slag has not been completely oxidized to Fe^{3+} at this temperature. This phenomenon may be caused by the calcination temperature which is not enough to complete the conversion of magnetite, or the oxidation of fayalite still proceed at this temperature, in other words, R1 and R2 take place simultaneously.

In summary, the higher the calcination temperature, the higher the degree of oxidation of the copper slag. However, Scanning Electron Microscope (SEM) results were shown in **Figure 3**, which indicated the most severe sintering occurred at 1,100°C. Based on this, it is better to control the calcined temperature at 1,000°C to ensure OC has more lattice oxygen and to avoid serious sintering in chemical looping process.



Phase Transformation of Copper Slag by Reduction

The calcined copper slag in reduction condition is shown in **Figure 2**. It was shown that the $\text{Fe}^{+8/3}$ in Fe_3O_4 phase gradually disappeared, while the Fe^{2+} existing in $\text{CaFeSi}_2\text{O}_6$ and $\text{Ca}_3\text{Si}_3\text{O}_9$ enhanced with the increasing of reduction temperature. The reduction processes are carried out step by step respectively: $\text{FeO} \cdot \text{SiO}_2 \rightarrow \text{FeO} \rightarrow \text{Fe}$, $\text{Fe}_3\text{O}_4 \rightarrow \text{FeO} \rightarrow \text{Fe}$ (Yang et al., 2011). During the reduction process, coal powder as a reductant reacted with various iron oxides in the copper slag to produce CO and further generate CO_2 , and simultaneously yield wollastonite $\text{Ca}_3\text{Si}_3\text{O}_9$ and hedenbergite $\text{CaFeSi}_2\text{O}_6$ (Yang et al., 2011). The reduction of iron oxide with C is called direct reduction (R3-R4) and with CO is called indirect reduction (R5-R6) (Bafghi et al., 1993). In the gas phase, the conversion reaction of CO_2 , CO, and C is a Boudouard reaction (R7) (Zuo et al., 2020a).



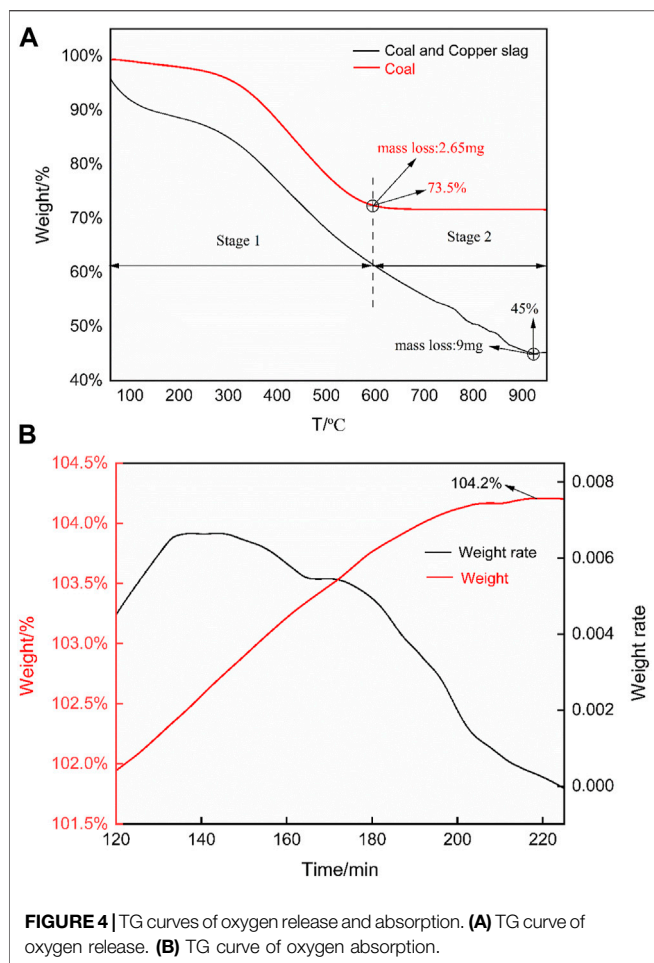


FIGURE 4 | TG curves of oxygen release and absorption. **(A)** TG curve of oxygen release. **(B)** TG curve of oxygen absorption.



In this study, the Reaction Equations part of the HSC6.3 simulation software was used to confirm the initial reduction reaction temperature based on Gibbs free energy calculation. It was found that the initial temperature for R3, R4, and R6 are approximately 800, 700, and 790°C. If temperature higher than 800°C, these reactions occur spontaneously, moreover, the reduction reactions of C are easier than the reduction reactions of CO for iron oxide in solid copper slag. However, The Gibbs free energy for reduction reactions of CO and 2FeO-SiO₂ can't take place spontaneously. In summary, the reduction temperature of C and copper slag should be set above 800°C. The above reactions are all endothermic reactions, which demonstrates that improving the temperature will promote the reduction reaction. Therefore, the copper slag calcined at 1,000°C has higher reduction degree and is more suitable as an oxygen carrier to a certain extent. This simulation conclusion is consistent with the results shown in the XRD plot.

The XRD results **Figure 2** show that in addition to the three main phases of 2FeO-SiO₂, Fe₃O₄, and SiO₂, there is a weaker CaFeSi₂O₆ characteristic peak at a reduction temperature of 800°C. Since the CaFeSi₂O₆ is a silicate composed of Ca²⁺, Fe²⁺ and Si₂O₆, Fe²⁺ has relatively strong reducibility. To a certain extent, the appearance of

characteristic peak of CaFeSi₂O₆ indicates the improvement of reduction degree. When the reduction temperature increased to 900 °C, the diffraction peaks of 2FeO-SiO₂ and Fe₃O₄ gradually weakened and decomposed into the characteristic peaks of FeO and Fe, there was simultaneously a large amount of 2FeO-SiO₂ in the oxygen carrier. Until the temperature rose to 1,000°C, almost all the iron phase was converted to iron metal.

At 1,000°C, the oxygen carrier has the deepest reduction degree and excellent reduction performance, which provides theoretical references for the operating characteristics and parameters of OC.

The Analysis of Thermal-Gravimetric

To further test the release and absorption oxygen performance of the calcined copper slag, two experiments were conducted by TG method:

- 1) The oxygen release characteristics of 1,000 (OX) was tested in a N₂ atmosphere.
- 2) The oxygen absorption of 1,000 (RE) was tested in an air atmosphere.

The TG curve of 1,000 (OX) oxygen release is shown in **Figure 4**. There are two obvious weight loss stages, 25–600 and 600–1,000°C. The stage 1 is mainly caused by the pyrolysis of coal powder. In the stage 2, pyrolysis of coal powder is basically completed and the reduction reaction between the coal powder and 1,000 (OX) lead the mass loss. It was calculated that the mass loss caused by the oxygen release process accounts for 70.57% of the total loss. The curve of oxygen release as shown in **Figure 3**, the surface lattice oxygen of OC was captured by C element in the pulverized coal to produce CO/CO₂, meanwhile the oxygen vacancies generated by the outer lattice oxygen enforce the inner lattice oxygen move to the surface quickly to provide more lattice oxygen and to achieve the purpose of releasing oxygen (Zeng et al., 2012). Thus, the degree of mass loss reflects the reduction degree of oxygen release performance. In general, this curve has two vividly mass loss region, the result is consistent with Zuo (Zuo et al., 2021b). In first region, pyrolysis reactions of coal take place; The second region is the oxygen release reaction of OC, taking place at 600–1,000°C, which is the main reaction stage causes the loss of mass. Moreover, it is calculated that the mass loss caused by the oxygen release process accounts for 70.57% of the total loss. From this aspect, the granulated copper slag after calcination has a good oxygen release performance.

Figure 4 shows the oxygen absorption process of 1,000 (RE). The oxygen absorption is an isothermal process. OC was heated in an inert gas N₂ before 120 min, then N₂ was switched to air and kept 2 h to accomplish oxygen absorption. In other words, the actual oxygen absorption process took place between 120 and 240 min, so the x-axis of TG curve starts from 120. The longer the oxidation process, the heavier the OC, eventually the mass of OC increased by 4.2%. This phenomenon indicates the OC after redox calcination has an ability to absorb oxygen.

In summary, granulated copper slag as a precursor makes full use of waste heat resources. OC calcined at 1,000°C has the best redox reactivity and has a fine ability of oxygen release and absorption. This study provided a reference for the operating

temperature of OC in the chemical looping technology, as well as offered a new idea for the comprehensive utilization of metal oxide-containing metallurgical slag.

CONCLUSIONS

This paper proposed the preparation of oxygen carriers using granulated copper slag as a precursor. and the main findings have been summarized below:

- 1) Copper slag calcined at different temperatures was tested through XRD and TG method to analyze the iron phase transition mechanism and the lattice oxygen transport performance of the oxygen carrier. The oxygen carrier showed excellent performance at 1,000°C.
- 2) There were obvious quality changes of OC during the TG experiment indicating the fine lattice oxygen transfer ability. At the same time, this research also provided theoretical temperature range of OC circulating between two reactors in practical chemical looping applications.

REFERENCES

- Abuelgasim, S., Wang, W., and Abdalazeez, A. (2021). A Brief Review for Chemical Looping Combustion as a Promising CO₂ Capture Technology: Fundamentals and Progress. *Sci. Total Environ.* 764, 142892. doi:10.1016/j.scitotenv.2020.142892
- Adánez, J., Cuadrat, A., Abad, A., Gayán, P., de Diego, L. F., and García-Labiano, F. (2010). Ilmenite Activation during Consecutive Redox Cycles in Chemical-Looping Combustion. *Energy Fuels* 24 (2), 1402–1413. doi:10.1021/ef900856d
- Alp, İ., Deveci, H., and Süngün, H. (2008). Utilization of Flotation Wastes of Copper Slag as Raw Material in Cement Production. *J. Hazard. Mater.* 159 (2–3), 390–395. doi:10.1016/j.jhazmat.2008.02.056
- Bafghi, M. S., Fukuda, M., Ito, Y., Yamada, S., and Sano, M. (1993). Effect of CO Gas Formation on Reduction Rate of Iron Oxide in Molten Slag by Graphite. *ISIJ Int.* 33 (11), 1125–1130. doi:10.2355/isijinternational.33.1125
- Bao, J., Li, Z., and Cai, N. (2013). Promoting the Reduction Reactivity of Ilmenite by Introducing Foreign Ions in Chemical Looping Combustion. *Ind. Eng. Chem. Res.* 52 (18), 6119–6128. doi:10.1021/ie400237p
- Chen, W.-H., Chen, K.-H., Ubando, A. T., Lee, W.-J., and Chio, M.-H. (2021). Redox Degrees of Iron-Based Oxygen Carriers in Cyclic Chemical Looping Combustion Using Thermodynamic Analysis. *Chem. Eng. J.* 426, 130834. doi:10.1016/j.cej.2021.130834
- Cheng, Z., Qin, L., Fan, J. A., and Fan, L.-S. (2018). New Insight into the Development of Oxygen Carrier Materials for Chemical Looping Systems. *Engineering* 4 (3), 343–351. doi:10.1016/j.eng.2018.05.002
- Deng, Z., Huang, Z., He, F., Zheng, A., Wei, G., Meng, J., et al. (2019). Evaluation of Calcined Copper Slag as an Oxygen Carrier for Chemical Looping Gasification of Sewage Sludge. *Int. J. Hydrogen Energ.* 44 (33), 17823–17834. doi:10.1016/j.ijhydene.2019.05.039
- Dong, N., Huo, R., Liu, M., Deng, L., Deng, Z., Chang, G., et al. (2021). Chemical Looping Gasification of Sewage Sludge Using Copper Slag Modified by NiO as an Oxygen Carrier. *Chin. J. Chem. Eng.* 29, 335–343. doi:10.1016/j.cjche.2020.09.007
- Durmaz, M., Dılmaç, N., and Dılmaç, Ö. F. (2020). Evaluation of Performance of Copper Converter Slag as Oxygen Carrier in Chemical-Looping Combustion (CLC). *Energy* 196, 117055. doi:10.1016/j.energy.2020.117055
- Fang, S., Deng, Z., Lin, Y., Huang, Z., Ding, L., Deng, L., et al. (2021). Investigation of the Nitrogen Migration Characteristics in Sewage Sludge during Chemical Looping Gasification. *Energy* 216, 119247. doi:10.1016/j.energy.2020.119247

DATA AVAILABILITY STATEMENT

The original contributions presented in the study are included in the article/Supplementary Material, further inquiries can be directed to the corresponding authors.

AUTHOR CONTRIBUTIONS

ZZ proposed the concept of the research; SL designed the experiment; YF contributed significantly to analysis and article writing; QY performed the experiment; DR and LH helped performing the analysis with constructive discussions.

FUNDING

This research has been supported by the Natural Science Foundation of China (52104397), the Natural Science Foundation of Shandong Province (ZR2020QE150, ZR2019MEE015).

- García-Labiano, F., de Diego, L. F., Gayán, P., Abad, A., Cabello, A., Adánez, J., et al. (2014). Energy Exploitation of Acid Gas with High H₂S Content by Means of a Chemical Looping Combustion System. *Appl. Energ.* 136, 242–249. doi:10.1016/j.apenergy.2014.09.041
- García-Labiano, F., de Diego, L. F., Cabello, A., Gayán, P., Abad, A., Adánez, J., et al. (2016). Sulphuric Acid Production via Chemical Looping Combustion of Elemental sulphur. *Appl. Energ.* 178, 736–745. doi:10.1016/j.apenergy.2016.06.110
- Gorai, B., Jana, R. K., and Premchand (2003). Characteristics and Utilisation of Copper Slag—A Review. *Resour. Conserv. Recycl.* 39 (4), 299–313. doi:10.1016/s0921-3449(02)00171-4
- Gu, H., Shen, L., Xiao, J., Zhang, S., Song, T., and Chen, D. (2012). Iron Ore as Oxygen Carrier Improved with Potassium Carrier during Chemical Looping Combustion of Anthracite Coal. *Combust. Flame* 159 (7), 2480–2490. doi:10.1016/j.combustflame.2012.03.013
- Gu, H., Shen, L., Zhong, Z., Zhou, Y., Liu, W., Niu, X., et al. (2015). Interaction between Biomass Ash and Iron Ore Oxygen Carrier during Chemical Looping Combustion. *Chem. Eng. J.* 277, 70–78. doi:10.1016/j.cej.2015.04.105
- Gyurov, S., Kostova, Y., Klitcheva, G., and Ilinkina, A. (2011). Thermal Decomposition of Pyrometallurgical Copper Slag by Oxidation in Synthetic Air. *Waste Manag. Res.* 29 (2), 157–164. doi:10.1177/0734242X10379495
- He, F., Galinsky, N., and Li, F. (2013). Chemical Looping Gasification of Solid Fuels Using Bimetallic Oxygen Carrier Particles - Feasibility Assessment and Process Simulations. *Int. J. Hydrogen Energ.* 38 (19), 7839–7854. doi:10.1016/j.ijhydene.2013.04.054
- Jiang, S., Shen, L., Wu, J., Yan, J., and Song, T. (2017). The Investigations of Hematite-CuO Oxygen Carrier in Chemical Looping Combustion. *Chem. Eng. J.* 317, 132–142. doi:10.1016/j.cej.2017.01.091
- Kang, K.-S., Kim, C.-H., Bae, K.-K., Cho, W.-C., Kim, S.-H., and Park, C.-S. (2010). Oxygen-carrier Selection and thermal Analysis of the Chemical-Looping Process for Hydrogen Production. *Int. J. Hydrogen Energ.* 35 (22), 12246–12254. doi:10.1016/j.ijhydene.2010.08.043
- Li, F., Kim, H. R., Sridhar, D., Wang, F., Zeng, L., Chen, J., et al. (2009). Syngas Chemical Looping Gasification Process: Oxygen Carrier Particle Selection and Performance. *Energy Fuels* 23 (8), 4182–4189. doi:10.1021/ef900236x
- Luo, M., Wang, S., Wang, L., and Lv, M. (2014). Reduction Kinetics of Iron-Based Oxygen Carriers Using Methane for Chemical-Looping Combustion. *J. Power Sourc.* 270, 434–440. doi:10.1016/j.jpowsour.2014.07.100
- Mayer, K., Schanz, E., Pröll, T., and Hofbauer, H. (2018). Performance of an Iron Based Oxygen Carrier in a 120 kWth Chemical Looping Combustion Pilot Plant. *Fuel* 217, 561–569. doi:10.1016/j.fuel.2018.01.014

- Shi, C., Meyer, C., and Behnood, A. (2008). Utilization of Copper Slag in Cement and Concrete. *Resour. Conserv. Recycl.* 52 (10), 1115–1120. doi:10.1016/j.resconrec.2008.06.008
- Yang, H., Jing, L., and Dang, C. (2011). Direct Reduction and Magnetic Separation Recovery of Iron Components in Copper Slag. *Chin. J. Nonferrous Met.* 21 (05), 1165–1170. doi:10.19476/j.ysxb.1004.0609.2011.05.034
- Yonghao, W., Ming, L., Nanhong, D., Yan, L., Guozhang, C., Guoqiang, W., et al. (2020). Chemical Looping Gasification of High Nitrogen wood Waste Using a Copper Slag Oxygen Carrier Modified by Alkali and Alkaline Earth Metals. *Chem. Eng. J.* 410, 128344, 2020 . (prepublish). doi:10.1016/j.cej.2020.128344
- Zeng, L., Kathe, M. V., Chung, E. Y., and Fan, L.-S. (2012). Some Remarks on Direct Solid Fuel Combustion Using Chemical Looping Processes. *Curr. Opin. Chem. Eng.* 1 (3), 290–295. doi:10.1016/j.coche.2012.05.001
- Zuo, Z., Luo, S., Zhang, J., Yu, Q., Guo, J., Bi, X., et al. (2020a). C and CO Reduction Proportional Fraction with Copper Slag by a Phase Equilibrium Calculation Model (PECM). *Energy Fuels* 34 (1), 698–708. doi:10.1021/acs.energyfuels.9b03384
- Zuo, Z., Yu, Q., Luo, S., Zhang, J., and Zhou, E. (2020b). Effects of CaO on Two-step Reduction Characteristics of Copper Slag Using Biochar as Reducer: Thermodynamic and Kinetics. *Energy Fuels* 34 (1), 491–500. doi:10.1021/acs.energyfuels.9b03274
- Zuo, Z., Feng, Y., Li, X., Luo, S., Ma, J., Sun, H., et al. (2021a). Thermal-Chemical Conversion of Sewage Sludge Based on Waste Heat Cascade Recovery of Copper Slag: Mass and Energy Analysis. *Energy* 235, 121327. doi:10.1016/j.energy.2021.121327
- Zuo, Z., Luo, S., Liu, S., Zhang, J., Yu, Q., and Bi, X. (2021b). Thermokinetics of Mass-Loss Behavior on Direct Reduction of Copper Slag by Waste Plastic Char. *Chem. Eng. J.* 405, 126671. doi:10.1016/j.cej.2020.126671

Conflict of Interest: The authors declare that the research was conducted in the absence of any commercial or financial relationships that could be construed as a potential conflict of interest.

Publisher's Note: All claims expressed in this article are solely those of the authors and do not necessarily represent those of their affiliated organizations, or those of the publisher, the editors and the reviewers. Any product that may be evaluated in this article, or claim that may be made by its manufacturer, is not guaranteed or endorsed by the publisher.

Copyright © 2021 Feng, Yang, Zuo, Luo, Ren and Lin. This is an open-access article distributed under the terms of the Creative Commons Attribution License (CC BY). The use, distribution or reproduction in other forums is permitted, provided the original author(s) and the copyright owner(s) are credited and that the original publication in this journal is cited, in accordance with accepted academic practice. No use, distribution or reproduction is permitted which does not comply with these terms.



Numerical and Experimental Analysis of Influence of Impeller Structures on Slurry Pump Performance

Guangjie Peng^{1*}, Jialin Du¹, Hao Chang^{1*}, Qiang Chen¹, Jiahui Li², Chengxiang Pan² and Yongfei Yang³

¹Research Center of Fluid Machinery Engineering and Technology, Jiangsu University, Zhenjiang, China, ²Xiangyang Wuerwu Pump Co., Ltd, Xiangyang, China, ³School of Mechanical Engineering, Nantong University, Nantong, China

OPEN ACCESS

Edited by:

Lin Teng,
Fuzhou University, China

Reviewed by:

Lei Tan,
Tsinghua University, China
Shi Guangtai,
Xihua University, China

*Correspondence:

Guangjie Peng
pgj@ujs.edu.cn
Hao Chang
changhao@ujs.edu.cn

Specialty section:

This article was submitted to
Advanced Clean Fuel Technologies,
a section of the journal
Frontiers in Energy Research

Received: 21 August 2021

Accepted: 27 September 2021

Published: 22 November 2021

Citation:

Peng G, Du J, Chang H, Chen Q, Li J,
Pan C and Yang Y (2021) Numerical
and Experimental Analysis of Influence
of Impeller Structures on Slurry
Pump Performance.
Front. Energy Res. 9:762159.
doi: 10.3389/fenrg.2021.762159

Slurry pump as an important equipment for transporting coal, which are widely used in power plants, mines and other fossil energy field. Therefore, the improvement of slurry pump performance can effectively reduce the energy loss of fossil energy industry. In this paper, a novel impeller with splitter blade structure was proposed, and the internal flow field of slurry pumps with different impeller structures was analyzed. Meanwhile, according to the shape and structure of the vortex in slurry pump, the vortex can be divided into leading edge vortex, trailing edge vortex and gap leakage vortex by employing the Q criterion, and the generation mechanism of each vortex and relationship between vortex strength and flow condition were analyzed. What is more, the entropy generation theory was employed to study the energy loss of slurry pump. The pressure distribution and wear characteristics of different impeller structures under two-phase flow conditions are studied. The result shows that the energy loss caused by entropy production in the slurry pump can be declined by employing the splitter blades, which can restrain the flow separation at the impeller outlet. Thus, the impeller with splitter blades not only can reduce the energy loss of the slurry pump, but also enhance the wear characteristics of impeller under two-phase flow conditions. Finally, the result can provide the guidelines for the design optimization of slurry pump.

Keywords: slurry pump, energy loss, entropy production, wear characteristic, energy-saving technology

INTRODUCTION

Slurry pump as an important equipment for transporting coal, which are widely used in power plants, mines and other fossil energy field. Since the conveyed medium is solid-liquid two-phase flow, the wear characteristic and hydraulic performance of the slurry pump as the important influence factor. Therefore, a lot of investigations were carried out to improve the performance of slurry pump. Wang et al. (2021a) studied the influence of migration characteristics of particles on the flow and wear of the pump based on CFD-DEM coupling algorithm, they found that the intensity and scale of the vortex can be enhanced by increasing particle diameter. Abdolahnejad et al. (2021) studied the influence of slip factor variations on the head of centrifugal pumps, the Newtonian glass bead-water (GBW) and non-Newtonian kaolin water (KW) slurry flows were employed as the analysis medium, the result shows that decrement of slip factor for GBW is more severe than KW. Alawadhi et al. (2021) applied the response surface methodology to optimize the vane and blade geometry parameters of slurry pump. F. Khalil et al. (2013) investigated the impaction of pump

performance under different concentrations of fluid. The influence of the solid concentration, specific gravity, and particle size on the head reduction was obtained. Kumar et al. (2014) studied the relationship between the slurry pump performance and the viscosity of conveying fluid by experiment. The result presents that with the decline of conveying fluid viscosity, the head and efficiency of slurry pump are continuously decreased. Meanwhile, Duarte et al. (2015) analyzed the erosion characteristic of solid-liquid two-phase flow in an elbow. They showed that when the particle concentration is higher than 20%, as the particle concentration increases, the growth efficiency of tube wall wear gradually decreases, which results from the buffer effect. Salim et al. (2015) studied the effect of size and slurry concentration on the performance of the slurry pump at different speeds, the result reported that with the increase of particle size, specific gravity, and solid concentration, the head and efficiency gradually decrease, but the input power continuously increases. Sellgren and Addie (2010) analyzed the pump efficiency and head under different particle concentrations by experiment. Results observed that when the weight concentration of solid particles in the conveying fluid is greater than 40%, the decreased amplitude of efficiency is greater than the decreased amplitude in the head. Tarodiya and Gandhi (2019) used the sliding grid method to study the impact of three different particle sizes on the performance of slurry pumps. They found that particles with high specific gravity have little effect on the head and efficiency. Tarodiya and Gandhi (2021) combined an erosion model to analyze the wear of the impeller and volute by simulation. The result presents that surface material removal rate and higher erosion zone were mainly caused by the variation of flow rate and solid particle size. Wang et al. (2012) used the Eulerian multiphase model to study the effect of particle concentration on the performance of slurry pumps. They observed that at high concentrations, the decrease in pump performance is mainly caused by friction loss. Xiao et al. (2019) analyzed the influence of different fluid flow characteristics on erosion by tracking particles in the Lagrangian frame. They found that the flow characteristics and the type of erosion are mainly caused by variations in the geometry of the flow components. Peng et al. (2020) applied the Euler-Euler method to analyze the flow performance of slurry pumps under different particle concentrations and small flow conditions. The result shows that when the slurry pump under part-load flow condition, the internal flow field is unstable and local wear is severe. Wang et al. (2021b) studied the unsteady flow of slurry pumps under different particle diameters, and they found that particles with different diameters have a limited impact on the hydraulic performance of the pump at low concentrations.

It can be seen that much research about the influence of particle properties on pump performance was carried out. However, most research focuses on the effect of different solid-phase particle parameters on the hydraulic performance of slurry pumps, but there are few studies on optimizing the design of slurry pump flow components to improve their service life. In this paper, a new impeller with splitter blade structure was proposed, and the internal flow field of slurry pumps with

different impeller structures was analyzed. The pressure distribution, vortex structure, entropy generation are investigated by employing the Q criterion and entropy generation theory, and the wear characteristics of impeller under two-phase flow conditions are studied. Finally, the result of this paper can provide the guidelines for the design optimization of slurry pump.

COMPUTATIONAL METHODS

Computational Model

In this paper, a splitter blade is designed which arranged at the exit of impeller flow channel, as shown in **Figure 1**. The number of splitter blades is the same as the blades, and the splitter blades profile is close to the blade profile. The main geometric parameters are shown in **Table 1**. The arrangement of splitter blades on the hub is shown in **Figure 1**.

Mesh Generation

In this paper, the computational domain of slurry pump is meshed by ICEM-CFD. The quality and quantity of grid have a great influence on the convergence and reliability of the numerical simulation results. The greater number of grids and higher grids quality, which ensure more accurate calculation results can be obtained. However, too many grids will consume a lot of computing resources. Therefore, to ensure the accuracy of the numerical simulation results and rational consumption of computer resources, the grid independence of the computational domain is carried out. The calculation domain of main components is divided into a hexahedral structured grid. The structure grid is shown in **Figure 2**.

In this section, five sets of slurry pump models with different grid numbers are selected to carry out the steady flow calculations under optimal flow conditions. Finally, a set of reasonable grid numbers are selected by observing fluctuations in head and efficiency. As shown in **Table 2**, as the number of grids changes, the fluctuation of the head is within 0.9%, and the fluctuation of the efficiency is within 0.3%. When the grid number at 1.56 million, the fluctuation of the external

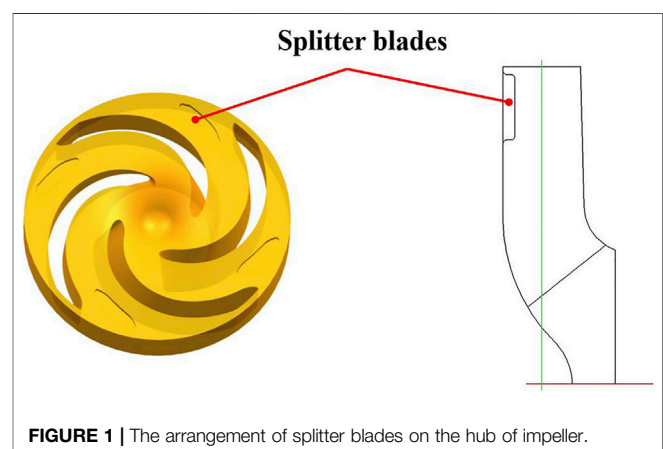


FIGURE 1 | The arrangement of splitter blades on the hub of impeller.

TABLE 1 | Main parameters of slurry pump.

Parameter	Symbol	Value
Design flow condition	Q_{BEP}	26 m ³ /h
Head	H	11 m
Rotation speed	n	1,500 rpm
Number of splitter blades	Z_i	4
Impeller outlet diameter	D_2	178 mm
Height of splitter blades	b_i	3.3 mm
The length of the splitter blades	L_i	18.3 mm

characteristics is already less than 1.0%. Therefore, the grid number is 1.56 million and the Y^+ is less than 30, which can meet the requirements of numerical simulation.

Computational Set-Up and Boundary Conditions

In the unsteady calculation process, the 3° rotation of impeller is set as a time step size, and 120-time steps are required for one revolution of impeller. The speed of the impeller is set as $n = 1,500$ rpm, and the time step is set as $t = 3.33 \times 10^{-4}$ s. The number of time steps is set as 1,200 steps, that is, the impeller rotates for 10 cycles in total, and the max iterations per time step is set as 20 steps. In the clean water simulation, the fluid medium is incompressible water at 25°C. The total pressure inflow (1atm), mass flow outflow, and standard k- ϵ turbulence model are employed for simulation. The impeller is set as the rotating domain and the inlet and outlet sections as the static domain. The convergence accuracy is set to 1.0×10^{-5} .

Figure 3 is the external characteristic curve of simulation and test of slurry pump. The measurement error of the turbine flowmeter and speed sensor are less than 0.1%, and the measurement error of the torque sensor is less than 0.5%, the measurement error of the inlet and outlet pressure sensor is less than 0.1%, while the measurement of test bench is less than 0.37%. It can be seen from the figure that the numerical

simulation results are larger than the experimental data. The main reason is that the leakage loss, disc friction loss, and friction loss between the bearing and sealing device are not considered in the numerical calculation. The maximum error of the head is at $Q = 38$ m³/h, the error is 3.35%. The maximum error of efficiency is at $Q = 17$ m³/h, the error is 1.41%. Therefore, the head and efficiency of numerical simulation can satisfy the accuracy of the investigation.

In this paper, an impeller with splitter blades is selected as scheme 1, and an impeller without splitter blades is set as scheme 2 to analyze the influence of impeller structures on the internal flow and wear characteristic of the slurry pump.

RESULTS AND DISCUSSIONS

Pressure Distribution Analysis

According to the unsteady calculation results, the impeller pressure distribution under different flow conditions is shown in **Figure 4** and **Figure 5**. The pressure distribution of the two schemes is similar, pressure gradually increases from the leading edge of the blade to the trailing edge, and the pressure contour is perpendicular to the shroud and hub. Meanwhile, the pressure distribution on the pressure surface and suction surface of the blade is not symmetrically. This phenomenon is attributed to the impeller is symmetrical geometry, while the volute is an asymmetric structure. When the impeller rotates in the volute, under the effect of rotor-stator interaction, which results in the uneven pressure distribution on the blade surface. Due to the continuous increase of the fluid linear velocity along the flow path of impeller, which makes the functional power of the blades gradually increases, thereby realizing the conversion of energy to kinetic energy and potential energy. Therefore, the pressure on the pressure side of the blade is higher than suction side at the same radius of the blade. By comparing the pressure distribution with different flow conditions, the pressure distribution at the outlet of impeller under part-load conditions is not uniform,

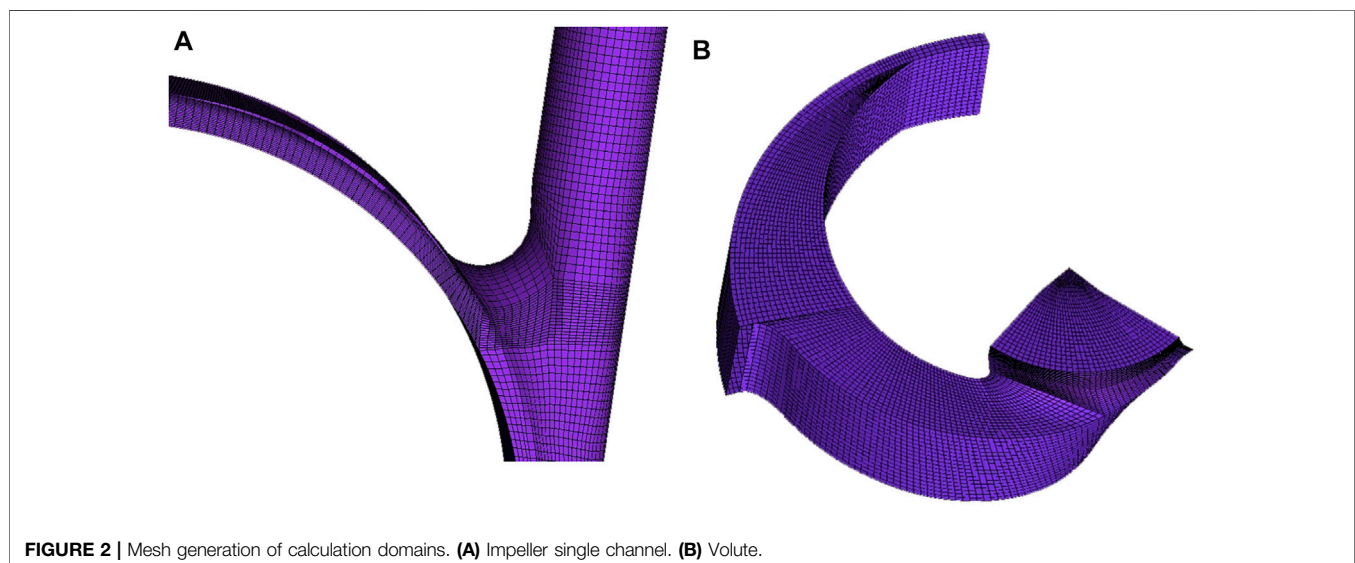
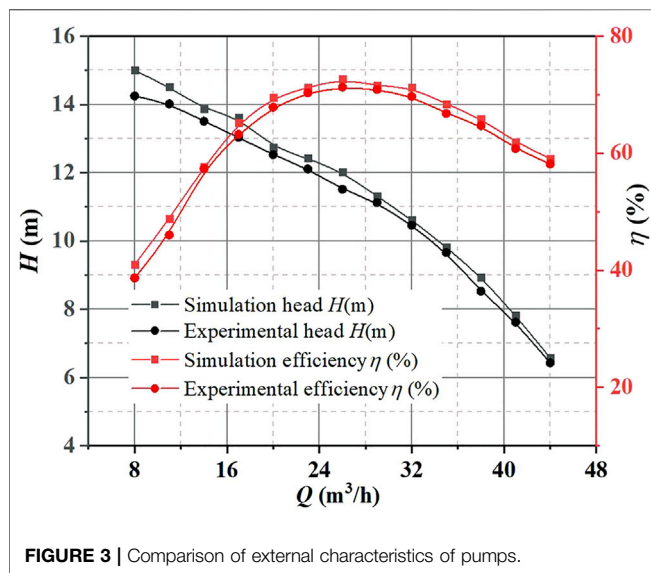


TABLE 2 | Performance comparison of different mesh numbers under optimal flow conditions.

Number of grids	Head (m)	Efficiency (%)
978990	12.07	72.81
1566234	12.01	72.69
2716867	11.97	72.64
3656186	11.98	72.62

**FIGURE 3** | Comparison of external characteristics of pumps.

which is caused by the instability of the impeller internal flow. It can be observed that the minimum pressure appears at the leading edge near the suction surface, where the pump is most prone to cavitation. As the flow rate increases, the impeller pressure gradually decreases, and the pressure distribution gradient becomes more uniform. As shown in **Figures 4, 5**, the pressure distributions of two schemes are similar, so the difference of head is very small.

Analysis of Vortex Structure Characteristic

Due to the complex flow in the slurry pump, several different types of vortices are generated in the internal flow, which will destroy the stability of the operation. Hence, in this section, the Q criterion is employed to study the vortex structure and its evolution law. At the same time, the corresponding pressure distribution is loaded on the vortex structure.

The three-dimensional vortex structure distribution inside the impeller of two schemes under the conditions of $0.6Q_{BEP}$, $1.0Q_{BEP}$, and $1.5Q_{BEP}$ are depicted in **Figures 6, 7**. According to the shape and structure of the vortex in the figure, it can be divided into leading edge vortex, trailing edge vortex, and gap leakage vortex. Since the inlet flow is affected by the rotation of the impeller, a small number of leading edge vortices can be observed at the impeller inlet. By comparing the leading edge vortices under different flow conditions, it can be found that as

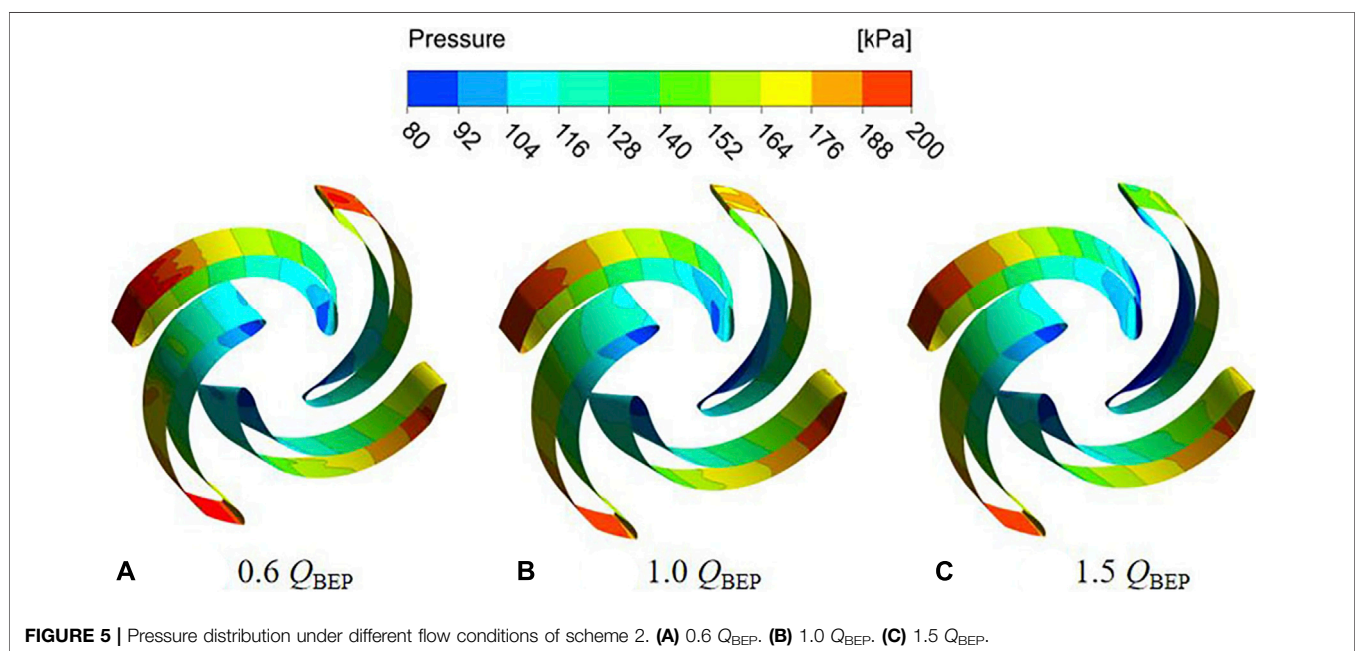
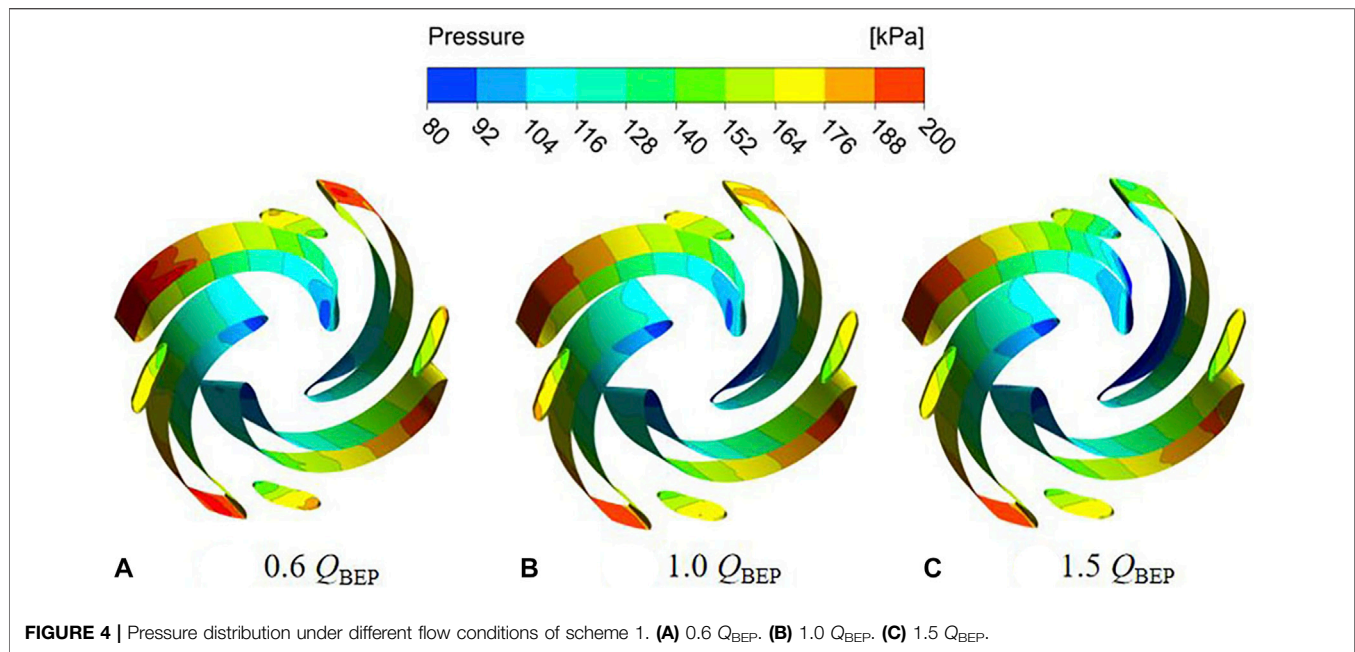
the flow rate increases, the strength of the leading edge vortices gradually increases. At the same time, the gap leakage vortices are mainly generated in the gap between the blade and volute. The overall structure of the gap leakage vortices looks like a rope, which is caused by the pressure difference between the pressure surface and suction surface of blade. Due to the pressure difference, the fluid flows from the gap between pressure surface and volute to suction surface and interacts with the main flow in the impeller channel. The rotation direction of gap leakage vortices is the same as that of the impeller. As the flow rate increases, the pressure difference between the pressure surface and suction surface will be gradually decreased, and gap leakage vortices will also gradually decrease. Furthermore, with the increase of flow rate, the trailing edge vortex will be gradually decreased. By comparing the vortex structure characteristic of two schemes under optimal flow conditions, due to the existence of splitter blades, vortices will be generated when the fluid flows through the splitter blades in the scheme 1. Therefore, the size and strength of the trailing edge vortex and gap leakage vortices are larger than those in scheme 2.

Entropy Generation Analysis

The unstable phenomenon such as back-flow, secondary flow, rotor-stator interaction is generated during the slurry pump operation, which has a great influence on the performance of slurry pump. In this section, the concept of entropy generation is introduced to calculate the energy loss caused by unstable phenomenon. The analysis method of entropy generation combines the theory of heat conduction and fluid mechanics, which is proposed from the second law of thermodynamics. It can effectively elaborate the consumption of the energy inside the system and the magnitude of the corresponding amplitude. In the numerical calculations of this paper, incompressible water at 25°C is selected as the medium, so the entropy generation transport equation in the system can be expressed as (Chang et al., 2019):

$$\rho \left(\frac{\partial s}{\partial t} + u \frac{\partial s}{\partial x} + v \frac{\partial s}{\partial y} + w \frac{\partial s}{\partial z} \right) = \text{div} \left(\frac{\bar{q}}{T} + \frac{\Phi}{T} + \frac{\Phi_{\theta}}{T^2} \right) \quad (1)$$

Where, ρ represents the density of 25°C clear water; s represents the entropy production rate, namely, the increment of entropy production in the system per unit time; x , y , and z represent the three directions in the three-dimensional coordinate system, respectively. And u , v , and w , respectively represent the corresponding velocity components of the internal velocity field of the system in the three coordinate directions of x , y , and z ; T represents the system temperature (K); Φ represents the energy dissipation variable; \bar{q} represents the heat flow density; Φ_{θ} represents the heat transfer and dissipation variables between temperature differences. Where Φ/T represents the entropy production of the system caused by energy loss and Φ_{θ}/T^2 represents the entropy production of the system caused by heat transfer and dissipation between temperature differences, furthermore these two terms are source terms, so they are always positive values. The energy dissipation variable formula can be expressed as:

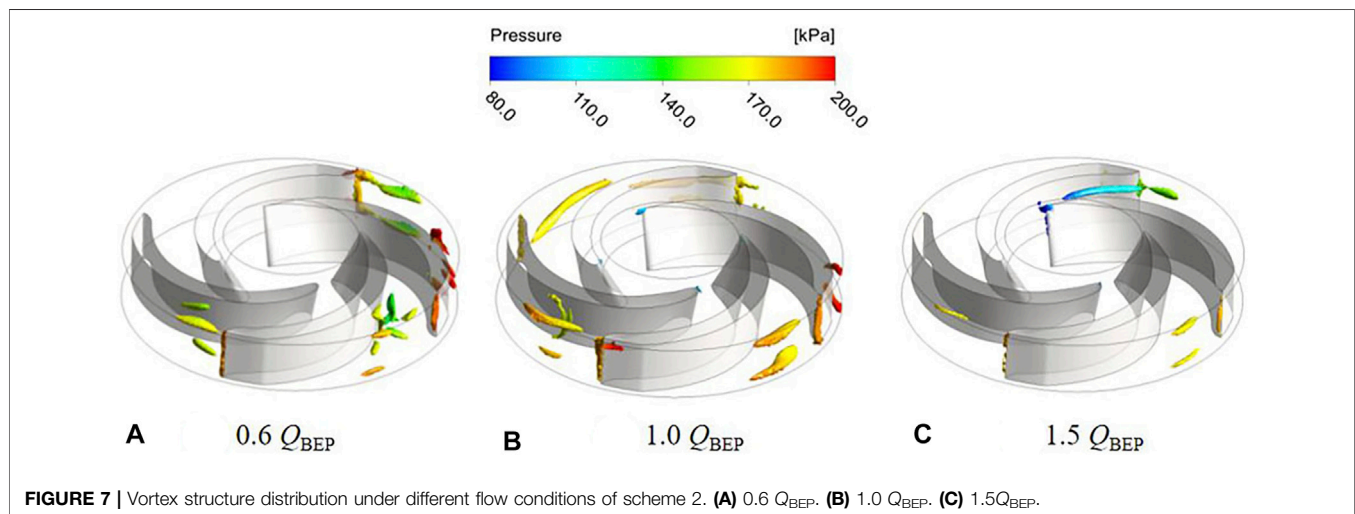
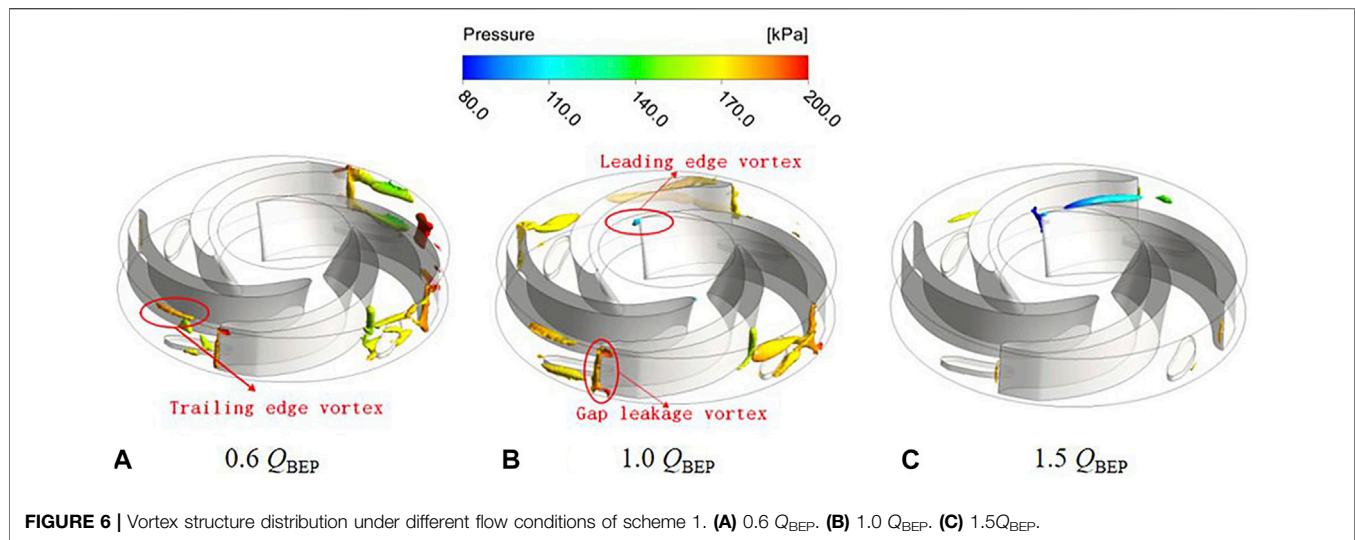


$$\Phi = \mu \left[2 \left(\frac{\partial u}{\partial x} \right)^2 + \left(\frac{\partial v}{\partial y} \right)^2 + \left(\frac{\partial w}{\partial z} \right)^2 \right] + \left[\left(\frac{\partial u}{\partial y} + \frac{\partial v}{\partial x} \right)^2 + \left(\frac{\partial u}{\partial z} + \frac{\partial w}{\partial x} \right)^2 + \left(\frac{\partial v}{\partial z} + \frac{\partial w}{\partial y} \right)^2 \right] \quad (2)$$

Since the instantaneous motion is superimposed by the time-averaged and pulsating motion. Therefore, the system entropy production caused by energy dissipation is processed by the Reynolds time average. It can be expressed as:

$$s_{VD} = \mu \left[2 \left(\frac{\partial \bar{u}}{\partial x} \right)^2 + \left(\frac{\partial \bar{v}}{\partial y} \right)^2 + \left(\frac{\partial \bar{w}}{\partial z} \right)^2 \right] + \left[\left(\frac{\partial \bar{u}}{\partial y} + \frac{\partial \bar{v}}{\partial x} \right)^2 + \left(\frac{\partial \bar{u}}{\partial z} + \frac{\partial \bar{w}}{\partial x} \right)^2 + \left(\frac{\partial \bar{v}}{\partial z} + \frac{\partial \bar{w}}{\partial y} \right)^2 \right] \quad (3)$$

Where, \bar{u} , \bar{v} , and \bar{w} represent the time-average velocity component respectively, μ represents the dynamic viscosity, T represents the temperature, the symbol “-” represents the time average parameter variable, s_{VD} represents the viscous entropy production caused by viscous dissipation.



$$s_{TD} = \frac{\mu}{T} \left[2 \left(\overline{\left(\frac{\partial u'}{\partial x} \right)^2} + \overline{\left(\frac{\partial v'}{\partial y} \right)^2} + \overline{\left(\frac{\partial w'}{\partial z} \right)^2} \right) + \left[\overline{\left(\frac{\partial u'}{\partial y} + \frac{\partial v'}{\partial x} \right)^2} + \overline{\left(\frac{\partial u'}{\partial z} + \frac{\partial w'}{\partial x} \right)^2} + \overline{\left(\frac{\partial v'}{\partial z} + \frac{\partial w'}{\partial y} \right)^2} \right] \right] \quad (4)$$

Where, u' , v' , and w' represent velocity fluctuation component respectively, the symbol “ $\overline{}$ ” represents the pulsating parameter variable, s_{TD} represents the entropy production of turbulent kinetic energy caused by turbulent kinetic energy dissipation.

However, in the actual calculation process, the pulsation velocity is difficult to obtain by direct measurement. Hence, Herwig et al. (2008) proposed a new calculation method to directly solve the turbulent energy dissipation entropy generation by using the turbulent energy dissipation rate, the calculation formula between the entropy production of turbulent

kinetic energy and the rate of turbulent energy dissipation can be expressed as:

$$s_{TD} = \frac{\rho \varepsilon}{T} \quad (5)$$

Where, ε represents the turbulent energy dissipation rate, T represents the system temperature (K).

At the same time, considering the system entropy production generated by heat transfer between temperatures, Duan et al. (2014) found that the entropy production caused by heat transfer between time-average temperature differences is consistent with the entropy production caused by heat transfer between fluctuating temperature differences. Therefore, the entropy production of heat transfer between temperature differences can be obtained. The calculation formula can be expressed as:

$$s_T = \frac{\lambda_{eff}}{T^2} \left[\left(\frac{\partial \bar{T}}{\partial x} \right)^2 + \left(\frac{\partial \bar{T}}{\partial y} \right)^2 + \left(\frac{\partial \bar{T}}{\partial z} \right)^2 \right] \quad (6)$$

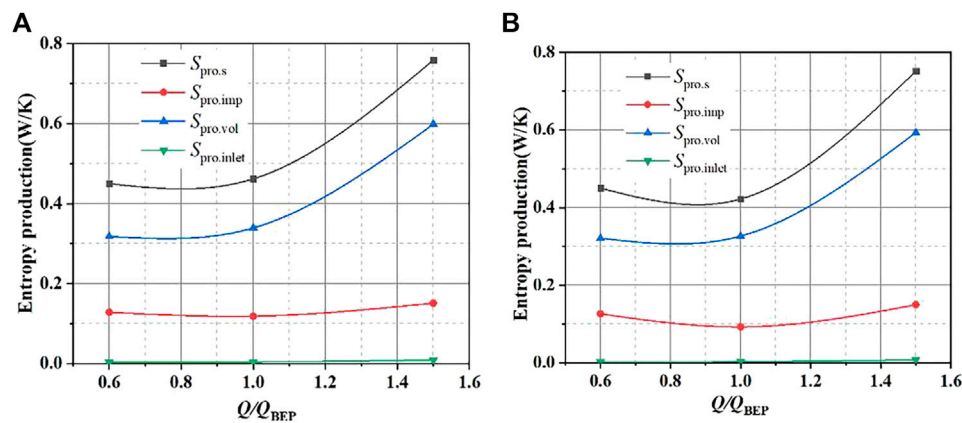


FIGURE 8 | Entropy production analysis. (A) Scheme 1. (B) Scheme 2.

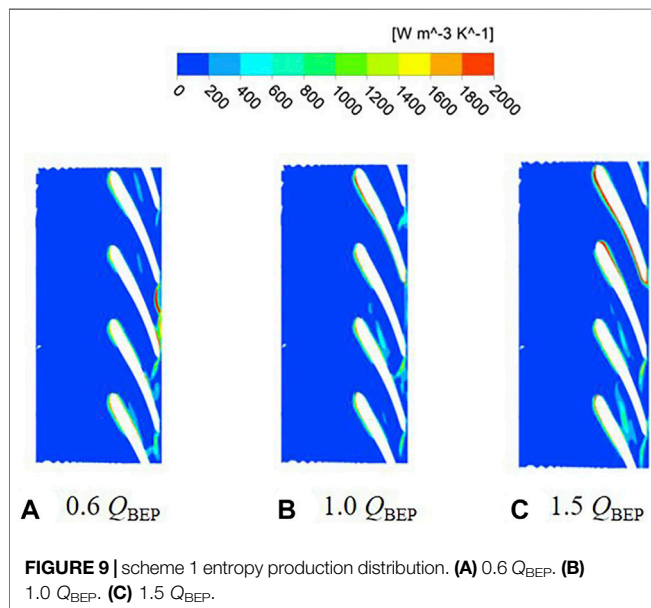


FIGURE 9 | scheme 1 entropy production distribution. (A) $0.6 Q_{BEP}$. (B) $1.0 Q_{BEP}$. (C) $1.5 Q_{BEP}$.

Where λ represents the thermal conductivity, λ_{eff} represents the effective thermal conductivity, which can be calculated by the following formula:

$$\lambda_{eff} = \lambda + \lambda_t \quad (7)$$

Where λ_t represents the turbulent thermal conductivity, which can be calculated by the following formula:

$$\lambda_t = \frac{c_p \mu_t}{Pr_t} \quad (8)$$

Where c_p represents the specific heat capacity at constant pressure, μ_t represents the turbulent viscosity, and Pr_t represents the turbulent Prandtl number.

At the same time, the viscous entropy production and the turbulent kinetic energy entropy production in the calculation

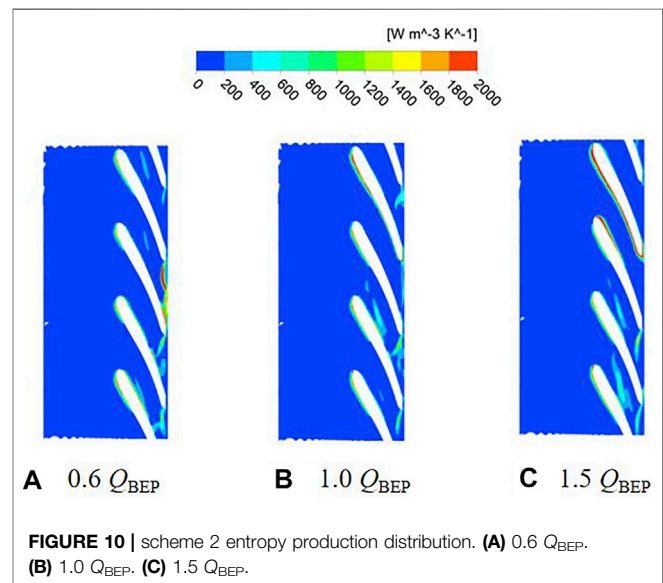


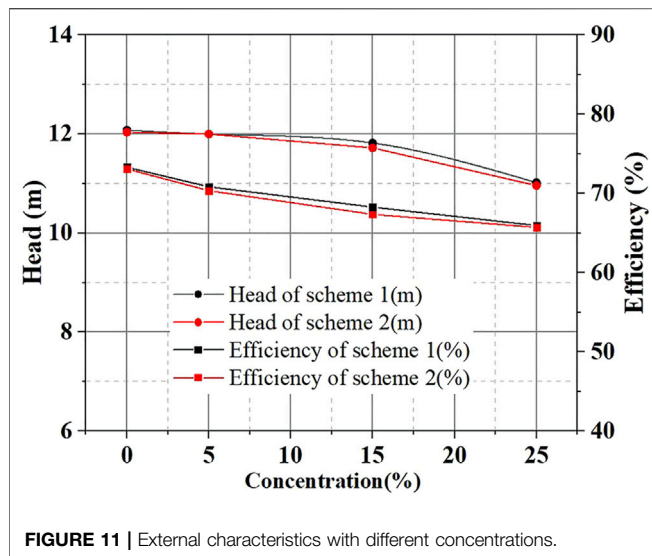
FIGURE 10 | scheme 2 entropy production distribution. (A) $0.6 Q_{BEP}$. (B) $1.0 Q_{BEP}$. (C) $1.5 Q_{BEP}$.

domain are respectively integrated and calculated. Therefore, the total viscosity entropy production and total turbulent kinetic energy entropy production can be obtained as follows:

$$S_{VD} = \int_V S_{vd} dV \quad (9)$$

$$S_{VD} = \int_V S_{vd} dV \quad (10)$$

The total entropy production of the system can be obtained by integrating the viscous entropy production and turbulent kinetic energy entropy production in the computational domain grid volume by Eqs 9, 10. Because the slurry pump is simulated under normal temperature and pressure, the simulated water temperature is 298K, considering that the temperature change in the simulation process is minimal, so the entropy production



caused by the temperature difference can be ignored. In the simulation process, only viscous entropy production and turbulent kinetic energy entropy production are analyzed.

Figure 8 shows the total entropy production of the two pumps and the corresponding entropy production in different areas under different flow conditions. Where $S_{pro,s}$ represents the total entropy production, $S_{pro,imp}$ represents the entropy production in the impeller, and $S_{pro,vol}$ represents the entropy production in the volute, $S_{pro,inlet}$ represents the entropy production in the inlet section. It can be seen from figure that the total entropy production of two schemes shows the same variation trend. The total entropy production of different regions presents first decrease and then increase with the increase of flow rate. Finally, reaching the minimum value under optimal flow conditions. Among them, the entropy production of the volute, the impeller, and the inlet section decreases sequentially. The total entropy production of scheme 1 under optimal flow conditions is 0.42W/K, and the total entropy production of scheme 2 under the optimal flow conditions is 0.46W/K. Namely, the energy loss caused by entropy production in the slurry pump can be declined by employing the splitter blades.

The total entropy production analysis of the expanded cross-section on impeller span = 0.5 is shown in **Figures 9, 10**. It can be seen from the figure that the internal losses of the impeller are mainly concentrated at the trailing edge and leading edge of the blade. When the fluid enters the impeller, obvious impaction is generated at the leading edge of blade. As the flow rate increases, the fluid velocity increases which intensifies the fluid shock, resulting in a greater impact loss at the leading edge of blade. At the same time, the energy loss at the trailing edge of blade is caused by the rotor-stator interaction between impeller and volute. Due to the splitter blades restrain the flow separation at impeller outlet, therefore, the entropy production of scheme 1 is less than scheme 2. From the previous analysis of the vortex structure, an obvious vortex structure is generated at the leading

edge and trailing edge of blade, and the vortex structure will form energy loss and further generate entropy production. The entropy production near the suction surface of the blade is greater than the entropy production near the pressure surface of the blade, and the total entropy production is larger at the trailing edge of blade.

However, under part-load flow conditions, the total entropy production distribution of each flow channel in the impeller is different. This phenomenon is attributed to the flow of each channel in impeller is significantly different under part-load flow conditions. As the flow rate increases, the entropy production is concentrated on the suction surface of blade, which results from the positive attack angle of blade was employed. With increasing flow rate, the angle of attack at the leading edge of the blade enhances, thereby causing a greater energy loss in the area of the suction surface of the blade.

Wear Analysis of Different Impeller Structures

The abrasion of the slurry pump is an important factor, which affects its efficient operation when conveying solid-liquid two-phase slurry, and it directly determines the service life of slurry pump. Therefore, research on the wear of slurry pumps is an important part of optimizing the slurry pump impeller. In this section, solid-liquid two-phase flow analysis of slurry pumps with different impeller structures is carried out.

The external characteristic curve of the slurry pump with different concentrations is shown in **Figure 11**, the brown aluminium oxide is employed as the solid particles, and the diameter of the solid particles is 0.6 mm, the density of brown aluminium oxide is 2900 kg/m³. It can be seen from figure that as the concentration increases, the head and efficiency of the pump present a declining trend. The descent rate of the head gradually improves with the increase of concentration. Whereas the descent rate of head gradually declines with the increase of the concentration. It found that the external characteristics of impeller with splitter blades are slightly higher than scheme 1. When the solid phase volume concentration improves to $C_V = 25\%$, the head of scheme 1 drops by 8.77%, and the efficiency drops by 10.01%, and the head of scheme 2 drops by 8.97% and the efficiency drops by 10.11%. Therefore, to analyze and compare the wear characteristic of the slurry pump impeller, the solid phase two-phase flow simulation of the slurry pump impeller under $C_V = 15\%$ and particle diameter with 0.6 mm are selected for further research.

Figure 12 present the solid phase volume fractions distribution of two schemes under optimal flow conditions. It can be seen from figure that the solid phase volume fraction distribution on the blade surface is not uniform, and the solid phase volume fraction is relatively high at the leading edge of the blade, the junction between the blade pressure surface and hub, and the junction between the suction surface of the blade and shroud. This phenomenon is attributed to the solid particles enter the impeller, under the effect of inertial force and centrifugal force, obvious impaction is generated at the junction between the blade pressure surface and hub. The volume fraction of the solid phase between suction surface of the blade and shroud is smaller

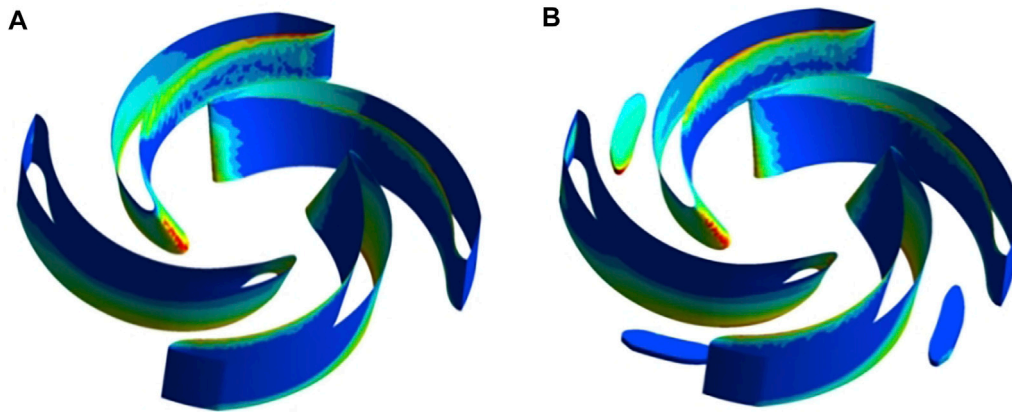


FIGURE 12 | Solid volume fraction distribution on the blade. **(A)** Scheme 1. **(B)** Scheme 2.

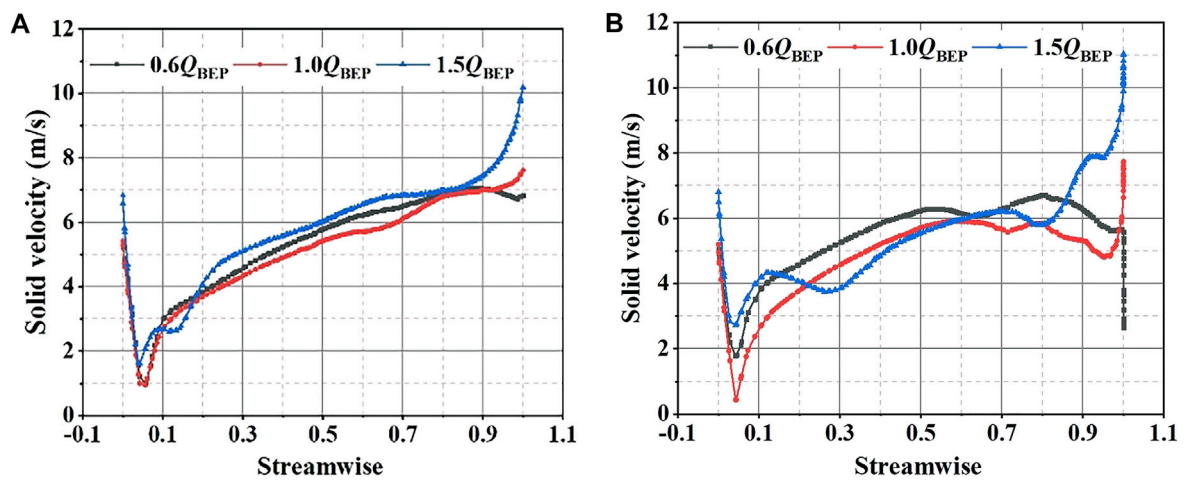


FIGURE 13 | The solid velocity of blade pressure surface. **(A)** Scheme 1. **(B)** Scheme 2.

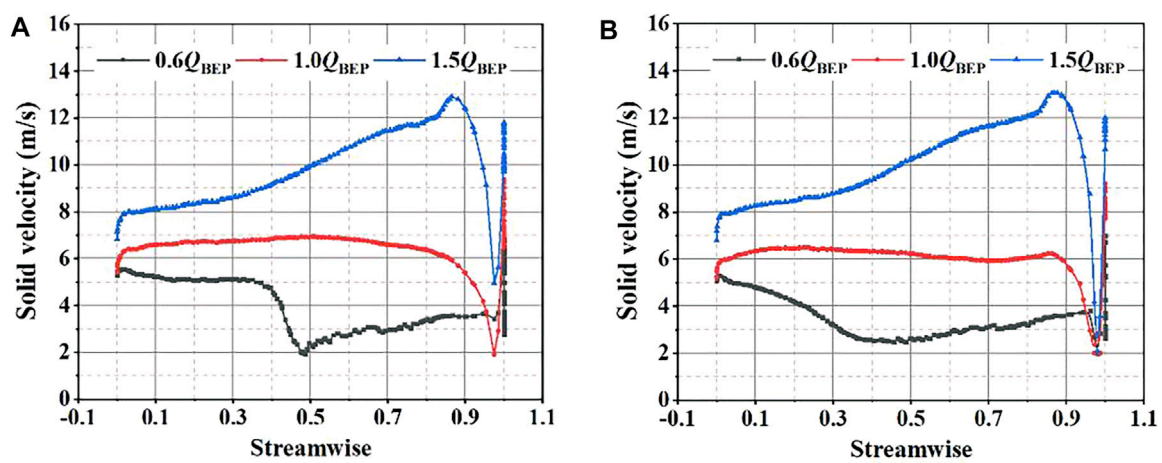


FIGURE 14 | The solid velocity of blade suction surface. **(A)** Scheme 1. **(B)** Scheme 2.

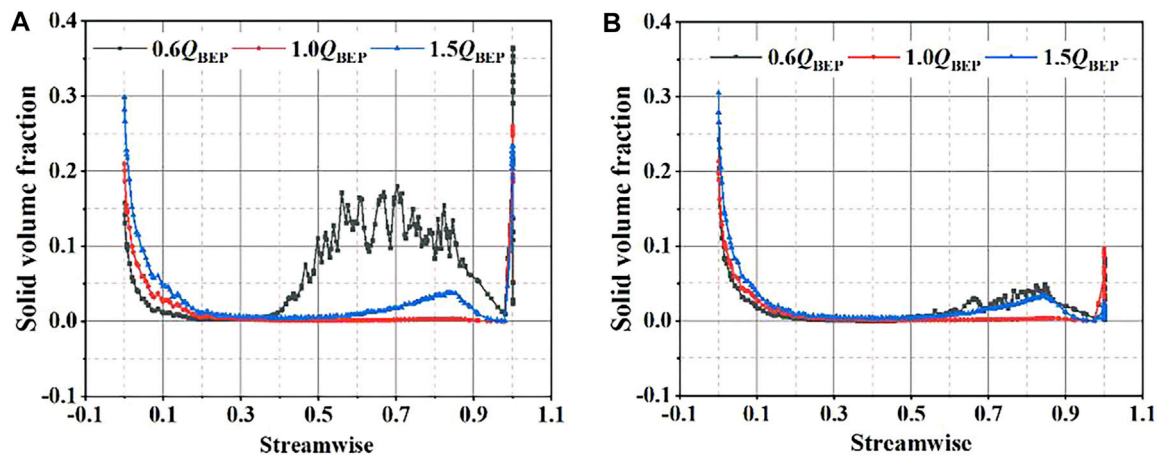


FIGURE 15 | The solid volume fraction of blade pressure surface. (A) scheme 1. (B) scheme 2.

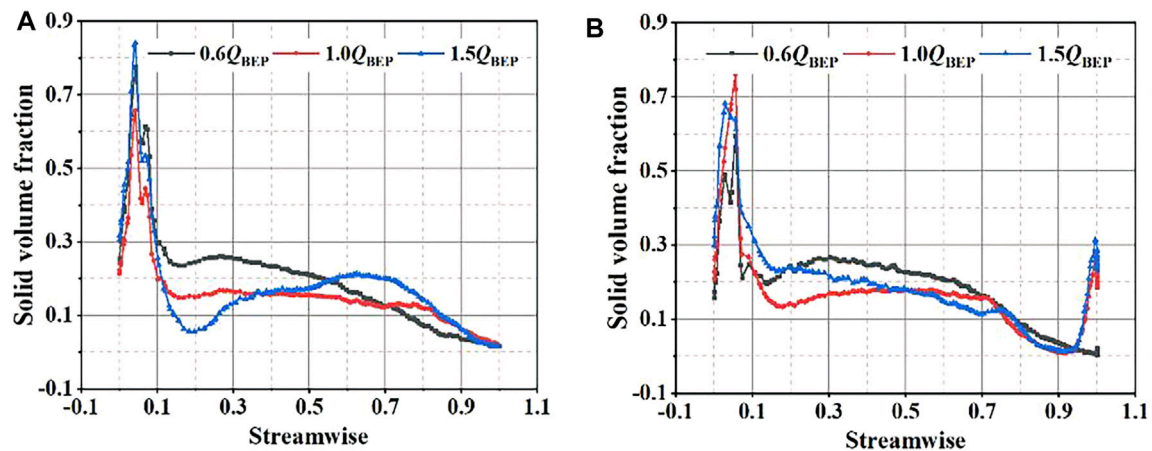


FIGURE 16 | The solid volume fraction of blade suction surface. (A) scheme 1. (B) scheme 2.

than the junction of the pressure surface and hub. Due to the inertial force of the particles, more solid particles move to the hub.

Furthermore, the solid phase volume fraction and solid-phase slip velocity on the blade middle section are analyzed to compare the wear characteristic with different impeller structures. As shown in Figures 13, 14, the solid-phase slip velocity on the blade pressure surface first declines and then increases, which reaches the maximum at the trailing edge. It results from that the dual effect of centrifugal force and inertial force, which lead to the velocity of solid particles first decreases and then increases. At the same time, with the increase of the flow rate, the solid-phase slip velocity on the suction surface is gradually higher than the pressure surface, and the wear of the suction surface is aggravated. What is more, due to the effect of splitter blades, the slight fluctuations in the solid-phase slip velocity are generated at the trailing edge of the pressure surface, while the splitter blades have

almost no effect on the sliding velocity of solid particles on the suction surface.

The solid volume fraction distribution on the middle section of the blade is shown in Figures 15, 16. It can be seen from the figure that the volume fraction of the solid phase at the leading edge of blade is relatively large. This mainly results from that the particle impact at the impeller inlet, and under the interaction effect of centrifugal force and inertial force, which will cause the particles accumulation on the leading edge of blade. It can be found that the solid particles are more likely to accumulate due to the lower speed of the solid particles driven by the liquid under $0.6Q_{BEP}$. As the flow rate increases, the volume fraction of the solid phase on the blade continuously declines, and the volume fraction of the solid phase on the pressure surface of the blade is greater than the suction surface. What is more, in scheme 1, when the streamwise of the blades is between 0.9 and 1.0, the blockage is generated by

the splitter blades of particle impaction, resulting in the accumulation of solid particles, which makes the solid phase volume fraction of scheme 1 larger than in the scheme 2. Therefore, the wear characteristic of scheme 1 with splitter blades is better than scheme 2.

CONCLUSION

In this paper, the internal flow field of slurry pumps with different impeller structures was analyzed. The pressure distribution, vortex structure, entropy generation are investigated by employing the Q criterion and entropy generation theory, and the wear characteristics of the impeller under two-phase flow conditions are studied. The following conclusions can be obtained:

- 1) A new impeller with splitter blades arranged at the exit of impeller flow channel was proposed. The pressure distribution of different impeller structures under diverse flow conditions was analyzed. Due to the continuous increase of the fluid linear velocity along the flow path of impeller, which makes the functional power of the blades gradually increases. Therefore, the pressure on the pressure side of blade is higher than suction side at the same radius of the blade. As the flow rate increases, the impeller pressure gradually decreases, and the pressure distribution gradient becomes more uniform.
- 2) According to the shape and structure of the vortex in the slurry pump, it can be divided into leading edge vortex, trailing edge vortex, and gap leakage vortex by employing the Q criterion. The generation mechanism of each vortex was analyzed. Meanwhile, as the flow rate increases, the strength of the leading edge vortices gradually increases, but the trailing edge vortex and gap leakage vortex continuously decline. By comparing the vortex structure characteristic of two schemes under optimal flow conditions, due to the existence of splitter blades, the blockage will be generated when the fluid flows through the splitter blades in scheme 1. Therefore, the size and strength of the trailing edge vortex and gap leakage vortices are larger than those in scheme 2.
- 3) Entropy production theory was introduced to investigate the energy loss of the slurry pump. The main energy loss is generated by viscous entropy production and turbulent kinetic energy entropy production. The total entropy production of different regions presents first decrease and then increase with the increase of flow rate. Finally, reach the minimum value under optimal flow conditions. And the total entropy production of scheme 1 under optimal flow conditions

is 0.42W/K, and the total entropy production of scheme 2 under the optimal flow conditions is 0.46W/K. Namely, the energy loss caused by entropy production in the slurry pump can be declined by employing the splitter blades, which can restrain the flow separation at the impeller outlet.

- 4) The wear characteristics of the slurry pump were studied, with the increase of the flow rate, the solid-phase slip velocity on the suction surface is gradually higher than the pressure surface, and the wear of the suction surface is aggravated. What is more, due to the effect of splitter blades, the slight fluctuations in the solid-phase slip velocity are generated at the trailing edge of the pressure surface, while the splitter blades have almost no effect on the sliding velocity of solid particles upon the suction surface. When the streamwise of the blades is between 0.9 and 1.0, the blockage is generated by the splitter blades of particle impaction, resulting in the accumulation of solid particles, which makes the solid phase volume fraction of scheme 1 larger than in scheme 2. Therefore, the wear characteristic of scheme 1 with splitter blades is better than scheme 2.

DATA AVAILABILITY STATEMENT

The raw data supporting the conclusion of this article will be made available by the authors, without undue reservation.

AUTHOR CONTRIBUTIONS

This is a joint work and the authors were in charge of their expertise and capability: GP for investigation, analysis, writing and revision; JD and HC for methodology and revision; QC for validation and revision; JL and CP for data analysis; YY for manuscript revision.

FUNDING

Open Research Fund Program of State key Laboratory of Hydro-science and Engineering grant number: sklhse-2020-E-01; Open Research Subject of Key Laboratory of Fluid Machinery and Engineering (Xihua University) grant number LTJX2021-003; Open Research Subject of Hubei Key Laboratory of Hydroelectric Machinery Design and Maintenance (China Three Gorges University) grant number 2020KJX07; The 69th batch of general funding from the China Postdoctoral Science Foundation grant number: 2021M691298; Priority Academic Program Development of Jiangsu Higher Education Institutions (PAPD).

REFERENCES

- Abdolahnejad, E., Moghimi, M., and Derakhshan, S. (2021). Experimental and Numerical Investigation of Slip Factor Reduction in Centrifugal Slurry Pump [J]. *J. Braz. Soc. Mech. Sci. Eng.* 43 (4), 1–14. doi:10.1007/s40430-021-02831-x
- Alawadhi, K., Alzuwayer, B., Mohammad, T. A., and Buhemdi, M. H. (2021). Design and Optimization of a Centrifugal Pump for Slurry Transport Using the Response Surface Method. *Machines* 9 (3), 60. doi:10.3390/machines9030060
- Chang, H., Shi, W., Li, W., and Liu, J. (2019). Energy Loss Analysis of Novel Self-Priming Pump Based on the Entropy Production Theory. *J. Therm. Sci.* 28 (2), 306–318. doi:10.1007/s11630-018-1057-5

- Duan, L., Wu, X., and Ji, Z. (2014). Application of Entropy Generation Method for Analyzing Energy Loss of Cyclone Separator[J]. *J. Chem. Industry Eng.* 65, 583–592.
- Duarte, C. A. R., de Souza, F. J., and dos Santos, V. F. (2015). Numerical Investigation of Mass Loading Effects on Elbow Erosion. *Powder Tech.* 283, 593–606. doi:10.1016/j.powtec.2015.06.021
- F. Khalil, M., Z. Kassab, S., A. Abdel Naby, A., and Azouz, A. (2013). Performance Characteristics of Centrifugal Pump Conveying Soft Slurry. *Ajme* 1 (5), 103–112. doi:10.12691/ajme-1-5-1
- Herwig, H., Gloss, D., and Wenterodt, T. (2008). A New Approach to Understanding and Modelling the Influence of wall Roughness on Friction Factors for Pipe and Channel Flows. *J. Fluid Mech.* 613, 35–53. doi:10.1017/s0022112008003534
- Kumar, S., Gandhi, B. K., and Mohapatra, S. K. (2014). Performance Characteristics of Centrifugal Slurry Pump with Multi-Sized Particulate Bottom and Fly Ash Mixtures. *Particulate Sci. Tech.* 32 (5), 466–476. doi:10.1080/02726351.2014.894163
- Peng, G., Huang, X., Zhou, L., Zhou, G., and Zhou, H. (2020). Solid-liquid Two-phase Flow and Wear Analysis in a Large-Scale Centrifugal Slurry Pump. *Eng. Fail. Anal.* 114, 104602. doi:10.1016/j.engfailanal.2020.104602
- Salim, B., Bajawi, H. Y., and Suhaibani, Z. (2015). Performance of a Centrifugal Slurry Pump with Clinker Slurry [J]. *Indian J. Sci. Tech.* 8 (12), 1. doi:10.17485/ijst/2015/v8i12/56300
- Sellgren, A., and Addie, G. (2010). Effects of Highly Concentrated Slurries on the Performance of Centrifugal Pumps. [J] 78 (4), 764–769.
- Tarodiya, R., and Gandhi, B. (2021). Numerical Investigation of Erosive Wear of a Centrifugal Slurry Pump Due to Solid-Liquid Flow [J]. *J. Tribology* 143, 1–24. doi:10.1115/1.4049596
- Tarodiya, R., and Gandhi, B. K. (2019). Numerical Simulation of a Centrifugal Slurry Pump Handling Solid-Liquid Mixture: Effect of Solids on Flow Field and Performance. *Adv. Powder Tech.* 30 (10), 2225–2239. doi:10.1016/j.appt.2019.07.003
- Wang, P. W., Zhao, J., Zou, W. J., and Hu, S. G. (2012). Experimental Study and Numerical Simulation of the Solid-phase Particles' Influence on outside Characteristics of Slurry Pump. *IOP Conf. Ser. Earth Environ. Sci.* 15 (6), 062057, 2012. IOP Publishing. doi:10.1088/1755-1315/15/6/062057
- Wang, R., Guan, Y., Jin, X., Tang, Z., Zhu, Z., and Su, X. (2021). Impact of Particle Sizes on Flow Characteristics of Slurry Pump for Deep-Sea Mining. *Shock and Vibration* 2021, 1–13. doi:10.1155/2021/6684944
- Wang, Y., Chen, B., Zhou, Y., Ma, J., Zhang, X., Zhu, Z., et al. (2021). Numerical Simulation of Fine Particle Solid-Liquid Two-phase Flow in a Centrifugal Pump. *Shock and Vibration* 2021 (20), 1–10. doi:10.1155/2021/6631981
- Xiao, Y., Guo, B., Ahn, S.-H., Luo, Y., Wang, Z., Shi, G., et al. (2019). Slurry Flow and Erosion Prediction in a Centrifugal Pump after Long-Term Operation. *Energies* 12 (8), 1523. doi:10.3390/en12081523

Conflict of Interest: Author GP is employed by Jiangsu University.

The remaining authors declare that the research was conducted in the absence of any commercial or financial relationships that could be construed as a potential conflict of interest.

Publisher's Note: All claims expressed in this article are solely those of the authors and do not necessarily represent those of their affiliated organizations, or those of the publisher, the editors and the reviewers. Any product that may be evaluated in this article, or claim that may be made by its manufacturer, is not guaranteed or endorsed by the publisher.

Copyright © 2021 Peng, Du, Chang, Chen, Li, Pan and Yang. This is an open-access article distributed under the terms of the Creative Commons Attribution License (CC BY). The use, distribution or reproduction in other forums is permitted, provided the original author(s) and the copyright owner(s) are credited and that the original publication in this journal is cited, in accordance with accepted academic practice. No use, distribution or reproduction is permitted which does not comply with these terms.



Mathematical Model of the Deaeration of Finely Dispersed Solid Media in a Spherical Matrix of a Roller-Type Apparatus

Anna Kapranova*, Mikhail Tarshis, Natalya Badaeva and Irina Sheronina

Yaroslavl State Technical University, Yaroslavl, Russia

OPEN ACCESS

Edited by:

Zheng Li,

Vanderbilt University, United States

Reviewed by:

Xiaoyu Zhang,

Vanderbilt University, United States

Bo Jiang,

Nanjing University of Science and Technology, China

*Correspondence:

Anna Kapranova

kapranova_anna@mail.ru

Specialty section:

This article was submitted to

Advanced Clean Fuel Technologies,

a section of the journal

Frontiers in Energy Research

Received: 02 September 2021

Accepted: 27 October 2021

Published: 24 November 2021

Citation:

Kapranova A, Tarshis M, Badaeva N and Sheronina I (2021) Mathematical Model of the Deaeration of Finely Dispersed Solid Media in a Spherical Matrix of a Roller-Type Apparatus. *Front. Energy Res.* 9:769940. doi: 10.3389/fenrg.2021.769940

The additional operation of deaeration (compaction) of powders affects the quality of many products of chemical industries, the conditions for their delivery. Otherwise, energy consumption increases significantly. The aim of this work is the modeling of the deaeration of solid finely dispersed media in a gap with perforated hemispherical shapes on the surfaces of the shaft and conveyor belt within the framework of the mechanics of heterogeneous systems. A plane-deformation model is described, neglecting the forces of interphase interaction and taking into account the compressibility of a solid-particle-gas mixture without elastoplastic deformations. The model assumes consideration of the movement of (1) the components of the solid skeleton together with the carrying phase as a whole; (2) gas in an isothermal state through the pores of a finely dispersed material. This work is devoted to the study of part (a), i.e., behavior of the solid particle-gas system as a whole. The efficiency of the seal-deaerator is estimated using the obtained analytical dependencies for the main strength and speed indicators. The change in the degree of compaction of a spherical granule made of kaolin with given strength characteristics is investigated. It is shown that for the initial time interval up to 3.7×10^{-2} s, the growth of the porosity value relative to the horizontal coordinate along the conveyor belt is exponential and increases by a factor of 1.1. After eight such time intervals, the porosity values stabilize along the indicated coordinate with an increase of more than 1.4 times from the initial value.

Keywords: model, deaeration (densification), finely dispersed medium, roller, porosity

INTRODUCTION

Preliminary deaeration (compaction) of powder components (Akiyama et al., 1986; Kapranova and Zaitzev, 2011; Francis, 2016), including soot and kaolin, affects the strength characteristics of the finished product, for example, car tires, and other polymer products. Transportation of sealed containers with a powder product with a high content of gas in its pores, in particular, for construction or food purposes, violates the principles of energy saving and energy efficiency. In contrast to the pressing of powders (Pizette et al., 2010; Bayle et al., 2016; Seong et al., 2020) or larger particles (Gai et al., 2005), deaeration refers to its initial stage, when there is no destruction of particles of the compacting medium. If it is necessary to obtain a special structure of a dispersed medium with given strength characteristics, it is advisable to use a mechanical deaeration method (Akiyama et al., 1986; Kapranova and Zaitzev, 2011) in particular, when obtaining granules from bitumen and mineral powder (Zaitsev et al., 2010), dry dye mixtures.

The design of roller devices for the deaeration of dispersed media is associated with the formation of theoretical foundations (Kapranova et al., 2000; Kapranova, 2010; Kapranova et al., 2015) for the engineering calculation of the parameters of these devices (Kapranova et al., 2001; Kapranova et al., 2006a; Kapranova et al., 2006b). For example, this is relevant in the manufacture of granules (Zaitsev et al., 2010) from bitumen (Santos et al., 2014; Fingas and Fieldhouse, 2009) and mineral powder (Renner et al., 2007). For these purposes, as a rule, the mechanics of heterogeneous systems are used (Nigmatulin, 1978; Generalov, 2002). The analytical results (Kapranova et al., 2000; Kapranova, 2010; Kapranova et al., 2015) when describing the behavior of the system solid particles-gas have some advantages over numerical solutions, (Pizette et al., 2010; Bayle et al., 2016; Seong et al., 2020) for example, when choosing rational ranges for changing the main parameters of the compaction process or when evaluating their optimal values (Kapranova et al., 2001; Kapranova et al., 2006a; Kapranova et al., 2006b). The importance of understanding the mechanism of the behavior of compacted materials is obvious for any type of modeling methods: analytical (Kapranova and Zaitsev, 2011; Kapranova et al., 2015; Udalov et al., 2019) or numerical (Khoei, 2005; Pizette et al., 2010; Bayle et al., 2016; Seong et al., 2020).

There are two sufficiently developed classical approaches to the formation of the initial model for calculating the main indicators of the powder compaction process. In the first method (roller rolling of metal powders) (Generalov, 2002; Wang et al., 2015), the conditions of air outflow from volumes are experimentally investigated depending on the shape of the constituent particles during their granulometric analysis (Vinogradov et al., 1969; Pimenov et al., 2015). In this case, scaling methods are used (Pimenov et al., 2015) within the framework of the Pi-Buckingham theorem (Buckingham, 1915; Annenkov et al., 2005); equilibrium equations (Generalov, 2002; Misic et al., 2010) and the limit state in the linearized representation (Tselikov et al., 1980; Generalov et al., 1984); indicators of changes in the volume of the specified workpiece (Generalov and Chainikov, 1972; Tselikov et al., 1980; Hu et al., 2021). The second method of description (Torner, 1977) does not make it possible to consider the compressibility of the system solid particles - gas when air is removed from the pores.

Two factors here are two factors that determine the modeling approach to modeling based on (Nigmatulin, 1978): (1) a significant content of the carrier phase in the composition of the specified system of solid particles—gas; (2) the maximum possible value of the degree of compaction of the material. This method makes it possible to carry out analytical calculations for the main indicators of the process under study, depending on the coordinates, time, design, and operating parameters, in particular, for the porosity of the mixture of solid particles-gas and the components of the velocity of the phases.

THEORY

Hemispherical shaft and belt surfaces are used to obtain deaerated portions of powder (Figure 1) with radius r . The Cartesian

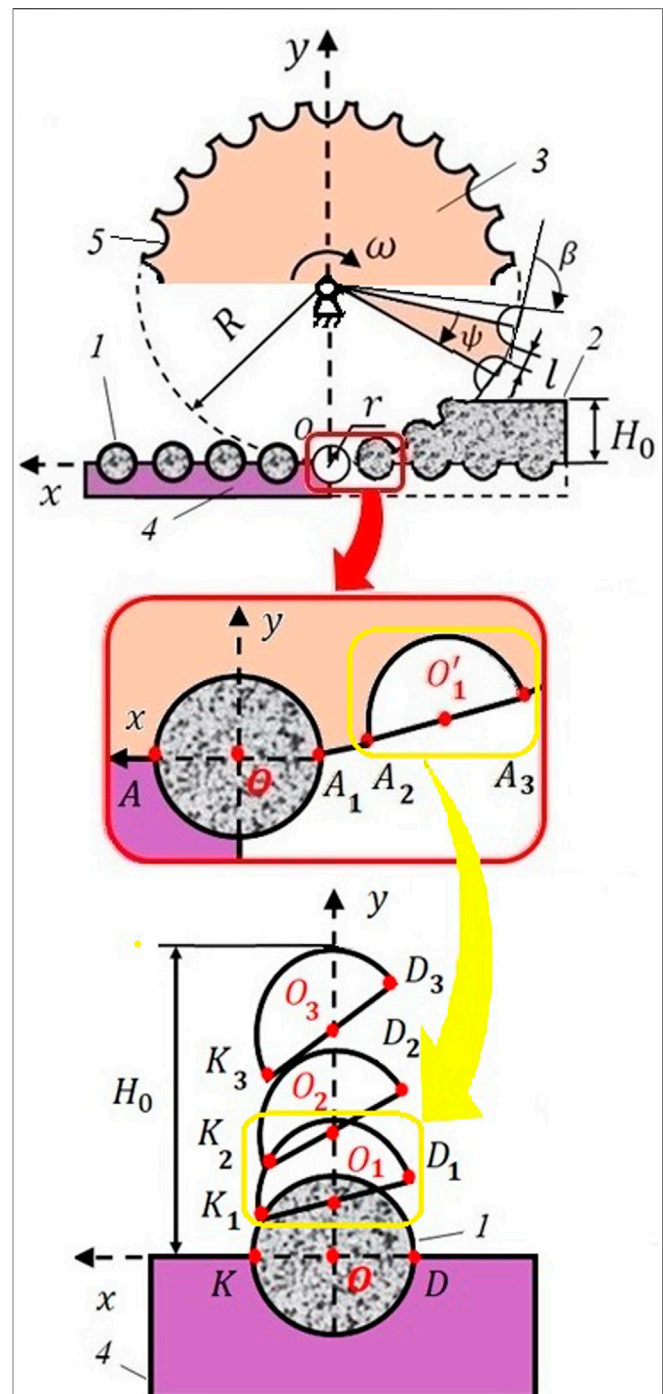


FIGURE 1 | Conditional scheme for the movement of the compacted finely dispersed medium in the gap of the shaft-conveyor belt: 1—deaerated granule-sphere; 2—solid finely dispersed material; 3—shaft; 4—conveyor belt; 5—hemispherical shapes (cells).

coordinate system Oxy and the “inverted” motion method (Kapranova et al., 2000; Kapranova et al., 2015) are used when the horizontal tape appears to be stationary. The planar motion of the surfaces of the shaft forms is assumed when decomposed into translational motion together with the K_i pole (Figure 1).

Let the total number of flat cells on the rim of the shaft section be N and the number of centers belonging to a quarter of the rim is denoted $n = N/4$. Then the coordinates of the points K_i , D_i , and O_i (**Figure 1**) are determined by the recurrent formulas ($i = 1, n_0 - 1$).

$$x_{K_i} = r; y_{K_i} = 2r \sin[(i-1)\varphi] + l \sum_{j=0}^{i-1} \sin[(2j+1)\gamma] \quad (1)$$

$$x_{D_i} = r(1 - 2 \cos i\varphi); y_{D_i} = l \sum_{j=0}^{i-1} \sin[(2j+1)\gamma] + 2r \sum_{j=0}^{i-1} \sin j\varphi \quad (2)$$

$$x_{O_i} = \frac{r}{R+r} y_{O_i}; y_{O_i} = y_O + \omega \frac{(R+r)}{\sin \alpha} (t_{O_i} - t_O) \quad (3)$$

Here it is indicated: n_0 is the number of cells for the section of the shaft, filled with powder; γ, φ are characteristic angles; $t_{O_i} = (x_{O_i} \sin \alpha) / (r\omega)$; ω is the angular velocity of rotation of the shaft. The values of n_0, γ, φ are determined by geometric parameters (linear R, r, l, H_0 and angular ψ, β) according to **Figure 1**.

Let for a dispersed system solid particles-gas in further designations the subscript "2" corresponds to the dispersed phase (solid skeleton), the subscript "1"-to the carrier phase. The classical conditions for the proportionality of the reduced ρ_i and true ρ_{tri} values of the phase densities are valid $\rho_i = \alpha_i \rho_{tri}, i = 1, 2$ (Nigmatulin, 1978). The developed method for modeling the process of deaeration of finely dispersed media (Kapranova and Zaitzev, 2011), due to its rather slow course, allows us to consider the movements of (1) the components of the solid skeleton of the dispersed medium together with the carrier phase as a whole; and (2) gas in an isothermal state through the pores of a finely dispersed material.

This work is devoted to the study of part (1), i.e., motion at a speed v_{12} of the solid particles-gas system as a whole, when the following conditions are met: $v_2 \gg v_1; v_{12} \approx v_2$ for the velocities of the phases $v_i, i = 1, 2$. Part (2) was studied by the authors in (Kapranova et al., 2010; Kapranova et al., 2011).

The following assumptions are made: $\rho_1 \ll \rho_2$; there is no sliding of the dispersed medium on the surfaces of hemispherical shapes. The gravitational and inertial forces are neglected in comparison with the action of surface forces. The flow of the medium in the specified gap is laminar and one-dimensional with significant compressibility and gas permeability in contrast (Akiyama et al., 1986) to the models of the motion of polymer compositions (Nigmatulin, 1978; Generalov, 2002). Let there be a linear relationship between changes in the velocity components of the rigid skeleton in coordinates and shear stresses. Similar to the generalized Hooke's law (Alcoverro, 2003) the linear dependence between the components of the averaged effective stress tensor σ_x, σ_y and of the averaged strain tensor deformations $\varepsilon_{2x}, \varepsilon_{2y}$ of the dispersed phase is reflected by expressions according to the form

$$\sigma_x = \alpha_2 [\lambda(\varepsilon_{2x} + \varepsilon_{2y}) + 2\mu\varepsilon_{2x}]; \sigma_y = \alpha_2 [\lambda(\varepsilon_{2x} + \varepsilon_{2y}) + 2\mu\varepsilon_{2y}], \quad (4)$$

where α_2 is the porosity of the powder, and λ, μ are the Lamé coefficients. Additionally, the condition of limiting equilibrium is assumed (Kapranova and Zaitzev, 2011; Kapranova et al., 2015). According to Kapranova and Zaitzev (2011), neglecting the

deformations of the dispersed medium along the z coordinate, the following representations are used for the equation of porosity change and the relation for shear stresses, respectively.

$$\alpha_2 = \frac{\alpha_{20}}{(1 - \varepsilon_{2x} - \varepsilon_{2y})} \quad (5)$$

$$\tau_{xy} = \zeta_0 (\alpha_2 - \alpha_{20}) \quad (6)$$

where $\zeta_0 \equiv \lambda + 2\mu$. Here α_{20} is the initial value of the porosity of the powder. The last relation (6) was obtained from the conditions $\sigma_z = (\sigma_x + \sigma_y)/2; \tau_{xy} = \zeta_0 (\varepsilon_{2x} + \varepsilon_{2y})$.

In addition, for shear stresses, the vertical component of the velocity of the solid skeleton along the x coordinate is neglected, i.e., communication is performed

$$\tau_{xy} = \mu_0 \partial v_{2x} / \partial y \quad (7)$$

where coefficient μ_0 is determined from the condition of adhesion of the compacted material to the surface of the hemispherical matrix.

The system of **Equations 4–6** in Cartesian coordinates is supplemented by the equations of motion of the medium with the true density of the solid phase ρ_{tr2} taking into account external pressure P .

$$\frac{\partial P}{\partial x} = \frac{\partial \tau_{xy}}{\partial y} - \frac{\rho_{tr2} \alpha_2 v_{2y} \partial v_{2x}}{\partial y} \quad (8)$$

$$0 = \frac{\partial \tau_{xy}}{\partial x} - \frac{\rho_{tr2} \alpha_2 v_{2x} \partial v_{2y}}{\partial x} \quad (9)$$

and the following equation of continuity of the solid

$$v_{2x} \frac{\partial \alpha_2}{\partial x} + v_{2y} \frac{\partial \alpha_2}{\partial y} = 0 \quad (10)$$

System (8)–(10) allows you to obtain analytical approximations for the main indicators of the process. The applied solution methods include a combination of the method of model equations and the method of substitution of constants instead of variable parameters (Kapranova et al., 2010; Kapranova et al., 2011; Kapranova et al., 2009).

By **Equations 8–10**, taking into account the slow nature of powder deaeration, we have

$$\alpha_2^{(1)}(x, y, t) = \alpha_{20} + \frac{\mu_0}{\zeta_0} [h_n \gamma_1(t) + h_1(x, y) \gamma_2(t)] \quad (11)$$

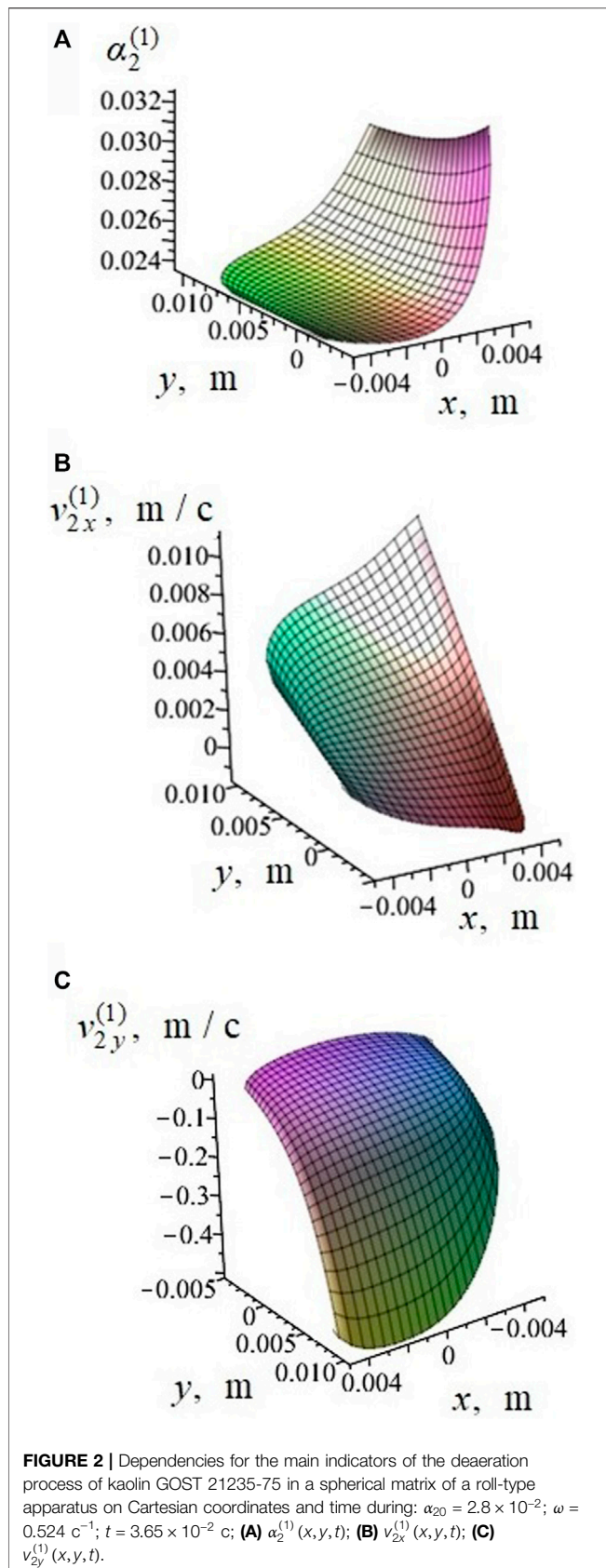
$$\tau_{xy}^{(1)}(x, y, t) = \zeta_0 [\alpha_2^{(0)}(x, y, t) - \alpha_{20}] \quad (12)$$

$$v_{2x}^{(1)}(x, y, t) = S_1(t) + h_0(x, y) S_2(t) \quad (13)$$

$$v_{2y}^{(1)}(x, y, t) = \Omega_3(y) \gamma_2(t) v_{2x}^{(1)}(x, y, t) \quad (14)$$

Here are the first approximations for tangential stresses $\tau_{xy}^{(1)}$; velocity components $v_{xy}^{(1)}$ for the rigid skeleton. Expressions (11), (13) contain a function $h_0(x, y)$ that is determined by integration $h_1(x, y)$ over the y -coordinate. Dependencies $S_1(t), S_2(t)$ from **Eq. (13)** are set according to the assumption that there is no movement of the powder at the bottom of the cell cross-section DK (**Figure 1**), then

$$v_{2x}^{(1)}(x_{D1}, y_{D1}, 0) = v_{2xA3}; v_{2x}^{(1)}(0, -r, 0) = 0 \quad (15)$$



The auxiliary functions included in Expressions (11)–(14) are

$$\begin{aligned} \gamma_1(t) &\equiv \frac{\exp\left(\frac{t}{t_n} - 1\right) - \exp(1)}{1 - \exp(1)}; \gamma_2(t) \equiv \frac{\exp\left(\frac{t}{t_n}\right) - \exp(1)}{1 - \exp(1)}; \\ S_1(t) &\equiv \frac{v_{2xN_3}\gamma_2(t)u_nu_0 - c_0h_nr\gamma_1(t)}{S_0(t)}; S_2(t) \equiv -c_0\frac{v_{2xA_3}}{S_0(t)}; \\ S_0(t) &\equiv \gamma_2(t)u_nu_0 - c_0h_nr[y_{D_1} + r\gamma_1(t)]; \\ h_0(x, y) &\equiv a_n\theta_1(x)\Omega_1(y); h_1(x, y) \equiv a_n\theta_1(x)\Omega_2(y); \\ \Omega_1(y) &\equiv C_3\theta_2(y) - \frac{y}{c_0}; \Omega_2(y) \equiv c_2C_3\theta_2(y) - \frac{1}{c_0}; \\ \Omega_3(y) &\equiv \frac{C_1}{c_2} \left[\frac{1}{c_0c_2C_3\theta_2(y)} - 1 \right]; \\ \theta_1(x) &\equiv \exp(C_1x); \theta_2(y) \equiv \exp(c_2y). \end{aligned}$$

In this case, the constants $c_0, C_1, c_2, C_3, a_n, h_n$ are set by the values of the coordinates of the points K_i, D_i from **Equations (1–3)** and the characteristics of the physical and mechanical properties of the compacted material, including the angle of friction of the dispersed medium ρ (Kapranova and Zaitzev, 2011; Kapranova et al., 2015) and the adhesion coefficient of the material $H = k_s\rho$ (Kapranova and Zaitzev, 2011; Kapranova et al., 2015), where k_s is the parameter of caking (adhesion).

Thus, expressions (11)–(14) can be used to form engineering methods for calculating the swath device (Kapranova et al., 2010; Kapranova et al., 2011; Kapranova et al., 2009).

RESULTS AND DISCUSSION

The calculation of the basic characteristics of the process of mechanical compaction of a dispersed medium $W_b = \{\alpha_2^{(1)}, v_{2x}^{(1)}\}$ when receiving granules-spheres in a roller device (**Figure 1**) is carried out using the example of deaeration of kaolin GOST 21235-75 (**Figures 2A,B**) according to (11) and (13). Additionally, the dependence $v_{2y}^{(1)}(x, y, t)$ was analyzed using expression (15) (**Figure 2C**). The values of the main parameters are: $\alpha_{20} = 2.8 \times 10^{-2}$; $R = 7.0 \times 10^{-2} \text{ m}$; $r = 5.0 \times 10^{-2} \text{ m}$; $\omega = 0.524 \text{ s}^{-1}$; $H_0 = 2.0 \times 10^{-3} \text{ m}$; $\rho_{tr2} = 2.6 \times 10^3 \text{ kg/m}^3$; $\lambda = 5.1 \times 10^5 \text{ Pa}$; $\mu = 3.1 \times 10^5 \text{ Pa}$; $k_s = 2.65 \times 10^4 \text{ Pa}$; $\rho = 0.471 \text{ rad}$ according to (Kapranova and Zaitzev, 2011) using the techniques (Andrianov, 1982; Bessonov et al., 2001; Kapranova and Zaitzev, 2011).

The surfaces shown in **Figure 2** correspond to a fixed point in time $3.65 \times 10^{-2} \text{ s}$ for the position of the form K_2D_2 (**Figure 1**).

According to the results obtained for the porosity function from Equation (11) (**Figure 2A**), the process of deaeration of the powder in the specified gap begins from the area surrounding the point $K_3, s = n_0 - 1$ at $t_0 = 0$ or point A_1 (**Figure 1**). Stabilization of $\alpha_2^{(1)}$ along the indicated coordinates on the last stage of closing hemispherical shapes on the shaft and conveyor (see arc section KD , **Figure 1**). Thus, for the initial time interval ($t_0 \leq t < t_1 = 3.7 \times 10^{-2} \text{ s}$), the growth of $\alpha_2^{(1)}$ (**Figure 2A**) relative to the horizontal coordinate along the conveyor belt is exponential and increases by 1.1 times. After eight such time intervals (at $t_3 = 3.21 \times 10^{-1} \text{ s}$), the porosity values

stabilize along the indicated coordinate with an increase of more than 1.4 times from the initial value of α_{20} .

Analysis of surfaces for $v_{2x}^{(1)}(x, y, t)$, $v_{2y}^{(1)}(x, y, t)$ (Figures 2B,C) from Equations (13) and (14) during its deaeration in the spherical matrix of the described apparatus (Figure 1) showed the presence of a shift of the layers of the compacted material, starting from the time $t_0 = 0$; $v_{2x}^{(1)}(0, 0, t_3)/v_{2x}^{(1)}(0, r, t_3) \approx 0.5$; $\Delta v_{2y}^{(1)} = v_{2y\max}^{(1)}(x, y, t_3) - v_{2y\min}^{(1)}(x, y, t_3) \leq 2 \times 10^{-11}$ m/s.

KEY FINDINGS AND RESULTS

- The plane-deformation modeling of the movement of the solid skeleton of the dispersed medium together with the carrier phase as a whole in the working volume of the specified roller apparatus is carried out, as part (1) for the complete deaeration model (Kapranova and Zaitzev, 2011). The description of the movement of gas in an isothermal state through the pores of a finely dispersed material, as part (2) of this model, is discussed in the works of the authors (Kapranova et al., 2010; Kapranova et al., 2011; Kapranova et al., 2009).
- The theoretical substantiation of the possibility of realizing deaeration of dispersed media in a roller device with a spherical matrix on the surfaces of the shaft and conveyor is obtained based on the results of the performed simulation.
- The proposed plane-deformation model contributes to the development of methods for modeling the behavior of dispersed media in the working volumes of seals-deaerators, identifying the main information variables of the deaeration process, for example, according to the approaches, tested for the processing of solid dispersed materials (Kapranova et al., 2020a; Kapranova et al., 2020b) or when transporting liquid media (Kapranova et al., 2020c; Kapranova et al., 2020d).

REFERENCES

- Akiyama, T., Miyamoto, Y., Yamanaka, N., and Zhang, J. Q. (1986). Densification of Powders by Means of Air, Vibratory and Mechanical Compactions. *Powder Technol.* 46 (2-3), 173–180. Available from: <https://www.sciencedirect.com/science/article/abs/pii/0032591086800249?via%3Dihub> (Accessed November 12, 2021). doi:10.1016/0032-5910(86)80024-9
- Alcoverro, J. (2003). The Effective Stress Principle. *Math. Comp. Model.* 37 (5), 457–467. doi:10.1016/S0895-7177(03)00038-4
- Andrianov, E. I. (1982). *Methods for Determining the Structural - Mechanical Characteristics of Powdered Materials*. Moscow: Khimiya Chemistry, 256.
- Annenkov, U. M., Ivaschutenko, A. S., and Kondratyuk, A. A. (2005). "Comparative Analysis of Alumina-Zirconium Powders Compressibility with Different Dispersibility," in Proceedings. The 9th Russian-Korean International Symposium on Science and Technology, Novosibirsk, Russia, July 2005 (KORUS), 415–417. doi:10.1109/KORUS.2005.1507746
- Bayle, J.-P., Reynaud, V., Gobin, F., Brenneis, C., Tronche, E., Ferry, C., et al. (2016). Modelling of powder die compaction for press cycle

CONCLUSION

An analytical method is proposed for assessing the efficiency of the deaeration process of solid dispersed components in a gap with perforated hemispherical shapes on the surfaces of the shaft and conveyor belt within the framework of the mechanics of heterogeneous systems taking into account the compressibility. It is noted that the porosity of the finished granule-sphere at the final stage of deaeration in the described gap of the conveyor shaft with a spherical matrix almost uniformly reaches its limiting value. In this case, the difference between the maximum and minimum porosity values does not exceed 2×10^{-12} . Up to time values of 3.7×10^{-2} s, the increase in porosity concerning the horizontal coordinate along the conveyor belt exponentially with an increase of 1.1 times in comparison with the initial value of this indicator. After eight such time intervals (when reaching 3.21×10^{-1} s), the porosity values stabilize along the indicated coordinate with an increase in this characteristic of the deaeration process by more than 1.4 times from its initial value. So, the proposed method for modeling the compaction process of solid dispersed components provides a theoretical justification for the possibility of implementing this technological operation in a gap with perforated hemispherical shapes on the surfaces of the shaft and the conveyor belt.

DATA AVAILABILITY STATEMENT

The original contributions presented in the study are included in the article/Supplementary Material, further inquiries can be directed to the corresponding author.

AUTHOR CONTRIBUTIONS

All authors contributed to manuscript revision, and read and approved the submitted version.

optimization. *EPJ Nucl. Sci. Technol.* 2 (25), 25–29. doi:10.1051/epjn/2016018

- Bessonov, A. I., Kutuzova, O. A., and Toporov, Y. P. (2001). A Cell for Measuring Shear Strength of Powdered Disperse Systems. *Colloid J.* 63, 788–789. doi:10.1023/A:1013244524903
- Buckingham, E. (1915). The Principle of Similitude. *Nature* 96 (2406), 396–397. doi:10.1038/096396d0
- Fingas, M., and Fieldhouse, B. (2009). Studies on Crude Oil and Petroleum Product Emulsions: Water Resolution and Rheology. *Colloids Surf. A: Physicochemical Eng. Aspects* 333 (1-3), 67–81. doi:10.1016/j.colsurfa.2008.09.029
- Francis, L. F. (2016). "Powder Processes," in *Materials Processing. A Unified Approach to Processing of Metals, Ceramics and Polymers* (University of Minnesota), 343–414. Available at: <https://www.sciencedirect.com/science/article/pii/B9780123851321000057?via%3Dihub> (Accessed November 12, 2021). doi:10.1016/B978-0-12-385132-1.00005-7
- Gai, G.-S., Yang, Y.-F., Fan, S.-M., and Cai, Z.-F. (2005). Preparation and Properties of Composite mineral Powders. *Powder Technol.* 153 (3), 153–158. doi:10.1016/j.powtec.2005.03.013
- Generalov, M. B., and Chainikov, N. A. (1972). Rolling of Powders onto Parts. *Powder Metall. Met. Ceram.* 11, 525–531. doi:10.1007/BF00798188

- Generalov, M. B., Klassen, P. V., Stepanova, A. R., and Shomin, I. P. (1984). *Design of Mineral Fertilizer Granulation Equipment [Raschet Oborudovaniya Dlya Granulirovaniya mineral'nykh Udobrenii]*. Moscow: Mashinostroenie, 191.
- Generalov, M. B. (2002). *Mechanics of Particulate Media in Chemical Processes [Mekhanika Tverdykh Dispersnykh Sred V Protssakh Khimicheskoi Tekhnologii]*. Kaluga: Izd. N. Bochkarevov 592.
- Hu, Y., Sun, J., Peng, W., and Zhang, D. (2021). A Novel Forecast Model Based on CF-PSO-SVM Approach for Predicting the Roll gap in Acceleration and Deceleration Process. *Eng. Computations* 38 (3), 1117–1133. doi:10.1108/EC-08-2019-0370
- Kapranova, A. B., and Zaitzev, A. I. (2011). *Mechanical Compaction of Finely Dispersed Materials*. Moscow: Ekon-inform, 247. Available from: <https://search.rsl.ru/ru/record/01004975377> (Accessed November 12, 2021).
- Kapranova, A. V., Zaitsev, A. I., and Nikitina, T. P. (2000). Taking into Account wall Slip and Friction in Calculating the Degree of Compaction of a Powder in a Screw Machine. *Theor. Found. Chem. Eng.* 34 (6), 592–599. Available from: https://www.researchgate.net/publication/225827276_Taking_into_Account_Wall_Slip_and_Friction_in_Calculating_the_Degree_of_Compaction_of_a_Powder_in_a_Screw_Machine (Accessed November 12, 2021). doi:10.1023/A:100523326377
- Kapranova, A. V., Zaitsev, A. I., and Nikitina, T. P. (2001). Design of a Screw Powder Compactor. *Theor. Found. Chem. Eng.* 35 (1), 90–94. Available from: https://link.springer.com/article/10.1023/A:1005233205559?error=cookies_not_supported&code=27bd158d-2c37-42a7-8884-90f3327e41d1 (Accessed November 12, 2021). doi:10.1023/A:1005233205559
- Kapranova, A., Zaitzev, A. I., Bushmelev, A. V., and Lebedev, A. E. (2006a). “The Optimization Problem of the Curvilinear Blades from in the Powder Densification Set-Up,” in 17-th Int. Congr of Chem. and Process Eng. – CHISA’2006, Prague, Czech. Republic, 27 August 2006 - 31 August 2006. ISBN 8086059456, 978-808605945-7. Available at: <https://www.scopus.com/record/display.uri?eid=2-s2.0-34748857979&origin=resultslist>, 878, 2006a Book of abstracts.
- Kapranova, A., Zaitzev, A. I., Bushmelev, A. V., and Kuzmin, I. O. (2006b). “The Investigation of the Densification Powder Sliding Effect in the Cell of the Set-Up with the Curvilinear Blades,” in 17-th Int. Congr of Chem. and Process Eng. – CHISA’2006, Prague, Czech. Republic, 27 August 2006 - 31 August 2006. ISBN 8086059456, 978-808605945-7. Available at: <https://www.scopus.com/authid/detail.uri?authorId=22034771200>, 875, 2006b Book of abstracts. (Accessed November 12, 2021).
- Kapranova, A. B., Lebedev, A. E., and Vasiliev, A. M. (2010). On the Movement of the Carrying Phase of a Dispersed Medium during its Degassing in the gap of a Roll Deaerator with a Spherical Matrix [Ekspress-Metod Otsenki Odnorodnosti Smesey Sypuchikh Materialov] Russian Journal of Chemistry and Chemical Technology [Izvestiya Vysshikh Uchebnykh Zavedeniy. Seriya: Khimiya I Khimicheskaya Tekhnologiya]. *Elibrary* 53 (6), 101–103. Available from: https://www.elibrary.ru/download/elibrary_15125889_14369485.pdf (Accessed November 12, 2021).
- Kapranova, A. B., Zaitsev, A. I., Dubrovin, A. V., Vasiliev, A. M., and Nikitina, Y. V. (2011). Movement Model of Carrying Phase of Bulk Mixture in Rolling gap with Spherical Matrix [Ekspress-Metod Otsenki Odnorodnosti Smesey Sypuchikh Materialov] Russian Journal of Chemistry and Chemical Technology [Izvestiya Vysshikh Uchebnykh Zavedeniy. Seriya: Khimiya I Khimicheskaya Tekhnologiya]. *Elibrary* 54 (8), 97–99. Available from: https://www.elibrary.ru/download/elibrary_16388583_98787057.pdf (Accessed November 12, 2021).
- Kapranova, A. B., Dubrovin, A. V., and Zaitsev, A. I. (2009). To the Question of Evaluating the External Pressure in the gap of the Roller Deaerator of Powders with a Spherical Matrix [Ekspress-Metod Otsenki Odnorodnosti Smesey Sypuchikh Materialov] Russian Journal of Chemistry and Chemical Technology [Izvestiya Vysshikh Uchebnykh Zavedeniy. Seriya: Khimiya I Khimicheskaya Tekhnologiya]. *Elibrary* 52 (12), 116–118. Available from: https://www.elibrary.ru/download/elibrary_12971400_26424233.pdf (Accessed November 12, 2021).
- Kapranova, A. B., Zaitsev, A. I., and Kuz'min, I. O. (2015). Studying the Porosity of Powders under Pressure Compaction in Deaeration Mixers. *Theor. Found. Chem. Eng.* 49 (4), 436–446. Available from: https://link.springer.com/article/10.1134/S0040579515040272?error=cookies_not_supported&code=7b22ff21-cb92-4ddb-b226-46340f3125b9 (Accessed November 12, 2021). doi:10.1134/S0040579515040272
- Kapranova, A., Verloka, I., Bahaeva, D., Tarshis, M., and Cherpitsky, S. (2020a). To the Calculation of the Average Value of the Volume Fraction of the Key Bulk Component at the Intermediate Stage of Mixing with an Inclined Bump. *Front. Eng. Res.* 8, 1–11. doi:10.3389/feng.2020.00135
- Kapranova, A. B., Verloka, I. I., and Bahaeva, D. D. (2020b). “About Preparation of the Analytical Platform for Creation of a Cyber-Physical System of Industrial Mixture of Loose Components,” in *Cyber-Physical Systems: Advances in Design & Modelling. Studies in Systems, Decision and Control*. Editors A. Kravets, A. Bolshakov, and M. Shcherbakov (Cham: Springer), 259, 81–91. doi:10.1007/978-3-030-32579-4_7
- Kapranova, A., Neklyudov, S., Lebedev, A., Meltser, A., and Voronin, D. (2020c). Engineering Method for Calculating of an Axial Valve Separator with an External Location of the Locking Part. *Front. Eng. Res.* 8, 1–17. doi:10.3389/feng.2020.00032
- Kapranova, A. B., Lebedev, A. E., Melzer, A. M., and Neklyudov, S. V. (2020d). “About Formation of Elements of a Cyber-Physical System for Efficient Throttling of Fluid in an Axial Valve,” in *Cyber-Physical Systems: Advances in Design & Modelling. Studies in Systems, Decision and Control*. Editors A. Kravets, A. Bolshakov, and M. Shcherbakov (Cham: Springer), 259, 109–119. doi:10.1007/978-3-030-32579-4_9
- Kapranova, A. B. (2010). Powder Densification Process in a Centrifugal Apparatus with Curvilinear Blades. *Math. Models Comput. Simul* 2 (1), 63–75. Available from: https://link.springer.com/article/10.1134/S2070048210010072?error=cookies_not_supported&code=202ef76c-3a51-483a-9a76-ee9c2b1f041a (Accessed November 12, 2021). doi:10.1134/S2070048210010072
- Khoei, A. R. (2005). “Finite Element Model,” in *Computational Plasticity in Powder Forming Processes* (Elsevier), 19–43. Available at: <https://www.sciencedirect.com/science/article/pii/B978008044636350002X> (Accessed November 12, 2021). doi:10.1016/B978-008044636-3/50002-X
- Misic, T., Najdanovic-Lukic, M., and Nesic, L. (2010). Dimensional Analysis in Physics and the Buckingham Theorem. *Eur. J. Phys.* 31 (4), 893–906. doi:10.1088/0143-0807/31/4/019
- Nigmatulin, R. I. (1978). *Fundamentals of Heterogeneous Medium Mechanics [Osnovy Mekhaniki Geterogenykh Sred]*. Moscow: Nauka, 336.
- Pimenov, V. A., Babushko, Y. Y., and Bakhtin, S. V. (2015). Reversible Cold Rolling of Thin High-Silicon Steel Strip. *Steel Transl.* 44 (10), 764–768. doi:10.13013/S0967091214100131
- Pizette, P., Martin, C. L., Delette, G., Sornay, P., and Sans, F. (2010). Compaction of Aggregated Ceramic Powders: From Contact Laws to Fracture and Yield Surfaces. *Powder Technol.* 198 (2), 240–250. Available from: https://www.researchgate.net/publication/244157915_Compaction_of_Aggregated_Ceramic_Powders_From_Contact_Laws_to_Fracture_and_Yield_Surfaces (Accessed November 12, 2021). doi:10.1016/j.powtec.2009.11.013
- Renner, J., Siddiqi, G., and Evans, B. (2007). Plastic Flow of Two-Phase Marbles. *J. Geophys. Res.* 112 (B7). doi:10.1029/2005JB004134
- Santos, R. G., Loh, W., Bannwart, A. C., and Trevisan, O. V. (2014). An Overview of Heavy Oil Properties and its Recovery and Transportation Methods. *Braz. J. Chem. Eng.* 31 (3), 571–590. doi:10.1590/0104-6632.20140313s00001853
- Seong, Y., Yim, D., Jang, M. J., Park, J. M., Park, S. J., and Kim, H. S. (2020). Physics-Based Constitutive Model of Porous Materials for Die/Isostatic Compaction of Metallic Powders. *Met. Mater. Int.* 26, 221–229. doi:10.1007/s12540-019-00317-z
- Torner, R. V. (1977). “Theoretical Foundations of Polymer Processing [Teoreticheskie Osnovy Pererabotki Polimerov], Khimiya, Moscow,” in *Theoretical Foundations of Polymer Processing* (Moscow: Khimiya Chemistry), 462.
- Tselikov, A. I., Nikitin, G. S., and Rokotyay, S. E. (1980). *Lengthwise Rolling Theory [Teoriya Prodol'noi Prokatki]*. Moscow: Metallurgiya, 319.
- Udalov, A. A., Parshin, S. V., Udalov, A. V., and Vasilyevykh, S. L. (2019). Power Parameters of the Process of Hardening of Cylindrical Parts by a Toroidal Roller by the Method of Surface Plastic Deformation. *J. Phys. Conf. Ser.* 1210, 012150. doi:10.1088/1742-6596/1210/1/012150
- Vinogradov, G. A., Semenov, Y. N., Katrus, O. A., and Katashinskii, V. N. (1969). *Metal Wire Rolling [Prokatka Metallicheskih Poroshkov]*. Moscow: Metallurgiya, 382.
- Wang, Z.-L., and Xiao, H. (2015). “A Study of Metal Fatigue Failure as Inherent Features of Elastoplastic Constitutive Equations,” in *From*

Creep Damage Mechanics to Homogenization Methods Advanced Structured Materials. Editors H. Altenbach, T. Matsuda, and D. Okumura (Cham: Springer), 64, 529–540. doi:10.1007/978-3-319-19440-0_23

Zaitsev, A. I., Lebedev, A. E., Dubrovin, A. V., and Gotovtsev, V. M. (2010). Aggregate for Obtaining Coated Granular Material. Patent 2385762 Russian Federation, IPC C 10 C 3/14. *Bull. N. 10*, 1 4. Available at: https://fips.ru/registers-doc-view/fips_servlet?DB=RUPAT&rn=5649&DocNumber=2385762&TypeFile=html (Accessed September 03, 2020).

Conflict of Interest: The authors declare that the research was conducted in the absence of any commercial or financial relationships that could be construed as a potential conflict of interest.

Publisher's Note: All claims expressed in this article are solely those of the authors and do not necessarily represent those of their affiliated organizations, or those of the publisher, the editors, and the reviewers. Any product that may be evaluated in this article, or claim that may be made by its manufacturer, is not guaranteed or endorsed by the publisher.

Copyright © 2021 Kapranova, Tarshis, Badaeva and Sheronina. This is an open-access article distributed under the terms of the Creative Commons Attribution License (CC BY). The use, distribution or reproduction in other forums is permitted, provided the original author(s) and the copyright owner(s) are credited and that the original publication in this journal is cited, in accordance with accepted academic practice. No use, distribution or reproduction is permitted which does not comply with these terms.



Effect of Fin Number and Position on Non-linear Characteristics of Natural Convection Heat Transfer in Internally Finned Horizontal Annulus

Kun Zhang^{1,2*}, Yu Zhang^{1,2}, Xiaoyu Wang^{1,2} and Liangbi Wang^{1,2}

¹School of Mechanical Engineering, Lanzhou Jiaotong University, Lanzhou, China, ²Key Laboratory of Railway Vehicle Thermal Engineering, Lanzhou Jiaotong University, Lanzhou, China

OPEN ACCESS

Edited by:

Xuwen Cao,
China University of Petroleum, China

Reviewed by:

Dongsheng Xia,
Dalian Maritime University, China
Liping Geng,
Shanghai Dianji University, China

*Correspondence:

Kun Zhang
zhangkun52015@163.com

Specialty section:

This article was submitted to
Advanced Clean Fuel Technologies,
a section of the journal
Frontiers in Energy Research

Received: 28 October 2021

Accepted: 22 November 2021

Published: 24 December 2021

Citation:

Zhang K, Zhang Y, Wang X and
Wang L (2021) Effect of Fin Number
and Position on Non-linear
Characteristics of Natural Convection
Heat Transfer in Internally Finned
Horizontal Annulus.
Front. Energy Res. 9:804094.
doi: 10.3389/fenrg.2021.804094

Detailed numerical calculations are performed for investigating the effect of fin number and position on unsteady natural convection heat transfer in internally finned horizontal annulus. The SIMPLER algorithm with Quick scheme is applied for solving the Navier Stokes equations of flow and heat transfer. The results show that the heat transfer rate in annulus with fins increases with the increasing numbers of fin and Rayleigh numbers. For $Ra = 2 \times 10^5$, the effect of numbers of fins and fins position at the bottom part on the unsteady solutions can be neglected, because the self-oscillation phenomenon is mainly affected by natural convection at the upper part of annulus. Although the fin positions cannot increase heat transfer rate significantly in the case of four fins, the self-oscillated solutions can be suppressed by altering fins position.

Keywords: non-linear characteristic, natural convection, periodic oscillation, fin number, fin position

INTRODUCTION

Natural convection heat transfer in annulus has been the topic of many investigations until recently, since it has many industrial applications including solar heating, electronic components, and reactor design. A large number of literatures on both experimental and numerical studies were published in the past few decades (Yong et al., 2006; Ghasemi et al., 2012; EI-Maghlany et al., 2015; Gholamalipour et al., 2019). The most fundamental studies were reported by Kuehn and Goldstein (Kuehn and Goldstein, 1976; Kuehn and Goldstein, 1978; Kuehn and Goldstein, 1980) in which experimental and numerical results were obtained for improving the knowledge of heat transfer performance, natural convection, and temperature fields in horizontal annulus. The natural convection heat transfer in annulus is limited by the heat transfer area of the inner cylinder. Therefore, the internal fins are sometimes employed for the purpose of increasing the heat transfer area, leading to an increasing heat transfer rate in annulus.

Numerical investigations of the natural convection heat transfer in annulus with internal fins were studied by many researchers (Chen and Hsu, 2007; Kim et al., 2013; Senapati et al., 2017; Liu et al.,

Abbreviations: F_0 , dimensionless time; K_{eq} , average dimensionless equivalent thermal conductivity of whole cylinder; K_{eqb} , local dimensionless equivalent thermal conductivity; k_f , thermal conductivity for fluid, W/m·K; L , gap width, m; L_f , height of fins, m; n_{fin} , number of fins; Pr , Prandtl number; q_b , local heat transfer rate, W; r , radial coordinate; r_b , radius of inner circle, m; r_o , radius of envelope circle, m; Ra , Rayleigh number; Ra_m , modified Rayleigh number; T_b , temperature of inner circle, K; T_o , temperature of envelope circle, K; U , dimensionless tangential velocity; V , dimensionless radial velocity; α , angle of fins, rad; δ , thickness of fins; θ , angular coordinate.

2021). Maakoul (El Maakoul et al., 2020) numerically studied the thermal performance of longitudinal fins in the double-pipe heat exchanger. Their results showed that the smallest internal fins with the size of 166 mm can provide the highest thermal performance and the heat transfer rate with longitudinal fins is higher than other cases under the same flow velocity. Chai and Patankar (1993) numerically investigated flow and heat transfer under gravity in horizontal annulus in the case of six fins. Their results indicated that the effect of the fins orientations is not obvious for improving the rate of averaged heat transfer, and the averaged heat transfer rate can increase with the increasing values of Rayleigh number and decrease with the increasing value of fin height. Farinas et al. (Farinas et al., 1997) investigated the effect of fins with different configurations on the flow pattern, temperature field, and heat transfer rate in annulus. Rahnama et al. (Rahnama et al., 1999; Rahnama and Farhadi, 2004) also studied natural convection heat transfer in annulus with radial fins. The existence of fins can improve the heat transfer rate while high fins resist the development of natural convection and decrease the value of local Nusselt number. Nada and Said (Nada and Said, 2019) studied the effects of Rayleigh numbers, internal cylindrical diameters, fins numbers, shapes, and arrangements on the heat transfer rate, flow pattern and effective thermal conductivity of the annulus. Alshahrani and Zeitoun (2005) numerically investigated the thermal resistance of finned annuli using conduction analysis and the correlation. Their results indicated that the thermal resistance becomes larger when the fin length increases in their parameter scope. Kiwan and Zeitoun (2008) studied the heat transfer rate in the annulus with fins made of porous material and the effect of fin conductivities, Darcy numbers, and Rayleigh numbers on thermal performance. Shadlaghani et al. (2019) studied the effect of internal fins on flow and heat transfer using control volume method. Their results showed that although the heat transfer coefficient between the two fins is reduced, fins increase the total heat transfer rate of both inner and outer walls of annulus and fins efficiencies are decreased with the increasing value of Rayleigh number.

Natural convection may occur in the annulus recurrently, and most of these flows are unsteady even under the steady boundary conditions, especially those encountered in the complex domain (Zhang et al., 2011; Zhang et al., 2014). Many numerical studies have been carried out to investigate the non-linear characteristics of natural convection heat transfer in annulus. Labonia and Guj (2000) experimentally investigated the transition process from steady laminar flow and heat transfer to chaotic state in annulus by increasing the values of Rayleigh numbers. Yoo and Han (Yoo, 1998; Yoo and Han, 2000) numerically studied the bifurcation sequences from steady to chaos of flow in annulus and a transition from a steady flow with the pattern of unicellular to an oscillatory multicellular flow pattern. Borjini et al. (2005) studied a reverse transition of natural convection from the quasi-periodic solutions to the periodic solutions with the increasing value of Rayleigh number in a very narrow annulus. Usman et al. (2021) investigated a transition from steady to oscillated solutions of natural convection in annulus when the Prandtl number is equal to 0.1. The numerical results revealed that the heat transfer

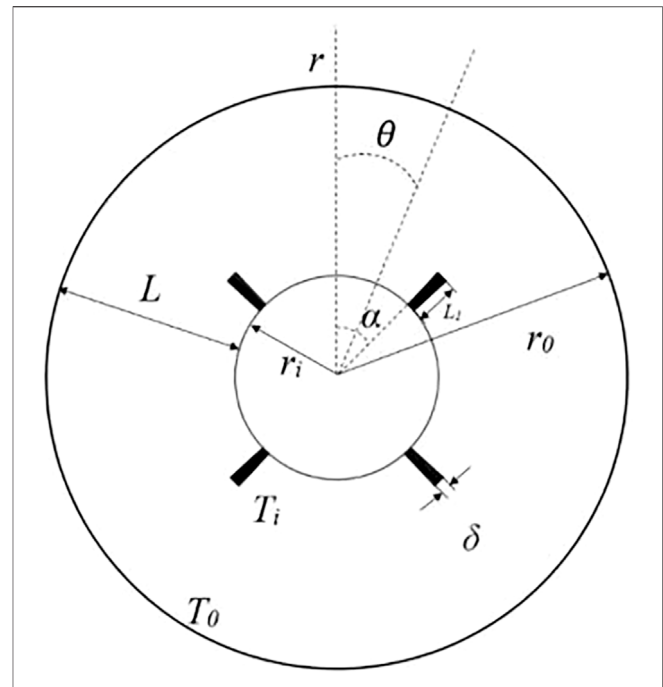


FIGURE 1 | Schematic diagram of annuli with fins.

rate increases suddenly in a narrow range of Rayleigh numbers, and this increase in heat transfer rate is related to a transition into chaos. Yang and Kong (Yang and Kong, 2019) studied the unsteady natural convection heat transfer in annulus with different Rayleigh numbers and Prandtl numbers.

Comparatively, a few studies have been reported on the non-linear characteristics of flow and heat transfer in annulus with fins. Idrissi et al. (2016) studied the natural convection heat transfer in annulus in the case of two fins attached to the upper surface of inner annulus. Their results indicated that the existence of a bifurcation point can separate two kinds of flow patterns, and the heat transfer rate increases for Rayleigh numbers higher than the critical value. Touzani et al. (2019) investigated the effect of the Rayleigh number from 10^3 to 10^4 on the flow pattern and heat transfer rate in the finned internally annulus. A bi-cellular or unicellular flow patterns can be observed, and the overall heat transfer rate is increased by adding fins. Gao et al. (2020) numerically studied the steady state, static branching and self-sustained oscillated solutions of natural convection heat transfer in annuli with fins. A series of critical Rayleigh numbers was obtained when the different initial conditions are selected. However, most of previous studies focus on the process of evolution from steady to chaotic flow for different non-dimensional parameters such as Rayleigh numbers or Prantal numbers, and only in a few of the works the effect of fin numbers and positions on the non-linear phenomenon of natural convection heat transfer were considered in detail.

The objective of this paper is to study the flow and heat transfer in annulus with different fin number and positions by SIMPLER algorithm with Quick scheme. The effect of fin number and positions on the steady or oscillated phenomenon of flow and heat transfer under the steady boundary conditions will be

studied in detail. The space trajectory of velocity at the sample point and the time signal of the average dimensionless equivalent thermal conductivity will be calculated for evaluating the effect of fin position and number on the non-linear characteristics.

PHYSICAL MODEL AND NUMERICAL METHOD

A schematic diagram of the horizontal annulus with fins is illustrated in **Figure 1**. The temperatures of the inner and outer cylinders are maintained at uniform but different values of T_i and T_o , respectively. The natural convection heat transfer occurs for $T_i > T_o$. The radius of the inner cylinder is denoted by r_i and at the same time that of the outer cylinder is denoted by r_o . The two concentric cylinders, consisting of an annulus, are assumed to be long enough that a two dimensional model can be applied. The natural convection resulting from the temperature difference between the cylinders is assumed to be unsteady and laminar. The fins of height L_f and the thickness of δ are evenly attached to the surface of inner cylinder. The thermo-physical properties of the fluid are assumed to be independent of temperature, and the flow in annulus follows the Boussinesq approximation.

The unsteady-state flow and heat transfer equations for natural convection heat transfer in annulus with fins in this investigation are described in Ref. (Gao et al., 2020). The Quick scheme is employed to discretize the convection terms while the deferred correction method is added into the computational process to improve the convergence of iterations. The SIMPLER algorithm with Quick scheme is selected for solving the Navier-Stokes equations of flow and heat transfer. The whole annulus with fins is considered as the calculating domain and the flow velocities of solid regions are set to zero. The dimensionless governing equations are solved numerically using the control-volume based finite volume method. An alternating direction scheme is applied where all the equations can be solved iteratively until the convergence criteria are met. The iterative calculation can be terminated when the relative residual of all variables is less than 10^{-6} for each time step.

The local dimensionless equivalent thermal conductivity based on the outer cylindrical envelope is used for evaluating the local heat transfer effect, and its definition formulation is written as follows.

$$K_{eq} = \frac{q_\theta}{2\pi\pi_f(T_i - T_o)} \ln \frac{r_o}{r_i} \quad (1)$$

where q_θ is the local heat transfer rate along the surface of the outer cylinder at the fin positioned angle θ , and k_f is the thermal conductivity of fluid.

To study the overall heat transfer effect, the average dimensionless equivalent thermal conductivity based on the whole outer cylindrical envelope is defined as

$$K_{eq} = \int_0^{2\pi} K_{eq} d\theta \quad (2)$$

ALGORITHM AND GRID CHECK

The check of grid independence is calculated under the parameters of $n_{fin} = 6$, $\delta/L = 0.05$, $Ra = 10^5$, $Pr = 0.701$. The dimensionless time step $\Delta\tau = 0.1$ is taken to calculate for obtaining time-step independent solutions. The number of grid nodes 160×400 is used to achieve grid independence. To verify the numerical code, the average dimensionless equivalent thermal conductivity is calculated numerically with modified Rayleigh numbers. The modified Rayleigh number Ra_m is defined by Alshahrani and Zeitoun (2005). The calculated solutions are compared with the results from Alshahrani and Zeitoun (2005) and Kiwan and Zeitoun (2008). It can be seen in **Figure 2** that the numerical results in this study agreed very well with other experimental and numerical results.

RESULTS AND DISCUSSIONS

The flow pattern, temperature distribution, and heat transfer rate of natural convection heat transfer in annulus with fins will be numerically investigated in detail. The effect of fin positions and number on the nonlinear characteristic of heat transfer will be analyzed in this section.

Flow and Temperature Fields at Low Rayleigh Numbers

Numerical simulations of the flow and heat transfer in horizontal annulus with fins are performed in the case of $Ra \leq 5 \times 10^3$. The numerical simulations indicate that the steady solution can be obtained from the initial conditions of stationary flow and uniform temperature field. **Figures 3, 4** show the flow and temperature fields at lower Rayleigh numbers with different fin numbers and positions for $Ra = 5 \times 10^3$, respectively. In the case of $n_{fin} = 2$, the effect of fin angle on the flow fields can be seen in **Figures 3A–D**. There are two symmetric and big vortices in the case of $\alpha = 0$ in **Figure 3A**. The fluid flows up along the inner heated cylinder by the buoyancy forces, as it gets closer to the top of the outer wall, it then moves down along the sidewall of the outer cylinder. The temperature fields in **Figure 4A** are also symmetrical with respect to the mid axial line accordingly. The existence of fins can increase the heat transfer areas and influence the isotherms. The heat transfer rate is very low at the root of fin and increases along the fin until it arrives at the greatest value on the top of the fin.

In the case of $\alpha = \pi/6$, one new vortex appears at the upper part of the annulus and at the same time the right vortex becomes small because of the suppression of the fin at the right side, as shown in **Figure 3B**. The new vortex becomes larger and the right vortex shrinks gradually as the fin angle increases, as can be seen in **Figures 3C, D**. At the same time, the left vortex becomes smaller and rises up, providing space for the development of another new vortex. In the case of $\alpha = \pi/2$, the fluid flows up and it is forced to alter the orientation when it meets the fins located at the center of the annulus, as shown in **Figure 3E**. There are four big vortices formed in the horizontal annulus. Two of them are in

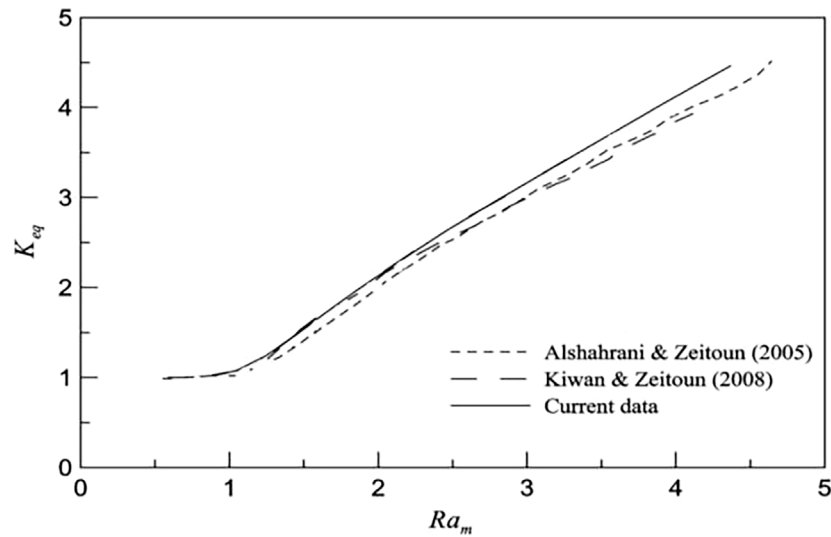


FIGURE 2 | Comparison of current and previous results of the average dimensionless equivalent thermal conductivity of whole cylinder (K_{eq}).

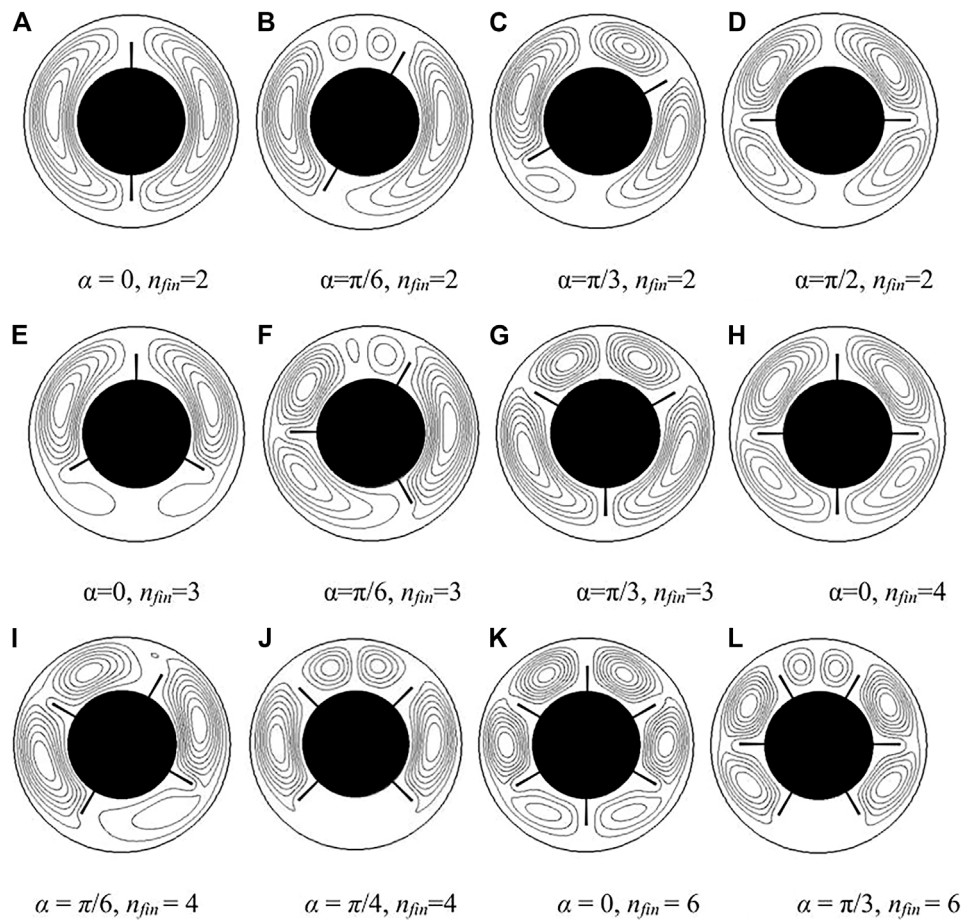


FIGURE 3 | Flow fields with different fin numbers and positions for $Ra = 5 \times 10^3$. (A) $\alpha = 0, n_{fin} = 2$ (B) $\alpha = \pi/6, n_{fin} = 2$ (C) $\alpha = \pi/3, n_{fin} = 2$ (D) $\alpha = \pi/2, n_{fin} = 2$ (E) $\alpha = 0, n_{fin} = 3$ (F) $\alpha = \pi/6, n_{fin} = 3$ (G) $\alpha = \pi/3, n_{fin} = 3$ (H) $\alpha = 0, n_{fin} = 4$ (I) $\alpha = \pi/6, n_{fin} = 4$ (J) $\alpha = \pi/4, n_{fin} = 4$ (K) $\alpha = 0, n_{fin} = 6$ (L) $\alpha = \pi/3, n_{fin} = 6$. Ra , Rayleigh number; α , angle of fins; n_{fin} , number of fins.

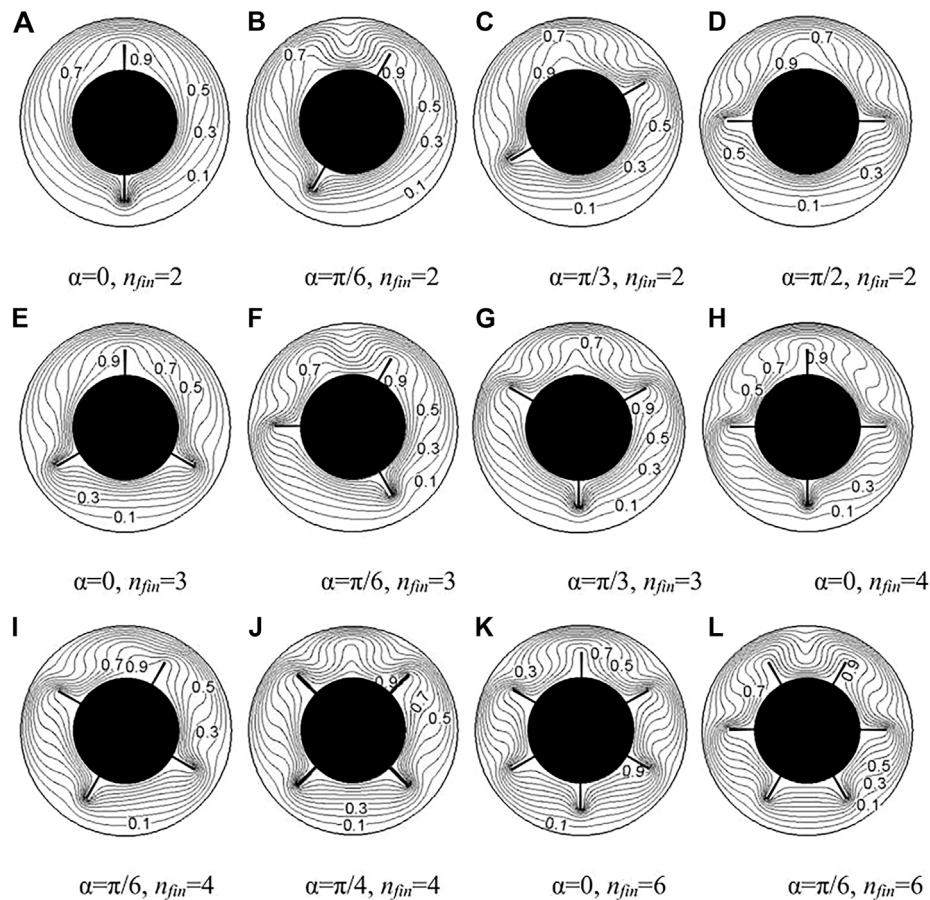


FIGURE 4 | Temperature fields with different fin numbers and positions for $Ra = 5 \times 10^3$. (A) $\alpha = 0$, $n_{fin} = 2$ (B) $\alpha = \pi/6$, $n_{fin} = 2$ (C) $\alpha = \pi/3$, $n_{fin} = 2$ (D) $\alpha = \pi/2$, $n_{fin} = 2$ (E) $\alpha = 0$, $n_{fin} = 3$ (F) $\alpha = \pi/6$, $n_{fin} = 3$ (G) $\alpha = \pi/3$, $n_{fin} = 3$ (H) $\alpha = 0$, $n_{fin} = 4$ (I) $\alpha = \pi/6$, $n_{fin} = 4$ (J) $\alpha = \pi/4$, $n_{fin} = 4$ (K) $\alpha = 0$, $n_{fin} = 6$ (L) $\alpha = \pi/6$, $n_{fin} = 6$.

the right side of the annulus and the other two are in the left side. The isotherms changes obviously especially at the upper part of annulus, as depicted by **Figures 4B–E**. The isotherm concentration in the upper part of the annulus is more than that in the other places. The largest temperature gradient occurs at the middle top of the outer cylinder. As the number of fins increases, the heat transfer area also increases and the flow structure becomes more complex. When there exists two fins in the lower part of the annulus, the fluid motion in the lower part is very weak due to the fact that high temperature surface is over that with low temperature as shown in **Figures 3E, J, L**. It is due to the dominated mechanism of conduction heat transfer in the lower part of the annulus.

Comparisons of Average Dimensionless Equivalent Thermal Conductivity of Whole Cylinder With Different Fin Numbers and Positions

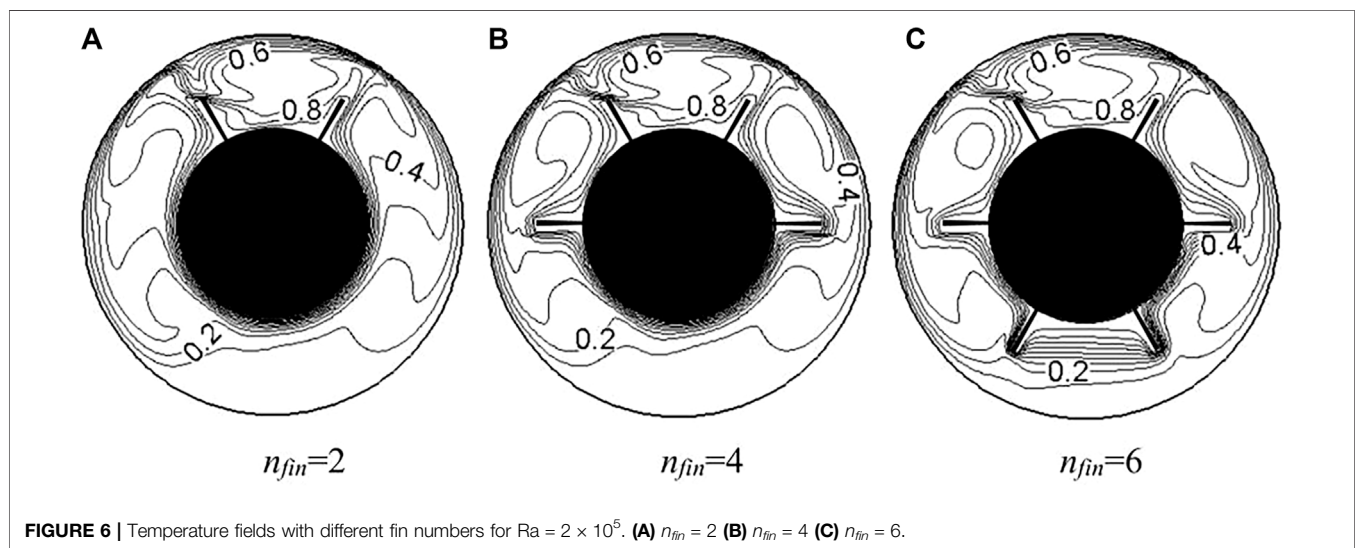
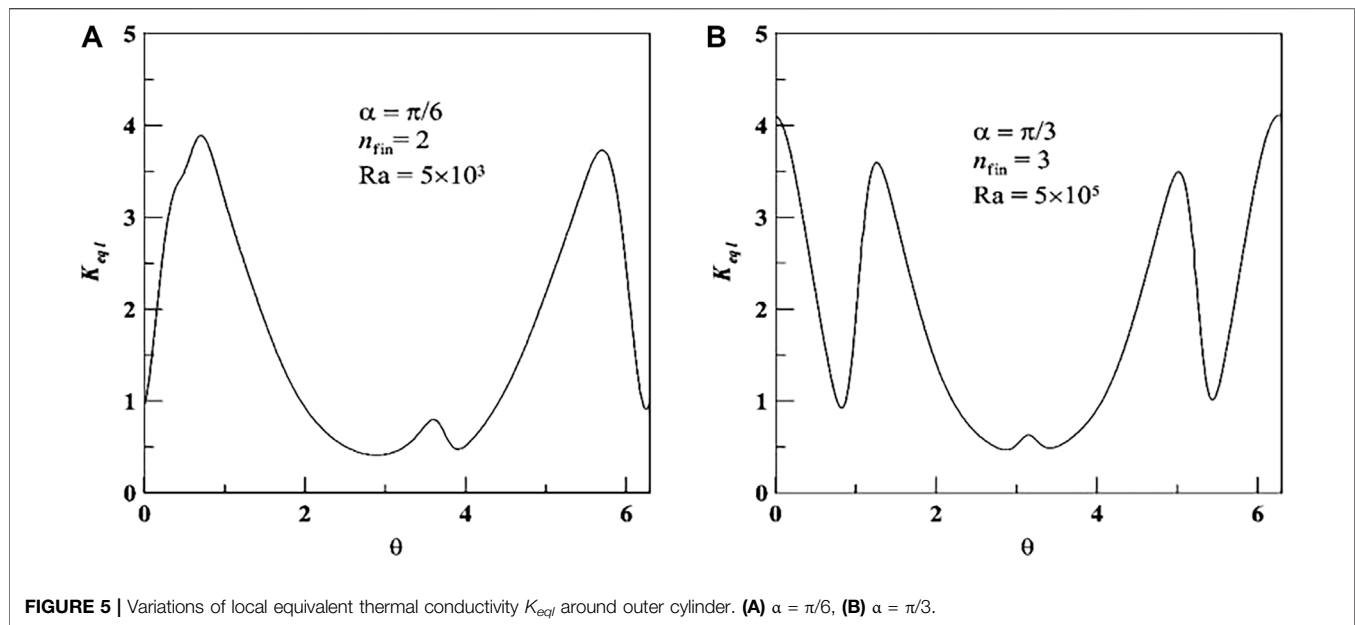
Table 1 shows the average dimensionless equivalent thermal conductivity K_{eq} for different fin numbers and angles at

TABLE 1 | The value of K_{eq} for different fin numbers and angles at $Ra = 5 \times 10^3$.

	$\alpha = 0$	$\alpha = \pi/6$	$\alpha = \pi/3$	$\alpha = \pi/2$
$n_{fin} = 2$	1.64	1.76	1.72	1.71
$n_{fin} = 3$	1.70	1.86	1.88	—
$n_{fin} = 4$	1.88	1.87	—	—
$n_{fin} = 6$	2.10	2.06	—	—

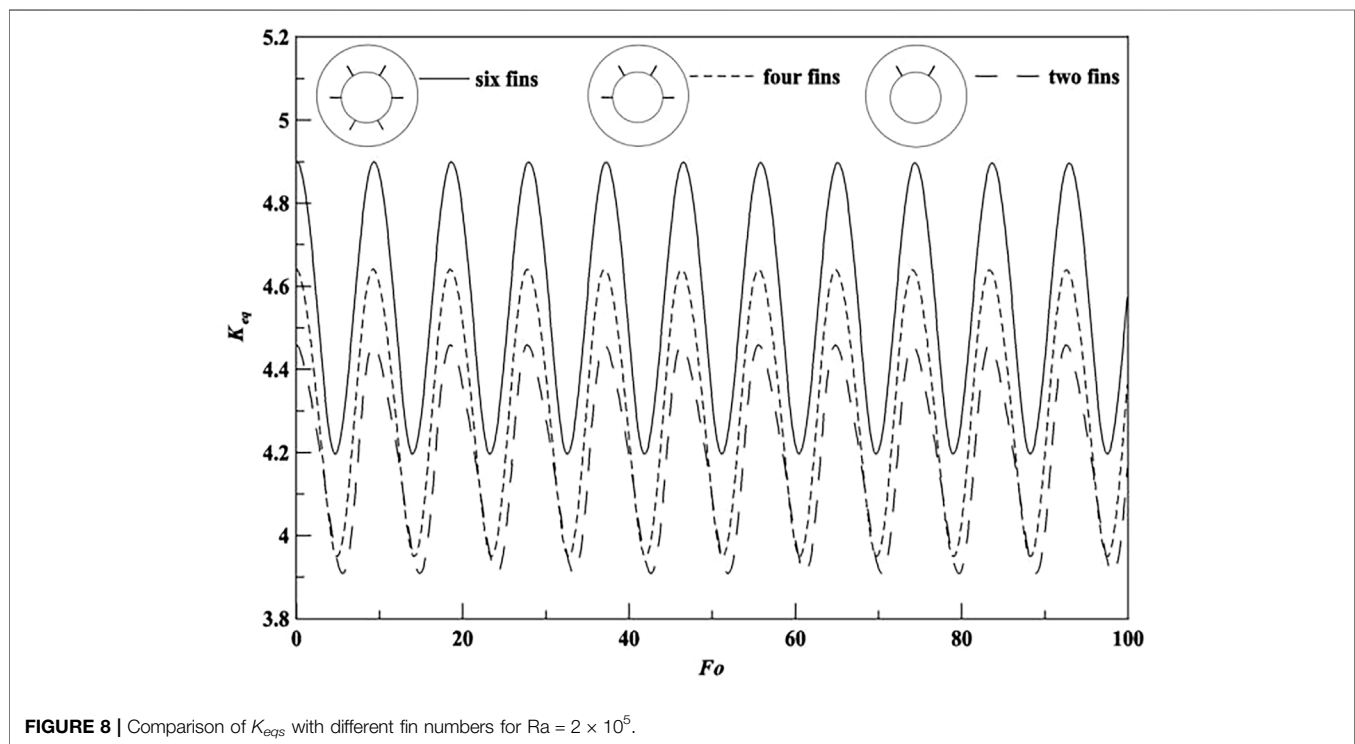
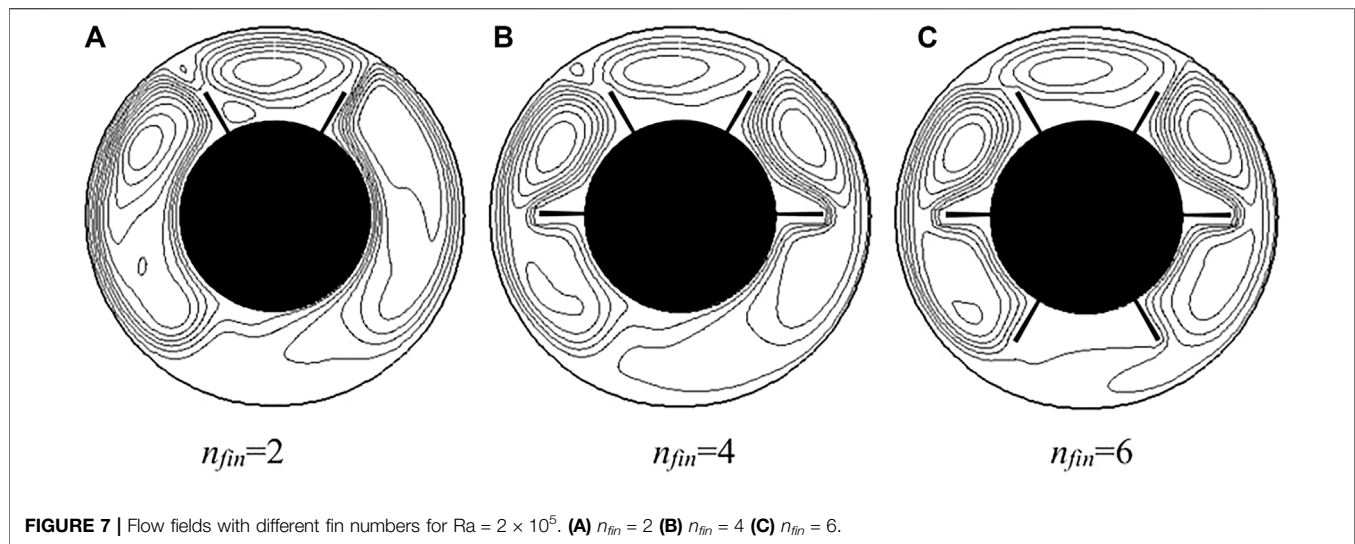
Note. K_{eq} , average dimensionless equivalent thermal conductivity of whole cylinder; Ra , Rayleigh number; α , angle of fins; n_{fin} , number of fins.

$Ra = 5 \times 10^3$. The total heat transfer rate mainly depends on the surface area of the heat transfer, the flow pattern, and the velocity. The values of K_{eq} increases with the increase of the fin number. In the case of $\alpha = \pi/6$, the value of K_{eq} with two fins is 1.64, while the corresponding value of K_{eq} with six fins is 2.1. The value of K_{eq} increases by 28% when the fin number increases from two to six. Accordingly, the value of K_{eq} increases by 17% in the case of $\alpha = \pi/3$. This result can be expected since the heat transfer area increases obviously with the increasing fin number. It also can be seen in **Table 1** that the effect of fin position on the average



equivalent thermal conductivity. In the case of the fin number larger than four, the effects of fin position on the heat transfer rate are negligible. In the case of the fin number less or equal to three, the effect of the fin position on the heat transfer rate cannot be neglected. The values of K_{eq} in the case of $n_{fin} = 2$ increases about 7% from the fin angle 0 to $\pi/6$ and it increases about 9.4% in the case of $n_{fin} = 3$. The results indicate that the fin position has significant effect in convection-dominated regime. The fin attached to the top surface of the inner cylinder resists the development of natural convection in the upper part of the annulus, and therefore, it can alter the flow patterns or heat transfer rate.

Figure 5 shows the variations of local equivalent thermal conductivity $K_{eq,l}$ around the outer cylinder. The asymmetric solution of $K_{eq,l}$ can be obtained under the condition of asymmetric geometric structure with $\alpha = \pi/6$. The maximum value of $K_{eq,l}$ occurs at the right top surface of the outer cylinder because of the synthesized effect. In the case of $\alpha = \pi/3$, the symmetric solutions of $K_{eq,l}$ can be obtained on the symmetric boundary condition, as shown in **Figure 5B**. The maximum value of $K_{eq,l}$ occurs at the middle top surface of the outer cylinder and its value can be arrived at 4.1 because of the heat transfer dominated by natural convection. The local peak value of $K_{eq,l}$ is related to the effect of fins attached to the inner cylinder. The results indicated

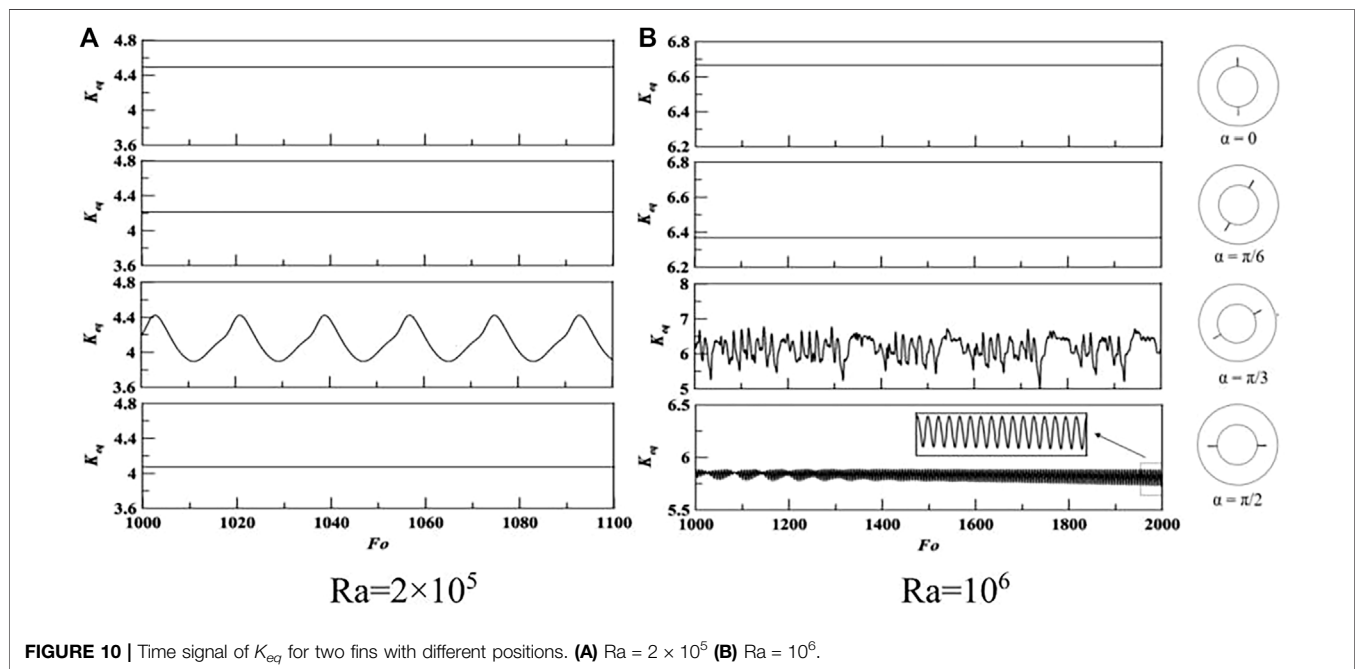
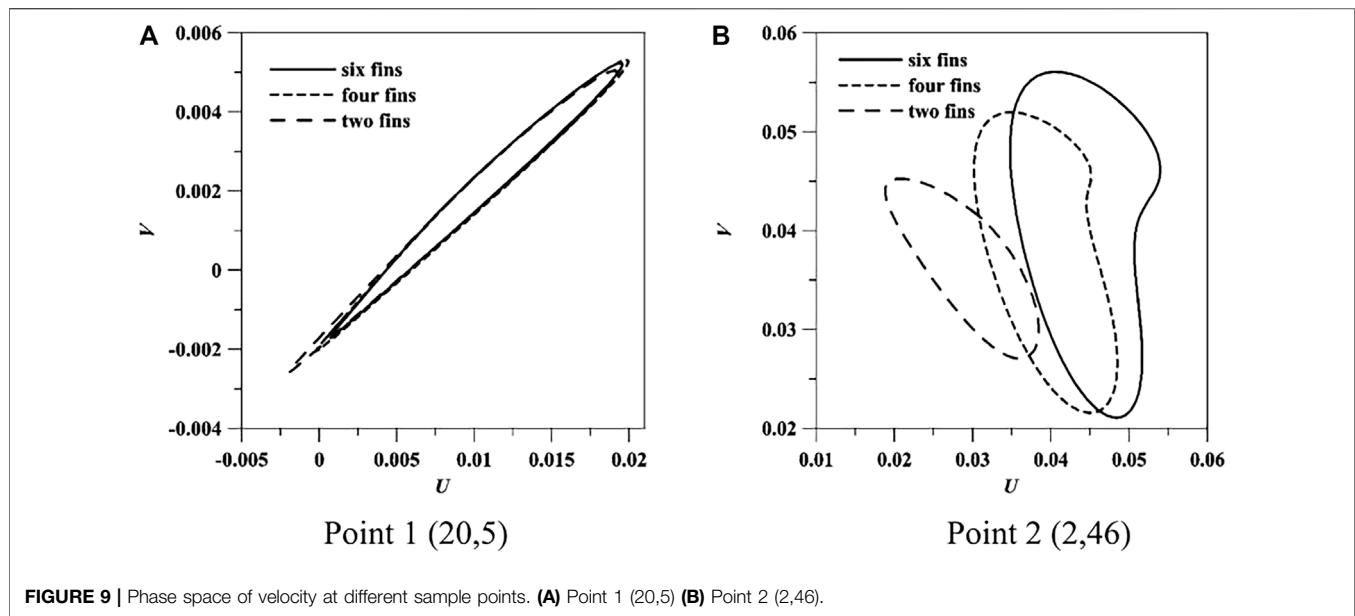


that the heat transfer rate on the upper wall of the outer cylinder is obviously larger than that on the bottom wall because it can be improved by two ways of natural convection and by adding fins.

Effect of Fin Number on Self-Sustained Oscillations

Numerical simulations of natural convection from the zero initial flow field and uniform temperature fields are calculated for different fin numbers. When time required are sufficiently long, self-oscillated solutions can be obtained in the case of

$Ra = 2 \times 10^5$. **Figure 6** shows the temperature fields with different fin numbers when the heat transfer rate arrived at maximum. The asymmetric and unsteady solutions can be obtained with the axisymmetric and steady boundary conditions. In the case of $n_{fin} = 2$, the existence of fins increases the thickness of flow and thermal boundary layer along the bottom part of the inner cylinder and the heat transfer area, and at the same time the fins decrease the thickness of boundary layer along the surface of the outer cylinder, as shown in **Figure 6A**. The heat transfer rate increases with the increasing number of fins at the lower



surface of inner cylinder. However, the temperature distributions on the upper part of annulus for $n_{fin} = 4$ or $n_{fin} = 6$ are almost the same because of the similar geometric structure on this part. The flow fields for different fins at the maximum value of K_{eq} are shown in **Figure 7**. The number of flow vortex increases with the increasing fin numbers. There are three big vortices in the whole annulus for $n_{fin} = 2$. One exists between the two fins at the top of the annulus and the other two are in the middle part of the annulus. The number of vortices increases and the big vortex in the middle part of the annulus is separated by the fins located at the center of the annulus. However, the flow pattern does not

change at the top part of the annulus for all the cases. The results indicate that the heat transfer rate at the top of the annulus can be enhanced more obviously than that at the other part of the annulus. The changing of fin number at the bottom part of the annulus does not make obvious effects on the temperature distribution and the flow pattern at the upper part.

Figure 8 shows the time signal of K_{eq} with different fin numbers for $Ra = 2 \times 10^5$. The initial condition is given that the temperature and flow fields are at the maximum values of K_{eq} . The value of K_{eq} increases with the increasing area of heat transfer and the oscillated phenomenon occurs at all the cases

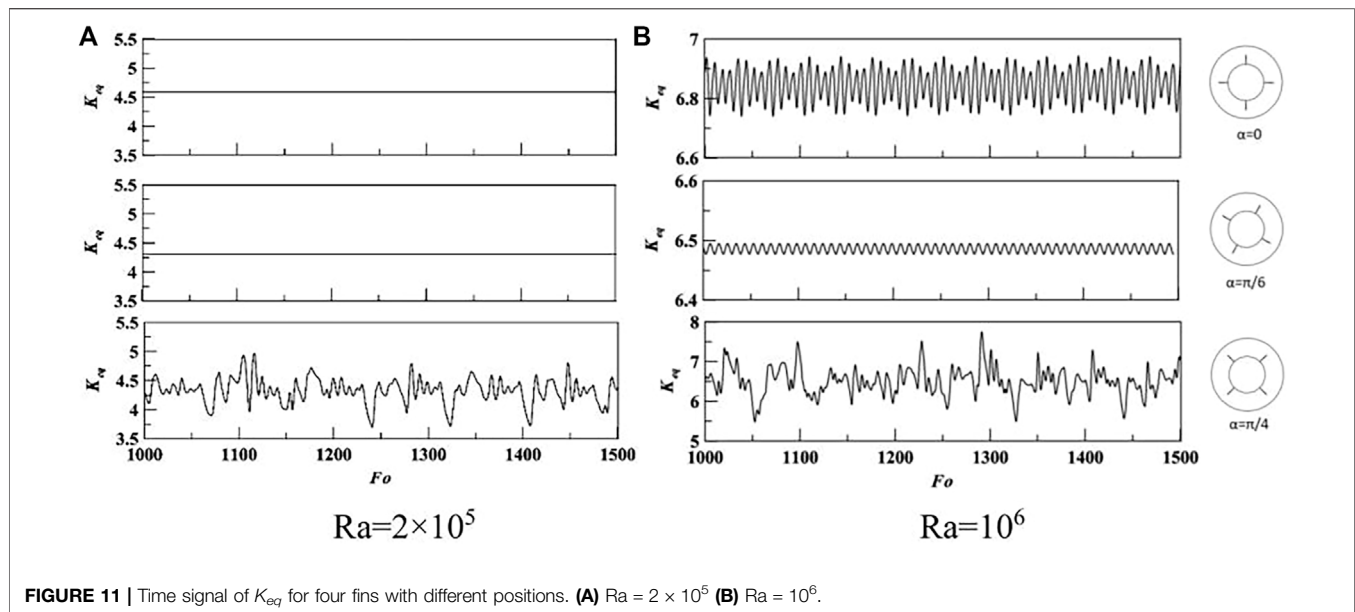


FIGURE 11 | Time signal of K_{eq} for four fins with different positions. (A) $Ra = 2 \times 10^5$ (B) $Ra = 10^6$.

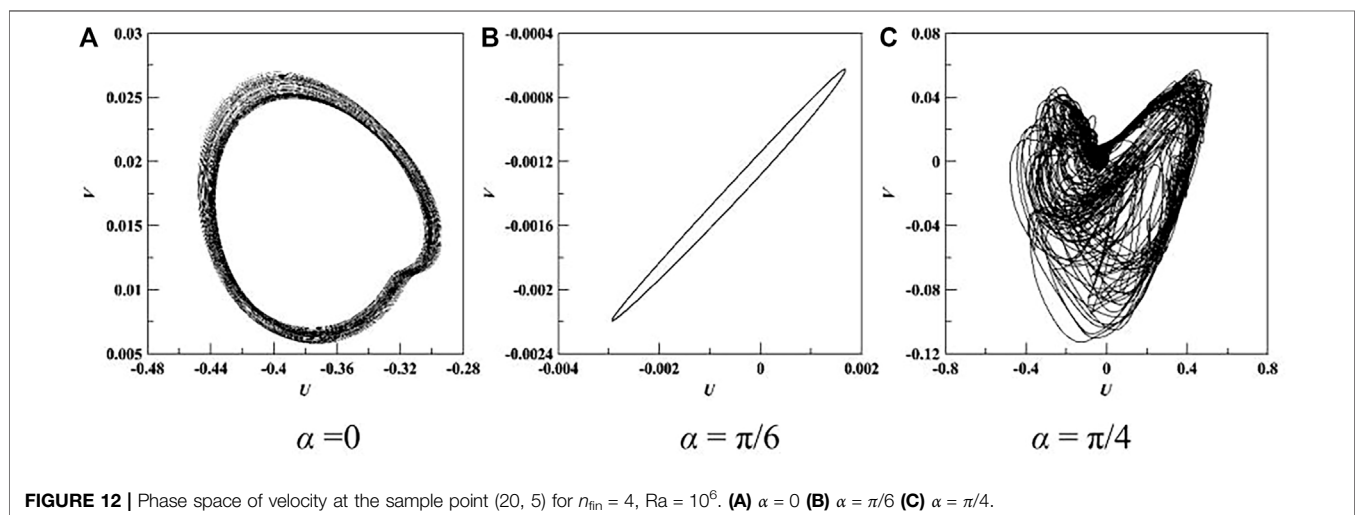


FIGURE 12 | Phase space of velocity at the sample point (20, 5) for $n_{fin} = 4$, $Ra = 10^6$. (A) $\alpha = 0$ (B) $\alpha = \pi/6$ (C) $\alpha = \pi/4$.

and the oscillated period can keep almost the same with the increasing number of fins at the bottom surface of the inner cylinder. The nonlinear phenomenon of natural convection heat transfer is analyzed by using phase space of velocity at points (20, 5) and (2, 46). The sample points are selected for evaluating the nonlinear characteristics of natural convection heat transfer. Some points at the lower part of the annulus or near boundary cannot be chosen because of the small amplitudes. When the dimensionless time is less than 1,000, the data of K_{eq} is not given in those figures for the purpose of convenience presentation. The phase trajectories of velocity at the selected points are shown in **Figure 9**. The system of natural convection heat transfer loses its stability and the phase trajectory of velocity becomes a cycle after the first Hopf bifurcation in the case of $Ra = 2 \times 10^5$. The result indicated that the heat transfer rate and the amplitude of oscillation

increase with the increasing number of fins, while the flow and heat transfer still oscillated with the same period. It means that the oscillation phenomenon of flow and heat transfer are related to the geometric structure at the upper part of the annulus and the natural convection is the most important factor for effecting the nonlinear characteristics.

Effect of Fin Positions on Self-Sustained Oscillations

Numerical simulations of the unsteady natural convection are performed for different fin positions. **Figure 10** shows the time signal of K_{eq} for two fins with different positions. The heat transfer rate increases with the increasing value of Rayleigh numbers and the nonlinear phenomenon is also affected by the value of Rayleigh numbers. When the fin is located at the top

surface of the inner cylinder in the case of $\alpha = 0$ and $\alpha = \pi/6$, the natural convection is easily limited by the fins and the steady solution can be obtained in the case of Rayleigh number from 2×10^5 to 10^6 . In the case of $\alpha = \pi/3$, the natural convection can be developed without obstacles at the upper part of the annulus and the nonlinear phenomenon occurs at $Ra = 2 \times 10^5$. In the case of $\alpha = \pi/2$, the periodic oscillations of flow and heat transfer after a critical Rayleigh numbers between 2×10^5 and 10^6 . The results show that the effect of the fin positions on the nonlinear characteristics is obvious, and the oscillated solution can be easily obtained when there is no fin at the upper part of the annulus. The effect of fins attached to the top surface of the inner cylinder on the natural convection and nonlinear characteristics can be also obtained in the case of four fins, as shown in **Figure 11**. For $Ra = 10^6$, the steady solutions can be calculated for $\alpha = 0$ and $\alpha = \pi/6$ while the unsteady solutions appear for $\alpha = 0$ and $\alpha = \pi/6$. Therefore, the effect of fin position on heat transfer rate is negligible in the case of four fins, but the oscillated phenomenon can be partially suppressed by altering fin positions. This is because the natural convection can be developed easily at the upper part of annulus when the temperature of the bottom surface is higher than that at the other surfaces. When the fins are added at the upper part of the annulus, the temperature distribution can be disturbed and sometimes steady flow and temperature fields can be obtained, as shown in **Figure 11A**.

In order to investigate further the nonlinear characteristics, the numerical solutions of velocity at the sample point (20, 5) is obtained for different fin positions in **Figure 12**. It can be seen that the system loses its stability and the phase trajectory of velocity is a circle for $\alpha = \pi/6$. A quasi-periodic system can be achieved for $\alpha = 0$, and the system progresses toward chaos for $\alpha = \pi/4$. The numerical investigation revealed that the nonlinear phenomenon of natural convection heat transfer in annulus with fins can be affected by the fin positions and Rayleigh numbers.

CONCLUSION

Numerical convection heat transfer in annulus with fins attached to the inner cylinder has been presented. Governing equations are solved using the SIMPLER algorithm with QUICK scheme. The

effect of fin numbers and position on non-linear characteristics was investigated in detail.

In the case of $Ra \leq 5 \times 10^3$, the steady and symmetrical solutions can be reached from the initial zero velocity and uniform field for different fin numbers and positions. The heat transfer rate increases with the increasing numbers of fin and Rayleigh numbers. For $n_{fin} = 2$, $\alpha = \pi/6$ and $Ra = 2 \times 10^5$, the natural convection heat transfer in the annulus loses its stability and the periodic oscillation solution can be obtained after a sufficient long time. The heat transfer rate and the amplitude of oscillation increase with the increasing fin located at other places while the flow and heat transfer still oscillated with the same period. It means that the oscillation phenomenon of flow and heat transfer is related to the geometric structure at the upper part of the annulus and the development of natural convection is the most important factor for nonlinear characteristics. The effect of fin position on the unsteady natural convection is obvious for the same number of fins. In the case of $n_{fin} = 4$ and $Ra = 10^6$, three different kinds of oscillated solutions can be obtained by changing fin inclination angles. Therefore, the nonlinear characteristics of the whole system mainly depend on the natural convection at the upper part of the annulus, and the oscillated phenomenon can be partially suppressed by altering fin positions.

DATA AVAILABILITY STATEMENT

The original contributions presented in the study are included in the article/Supplementary Materials, further inquiries can be directed to the corresponding author.

AUTHOR CONTRIBUTIONS

All authors listed have made a substantial, direct, and intellectual contribution to the work and approved it for publication.

FUNDING

The financial support was granted by the Chinese National Natural Science Foundation under Grant No. 51866008 and the Foundation of A Hundred Youth Talents Training Program of Lanzhou Jiaotong University.

REFERENCES

- Alshahrani, D., and Zeitoun, O. (2005). Natural Convection in Air-Filled Horizontal Cylindrical Annuli. *Alexandria Eng. J.* 44 (6), 814–824.
- Borjini, M. N., Abidi, A., and Aissia, H. B. (2005). Prediction of Unsteady Natural Convection within a Horizontal Narrow Annular Space Using the Control-Volume Method. *Numer. Heat Transfer, A: Appl.* 48 (8), 811–829. doi:10.1080/10407780500196576
- Chai, J. C., and Patankar, S. V. (1993). Laminar Natural Convection in Internally Finned Horizontal Annuli. *Numer. Heat Transfer, Part A: Appl.* 24 (1), 67–87. doi:10.1080/10407789308902603
- Chen, H. T., and Hsu, W. L. (2007). Estimation of Heat Transfer Coefficient on the Fin of Annular Finned Tube Heat Exchangers in Natural Convection for Various Fin Spacings. *Int. J. Heat Mass. Tran.* 10 (50), 1750–1761. doi:10.1016/j.ijheatmasstransfer.2006.10.021
- Ei-Maghlay, W. M., Sorour, M. M., and Hozien, O. (2015). Experimental Study of Natural Convection in an Annulus between Two Eccentric Horizontal Square Ducts. *Exp. Therm. Fluid Sci.* 65, 65–72. doi:10.1016/j.expthermflusci.2015.03.006
- El Maakoul, A., Feddi, K., Saadeddine, S., Ben Abdellah, A., and El Metoui, M. (2020). Performance Enhancement of Finned Annulus Using Surface Interruptions in Double-Pipe Heat Exchangers. *Energ. Convers. Manag.* 210, 112710. doi:10.1016/j.enconman.2020.112710

- Farinas, M.-I., Garon, A., and Saint-Louis, K. (1997). Study of Heat Transfer in a Horizontal cylinder with Fins. *Revue Générale de Thermique* 36 (5), 398–410. doi:10.1016/s0035-3159(97)81601-7
- Gao, Q., Zhang, K., and Wang, L. B. (2020). Numerical Analysis of Natural Convection in Internally Finned Horizontal Annuli. *Front. Heat Mass Transfer* 14, 29. doi:10.5098/hmt.14.29
- Ghasemi, E., Soleimani, S., and Bararnia, H. (2012). Natural Convection between a Circular Enclosure and an Elliptic cylinder Using Control Volume Based Finite Element Method. *Int. Commun. Heat Mass Transfer* 39, 1035–1044. doi:10.1016/j.icheatmasstransfer.2012.06.016
- Gholamalipour, P., Siavashi, M., and Doranehgard, M. H. (2019). Eccentricity Effects of Heat Source inside a Porous Annulus on the Natural Convection Heat Transfer and Entropy Generation of Cu-Water Nanofluid. *Int. Commun. Heat Mass Transfer* 109, 104367. doi:10.1016/j.icheatmasstransfer.2019.104367
- Idrissi, A., Cheddadi, A., and Ouazzani, M. T. (2016). Heat Transfer in an Annular Space Fitted with Heating Isothermal Blocks: Numerical Bifurcation for Low Blocks Height. *Case Stud. Therm. Eng.* 7, 1–7. doi:10.1016/j.csite.2015.11.002
- Kim, H. J., An, B. H., Park, J., and Kim, D.-K. (2013). Experimental Study on Natural Convection Heat Transfer from Horizontal Cylinders with Longitudinal Plate Fins. *J. Mech. Sci. Technol.* 27 (2), 593–599. doi:10.1007/s12206-012-1236-3
- Kiwan, S., and Zeitoun, O. (2008). Natural Convection in a Horizontal Cylindrical Annulus Using Porous Fins. *Int. Jnl Num Meth HFF* 18 (5), 618–634. doi:10.1108/09615530810879747
- Kuehn, T. H., and Goldstein, R. J. (1976). An Experimental and Theoretical Study of Natural Convection in the Annulus between Horizontal Concentric Cylinders. *J. Fluid Mech.* 74, 695–719. doi:10.1017/s0022112076002012
- Kuehn, T. H., and Goldstein, R. J. (1978). An Experimental Study of Natural Convection Heat Transfer in Concentric and Eccentric Horizontal Cylindrical Annuli. *J. Heat Transfer* 100, 635–640. doi:10.1115/1.3450869
- Kuehn, T. H., and Goldstein, R. J. (1980). Numerical Solution to the Navier-Stokes Equations for Laminar Natural Convection about a Horizontal Isothermal Circular cylinder. *Int. J. Heat Mass Transfer* 23 (7), 971–979. doi:10.1016/0017-9310(80)90071-x
- Labonia, G., and Guj, G. (2000). Natural Convection in a Horizontal Concentric Cylindrical Annulus: Oscillatory Flow and Transition to Chaos. *J. Fluid Mech.* 375 (375), 179–202. doi:10.1017/S0022112098002754
- Liu, L., Cao, Z., Shen, T., Zhang, L., and Zhang, L. (2021). Experimental and Numerical Investigation on Flow and Heat Transfer Characteristics of a Multi-Waves Internally Spiral Finned Tube. *Int. J. Heat Mass Transfer* 172, 121104. doi:10.1016/j.ijheatmasstransfer.2021.121104
- Nada, S. A., and Said, M. A. (2019). Effects of Fins Geometries, Arrangements, Dimensions and Numbers on Natural Convection Heat Transfer Characteristics in Finned-Horizontal Annulus. *Int. J. Therm. Sci.* 137, 121–137. doi:10.1016/j.ijthermalsci.2018.11.026
- Rahnama, M., and Farhadi, M. (2004). Effect of Radial Fins on Two-Dimensional Turbulent Natural Convection in a Horizontal Annulus. *Int. J. Therm. Sci.* 43, 255–264. doi:10.1016/j.ijthermalsci.2003.07.002
- Rahnama, M., Mehrabian, M. A., Mansouri, S. H., Sinaie, A., and Jafarholi, K. (1999). Numerical Simulation of Laminar Natural Convection in Horizontal Annuli with Radial Fins. *Proc. Inst. Mech. Eng. E: J. Process Mech. Eng.* 213 (2), 93–97. doi:10.1243/0954408991529780
- Senapati, J. R., Dash, S. K., and Roy, S. (2017). Numerical Investigation of Natural Convection Heat Transfer from Vertical cylinder with Annular Fins. *Int. J. Therm. Sci.* 111, 146–159. doi:10.1016/j.ijthermalsci.2016.08.019
- Shadlaghani, A., Farzaneh, M., Shahabadi, M., Tavakoli, M. R., Safaei, M. R., and Mazinani, I. (2019). Numerical Investigation of Serrated Fins on Natural Convection from Concentric and Eccentric Annuli with Different Cross Sections. *J. Therm. Anal. Calorim.* 135, 1429–1442. doi:10.1007/s10973-018-7542-y
- Touzani, S., Idrissi, A., Cheddadi, A., and Ouazzani, M. T. (2019). Numerical Study of Laminar Natural Convection in a Finned Annulus: Low Isothermal Blocks Positions. *J. Eng. Phys. Thermophy* 92 (4), 1064–1071. doi:10.1007/s10891-019-02021-6
- Usman, M., Son, J. H., and Park, I. S. (2021). A Low-Rayleigh Transition into Chaos for Natural Convection inside a Horizontal Annulus at Prandtl Number 0.1. *Int. J. Heat Mass Transfer* 179 (2), 121658. doi:10.1016/j.ijheatmasstransfer.2021.121658
- Yang, X., and Kong, S.-C. (2019). Numerical Study of Natural Convection in a Horizontal Concentric Annulus Using Smoothed Particle Hydrodynamics. *Eng. Anal. Boundary Elem.* 102, 11–20. doi:10.1016/jenganabound.2019.02.007
- Yong, S., Zhao, T. S., and Guo, Z. L. (2006). Finite Difference-Based Lattice Boltzmann Simulation of Natural Convection Heat Transfer in a Horizontal Concentric Annulus. *Comput. Fluids* 35 (1), 1–15. doi:10.1016/j.compfluid.2004.11.003
- Yoo, J.-S., and Han, S.-M. (2000). Transitions and Chaos in Natural Convection of a Fluid with $Pr = 0.1$ in a Horizontal Annulus. *Fluid Dyn. Res.* 27 (4), 231–245. doi:10.1016/s0169-5983(00)00004-6
- Yoo, J.-S. (1998). Natural Convection in a Narrow Horizontal Cylindrical Annulus: $Pr \leq 0.3$. *Int. J. Heat Mass Transfer* 41 (20), 3055–3073. doi:10.1016/s0017-9310(98)00051-9
- Zhang, K., Yang, M., Wang, J., and Zhang, Y. (2014). Experimental Study on Natural Convection in a Cylindrical Envelope with an Internal Concentric cylinder with Slots. *Int. J. Therm. Sci.* 76, 190–199. doi:10.1016/j.ijthermalsci.2013.09.005
- Zhang, K., Yang, M., and Zhang, Y. (2011). Numerical Analysis of Natural Convection in a Cylindrical Envelope with an Internal Concentric cylinder with Slots. *Numer. Heat Transfer, Part A: Appl.* 59 (10), 739–754. doi:10.1080/10407782.2011.572762

Conflict of Interest: The authors declare that the research was conducted in the absence of any commercial or financial relationships that could be construed as a potential conflict of interest.

Publisher's Note: All claims expressed in this article are solely those of the authors and do not necessarily represent those of their affiliated organizations, or those of the publisher, the editors, and the reviewers. Any product that may be evaluated in this article, or claim that may be made by its manufacturer, is not guaranteed or endorsed by the publisher.

Copyright © 2021 Zhang, Zhang, Wang and Wang. This is an open-access article distributed under the terms of the Creative Commons Attribution License (CC BY). The use, distribution or reproduction in other forums is permitted, provided the original author(s) and the copyright owner(s) are credited and that the original publication in this journal is cited, in accordance with accepted academic practice. No use, distribution or reproduction is permitted which does not comply with these terms.



Numerical Simulation of the Influence of CO₂ on the Combustion Characteristics and NO_x of Biogas

Jinshuang Ma¹, Chuanjia Qi^{1,2}, Siyi Luo^{1,3*} and Zongliang Zuo^{1,3}

¹School of Environmental and Municipal Engineering, Qingdao University of Technology, Qingdao, China, ²School of Energy and Power Engineering, Shandong University, Jinan, China, ³Key Lab of Industrial Fluid Energy Conservation and Pollution Control (Qingdao University of Technology), Ministry of Education, Qingdao, China

OPEN ACCESS

Edited by:

Chuang Wen,
University of Exeter, United Kingdom

Reviewed by:

Pengfei Li,
Huazhong University of Science and
Technology, China
Jo-Han Ng,
University of Southampton Malaysia,
Malaysia
Grzegorz Przybyła,
Silesian University of Technology,
Poland

*Correspondence:

Siyi Luo
luosiyi666@126.com

Specialty section:

This article was submitted to
Advanced Clean Fuel Technologies,
a section of the journal
Frontiers in Energy Research

Received: 08 November 2021

Accepted: 14 December 2021

Published: 06 January 2022

Citation:

Ma J, Qi C, Luo S and Zuo Z (2022)
Numerical Simulation of the Influence
of CO₂ on the Combustion
Characteristics and NO_x of Biogas.
Front. Energy Res. 9:811037.
doi: 10.3389/fenrg.2021.811037

The existence of inert gases such as N₂ and CO₂ in biogas will reduce the proportion of combustible components in syngas and affect the combustion and NO_x formation characteristics. In this study, ANSYS CHEMKIN-PRO software combined with GRI-MECH 3.0 mechanism was used to numerically simulate the effects of different CO₂ concentrations (CO₂ volume ratio in biogas is 0–41.6%) on flame combustion temperature, flame propagation speed and nitrogen oxide formation of complex biogas with low calorific value. The results showed that when the combustion reaches the chemical equilibrium, the flame combustion temperature and flame propagation speed decrease with the increase of CO₂ concentration, and the flame propagation speed decreases even more slowly. Meanwhile, the molar fraction of NO at chemical equilibrium decreases with the increase of CO₂ concentration and the decrease is decreasing, which indicates that the effect of CO₂ concentration in biogas on NO is simpler. While the molar fraction of NO₂ does not change regularly with the change of CO₂ concentration, the effect of CO₂ concentration in biogas on NO₂ is complicated. The highest molar fraction of NO₂ was found at chemical equilibrium when the CO₂ concentration was 33.6%, when the target was a typical low calorific value biogas.

Keywords: simulation, biogas, CO₂ concentration, combustion characteristics, NO_x

INTRODUCTION

Biomass is a kind of clean and convenient energy with rich reserves, which is a promising green renewable energy (Zhang et al., 2005). Nowadays, direct combustion is a main utilization method for biomass (Yang et al., 2020). However, it has the disadvantages of low utilization ratio, massive content of dust and NO_x in flue gas (Zhao and Su, 2019; Wang et al., 2020). To solve above issues, the biogas obtained from pyrolysis or gasification of biomass can be combusted with pulverized coal as boiler fuel, which not only reduces the consumption of coal, but also decreases the NO_x emission significantly (Zhang et al., 2017). Therefore, biomass gasification is considered as a more effective, promising and valuable application mode for biomass utilization (Cao et al., 2019). However, the composition of biogas is complex, especially the existence of inert gases such as CO₂ and N₂ will have a great impact on the combustion characteristics of flame and the formation of NO_x (Chu et al., 2021).

In recent years, many scholars have studied the effects of simple component gases on flame characteristics and NO_x emission in laminar premixed combustion: Studies by many scholars have shown that the increase of H₂ content will lead to higher combustion temperature and laminar flame

speed, but the emission of nitrogen oxides will also increase correspondingly (Azimov et al., 2011; Wang et al., 2021). The premixed combustion of syngas under different H₂/CO ratio was studied, the results suggested that increasing the H₂/CO ratio led to a decrease in the temperature as well as the NO concentration near the flame (Asgari et al., 2017). The combustion characteristics of NH₃/H₂/air, H₂/CO/syngas, propane/hydrogen/air and other mixtures have also been extensively studied (Tang et al., 2008; Nozari and Karabeyoglu, 2015; Chen and Jiang, 2021).

Although many scholars have studied the flame combustion characteristics of biogas, most of them are limited to study some kind of combustible gas, or changing the ratio of two kinds of gas in the combustible gas. A small number of people have studied the effects of inert gas on combustion characteristics and NO_x emission: The effects of N₂ dilution on laminar burning speed, adiabatic flame temperature, intermediate radicals and NO_x emissions of methane were investigated under different equivalence ratio conditions. Results showed that under the same equivalence ratio, the mole fraction of NO_x decreased as the N₂ doping ratio increased (Resende et al., 2019; Chu et al., 2021). The effect of CO₂ and N₂ dilution on CH₄/air flame by flame temperature distribution measurement and flame calculation was analyzed. At ambient temperature (298K), the specific heat capacity of N₂ is 1042 J/kg·K, H₂ is 14,300 J/kg·K and that of CO₂ is 839 J/kg·K. Results indicated that CO₂ addition shows more significant effects on the thermal properties of flame, except for flame thickness (Zhang et al., 2016). Numerical simulation was used to study the combustion characteristics of laminar premixed biological combustion flames with different equivalence ratios (0.6–1.6) under standard conditions by using ANSYS CHEMKIN-PRO and GRI-MECH 3.0 mechanism. The results showed that the laminar flame speed has a good positive correlation with the adiabatic temperature under different equivalent ratios. The inhibition effect of CO₂ is stronger than N₂, which may be related to the chemical effect and heat capacity of CO₂ (Sun et al., 2021). It can be seen from the above that the change of CO₂ concentration has a stronger influence on combustion characteristics than N₂, and most scholars have studied the influence of inert gas on combustion characteristics of simple components (methane, methane-air mixture, etc.). The research on combustion characteristics and nitrogen oxide emission of complex biogas which close to actual biogas components by using simulation software is relatively rare, and further research is necessary.

Because CHEMKIN software has relatively perfect mechanism files for solving complex chemical reaction problems, it is often used to study flame combustion characteristics and NO_x conversion mechanism. It was proved to be very effective to study the combustion characteristics and NO_x emissions by using the PREMIX code of CHEMKIN (Chen et al., 2011; Gong et al., 2018). CHEMKIN and GRI-MECH 3.0 chemical kinetic models were used to simulate combustion process, which has outstanding advantages in predicting combustion chamber pressure, temperature, distribution of main combustion species and formation of nitrogen oxides (Mansha et al., 2010). Chemical dynamics simulation with hedged flame model in CHEMKIN

software was carried out, and the influence mechanism of water vapor on combustion flame characteristics was analyzed, the simulated data were in good agreement with the experimental results. (Cui et al., 2020). Wilk, M. studied the combustion characteristics of carbonized biomass by TGA (Thermo Gravimetric Analyzer) analysis and CHEMKIN calculation, and the results showed that the change of gas products calculated by CHEMKIN during combustion was consistent with the results of TGA analysis (Wilk et al., 2017). The above research shows that the simulation of combustion characteristics and nitrogen oxides emission by CHEMKIN software is in good agreement with the actual situation, so it can be used to study the combustion mechanism.

The influence of one or more combustible gases on flame combustion characteristics and NO_x formation mechanism has been extensively studied, and the effects of nitrogen and carbon dioxide dilution on combustion characteristics are well explored, studies on combustion characteristics and NO_x formation mechanism of syngas flame with complex components under different inert gas concentrations are relatively scarce seldom. Therefore, in this study, typical low calorific value biogas (Li, 2019) which is closer to the real biogas composition (the composition of typical low calorific value biogas is shown in **Table 2 of Section 2.1**) was selected to study one-dimensional laminar premixed flame, and CHEMKIN software was used to simulate the influence of CO₂ concentration change on flame combustion characteristics and the formation of nitrogen oxides, aiming at providing help for the design of biomass gas burner and theoretical support for emission reduction of biomass gas boiler.

METHODS

Mechanism

In this study, based on CHEMKIN software, the premixed laminar flame characteristics and NO_x conversion mechanism of material gas were studied. All calculations in CHEMKIN software are based on mechanism files. This simulation uses two mechanism files. One is the Flame-speed-parameter-study case in CHEMKIN software, which contains C, H, O and N elements. The components include all the components in the biogas, which can well simulate the combustion process of the selected biogas. Since the generation of NO_x is not involved in this mechanism document, GRI-MECH3.0 methane mechanism document is selected for the concentration variation law of NO and NO₂. The above two mechanism documents can be used to complete the combustion characteristics of the flame and NO_x conversion mechanism.

Assuming that the gas inlet is a one-dimensional steady flow, the governing equation can be simplified as follows (Kuo, 2005; Sun et al., 2021):

Continuity

$$\dot{M} = \rho u A \quad (1)$$

In the above formula, \dot{M} represents the total mass flow rate of gas components, ρ means the density of the mixture, u represents

TABLE 1 | The main gas components of different types of biomass.

CO	H ₂	CH ₄	N ₂	CO ₂
%	%	%	%	%
6.56	14.18	15.7	50.99	3.96
8.29	13.16	14.76	46.16	7.24
20.62	5.37	5.79	47.33	15.52
16.67	8.96	9.77	42.92	21.68
25	27	3.6	0.27	23
28	30	10	5	27

the speed of the mixed fluid in the x direction, and A indicates the cross-sectional area of the flow tube.

Energy

$$\dot{M} \frac{dT}{dx} - \frac{1}{C_p} \frac{d}{dx} \left(\lambda A \frac{dT}{dx} \right) + \frac{A}{C_p} \sum_{k=1}^k \rho Y_k V_k C_{pk} \frac{dT}{dx} + \frac{A}{C_p} \sum_{k=1}^k \dot{\omega}_k h_k W_k + \frac{A}{C_p} \dot{Q}_{rad} = 0 \quad (2)$$

where x represents the one-dimensional coordinates, T represents the temperature, λ is the heat conductivity of the gas, C_p represents the heat capacity of the mixed gas at constant pressure, C_{pk} expresses the k th species heat capacity at constant pressure, Y_k denotes the k th species mass fraction, V_k indicates the diffusion rate of the k th gas, h_k indicates the specific enthalpy of the k th gas, W_k represents molecular weight of the k th species, $\dot{\omega}_k$ is the production molar rate through the chemical reaction of the k th species every unit volume, and \dot{Q}_{rad} expresses the radiation heat loss of mixture.

Species

$$\dot{M} \frac{dY_k}{dx} + \frac{d}{dx} (\rho A Y_k V_k) - A \dot{\omega}_k W_k = 0, (k = 1, \dots, K_g) \quad (3)$$

Equation of state

$$\rho = \frac{P\bar{W}}{RT} \quad (4)$$

In Eq. 4, P represents the pressure in the x direction, R is the general constant of gas, and \bar{W} represents the average molecular weight of the mixture.

Material

Table 1 shows the main gas components of different types of biomass gasification processes in the references (Wu et al., 2009; Kim et al., 2011; Miao et al., 2013; Wang et al., 2015). It can be noticed that the variation range of CO₂ concentration in biogas is 0–30%. In addition, related reference also showed that when the proportion of CO₂ is about 40% (Li, 2019) the fuel has better combustion characteristics and low NO_x generation. It can be seen that the influence range of CO₂ concentration on combustion characteristics and NO_x is about 0–40%, so we choose the biogas synthesized in the laboratory, that is, the typical low calorific value biogas (the composition of typical low calorific value biogas is shown in **Table 2**) as the control group for numerical simulation, and study it in the range of CO₂ concentration of 0–41.6%.

TABLE 2 | Composition of typical low calorific value biogas.

CO	H ₂	CH ₄	N ₂	CO ₂	Calorific value of gas
%	%	%	%	%	kcal/Nm ³
9.35	13.05	7.5	36.5	33.6	1260

TABLE 3 | The biogas composition under different CO₂ volume ratios.

CO	H ₂	CH ₄	N ₂	CO ₂
%	%	%	%	%
14.08	19.65	11.30	54.97	0
12.73	17.76	10.22	49.69	9.60
11.60	16.19	9.31	45.30	17.60
10.48	14.62	8.41	40.89	25.60
9.35	13.05	7.50	36.50	33.60
8.22	11.48	6.60	32.10	41.60

Calculation Conditions

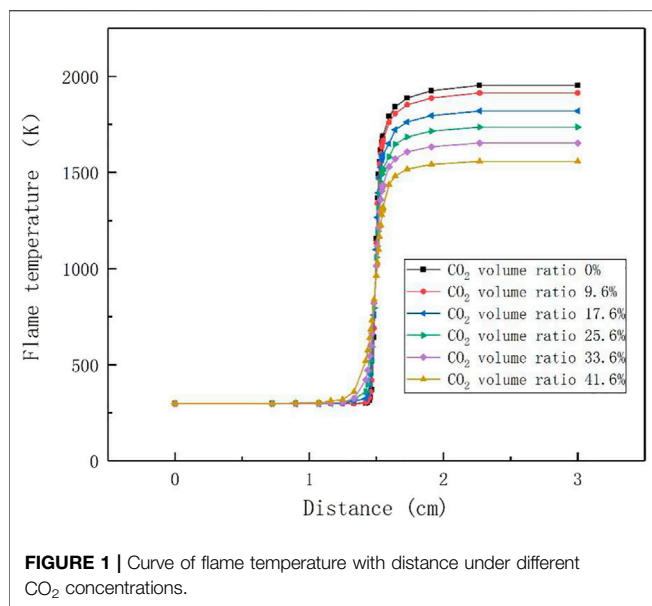
To ensure that the flame is close to the real burning condition, the flame speed calculator simulates a freely propagating flame at 298 K and 1 atm. At the equivalent ratio of 1.0, the laminar flame is the fastest and the flame is stable (Liu et al., 2020), so the simulation is performed at the equivalent ratio of 1.0. The initial flow rate parameter of the biogas was set to 50 cm/s. In the simulation process, the proportion of other gases remains unchanged, only the concentration of CO₂ to be studied will be changed. **Table 3** shows the biogas composition under different CO₂ volume ratios.

RESULTS AND DISCUSSION

Effect of CO₂ Concentration on Flame Combustion Temperature

CO₂ has a high specific heat capacity and a relatively high heat absorption capacity, which has a certain influence on the flame combustion temperature, and the flame combustion temperature will have an influence on the formation of some temperature-sensitive intermediate products (Zhang, 2020). Reasonable control of the combustion temperature ensures that the fuel is fully burned, and the generation of intermediate products can be controlled to reduce the formation of pollutants while ensuring combustion efficiency.

Figure 1 illustrates the variation curve of flame temperature with distance for different CO₂ compositions simulated by CHEMKIN. For typical low calorific value biogas, when the volume ratio of CO₂ is 33.60%, it can be used as a control group to compare the influence of CO₂ concentration change on flame combustion temperature. It can be seen from **Figure 1** that with the increase of the distance and the continuation of the reaction, the temperature of the flame keeps rising. When the combustion reaches chemical equilibrium, the final temperature of the reaction keeps decreasing with the increase of CO₂ concentration. As the percentage of CO₂ increases from 0 to 41.6%, the flame temperature decreases by about 395 K, which can be explained by the fact that the concentration of small molecular intermediates such as H, O and OH in the flame decreases as the

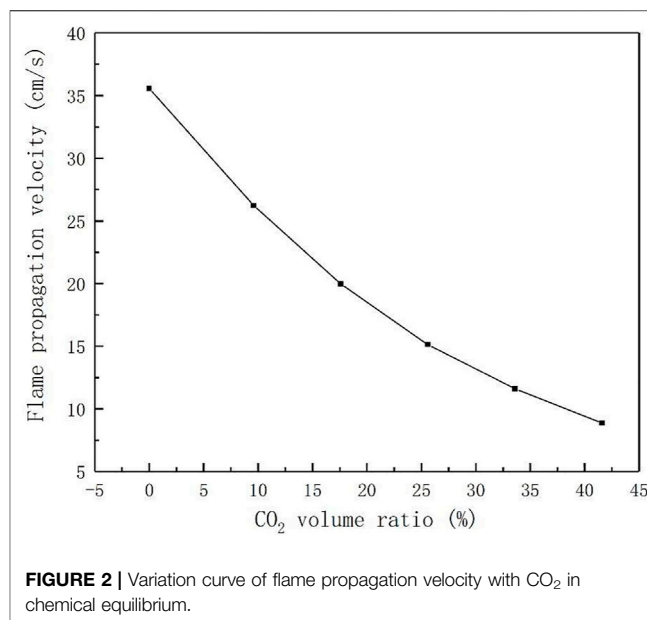


concentration of CO₂ increases, and the maximum flame temperature falls with the increase of CO₂, while the high temperature area also decreases (Cao and Zhu, 2012). The research results of Park et al. showed that with the increase of CO₂ concentration from 0 to 0.4, the flame burning temperature decreases by about 400K (Park et al., 2007), which is highly consistent with our simulation results. The effect of CO₂ concentration on combustion temperature provides a theoretical basis for adding CO₂ as a diluent to the fuel.

Effect of CO₂ Concentration on Flame Propagation Speed

The flame propagation speed of laminar flow can fully reflect the fuel activity, the basic characteristics of heat and mass transfer of combustion reaction, and the tempering characteristics of flame, etc (De Goey et al., 2011). However, the addition of CO₂ has a great influence on the flame propagation speed, so studying the influence of CO₂ concentration on the flame propagation speed can provide great help to the design of burner. Therefore, the flame propagation speed was simulated numerically using CHEMKIN software, and the variation curve of flame propagation speed with CO₂ concentration was obtained as shown in **Figure 2**. It can be seen that the flame propagation speed decreases with the increase of the volume ratio of CO₂, the flame propagation speed at 40% CO₂ concentration is 64.2% lower than that at 10%, which is consistent with the results of Hinton and Cohe (Cohe et al., 2009; Hinton and Stone, 2014). In addition, the simulation results are in good agreement with the experimental results of Maria Mitu (Mitu et al., 2017). With the increase of CO₂ concentration, the laminar flame combustion velocity decreases from the initial 35 cm/s to about 10 cm/s.

The reason why the existence of CO₂ reduces the flame propagation speed is that although CO₂ is an inert gas, it also participates in the primitive reaction $\text{CO}_2 + \text{H} \rightarrow \text{CO} + \text{OH}$ (Glarborg and Bentzen, 2008), which inhibits the oxidation

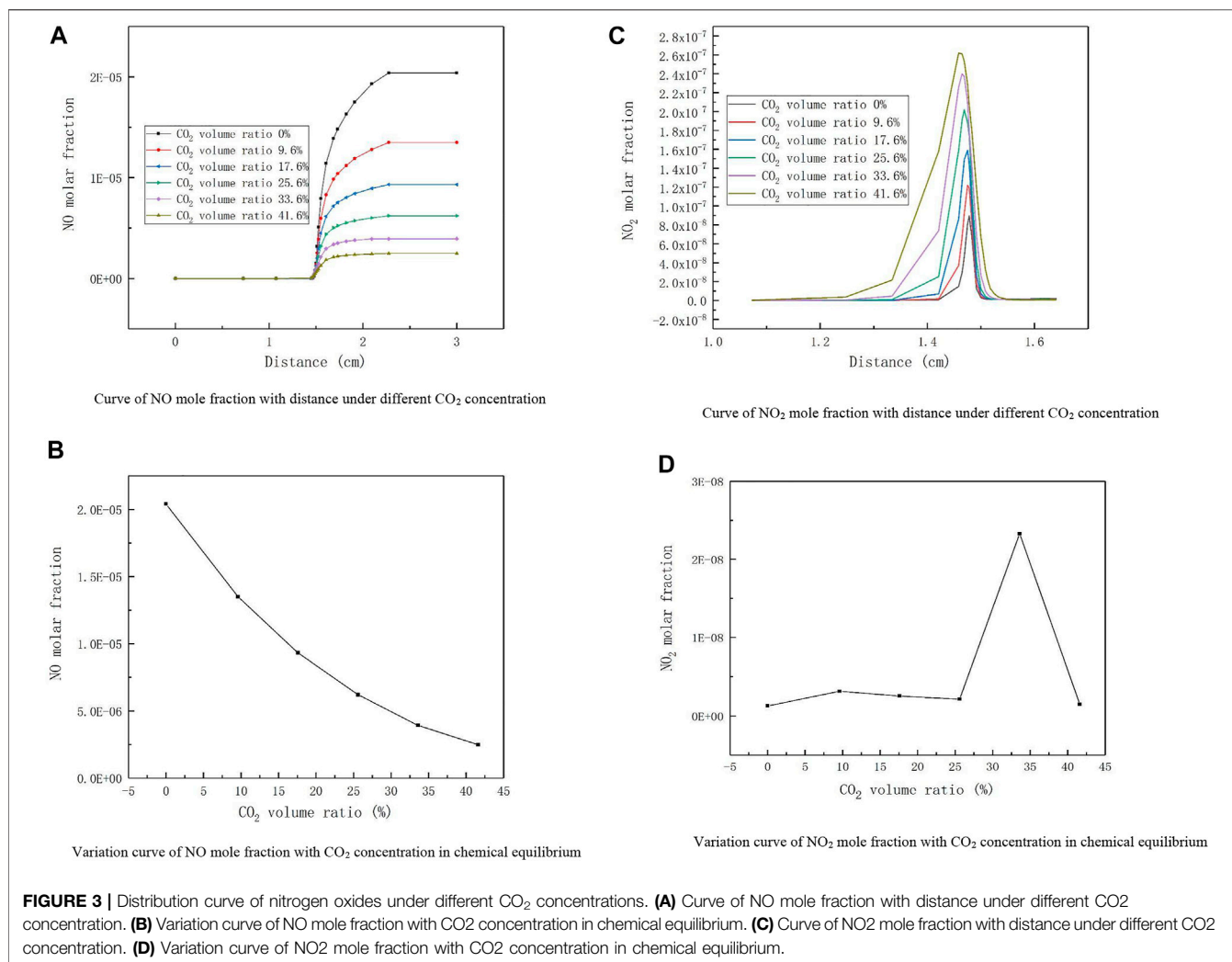


of CO. It will also compete with the branch reaction of the main chain for H element, leading to the reduction of H group and OH group (Huang, 2011), and these two free radicals have a great promotion effect on the flame propagation speed. Consequently, the volume ratio of CO₂ in syngas should be controlled to ensure a reasonable combustion rate.

Effect of CO₂ Concentration on the Formation of NO and NO₂

The emission of nitrogen oxides is a problem to be considered in small-capacity boilers, because the nitrogen oxides produced by any fossil fuel combustion will lead to the formation of acid rain and photochemical smog, which are important causes of air pollution (Werle, 2015). Thus, studying the effect of CO₂ concentration on NO_x formation can reduce the pollutant generation at the source and can provide theoretical support for reducing NO_x emissions for biomass gas boilers.

Figure 3A shows the curve of NO mole fraction with distance under different CO₂ concentration, and **Figure 3B** presents the variation curve of NO mole fraction with CO₂ concentration in chemical equilibrium. From the above two figures, it can be observed that the molar fraction of NO keeps increasing with the distance and the reaction proceeds continuously. When the biogas is devoid of CO₂, the molar fraction of NO increases fastest with distance, and when the combustion reaches chemical equilibrium, the proportion of NO produced is the largest, and the molar fraction of NO produced at equilibrium declines as the volume proportion of CO₂ in the fuel increases. This is in agreement with the findings of Tang (Tang et al., 2009). The influence of CO₂ concentration on NO generation was studied by using a tube furnace with Li of 1373K and equivalent ratio of 1. The experimental results showed that with the increase of CO₂ concentration, NO concentration decreases from 14.8 to 5.9 ppm (Li, 2019), which is consistent with our simulation results.



Because of the different gas composition and the influence of experimental operation process, the specific values are different. Liu and Dong et al. demonstrated that $\text{CO}_2 + \text{H} \rightarrow \text{CO} + \text{OH}$ and $\text{CO}_2 + \text{CH} \rightarrow \text{HCO} + \text{CO}$ are the main chemical reaction in which CO₂ participates, while these two reactions indirectly affect the production of the NO precursor HCN, thus inhibiting the production of NO_x (Liu et al., 2001; Dong et al., 2014).

Figure 3C shows the curve of NO₂ mole fraction with distance under different CO₂ concentration, and **Figure 3D** presents the variation curve of NO₂ mole fraction with CO₂ concentration in chemical equilibrium. From **Figure 3C**, it can be found that the molar fraction of NO₂ at the peak is highest when the volumetric proportion of CO₂ in the biogas is 41.6%, with a value of 2.06E-07. As the volumetric proportion of CO₂ in the biogas decreases, the molar fraction of NO₂ at the peak also reduces. As can be noticed from **Figure 3D**, the molar fraction of NO₂ produced at equilibrium is maximum for the selected typical low calorific value biogas whose CO₂ concentration is around 33.6%, and the molar fraction of NO₂ produced is significantly lower in other cases. Thus, it can be seen that the effect of the variation of CO₂ concentration on NO₂ is very complex. This may be due to the fact that the concentration of H, O,

and HO₂ changes with different CO₂ concentrations, leading to unstable formation of NO₂ (Glarborg and Bentzen, 2008). Since the combustion mechanism is very complex the exact cause needs to be further verified.

CONCLUSIONS

In this paper, the influence of CO₂ concentration on flame combustion characteristics and NO_x formation was studied by using CHEMKIN software. The main research results are as follows.

- (1) With the increase of CO₂ concentration, the flame combustion temperature and flame propagation speed gradually decrease, and the flame propagation speed decreases even more slowly. Compared with syngas without CO₂, when the CO₂ concentration in biogas is 41.6%, the flame temperature is 395 K lower and the flame propagation speed decreases by 64.2%. It can be seen that the existence of CO₂ in biogas not only reduces the combustion temperature of the flame, but also greatly reduces the propagation speed of the laminar flame.

- (2) After the combustion reaches the chemical equilibrium, the molar fraction of NO in the product decreases with the increase of CO₂, while the molar fraction of NO₂ does not show regularity with the change of CO₂ concentration. When the concentration of carbon dioxide is 33.6%, that is, when the research object is typical low calorific value biogas, the mole fraction of nitrogen dioxide in chemical equilibrium is the highest.

DATA AVAILABILITY STATEMENT

The original contributions presented in the study are included in the article/supplementary material, further inquiries can be directed to the corresponding author.

REFERENCES

- Asgari, N., Ahmed, S. F., Farouk, T. I., and Padak, B. (2017). NO_x Formation in post-flame Gases from Syngas/air Combustion at Atmospheric Pressure. *Int. J. Hydrogen Energ.* 42 (38), 24569–24579. doi:10.1016/j.ijhydene.2017.08.017
- Azimov, U., Tomita, E., Kawahara, N., and Harada, Y. (2011). Effect of Syngas Composition on Combustion and Exhaust Emission Characteristics in a Pilot-Ignited Dual-Fuel Engine Operated in PREMIER Combustion Mode. *Int. J. Hydrogen Energ.* 36 (18), 11985–11996. doi:10.1016/j.ijhydene.2011.04.192
- Cao, Y., Wang, Q., Du, J., and Chen, J. (2019). Oxygen-enriched Air Gasification of Biomass Materials for High-Quality Syngas Production. *Energ. Convers. Manage.* 199, 111628. doi:10.1016/j.enconman.2019.05.054
- Cao, Z., and Zhu, T. (2012). Effects of CO₂ Dilution on Methane Ignition in Moderate or Intense Low-Oxygen Dilution (MILD) Combustion: A Numerical Study. *Chin. J. Chem. Eng.* 20 (4), 701–709. doi:10.1016/S1004-9541(11)60238-3
- Chen, G.-B., Li, Y.-H., Cheng, T.-S., Hsu, H.-W., and Chao, Y.-C. (2011). Effects of Hydrogen Peroxide on Combustion Enhancement of Premixed Methane/air Flames. *Int. J. Hydrogen Energ.* 36 (23), 15414–15426. doi:10.1016/j.ijhydene.2011.07.074
- Chen, Z., and Jiang, Y. (2021). Numerical Investigation of the Effects of H₂/CO/ syngas Additions on Laminar Premixed Combustion Characteristics of NH₃/air Flame. *Int. J. Hydrogen Energ.* 46 (21), 12016–12030. doi:10.1016/j.ijhydene.2021.01.054
- Chu, H., Xiang, L., Meng, S., Dong, W., Gu, M., and Li, Z. (2021). Effects of N₂ Dilution on Laminar Burning Velocity, Combustion Characteristics and NO_x Emissions of Rich CH₄-Air Premixed Flames. *Fuel* 284, 119017. doi:10.1016/j.fuel.2020.119017
- Cohé, C., Chauveau, C., Gökalp, I., and Kurtuluş, D. F. (2009). CO₂ Addition and Pressure Effects on Laminar and Turbulent Lean Premixed CH₄ Air Flames. *Proc. Combustion Inst.* 32, 1803–1810. doi:10.1016/j.proci.2008.06.181
- Cui, G., Dong, Z., Wang, S., Xing, X., Shan, T., and Li, Z. (2020). Effect of the Water on the Flame Characteristics of Methane Hydrate Combustion. *Appl. Energ.* 259, 114205. doi:10.1016/j.apenergy.2019.114205
- De Goey, L. P. H., Van Oijen, J. A., Kornilov, V. N., and ten Thijs Boonkamp, J. H. M. (2011). Propagation, Dynamics and Control of Laminar Premixed Flames. *Proc. Combustion Inst.* 33 (1), 863–886. doi:10.1016/j.proci.2010.09.006
- Dong, H., Zhang, Y., and Gu, Z. (2014). Effects of Diluents on NO_x Formation in Coflow CH₄/air Diffusion Flames. *Korean J. Chem. Eng.* 31 (6), 1002–1007. doi:10.1007/s11814-014-0035-1
- Glarborg, P., and Bentzen, L. L. B. (2008). Chemical Effects of a High CO₂ Concentration in Oxy-Fuel Combustion of Methane. *Energ. Fuels* 22 (1), 291–296. doi:10.1021/ef7005854
- Gong, C., Li, Z., Li, D., Liu, J., Si, X., Yu, J., et al. (2018). Numerical Investigation of Hydrogen Addition Effects on Methanol-Air Mixtures Combustion in Premixed Laminar Flames under Lean Burn Conditions. *Renew. Energ.* 127, 56–63. doi:10.1016/j.renene.2018.04.047
- Hinton, N., and Stone, R. (2014). Laminar Burning Velocity Measurements of Methane and Carbon Dioxide Mixtures (Biogas) over Wide Ranging Temperatures and Pressures. *Fuel* 116, 743–750. doi:10.1016/j.fuel.2013.08.069
- Huang, M. (2011). *Research on Biomass Gasification and Co-combustion Processmaster's Thesis*. Zhengzhou, Henan: North China University of Water Resources and Electric Power.
- Kim, J.-W., Mun, T.-Y., Kim, J.-O., and Kim, J.-S. (2011). Air Gasification of Mixed Plastic Wastes Using a Two-Stage Gasifier for the Production of Producer Gas with Low Tar and a High Caloric Value. *Fuel* 90 (6), 2266–2272. doi:10.1016/j.fuel.2011.02.021
- Kuo, K. (2005). *Principles of Combustion*. New York: Wiley.
- Li, Y. (2019). "Study on Combustion Characteristics and Numerical Simulation of Biomass Gasification Gas," (Zhejiang: Zhejiang University). master's thesis.
- Liu, F., Guo, H., Smallwood, G. J., and Gülder, Ö. L. (2001). The Chemical Effects of Carbon Dioxide as an Additive in an Ethylene Diffusion Flame: Implications for Soot and NO_x Formation. *Combustion and Flame* 125 (1), 778–787. doi:10.1016/S0010-2180(00)00241-8
- Liu, S., Pei, H., Wang, Z., Li, Y., and Yao, H. X. (2020). Laminar Combustion Characteristics of Premixed Shale Gas and Air Flames. *J. Energ. Eng.* 146 (3), 04020014. doi:10.1061/(ASCE)EY.1943-7897.0000669
- Mansha, M., Saleemi, A. R., and Ghauri, B. M. (2010). Kinetic Models of Natural Gas Combustion in an Internal Combustion Engine. *J. Nat. Gas Chem.* 19 (1), 6–14. doi:10.1016/S1003-9953(09)60024-4
- Miao, Q., Zhu, J., Barghi, S., Wu, C., Yin, X., and Zhou, Z. (2013). Modeling Biomass Gasification in Circulating Fluidized Beds. *Renew. Energ.* 50, 655–661. doi:10.1016/j.renene.2012.08.020
- Mitu, M., Giurcan, V., Razus, D., and Oancea, D. (2017). Inert Gas Influence on the Laminar Burning Velocity of Methane-Air Mixtures. *J. Hazard. Mater.* 321, 440–448. doi:10.1016/j.jhazmat.2016.09.033
- Nozari, H., and Karabeyoğlu, A. (2015). Numerical Study of Combustion Characteristics of Ammonia as a Renewable Fuel and Establishment of Reduced Reaction Mechanisms. *Fuel* 159, 223–233. doi:10.1016/j.fuel.2015.06.075
- Park, J., Park, J. S., Kim, H. P., Kim, J. S., Kim, S. C., Choi, J. G., et al. (2007). NO Emission Behavior in Oxy-Fuel Combustion Recirculated with Carbon Dioxide. *Energ. Fuels* 21, 121–129. doi:10.1021/ef060309p
- Resende, P. R., Afonso, A., Pinho, C., and Ayoobi, M. (2019). Impacts of Dilution on Hydrogen Combustion Characteristics and NO_x Emissions. *J. Heat Transfer-Transactions Asme* 141 (1), 012003. doi:10.1115/1.4041623
- Sun, H., Li, R., Huang, M., Li, Z., and Xu, J. (2021). Numerical Simulations of the Influence of Inert Gases (N₂/CO₂) on Combustion Characteristics of Laminar-Premixed Biosyngas Flame. *ACS Omega* 6 (22), 14585–14597. doi:10.1021/acsomega.1c01729
- Tang, C., Huang, Z., Jin, C., He, J., Wang, J., Wang, X., et al. (2008). Laminar Burning Velocities and Combustion Characteristics of Propane-Hydrogen-Air Premixed Flames. *Int. J. Hydrogen Energ.* 33 (18), 4906–4914. doi:10.1016/j.ijhydene.2008.06.063
- Tang, G. T., Lv, J. F., Yue, G. X., and Zhang, H. (2009). Effects of CO₂ Dilution on NO_x Formation Characteristics in Syngas Diffusion Flames. *J. Combustion Sci. Tech.* 15 (03), 226–231. 1006-8740(2009)03-0226-06.

AUTHOR CONTRIBUTIONS

JM performed the data analysis and wrote the manuscript. CQ performed the simulations using software. SL provided ideas and directed the analysis of the data. ZZ provided constructive comments on revisions to the manuscript.

FUNDING

This work supported by the National Key Research and Development of China (2020YFD1100302), 2020 science and technology project of Qingdao West Coast New Area (Science and technology benefiting the people) (2020–99).

- Wang, X., Zhu, Y., Hu, Z., Zhang, L., Yang, S., Ruan, R., et al. (2020). Characteristics of Ash and Slag from Four Biomass-Fired Power Plants: Ash/slag Ratio, Unburned Carbon, Leaching of Major and Trace Elements. *Energy. Convers. Manage.* 214, 112897. doi:10.1016/j.enconman.2020.112897
- Wang, Y., Zhou, X., and Liu, L. (2021). Theoretical Investigation of the Combustion Performance of Ammonia/hydrogen Mixtures on a marine Diesel Engine. *Int. J. Hydrogen Energy*. 46 (28), 14805–14812. doi:10.1016/j.ijhydene.2021.01.233
- Wang, Z., He, T., Qin, J., Wu, J., Li, J., Zi, Z., et al. (2015). Gasification of Biomass with Oxygen-Enriched Air in a Pilot Scale Two-Stage Gasifier. *Fuel* 150, 386–393. doi:10.1016/j.fuel.2015.02.056
- Werle, S. (2015). Nitrogen Oxides Emission Reduction Using Sewage Sludge Gasification Gas Reburning Process/Obniżenie Emisji Tlenków Azotu Przy Użyciu Procesu Reburningu Gazem Ze Zgazowania Osadów Ściekowych. *Ecol. Chem. Eng. S-Chemia Inżynieria Ekologiczna S* 22 (1), 83–94. doi:10.1515/eces-2015-0005
- Wilk, M., Magdziarz, A., Gajek, M., Zajemska, M., Jayaraman, K., and Gokalp, I. (2017). Combustion and Kinetic Parameters Estimation of Torrefied pine, acacia and Miscanthus Giganteus Using Experimental and Modelling Techniques. *Bioresour. Tech.* 243, 304–314. doi:10.1016/j.biortech.2017.06.116
- Wu, C.-z., Yin, X.-l., Ma, L.-l., Zhou, Z.-q., and Chen, H.-p. (2009). Operational Characteristics of a 1.2-MW Biomass Gasification and Power Generation Plant. *Biotechnol. Adv.* 27 (5), 588–592. doi:10.1016/j.biotechadv.2009.04.020
- Yang, S., Wang, H. Y., Zhang, J., Song, C. D., Ding, K., and Ma, Y. H. (2020). General Situation and prospect of Biomass Energy Development and Utilization. *Technology Wind* (22), 193–194. doi:10.19392/j.cnki.1671-7341.202022158
- Zhang, C., Hu, G., Liao, S., Cheng, Q., Xiang, C., and Yuan, C. (2016). Comparative Study on the Effects of Nitrogen and Carbon Dioxide on Methane/air Flames. *Energy* 106 (Jul.1), 431–442. doi:10.1016/j.energy.2016.03.087
- Zhang, L. (2020). *Effect of CO₂ Addition on Natural Gas Combustion Process and NO Formation*. Heilongjiang: Harbin Institute of Technology. doctoral thesis.
- Zhang, M., Yuan, Y., and Liu, Y. (2005). Research on Biomass Waste Combustion Technologies. *Energy. Res. Inf.* 21, 15–20. doi:10.13259/j.cnki.eri.2005.01.003
- Zhang, X., Wen, M., Ding, Q., and Liu, Y. (2017). Numerical Simulation Study on the Boiler Combustion Performance for Biomass Gas Co-firing with Pulverized Coal. *J. Eng. Therm. Energy. Power* 32, 82–87. doi:10.16146/j.cnki.rndlgc.2017.03.013
- Zhao, B., and Su, Y. (2019). Emission and Conversion of NO from Algal Biomass Combustion in O₂/CO₂ Atmosphere. *J. Environ. Manage.* 250, 109419. doi:10.1016/j.jenvman.2019.109419

Conflict of Interest: The authors declare that the research was conducted in the absence of any commercial or financial relationships that could be construed as a potential conflict of interest.

Publisher's Note: All claims expressed in this article are solely those of the authors and do not necessarily represent those of their affiliated organizations, or those of the publisher, the editors and the reviewers. Any product that may be evaluated in this article, or claim that may be made by its manufacturer, is not guaranteed or endorsed by the publisher.

Copyright © 2022 Ma, Qi, Luo and Zuo. This is an open-access article distributed under the terms of the Creative Commons Attribution License (CC BY). The use, distribution or reproduction in other forums is permitted, provided the original author(s) and the copyright owner(s) are credited and that the original publication in this journal is cited, in accordance with accepted academic practice. No use, distribution or reproduction is permitted which does not comply with these terms.



A Semi-Analytical Mathematical Model for Off-Center Fractured Vertical Wells With Asymmetrical Fractures in Columnar Coalbed Methane

Anzhao Ji^{1*}, Zhanjun Chen¹, Yufeng Wang¹, Guangsheng Zhang¹, Zhenglin Mao² and Fenjun Chen³

¹School of Energy Engineering, Longdong University, Qingyang, China, ²Research Institute of Exploration Development, PetroChina Southwest Oil & Gasfield Company, Chengdu, China, ³Research Institute of Exploration Development, PetroChina Qinghai Oil Field Company, Dunhuang, China

OPEN ACCESS

Edited by:

Jiang Bian,
China University of Petroleum (East
China), China

Reviewed by:

Hu Guo,
China University of Petroleum, Beijing,
China

Yang Xiao,

Xi'an University of Science and
Technology, China

*Correspondence:

Anzhao Ji
jianzhao_831024@163.com

Specialty section:

This article was submitted to
Advanced Clean Fuel Technologies,
a section of the journal
Frontiers in Energy Research

Received: 06 December 2021

Accepted: 14 January 2022

Published: 25 February 2022

Citation:

Ji A, Chen Z, Wang Y, Zhang G, Mao Z
and Chen F (2022) A Semi-Analytical
Mathematical Model for Off-Center
Fractured Vertical Wells With
Asymmetrical Fractures in Columnar
Coalbed Methane.
Front. Energy Res. 10:829914.
doi: 10.3389/fenrg.2022.829914

Coalbed methane (CBM) is one of the important unconventional oil and gas resources. Since the permeability of the CBM reservoir is very low, CBM is usually developed by hydraulic fracturing technology to enhance gas productivity. In fact, most of the wells are not at the center of the columnar CBM reservoirs, which leads to different wellbore pressure responses. It is meaningful to analyze the wellbore pressure response of the off-center fractured vertical wells with asymmetrical fracture. The adsorption-desorption, fracture asymmetry are considered and a semi-analytical mathematical model is established. The pressure wellbore solution of the Laplace domain can be obtained by Laplace transformation, model coupling, and Gauss elimination. Then, the Stehfest numerical inversion is employed to obtain the pressure solution and rate distribution in the real-time domain. This semi-analytical solution is verified; the results show that the wellbore pressure includes six flow regimes, which include bilinear flow, linear flow, elliptic flow, radial flow, arc boundary reflection, and boundary dominated flow regime. The influence of fracture angle, dimensionless conductivity, and off-center distance on wellbore pressure and rate distribution are discussed in detail.

Keywords: hydraulically fractured well, coalbed methane, off-center well, asymmetrical fracture, pressure transient response

INTRODUCTION

Owing to the complicated seepage mechanism of CBM, CBM is classified as an unconventional natural gas resource. As one of the vital unconventional resources, development of CBM has been a global concern. The gas is stored in coal beds and there are many natural fractures in CBM reservoirs, which provide the seepage channels for gas flow (Zuber and Kuuskraa, 1990; Aminian and Ameri, 2009). Since the permeability of the CBM reservoir is very low, hydraulic fracturing measures are employed to enhance the production of coalbed methane. The complexity of formation conditions leads to the hydraulic fracture being asymmetric to the wellbore. Pressure transient analysis is an important approach for reservoir evaluation and production performance prediction. Therefore, we can diagnose whether the well is in the

center of the reservoir and calculate the distance from the well to the center of the reservoir by pressure transient analysis.

The main component of CBM is methane. CBM reservoirs consist of matrix and natural fractures systems, and there are many small-diameter pores in coal matrix particles. The transport of CBM includes the desorption and diffusion of CBM in small-diameter pores, and flow through a network of natural fractures (Liu et al., 2020; Nie et al., 2012; Pillalamarry et al., 2011; H.; Wang et al., 2021). However, the above-cited research mainly focuses on micro seepage. There is no research on the unsteady seepage of wellbore pressure in CBM, which cannot evaluate pressure wave propagation directly.

Hydraulic fracturing technology is often used to enhance the production of CBM. Many scholars have carried out research on the unsteady flow theory of vertically fractured wells (Cinco-Ley and Meng, 1988; Huang et al., 2015; Wang and Wang, 2014; L.; Wang et al., 2012). Cinco-Ley and Meng, (1988) presented the approach to couple the hydraulic fracture model and surface source solution firstly, then Huang et al. (2015) and presented an analytical model of a vertically fractured well to stimulate the relationship between wellbore pressure and production time. However, their works assumed that the fractures are symmetrical around the wellbore, which is not consistent with the reality.

In practice, the complexity of the conditions of the reservoir leads to hydraulic fracture being asymmetric around the wellbore. Some scholars simulated wellbore pressure transient response via numerical simulation (Bennett et al., 1983; Berumen et al., 2000; Crawford and Landrum, 1955; Narasimhan and Palen, 1979) and semi-analytical approach (Rodriguez et al., 1992; Tiab et al., 2010; Wang et al., 2019; Wang et al., 2013; Wang and Wang, 2014; Wang and Xue, 2018; Zhao et al., 2019). Crawford and Landrum (1955) firstly introduced a fracture asymmetry mathematical model but meaningful conclusions could not be drawn. Bennett et al. (1983) discussed the influence of the asymmetrical fracture on the rate decline curve by the numerical simulation methods. Wellbore pressure response curve under the condition of constant rate is analyzed by employing the numerical simulation methods (Berumen et al., 2000; Narasimhan and Palen, 1979). Their results showed that fracture asymmetry has an obvious influence on the wellbore pressure curve during the bilinear flow regime. Since the numerical solution is low efficiency and accuracy, some scholars introduced the analytical and semi-analytical approaches to obtain the wellbore pressure. Rodriguez et al. (1992) and Tiab et al. (2010) introduced the analytical method of vertical well with asymmetric hydraulic fracture firstly, but their model only gives the pressure solution of the hydraulic fracture. In order to couple the hydraulic fracture model and reservoirs model, (Wang et al., 2013, 2014, 2018, 2019) introduced the fracture Green's function and coupled the hydraulic fracture and reservoirs model. Finally, a wellbore pressure curve during the whole flow regime is obtained. Zhao et al. (2019) analyzed the wellbore pressure curve of fractured wells with asymmetric fractures by combining the boundary element method and source function. Although they had carried out a lot of research on the wellbore pressure response of fractured wells with asymmetric fractures, their models assumed that vertical well is the center of the CBM reservoirs.

Assuming the well is the center of the reservoir is an ideal model. Based on an "equivalent well block radius," Peaceman (1990) presented the simulation method of an off-center well by reservoir numerical simulation. Rosa et al. (1996) presented the off-center vertical well analytical model of radial composite reservoirs with an internal circular discontinuity. However, their research object is vertical wells. Deng et al. (2017) presented the semi-analytical model of the off-center vertical fractured well with a bi-wing symmetrical fracture in a multi-region heterogeneous reservoir to analyze the wellbore pressure behavior. Zhao et al. (2017) presented the semi-analytical solution of the off-center vertical fractured well with bi-wing symmetrical fracture by combining the boundary element method and source function. Although they were given the semi-analytical solution of hydraulic fractured well, their model assumed that the fracture is symmetrical about the wellbore.

Based on the above literature and research, there is no research about off-center fractured vertical wells with an asymmetrical fracture in columnar coalbed methane. In fact, for columnar gas reservoirs with circular closed boundaries, wellbore is not often the center of circle closed reservoirs and the bi-wing of hydraulic fracture is unequal length because of the influence of reservoir anisotropy. Therefore, the major work of this paper can be summarized as follows.

- An efficient semi-analytical mathematical model of off-center fractured well with an asymmetrical fracture is established and solved.
- Wellbore pressure characteristics curve is discussed and verified with numerical solution.
- The influence of key parameters on wellbore pressure and rate distribution curve is discussed.

Firstly, some assumptions are made and a physical model schematic diagram is shown. Secondly, the governing equations of the 2D CBM reservoirs model and 1D hydraulic fracture are established and solved. Thirdly, discretizing fracture as many small segments, and pressure drop superposition is used to obtain the relationship between wellbore pressure and time. Finally, the influence of some parameters on wellbore pressure and rate distribution curve is analyzed.

PHYSICS MODEL AND BASIC ASSUMPTION

The CBM reservoirs are composed of matrix and natural fracture systems and natural fracture is the main seepage channel to connect with hydraulic fracture. The wellbore is not the center of the CBM reservoir, and hydraulic fracture is asymmetric towards the wellbore (**Figure 1**). Desorption and diffusion in the matrix are considered. Some basic assumptions are given as follows:

- The gas well product by constant rate q_{sc} .
- The distance from the wellbore to the gas reservoir center is r_o .
- There is an angle, θ_F , between fracture and horizontal direction.

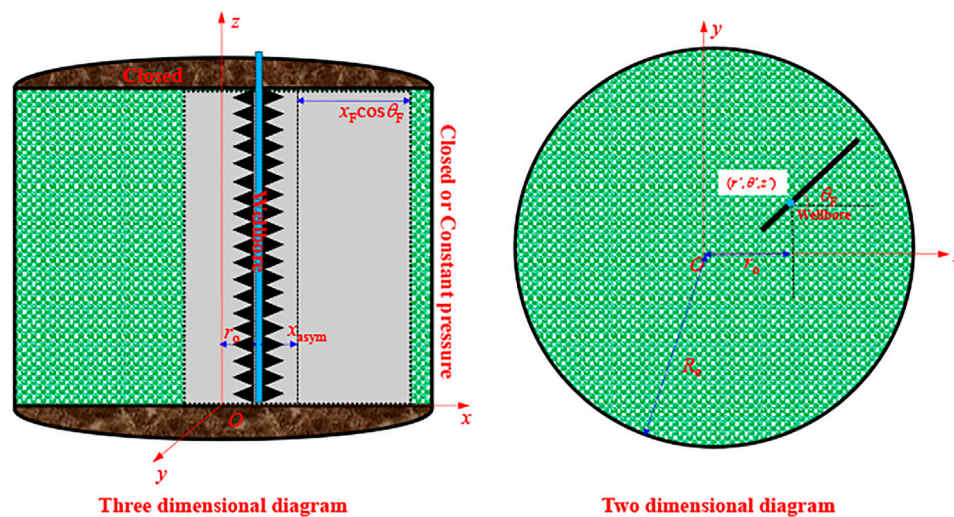


FIGURE 1 | Schematic diagram of off-centered fractured well with asymmetric fracture.

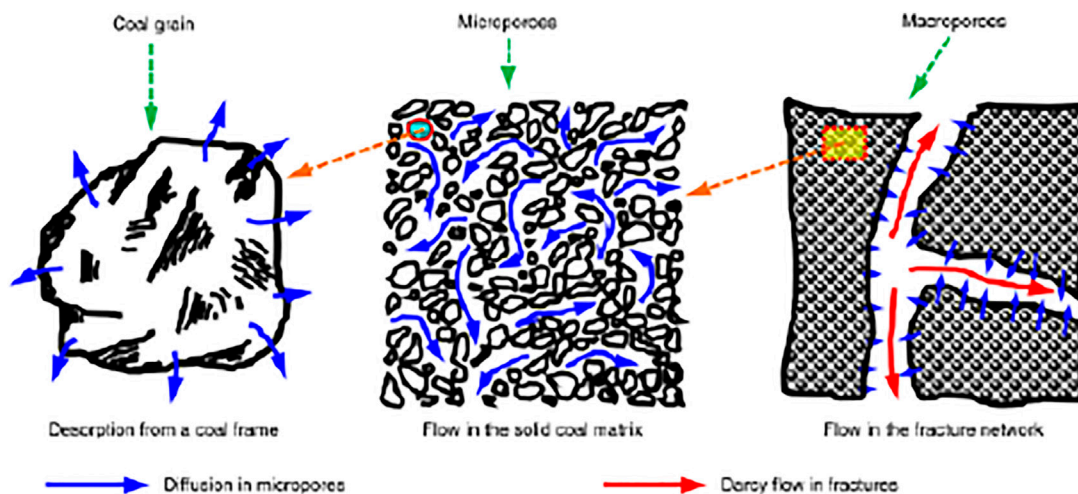


FIGURE 2 | Schematic diagram of microflow mechanism of coalbed methane (Zhao et al., 2016).

- The two wings of fracture are not equal and the distance from the wellbore to the hydraulic fracture center is x_{asym} .
- The gas flow obeys isothermal Darcy seepage in hydraulic fracture and reservoirs.
- The desorption of adsorbed gas in the coal matrix can be described by Langmuir's isothermal adsorption (Figure 2).
- The outer boundary of the reservoir is a circle closed.

$$V = V_L \frac{p}{p_L + p} \quad (1)$$

Where: V_L is Langmuir volume, sm^3/m^3 ; p_L is Langmuir pressure, Pa; p is Reservoirs pressure, Pa; V is Shale gas adsorption volume, sm^3/m^3 .

In order to find the linear governing equation, pseudo-pressure is defined as:

$$\psi = 2 \int_{p_0}^p \frac{p}{\mu Z} dp \quad (2)$$

Where: μ is CBM viscosity, cp.; Z is gas deviation factor, dimensionless; ψ is pseudo-pressure, Pa/s.

MATHEMATICAL MODEL AND SOLUTION

Off-Center Linear Source Function

Langmuir's isothermal adsorption equation is (Langmuir, 1917; Chen et al., 2016; Zhao et al., 2016; Xu et al., 2020).

TABLE 1 | dimensionless variable definition.

Dimensionless pseudo-pressure	$\psi_{FD} = \frac{\pi k h T_{sc}}{p_{sc} T_{sc}} (\psi_e - \psi_f)$	Dimensionless outboundary radius	$R_{eD} = \frac{R_e}{L_{ref}}$
Dimensionless radial distance	$r_D = \frac{r}{L_{ref}}$	Dimensionless asymmetry factor	$x_{asymD} = \frac{x_{asym}}{L_{ref}}$
Dimensionless time	$t_D = \frac{k_i}{(\phi_f C_{ft} + \phi_m C_{mt}) \mu L_{ref}^2} t$	Dimensionless off-left distance	$r_{oD} = \frac{r_o}{L_{ref}}$
Storativity ratio	$\omega = \frac{\phi_f C_{ft}}{\phi_f C_{ft} + \phi_m C_{mt}}$	Dimensionless fracture conductivity	$C_{FD} = \frac{k_F w_F}{k_i L_{ref}}$
Interporosity coefficient of transient state crossflow	$\lambda = \alpha_m \frac{k_m}{k_i} L_{ref}^2$	Dimensionless surface rate	$\bar{q}_D = \frac{\bar{q} L_{ref}}{Q_{sc}}$
Interporosity coefficient of pseudo-state state crossflow	$\lambda = \frac{15 k_m L_{ref}^2}{k_i r_{ms}^2}$	Dimensionless fracture length	$L_{FD} = \frac{L_F}{L_{ref}}$

For the convenience of mathematical model solving, the following dimensionless variable definition is given in **Table 1**.

Where: r is the radial distance in x-y plane, m; h is reservoirs thickness, m; T_{sc} is temperature under standard conditions, K; T is reservoirs temperature, K; p_{sc} is pressure under standard conditions, Pa; ϕ_m is matrix porosity, decimal; ϕ_f is natural fracture porosity, decimal; C_{mt} is matrix system compressibility coefficient, Pa^{-1} ; C_{ft} is natural fracture system compressibility coefficient, Pa^{-1} ; C_{FD} is Dimensionless fracture conductivity, dimensionless; μ is the CBM viscosity, cp; \bar{q} is the continuous unite length source strength, m^3/s ; k_f is the permeability of natural fracture system, m^2 ; k_m is the permeability of matrix system, m^2 ; k_F is the permeability of hydraulic fracture, m^2 ; θ is the angle from linear source to center of reservoirs, degree; L_{ref} is reference length, m; L_F is fracture length, m; α_m is matrix shape factor, dimensionless; R_e is closed boundary radius, m; r_o is off-center distance, m; x_{asym} is distance from the center of hydraulic fracture to wellbore, m; ω is the storativity-ratio, dimensionless; λ is interporosity coefficient, dimensionless; subscript D is the dimensionless.

In cylindrical coordinate system r - θ - z , the location of the line source is assumed to be (r', θ', z') . According to the work of Guo et al. (2016) and Xu et al. (2020), the two-dimension governing equation in the radial cylindrical system (Ozkan, 1994; Deng et al., 2017) is

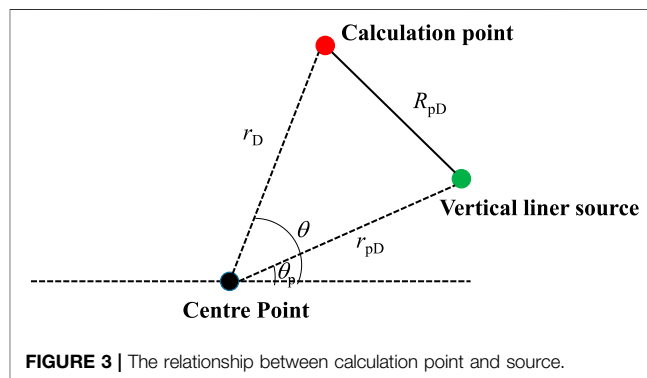
$$\begin{aligned} \frac{1}{r_D} \frac{\partial}{\partial r_D} \left(r_D \frac{\partial \Delta \bar{\psi}_f}{\partial r_D} \right) + \frac{1}{r_D^2} \frac{\partial}{\partial \theta} \left(\frac{\partial \Delta \bar{\psi}_f}{\partial \theta} \right) \\ + \frac{1}{r_D} \frac{\bar{q} L_{ref}}{\pi k_f h} \frac{T_{p_{sc}}}{T_{sc}} \delta(\theta - \theta') \delta(r_D - r'_D) \\ = f(s) \Delta \bar{\psi}_f \end{aligned} \quad (3)$$

Where:

$$f(s) = \begin{cases} \omega s + \frac{s \beta_m \lambda (1 + \sigma)(1 - \omega)}{\beta_m \lambda + s(1 + \sigma)(1 - \omega)}, & \text{Transient state} \\ \omega s + \frac{\beta_m \lambda}{5} \left[\sqrt{\frac{s(1 + \sigma)(1 - \omega)}{\beta_m \lambda}} \coth \left(\sqrt{\frac{s(1 + \sigma)(1 - \omega)}{\beta_m \lambda}} \right) - 1 \right], & \text{Pseudo-steady state} \end{cases}$$

Where: r' is the distance from linear source to the center of reservoir, m; θ' is the angle from linear source to the center of reservoir, degree; β_m is matrix apparent permeability coefficient, dimensionless; σ is adsorption gas desorption coefficient, dimensionless.

The general solution of **Eq. 3** is (Ozkan, 1994).

**FIGURE 3** | The relationship between calculation point and source.

$$\Delta \bar{\psi}_f = P + E \quad (4)$$

Where: P is a center linear source solution of coal gas reservoirs, this solution can be obtained easily. E is chosen such that $P + E$ satisfies the boundary condition at $r = R_e$ and the contribution of E to the flux vanishes as $\theta \rightarrow \theta'$ and $r \rightarrow r'$.

The position relationship between the calculation point and the vertical line source is shown in **Figure 3**.

According to the previous research work, the center linear source solution P is (Ozkan and Raghavan, 1991)

$$P = \frac{\mu \bar{q}}{2 \pi k h L_{ref}} \left[K_0 \left(R_{pD} \sqrt{f(s)} \right) + D_0 I_0 \left(R_{pD} \sqrt{f(s)} \right) \right] \quad (5)$$

Where: $R_{pD} = \sqrt{r_D^2 + r'^2_D - 2 r_D r'_D \cos(\theta - \theta')}$

According to the addition theorem of the Bessel function (Carslaw and Jaeger, 1959)

$$I_k(a R_{pD}) = \sum_{k=-\infty}^{+\infty} (-1)^k I_k(ar_D) I_k(ar'_D) \cos k(\theta - \theta') \quad r_D < R_{eD} \quad (6)$$

$$K_0(a R_{pD}) = \begin{cases} \sum_{k=-\infty}^{+\infty} I_k(ar_D) K_k(ar'_D) \cos k(\theta - \theta') & r_D < r'_D \\ \sum_{k=-\infty}^{+\infty} I_k(ar'_D) K_k(ar_D) \cos k(\theta - \theta') & r_D \geq r'_D \end{cases} \quad (7)$$

Where: $I_k(x)$ is the k order first type Bessel function; $K_k(x)$ is the k order second type Bessel function.

Therefore, E can be written as

$$E = \frac{\mu \bar{q}}{2\pi k_f h_D L_{ref}} 2 \sum_{k=1}^{\infty} D_k I_k(ar_D) I_k(ar'_D) \cos k(\theta - \theta') \quad (8)$$

Finally, when the vertical linear source is not the center of coal gas reservoirs, the general solution can be written as:

$$\Delta \bar{\psi}_f = \frac{\mu \bar{q}}{2\pi k_f h_D L_{ref}} \left[K_0 \left(R_{pD} \sqrt{f(s)} \right) + D_0 I_0 \left(R_{pD} \sqrt{f(s)} \right) + 2 \sum_{k=1}^{\infty} D_k I_k(ar_D) I_k(ar'_D) \cos k(\theta - \theta') \right] \quad (9)$$

For circle closed boundary.

$$\left. \frac{\partial \Delta \bar{\psi}_f}{\partial r_D} \right|_{r_D=R_{eD}} = 0 \quad (10)$$

For circle constant-pressure boundary.

$$\Delta \bar{\psi}_f|_{r_D=R_{eD}} = 0 \quad (11)$$

Substituting **Eq. 9** into **Eqs 10, 11**, coefficient D_k ($k = 0, 1, 2, \dots, \infty$) can be obtained for circle closed and constant-pressure boundary.

$$D_k = \begin{cases} -\frac{K'_k \left(\sqrt{f(s)} R_{eD} \right)}{I'_k \left(\sqrt{f(s)} R_{eD} \right)}, & \text{Closed} \\ -\frac{K_k \left(\sqrt{f(s)} R_{eD} \right)}{I_k \left(\sqrt{f(s)} R_{eD} \right)}, & \text{Constant pressure} \end{cases} \quad (k = 0, 1, 2, \dots, \infty) \quad (12)$$

Off-Center Surface Source Function

Substituting **Eq. 12** into **Eq. 9** and using with the dimensionless variable definition in **Table 1**. The linear source is integrated along the fracture direction and a uniform flux surface source solution can be obtained.

$$\bar{\psi}_{fD} = \frac{1}{2} \int_{L_D} \bar{q}_D \left[K_0 \left(R_{pD} \sqrt{f(s)} \right) + D_0 I_0 \left(R_{pD} \sqrt{f(s)} \right) + 2 \sum_{k=1}^{\infty} D_k I_k(ar_D) I_k(ar'_D) \cos k(\theta - \theta_p) \right] ds_D \quad (13)$$

However, integration of **Eq. 13** is very difficult directly. Therefore, according to the triangle similarity and Pythagorean law, there is the following mathematical relationship.

$$r'_D = r_{oD} \frac{\sin \theta_F}{\sin(\theta_F - \theta')}, \quad (\theta_F \neq 0, \pi) \quad (14)$$

Where: θ_F is the angle between hydraulic fracture and horizontal line, degree.

In order to improve the calculation speed and accuracy, the grid needs to be divided into unequal distances (**Figure 4**). Dividing the hydraulic fracture into $2N$ segments, and the segment numbers of wellbore left fracture and wellbore right fracture is set as N .

The grid end-point coordinates can be expressed as in local coordinate system (r_F - θ)

$$r_{FDi} = \begin{cases} L_{FRD} \frac{(N-i+1)}{N}, & (1 \leq i \leq N+1) \\ L_{FLD} \frac{(i-N-1)}{N}, & (N+2 \leq i \leq 2N+1) \end{cases} \quad (15)$$

Where: L_{FRD} is the dimensionless right fracture length; L_{FLD} is the dimensionless left fracture length; N is the fracture segments number. r_{FDi} is the i -th segment end-point in the local coordinate system.

The grid mid-point coordinates can be expressed as local coordinate system (r_F - θ)

$$r_{mFDi} = \frac{r_{FDi} + r_{FDi+1}}{2} \quad (1 \leq i \leq 2N) \quad (16)$$

Where: r_{mFDi} is the i -th segment mid-point in the local coordinate system.

The grid end-point coordinates can be expressed as in coordinate system (r - θ)

$$\begin{cases} r_{Di} = \sqrt{r_{oD}^2 + r_{FDi}^2 - 2r_{oD}r_{FDi} \cos(\pi - \theta_F)} \\ \theta_i = \tan^{-1} \frac{r_{FDi} \sin \theta_F}{r_{oD} + r_{FDiD} \cos \theta_F} \end{cases} \quad (17)$$

The grid mid-point coordinates can be expressed as in coordinate system (r - θ)

$$\begin{cases} r_{mDi} = \sqrt{r_{oD}^2 + r_{mFDi}^2 - 2r_{oD}r_{mFDi} \cos(\pi - \theta_F)} \\ \theta_{mj} = \tan^{-1} \frac{r_{mFDi} \sin \theta_F}{r_{oD} + r_{mFDiD} \cos \theta_F} \end{cases} \quad (18)$$

Where: r_{mDi} is the i -th segment mid-point in r - θ coordinate system; r_{Di} is the i -th segment end-point in r - θ coordinate system; θ_{mi} is the i -th segment mid-point degree in r - θ coordinate system; θ_i is the i -th segment end-point degree in r - θ coordinate system.

However, the pressure drop of the i -th segment is.

$$\bar{\psi}_{fD}(r_{mDi}, \theta_{mi}) = \sum_{j=1}^{2N} \bar{q}_{Dj} \int_{r_{Dj}}^{r_{Dj+1}} C_{\theta} \left(K_0 \left(\varepsilon_0 \sqrt{[r_{mDi} \cos(\theta_{mi} - \theta') - r'_{Di}]^2 + r_{pD}^2 \sin^2(\theta_{mi} - \theta')^2} \right) + D_0 I_0(\varepsilon_0 r_{mDi}) I_0(\varepsilon_0 r'_{Di}) + 2 \sum_{k=1}^{\infty} D_k I_k(\varepsilon_0 r_{mDi}) I_k(\varepsilon_0 r'_{Di}) \cos k(\theta_{mi} - \theta') \right) dr'_{Di} \quad (19)$$

Where: $C_{\theta} = \frac{r_{oD} \sin \theta_F}{\sin(\theta_F - \theta')^2}$; $\theta' = \theta_F - \sin^{-1} \frac{r_{oD} \sin \theta_F}{r'_{Di}}$

Wellbore pressure of the off-center vertical fractured well with asymmetric infinite conductivity fracture can be written as.

$$\bar{\psi}_{fD} = \sum_{i=1}^M \bar{\psi}_{fD}(r_{mDi}, \theta_{mi}) \quad (20)$$

Where: M is the fracture number.

Fracture Flow Model and Coupling

The fluid flow of fracture is only considered as linear flow. The two wing lengths of hydraulic fracture are unequal. Fracture tips

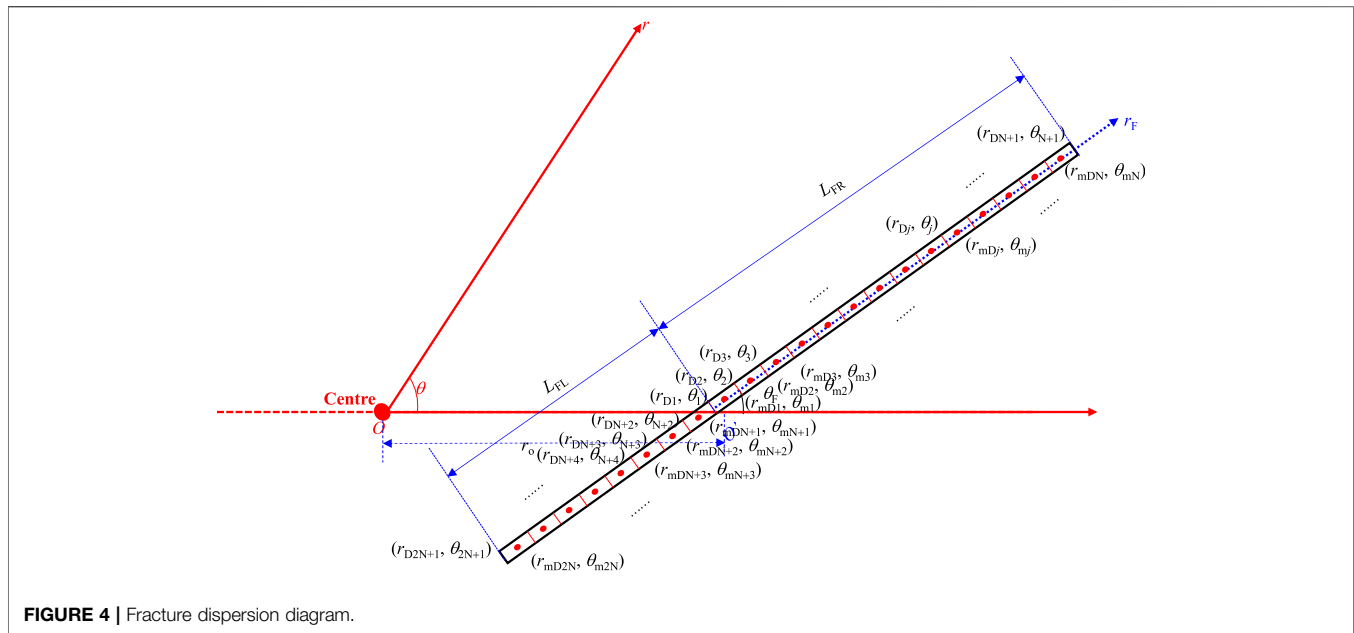


FIGURE 4 | Fracture dispersion diagram.

have no fluid supplement. According to the work of Wang (Wang and Wang, 2014), the solution of hydraulic fracture can be written as:

$$\bar{\psi}_{fD}(r_{FD}, s) = \bar{\psi}_{fD,avg} + \frac{\pi}{C_{FD}} \int_{-1}^1 G(r', r_{FD}) \bar{q}_D(r', s) dr' - \frac{2\pi}{C_{FD}} G(x_{asymD}, r_{FD}) \quad (21)$$

Where:

$$G(r', r_{FD}) = \begin{cases} -\frac{1}{4} \left[(r' + 1)^2 + (r_{FD} - 1)^2 - \frac{4}{3} \right] - 1 \leq r' \leq r_{FD} \\ -\frac{1}{4} \left[(r' - 1)^2 + (r_{FD} + 1)^2 - \frac{4}{3} \right] - 1 \leq r' \leq r_{FD} \end{cases};$$

$$\bar{\psi}_{fD,avg} = \frac{1}{2} \int_{-1}^1 \bar{\psi}_{fD}(r', s) dr'$$

Where: $\bar{\psi}_{fD,avg}$ is the dimensionless average reservoir pressure; C_{FD} is the dimensionless conductivity. $G(x)$ is the Green function.

The left term of Eq. 21 is the wellbore pressure of infinite conductivity fracture and it can be replaced by Eq. 20. Therefore, the discrete linear equations of Eq. 21 can be written as

$$\sum_{j=1}^{2N} \bar{q}_{Dj} \int_{r_{Dj}}^{r_{Dj+1}} C_{\theta} \left(K_0 \left(\varepsilon_0 \sqrt{[r_{mDi} \cos(\theta_{mi} - \theta_p) - r_{pD}]^2 + r_{pD}^2 \sin(\theta_{mi} - \theta_p)^2} \right) + D_0 I_0(\varepsilon_0 r_{mDi}) I_0(\varepsilon_0 r_{pD}) + 2 \sum_{k=1}^{+\infty} D_k I_k(\varepsilon_0 r_{mDi}) I_k(\varepsilon_0 r_{pD}) \cos k(\theta_{mi} - \theta_p) \right) dr_{pD} = \bar{\psi}_{fD,avg} + \frac{\pi}{C_{FD}} \sum_{j=1}^{2N} \int_{r_{FDj}}^{r_{FDj+1}} G(r', r_{mFDj}) \bar{q}_{Dj}(r', s) - \frac{2\pi}{C_{FD}} G(x_{asymD}, r_{mFDj}) \quad 1 \leq i \leq N \quad (22)$$

In addition, according to the mass conservation.

$$\frac{1}{2} \sum_{j=1}^{2N} \bar{q}_{Dj} = \frac{1}{s} \quad (23)$$

Where: s is the Laplace variable.

Combining with Eqs 22, 23, the $2N + 1$ linear equation can be obtained and solved by the Gauss elimination method. However, Wellbore pressure still cannot be obtained. Taking surface flux and average pressure into Eq. 21 and letting the $r_{FD} = x_{asymD}$, the wellbore pressure of off-center vertical well with asymmetric finite conductivity fracture can be obtained.

Wellbore pressure skin effect and wellbore storage are calculated by Eq. 24 (Van Everdingen and Hurst, 1949).

$$\bar{\psi}_{wD} = \frac{s \bar{\psi}_{fD} + S}{s + C_D s^2 (s \bar{\psi}_{fD} + S)} \quad (24)$$

Where: C_D is dimensionless well storage; S is the skin, $\bar{\psi}_{wD}$ is the dimensionless wellbore pressure.

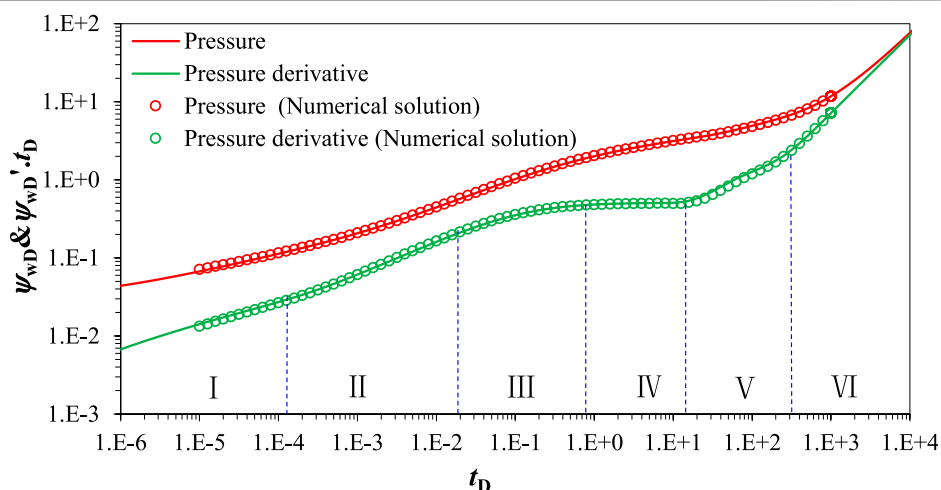
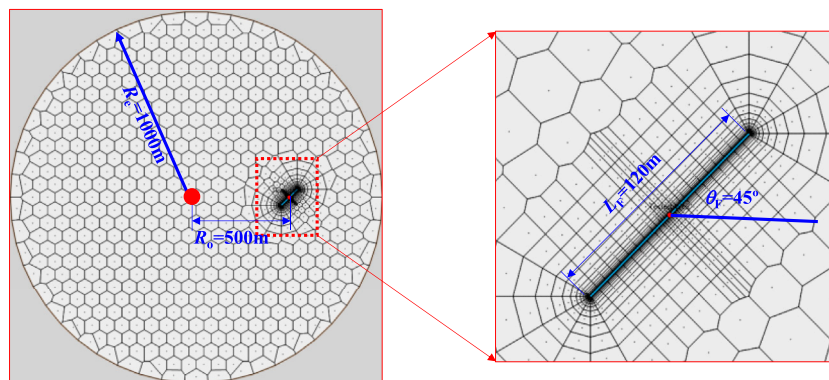
MODEL VERIFICATION

The model of this paper can be verified by comparing it with a numerical solution. If $x_{asymD} = 0$, $\sigma = 0$ and $\beta_m = 1$, our model can be simplified as an off-center fractured well with a finite symmetrical fracture in conventional reservoirs. The model verification basic parameter of this paper and numerical model is shown in Table 2. The Saphir numerical physical model is shown in Figure 5. Based on the same parameter, the wellbore can be obtained by this paper, and by Saphir, and the comparison figure is shown in Figure 6.

Points on Figure 6 represent the numerical results by the Saphir, the solid line represents the results of the semi-analytical solution of this paper. It can be seen from Figure 6 that the numerical solution and the semi-analytical solution are matched well. According to the pressure derivative curve, the six flow regimes are

TABLE 2 | Model verification basic parameter.

Parameter	Value	Parameter	Value
Storativity ratio	1	Formation volume factor	0.01
Reservoirs thickness	10 m	Formation permeability	0.1 mD
Initial reservoirs pressure	35 MPa	Gas reservoirs temperature	100°C
Total compressibility	0.001 MPa ⁻¹	Fracture half-length	60 m
Reservoirs porosity	0.05	Fracture conductivity	44208 mD-m
Hydraulic fracture angle	45°	Distance from wellbore to coal reservoir center	500 m
Circle closed boundary radius	1000 m		

**FIGURE 5** | Wellbore pressure comparison curves.**FIGURE 6** | Numerical physical model of the off-center fractured well.

distinguished. The pressure derivative curve characteristic of every flow regime is shown in Table 3.

PARAMETER SENSITIVITY ANALYSIS

According to the file data analysis result, the basic parameter is given under every figure. Based on these basic parameters, we can

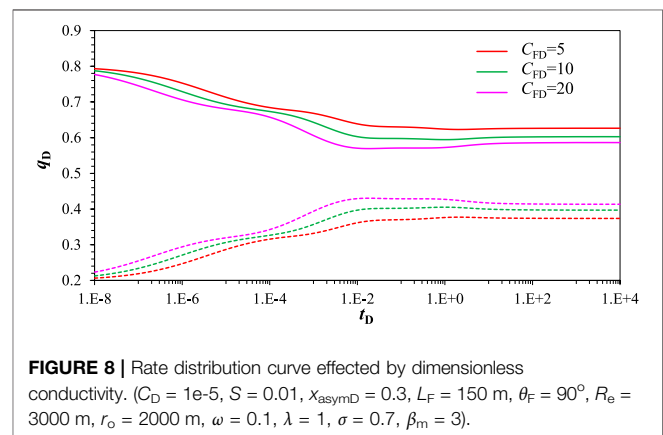
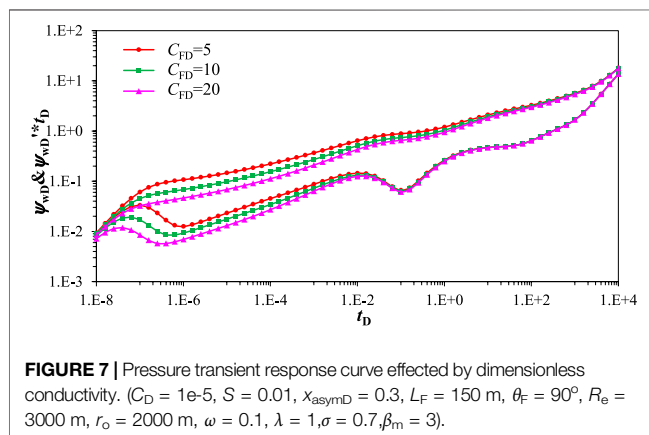
analyze the influence of every parameter on wellbore pressure and rate distribution.

Conductivity

Figure 7 displays the wellbore pressure curve is affected by dimensionless conductivity. The dimensionless conductivity has an obvious influence on wellbore pressure during the linear and bilinear regimes. Large dimensionless conductivity

TABLE 3 | Flowing regime and characteristic of derivative curve.

Flow regime	Physical process	Sketch map
Regime I	Bilinear flow regime: This flow regime mainly reflects the superposition of the linear flow from reservoirs to hydraulic and the linear flow in hydraulic fracture. The characteristic of the derivative curve is a 0.25-slope straight line Cinco-Ley et al. (1978)	
Regime II	Linear flow regime: This flow regime mainly reflects the superposition of the linear flow from reservoirs to hydraulic. The characteristic of the derivative curve is a 0.5-slope straight line Cinco-Ley et al. (1978)	
Regime III	Elliptical flow regime: Since the length of hydraulic fracture is longer than the width of hydraulic fracture, the CBM flow to fractured well by elliptical approach. The characteristic of the derivative curve is a 0.36-slope straight line. It is noted that the elliptical flow regime is not obvious for the actual situation	
Regime IV	Radial flow regime: As the pressure wave continues to spread, the CBM flow fractured well by radial approach. The characteristic of the derivative curve is a 0.5-horizontal line	
Regime V	Arc boundary reflection regime: When pressure wave spread to closed circle boundary, the arc boundary reflection regime appears and the characteristic of the derivative curve is an "up-warping" curve	
Regime VI	Boundary dominated flow regime: The characteristic of the derivative curve is a 1-slope straight line	—



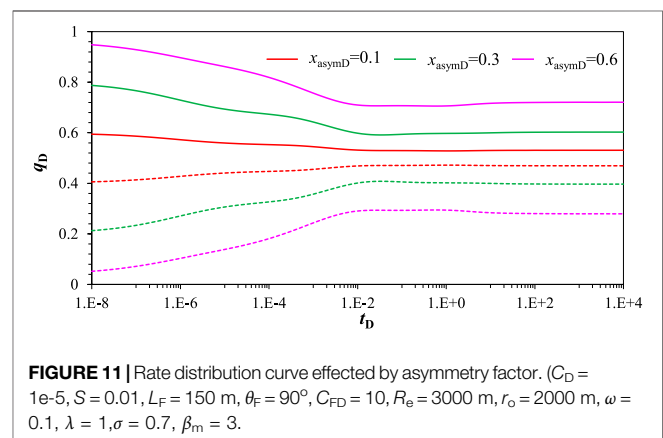
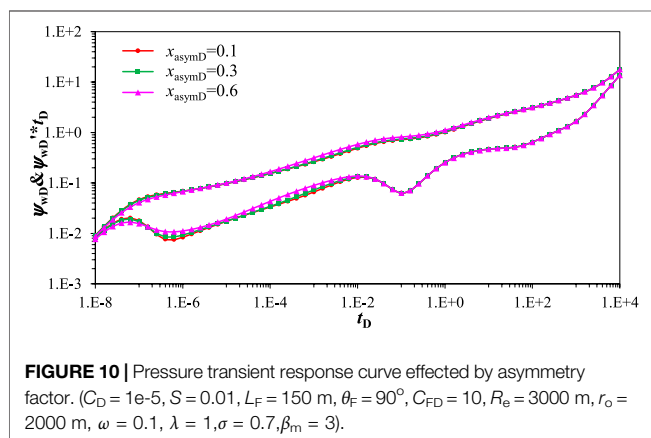
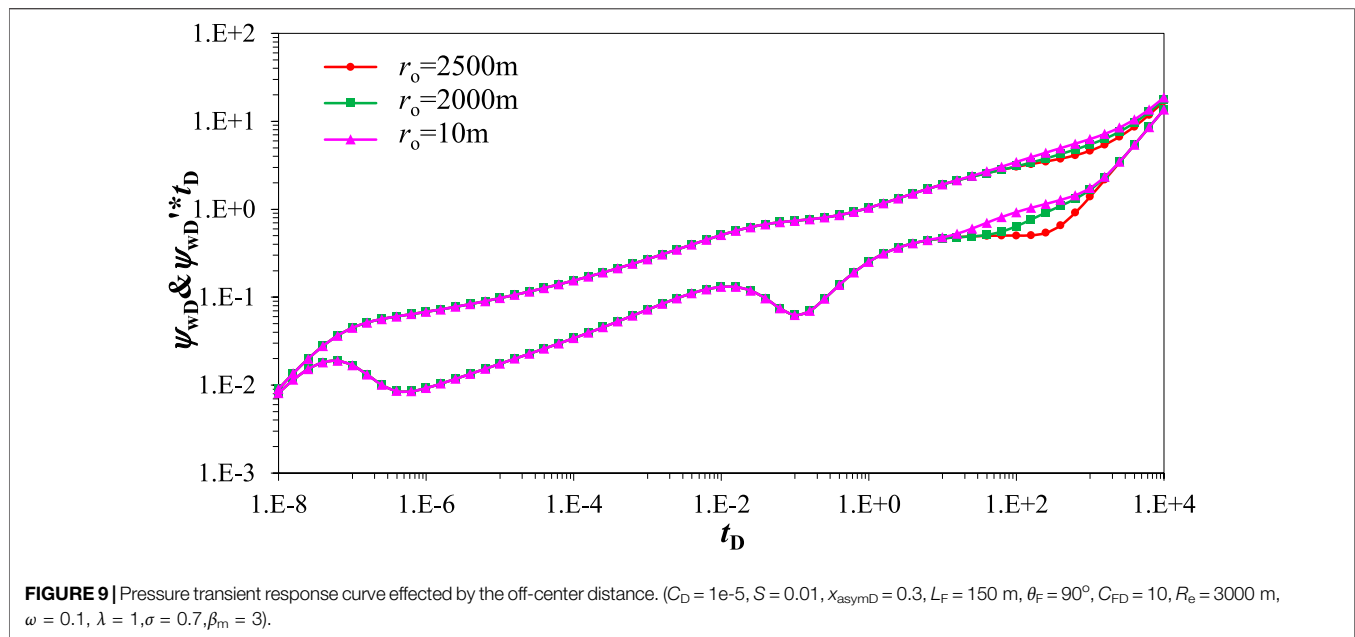
indicates small seepage resistance in hydraulic fracture. Therefore, the larger dimensionless conductivity is the smaller dimensionless wellbore pressure during bilinear and linear flow regime is. Therefore, in the actual fracturing process, it is helpful for improving the production of the CBM wells to increase the fracture conductivity.

Figure 8 displays the rate distribution curve is influenced by dimensionless conductivity. The solid line represents the rate distribution of short fracture and the dots lines represent the rate distribution of the long fracture. The dimensionless conductivity has an obvious influence on rate distribution. Since hydraulic fracture is asymmetric about wellbore, pressure wave around the short fracture wing spreads to reservoir quickly, so rate contribution of short fracture wing is higher than that of length fracture wing during while flow regime. However, as time progresses, since the control radius of short fracture wing is smaller than that of long fracture wing,

rate contribution of short fracture wing decreases and rate contribution of long fracture wing increases with time increasing before linear flow regime. Rate contribution of short and long fracture wing keep an approximate constant. Therefore, the large dimensionless conductivity leads to a small rate of short fracture wing and a large of long fracture wing in the whole flow regime.

Off-Center Distance

Figure 9 displays the wellbore pressure curve is affected by the off-center distance. As is shown in **Figure 9**, the off-center distance has an obvious effect on wellbore pressure during the arc boundary reflection regime. The larger off-center distance indicates that the well is closed to the circle closed boundary. Pressure waves propagate quickly to the boundary and boundary reaction characteristics appear in advance, which leads to the obvious "upwarping" characteristic of the derivative curve. Therefore, the larger the off-center distance is,



the earlier the time of the arc boundary reflection regime and derivative curve “upwarping” is.

Asymmetry Factor

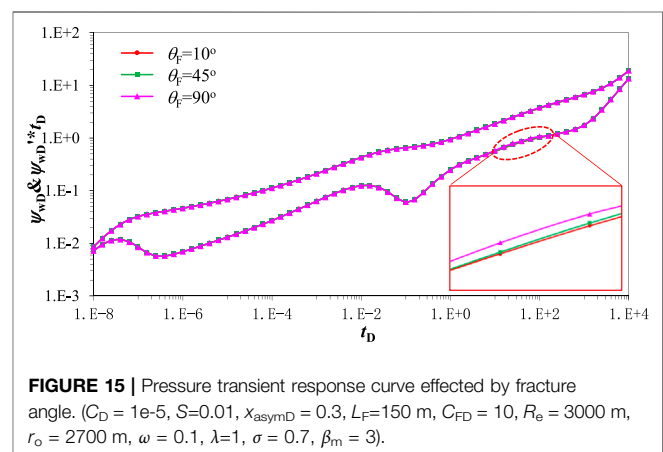
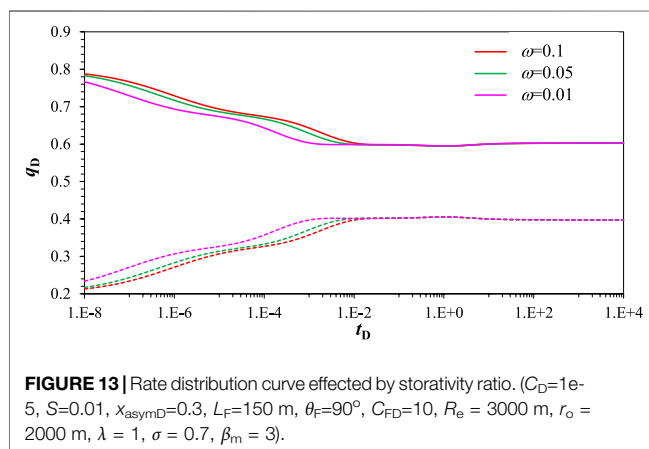
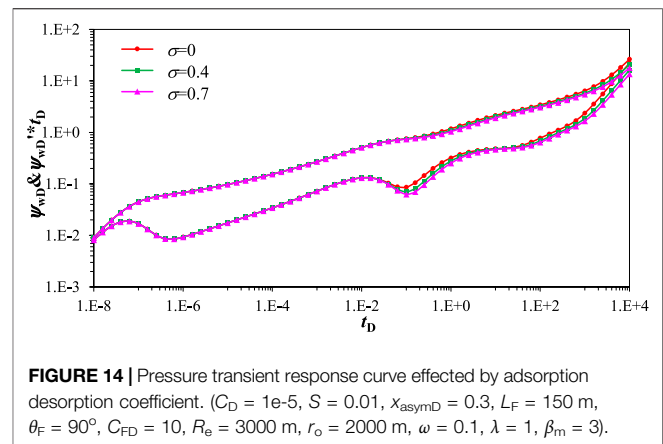
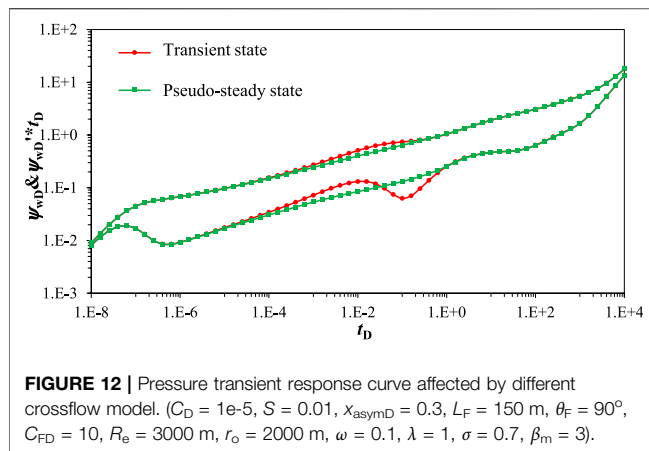
Figure 10 displays that the wellbore pressure curve is affected by the asymmetry factor. The asymmetry factor has an obvious effect on wellbore pressure during bilinear and linear flow regimes. It is assumed that the fracture length is equal for different asymmetry factors. The larger asymmetry factor indicates that the wellbore is closed to the fracture end-point, which leads that the fluid flows time longer in the long fracture. Therefore, the larger asymmetry factor leads to the larger seepage resistance. That is to say, the larger the asymmetry factor is, the higher of pressure and derivative curve before the radial flow regime is.

Figure 11 displays how the rate distribution curve is affected by the asymmetry factor. The solid line represents the rate distribution of the short fracture and the dots lines represent the rate distribution of the long fracture. The asymmetry factor has an obvious influence on

rate distribution. Since hydraulic fracture is asymmetric about wellbore, pressure wave around the short fracture wing spread to reservoir quickly, so rate contribution of short fracture wing is higher than that of length fracture wing during while flow regime. However, as time progresses, since the control radius of the short fracture wing is smaller than that of the long fracture wing, the rate contribution of the short fracture wing decreases and the rate contribution of the long fracture wing increase with time increasing before linear flow regime. For shorter fracture wing, the larger asymmetry factor leads to a larger pressure drop between the wellbore and hydraulic fracture surface. Therefore, the larger asymmetry factor indicates a larger rate contribution of the short wing. On the contrary, the larger asymmetry factor indicates a larger rate contribution of the short wing with consideration of rate conservation.

Crossflow Model and Storativity Ratio

Figure 12 displays that the wellbore pressure curve is influenced by different crossflow models. As is shown in **Figure 12**, a



different crossflow model has an obvious influence on wellbore pressure during the crossflow regime. Transient state crossflow shows that the CBM of matrix system can crossflow into naturally fracture system quickly when the pressure of the natural fracture system decreases. On the contrary, pseudo-steady state crossflow shows that the CBM of matrix system cannot crossflow into the natural fracture system quickly when the pressure of the natural fracture system decreases. The CBM of the matrix system can flow out the surface of matrix particles by the seepage type. Therefore, the “concavity” of pressure derivative of transient state crossflow is deeper than that of pseudo-steady state crossflow during crossflow regime.

Figure 13 is the rate distribution curve affected by the storativity ratio. The solid line represents the rate distribution of the short fracture and the dotted lines represent the rate distribution of the long fracture. It is assumed that the crossflow model is transient state crossflow. A large storativity ratio indicates larger storativity volume and a more natural fracture network, which indicates more natural fractures can connect with hydraulic fractures. In addition, since the short fracture wing is closer to the wellbore, the rate contribution of short fracture wing is higher than that of long fracture wing. Therefore, the larger storativity ratio leads to the higher rate contribution of

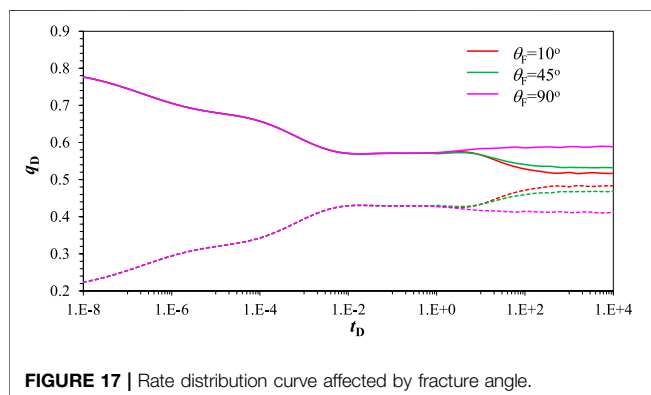
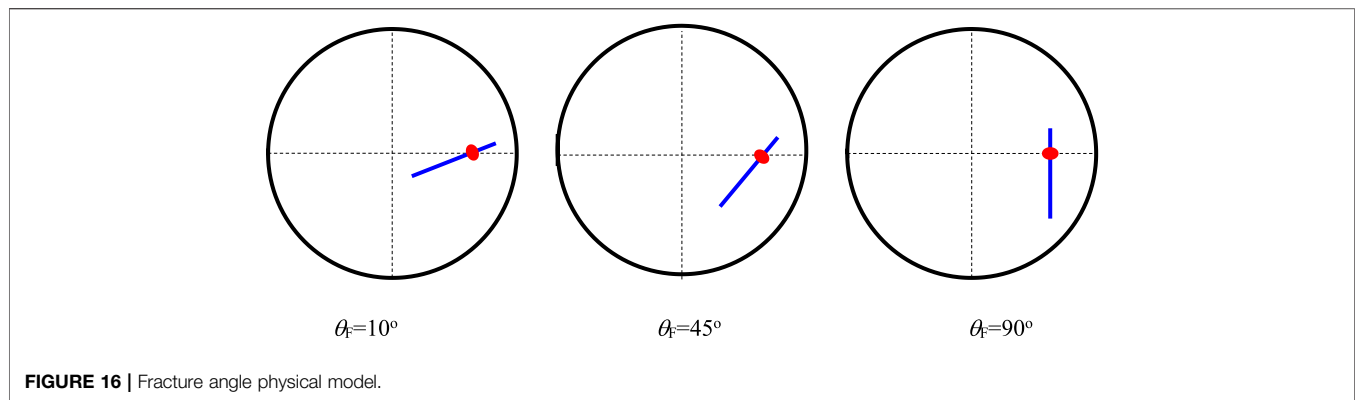
short fracture wing and small rate contribution of long fracture wing before crossflow regime.

Adsorption Desorption Coefficient

Figure 14 is the pressure transient response curve affected by adsorption-desorption coefficient. The adsorption-desorption coefficient mainly affects the typical curve shape after the crossflow regime. The smaller the value of adsorption-desorption coefficient is, the narrower and shallower the “concave” on the pressure derivative curve is. On the contrary, the larger the value of the adsorption-desorption coefficient is, the wider and deeper the “concave” on the pressure derivative curve is. The larger the amount of adsorbed gas in the coal matrix is, the more obvious the characteristics of crossflow after desorption are.

Fracture Angle

Figure 15 is a pressure transient response curve influenced by fracture angle. The influence of fracture angle on the pressure derivative curve is not very obvious. The fracture angle physical model is shown in **Figure 16**. The blue is the hydraulic and the red circle is the wellbore. Since fluid cannot flow into the hydraulic fracture and the largest rate supplement of the hydraulic fracture comes from fracture surface, the pressure

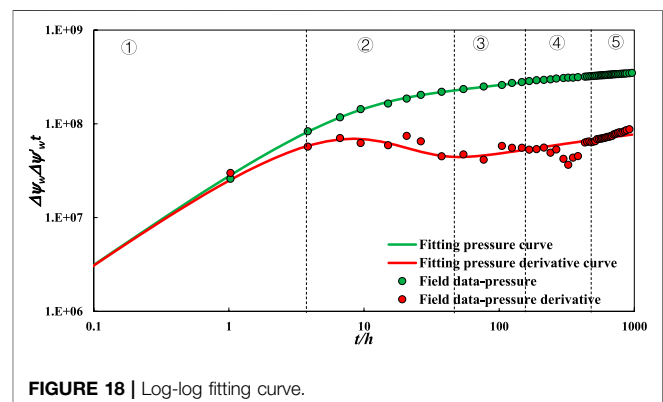


wave can spread to closed boundary quickly with the increasing of the hydraulic fracture angle. Therefore, a larger fracture angle leads to higher pressure derivative curve during the arc boundary reflection regime. However, since the off-center distance is very large, the influence of a larger fracture angle on the pressure derivative curve is not very obvious.

Figure 17 is the rate distribution curve affected by fracture angle. The solid line represents the rate distribution of the short fracture and the dotted lines represent the rate distribution of the long fracture. The fracture angle physical model is shown in **Figure 16**. The fracture angle has no influence on rate distribution curve before the arc boundary reflection regime. Rate supply around the boundary is finite, so short fracture wing rate contribution decrease with the decreasing of the fracture angle during the arc boundary reflection regime.

FIELD DATA ANALYSIS

The field data is used to verify and apply the research results of this paper. The basic parameters are as follows: the wellbore radius is 0.1397 m, the height of the reservoir is 5 m, reservoir porosity is 0.103, the average gas rate is 5500 m³/d, the CBM viscosity is 1.82×10^{-2} mPa s, relative density is 0.568, volume factor is 5.568×10^{-3} , compressibility coefficient is 4.138×10^{-2} MPa⁻¹, compressibility coefficient of rock is 4.138×10^{-4} MPa⁻¹, the total compressibility coefficient is 4.388×10^{-2} MPa⁻¹.



According to the pressure derivative curve, the five flow regimes can be diagnosed, which include well storage regime (①), skin reflection region (②), radial flow regime (③), crossflow regime (④), and arc boundary reflection regime (⑤). However, since well storage is very large, the bilinear and linear flow regimes are covered up. The fitting is shown in **Figure 18**. The fitting permeability is 25.3 mD, well storage is 0.08 m³/MPa, the storativity-ratio is 0.186, and the interporosity coefficient is 1.25×10^{-7} . Matrix apparent permeability coefficient is 1.2, dimensionless; adsorption gas desorption coefficient is 0.4. Off-center distance is 3610 m and the control radius of a single well is 3,726.4 m. Distance from the center of hydraulic fracture to the wellbore is 40m, and the half-length of hydraulic fracture is 78 m.

CONCLUSION

Based on the micro seepage mechanism of the CBM, the semi-analytical model of off-center fractured well with asymmetric finite conductivity fracture. According to the pressure derivative curve characteristic and parameter sensitivity analysis, the following main conclusion can be drawn in this paper.

- 1) This semi-analytical solution is verified with a numerical solution and the calculation speed of our semi-analytical model is greater than numerical simulation.

- 2) Compared to center fractured well, our semi-analytical model has the ability to identify six flow regimes, which include bilinear flow, linear flow, elliptic flow, radial flow, arc boundary reflection, and boundary dominated flow regimes.
- 3) Off-center distance and fracture angle have an influence on the starting-time of arc boundary reflection. Compared to fracture angle, off-center distance has a sensitive influence on the pressure derivative curve of the arc boundary reflection regime. The larger off-center distance and fracture angle lead to a larger pressure derivative curve during the arc boundary reflection regime.
- 4) Fracture conductivity, asymmetry factor has obvious influence on the early flow regime. As the fracture conductivity increases, the asymmetry factor decreases, pressure, and the derivative curve is smaller during bilinear flow and linear flow regime.
- 5) Our application also evaluates hydraulic fracturing result and provide guidance to diagnose well location to the closed boundary.

DATA AVAILABILITY STATEMENT

The original contributions presented in the study are included in the article/**Supplementary Material**, further inquiries can be directed to the corresponding author.

REFERENCES

- Aminian, K., and Ameri, S. (2009). Predicting Production Performance of Cbm Reservoirs. *J. Nat. Gas Sci. Eng.* 1 (1), 25–30. doi:10.1016/j.jngse.2009.03.003
- Bennett, C. O., Rosato, N. D., and Reynolds, A. C. (1983). Influence of Fracture Heterogeneity and wing Length on the Response of Vertically Fractured wells. *SPE-98-PAJ Soc. Pet. Eng. J.* 23 (02), 219–230. doi:10.2118/9886-PA
- Berumen, S., Tiab, D., and Rodriguez, F. (2000). Constant Rate Solutions for a Fractured Well with an Asymmetric Fracture. *J. Pet. Sci. Eng.* 25 (1), 49–58. doi:10.1016/S0920-4105(99)00053-4
- Carlslaw, H. S., and Jaeger, J. C. (1959). *Conduction of Heat in Solids*. second edition. London: Oxford University Press.
- Chen, Z., Liao, X., Zhao, X., Dou, X., and Zhu, L. (2016). A Semi-analytical Mathematical Model for Transient Pressure Behavior of Multiple Fractured Vertical Well in Coal Reservoirs Incorporating with Diffusion, Adsorption, and Stress-Sensitivity. *J. Nat. Gas Sci. Eng.* 29, 570–582. doi:10.1016/j.jngse.2015.08.043
- Cinco L., H. H., Samaniego V., F. F., and Dominguez A., N. (1978). Transient Pressure Behavior for a Well with a Finite-Conductivity Vertical Fracture. *SPE-98-PA* 18 (04), 253–264. doi:10.2118/6014-PA
- Cinco-Ley, H., and Meng, H.-Z. (1988). *Pressure Transient Analysis of wells with Finite Conductivity Vertical Fractures in Double Porosity Reservoirs*. Houston, Texas: Paper presented at the SPE Annual Technical Conference and Exhibition. doi:10.2118/18172-MSP
- Crawford, P. B., and Landrum, B. L. (1955). Effect of Unsymmetrical Vertical Fractures on Production Capacity. *Trans. AIME* 204 (01), 251–254. doi:10.2118/433-G
- Deng, Q., Nie, R.-S., Jia, Y.-L., Guo, Q., Jiang, K.-J., Chen, X., et al. (2017). Pressure Transient Behavior of a Fractured Well in Multi-Region Composite Reservoirs. *J. Pet. Sci. Eng.* 158, 535–553. doi:10.1016/j.petrol.2017.08.079
- Guo, J., Wang, H., and Zhang, L. 2016. Transient Pressure and Production Dynamics of Multi-Stage Fractured Horizontal wells in Shale Gas Reservoirs with Stimulated Reservoir Volume. *J. Nat. Gas Sci. Eng.*, 35: 425–443. doi:10.1016/j.jngse.2016.08.074

AUTHOR CONTRIBUTIONS

AJ: Writing-original draft, conceptualization, code, methodology, model validation. ZC: Writing- review and editing, participated the discussions YW: Participated the discussions GZ: Data curation, supervision, constructive discussions guidance ZM: Figure description, supervision, model validation FC: Field application.

FUNDING

This article was supported by the Natural Science Foundation of Gansu Province (21JR1RM327), Innovation Foundation of Colleges and Universities in Gansu Province (2021A-127), and National Natural Science Foundation of China Regional Science Foundation Project (42162015).

SUPPLEMENTARY MATERIAL

The Supplementary Material for this article can be found online at: <https://www.frontiersin.org/articles/10.3389/fenrg.2022.829914/full#supplementary-material>

- Huang, T., Guo, X., and Chen, F. (2015). Modeling Transient Pressure Behavior of a Fractured Well for Shale Gas Reservoirs Based on the Properties of Nanopores. *J. Nat. Gas Sci. Eng.* 23, 387–398. doi:10.1016/j.jngse.2015.02.020
- Langmuir, I. (1917). The Constitution and Fundamental Properties of Solids and Liquids. Part II-Liquids. *J. Franklin Inst.* 184 (5), 721. doi:10.1016/S0016-0032(17)90088-2
- Lei, W., Xiao-dong, W., Xu-min, D., Li, Z., and Chen, L. (2012). Rate Decline Curves Analysis of a Vertical Fractured Well with Fracture Face Damage. *J. Energ. Resour. Technology-Transactions Asme* 134 (3). doi:10.1115/1.4006865
- Liu, Y., Xu, H., Tang, D., Xu, F., Mathews, J. P., Hou, W., et al. (2020). Coalbed Methane Production of a Heterogeneous Reservoir in the Ordos basin, china. *J. Nat. Gas Sci. Eng.* 82, 103502. doi:10.1016/j.jngse.2020.103502
- Narasimhan, T. N., and Palen, W. A. (1979). *A Purely Numerical Approach for Analyzing Fluid Flow to a Well Intercepting a Vertical Fracture*. Paper presented at the. California: SPE California Regional Meeting.
- Nie, R.-S., Meng, Y.-F., Guo, J.-C., and Jia, Y.-L. (2012). Modeling Transient Flow Behavior of a Horizontal Well in a Coal Seam. *Int. J. Coal Geology.* 92, 54–68. doi:10.1016/j.coal.2011.12.005
- Ozkan, E. (1994). New Solutions for Well-Test-Analysis Problems: Part Iii-Additional Algorithms. *Paper presented SPE Annu. Tech. Conf. Exhibition.* doi:10.2118/28424-ms
- Ozkan, E., and Raghavan, R. 1991. New Solutions for Well-Test-Analysis Problems: Part 1-analytical Considerations(includes Associated Papers 28666 and 29213). *SPE Formation Eval.*, 6(3): 359–368. doi:10.2118/18615-PA
- Peaceman, D. W. (1990). Interpretation of Wellblock Pressures in Numerical Reservoir Simulation: Part 3 -- off-center and Multiple wells within a wellblockSPE Reservoir Engineering. *SPE Reservoir Eng.* 5 (02), 227–232. doi:10.2118/16976-PA
- Pillalamarry, M., Harpalani, S., and Liu, S. (2011). Gas Diffusion Behavior of Coal and its Impact on Production from Coalbed Methane Reservoirs. *Int. J. Coal Geology.* 86 (4), 342–348. doi:10.1016/j.coal.2011.03.007
- Rodriguez, F., Cinco-Ley, H., and Samaniego, -V., F. (1992). Evaluation of Fracture Asymmetry of Finite-Conductivity Fractured wellsSPE Production Engineering. *SPE Prod. Eng.* 7 (02), 233–239. doi:10.2118/20583-PA
- Rosa, A. J., Magalhaes, A. A. C., and Horne, R. N. (1996). Pressure Transient Behavior in Reservoirs with an Internal Circular Discontinuity. *SPE J.* 1 (01), 83–92. doi:10.2118/26455-PA

- Tiab, D., Lu, J., Nguyen, H., and Owayed, J. (2010). Evaluation of Fracture Asymmetry of Finite-Conductivity Fractured wells. *J. Energ. Resour. Tech.* 132 (1). doi:10.1115/1.4000700
- Van Everdingen, A. F., and Hurst, W. (1949). The Application of the Laplace Transformation to Flow Problems in Reservoirs. *J. Pet. Tech.* 1 (12), 305–324. doi:10.2118/949305-G
- Wang, H., Kou, Z., Guo, J., and Chen, Z. (2021). A Semi-analytical Model for the Transient Pressure Behaviors of a Multiple Fractured Well in a Coal Seam Gas Reservoir. *J. Pet. Sci. Eng.* 198, 108159. doi:10.1016/j.petrol.2020.108159
- Wang, L., Dai, C., Li, X., Chen, X., and Xia, Z. (2019). Pressure Transient Analysis for Asymmetrically Fractured wells in Dual-Permeability Organic Compound Reservoir of Hydrogen and Carbon. *Int. J. Hydrogen Energ.* 44 (11), 5254–5261. doi:10.1016/j.ijhydene.2018.08.082
- Wang, L., Wang, X., Li, J., and Wang, J. (2013). Simulation of Pressure Transient Behavior for Asymmetrically Finite-Conductivity Fractured wells in Coal Reservoirs. *Transp Porous Med.* 97 (3), 353–372. doi:10.1007/s11242-013-0128-z
- Wang, L., and Wang, X. (2014). Type Curves Analysis for Asymmetrically Fractured wells. *J. Energ. Resour. Technology-Transactions Asme* 136 (2). doi:10.1115/1.4025712
- Wang, L., and Xue, L. (2018). A Laplace-Transform Boundary Element Model for Pumping Tests in Irregularly Shaped Double-Porosity Aquifers. *J. Hydrol.* 567, 712–720. doi:10.1016/j.jhydrol.2018.06.027
- Warren, J. E., and Root, P. J. (1963). The Behavior of Naturally Fractured Reservoirs. *SPE-98-PA* 3 (03), 245–255. doi:10.2118/426-PA
- Xu, Y., Li, X., and Liu, Q. (2020). Pressure Performance of Multi-Stage Fractured Horizontal Well with Stimulated Reservoir Volume and Irregular Fractures Distribution in Shale Gas Reservoirs. *J. Nat. Gas Sci. Eng.* 77, 103209. doi:10.1016/j.jngse.2020.103209
- Zhao, Y.-l., Shan, B.-c., and Zhang, L.-h. (2019). Pressure Dynamics of Asymmetrically Fractured wells in an Arbitrarily Shaped Reservoir. *J. Hydrodyn* 31 (4), 767–777. doi:10.1007/s42241-018-0166-7
- Zhao, Y.-l., Zhang, L.-H., Feng, G.-Q., Zhang, B.-N., and Kang, B. (2016). Performance Analysis of Fractured wells with Stimulated Reservoir Volume in Coal Seam Reservoirs. *Oil Gas Sci. Technol. – Rev. IFP Energies Nouvelles* 71 (1), 8.
- Zhao, Y., Li, H., Zhang, L., and Kang, B. (2017). Pressure Transient Analysis for Off-Centered Fractured Vertical wells in Arbitrarily Shaped Gas Reservoirs with the Bem. *J. Pet. Sci. Eng.*, 156: 167–180. doi:10.1016/j.petrol.2017.05.015
- Zuber, M. D., and Kuuskraa, V. A. (1990). Optimizing Well Spacing and Hydraulic-Fracture Design for Economic Recovery of Coalbed methane Formation Evaluation. *SPE Formation Eval.* 5 (01), 98–102. doi:10.2118/17726-PA

Conflict of Interest: Author ZM was employed by the company PetroChina Southwest Oil & Gasfield Company. Author FC was employed by the company PetroChina Qinghai Oil Field Company.

The remaining authors declare that the research was conducted in the absence of any commercial or financial relationships that could be construed as a potential conflict of interest.

Publisher's Note: All claims expressed in this article are solely those of the authors and do not necessarily represent those of their affiliated organizations, or those of the publisher, the editors, and the reviewers. Any product that may be evaluated in this article, or claim that may be made by its manufacturer, is not guaranteed or endorsed by the publisher.

Copyright © 2022 Ji, Chen, Wang, Zhang, Mao and Chen. This is an open-access article distributed under the terms of the Creative Commons Attribution License (CC BY). The use, distribution or reproduction in other forums is permitted, provided the original author(s) and the copyright owner(s) are credited and that the original publication in this journal is cited, in accordance with accepted academic practice. No use, distribution or reproduction is permitted which does not comply with these terms.



Stress Analysis of the Effect of Additional Load on the Butt Weld of Suspended Pipeline With Variable Wall Thickness

Fang Yingchao¹, Yu Dongliang¹, Wang Binbin^{1*}, Xu Jian², Xuan Heng¹, Hou Hao¹ and Wang lin²

¹Southwest Pipe Company of Pipe China, Chengdu, China, ²School of Mechatronic Engineering, Southwest Petroleum University, Chengdu, China

OPEN ACCESS

Edited by:

Jiang Bian,
China University of Petroleum (East
China), China

Reviewed by:

Xiaoben Liu,
China University of Petroleum, Beijing,
China

Ying Zeng,

National University of Singapore,
Singapore

*Correspondence:

Wang Binbin
wangbb@pipechina.com.cn

Specialty section:

This article was submitted to
Advanced Clean Fuel Technologies,
a section of the journal
Frontiers in Energy Research

Received: 10 October 2021

Accepted: 03 December 2021

Published: 24 March 2022

Citation:

Yingchao F, Dongliang Y, Binbin W,
Jian X, Heng X, Hao H and lin W (2022)
Stress Analysis of the Effect of
Additional Load on the Butt Weld of
Suspended Pipeline With Variable
Wall Thickness.
Front. Energy Res. 9:792508.
doi: 10.3389/fenrg.2021.792508

Under the special geological environment of the buried pipe, the ground is lost at the bottom of the pipe, which is created by various kinds of external factors. The pipe in the suspended state would be greatly deformed due to its own weight, internal pressure, and other factors, resulting in the failure of the pipeline. When a variable wall thickness weld occurs in the suspended section of the pipeline, the change of the pipeline stress will be more complicated and changeable. In this study, ABAQUS software is used to establish a pipe-soil model of variable wall thickness butt welds of suspended pipelines. The axial stress distribution with different affected factors in the pipe, the change of curvature, and Mises stress change of the entire pipe along the axial direction are obtained by analyzing the internal pressure, wall thickness ratio, suspended length, weld position, and cone length. The results show that the stress at the root of the weld changes significantly; therefore, the weld has a greater impact on the stress of the entire pipeline. The change of internal pressure has little effect on the stress at the pipe weld. As the suspended length increases, the change in stress at the weld is more obvious. When the weld seam is close to the soil, the support of the soil will gradually shift the maximum stress position of the pipe from the top of the pipe to the bottom of the pipe. With the increase in cone length, it will reduce the sudden change of pipe section and the change in stress effectively. The places where the curvature greatly changes along the axial direction are at the pipe-soil separation and the middle of the pipeline, while the stress reaches the maximum at the pipe-soil separation, and the place with the largest stress change is the weld in the middle of the pipeline.

Keywords: variable wall thickness weld, suspended pipeline, finite element analysis, axial stress, curvature

Abbreviations: A, cross-sectional area of the pipe; D, pipe diameter; F, axial force on the pipe; K, curvature; K₀, stress concentration factor; M, bending moment of the pipe; P, internal pressure; U, vertical displacement of the pipeline; W, bending section coefficient; e, cone length of weld seam; t, wall thickness; t₁, thickness of small diameter pipe; t₂, thickness of large diameter pipe; ν, Poisson ratio; σ_t, axial stress of the pipe; σ_{hot}, hot spot stress; σ_{nom}, nominal stress; δ_t, axis deviation value caused by the wall thickness transition; δ_m, pipe offset value.

INTRODUCTION

As the main transportation method of oil and natural gas, pipelines play an indispensable role in the petroleum industry. Mountains and hills occupy 1/3 of the total land area in China. The completed pipeline inevitably crosses various complex terrain conditions. Many pipelines are laid in areas with special geology or frequently washed by rain, so the pipelines are very sensitive to ground deformation. The soil loss will make buried pipelines suspended. Under the influence of external loads such as gravity and pipe-soil interaction, the pipeline will produce large deformation and stress concentration because of the large span of suspension (Nishida, 1967; Li et al., 2011; Ma et al., 2012; Terán et al., 2013; Dabiri et al., 2017; Zhu et al., 2017; Wang et al., 2018). The geological loads will cause large displacement, creep, and buckling and even cause the pipeline to rupture due to large deformation and cause pipeline leakage. In some special geological environments, the variable wall thickness often generates due to actual needs and economic aspects, and different wall thicknesses inevitably involve welding between pipelines. In the process of pipe production, pipe butt welds are usually made outside, although after welding, grinding and other operations are carried out to reduce stress concentration. However, due to the existence of variable wall thickness and sudden changes in the cross section, there will still be stress concentration and stress increase at the joints. The butt weld is the key part of fatigue. Fatigue cracking may occur at the root or toe of the weld (Lotsberg, 2009), thereby shortening the service life of the pipeline (Guo et al., 2019a; Guo et al., 2019b; Li et al., 2021) and affecting the reliability of the pipeline (Yuan et al., 2016; Yuan and Li, 2016; Yuan et al., 2018; Yuan et al., 2019).

Zhu et al. (2021) studied the response characteristics and mechanism of weld during deformation. Lotsberg (2009) proposed a more detailed formula for evaluating the stress concentration factor in the tube-packed structural parts based on the classical shell theory. Midawi et al. (2020) used indentation technology and DIC technology to measure the anisotropic behavior of weld metal yield strength, highlighting the importance of developing new technologies to characterize the local characteristics of welded structures. Liu et al. (2021) used Marc finite element software for numerical simulation, used the magnetic method for stress test, and obtained the stress distribution law of pipeline welding parts. There was large tensile stress near the welding area, which was easy to fracture and led to structural damage.

In practical engineering applications, it is difficult to measure stress at the weld due to the complex changes in stress (Dabiri et al., 2017). In this study, the finite element analysis method is used to analyze the axial stress of the variable wall thickness butt weld of the suspended pipeline. The axial stress of the pipeline is mainly generated by the internal pressure of the pipeline, followed by the force and moment generated by the dead weight and thermal expansion of the pipeline, or the force or moment generated by other forms of load (Z, 2009).

$$\sigma_t = \frac{P(D-t)}{2t} + \frac{M}{W} + \frac{F}{A} \quad (1)$$

Among them, σ_t is the axial stress of the pipe, MPa; M is the bending moment of the pipe, Nm; W is the bending section coefficient, mm^3 ; F is the axial force on the pipe, N; and A is the cross-sectional area of the pipe, mm^2 .

When the pipeline is suspended, the pipeline always has certain bending due to the influence of external loads. The bending degree of the pipeline can be described by the curvature of the pipeline in the suspended state. The relationship between the curvature and the bending degree is described (Jian, 2015) as follows:

$$K = \frac{U''}{(1+U'^2)^{\frac{3}{2}}}, \quad (2)$$

where K is the curvature (the positive and negative values of K represent the bending direction of the pipeline. The upward bending is positive, and the downward bending is negative) and U is the vertical displacement of the pipeline.

For the stress concentration factor, the ratio of the hot spot stress to the nominal stress is defined as the stress concentration factor, which can generally reflect the local stress status of the pipeline with the same stress. According to a large number of pipeline failure accidents, it indicates that the possibility of cracks increases greatly in areas with large stress or stress concentration factors. From the point of mechanics, the greater the stress, the higher will be the degree of stress concentration, and the probability of pipeline failure will increase. For the suspended pipeline with a variable wall thickness butt weld, the weld is the weakest part of the pipeline, so it is necessary to analyze the local position of the weld. On the basis of the classical shell theory, Lotsberg proposed a more detailed evaluation formula for the stress corrosion of tubular structures. The influence of manufacturing tolerance, thickness transition, and annular parts on the stress corrosion was verified by comparing with the finite element analysis results (Jian, 2015).

The suspended pipe with weld is studied in this work, which is a lack of research on suspended pipeline. The stress state of the variable wall thickness butt weld is studied by establishing the model of the variable wall thickness butt weld of suspended pipeline under self-weight and internal pressure load. The stress values are acquired by analyzing the internal pressure, wall thickness ratio, suspension length, weld position, weld cone length, and different curvatures, which are used to reflect the reliability of the variable wall thickness butt weld of suspended pipeline during operation. According to the change of stress, relevantly constructive suggestions are put forward for pipeline operation, which is of certain value for the safety evaluation of oil and gas pipelines.

NUMERICAL MODEL

Model Assumption

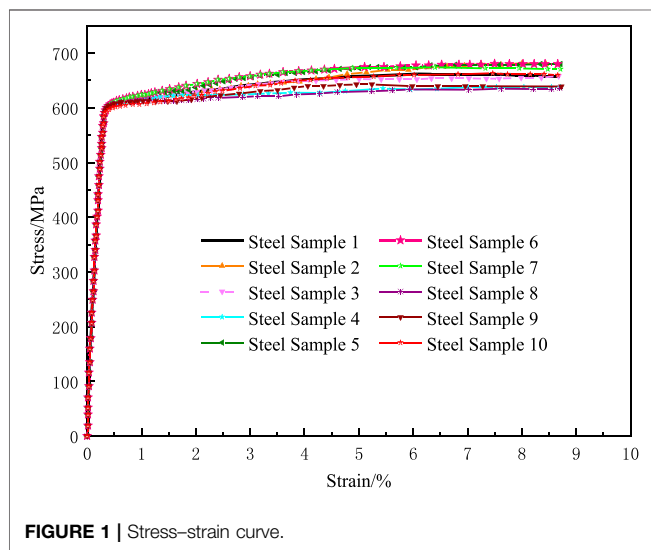
The suspended pipelines are located in a complicate and changing external environment, in order to ensure the pertinence of the simulation model, and the single-factor analysis is adopted. At the same time, in order to ensure the accuracy of the results and the

TABLE 1 | Pipe parameters.

Piping classification	X80	Diameter D/mm	1016
Density ρ /(kg/m ³)	7800	Elasticity modulus E/MPa	2.1×10^5
Poisson's ration ν	0.3	Operating pressure P/MPa	7.2
Yield strength σ_y /MPa	570	Tensile strength σ_b /MPa	645

TABLE 2 | Plastic stress and strain.

Stress MPa	570	595.494	601.311	607.14	613.013
Plastic strain %	0	0.06333	0.11053	0.23641	0.62976
Stress MPa	617.426	621.848	629.173	636.513	645
Plastic strain %	0.97592	1.38501	1.77836	2.26613	2.90992

**FIGURE 1** | Stress-strain curve.

speed of calculation, the simplified assumptions are made in the model as follows:

- (1) The base metal and welding material are ideally elastic-plastic materials, with equal intensity matching and no weld defects.
- (2) Considering only internal pressure and self-weight load, the factors such as temperature, covering soil, fluid, and their influence with load are ignored.
- (3) The pipeline is a straight pipe section and laid horizontally without difference of elevation in the vertical. The surrounding soil is isotropic and saturated.
- (4) An ideal weld has variable wall thickness with a regular and uniform butt weld.

The finite element method is carried out by ABAQUS software, which has good ability to analyze non-linear problem. The butt weld model of the suspended pipeline with variable wall thickness is established by considering the non-

TABLE 3 | Soil parameters.

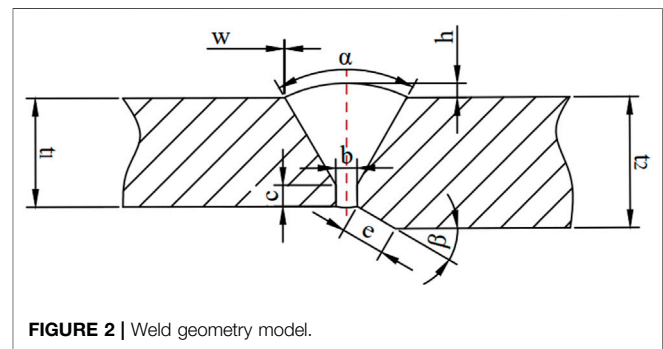
Model type	Mohr-coulomb	Density ρ /(kg/m ³)	1400
Poisson's ration ν	0.44	Elasticity modulus E/MPa	33
Cohesive force c/KPa	24.6	Internal friction angle φ °	11.7

TABLE 4 | Model verification.

Wall ratio	1.1	1.2	1.3	1.4
K_t -Lotsberg	1.21	1.30	1.38	1.45
K_t -Finite element	1.13	1.23	1.32	1.41
Error/%	5.8	5.4	4.3	2.8

TABLE 5 | Grid independence verification.

Type	Grid quantity	Mises stress/MPa	Error/%
Mesh 1	93304	203.123	1.88
Mesh 2	160934	207.019	0
Mesh 3	194204	207.201	0.088

**FIGURE 2** | Weld geometry model.

linear coupling between the pipe and soil, and the large deformation of the pipe and soil.

Parameter Settings

Taking X80 pipeline steel, which is most commonly used in oil and gas pipelines as the research object, the relevant parameters are listed in **Table 1**:

Mechanical properties of X80 pipeline steel were tested by using a universal testing machine, and the test was carried out according to Gao and Liang (2012). Tensile tests were carried out by a microcomputer-controlled universal testing machine to obtain stress-strain curves, as shown in **Figure 1**. One of the typical stress-strain data is selected as the constitutive relation of X80 pipeline steel, and the data are extracted. The Mohr-Coulomb model is adopted in the soil model, and the relevant parameters are listed in **Table 3** (Jian, 2015).

Finite Element Model

In this study, the welding seam of the China-Myanmar natural gas pipeline is mainly V-type, double-sided, and butted groove,

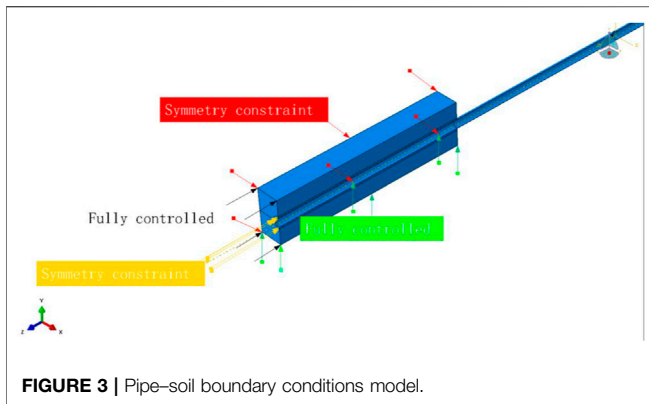


FIGURE 3 | Pipe-soil boundary conditions model.

and the weld cross section is shown in **Figure 2**. The groove size can be found in Reference GB/T 985.2-2008, GB 50236-2011, GB 50251-2015, and other relevant standards.

Among them, t_1 and t_2 are the thickness of the thin wall and thick wall, mm; α is the slope angle, 60° ; b is the root gap, 3 mm; c is the thickness of the blunt edge, 3 mm; h is the weld residual height, 2 mm; β is the cutting angle (wall thickness transition angle), 60° ; and w is the weld width of cover.

Considering the complexity of the weld grid, the field welding process, and other factors, the geometric model of the weld is appropriately simplified, at the same time, not considering the weld width of cover and residual height of weld root (It is supposed a linear transition).

The model of the suspended pipeline with a variable wall thickness butt weld is established on the basis of the aforementioned material parameters. The buried depth of the pipeline is 2.5 m. The initial weld is set in the middle of the suspended pipeline, and the soil length is 1/2 of the suspended length of the pipeline. The contact friction between the soil and pipe is penalty function, the normal friction coefficient is 0.5, and the tangential property is hard contact. The cross sections of both ends of the pipeline are symmetrical constraint along the normal direction. Symmetrical constraint along the normal direction is adopted for the side of the soil. The end face and undersurface of the soil are completely constrained, and the upper surface of the soil is completely free. Gravity load is applied to the whole pipe-soil model, and internal pressure load is applied to the pipe. The whole model is meshed by a hexahedral structure. Because the stress changes greatly at the weld of the pipeline, the mesh is encrypted by using the distributional method of single precision at the weld; besides, the part of soil close to the pipe-soil coupling is also encrypted. In order to improve the calculative efficiency, a 1/2 symmetric pipe-soil model is established for calculation. **Figure 3** shows the boundary conditions of the pipe-soil model. **Figure 4** shows the overall pipe-soil model.

Model Verification

The feasibility verification of the model is usually carried out by comparing the experimental analysis with the theoretical results. For the model of the suspended pipeline with weld, due to the difficulty and cost of the experiment, the experimental data are

scarce. Therefore, the feasibility of the model will be verified by comparing the theory with the finite element method.

In the calculation of the finite element, the ratio of hot spot stress to nominal stress is commonly used to define the stress concentration factor in engineering, as shown in the following formula (Wang et al., 2020):

$$K_t = \frac{\sigma_{hot}}{\sigma_{nom}} \quad (3)$$

Among them, K_t is the stress concentration factor; σ_{hot} is the hot spot stress, MPa, that is, the maximum stress of the dangerous section around the weld; and σ_{nom} is the nominal stress, MPa, that is, mean stress at the root of the weld.

In the early engineering practice, the reference to the empirical formula was mainly the formula proposed by Jian (2015):

$$K_t = 1 + \frac{2.6(\delta_t + \delta_m)}{t_1 [1 + 0.7(t_2/t_1)^{1.4}]} \quad (4)$$

Among them, t_1 is the thickness of the thin wall, mm; t_2 is the thickness of the thick wall, mm; δ_t is the axis deviation value caused by the wall thickness transition, $\delta_t = (t_2 - t_1)/2$, mm; and δ_m is the pipe offset value; this article only has the factor about variable wall thickness, $\delta_m = 0$, mm.

Afterward, Lotsberg deduced the stress concentration factor of weld under externally axial force by the shell theory, and the formulas have been modified by Lotsberg. The formulas are as follows (Lotsberg, 2009):

$$K_t = 1 + \frac{2 - \nu}{\gamma} \sqrt{\frac{3}{1 - \nu^2}} \left(1 - \frac{t_1}{t_2} \right) + \frac{3(t_2 - t_1)}{t_1} \frac{1}{1 + (t_2/t_1)^{2.5}} e^{-\alpha} \quad (5)$$

$$\alpha = \frac{1.82e}{\sqrt{(D - t_1)t_1}} \frac{1}{1 + (t_2/t_1)^{2.5}} \quad (6)$$

$$\gamma = \frac{2(t_1^{2.5} + t_2^{2.5})}{t_2^{2.5} - t_1^{0.5}t_2} \left(1 + \left(\frac{t_1}{t_2} \right)^{1.5} \right) + \left(\frac{t_1}{t_2} \right)^2 - 1 \quad (7)$$

Among them, ν is Poisson ratio and e is the cone length of weld seam.

The results are shown in **Table 4**, comparing the results of stress by using the finite element method with the results of stress by using the empirical formula, as well as comparing the stress concentration coefficient with different wall thickness ratios, show that the maximum error is 5.8% and the error rate is small, which can ensure the accuracy of the analysis, and the pipe-soil model is feasible.

Grid Independence Validation

The purpose of mesh independence verification is to verify the influence of the analytical results by using the finite element method with different mesh densities. Three different mesh densities are established, and the stress extracted from the weld root is compared with each other. The results are shown in **Table 5**, from the analysis of the comparative results, when dividing the grid with the density of mesh 1, the rate of error is large. (The rate of error is calculated based on the size of grid 2). When the grid reaches more than 100,000 level, the increase

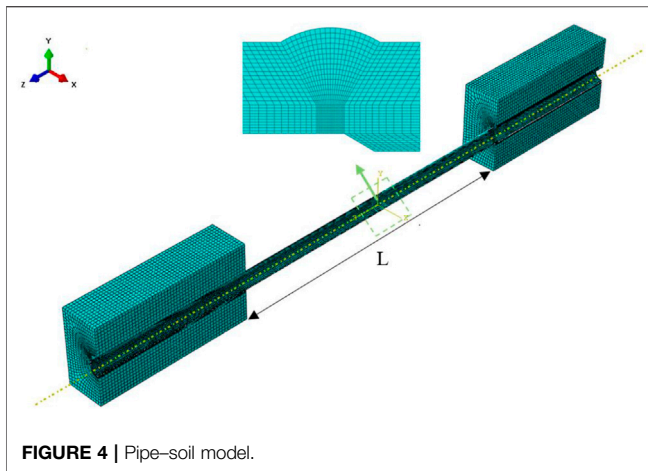


FIGURE 4 | Pipe-soil model.

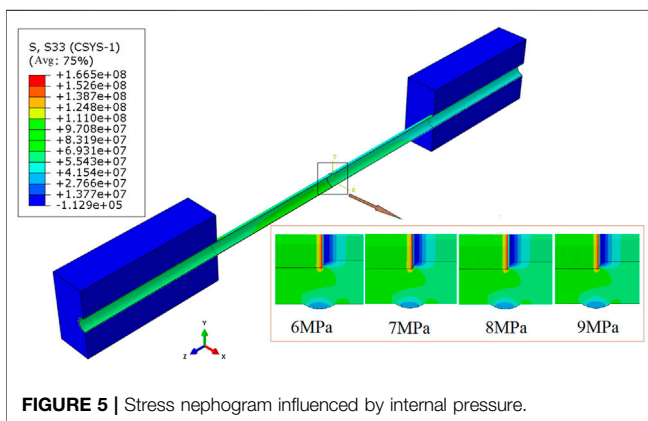


FIGURE 5 | Stress nephogram influenced by internal pressure.

density of grid has little effect on the stress analysis. Therefore, the density of grid 2 is used to divide the model.

RESULTS AND DISCUSSION

Through the analysis of the variable wall thickness butt weld model of the suspended pipeline, the values of axial stress are extracted from the weld root anticlockwise along the top of the pipeline to obtain the law of stress of the variable wall thickness butt weld model of the suspended pipeline.

Internal Pressure Effects

When analyzing the influence of internal pressure on the variable wall thickness butt weld of the suspended pipeline, the wall thickness ratio is $t_2/t_1 = 1.2$, the buried depth is 2.5 m, the suspended length of pipeline is $20D$, and the soil length is $10D$. The local stress nephogram is obtained from the bottom of the pipeline (Figure 5), which shows that the stress at the weld root of the pipeline is significantly greater than other parts at the bottom of the pipeline, due to the influence of the dual load of pipeline self-weight and internal pressure. The wall thickness of the conical part and the top of the weld has the tendency to

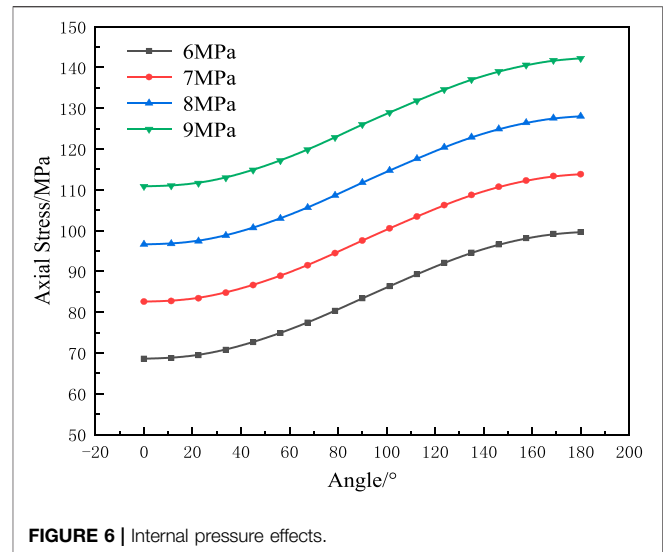


FIGURE 6 | Internal pressure effects.

change, and the stress is relatively small due to insufficient stress. The influence of internal pressure on axial stress of the weld with variable wall thickness is shown in Figure 6.

As can be seen from Figure 6, when the internal pressure increases from 6 to 9 MPa, the axial stress at the weld root increases gradually. When the internal pressure increases from 6 to 7 MPa, the stress increases about 17%. When the internal pressure increases from 7 to 8 MPa and then 8 to 9 MPa, the stress increases about 15 and 13%, respectively. Furthermore, under the same internal pressure, the difference of stress between the top and bottom of the pipeline is about 31 MPa.

Wall Thickness Ratio Effects

When analyzing the influence of the wall thickness ratio on variable wall thickness butt weld of the suspended pipeline, the operating pressure is 7.2 MPa, the buried depth is 2.5 m, the suspended length of pipeline is $20D$, and the soil length is $10D$. It can be seen from the local stress nephogram at the bottom of the pipeline (Figure 7), the stress is red, and the largest value is at the weld root. However, in the transition section of tapered wall thickness, the stress is blue. With the increase in the wall thickness ratio, the blue area of stress is also increasing in the conical transition section, and the stress difference between the welding root and the other parts is larger.

The stress law is analyzed by changing different wall thickness ratios, as shown in Figure 8. When the wall thickness ratio increases from 1.1 to 1.4, the axial stress at the weld root tends to increase. When the wall thickness ratio increases from 1.1 to 1.2, the stress increases by 26%. When the wall thickness ratio increases from 1.2 to 1.3, the stress increases by 19%. When the wall thickness ratio increases from 1.3 to 1.4, the stress increases by 28%. It indicates that the influence of the wall thickness ratio on pipeline stress cannot be ignored. At the same time, when the wall thickness ratio is increasing, the difference between the inner wall of the thin-walled pipeline and the thick-walled pipeline is also increasing, which will lead to the greater stress at the weld root and the more obvious stress concentration.

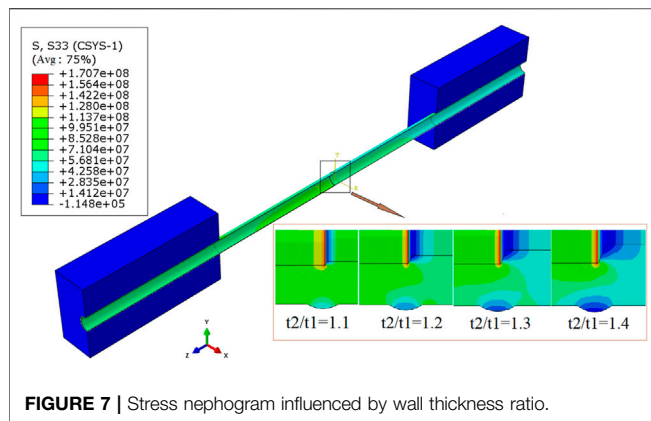


FIGURE 7 | Stress nephogram influenced by wall thickness ratio.

Suspension Length Effects

When analyzing the influence of suspended length on the variable wall thickness butt weld of suspended pipeline, the operating pressure is 7.2 MPa, the buried depth is 2.5 m, the wall thickness ratio is 1.2, and the soil length is 1/2 times the length of suspended length. It can be seen from the local stress nephogram at the bottom of the pipeline that the maximum stress is at the junction of the welding root and the thick wall pipeline (Figure 9). With the increase in suspended length, the stress in the thin-walled pipe section increases gradually. Meanwhile, the stress at the transitional part of the cone is also gradually increasing. It indicates that with the increase in the suspended length, the deformation of the pipeline is increasing, and the stress will concentrate to the weakest part of the pipeline, and the stress of floating is more obvious at the changeable part of the pipe diameter.

Analyzing the stress law by changing the lengths of the suspended pipeline (20D, 40D, 60D, 80D) is shown in Figure 10. When the suspended length increases from 20D to 80D, the longer the suspended length of the pipeline, the greater is the stress variation amplitude at the top and bottom of the pipeline. When the suspended length is 20D, the stress difference between the top and bottom of the pipe at the welding root is about 31.27 MPa. When the suspended length is 40D, the stress difference between the top and bottom of the pipe at the welding root is about 93.03 MPa. When the suspended length is 60D, the stress difference between the top and bottom of the pipe at the welding root is about 216.33 MPa. When the suspended length is 80D, the stress difference between the top and bottom of the pipe at the welding root is about 382.96 MPa. It indicates that the longer the suspension, the more obvious is the gap of stress. As a result of the pipeline in a suspended state, the influence of gravity on the pipeline, the longer the suspended length, the greater will be the weight of the pipeline, and the deformation of the pipeline about bending and stretching will also increase. Nevertheless, at the top of the pipe, the tensile force of the weld with variable wall thickness decreases with the increase in the suspended length, so the stress at the weld root at the top of the pipe will gradually decrease. At the bottom of the pipeline, due to the dual load of gravity and tension, the stress of

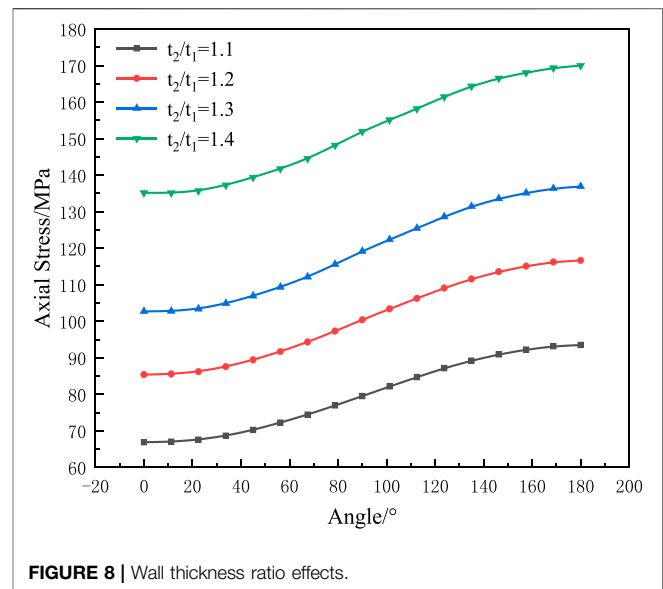


FIGURE 8 | Wall thickness ratio effects.

the weld with variable wall thickness changes greatly, and the degree of stress concentration will be more obvious, which will increase with the increase in the suspended length.

Weld Position Effects

When analyzing the influence in the weld position on variable wall thickness butt welds of suspended pipelines, the operating pressure is found to be 7.2 MPa, the buried depth 2.5 m, the wall thickness ratio 1.2, the suspended length 40D, and the soil length 20D. From the stress nephogram at the top and bottom of the pipeline (Figure 11), it can be seen that the stress at the top of the pipeline decreases with the gradual transfer of the weld to the middle of the suspended pipeline, and the blue stress area increases significantly. At the same time, the stress at the weld root at the top of the pipeline changes from red to blue. At the bottom of the pipeline, the stress at the change of weld root and wall thickness is red, and the red area is also gradually widened, which belongs to the most vulnerable part of the pipeline. At the same time, the stress at the top of the weld increases with the right shift of the weld position.

The stress law is analyzed by changing different welding positions (1/8L, 2/8L, 3/8L, and 4/8L), as shown in Figure 12. When the position of the pipeline weld moves from 1/8L to 4/8L, the farther the weld is away from the soil, the greater is the stress at the root of pipeline butt weld. When the welding position is at 1/8L, the stress difference between the top and bottom of the pipe at the weld root is about 17.36 MPa. When the weld position is at 2/8L, the stress difference between the top and bottom of the pipe at the weld root is about 46.96 MPa. When the weld position is at 3/8L, the stress difference between the top and bottom of the pipe at the weld root is about 83.31 MPa. When the weld position is at 4/8L, the stress difference between the top and bottom of the pipe at the weld root is about 92.32 MPa. It can be found from the stress diagram that when the weld seam is located at 1/8L, the stress at the weld root at the top of the pipeline is greater than that at the bottom of the pipeline. This is because at 1/8L, the pipe is

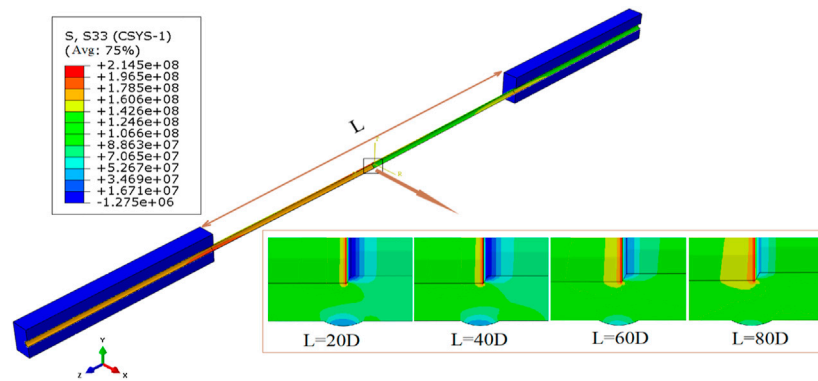


FIGURE 9 | Stress nephogram influenced by suspension length.

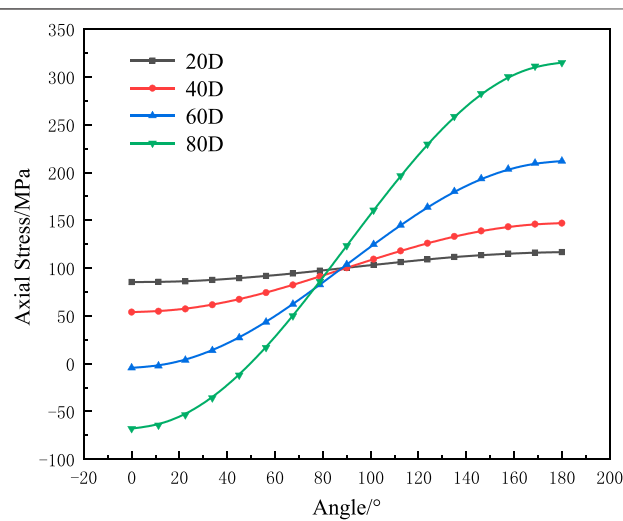


FIGURE 10 | Suspension length effects.

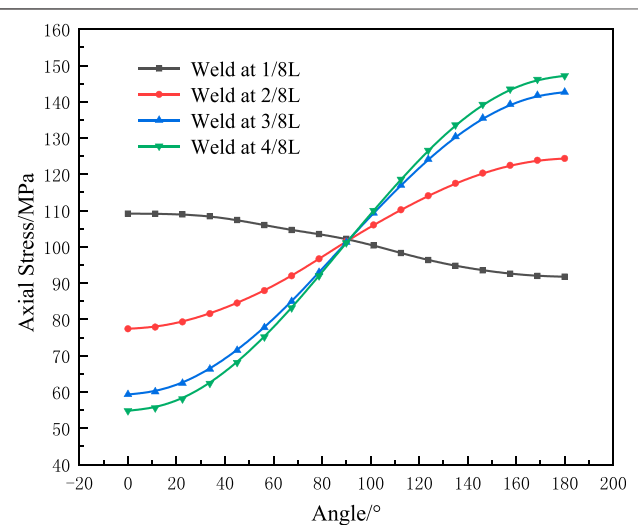


FIGURE 12 | Weld position effects.

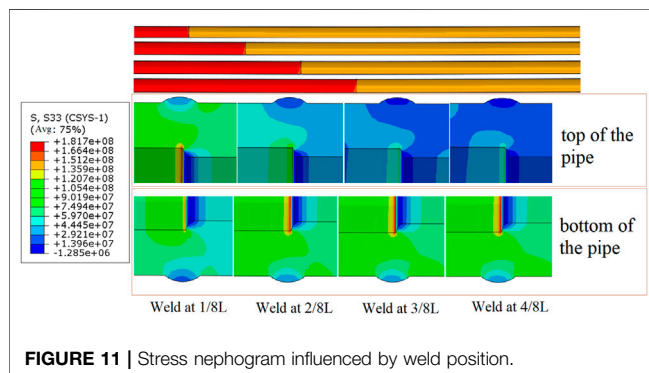


FIGURE 11 | Stress nephogram influenced by weld position.

close to the soil, the interaction between the pipe and the soil will have an impact on the stress of the pipeline. At this time, the stress change at the top of the pipe is larger than that at the bottom of the pipe. But when the weld position moves to the middle of the suspended pipeline as the position of the weld is farther and

farther from the soil, the influence of the interaction between the pipe and the soil is gradually reduced, the position where the stress changes greatly return to the bottom of the pipe.

Weld Conical Surface Length Effects

When analyzing the influence of weld cone length on variable wall thickness butt weld of the suspended pipeline, the operating pressure is 7.2 MPa, the buried depth is 2.5 m, the wall thickness ratio is 1.2, the suspended length is 20D, and the soil length is 10D. It can be seen from the stress nephogram from the bottom of the pipeline that the stress gradient changes more and more evenly at the weld root (Figure 13), and the area with larger stress is gradually decreasing. The stress law is analyzed by changing the length of the weld cone (3.5, 4, 5, 6 mm), as shown in Figure 14. When the cone length increases from 3.5 to 6 mm, the stress at the weld root also decreases. When the cone length increases from 3.5 to 4 mm, the stress decreases by 0.16%. When the cone length increases from 4 to 6 mm, the stress decreases by 0.57%. When the cone length increases from 5 to 6 mm, the stress decreases by

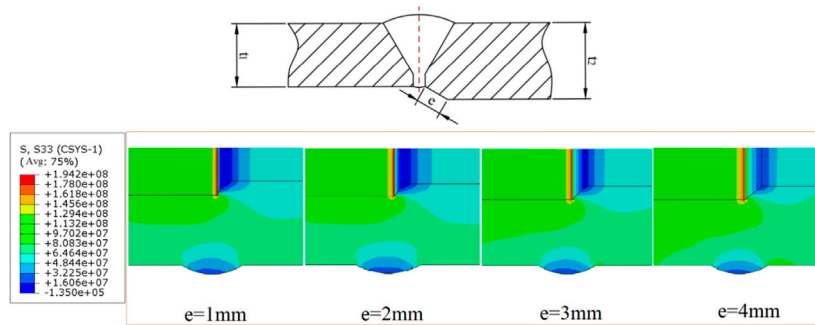


FIGURE 13 | Stress nephogram influenced by weld conical surface length.

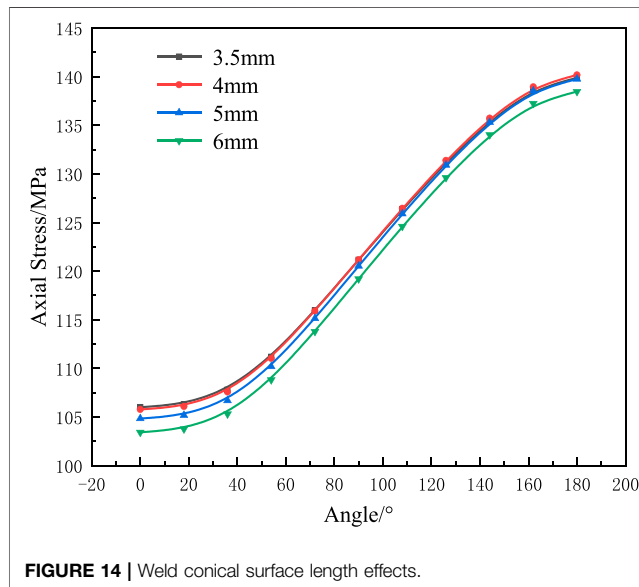


FIGURE 14 | Weld conical surface length effects.

1.13%. The influence of the cone length on the stress at the weld root decreases with the increase in the cone length because the degree of mutation will be reduced by increasing the cone length at the weld root at the inner wall of the pipe, and the cross-sectional stress distribution is more uniform.

Pipeline Curvature Analysis

The model used to analyze the curvature is a suspended pipeline about 60 m in length. Through finite element analysis, it can be seen that the pipeline has been deformed significantly (Figure 15). Extracting the vertical displacement of each node at the bottom of the whole pipeline and calculating the curvature (Figure 16, where Fig. (A) and Fig. (B) are local graphs of points a and b). It can be seen that the curvature variation of point A and point B at the separation of pipeline and soil is obvious, where the curvature of point A is 0.001 and that of point B is 0.0009. The position with the largest curvature is the middle of the pipeline weld, and the curvature is 0.05987. Under the action of self-weight and internal pressure, the suspended part of the pipeline lacks the support of soil to the pipeline, which can only rely on the

pipeline's own ability to resist deformation. At both ends of the pipeline, due to the support of soil, the deformation of the pipeline is small, the curvature is relatively small, and the curvature variation in the rest are not obvious. The left side of the pipeline is a thin-walled pipe because its ability to resist deformation is less than the thick-walled pipe on the right side, resulting in a greater curvature at point A than at point B.

As can be seen from Figure 17, in the pipe-soil separation part, the stress value at point A of the left thin-walled pipe section is 243 MPa, and the stress value at point B of the right thick-walled pipe section is 206 MPa. In the middle of the pipe, due to the existence of weld, the stress change of the pipe is greatly reduced from 202 to 155 MPa. For the Mises stress of the pipeline, the thin-walled pipe section has a large deformation due to its poor ability to resist deformation, and the stress of the whole thin-walled pipe section is larger than that of the thick-walled pipe section. The position with the largest curvature is not the position with the largest stress, and the position with the largest stress is not the position with the largest curvature. Only when the stress value changes greatly, the position with larger curvature changes.

Through the analysis of various influencing factors, it can be known that the key factor is the suspended length. When the suspended length exceeds $60D$, the increase in the stress value in the middle of the pipeline will gradually increase, so $60D$ is regarded as the critical value of suspension. In terms of internal pressure, the increase in internal pressure will elongate the pipe along the axial direction, and the axial stress will increase. In reference to the wall thickness ratio, the change in the wall thickness ratio affects the inner diameter at both ends of the weld. A larger wall thickness ratio makes the transition cone at both ends of the weld steeper and the stress concentration at the weld root more obvious. The suspended length will affect the dead weight of the pipeline; a larger suspended length will make the middle part of the pipeline bend gradually under the action of the dead weight, while the capacity of the soil at both ends to share the gravity of the pipeline does not increase. The larger suspended length of the pipeline will increase the deformation of the pipeline and the axial stress in the middle of the pipeline. In terms of the weld position factor, the change in the weld position affects the supporting effect of soil on the pipeline. The closer the

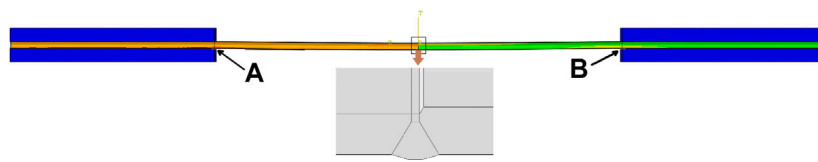


FIGURE 15 | Pipeline deformation diagram.

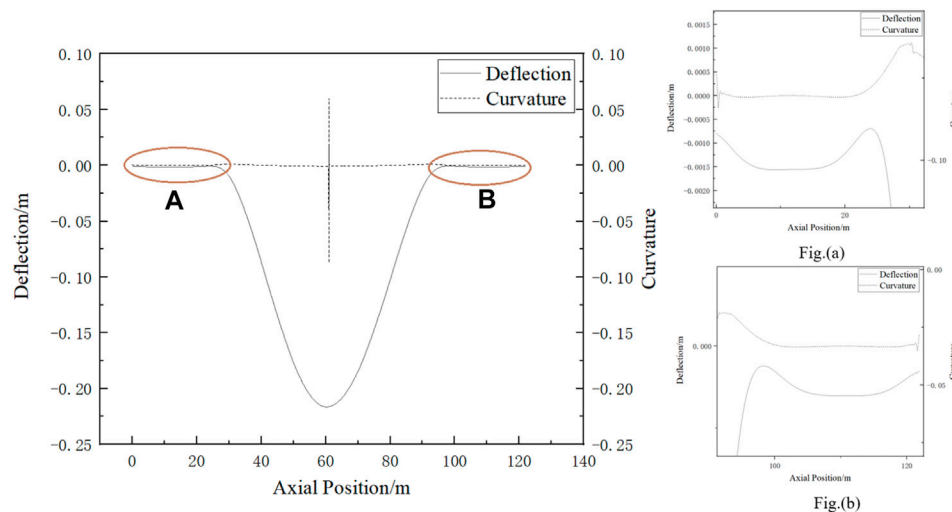


FIGURE 16 | Deflection and curvature diagram, where Figure (a) and Figure (b) are local graphs of points A and B. Point A is the junction of thin-walled pipe and soil. Point B is the junction of thick-walled pipe section and soil.

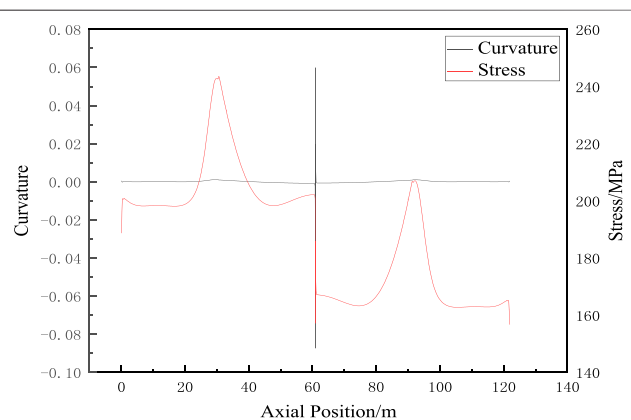


FIGURE 17 | Curvature and strain diagram.

weld is to the soil, the stronger will be the supporting effect of soil, and the smaller will be the axial stress of the pipeline. As far as the weld cone length factor is concerned, the change in the weld cone length affects the transition between large and small pipe diameters. On the premise that the wall thickness ratio remains unchanged, the longer the cone length is, the gentler will be the wall thickness transition, and the axial

stress will not increase sharply due to the sudden change of wall thickness.

CONCLUSION

The main studies of the work are about the influence of internal pressure, wall thickness ratio, suspended length, weld position, and cone length on the axial stress of the variable wall thickness butt weld of suspended pipeline and the analysis of curvature and stress at the weld root. Through the analysis of the finite element results, the following conclusions can be drawn as follows:

- The influence of single change in internal pressure on weld stress is smaller than the other four factors.
- The influence of the wall thickness ratio on the stress at the weld seam gradually increases with the increase in the wall thickness ratio. The larger the wall thickness ratio, the greater the difference between the inner diameters of the pipes at both ends, and the greater the stress change at the weld joint. Therefore, for variable wall thickness-welded pipelines, a small wall thickness ratio should be selected to increase the reliability of pipeline operation.
- The increase in the suspended length will significantly change the stress at the weld root, and the stress

difference between the top and bottom of the pipeline will also gradually increase. In a large suspended state, the probability of failure at the bottom of the pipeline is the largest. In practical engineering applications, large suspended pipeline should be avoided.

- When the weld position is close to the soil, the soil can give a larger supporting force to the suspended pipeline, so the stress at the weld will be smaller than the weld position far from the soil.
- With the increase in the cone length, the stress gradient at the welding root is more uniform, and the stress decreases. Increasing the cone length is conducive to reducing the cross-sectional mutation and sharing the stress change. When the pipeline is welded, maintaining a large cone length can reduce the failure rate of the pipeline during operation.
- When the pipeline is suspended, the curvature at the separation of the pipeline and the soil is increasing, but when it moves to the suspended section, the curvature decreases gradually. When it reaches the weld position located in the middle of the pipeline, the curvature changes to the peak, and the stress value changes greatly. Therefore, the position where the stress value changes greatly is the position where the curvature changes most. In the separation of pipe and soil, the curvature has a certain change, but it is not obvious. However, in the separation of pipe and soil, the stress is the

largest, and in the middle of the pipeline weld position, the stress change is the largest.

DATA AVAILABILITY STATEMENT

The original contributions presented in the study are included in the article/Supplementary Material; further inquiries can be directed to the corresponding author.

AUTHOR CONTRIBUTIONS

FY contributed to data curation, writing—original draft preparation, and writing—original draft. YD performed data curation and wrote the original draft. WB supervised the research and wrote the original draft. XJ worked on software. XH performed the validation. HH and WL contributed to writing—review and editing.

FUNDING

This work is supported by the research project of the Southwest Pipe Company of Pipe China (XNGD-JSZX-2020-JS-371-1).

REFERENCES

- Dabiri, M., Ghafouri, M., Raftar, H. R. R., and Björk, T. (2017). Neural Network-Based Assessment of the Stress Concentration Factor in a T-Welded Joint. *J. Constructional Steel Res.* 128, 567–578. doi:10.1016/j.jcsr.2016.09.024
- Gao, Y. F., and Liang, X. B. (2012). *GB/T 228.1-2010(Tensile Test of Metal Materials Part 1: Room Temperature Test method) Implementation Guide*. Beijing: Standards Press of China.
- Guo, J., Zheng, H., Li, B., and Fu, G. Z. (2019). A Bayesian Approach for Degradation Analysis with Individual Differences. *IEEE Access* 7, 175033–175040. doi:10.1109/access.2019.2955969
- Guo, J., Zheng, H., Li, B., and Fu, G. Z. (2019). Bayesian Hierarchical Model-Based Information Fusion for Degradation Analysis Considering Non-competing Relationship. *IEEE Access* 7, 175222–175227. doi:10.1109/access.2019.2955932
- Jian, S. (2015). *Pipeline Mechanics*. Beijing: Science Press.
- Li, H., Guo, J. Y., Yazdi, M., Nedjati, A., and Adesina, K. A. (2021). Supportive Emergency Decision-Making Model towards Sustainable Development with Fuzzy Expert System. *Neural Comput. Appl.* 33, 15619–15637. doi:10.1007/s00521-021-06183-4
- Li, Y., Lence, B. J., Shi-Liang, Z., and Wu, Q. (2011). Stochastic Fatigue Assessment for Berthing Monopiles in Inland Waterways. *J. Waterway, Port, Coastal, Ocean Eng.* 137 (2), 43–53. doi:10.1061/(asce)ww.1943-5460.0000063
- Liu, W. L. Z. Y., Jiang, W. M., Wang, X. L., He, Y. Z., and Long, B. (2021). Numerical Simulation of Welding Residual Stress of X80 Pipeline Joint in Eastern China - Russia Railway. *Oil Gas Storage Transp.* Available at: <https://kns.cnki.net/kcms/detail/13.1093.TE.20200611.1111.002.html>.
- Lotsberg, I. (2009). Stress Concentrations at Butt Welds in Pipelines. *Mar. Struct.* 22, 335–337. doi:10.1016/j.marstruc.2008.06.008
- Ma, T., Wu, J., Tang, Y., Hu, H., and Li, A. (2012). Maximum Suspended Length of Production Pipeline. *J. Southwest. Pet. Univ. Technol. Ed.* 34 (4), 165–173. doi:10.3863/j.issn.1674-5086.2012.04.025
- Midawi, A. R. H., Huda, N., Simha, C. H. M., and Gerlich, A. P. (2020). Characterization of Anisotropy of Strength in API-X80 Line Pipe Welds through Instrumented Indentation. *Metallogr. Microstruct. Anal.* 9, 884–894. doi:10.1007/s13632-020-00693-8
- Nishida, M. (1967). *Stress Concentration*. Beijing: Machinery Industry Press.
- Terán, G., Albiter, A., and Cuamatzi-Meléndez, R. (2013). Parametric Evaluation of the Stress Concentration Factors in T-Butt Welded Connections. *Eng. Struct.* 56, 1484–1495. doi:10.1016/j.engstruct.2013.06.031
- Wang, L., Bi, H., Yang, Y., Zhang, Y., and Li, Y. (2018). Response Analysis of an Aerial-Crossing Gas-Transmission Pipeline during Pigging Operations. *Int. J. Press. Vessels Piping* 165, 286–294. doi:10.1016/j.ijpvp.2018.07.011
- Wang, L., Tang, Y., Ma, T., Zhong, J., Li, Z., Zhang, Y., et al. (2020). Stress Concentration Analysis of Butt Welds with Variable wall Thickness of Spanning Pipelines Caused by Additional Loads. *Int. J. Press. Vessel. Pip.* 182, 104075. doi:10.1016/j.ijpvp.2020.104075
- Yuan, R., and Li, H. (2016). A Multidisciplinary Coupling Relationship Coordination Algorithm Using the Hierarchical Control Methods of Complex Systems and its Application in Multidisciplinary Design Optimization. *Adv. Mech. Eng.* 9, 168781401668522. doi:10.1177/1687814016685222
- Yuan, R., Li, H., and Wang, Q. (2018). An Enhanced Genetic Algorithm-Based Multi-Objective Design Optimization Strategy. *Adv. Mech. Eng.* 10, 168781401878483. doi:10.1177/1687814018784836
- Yuan, R., Meng, D., and Li, H. (2016). Multidisciplinary Reliability Design Optimization Using an Enhanced Saddlepoint Approximation in the Framework of Sequential Optimization and Reliability Analysis. *Proc. Inst. Mech. Eng. Part. O J. Risk Reliab.* 230, 570–578. doi:10.1177/1748006x16673500
- Yuan, R., Tang, M., Wang, H., and Li, H. (2019). A Reliability Analysis Method of Accelerated Performance Degradation Based on Bayesian Strategy. *IEEE Access* 7, 169047–169054. doi:10.1109/access.2019.2952337
- Z. F., S. (2009). *Stress Analysis and Safety Research on Special Pipe Section of Gas Pipeline*. East China: East China: China University of Petroleum.
- Zhu, L., Luo, J., Wu, G., Han, J., Chen, Y., and Song, C. (2021). Study on Strain Response of X80 Pipeline Steel during weld Dent Deformation. *Eng. Fail. Anal.* 123, 105303. doi:10.1016/j.engfailanal.2021.105303
- Zhu, Y., Du, Z., Ma, Z., and Jiao, S. (2017). Security Research of Pipeline with Unfitness Defect in Spanning State. *Pipeline Tech. Equip.*, 16–19. doi:10.3969/j.issn.1004-9614.2017.06.004

Conflict of Interest: FY, YD, WB, XH, and HH were employed by the Southwest Pipe Company of Pipe China.

The remaining authors declare that the research was conducted in the absence of any commercial or financial relationships that could be construed as a potential conflict of interest.

Publisher's Note: All claims expressed in this article are solely those of the authors and do not necessarily represent those of their affiliated organizations, or those of the publisher,

the editors, and the reviewers. Any product that may be evaluated in this article, or claim that may be made by its manufacturer, is not guaranteed or endorsed by the publisher.

Copyright © 2022 Yingchao, Dongliang, Binbin, Jian, Heng, Hao and lin. This is an open-access article distributed under the terms of the Creative Commons Attribution License (CC BY). The use, distribution or reproduction in other forums is permitted, provided the original author(s) and the copyright owner(s) are credited and that the original publication in this journal is cited, in accordance with accepted academic practice. No use, distribution or reproduction is permitted which does not comply with these terms.



Coupled Heat and Flow Analysis Inside a Diversion-Type Gas Heater With Vertical Guide Plate Structure

Yun Guo^{1*}, Xuning Zhang¹ and Zhongwei Zhou²

¹School of Mechanical and Automotive Engineering, Shanghai University of Engineering Science, Shanghai, China, ²Shanghai Petrochemical Co., Ltd, Shanghai, China

OPEN ACCESS

Edited by:

Jiang Bian,
China University of Petroleum, China

Reviewed by:

Meysam Atashafrooz,
Sirjan University of Technology, Iran
Balaji Kumar,
VIT University, India

*Correspondence:

Yun Guo
graceguo1980@126.com

Specialty section:

This article was submitted to
Advanced Clean Fuel Technologies,
a section of the journal
Frontiers in Energy Research

Received: 16 December 2021

Accepted: 22 February 2022

Published: 11 April 2022

Citation:

Guo Y, Zhang X and Zhou Z (2022)
Coupled Heat and Flow Analysis Inside
a Diversion-Type Gas Heater With
Vertical Guide Plate Structure.
Front. Energy Res. 10:837104.
doi: 10.3389/fenrg.2022.837104

In the natural gas heating process, the cylinder-type heater using water as an intermediate heating medium is the most extensively used. The heat exchange rate between the heating medium water and the fire and gas tubes in the great-capacity cylinder appears to be the most important element affecting a gas heater's thermal efficiency. The water heat flow field within a new diversion-type gas heater with vertical guide plate design is described in this paper. In contrast to prior research that concentrated on natural convection heat transfer in medium water, the radiation impact is included. The discrete-ordinate model was utilized to build a 2-D combined natural convection and participating medium radiation heat transfer model, which was solved using the finite volume technique with unstructured body-fitted grids. First, experimental data were used to validate the numerical model. The coupled heat flow fields with vertical guide plates of various heights were then analyzed. The numerical findings reveal that utilizing a vertical guide plate structure, the proportion of radiation heat transfer in the total heat transfer rate reaches 25.1%, indicating that water radiation cannot be ignored. The vertical guide plate structure might help to create a well-organized flow pattern in the cylinder, which would improve natural convection heat transfer while having no influence on water radiation. Installing a vertical guide plate with a height of 550 mm and a thickness of 5 mm can lower the overall heat transfer rate in the convective tube bundle by 2.04%. In China, this technique has been given a patent.

Keywords: gas heater, vertical guide plate, heat transfer enhancement, natural convection, radiation, thermal efficiency

INTRODUCTION

The use of natural gas necessitates the use of a gas heater, as heating is required in the natural gas usage process (Guo Y. and Guo Z., 2016). Because the process in gas-fired generating units needs high-temperature flue gas, the natural gas utilized in power plants must undergo heat treatment. During the gasification process, liquefied natural gas must also be heated (Yuan et al., 2001). In the engineering process, the cylindrical heater with intermediate heating medium is now commonly utilized as a gas heater (Al-Sammerrai, 1985; Guo et al., 2009; Su, 2013; Setoodeh et al., 2016).

Figure 1 depicts the structure of a general heater. The flame and smoke from fuel combustion fill the fire tube and flue tube bundles in the cylindrical heater; the convective tube bundle is filled with natural gas to be heated; and the intermediate heating medium fills the inner space of the entire cylinder except the fire tube, flue tube bundle, and convective tube bundle, transferring the heat created in the fire tube and flue tube bundle to reach completion. The most common intermediate heating medium is water (Li and Wang,

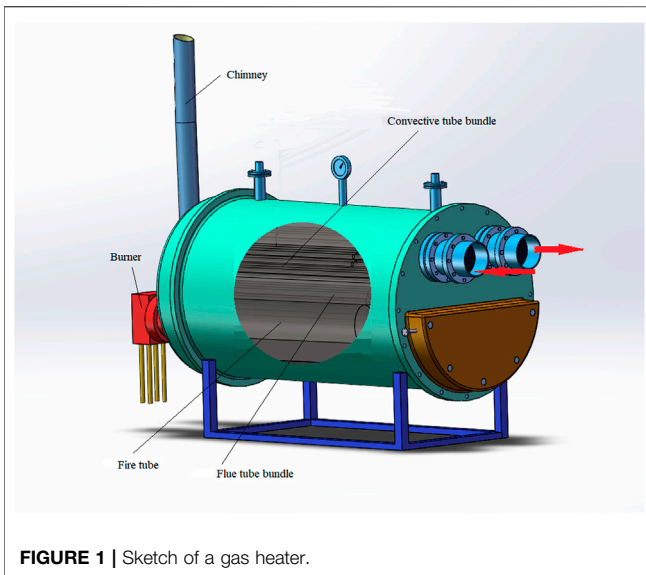


FIGURE 1 | Sketch of a gas heater.

2019). The typical heat exchange surface configuration of this gas heater has the following consequences: firstly, a high-temperature up-flow medium forms along the wall of the fire tube and flue tube bundle. Meanwhile, a low-temperature downflow medium is developed along the convection tube bundle's wall. These two mediums collide, resulting in a disordered flow field organization in the cylinder. Secondly, the small temperature difference between the upper and lower flow fields in the large cylinder causes natural convection to be weak and heat transfer efficiency to be low. Lastly, the entire flow field, including the bottom of the large cylinder, has many dead angles (Li and Zhang, 2007; Sun et al., 2011; Guo, 2012).

Previous research (Guo Y. and Guo Z. X., 2016; Wang, 2017) solely examined the natural convection heat transfer within the cylinder, but the influence of radiation was largely ignored. When radiation and convection effects are of similar importance, a separate calculation of these and superposition without considering their interaction leads to significant errors (Atashafrooz et al., 2015). To have more accurate and reliable results, the flowing fluid must be considered as a radiating medium (Atashafrooz and GandjalikhanNassab, 2013). Because the operating temperature of a water cylinder is usually above 350 K, the radiation between the water, the cylinder, and the tubes must be considered. As a result, water cannot be described as a non-participating medium. Participating medium radiation has become a research hotspot in recent years. However, the majority of research is concentrated on flue gas, with only a few studies focusing on alternative mediums such as water (Smith et al., 1982; Razzaque et al., 1984; Sun et al., 2016; Gao et al., 2019). This research analyzes the coupled heat and flow of natural convection as well as radiation in the cylinder to better understand the heat transfer mode within the gas heater.

Adding metallic plates to enhance convective heat transmission was a frequent method (Guo, 1999; Zhukova and Isaev, 2008; Guo et al., 2011; Sun et al., 2016; Gao et al., 2019). We suggest using a vertical guide plate structure to improve coupled heat transport within a gas heating cylinder.

MATHEMATICAL MODEL

The two-dimensional circular section in the center of a heating cylinder is used as the numerical model in this paper. The configuration information is provided where the heater's dimensions are given: D1 measures 1,300 mm, D2 measures 325 mm, b1 measures 540 mm, and b2 measures 510 mm. The flue tubes have a diameter of 42 mm and a spacing of 68 mm between adjacent tubes. The convective tubes have a diameter of 38 mm, b3 is 90 mm, b4 is 65 mm, and the angle ϕ is 60° . As illustrated in Figure 2A, there are nine measuring points designated from 0 to eight along the circular section that are used to determine the temperature distribution of the intermediate heating medium in the cylinder. The central temperature of the cylinder is measured at measuring point 0, which is located in the middle of the circular section.

Measuring point 1 is situated in the third pass area of the convective tube bundle, which is on the left side of the cylinder. Measuring point 2 is on the right side of the cylinder, in the second pass region of the convective tube bundle. The third measuring point is located in the fourth tube pass region on the cylinder's left side. Point 4 is located on the first tube pass region on the right side of the cylinder. Measuring point 5 is placed in the upper part of the flue tube, while measuring point 6 is situated in the upper part of the fire tube. The lowest half of the flue tube is where measuring point 7 is located, and the bottom of the cylinder is where measuring point 8 is located. Carbon steel is used for the cylinder and all tubes. Interested readers might refer to Guo et al. (Cimina et al., 2015) for further information on the experimental system.

Based on the Boussinesq assumption under steady laminar flow conditions (the maximum Rayleigh number in the present study is about 2.02×10^9 ; thus, a laminar flow model is considered), the two-dimensional governing equations for the steady-state coupled heat transfer of convection and radiation are as follows:

Continuity equation:

$$\frac{\partial u}{\partial x} + \frac{\partial v}{\partial y} = 0 \quad (1)$$

Momentum equations:

$$\rho \left(u \frac{\partial u}{\partial x} + v \frac{\partial u}{\partial y} \right) = -\frac{\partial p}{\partial x} + \mu \left(\frac{\partial^2 u}{\partial x^2} + \frac{\partial^2 u}{\partial y^2} \right) \quad (2)$$

$$\rho \left(u \frac{\partial v}{\partial x} + v \frac{\partial v}{\partial y} \right) = -\frac{\partial p}{\partial y} + \mu \left(\frac{\partial^2 v}{\partial x^2} + \frac{\partial^2 v}{\partial y^2} \right) + \rho g \beta (T - T_\infty) \quad (3)$$

Energy equation:

$$\rho c_p \left(u \frac{\partial T}{\partial x} + v \frac{\partial T}{\partial y} \right) = \lambda \left(\frac{\partial^2 T}{\partial x^2} + \frac{\partial^2 T}{\partial y^2} \right) - Q_s \quad (4)$$

Respectively, u, v , the velocity components on x, y directions; ρ , the medium density; μ , the dynamic viscosity; p , the pressure; β , the volume expansion coefficient; T , the temperature; T_∞ , the reference temperature; λ , the thermal conductivity; C_p , the specific heat; Q_s , and the radiative heat loss, which is written as

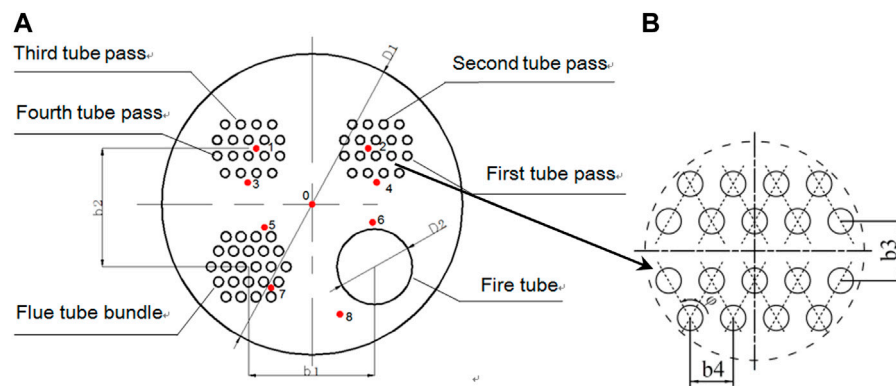


FIGURE 2 | (A) Cross-section of a gas heater simulated using a numerical model. **(B)** A zoom-in of the convective tube bundle.

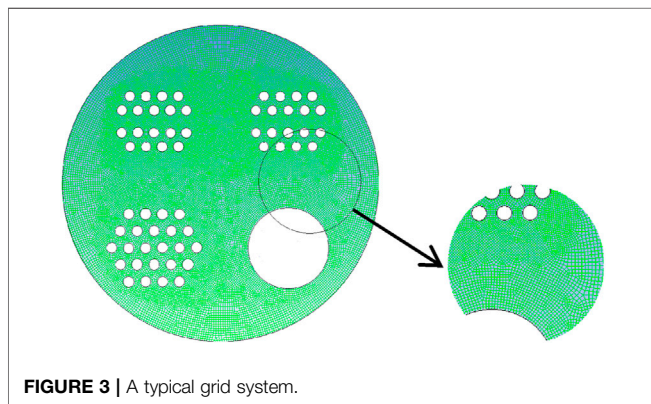


FIGURE 3 | A typical grid system.

$$Q_s = k_a \left[4\sigma T^4 - \int_0^{4\pi} I d\Omega \right] \quad (5)$$

where k_a denotes the medium's absorption coefficient, σ is the Stefan-Boltzmann constant, and I is the radiation intensity, which is calculated by solving the radiation transfer equation in water:

$$\mu^m \frac{\partial I^m}{\partial x} + \eta^m \frac{\partial I^m}{\partial y} = -k_a I^m + n^2 k_a I_b \quad (m = 1, 2, \dots, M) \quad (6)$$

where I^m denotes the radiation intensity in the m direction; I_b represents the blackbody radiation intensity; μ^m , η^m are direction cosine values in the direction of m ; and M is the discrete number.

The radiation boundary conditions for the opaque and diffuse wall surfaces are as follows:

$$I_\omega^m = n^2 \varepsilon_\omega I_{b\omega} + \frac{1 - \varepsilon_\omega}{\pi} \sum_{n_\omega \cdot s^{m'} < 0} I_\omega^{m'} |n_\omega \cdot s^{m'}| \omega^{m'} \quad (7)$$

ε_ω is the emissivity of the wall; n_ω is the normal vector outside the wall; $s^{m'}$ is the unit vector in the direction m' ; and $\omega^{m'}$ is the solid angle weight in the m' direction.

The following are the boundary conditions: the adiabatic boundary is the cylinder wall, with the average temperature

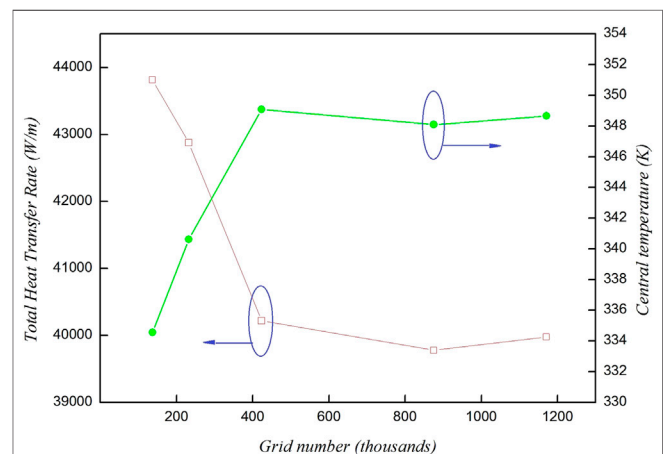


FIGURE 4 | Grid independence test of medium water.

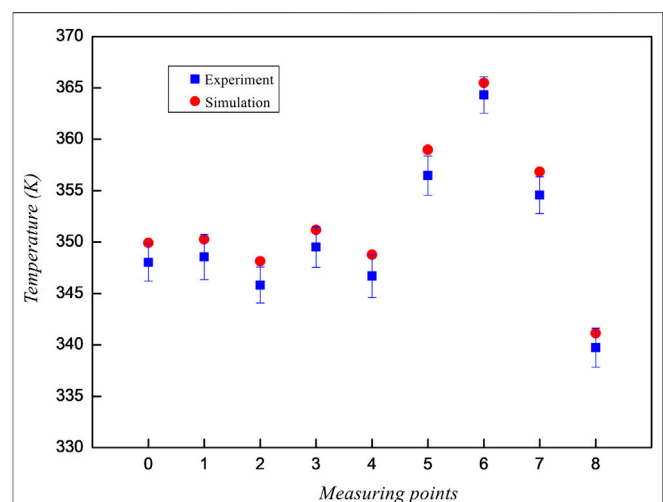


FIGURE 5 | Comparison of the simulation and measurement of temperatures at nine locations.

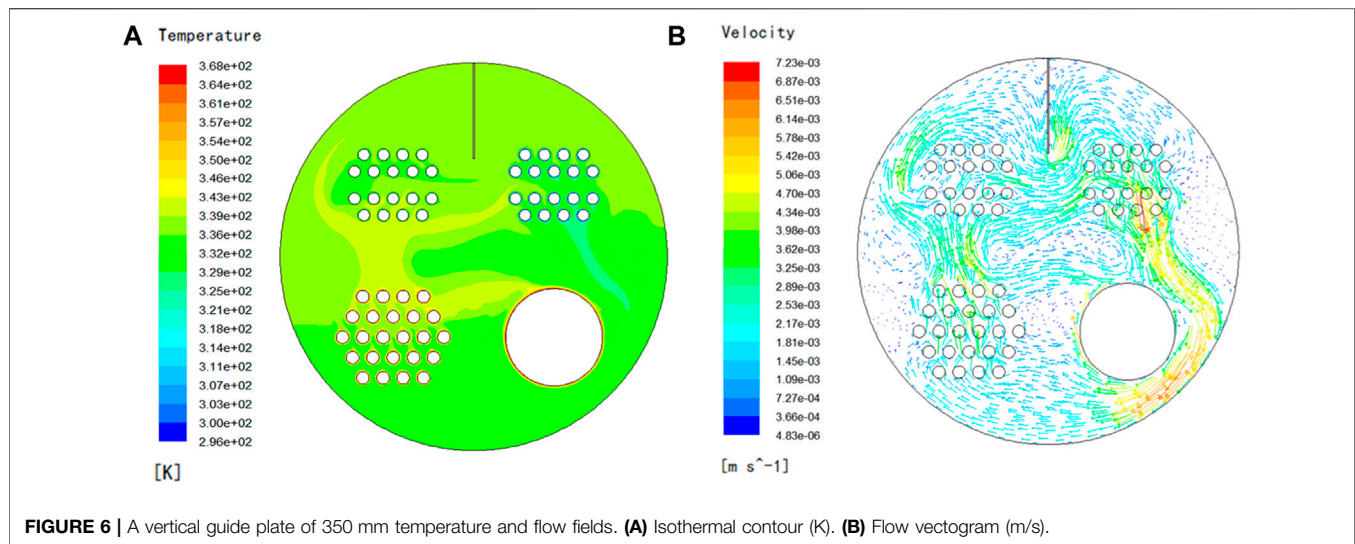


FIGURE 6 | A vertical guide plate of 350 mm temperature and flow fields. **(A)** Isothermal contour (K). **(B)** Flow vectogram (m/s).

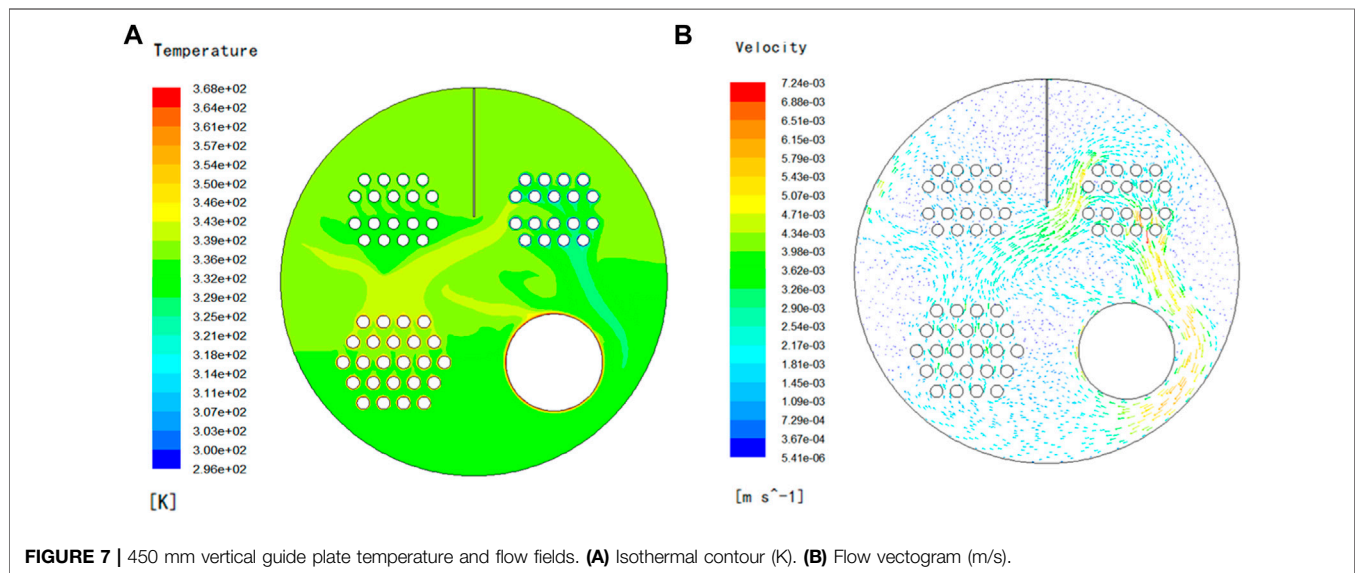


FIGURE 7 | 450 mm vertical guide plate temperature and flow fields. **(A)** Isothermal contour (K). **(B)** Flow vectogram (m/s).

of the fire tube wall set to 368 K, the average temperature of the flue tube bundle wall set to 363 K, and the convective tube bundle boundary condition expressed as follows:

$$-\lambda \frac{\partial T_w}{\partial n} = h(T_w - T_g) \quad (8)$$

where n denotes the normal direction of the wall, T_w represents the wall temperature, and T_g is the temperature of the heated gas. The average temperature of the heated gas in the first and second tube passes is 285 K, and the heated gas's average temperature in the third and fourth tube passes is 310 K. h , the heat transfer coefficient is computed by

$$h = \frac{Nu \lambda_g}{d} \quad (9)$$

The Nusselt number (Nu) is determined using the following equation: the gas inside the convective tube bundle has a thermal conductivity of λ_g ; the diameter of the convective tubes is d ; and the gas flow inside the tube is turbulent.

$$Nu = 0.023 Re^{0.8} Pr^{0.4} \quad (10)$$

The Reynolds number for the gas flow within the convective tubes is Re , and the Prandtl number for the gas flow is Pr .

Fluent 17 was used for numerical simulation in this work, while Gambit software was employed to create hybrid unstructured grids. The convection and radiation-coupled heat transfer in the gas heater are solved using the finite volume approach and discrete ordinate radiation model in Fluent, which is consistent with literatures (Wu et al., 2019), (Aghanajafi and Abjadpour, 2016). Under 350 K, water has an

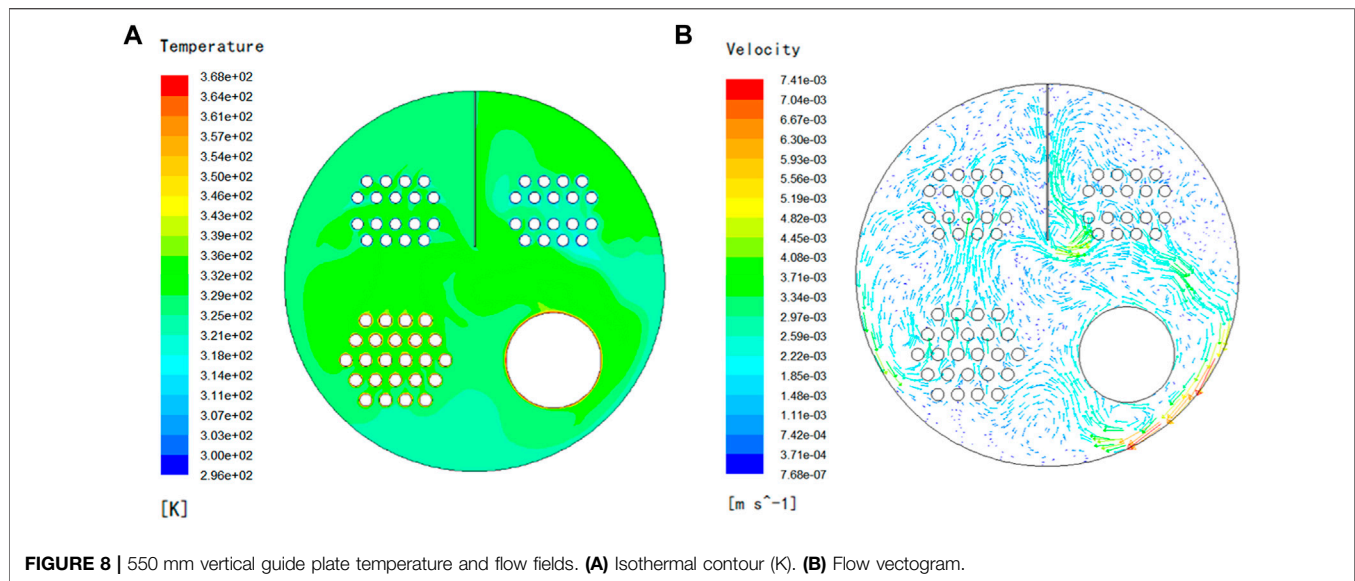


FIGURE 8 | 550 mm vertical guide plate temperature and flow fields. (A) Isothermal contour (K). (B) Flow vectogram.

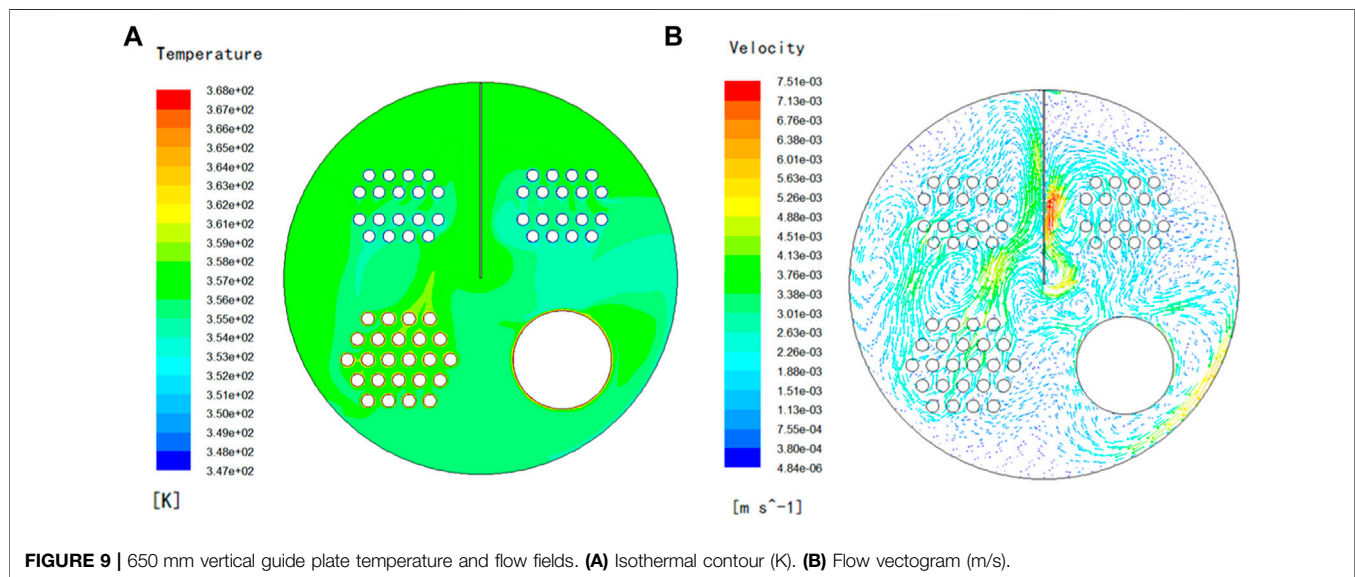


FIGURE 9 | 650 mm vertical guide plate temperature and flow fields. (A) Isothermal contour (K). (B) Flow vectogram (m/s).

emissivity of 0.922 and an absorption coefficient of $153,679 \text{ m}^{-1}$. The walls of the tubes are assumed to have constant steel characteristics with an emissivity of 0.8, and the thickness of the walls is not taken into account in the simulation.

In the area of the boundary surface, such as around the heating and cooling surfaces, where substantial velocity and temperature gradients exist, mesh refinement is required (Kim and Baek, 1997). Figure 3 depicts a typical grid system as well as a portion of the unstructured grid utilized in computation.

The grid independency was assessed using five different grid levels, including 136, 232, 423, 875, and 1,170,000 cells: the estimated total heat transfer rate in the convective tube

bundle (i.e., the heat utilized to heat up gas inside the convective tubes) is compared to the cylinder's central temperature in the case without the guide plate in Figure 4. With a finer grid system, the overall heat transfer rate and central temperature converge as predicted. The cumulative heat transfer rate inaccuracy between the finest grid with 1,170,000 cells and the grid with 423,000 cells is less than 0.6%, and the temperature at the cylinder center is less than 0.12%. It can be considered that this and a larger number of grids no longer affect the calculation results; considering the limited resources of the computer, the grid level of 423,000 cells may be employed to conduct research. The same grid-level setting procedure was adopted for all subsequent simulations.

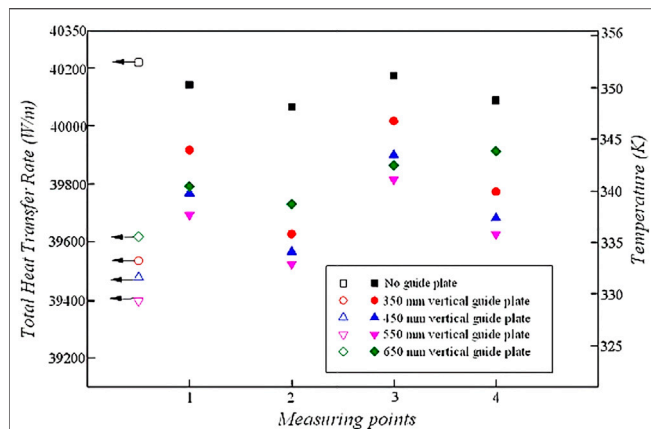


FIGURE 10 | The impact of vertical guide plates on total heat transmission and average temperature at the convective tube bundle.

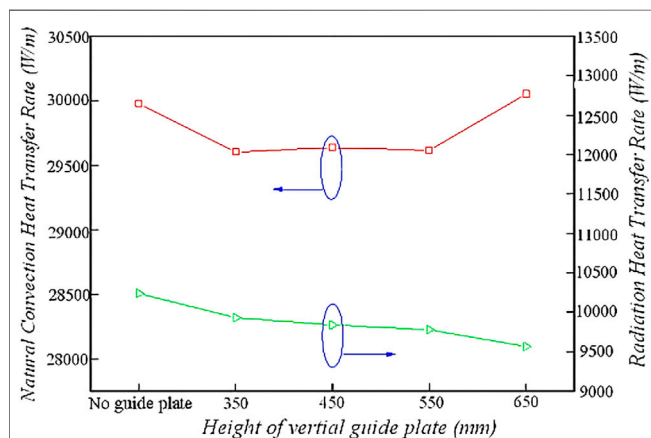


FIGURE 11 | Comparison of the rate of natural convection heat transfer and the rate of radiation heat transfer of vertical guide plates with various heights.

RESULTS AND DISCUSSION

The experiment was carried out under the boundary conditions specified in the previous article, and the data were read after the measured values of nine points were stable. The temperatures simulated are compared to the experimental results at the nine points highlighted in **Figure 2A** for the standard cylinder without the use of a guide plate before analyzing the improved heat transfer impact of the vertical guide plate. **Figure 5** depicts the contrast. The predicted temperatures agree with the experimental results, indicating that the model and boundary conditions are appropriately adjusted. Due to the neglect of the axial flow and heat dissipation through the cylinder wall in the simulation, the simulated temperatures are generally $1^{\circ}\text{C}\sim 2^{\circ}\text{C}$ greater than the corresponding temperatures experimentally measured.

In **Figure 5**, there is a clear thermal stratification at different heights of cylinder. The temperature is higher at measuring points 5–7 near the fire tube and flue tube bundle. The highest temperature appears at the measuring point 6 nearest to the fire tube. The temperature differences among the measuring points 1–4 at a different convective tube pass are small. The temperature of measuring point 8 at the bottom of the cylinder is the lowest. Obviously, the driving force of the flow field is weak in this traditional cylinder arrangement. So, it took about 4 h for the test to reach a thermal equilibrium condition in the experiment. The start-up of the gas heater was very slow. This indicates the necessity to enhance the efficiency inside the cylinder with modified structures.

A simple and effective heat-transfer improvement option is to install vertical guide plates along the cylinder's axial path. Subsequently, fluid flow and heat transfer using vertical guide plates of various heights are simulated. The vertical plates are 5 mm thick carbon steel plates. The heights of four plates are compared (350, 450, 550, and 650 mm). As a heating medium, still water is employed.

The temperature and flow fields of the gas heater with a 350 mm vertical guide plate positioned at the upper part are shown in **Figures 6A,B**. High-temperature zones emerge on the top half of the flue tube bundle and upper left side of the fire tube, as shown in **Figure 6A**. The water near the flue tube bundle generates an ascending flow that shifts to the left and right; the water near the third and fourth convective tube bundles forms a descending flow, as demonstrated in **Figure 6B**. The temperature variations among the multireturn of convective tube bundles will cause these two flows to collide and be impacted.

The temperature and flow fields of 450 mm with a vertical guide plate are shown in **Figures 7A,B**. High-temperature zones arise on the upper part of the flue tube bundle and the upper left side of the fire tube, which can be seen in **Figure 7A**. Those affections between the first and fourth returns of the convective tube bundle may be observed in **Figure 7B**.

Figures 8A,B depict the temperature and flow fields of a 550 mm vertical guide plate. High-temperature zones can be seen on the top of the fire tube and flue tube bundle in **Figure 8A**. Under the diversion of the vertical plate, two flow fields from the center to two sides are generated on the left and right sides of the circular cross-section in the cylinder independently, thus eliminating the collision phenomena.

The temperature and flow fields of a 650 mm vertical guide plate are shown in **Figures 9A,B**. High-temperature zones can be seen on the top-right side of the flue tube bundle and fire tube in **Figure 9A**. Although two flow fields are generated on both the left and right sides of the circular section in **Figure 9B**, due to the conflict of opposing water flows, a number of swirl zones are formed, which are not ideal for convective heat transfer.

Figure 10 shows the impact of the vertical guide plate on total heat transfer rates in the convective tube bundle and temperature at the measuring points around the convective tube bundle. Water temperatures surrounding the convective tube bundle without the use of a guide plate are much greater than in circumstances when vertical guide plates are employed. As a result, the construction of the gas heater must be optimized. Due to the varied heights of vertical

guide plates, there were differences in the temperature distribution around the multireturn passes of the convective tube bundle. Installing vertical guide plates can lower the overall heat transfer rate of the convective tube bundle by 1.49%–2.04% when heating the gas to the desired temperature. The vertical guide plate with a height of 550 mm has the lowest total heat transfer rate in the convective tube bundle.

The natural convection heat transfer rates and radiation heat transfer rates for various plate heights are shown in **Figure 11**. The effect of installing vertical plates on the participating medium radiation is less due to the small temperature difference among the multireturn of the convective tube bundle, but the proportion of radiation heat transfer in the total heat transfer rate still reaches 25.1% by using the vertical guide plate structure, indicating that the part of water radiation is not negligible.

CONCLUSION

The simulated results in this study demonstrated the feasibility and advantages of a heat transfer structure within a gas heater by using vertical guide plates installed along the axial direction of the large cylinder to improve the overall coupled heat transfer efficiency, overcoming the weakness that an effective hot circulating flow field cannot be formed around the cold gas tube inside the conventional gas heater.

REFERENCES

- Aghanajafi, C., and Abjadpour, A. (2016). Discrete Ordinates Method Applied to Radiative Transfer Equation in Complex Geometries Meshed by Structured and Unstructured Grids. *J. Braz. Soc. Mech. Sci. Eng.* 38 (3), 1007–1019. doi:10.1007/s40430-015-0397-2
- Al-Sammerrai, D. (1985). Study of Thermal Stabilities of Some Heat Transfer Oils. *J. Therm. Anal.* 30 (4), 763–770. doi:10.1007/BF01913304
- Atashafrooz, M., and Gandjalikhan Nassab, S. A. (2013). Simulation of Laminar Mixed Convection Recess Flow Combined with Radiation Heat Transfer. *Iranian J. Sci. Techn.* 37 (M1), 71–75.
- Atashafrooz, M., Nassab, S. A. G., and Lari, K. (2015). Application of Full-Spectrum K-Distribution Method to Combined Non-gray Radiation and Forced Convection Flow in a Duct with an Expansion. *J. Mech. Sci. Technol.* 29 (2), 845–859. doi:10.1007/s12206-015-0148-4
- Cimina, S., Wang, C., Wang, L., Niro, A., and Sunden, B. (2015). Experimental Study of Pressure Drop and Heat Transfer in a U-bend Channel with Various Guide Vanes and Ribs. *J. Enh. Heat Transf.* 22 (1), 29–45. doi:10.1615/jenhheattransf.2015013382
- Gao, B.-H., Qi, H., Yin, Y.-M., Wei, L.-Y., and Ren, Y.-T. (2019). Fast Reconstructing Two-Dimensional Temperature Distribution in Participating Media with Different Surfaces Conditions. *Infrared Phys. Techn.* 103, 103080. doi:10.1016/j.infrared.2019.103080
- Guo, Y., Cao, W.-W., Yan, P., Yu, C.-X., and Qian, S.-Y. (2011). Application and Research Progress of Heater in Natural Gas Industry. *Heat Transfer Eng.* 32, 1003–1008. doi:10.1080/01457632.2011.556473
- Guo, Y., Cao, W. W., Yan, P., and Qian, S. Y. (2009). Exploration and Development of Natural Gas Heaters with High Fuel Efficiency. *J. Nat. Gas Ind.* 29 (12), 97–100. doi:10.3787/j.issn.1000-0976.2009.12.030
- Guo, Y., and Guo, Z. (2016a). Flow and Heat Transfer inside a New Diversion-type Gas Heating Device. *Numer. Heat Transfer, Part A: Appl.* 70 (1), 1–13. doi:10.1080/10407782.2016.1173441
- Guo, Y., and Guo, Z. X. (2016b). *A Numerical Study on 2-D Flow and Heat Transfer in A Natural Gas Heater*, 2. Washington, DC: ASME Summer Heat Trans. Conf.
- Guo, Y. (2012). Investigation on Natural Gas Heater with Different Heat-Transfer Medium. *J. Chem. Industry Eng. Prog.* 6, 1206–1214.
- Installing vertical guide plates in the midst of the convective tube bundle's left and right passes might improve natural convection heat transfer while having a minor impact on water radiation. The total heat transfer rate in the convective tube bundle may be lowered by 1.49%–2.04%. The employment of the vertical guide plate with a height of 550 mm is the optimized case.

DATA AVAILABILITY STATEMENT

The raw data supporting the conclusion of this article will be made available by the authors, without undue reservation.

AUTHOR CONTRIBUTIONS

All authors listed have made a substantial, direct and intellectual contribution to the work, and approved it for publication.

FUNDING

This research paper is supported by the China National Natural Science Foundation (No. 51606116) and Shanghai Scientific and Technological Research Projects (No. 19195810800).

- Guo, Z. (1999). Enhancement of Heat and Mass Transfer in Metal Hydride Beds with the Addition of Al Plates. *Heat Mass. Transfer* 34, 517–523. doi:10.1007/s002310050290
- Kim, M. Y., and Baek, S. W. (1997). Analysis of Radiative Transfer in Cylindrical Enclosures Using the Finite Volume Method. *J. Thermophys. Heat Transfer* 11 (2), 246–252. doi:10.2514/2.6229
- Li, Q. F., and Zhang, G. Z. (2007). Optimal Structural Design of Oil Field Water Bathed Heater. *J. China Univ. Pet.* 31, 114–118. doi:10.3321/j.issn:1000-5870.2007.03.024
- Li, S., and Wang, Y. H. (2019). Transient Simulation and the Minimum Reversal Time of High Temperature Air Combustion in Oil-Field Jacket Heater. *J. East. China Univ. Sci. Techn.* 1, 1–12. doi:10.14135/j.cnki.1006-3080.20180723008
- Razzaque, M. M., Howell, J. R., and Klein, D. E. (1984). Coupled Radiative and Conductive Heat Transfer in a Two-Dimensional Rectangular Enclosure with Gray Participating Media Using Finite Elements. *J. Heat Trans.* 106 (106), 613–619. doi:10.1115/1.3246723
- Setoodeh, H., Keshavarz, A., Ghasemian, A., and Nasouhi, A. (2016). Subcooled Flow Boiling of Ethylene-Glycol/water Mixture in an Inclined Channel with A Hot Spot: An Experimental Study. *Int. Commun. Heat Mass Transfer* 78, 285–294. doi:10.1016/j.icheatmasstransfer.2016.09.020
- Smith, T. F., Shen, Z. F., and Friedman, J. N. (1982). Evaluation of Coefficients for the Weighted Sum of Gray Gases Model. *J. Heat Trans.* 104 (4), 602–608. doi:10.1115/1.3245174
- Su, H. P. (2013). Glycol-water Solution for Heating Process in Oil-Gas Gathering and Transportation. *J. Petrochem. Ind. Appl.* 32 (4), 97–100. doi:10.3969/j.issn.1673-5285.2013.04.026
- Sun, J. J., Yang, J., and Wang, L. L. (2011). Influence Factors of Structure Optimization of Water Jacket Furnace. *J. Oil Gas Field Surface Eng.* 4, 91. doi:10.3969/j.issn.1006-6896.2011.4.044
- Sun, J., Yi, H. L., and Tan, H. P. (2016). Meshless Finite Difference Method for Radiative Transfer in Participating Media. *J. Eng. Phys. Thermophys.* 37 (3), 653–656.
- Wang, Z. (2017). Numerical Study of Natural Gas Water Bath Heater. [Master's thesis]. Qing dao City (Shan dong Province): China University of Petroleum.
- Wu, Z., Shi, Y., Song, K., He, S., and Gao, M. (2019). Numerical Simulation of Heat Transfer Performance Enhancement of Cooling Water Jacket Used in the Carbon Industry. *J. Enh. Heat Transf.* 26 (3), 235–255. doi:10.1615/JEnhHeatTransf.2019029345

- Yuan, B., Yang, D. M., Wang, Y., and Wang, J. R. (2001). Gas Supply Technology for Combustion Gas Generating Unit. *J. Oil-Gas Field Surf. Eng.* 20 (2), 30–32.
- Zhukova, Y. V., and Isaev, S. A. (2008). Numerical Simulation of Laminar Flow of Oil and Heat Transfer Near a Circular Cylinder with Arched Guide Plates. *J. Eng. Phys. Thermophy* 81, 732–738. doi:10.1007/s10891-008-0086-4

Conflict of Interest: ZZ is employed by Shanghai Petrochemical Co., Ltd.

The remaining authors declare that the research was conducted in the absence of any commercial or financial relationships that could be construed as a potential conflict of interest.

Publisher's Note: All claims expressed in this article are solely those of the authors and do not necessarily represent those of their affiliated organizations, or those of the publisher, the editors and the reviewers. Any product that may be evaluated in this article, or claim that may be made by its manufacturer, is not guaranteed or endorsed by the publisher.

Copyright © 2022 Guo, Zhang and Zhou. This is an open-access article distributed under the terms of the Creative Commons Attribution License (CC BY). The use, distribution or reproduction in other forums is permitted, provided the original author(s) and the copyright owner(s) are credited and that the original publication in this journal is cited, in accordance with accepted academic practice. No use, distribution or reproduction is permitted which does not comply with these terms.



Application of the Material Balance Equation Based on the BET Multimolecular Fractal Theory in a Shale Gas Reservoir

Tingting Qiu, Shuyong Hu and Jiayi Zhang*

State Key Laboratory of Oil and Gas Reservoir Geology and Development Engineering, Southwest Petroleum University, Chengdu, China

OPEN ACCESS

Edited by:

Lin Teng,
Fuzhou University, China

Reviewed by:

Yang Xiao,
Xi'an University of Science and
Technology, China
Muhammad Wakil Shahzad,
Northumbria University,
United Kingdom

*Correspondence:

Jiayi Zhang
yixingjatie@163.com

Specialty section:

This article was submitted to
Advanced Clean Fuel Technologies,
a section of the journal
Frontiers in Energy Research

Received: 06 December 2021

Accepted: 21 March 2022

Published: 26 April 2022

Citation:

Qiu T, Hu S and Zhang J (2022)
Application of the Material Balance
Equation Based on the BET
Multimolecular Fractal Theory in a
Shale Gas Reservoir.
Front. Energy Res. 10:829800.
doi: 10.3389/fenrg.2022.829800

During shale gas reservoir development, obtaining actual formation pressure is challenging; therefore, it is challenging to obtain a single well production allocation using the current formation pressure based on a productivity equation. Different shale gas reservoirs with different rock adsorption properties and the traditional Langmuir isotherm adsorption equations are not accurate in describing the adsorption properties of shale gas reservoirs, causing significant errors. BET multimolecular adsorption, considering the shale gas surface fractal dimension theory to describe the adsorption properties, can describe the adsorption surface as a multimolecular layer and regard adsorption using a fractal dimension, describing the adsorption property of shale gas more accurately. According to the core adsorption test data and theory, the actual BET multimolecular adsorption is established by considering the shale gas surface fractal dimension. Therefore, the actual material balance equation was obtained using the theory, establishing the relationship between the formation pressure and cumulative shale gas production. A time-independent distribution and cumulative gas production chart were formed using the productivity equation. Consequently, the material balance equation, which takes advantage of the BET multimolecular fractal theory, was conducted. This allocation production method obtained from the material balance equation has significant importance in shale gas development.

Keywords: Langmuir isotherm adsorption equation, BET multimolecular adsorption, fractal dimension, material balance equation, allocation production method

Abbreviations: A and B, coefficient of binomial productivity equation and dimensionless parameter; B_g , natural gas volume factor, m^3/m^3 ; B_{gi} , original volume factor of shale gas, m^3/m^3 ; B_w , formation water volume factor, m^3/m^3 ; C, constant related to the energy of adsorption and liquefaction; C_m , shale rock compressibility factor of the matrix system, MPa^{-1} ; C_f , rock compressibility factor of the fracture system, MPa^{-1} ; C_w , formation water compressibility factor of the shale gas reservoir, MPa^{-1} ; D_s , —fractal dimension of the adsorption surface; G_f , surface free volume of the shale gas reservoir fracture system, m^3 ; G_m , surface free volume of the shale gas reservoir matrix system, m^3 ; M, —salinity of formation water, mg/L ; n, adsorption layer of the gas surface; N_1 , adsorption capacity of layer One; N_i , adsorption capacity of layer i; p_0 , saturated vapor pressure, MPa ; P_{cd} , critical desorption pressure, MPa ; P_i , original formation pressure, MPa ; P_s , pressure, $MPa \times 10$; R_s , natural gas solubility in the formation water, m^3/m^3 ; R_{si} , original formation water solubility of the shale gas reservoir, m^3/m^3 ; S_{wf} , water saturation of the shale gas reservoir fracture system, %; T, temperature, $^{\circ}C$; V_s , single well control volume of the shale rock, m^3 ; x, relative pressure $\frac{p}{p_0}$, MPa/MPa ; ρ_s , density of shale, g/cm^3 .

INTRODUCTION

Shale gas reserves comprised free, adsorbed, and dissolved gases, of which free and adsorbed gases are the main parts (Taghavinejad et al., 2020); (Mengal and Wattenbarger, 2011); (Huang and Zhao, 2017); (Boadu, 2000); (Sanyal et al., 2006); (Curtis, 2002); (Jenkins and Boyer, 2008). In this regard, the study of shale gas adsorption behavior is significant to reservoir volume calculation and development (Huang and Zhao, 2017); (Shao et al., 2017); (Wu et al., 2015). Currently, the Langmuir isotherm, BET equations, and other modified Langmuir and BET equations predominantly describe the adsorption behavior (Li et al., 2020); (Jaroniec et al., 1989); (Zhang et al., 2015). The classic Langmuir equation assumes that methane is monolayer-adsorbed, and the surface of the adsorbent is homogeneous with constant adsorption heat (Langmuir, 1918); (Langmuir, 2015). The adsorption behavior of shale gas is complex, and Langmuir's isotherm adsorption equation is too ideal and cannot describe it accurately. The BET adsorption theory considers the adsorption surface as a multilayer, and the adsorption capacity of every layer is the same (Myers, 1968); (Brunauer et al., 1940); (Zhou et al., 2019); (Myers and Prausnitz, 1965); (Ritter and Yang, 1987); (Dang et al., 2020). To simulate the enrichment and production of methane in shale gas reservoirs, an accurate gas adsorption model is critically required (Chareonsuppanimit et al., 2012), (Clarkson and Haghsheenas, 2013), (Huang et al., 2018a). Fortunately, the BET multi-molecular fractal theory, considering the surface fractal dimension of shale gas, can describe adsorption more accurately by considering the multilayer and fractal dimension of shale gas adsorption (Brunauer et al., 1938), (Wang et al., 2022), (Chai et al., 2019), (Zheng et al., 2019), (Wang et al., 2016), (Fan and Liu, 2021). Therefore, the material balance equation can enhance the accuracy of future reservoir prediction about reserves and formation pressure based on the adsorption theory (Zhang et al., 2017), (Canel and Rosbaco, 2006), (Fianu et al., 2019).

Ambrose et al. (2012), (Xiong et al., 2021), and (Memon et al., 2020) combined the Langmuir adsorption isotherm with the volume for free gas and formulated a new gas-in-place equation accounting for the pore space occupied by the adsorbed phase; however, the adsorption surface layer and fractal dimension were not considered (Pang et al., 2019). The material balance equation proposed by Daniel et al. (Orozco and Aguilera, 2015) simultaneously considered stress-dependent porosity and permeability, free gas, adsorbed gas, and dissolved gas but also excluded the adsorption surface layer and fractal dimension. Usually, the material balance equation combined with the shale gas productivity equation is used to calculate the reservoir reserves and conduct the relevant model for predicting the production rate and formation pressure versus time (Sun et al., 2019), (Gu et al., 2014), (Hu et al., 2019). The shale gas well allocation is usually based on this method to carry out well productivity tests (Deng et al., 2014), (Wheaton, 2019). According to the test, the shale gas well binomial productivity formula is determined. If the present reservoir pressure is calculated by the material balance equation, then the actual open flow capacity of a single well can be calculated. The reasonable gas well allocation is also determined. Nevertheless,

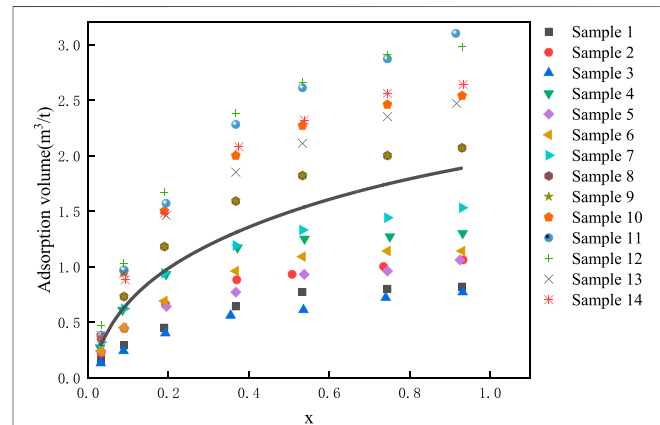


FIGURE 1 | Actual isotherm adsorption curve of shale gas Block XX.

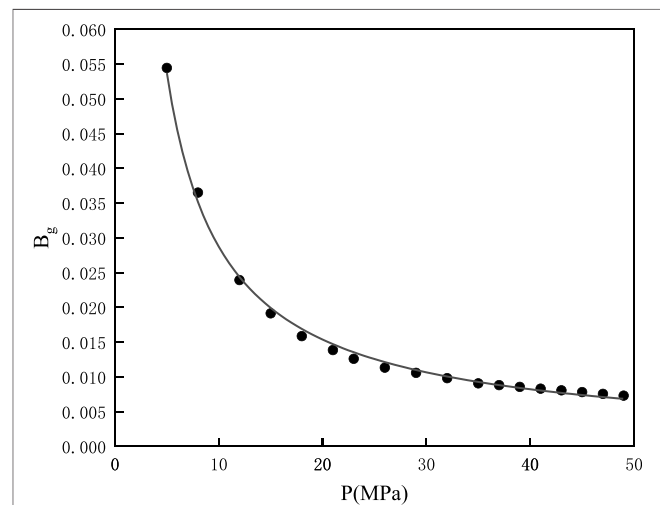


FIGURE 2 | Curve of the gas volume factor versus formation pressure of shale gas Block XX.

practical reservoir production requires convenient and efficient allocation progress. The aforementioned method aims at a certain moment, is complex, and cannot satisfy the practical production needs. Therefore, finding an efficient and convenient shale gas allocation method for the whole well life is necessary.

Huang et al. (2018b) proposed a new method. Shale reservoirs were depicted by the De Swaan dual porosity model, where the secondary and hydraulic fractures were characterized by discrete units to conduct the shale gas well productivity equation. This method can calculate more efficiently than the Eclipse simulator. Furthermore, it can describe the complex fracture network more correctly even though the calculating process and single shale gas well allocation of every production moment are complex. Sang et al. (2014) used a numerical model considering desorption and adsorption processes to establish and solve, under polar coordinates and Laplace space, respectively, predicting the

TABLE 1 | Test data of shale gas Block XX.

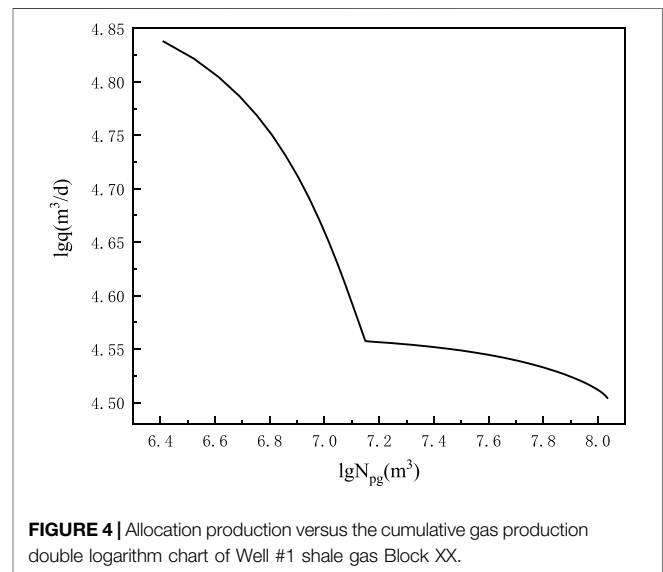
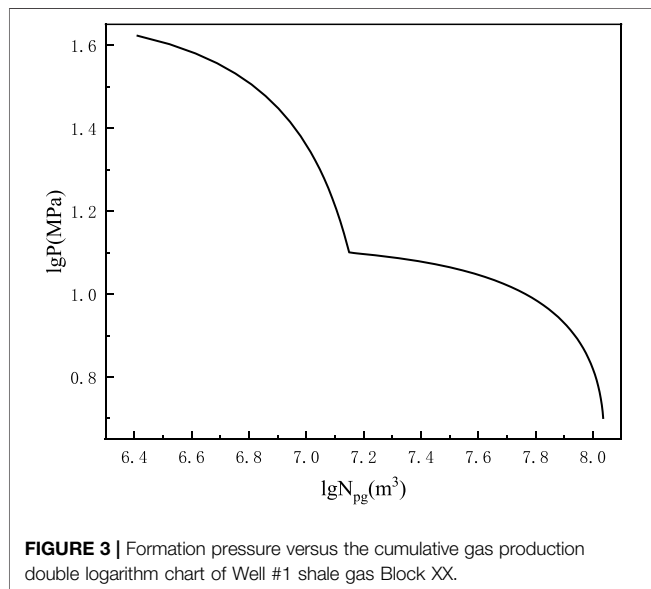
Sample	Pressure (MPa)	Adsorption volume (m ³ /t)	Sample	Pressure (MPa)	Adsorption volume (m ³ /t)
Sample 1	0.38	0.16	Sample 8	0.38	0.36
	1.04	0.29		1.04	0.73
	2.21	0.45		2.21	1.18
	4.28	0.64		4.28	1.59
	6.21	0.77		6.21	1.82
	8.67	0.8		8.67	2
Sample 2	10.83	0.82	Sample 9	10.83	2.07
	0.38	0.22		0.38	0.36
	1.05	0.44		1.04	0.73
	2.25	0.66		2.21	1.18
	4.31	0.88		4.28	1.59
	5.91	0.93		6.21	1.82
Sample 3	8.56	1	Sample 10	8.67	2
	10.86	1.06		10.83	2.07
	0.37	0.13		0.38	0.38
	1.03	0.24		1.04	0.95
	2.24	0.4		2.21	1.5
	4.13	0.56		4.28	2
Sample 4	6.24	0.61	Sample 11	6.21	2.27
	8.62	0.72		8.67	2.46
	10.85	0.77		10.83	2.54
	0.35	0.27		0.38	0.47
	1	0.61		1.04	1.03
	2.26	0.93		2.21	1.67
Sample 5	4.33	1.17	Sample 12	4.28	2.38
	6.27	1.25		6.21	2.66
	8.74	1.27		8.67	2.91
	10.85	1.3		10.83	2.98
	0.38	0.24		0.38	0.47
	1.04	0.45		1.04	1.03
Sample 6	2.27	0.64	Sample 13	2.21	1.67
	4.28	0.77		4.28	2.38
	6.26	0.93		6.21	2.66
	8.67	0.96		8.67	2.91
	10.77	1.06		10.83	2.98
	0.38	0.24		0.38	0.38
Sample 7	1.04	0.45	Sample 14	1.04	0.94
	2.21	0.69		2.26	1.46
	4.28	0.96		4.28	1.85
	6.21	1.09		6.21	2.11
	8.67	1.14		8.67	2.35
	10.83	1.14		10.67	2.47
	0.38	0.32		0.38	0.36
	1.04	0.62		1.08	0.88
	2.21	0.94		2.21	1.48
	4.28	1.19		4.37	2.08
	6.21	1.33		6.26	2.32
	8.67	1.44		8.67	2.56
	10.83	1.53		10.86	2.64

productivity of volume-fractured horizontal wells in shale gas reservoirs. This model can predict the production rate versus time, but the allocation production of the single well cannot be obtained. At present, the existing allocation methods combining the material balance equation with productivity formula cannot offer well the allocation of well life and satisfy the convenience of practical allocation apart from numeric simulation, decline analysis, and so on (Huang et al., 2018b); (Arps, 1945). As for the adsorption of shale gas reservoirs, we adopted the BET multi-molecular fractal theory. Creatively,

we developed a material balance equation based on the BET multi-molecular fractal theory, considering the dissolved gas of the formation water. Furthermore, we combined this new material balance equation with the productivity equation to obtain single well allocation production versus cumulative gas production for the well life cycle. As a result, we can offer the shale gas development worker an allocation plate, and there is no need for paying attention to complex equations about the well and gas reservoir properties. In a word, this method can not only calculate the adsorption gas volume but also propose

TABLE 2 | Formation physics and fluid property of Well #1 shale gas Block XX.

Parameter	Symbol	Unit	Value	Parameter classification
Surface-free volume of the shale gas reservoir matrix system	G_m	m^3	$G_m + G_f = 1.97 \times 10^7$	Shale gas geological parameter
Surface-free volume of the shale gas reservoir fracture system	G_f	m^3		
Original volume factor of shale gas	B_{gi}	m^3/m^3	0.0069	
Formation water compressibility factor of the shale gas reservoir	C_w	Mpa^{-1}	0.000453	
Shale rock compressibility factor of the matrix system	C_m	Mpa^{-1}	0.000419	
Original formation water solubility of the shale gas reservoir	R_{si}	m^3/m^3	0.647887	
Original formation pressure	P_i	MPa	48.6	
Water saturation of the shale gas reservoir fracture system	S_{wf}	%	45	
Rock compressibility factor of the fracture system	C_f	Mpa^{-1}	0.000419	
Formation water volume factor	B_w	m^3/m^3	0.993262	
Density of shale	ρ_s	g/cm^3	2.65	
Critical desorption pressure	P_{cd}	MPa	12.58	
Single well control volume of the shale rock	V_S	m^3	$4,382 \times 10^4$	
Natural gas volume factor	B_g	m^3/m^3	Variable	Shale gas geological parameter
Present solubility of formation water	R_s	m^3/m^3	Variable	
Coefficient of the binomial productivity equation	A	Dimensionless parameter	1.8633×10^{-8}	Test parameter
Coefficient of the binomial productivity equation	B	Dimensionless parameter	5.78×10^{-3}	



a convenient and fast life cycle allocation method for shale gas reservoirs.

MATERIAL BALANCE EQUATION OF A SHALE GAS WELL BASED ON THE BET MULTI-MOLECULAR FRACTAL THEORY

The material balance equation of the confining shale gas reservoir was established by considering the reservoir as a fracture-matrix dual system and the dissolved gas in the formation water to obtain the chart of shale gas dynamic allocation production. Furthermore, the BET multimolecular and fractal adsorption theory described the gas adsorption behavior.

The Actual Isotherm Adsorption Curve of Shale Gas Block XX

Brunauer et al. (1940) proposed the BET multimolecular adsorption theory in 1940, and it was an addition to the Langmuir monolayer molecular adsorption equation. The assumption of the BET multimolecular adsorption theory is as follows:

- 1) The gas adsorption is multimolecular, and it does not have to cover the first layer completely and then the second.
- 2) The heat of adsorption (E_i) of the first layer is a certain value; the other is the liquefaction heat (E_L) of the adsorbate.
- 3) The adsorption and desorption of the adsorbate are exposed on the surface of the gas phase directly.

Consequently, the BET multimolecular adsorption expression is described in Eq. 1.

$$\frac{V}{V_m} = \frac{Cx[1 - (n+1)x^n + nx^{n+1}]}{(1-x)[1 + (C-x) - Cx^{n+1}]} \quad (1)$$

In the equation, x is the relative pressure $\frac{P}{P_0}$, P_0 is the saturated vapor pressure, n is the adsorption layer of the gas surface, and C is the constant related to the energy of adsorption and liquefaction.

Eq. 2 shows the relationship of the adsorption capacity between layers i and One proposed by Fripiat et al., (1986) and (Zhou et al., 2019) based on numeric simulation.

$$f_i = \frac{N_i}{N_1} = i^{-(D_s-2)} \quad (2)$$

In Eq. 2, D_s is the fractal dimension of the adsorption surface, N_1 is the adsorption capacity of layer One, and N_i is the adsorption capacity of layer i . Therefore, the BET multimolecular adsorption, considering the fractal dimension of the adsorption surface expression, was obtained as Eq. 3.

$$V = \frac{V_m C \sum_{i=1}^n i^{2-D_s} \sum_{j=i}^n x^j}{1 + C \sum_{i=1}^n x^i} \quad (3)$$

According to Eq. 3, the actual isotherm adsorption curve of shale gas Block XX can be obtained by regression, as shown in Eq. 4, and Figure 1 shows the curve. The gas adsorption test data is showed in Table 1. According to the regression results, we obtained the following conclusions. The adsorption volume of shale gas Block XX was 1.19924 m³/t, and the constant related to the energy of adsorption and liquefaction was 9.86193, based on the fractal dimension 2.5 and the layer of surface molecular adsorption 3 (Figure 1).

$$V = 1.19924 \frac{9.86193 \times \left[\frac{P}{P_0} + \left(\frac{P}{P_0}\right)^2 + \left(\frac{P}{P_0}\right)^3 + 2^{2-2.5} \left(\left(\frac{P}{P_0}\right)^2 + \left(\frac{P}{P_0}\right)^3\right) + 3^{2-2.5} \left(\frac{P}{P_0}\right)^3 \right]}{1 + 9.86193 \times \left[\left(\frac{P}{P_0}\right) + \left(\frac{P}{P_0}\right)^2 + \left(\frac{P}{P_0}\right)^3 \right]} \quad (4)$$

Material Balance Equation of Shale Gas Block XX

The assumption of the material balance equation of shale gas Block XX is as follows:

- 1) The shale gas reservoir is an isotherm system; in other words, the reservoir temperature is unchanged during exploitation.
- 2) The water saturation of the matrix and fracture system is different.
- 3) There is no formation of water to be produced.

According to the principle of the material balance equation, the underground volume of the produced shale gas comprised

underground expansion, including free gas, formation water, rock, dissolved gas of formation water underground volume variation of the matrix, and fracture system. For the shale gas reservoir, it included the underground adsorption gas volume variation of the matrix system. When the shale gas reservoir proceeded to desorption, the material balance equation was as shown in Eq. 5.

$$\begin{aligned} G_{pg} B_g &= G_m (B_g - B_{gi}) + G_m B_{gi} \frac{C_w S_{mui}}{1 - S_{mui}} (P_i - P) + \\ &G_m B_{gi} \frac{C_m}{1 - S_{mui}} (P_i - P) + \frac{G_m B_{gi}}{(1 - S_{mui}) B_w} S_{mui} (R_{si} - R_s) B_g + \\ &G_f (B_g - B_{fi}) + G_f B_{fi} \frac{C_w S_{fui}}{1 - S_{fui}} (P_i - P) + \\ &G_f B_{fi} \frac{C_f}{1 - S_{fui}} (P_i - P) + \frac{G_f B_{fi}}{(1 - S_{fui}) B_w} S_{fui} (R_{si} - R_s) B_g \\ &+ \rho_s V_s \left\{ C \left[\frac{P_{cd}}{P_0} + \left(\frac{P_{cd}}{P_0}\right)^2 + \left(\frac{P_{cd}}{P_0}\right)^3 + 2^{2-D_s} \left(\left(\frac{P_{cd}}{P_0}\right)^2 + \left(\frac{P_{cd}}{P_0}\right)^3\right) \right] \right. \\ &\left. + 3^{2-D_s} \left(\frac{P_{cd}}{P_0}\right)^3 \right] \frac{V_m}{1 + C \left[\frac{P}{P_0} + \left(\frac{P}{P_0}\right)^2 + \left(\frac{P}{P_0}\right)^3 \right]} \right. \\ &\left. C \left[\frac{P}{P_0} + \left(\frac{P}{P_0}\right)^2 + \left(\frac{P}{P_0}\right)^3 + 2^{2-D_s} \left(\left(\frac{P}{P_0}\right)^2 + \left(\frac{P}{P_0}\right)^3\right) \right] \right. \\ &\left. + 3^{2-D_s} \left(\frac{P}{P_0}\right)^3 \right] \frac{V_m}{1 + C \left[\frac{P}{P_0} + \left(\frac{P}{P_0}\right)^2 + \left(\frac{P}{P_0}\right)^3 \right]} \right\} \end{aligned} \quad (5)$$

The high-pressure fluid parameter testing of shale gas Block XX regressed the relationship between the gas volume factor and formation pressure. Eq. 6 shows the function, and Figure 2 shows the curve of the gas volume factor versus the formation pressure.

$$B_g = 0.22919 P^{-0.902} \quad (6)$$

The empirical formula of the formation water property is as suggested by Yuanqian (Chen, 1990) and (Myers and Prausnitz, 1965), as shown in Eq. 7.

$$\begin{aligned} R_s = (T, M, P) &= -3.1670 \times 10^{-10} T^2 \times M + 1.997 \times 10^{-8} T \times M \\ &+ 1.0635 \times 10^{-10} P_s^2 \times M - 9.7764 \times 10^{-8} P_s \times M + 2.9745 \times 10^{-10} T \times P_s \times M \\ &+ 1.6230 \times 10^{-4} T^2 - 2.7879 \times 10^{-2} T - 2.0587 \times 10^{-5} P_s^2 \\ &+ 1.7323 \times 10^{-2} P_s + 9.5233 \times 10^{-6} T \times P_s + 1.1937. \end{aligned} \quad (7)$$

In the equation, R_s is the natural gas solubility in the formation water (m³/m³). T is the temperature (°C). P_s is the pressure (MPa $\times 10$), and M is the salinity of formation water (mg/L).

PRACTICAL MATERIAL BALANCE EQUATION OF SHALE GAS BLOCK XX

Based on the BET multimolecular adsorption theory equation (Eq. 4) of shale gas Block XX, the practical material balance equation of the shale gas Block XX can be established by considering the dissolved gas of formation water and adsorption of shale gas. The practical material balance

TABLE 3 | Cumulative gas production versus the formation pressure and single well allocation production.

Cumulative gas production (m ³)	Formation pressure (MPa)	Allocation (m ³ /d)
2,560,459	42	68,913
3,336,274	40	66,310
4,112,330	38	63,735
4,888,812	36	61,191
5,665,926	34	58,684
6,443,905	32	56,218
7,223,014	30	53,799
8,003,557	28	51,432
8,785,884	26	49,127
9,570,407	24	46,891
10,357,608	22	44,735
10,752,390	21	43,691
11,148,069	20	42,672
11,544,735	19	41,680
11,942,493	18	40,716
12,341,457	17	39,782
12,741,758	16	38,882
13,143,541	15	38,016
13,546,976	14	37,189
13,952,255	13	36,401
14,116,546	12.6	36,098
14,676,689	12.55	36,060
15,045,356	12.53	36,045
15,596,469	12.5	36,023
17,421,447	12.4	35,949
21,040,933	12.2	35,802
24,626,119	12	35,656
28,175,327	11.8	35,513
31,686,804	11.6	35,371
35,158,721	11.4	35,231
38,589,165	11.2	35,093
41,976,138	11	34,957
45,317,553	10.8	34,823
48,611,233	10.6	34,691
51,854,902	10.4	34,560
55,046,184	10.2	34,432
58,182,599	10	34,306
61,261,559	9.8	34,182
64,280,362	9.6	34,060
67,236,190	9.4	33,940
70,120,077	9.2	33,822
72,940,198	9	33,706
75,688,122	8.8	33,593
78,360,507	8.6	33,481
80,953,874	8.4	33,372
83,464,591	8.2	33,265
85,888,877	8	33,161
88,222,791	7.8	33,058
90,462,228	7.6	32,958
92,602,913	7.4	32,860
94,640,393	7.2	32,765
96,570,033	7	32,671
98,387,010	6.8	32,581
100,086,302	6.6	32,492
101,662,682	6.4	32,406
103,110,711	6.2	32,323
104,424,729	6	32,242
105,598,839	5.8	32,163
106,626,904	5.6	32,087
107,502,526	5.4	32,013
108,219,034	5.2	31,942
108,769,462	5	31,873

equation of Well #1 Block XX was obtained from Eq. 8 by substituting Eqs 6 and 7 into Eq. 5.

$$\begin{aligned}
 G_{pg} \times 0.22919P^{-0.902} &= G_m(0.22919P^{-0.902} - B_{gi}) + \\
 G_m B_{gi} \frac{C_w S_{mwi}}{1 - S_{mwi}} (P_i - P) &+ G_m B_{gi} \frac{C_m}{1 - S_{mwi}} (P_i - P) + \\
 \frac{G_m B_{gi}}{(1 - S_{mwi}) B_w} S_{mwi} &\left(R_{si} - \begin{pmatrix} 3.1670 \times 10^{-10} T^2 \times M + 1.997 \times 10^{-8} T \times M + \\ 1.0635 \times 10^{-10} P_s^2 \times M - 9.7764 \times 10^{-8} P_s \times M + \\ 2.9745 \times 10^{-10} T \times P_s \times M + 1.6230 \times 10^{-4} T^2 - \\ 2.7879 \times 10^{-2} T - 2.0587 \times 10^{-5} P_s^2 + \\ 1.7323 \times 10^{-2} P_s + 9.5233 \times 10^{-6} T \times P_s + 1.1937 \end{pmatrix} \right) \\
 0.22919P^{-0.902} &+ G_f(0.22919P^{-0.902} - B_{gi}) + G_f B_{gi} \frac{C_w S_{fwi}}{1 - S_{fwi}} (P_i - P) + \\
 G_f B_{gi} \frac{C_f}{1 - S_{fwi}} (P_i - P) &+ \frac{G_f B_{gi}}{(1 - S_{fwi}) B_w} S_{fwi} \\
 \left(R_{si} - \begin{pmatrix} 3.1670 \times 10^{-10} T^2 \times M + 1.997 \times 10^{-8} T \times M + \\ 1.0635 \times 10^{-10} P_s^2 \times M - 9.7764 \times 10^{-8} P_s \times M + \\ 2.9745 \times 10^{-10} T \times P_s \times M + 1.6230 \times 10^{-4} T^2 - \\ 2.7879 \times 10^{-2} T - 2.0587 \times 10^{-5} P_s^2 + \\ 1.7323 \times 10^{-2} P_s + 9.5233 \times 10^{-6} T \times P_s + 1.1937 \end{pmatrix} \right) &\times \\
 \left[\frac{P_{cd}}{P_0} + \left(\frac{P_{cd}}{P_0} \right)^2 + \left(\frac{P_{cd}}{P_0} \right)^3 + \right. & \\
 C \left[2^{2-D_s} \left(\left(\frac{P_{cd}}{P_0} \right)^2 + \left(\frac{P_{cd}}{P_0} \right)^3 \right) + \right. & \\
 \left. \left. 3^{2-D_s} \left(\frac{P_{cd}}{P_0} \right)^3 \right] \right] & \\
 V_m \left[\frac{1 + C \left[\frac{P}{P_0} + \left(\frac{P}{P_0} \right)^2 + \left(\frac{P}{P_0} \right)^3 \right]}{1 + C \left[\frac{P}{P_0} + \left(\frac{P}{P_0} \right)^2 + \left(\frac{P}{P_0} \right)^3 \right]} \right] & \\
 0.22919P^{-0.902} + \rho_s V_s &\left. \left[\frac{P}{P_0} + \left(\frac{P}{P_0} \right)^2 + \left(\frac{P}{P_0} \right)^3 + \right. \right. \\
 C \left[2^{2-D_s} \left(\left(\frac{P}{P_0} \right)^2 + \left(\frac{P}{P_0} \right)^3 \right) + \right. & \\
 \left. \left. 3^{2-D_s} \left(\frac{P}{P_0} \right)^3 \right] \right] & \\
 1 + C \left[\frac{P}{P_0} + \left(\frac{P}{P_0} \right)^2 + \left(\frac{P}{P_0} \right)^3 \right] & \left. \right\}.
 \end{aligned} \quad (8)$$

According to the formation of physics and fluid properties (Table 2), the practical material balance equation can be established, and a double logarithm chart (allocation versus cumulative gas production) can be obtained. Therefore, the allocation of a single shale gas well can be calculated according to the cumulative gas production using the chart in the progress of shale gas exploitation.

From the productivity test data, the gas well productivity equation was as in Eq. 9.

$$P^2 - P_{wf}^2 = Aq^2 + Bq. \quad (9)$$

The 1/5 times of the gas well open flow was often used as the allocation *in situ* production; therefore, the production allocation formula was as in Eq. 10.

$$q = \frac{1}{5} \cdot \left(\frac{-B + \sqrt{B^2 + 4A(P^2 - 0.1^2)}}{2A} \right). \quad (10)$$

CASE STUDY

As the description of the practical material balance equation of shale gas Block XX, at first, the shale gas material balance equation is conducted, considering multimolecular fractal adsorption about the single shale gas well. Second, the binomial productivity equation is obtained by regressing the productivity test data. Third, cumulative gas productivity is substituted into the first step regarding the material balance equation in order to obtain the present reservoir pressure. Fourth, the pressure is substituted into the second step productivity equation, and the single well allocation can be calculated. Finally, the abovementioned steps are repeated, and then, the allocation plate allocation production versus cumulative gas production double logarithm is drawn. According to the plate, the practical allocation process is guided quickly. The specific procedures are as follows.

Figures 3, 4 and Table 3 show the cumulative gas production chart versus formation pressure and single well production allocation chart taking advantage of Eqs 8–10.

By viewing the cumulative gas production in Figure 4, the allocation production can be obtained. Through analysis, in Figure 3, the decrease in the formation pressure on the cumulative gas production was gentle, and the allocation on cumulative gas production decreased similar to that in Figure 4 when the shale gas reservoir entered desorption. Thus, the formation pressure can keep well after desorption, and shale gas had a long dependable crop time.

CONCLUSION

Based on the practical BET multimolecular adsorption, considering the fractal dimension of the adsorption surface, a production allocation chart about Well #1 shale gas Block XX can be established using the material balance equation. The conclusions are as follows:

- 1) The adsorption volume of the shale gas Block XX was 1.19924 m³/t, and the constant related to the energy of adsorption and liquefaction was 9.86193, based on the fractal dimension 2.5 and the layer of surface molecular adsorption 3.
- 2) According to the production allocation chart of Well #1 shale gas Block XX, before the shale gas reservoir entered the desorption, the desorption pressure decreased faster, and the cumulative gas production increased slowly. However, when the reservoir entered the desorption stage, the decrease in the formation pressure was gentle, despite the low formation pressure. Furthermore, the shale gas production allocation can maintain a certain time, indicating that most

shale gas of the production well was exploited during the desorption stage.

DATA AVAILABILITY STATEMENT

The original contributions presented in the study are included in the article/Supplementary Material, further inquiries can be directed to the corresponding author.

AUTHOR CONTRIBUTIONS

TQ: responsible for the main writing of the thesis and the derivation of the formula. SH: responsible for guiding

the author's research and revision of the manuscript. JZ: responsible for the provision of experimental data and email communication.

FUNDING

This work was supported by the National Science and Technology Major Project “Zhaotong Shale Gas Exploration and Development Demonstration Project-Comprehensive Mountain Shale Gas Well Productivity Evaluation and Production System Optimization and Application” (Grant No. 2017ZX05063005-019) and The National Natural Science Fund (No. 51574199) administered by the National Natural Science Foundation of China.

REFERENCES

- Ambrose, R. J., Hartman, R. C., Diaz-Campos, M., Akkutlu, I. Y., and Sondergeld, C. H. (2012). Shale Gas-In-Place Calculations Part I: New Pore-Scale Considerations. *SPE J.* 17, 219–229. doi:10.2118/131772-PA
- Arps, J. J. (1945). Analysis of Decline Curves. *Trans.* 160, 228–247. doi:10.2118/945228-G
- Boadu, F. K. (2000). Predicting the Transport Properties of Fractured Rocks from Seismic Information: Numerical Experiments. *J. Appl. Geophys.* 44 (2–3), 103–113. doi:10.1016/S0926-9851(99)00020-8
- Brunauer, S., Deming, L. S., Deming, W. E., and Teller, E. (1940). On a theory of the van der Waals adsorption of gases. *J. Am. Chem. Soc.* 62, 1723–1732. doi:10.1021/ja01864a025
- Brunauer, S., Emmett, P. H., and Teller, E. (1938). Adsorption of Gases in Multimolecular Layers. *J. Am. Chem. Soc.* 60 (2), 309–319. doi:10.1021/ja01269a023
- Canel, C. A., and Rosbaco, J. (2006). “Compositional Material Balance: its Application to the Development of an Oil and Gas Field with Retrograde Condensation,” in Paper SPE 23647 presented at the Second Latin American Petroleum Engineering Conference, Caracas, Venezuela, January 01, 1992. 117–128 March. doi:10.2118/23647-MS
- Chai, D., Yang, G., Fan, Z., and Li, X. (2019). Gas Transport in Shale Matrix Coupling Multilayer Adsorption and Pore Confinement Effect. *Chem. Eng. J.* 370, 1534–1549. doi:10.1016/j.cej.2019.03.276
- Chareonsuppanimit, P., Mohammad, S. A., Robinson, R. L., and Gasem, K. A. M. (2012). High-pressure Adsorption of Gases on Shales: Measurements and Modeling. *Int. J. Coal Geology.* 95, 34–46. doi:10.1016/j.coal.2012.02.005
- Chen, Y. (1990). The Property of Formation Water Relevant Empirical Equation. *Well Test. Prod. Technology* 11 (3), 31–33.
- Clarkson, C. R., and Haghsheenas, B. (2013). “Modeling of Supercritical Fluid Adsorption on Organic-Rich Shales and Coal,” in Paper SPE 164532 presented at Unconventional Resources Conference-USA held in The Woodlands, Texas, USA, April 2013. doi:10.2118/164532-ms
- Curtis, J. B. (2002). Fractured Shale-Gas Systems. *AAPG Bull.* 86 (11), 1921–1938. doi:10.1306/61eaddbe-173e-11d7-8645000102c1865d
- Dang, W., Zhang, J., Nie, H., Wang, F., Tang, X., Wu, N., et al. (2020). Isotherms, Thermodynamics and Kinetics of Methane-Shale Adsorption Pair under Supercritical Condition: Implications for Understanding the Nature of Shale Gas Adsorption Process. *Chem. Eng. J.* 383, 123191. doi:10.1016/j.cej.2019.123191
- Deng, J., Zhu, W., and Ma, Q. (2014). A New Seepage Model for Shale Gas Reservoir and Productivity Analysis of Fractured Well. *Fuel* 124, 232–240. doi:10.1016/j.fuel.2014.02.001
- Fan, L., and Liu, S. (2021). A Novel Experimental System for Accurate Gas Sorption and its Application to Various Shale Rocks. *Chem. Eng. Res. Des.* 165, 180–191. doi:10.1016/j.cherd.2020.10.034
- Fianu, J., Gholinezhad, J., and Hassan, M. (2019). Application of Temperature-dependent Adsorption Models in Material Balance Calculations for Unconventional Gas Reservoirs. *Heliyon* 5 (5), e01721. doi:10.1016/j.heliyon.2019.e01721
- Fripiat, J. J., Gattineau, L., and Van Damme, H. (1986). Multilayer Physical Adsorption on Fractal Surfaces. *Langmuir* 2 (5), 562–567. doi:10.1021/la00071a006
- Gu, N., Zhu, X., and Xing, L. (2014). Oil and Gas Field Development. *Nat. Gas oil* 32 (6), 50–58.
- Hu, S., Hu, X., He, L., and Chen, W. (2019). A New Material Balance Equation for Dual-Porosity Media Shale Gas Reservoir. *Energ. Proced.* 158, 5994–6002. doi:10.1016/j.egypro.2019.01.520
- Huang, H., Sun, W., Xiong, F., Chen, L., Li, X., Gao, T., et al. (2018). A Novel Method to Estimate Subsurface Shale Gas Capacities. *Fuel* 232, 341–350. doi:10.1016/j.fuel.2018.05.172
- Huang, S., Ding, G., Wu, Y., Huang, H., Lan, X., and Zhang, J. (2018). A Semi-analytical Model to Evaluate Productivity of Shale Gas wells with Complex Fracture Networks. *J. Nat. Gas Sci. Eng.* 50, 374–383. doi:10.1016/j.jngse.2017.09.010
- Huang, X., and Zhao, Y.-P. (2017). Characterization of Pore Structure, Gas Adsorption, and Spontaneous Imbibition in Shale Gas Reservoirs. *J. Pet. Sci. Eng.* 159 (159), 197–204. doi:10.1016/j.petrol.2017.09.010
- Jaroniec, M., Lu, X., Madey, R., and Choma, J. (1989). Extension of the Langmuir Equation for Describing Gas Adsorption on Heterogeneous Microporous Solids. *Langmuir* 5 (3), 839–844. doi:10.1021/la00087a044
- Jenkins, C. D., and Boyer, C. M., II (2008). Coalbed- and Shale-Gas Reservoirs. *J. Pet. Technology* 60 (2), 92–99. doi:10.2118/103514-JPT
- Langmuir, I. (1918). The Adsorption of Gases on Plane Surfaces of Glass, Mica and Platinum. *J. Am. Chem. Soc.* 40 (9), 1361–1403. doi:10.1063/1.492960910.1021/ja02242a004
- Langmuir, I. (2015). The Adsorption of Gases on Plane Surfaces of Glass, Mica and Platinum. *J. Am. Chem. Soc.* 40 (12), 1361–1403.
- Li, J., Lu, S., Zhang, P., Cai, J., Li, W., Wang, S., et al. (2020). Estimation of Gas-In-Place Content in Coal and Shale Reservoirs: A Process Analysis Method and its Preliminary Application. *Fuel* 259, 116266. doi:10.1016/j.fuel.2019.116266
- Memon, A., Li, A., Jacqueline, N., Kashif, M., and Ma, M. (2020). Study of Gas Sorption, Stress Effects and Analysis of Effective Porosity and Permeability for Shale Gas Reservoirs. *J. Pet. Sci. Eng.* 193, 107370. doi:10.1016/j.petrol.2020.107370
- Mengal, S. A., and Wattenbarger, R. A. (2011). “Accounting for Absorbed Gas in Shale Gas Reservoirs,” in Paper SPE 141085 presented at SPE Middle East Oil and Gas Show and Conference, Manama, Bahrain, 25–28 September (MS). doi:10.2118/141085
- Myers, A. L. (1968). Adsorption of Gas Mixtures-A Thermodynamic Approach. *Ind. Eng. Chem.* 60 (5), 45–49. doi:10.1021/ie50701a007
- Myers, A. L., and Prausnitz, J. M. (1965). Thermodynamics of Mixed-Gas Adsorption. *Aiche J.* 11 (1), 121–127. doi:10.1002/aic.690110125
- Orozco, Daniel., and Aguilera, Roberto. (2015). “A Material Balance Equation for Stress-Sensitive Shale Gas Reservoirs Considering the Contribution of Free,

- Adsorbed and Dissolved Gas,” in Paper SPE-175964-MS presented at SPE/CSUR Unconventional Resources Conference held in Calgary, Alberta, Canada, October 2015. 10.2118/175964-MS. doi:10.2118/175964-ms
- Pang, Y., Tian, Y., Soliman, M. Y., and Shen, Y. (2019). Experimental Measurement and Analytical Estimation of Methane Absorption in Shale Kerogen. *Fuel* 240, 192–205. doi:10.1016/j.fuel.2018.11.144
- Ritter, J. A., and Yang, R. T. (1987). Equilibrium Adsorption of Multicomponent Gas Mixtures at Elevated Pressures. *Ind. Eng. Chem. Res.* 26 (8), 1679–1686. doi:10.1021/ie00068a032
- Sang, Y., Chen, H., Yang, S., Guo, X., Zhou, C., Fang, B., et al. (2014). A New Mathematical Model Considering Adsorption and Desorption Process for Productivity Prediction of Volume Fractured Horizontal wells in Shale Gas Reservoirs. *J. Nat. Gas Sci. Eng.* 19, 228–236. doi:10.1016/j.jngse.2014.05.009
- Sanyal, D., Ramachandrarao, P., and Gupta, O. P. (2006). A Fractal Description of Transport Phenomena in Dendritic Porous Network. *Chem. Eng. Sci.* 61 (2), 307–315. doi:10.1016/j.ces.2005.06.0010.1016/j.ces.2005.06.005
- Shao, X., Pang, X., Li, Q., Wang, P., Chen, D., Shen, W., et al. (2017). Pore Structure and Fractal Characteristics of Organic-Rich Shales: A Case Study of the Lower Silurian Longmaxi Shales in the Sichuan Basin, SW China. *Mar. Pet. Geology*. 80, 192–202. doi:10.1016/j.marpetgeo.2016.11.025
- Sun, H., Wang, H., Zhu, S., Nie, H., Liu, Y., Li, Y., et al. (2019). Reserve Evaluation of High Pressure and Ultra-high Pressure Reservoirs with Power Function Material Balance Method. *Nat. Gas Industry B* 6 (5), 509–516. doi:10.1016/j.ngib.2019.03.007
- Taghavinejad, A., Sharifi, M., Heidaryan, E., Liu, K., and Ostadhasan, M. (2020). Flow Modeling in Shale Gas Reservoirs: a Comprehensive Review. *J. Nat. Gas Sci. Eng.* 83, 103535. doi:10.1016/j.jngse.2020.103535
- Wang, P., Jiang, Z., Ji, W., Zhang, C., Yuan, Y., Chen, L., et al. (2016). Heterogeneity of Intergranular, Intraparticle and Organic Pores in Longmaxi Shale in Sichuan Basin, South China: Evidence from SEM Digital Images and Fractal and Multifractal Geometries. *Mar. Pet. Geology*. 72, 122–138. doi:10.1016/j.marpetgeo.2016.01.020
- Wang, Y., Cheng, H., Hu, Q., Liu, L., Jia, L., Gao, S., et al. (2022). Pore Structure Heterogeneity of Wufeng-Longmaxi Shale, Sichuan Basin, China: Evidence from Gas Physisorption and Multifractal Geometries. *J. Pet. Sci. Eng.* 208, 109313. doi:10.1016/j.petrol.2021.109313
- Wheaton, R. (2019). Modeling of Gas Flow in Fractured Shale. *Upstream Oil Gas Technology* 1, 100001. doi:10.1016/j.upstre.2020.100001
- Wu, K., Chen, Z., and Li, X. (2015). Real Gas Transport through Nanopores of Varying Cross-Section Type and Shape in Shale Gas Reservoirs. *Chem. Eng. J.* 281, 813–825. doi:10.1016/j.cej.2015.07.012
- Xiong, F., Rother, G., Gong, Y., and Moortgat, J. (2021). Reexamining Supercritical Gas Adsorption Theories in Nano-Porous Shales under Geological Conditions. *Fuel* 287, 119454. doi:10.1016/j.fuel.2020.119454
- Zhang, C.-Y., Chai, X.-S., and Xiao, X.-M. (2015). A Simple Method for Correcting for the Presence of Minor Gases when Determining the Adsorbed Methane Content in Shale. *Fuel* 150, 334–338. doi:10.1016/j.fuel.2015.02.050
- Zhang, W., Xu, J., Jiang, R., Cui, Y., Qiao, J., Kang, C., et al. (2017). Employing a Quad-Porosity Numerical Model to Analyze the Productivity of Shale Gas Reservoir. *J. Pet. Sci. Eng.* 157, 1046–1055. doi:10.1016/j.petrol.2017.07.031
- Zheng, S., Yao, Y., Liu, D., Cai, Y., Liu, Y., and Li, X. (2019). Nuclear Magnetic Resonance T2 Cutoffs of Coals: A Novel Method by Multifractal Analysis Theory. *Fuel* 241, 715–724. doi:10.1016/j.fuel.2018.12.044
- Zhou, S., Zhang, D., Wang, H., and Li, X. (2019). A Modified BET Equation to Investigate Supercritical Methane Adsorption Mechanisms in Shale. *Mar. Pet. Geology*. 105, 284–292. doi:10.1016/j.marpetgeo.2019.04.036

Conflict of Interest: The authors declare that the research was conducted in the absence of any commercial or financial relationships that could be construed as a potential conflict of interest.

Publisher’s Note: All claims expressed in this article are solely those of the authors and do not necessarily represent those of their affiliated organizations, or those of the publisher, the editors, and the reviewers. Any product that may be evaluated in this article, or claim that may be made by its manufacturer, is not guaranteed or endorsed by the publisher.

Copyright © 2022 Qiu, Hu and Zhang. This is an open-access article distributed under the terms of the Creative Commons Attribution License (CC BY). The use, distribution or reproduction in other forums is permitted, provided the original author(s) and the copyright owner(s) are credited and that the original publication in this journal is cited, in accordance with accepted academic practice. No use, distribution or reproduction is permitted which does not comply with these terms.



OPEN ACCESS

EDITED BY

Jiang Bian,
China University of Petroleum,
Huadong, China

REVIEWED BY

Guangchun Song,
China University of Petroleum, China
Shiyuan Zhan,
Chengdu University of Technology,
China

*CORRESPONDENCE

Chao Yang,
yangchao201001@163.com

SPECIALTY SECTION

This article was submitted to Advanced
Clean Fuel Technologies,
a section of the journal
Frontiers in Energy Research

RECEIVED 26 July 2022

ACCEPTED 13 September 2022

PUBLISHED 05 January 2023

CITATION

Yang C, Han Q, Liu H, Wang Y and
Cheng R (2023), Ignition characteristics
of methane-air mixture at low
initial temperature.
Front. Energy Res. 10:1003470.
doi: 10.3389/fenrg.2022.1003470

COPYRIGHT

© 2023 Yang, Han, Liu, Wang and
Cheng. This is an open-access article
distributed under the terms of the
[Creative Commons Attribution License](#)
(CC BY). The use, distribution or
reproduction in other forums is
permitted, provided the original
author(s) and the copyright owner(s) are
credited and that the original
publication in this journal is cited, in
accordance with accepted academic
practice. No use, distribution or
reproduction is permitted which does
not comply with these terms.

Ignition characteristics of methane-air mixture at low initial temperature

Chao Yang*, Qing Han, Haibo Liu, Yuanyuan Wang and
Ran Cheng

Shengli Oilfield, Dongying, China

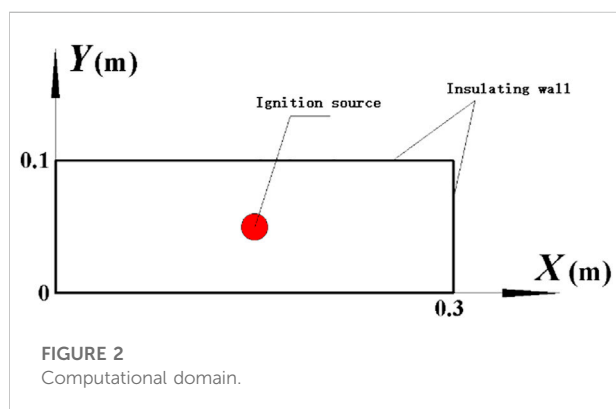
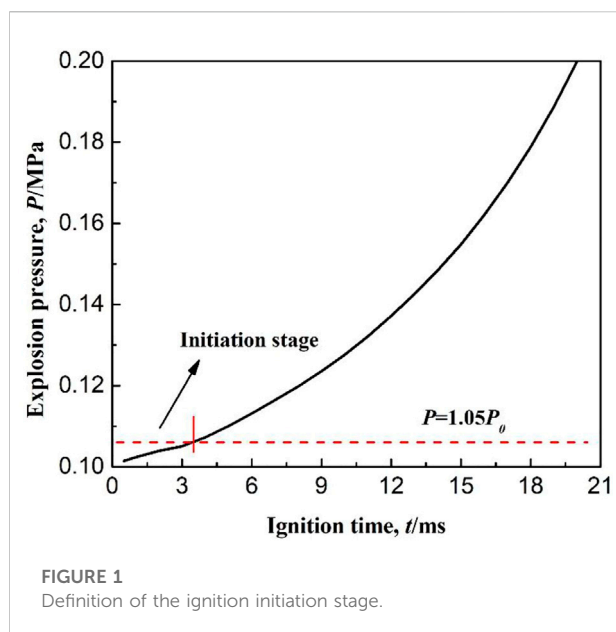
In this paper, FLUENT software coupled with the chemical reaction mechanism is used to study the ignition characteristics of methane-air mixtures at low temperature. Variations of the main free radical concentrations, the critical conditions for a successful ignition and the chemical reaction rate of each elementary reaction for a failure ignition are obtained, respectively. Results indicate that the consumption of methane immediately affects the concentration distribution of carbon monoxide, which presents the opposite relationship with that of methane. Mass fractions of the intermediate products and H, O free radicals are low in the burnt zone and unburnt zone, whereas reach the maximum on the flame front. OH is not only the intermediate free radical, but also the combustion product remained by the intermediate reactions. At a low temperature of 150 K, the critical radius and temperature of methane ignition are 4.6 mm and 1180 K, respectively. When ignition radius is smaller than the critical value, the failed ignition of methane is caused by the termination of the elementary reactions: R8: $H + O_2 = OH + O$, R9: $OH + O = O_2 + H$, R12: $O + H_2O = 2OH$ and R13: $2OH = O + H_2O$. However, when ignition temperature is lower than the critical value, because of the failed initiation of elementary reaction R1: $CH_4 = CH_3 + H$, the combustion of methane is not occurred.

KEYWORDS

methane, ignition, free radicals, critical conditions, elementary reactions, low temperature

1 Introduction

With an attention to environmental protection and increased energy demand all over the world, and the increasingly shortage of traditional energy such as oil, the development and utilization of liquid natural gas (LNG) and oxygen-bearing coal-bed methane have shown significant economic and social benefits (Gao et al., 2010; Hammond and Grady, 2017; Mikolajkov et al., 2017; Song et al., 2017). However, in the LNG storage and low temperature liquefaction of oxygen-bearing coal-bed methane, the methane concentration in the gas phase is within the explosion limit, which has an explosion risk and results in significant economic losses and casualties (Cui et al., 2015). At present, some experts at home and abroad have conducted some research on the combustion



characteristics of combustible gases at low temperatures. Karim et al. (1984) built a cylindrical stainless steel tube, and experimentally measured the lower flammability limit of methane at initial temperature of 143–298 K. Wierzbza et al. (1990) used the same experimental device to measure the upper flammability limit of combustible gases at normal pressure and low temperature. The temperature condition was from room temperature to 213 K. Then, Wierzbza et al. (1992) measured the flammability limits of hydrogen and some fuel mixtures at low temperature. Among, the initial temperature range for the upper flammability limits was from room temperature to 213 K, while for the lower flammability limits was from room temperature to 173 K. Li et al. (2011) from the Chinese Academy of Science have experimentally measured the flammability limits of different methane/nitrogen mixtures at a temperature range from 150 to 300 K. In recent years, our research team built an explosion test setup which was able to withstand a temperature as low as 113 K, and conducted a methane explosion experiment at

different low initial temperatures of 123–273 K, different initial pressure of 0.1–0.9 MPa and different equivalence ratios. The flammability limit and the MIE of methane at low initial temperatures were obtained (Cui et al., 2016a; Cui et al., 2016b).

To sum up, the above research results are focused on macroscopic explosion characteristics, such as flammability limits, minimum ignition energy, explosion pressure, and temperature. However, the characteristics of the ignition source itself is rarely studied. For the combustion process of methane in a confined vessel, it can be regarded as an unsteady hydrodynamic phenomenon with detailed chemical reactions. The ignition initiation stage is the beginning of the combustion, accompanied by the rapid growth of the flame kernel and the occurrence of a large number of chemical chain reactions. The current study does not give the critical value for a successful ignition. Moreover, variations in concentrations of reactants, products, and free radicals generated by chemical reactions are also not involved. Therefore, focusing on the ignition initiation characteristics of combustible gases has important implications for clarifying the nature of ignition.

For the combustion process of combustible gases, the most intuitive and effective way of research is experimental measurement. However, during the experiment, all the parameters that can be measured immediately are the macroscopic phenomena of combustion: combustion temperature and pressure, flame propagation speed, variations of flame shape and so on. However, some microscopic features such as variations of the detailed chemical reactions, critical values for ignition and the flow field during the flame propagation are hardly presented by experiment. Moreover, due to the special nature of low-temperature conditions, it is difficult to set a transparent observation window on the combustion vessel (caused by the cooling method and icing at low temperatures). Therefore, it is difficult to study the combustion of methane under low temperature conditions using experimental method. Numerical simulation is an important tool for studying the effect of some factors on the combustion characteristics which are hardly test or controlled by experimental method. Some researchers have studied the ignition characteristics by numerical methods. Yuasa et al. (2002) studied the influence of the energy retention on the minimum ignition energy using a two-dimensional numerical analysis. Kravchik and Sher (1994) studied ignition characteristic and flame propagation in methane/air mixture by numerical methods. Han et al. (2010) studied the spark ignition characteristics of methane/air mixture using detailed chemical reaction mechanisms. The ignition behavior of a hydrogen/air mixture was also studied by them using the same numerical model while heat loss was considered (Han et al., 2011). In Cui et al. (2018) study, premixed methane-air flame propagation in a confined vessel at low initial temperature was simulated using a multi-step chemical reaction mechanism. As explained above, the numerical simulation method can effectively study the combustion characteristics of combustible gas.

TABLE 1 Chemical kinetics mechanism of methane.

Component:CH₄, CH₃, CH, CH₂O, CO₂, CO, H₂, H, O₂, O, OH, H₂O

Primitive reaction	A	b	E(kJ/mol)
R1: CH ₄ = CH ₃ + H	4.23E + 15	0	455.06
R2: CH ₄ + OH = CH ₃ + H ₂ O	2.00E + 14	0	35.21
R3: CH ₄ + O = CH ₃ + OH	3.48E + 13	0	35.08
R4: CH ₄ + H = CH ₃ + H ₂	4.35E + 14	0	57.53
R5: CH ₃ + O ₂ = CH ₂ O + OH	5.29E + 11	0	7.12
R6: CH ₂ O + OH = CO + H ₂ O + H	5.87E + 14	0	20.43
R7: CO + OH = CO ₂ +H	1.45E + 14	0	994.78
R8: H + O ₂ = OH + O	2.24E + 14	0	70.34
Duplicate			
R9: OH + O = O ₂ + H	1.71E + 13	0	3.64
Duplicate			
R10: O + H ₂ = OH + H	1.74E + 13	0	39.56
Duplicate			
R11: OH + H=O + H ₂	7.70E + 12	0	31.74
Duplicate			
R12: O + H ₂ O = 2OH	5.75E + 13	0	75.78
Duplicate			
R13: 2OH = O + H ₂ O	5.38E + 12	0	43.96
Duplicate			
R14: OH + H ₂ = H ₂ O + H	2.19E + 13	0	21.56
Duplicate			
R15: H ₂ O + H=H ₂ +OH	8.41E + 13	0	84.15
Duplicate			
R16: H + OH + M = H ₂ O + M	2.00E + 19	-1.0	0
H ₂ /0.73/H ₂ O/3.65/CH ₄ /2.00/			
R17: O + O + M = O ₂ +M	8.90E + 14	-0.5	0
H ₂ /2.40/H ₂ O/15.40/CH ₄ /2.00/CO/1.75/CO ₂ /3.60/			
R18: H + H + M = H ₂ +M	1.00E + 18	-1.0	0
H ₂ /0.00/H ₂ O/0.00/CH ₄ /2.00/CO ₂ /0.00/			
R19: CH ₃ + O = CH + H ₂ O	2.80E + 08	0	0
R20: CH + O ₂ = CO + OH	6.00E + 10	0	0

Note: The corresponding rate expression in the table is: $k = AT^b \exp(-E/RT)$. Among them, k is the reaction rate, A is the pre-factor, b is the temperature index, and E is the activation energy. M in the elementary reaction represents the third body, Duplicate indicates that this elementary reaction is repeated in the detailed chemical reaction mechanism, but the values of each parameter are different.

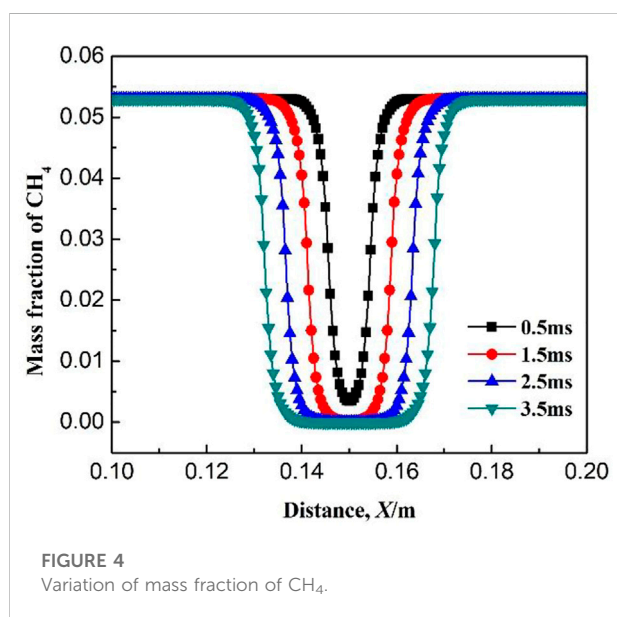
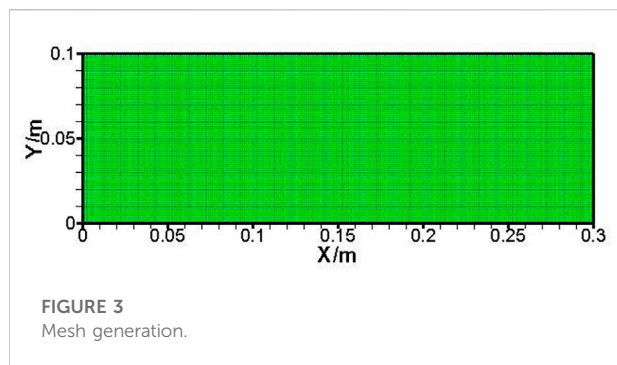
Therefore, in this paper, FLUENT software coupled with the chemical reaction mechanism is used to study the initiation process of methane combustion at low temperature. The variations of the main free radical concentrations during the growth of flame kernel are obtained. The critical ignition radius and critical ignition temperature for a successful ignition at low temperature are also calculated. Through the study on the chemical reaction rate of each elementary reaction for a failed ignition, the elementary reactions which induce the termination of the chemical reaction are obtained. The research results have important safety significance for LNG storage and low-temperature liquefaction production of oxygen-containing coalbed methane. In addition, the research results can be used for the research and development of LNG fire extinguishing agents, which can achieve

the purpose of extinguishing fire by interrupting the chemical reaction chain of methane combustion at low temperature.

2 Numerical methods

2.1 Definition of the initiation stage of methane combustion

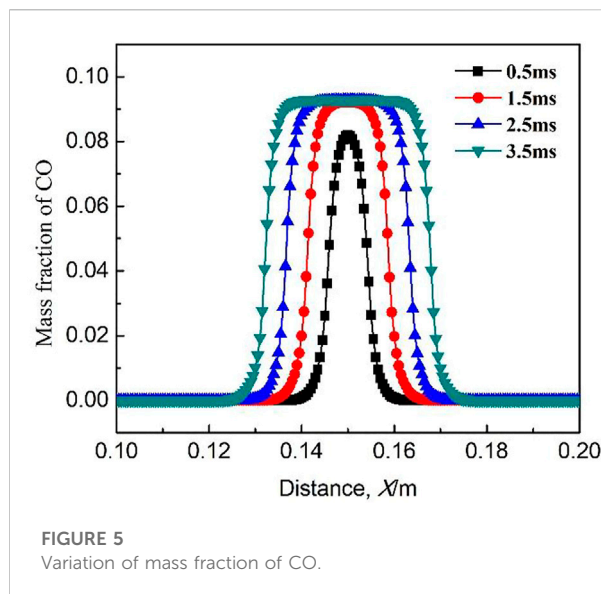
According to the standard BS EN 1839:2003, an explosion is considered to occur when the pressure rise in the confined vessel is 5% of the initial pressure. Based on this criterion, the initiation stage of methane combustion is defined as following: from the



moment of ignition, to the end when the combustion pressure at the center of the right end wall of the confined space increases by 5% of the initial pressure. As shown in Figure 1, the black solid line shows the variation of explosion pressure with ignition time. The red dashed line indicates that the explosion pressure is 1.05 times of the initial pressure. The intersection of the red dashed line and the black solid line is the moment when explosion occurs. The stage between the start of ignition and the moment when explosion occurs is the initiation stage of methane combustion. As seen from the figure, the ignition initiation period is from 0 to 3.5 ms.

2.2 Mathematical model

The equations describing the methane combustion at low temperatures are completely consistent with those previously published in Ref. (Cui et al., 2018), which are not repeated here. The ignition problem in the central axis of a cylindrical vessel can be



considered as a central symmetry problem centered on the axis. Because of the large amount of 3D simulation calculations, the model is simplified to a two-dimensional problem, which has been proved to be effective to model the flame propagation (Dunn-Rankin et al., 1988; Marra and Continillo, 1996; Kaltayev et al., 2000; Xiao et al., 2014). The size of the computational domain is exactly the same with the explosion vessel used in the literature (Cui et al., 2016a; Cui et al., 2016b), as also shown in Figure 2. In the figure, X represents the height direction of the cylindrical explosion vessel, and Y represents the diameter direction of the cylindrical explosion vessel. In the process of simulation, the size of the grid directly affects the accuracy of the calculation results and the calculation time. Therefore, before the calculation, the size of the grid should be studied first to obtain the optimal one, as shown in Figure 3. The study on grid optimization in this paper is consistent with that in the previously published paper (Cui et al., 2018) which will not be repeated here.

2.3 Chemical kinetics mechanism

In this paper, the eddy dissipation concept (EDC) model is chosen for solving because fluid dynamics calculation is coupled with chemical reaction mechanism. A simplified chemical kinetics mechanism are imported in FLUENT software for related calculations, as shown in Table 1 (Hu et al., 2000).

2.4 Initial and boundary conditions

For the combustion problem in a small confined space, we believe that the combustion is completed in an extremely short time. Therefore, the four walls of the model shown in Figure 2 are

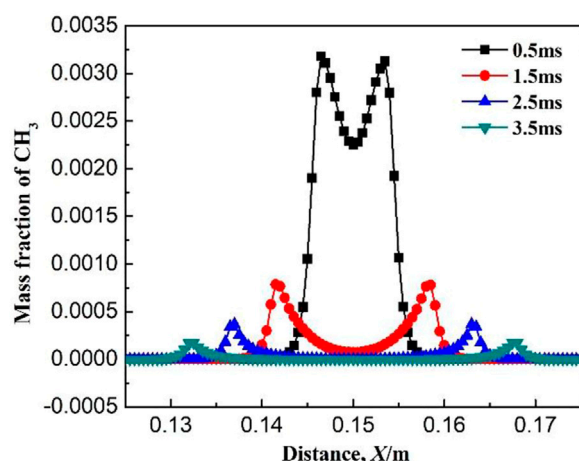


FIGURE 6
Variation of mass fraction of CH_3 .

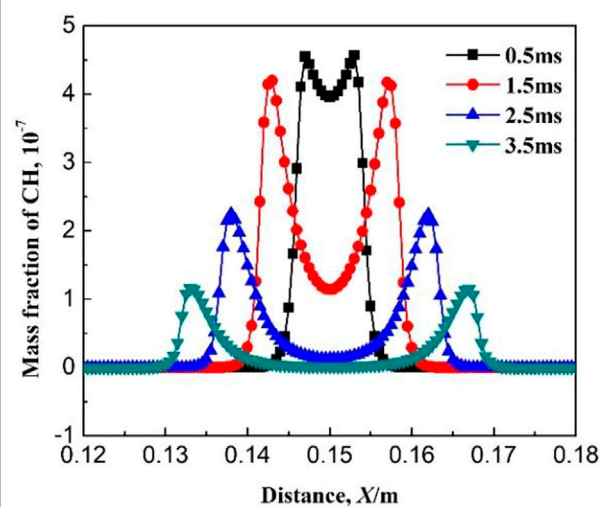


FIGURE 8
Variation of mass fraction of CH .

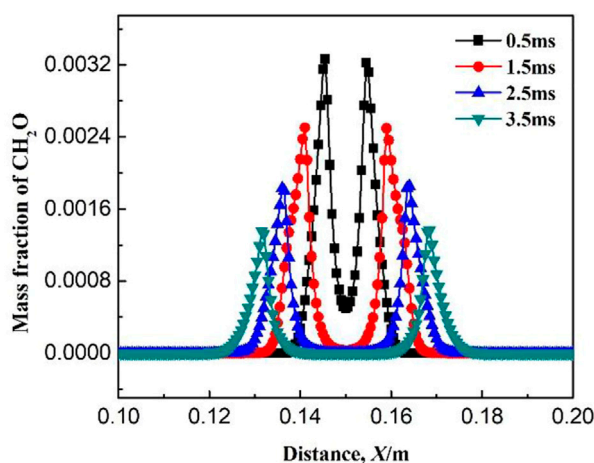


FIGURE 7
Variation of mass fraction of CH_2O .

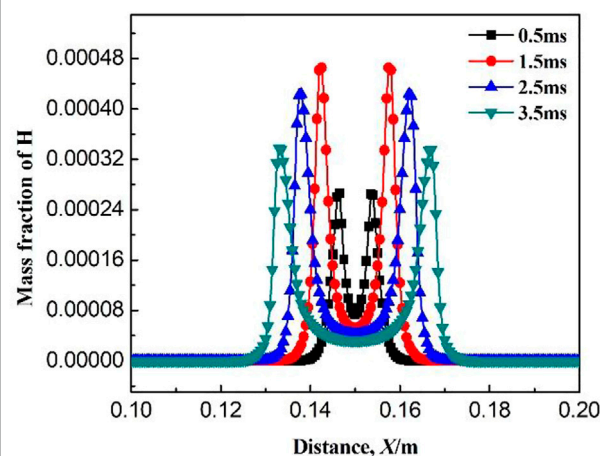


FIGURE 9
Variation of mass fraction of H .

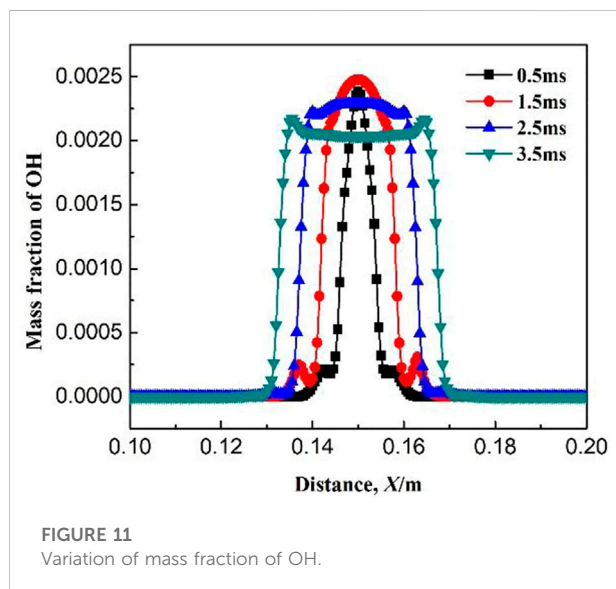
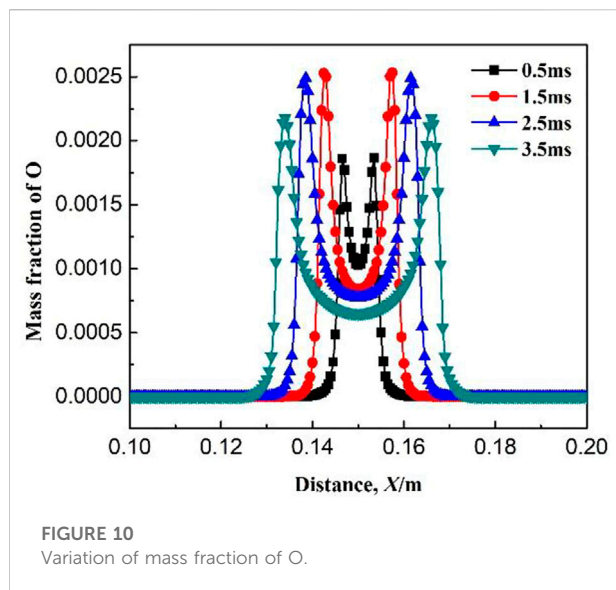
all set as adiabatic boundaries. The initial pressure is 0.1 MPa and the initial temperature is 150 K. When the equivalence ratio is 1, the mass fraction of methane is 0.053, mass fraction of oxygen is 0.21, mass fraction of nitrogen is automatically calculated in FLUENT and mass fractions of remaining components are all zero. The initial speeds in X and Y directions are also zero.

2.5 Ignition treatment

In this paper, the ignition source is set to a high temperature air mass instead of the actual spark. A circular zone is first created

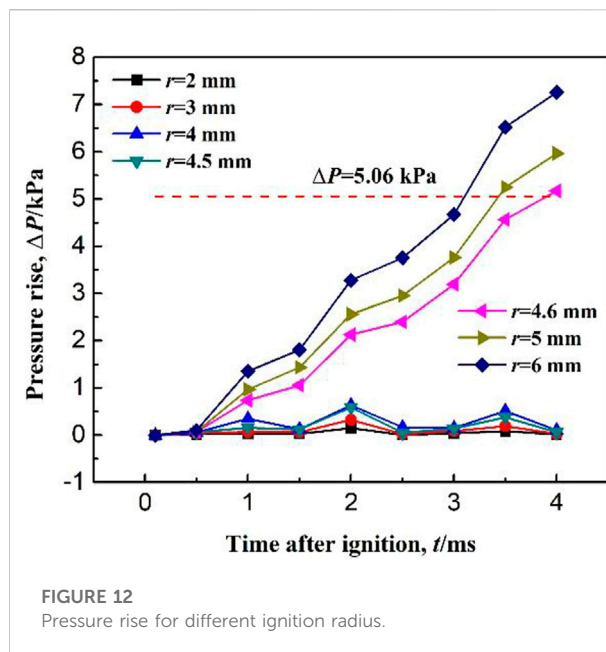
in which the gas consists of CH_4 , O_2 , and N_2 . The ratio of each component is the same as the initial condition. Then, the ignition source is set as a relatively high initial temperature (e.g., 1,400 K). The ignition source is the red circular with a radius r as shown in Figure 2.

The ignition source has two variable parameters: radius r and temperature T , which directly affect whether the combustible gas is ignited successfully. Therefore, by changing the ignition radius and temperature, the critical conditions for ignition are obtained.



2.6 Numerical methods

The finite volume method is used to discretize the corresponding control equations. The standard k - ϵ model is used for the turbulence equation, coupling with the non-equilibrium wall function method and the volumetric reaction. The SIMPLEC method is used for coupling the pressure and velocity fields. Second-order upwind scheme is used for the convective terms, while the time is advanced by the fully implicit Euler method. The time stepping method is successive over-relaxation. The relaxation factor of pressure, density, momentum and energy is set to 0.3, and the relaxation factor of each component is set to 1. The time step is set to 10^{-5} s.



3 Results and discussion

3.1 Variations in free radical concentration

For the free radical concentration at the ignition initiation stage, the concentration distribution on the central axis of the confined space is selected. Figure 4 shows the variation of mass fraction of CH_4 at different ignition times. The mass fraction of CH_4 inside the flame core is almost zero, while on the flame front, the methane concentration gradually increases from the burned zone to the unburned zone. It indicates that the combustion of methane mainly occurs on the flame front. With the increase in ignition time, the burned area and the flame front gradually expands to the surroundings. When the time is 0.5 ms after ignition, the mass fraction of CH_4 is not zero in the flame core, indicating that the consumption rate of CH_4 is slow at the initial stage. As seen in Table 1, the elementary reactions which promote the consumption of CH_4 are mainly R5: $\text{CH}_3 + \text{O}_2 = \text{CH}_2\text{O} + \text{OH}$, R6: $\text{CH}_2\text{O} + \text{OH} = \text{CO} + \text{H}_2\text{O} + \text{H}$, R8: $\text{H} + \text{O}_2 = \text{OH} + \text{O}$, and R9: $\text{OH} + \text{O} = \text{O}_2 + \text{H}$. The above elementary reactions are participated by free radicals. Due to the initial mass fraction of free radicals is low, the above elementary reactions are inactive and CH_4 is consumed slowly at the beginning of ignition. Moreover, the mass fraction of CH_3 is large at the beginning of ignition (as seen in Figure 6), which causes the reverse reaction rate of the elementary reactions R2: $\text{CH}_4 + \text{OH} = \text{CH}_3 + \text{H}_2\text{O}$ and R4: $\text{CH}_4 + \text{H} = \text{CH}_3 + \text{H}_2$ to be larger than the positive reaction rate. With the increase in ignition time (greater than 1.5 ms), the mass fraction of free radicals increases greatly and the mass fraction of CH_3 decreases a lot, which increases the consumption

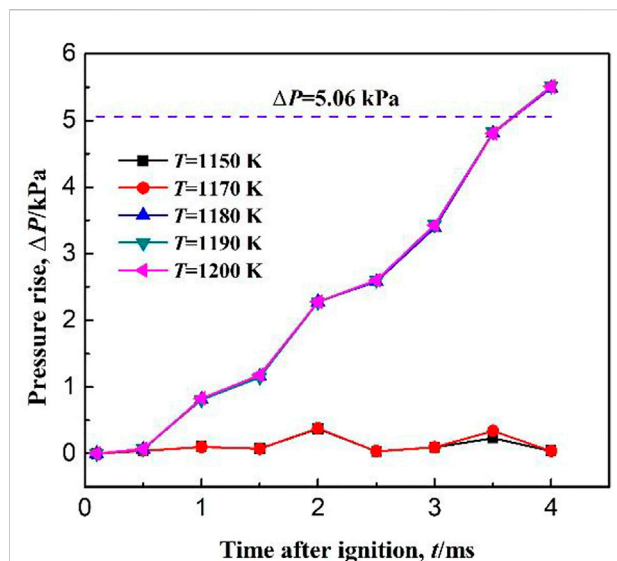


FIGURE 13
Pressure rise for different ignition temperature.

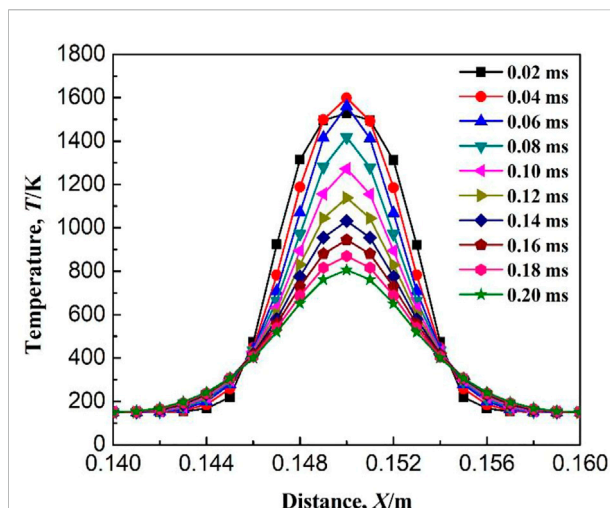


FIGURE 14
Variation of temperature with time when ignition radius is 4.5 mm.

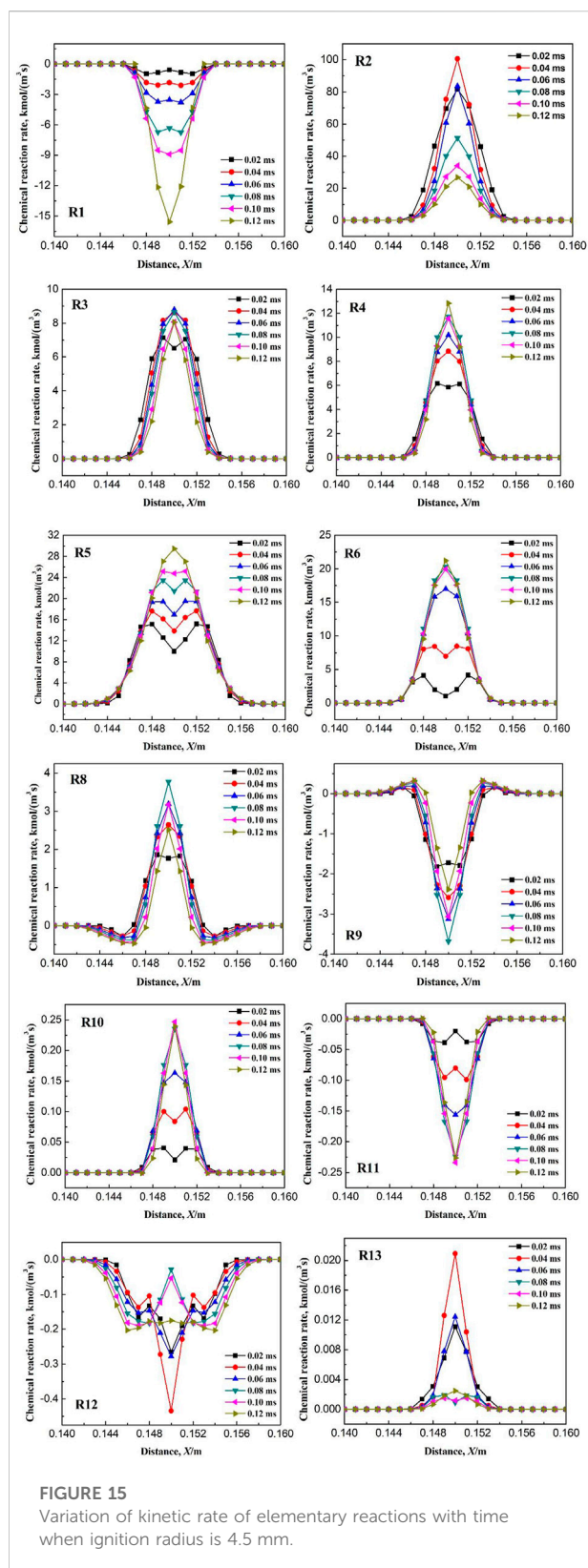
rate of methane. In the subsequent combustion process, the mass fraction of CH_4 inside the flame core is always equal to zero.

Figure 5 shows the variation of mass fraction of CO at different ignition time. The mass fraction of CO reaches the maximum in the burned area. On the flame front, the mass fraction of CO gradually decreases from the burned area to the unburned area. At the beginning of ignition, the mass fraction of CO is low because of the low concentration of free radicals and the slow reaction rate. Subsequently, with the increase in ignition time, the mass fraction of CO reaches the maximum in the flame core. When Figure 4 is compared with Figure 5, it is found that the distribution of mass fraction of methane shows an inverse relationship with that of CO.

Figures 6–8 show the variations of mass fraction of important intermediate products CH_3 , CH_2O , and CH. As seen in the figures, the mass fraction of the intermediate products in the burned and unburned areas is low while reaches the maximum on the flame front. It indicates that the chemical reaction takes place on the flame front. At the beginning of ignition, the mass fraction of the intermediate product on the flame front is high. With the increase in ignition time, the mass fraction of the intermediate product on the flame front decreases. The reactions for the generation of CH_3 in Table 1 includes R2: $\text{CH}_4 + \text{OH} = \text{CH}_3 + \text{H}_2\text{O}$, R3: $\text{CH}_4 + \text{O} = \text{CH}_3 + \text{OH}$, and R4: $\text{CH}_4 + \text{H} = \text{CH}_3 + \text{H}_2$. The main reaction for the consumption of CH_3 is R5: $\text{CH}_3 + \text{O}_2 = \text{CH}_2\text{O} + \text{OH}$. At the initial time (0.5 ms), the elementary reactions R2, R3, and R4 occurs severely, whereas elementary reaction R5 occurs gently. Therefore, a large amount of CH_3 is generated and accumulated which results in a large mass fraction of CH_3 on the flame front. As the combustion continues, the elementary reaction R5 gradually becomes active. Therefore, the

generated CH_3 is rapidly consumed and its mass fraction on the flame front greatly decreases. The main reaction for the generation of CH_2O is R5: $\text{CH}_3 + \text{O}_2 = \text{CH}_2\text{O} + \text{OH}$, while the main elementary reaction for the consumption of CH_2O is R6: $\text{CH}_2\text{O} + \text{OH} = \text{CO} + \text{H}_2\text{O} + \text{H}$. As shown in Figure 7, the mass fraction of CH_2O on the flame front gradually decreases with ignition time. This is because the elementary reaction R6 is much more reactive than R5. Figure 8 shows the variation of mass fraction of CH. Overall, the mass fraction of CH is very small, on the order of 10^{-7} , indicating that the elementary reactions R19: $\text{CH}_3 + \text{O} = \text{CH} + \text{H}_2\text{O}$ and R20: $\text{CH} + \text{O}_2 = \text{CO} + \text{OH}$ are very weak in the whole combustion process.

Figures 9–11 show the variations of mass fraction of the important free radicals H, O, and OH. The distribution of the mass fractions of free radicals H and O is similar to that of the intermediate products. The mass fractions in the burned and unburned areas are both low and reach the maximum on the flame front. At the beginning of ignition, the concentrations of H and O free radicals are low, which lead to slow chemical reaction rates at the initial stage (resulting in slow consumption rates of CH_4 and CH_3 , which is consistent with the above discussion). With the increase in ignition time, the concentrations of free radicals maintain at a high level, indicating that the reaction rate greatly increases. Figure 11 shows the variation of mass fraction of OH. Specially, the mass fraction of OH in the burned zone is not zero, but maintains a high value. As seen in Table 1, the consumption reactions of OH are R2, R6, and R7. The elementary reactions that OH serves as a chain carrier are R9, R11, R13, and R14. Therefore, OH is not only the intermediate free radical which participates in the reaction as the chain carrier, but also the combustion product remained by the intermediate reactions.



3.2 Critical conditions for methane ignition at low temperatures

In this paper, the ignition source is a spherical high temperature air mass, of which the temperature and radius are variables. If the ignition temperature is too low or the ignition radius is too small, the combustible gas cannot be successfully ignited. Therefore, there is a minimum ignition temperature or an ignition radius that can ignite methane successfully, i.e., the critical value for a successful ignition. Figure 12 shows the pressure rise in the confined space for different ignition radius r at an initial temperature of 150 K. The pressure is the monitoring data at the center of the right side wall. According to the standard BS EN 1839:2003, the explosion is considered to occur if the pressure rise in a confined space reaches 5% of the initial pressure. As seen in Figure 12, the explosion is considered to occur when the pressure rise curve exceeds $\Delta P = 5.06$ kPa (the initial pressure is 101.3 kPa). When the ignition radius $r < 4.6$ mm, the pressure rise maintains at a low level, and the maximum pressure rise is less than 1 kPa. Therefore, when the ignition radius $r < 4.6$ mm, the combustible gas cannot be ignited. However, when the ignition radius $r \geq 4.6$ mm, the pressure rise greatly increases and between $t = 3$ and 4 ms, the pressure rises exceeds 5.06 kPa, indicating that the combustible gas is successfully ignited. In summary, the critical value of the ignition radius at an initial temperature of 150 K is 4.6 mm. As also seen in Figure 12, with an increase in ignition radius, the pressure rise increases. This is because with the increase in ignition radius, the amount of combustible gas that is initially ignited increases. Thus, the heat released increases which induces a larger pressure rise. Therefore, the size of the ignition radius has a large effect on the methane ignition.

Figure 13 shows the pressure rise in the confined space for different ignition temperatures. When the ignition temperature is less than 1180 K, the pressure rise after ignition maintains a low level, and the maximum pressure rise is less than 5.06 kPa, indicating that the combustible gas is not ignited. When the ignition temperature $T \geq 1180$ K, the pressure rise increases rapidly and exceeds 5.06 kPa at about 3.5 ms, indicating that the combustible gas is successfully ignited. Therefore, at an initial temperature of 150 K, the critical ignition temperature is 1180 K. As also seen in Figure 13, the pressure rise curves basically coincide for different ignition temperatures, indicating that the ignition temperature has no effect on the methane ignition.

3.3 Terminated elementary reactions when the ignition radius is less than the critical value

Figure 14 shows the variation of flame temperature with ignition time when the ignition radius is 4.5 mm and the initial temperature is 150 K. First, the flame temperature gradually

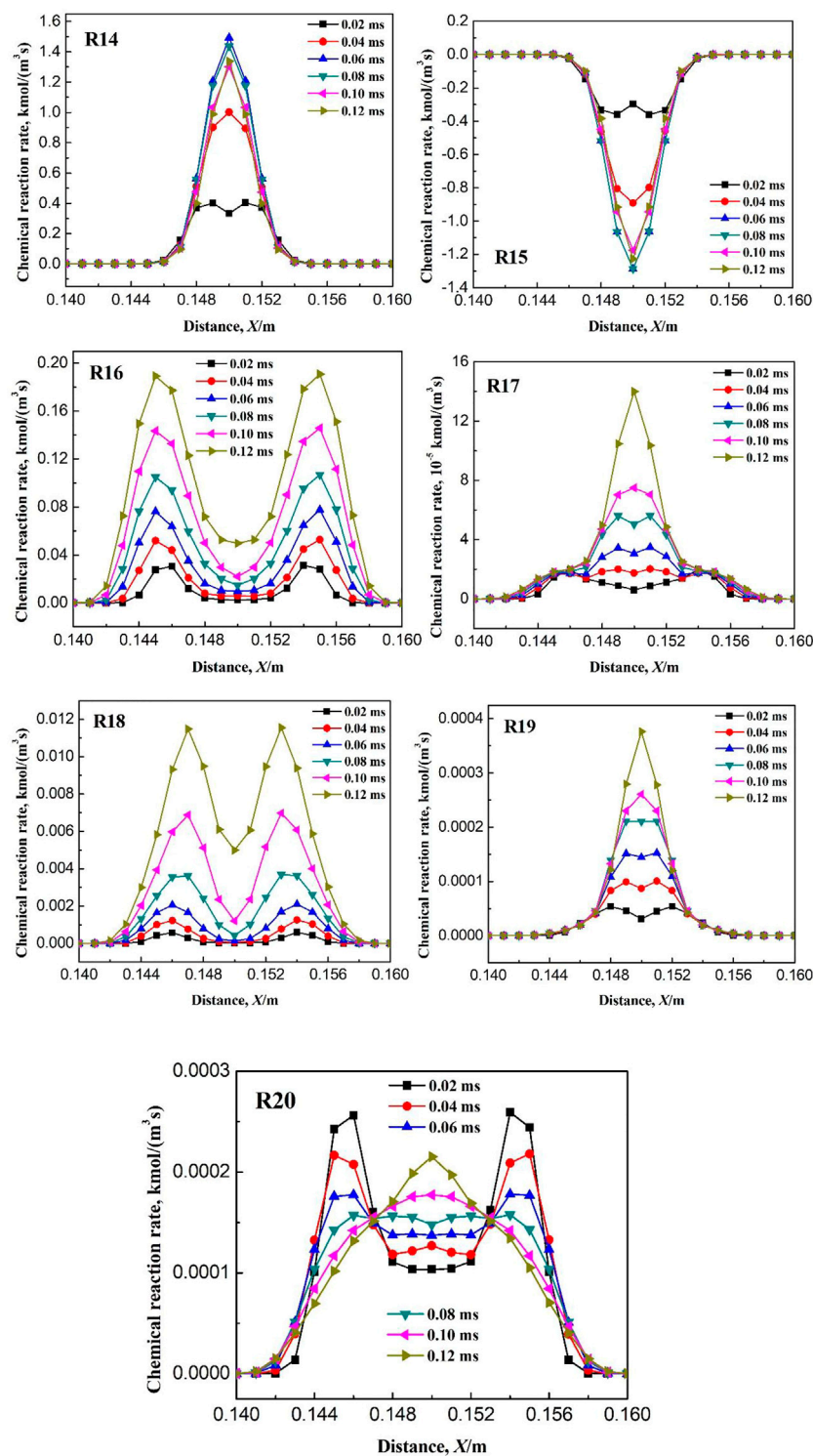


FIGURE 15
(Continued).

increases with time after ignition, and at the ignition time of 0.06 ms, the temperature reaches a maximum of 1640 K. With the further increase in ignition time, the flame temperature

gradually decreases. When the ignition time reaches 0.20 ms, the flame temperature decreases below 900 K. Therefore, combustible gas cannot be successfully ignited at an ignition

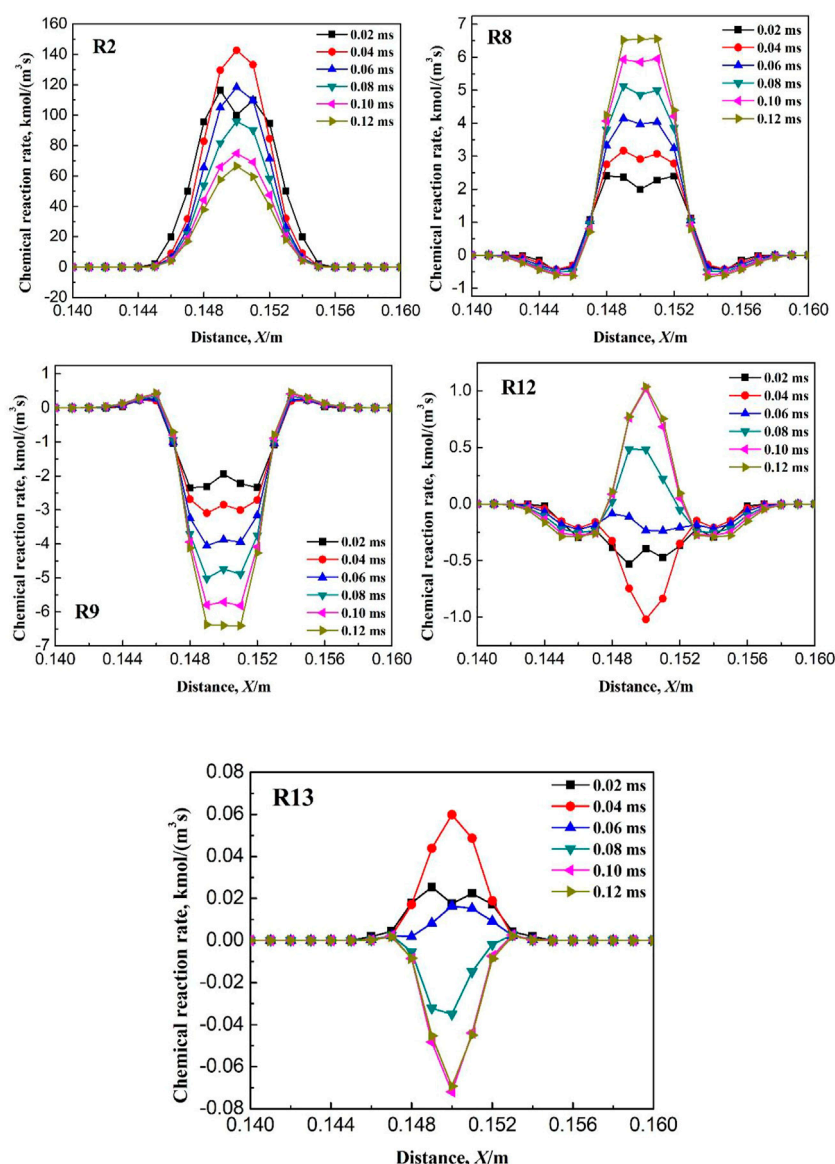


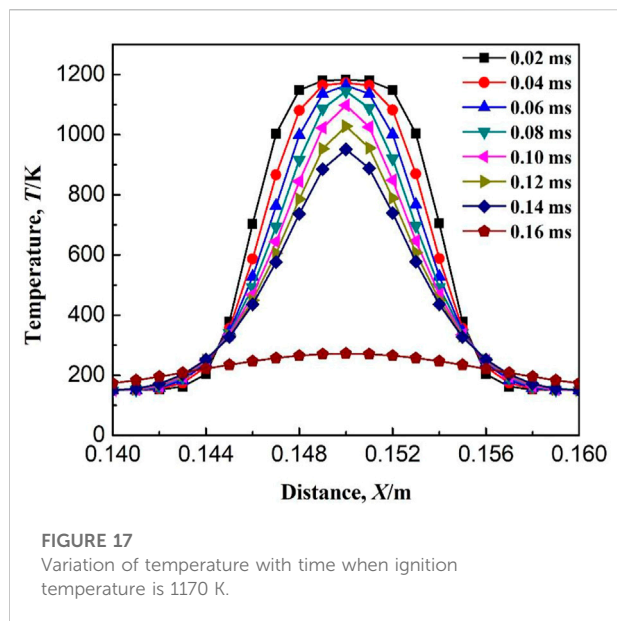
FIGURE 16

Variation of kinetic rate of elementary reactions with time when ignition radius is 4.6 mm.

radius of 4.5 mm. However, the increase in temperature after ignition indicates that some chemical reactions occur at the early stage of ignition. Because the ignition radius is less than the critical value, the energy released by the chemical reactions occurring at the initial stage is not enough to maintain the combustion of methane, and eventually lead to the failure of ignition. Methane combustion process consists of a chain reaction composed by a series of elementary reactions. The failure of methane ignition must be caused by the termination of one or more elementary reactions. In order to obtain the elementary reaction for the termination of methane combustion when the ignition radius is less than the critical value, variation of

the reaction rate of each elementary reaction with ignition time is studied, as shown in Figure 15. The chemical reaction rate reflects the activity of the elementary reaction. When the reaction rate of a certain elementary reaction suddenly drops to a low level, the elementary reaction is considered to be terminated.

As seen in Figure 15, after ignition, the chemical reaction rates of elementary reactions R1, R3, R4, R5, R6, R10, R11, R14, R15, R16, R17, R18, R19, and R20 increase gradually with the ignition time, or increase to a certain value and then maintain constants. However, the chemical reaction rates of the elementary reactions R2, R8, R9, R12, and R13 increase with ignition time to a certain value and then decrease greatly.

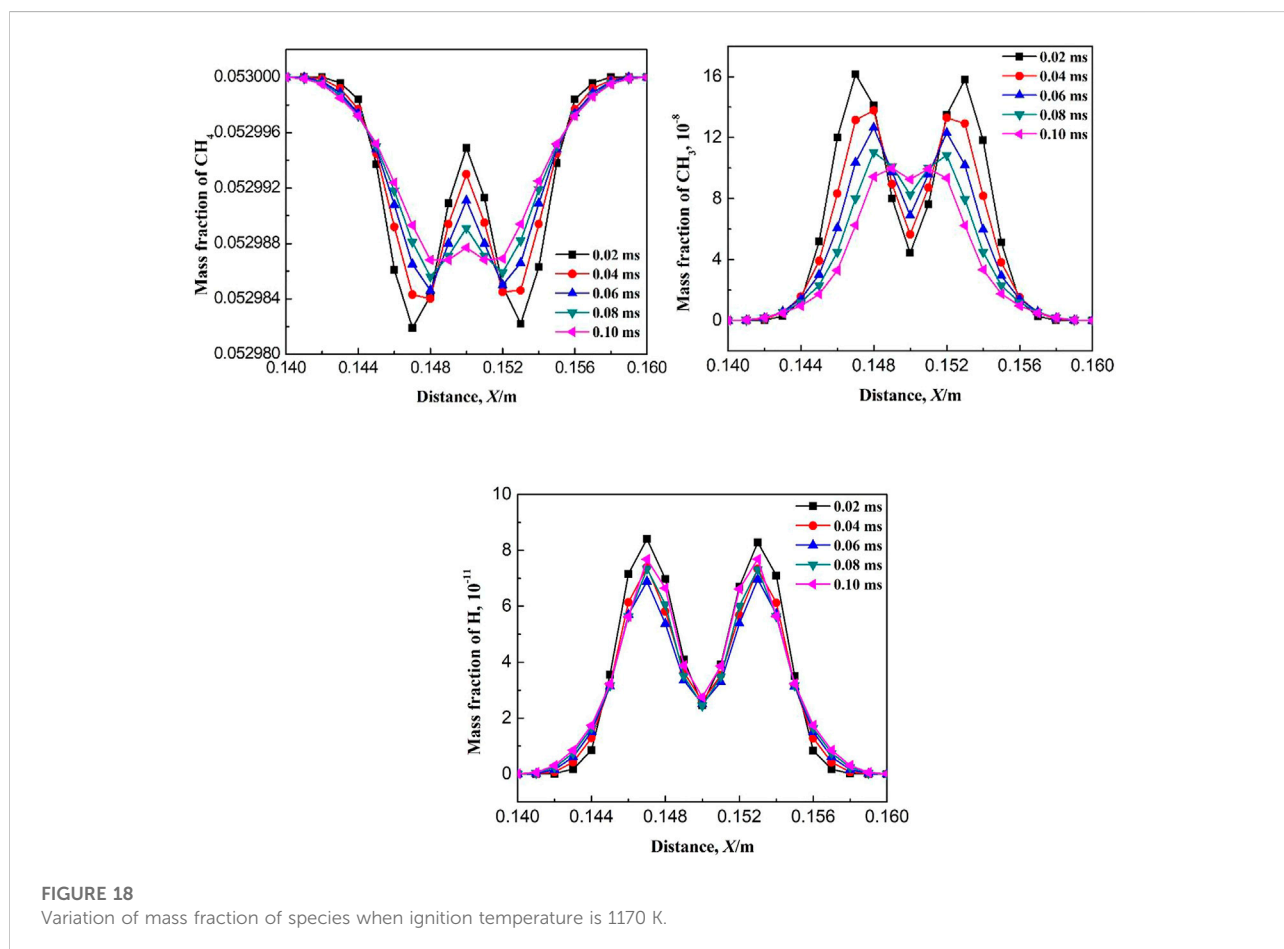


Therefore, the elementary reactions R2, R8, R9, R12, and R13 may be the termination reaction for the failure of the ignition. Next, variation of the reaction rate of the above five

elementary reactions with time are studied when the ignition radius is 4.6 mm (i.e., successful ignition), as shown in Figure 16. It can be seen that after ignition, variation of the chemical reaction rate of the elementary reaction R2 is the same as that when the ignition radius is 4.5 mm, therefore, R2 is not the terminated elementary reaction for the failure of ignition. In contrast, after ignition, the reaction rates of the elementary reactions R8, R9, R12, and R13 maintain at a high value and does not decrease, which is different from that when the ignition radius is 4.5 mm. To sum up, when the ignition radius is less than the critical value, the terminated elementary reactions resulting in the failure of ignition are R8, R9, R12, and R13.

3.4 Terminated elementary reactions when the ignition temperature is less than the critical value

Figure 17 shows the variation of flame temperature with ignition time at an ignition temperature of 1170 K. As seen in Figure 17, the flame temperature gradually decreases after ignition. When the time after ignition is greater than 0.14 ms, the flame temperature rapidly drops below 300 K. The



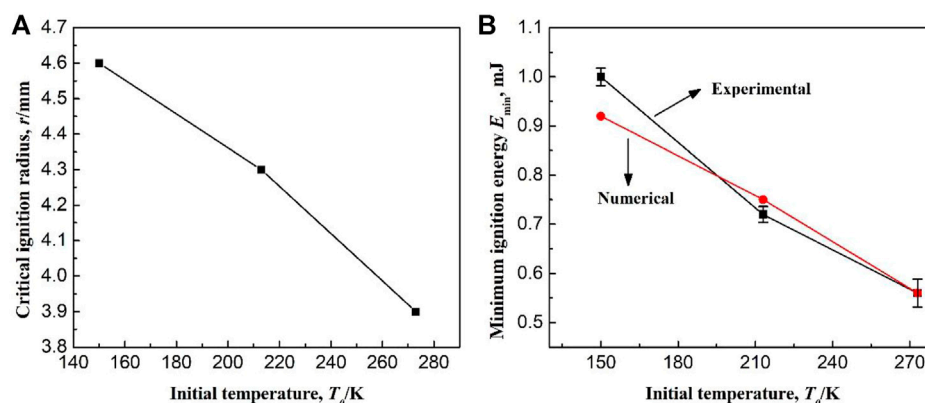


FIGURE 19

(A) Effect of initial temperature on the critical ignition radius; (B) Experimental and calculated minimum ignition energy at different initial temperatures.

continuous decrease in temperature indicates that no chemical reaction occurs after ignition. Figure 18 shows the variation of the mass fraction of some components with ignition time. It can be seen that the mass fraction of methane fluctuates after ignition. However, the volatility is only 0.00002, and it is assumed that CH₄ has not been consumed after ignition. As seen in Table 1, the start of the chemical reaction chain is the dehydrogenation of CH₄, and the corresponding elementary reactions are R1: CH₄ = CH₃ + H, R2: CH₄ + OH = CH₃ + H₂O, R3: CH₄ + O = CH₃ + OH, and R4: CH₄ + H = CH₃ + H₂. The initial stage does not exist H, OH, and O free radicals, therefore, the failure of ignition is due to the failure initiation of the elementary reaction R1. This is also confirmed by the fluctuations magnitude of the mass fractions of CH₃ (10⁻⁸) and H (10⁻¹¹), which is shown in Figure 18. Simply based on the elementary reaction, R1 is an endothermic reaction. Therefore, the occurrence of R1 needs enough energy to be provided. As seen from Table 1, the activation energy of the elementary reaction R1 is 455.06 kJ/mol, which induces a larger ignition energy, i.e., the reaction requires a sufficient ignition temperature.

3.5 Validation of the numerical results based on experimental data

In this paper, the ignition source is set to a high temperature air mass, and it is proposed for the first time to study the critical value of methane combustion at low temperature by changing the radius and temperature of the high temperature air mass. As for whether the above processing method can accurately simulate the actual spark, it needs to be verified by previous experimental results. According to the results in Section 3.5 in this paper, when the ignition temperature is lower than the critical value, the failure of ignition is due to the failure

initiation of the elementary reaction R1, which is the first reaction of the chemical reaction chain. Therefore, the initial temperature has no effect on the critical ignition temperature. However, the initial temperature has a large effect on the critical ignition radius, as shown in Figure 19A. After calculation using the numerical model in this paper, the critical ignition radius of methane is 4.6 mm at the low temperature of 150 K, while it is 3.9 mm at room temperature. Therefore, low temperature leads to an increase in the critical ignition radius. If the spark energy density of the ignition electrodes maintains a constant, the minimum ignition energy (MIE) increases with the increase in the critical ignition radius, which is consistent with the experimental results in Ref. (Cui et al., 2016b). In order to verify the correctness of the numerical simulation results, the MIEs based on the critical ignition radius are calculated. For the spark generator used in Ref. (Cui et al., 2016b), it is difficult to measure the spark energy density. At this point, at an initial temperature of 273 K, the calculated MIE is thought to be equal to the experimental value, which is 0.56 mJ. Therefore, the corresponding ignition energy density is calculated according to Equation 1, which is 0.002255 mJ/mm³. Based on this energy density value, the critical ignition energies (i.e., MIEs) of methane at different initial temperatures are calculated and compared with the experimental results, as shown in Figure 19B. As seen from the figure, with a decrease in initial temperature, the difference between the calculated and experimental results gradually increases. But overall, the maximum absolute error between those is 0.08 mJ. Therefore, the ignition initiation process of methane at low temperature can be well studied using the numerical model and the ignition method in this paper.

$$E = \frac{4}{3}\pi r^3 \rho \quad (1)$$

Here, E is the ignition energy, ρ is the ignition energy density, and r is the critical ignition radius.

4 Conclusion

In this paper, the initiation process of methane combustion at low temperature is studied and the following conclusion are drawn.

- (1) At the initial time after ignition (within 0.5 ms), due to the lower concentration of free radicals, CH_4 is consumed slowly and the mass fraction of CH_4 in the flame core is not zero. As the combustion reaction proceeds, an increase in free radical concentrations lead to the increase in CH_4 consumption rate. The consumption of CH_4 directly affects the concentration distribution of CO during the ignition initiation period, which causes an inverse relationship between CO concentration distribution and CH_4 concentration distribution.
- (2) The mass fraction of the intermediate product in the burned area and the unburned area is low and reaches the maximum on the flame front. Moreover, as the reaction proceeds, the maximum concentration of the intermediate product on the flame front gradually decreases.
- (3) Variations of the mass fraction of free radicals H and O are the same with those of the intermediate product: the mass fractions in the burned and unburned areas are both low and reach the maximum on the flame front. In the burned area, the OH mass fraction is not zero whereas maintains a high value. It indicates that OH is either a free radical which participates in the elementary reaction as a chain carrier, or a combustion reaction product remaining from the intermediate chain reaction.
- (4) The ignition radius has a large effect on the initiation stage of methane combustion. With an increase in ignition radius, the combustion pressure increases. However, the ignition temperature has no effect on the initiation stage of methane combustion. At a low temperature of 150 K, the critical ignition radius for methane initiation is 4.6 mm, while it is 3.9 mm at room temperature. Therefore, the low temperature leads to a large increase in the critical ignition radius. The initial temperature has no effect on the critical ignition temperature, which is 1,180 K at low or normal temperatures. The numerical simulation results and the experimental results show a good agreement.

- (5) When the ignition radius is less than the critical value, the failure of methane ignition is caused by the termination of the elementary reactions R8, R9, R12, and R13. However, when the ignition temperature is less than the critical value, methane is not ignited successfully because of the failed initiation of the elementary reaction R1.

Data availability statement

The original contributions presented in the study are included in the article/supplementary material, further inquiries can be directed to the corresponding author.

Author contributions

All authors listed have made a substantial, direct, and intellectual contribution to the work and approved it for publication.

Funding

This investigation has been supported by the Fundamental Research Funds for the Central Universities (No. 18CX02005A).

Conflict of interest

Authors CY, QH, HL, YW, and RC were employed by the company Shengli Oilfield.

Publisher's note

All claims expressed in this article are solely those of the authors and do not necessarily represent those of their affiliated organizations, or those of the publisher, the editors and the reviewers. Any product that may be evaluated in this article, or claim that may be made by its manufacturer, is not guaranteed or endorsed by the publisher.

References

- Cui, G., Li, Z. L., Li, H. B., Bi, Z. X., and Wang, S. (2018). Numerical study on premixed methane-air flame propagation in a confined vessel at low initial temperature. *Energy fuels*. 32, 2465–2478. doi:10.1021/acs.energyfuels.7b03433
- Cui, G., Li, Z. L., and Yang, C. (2016). Experimental study of flammability limits of methane/air mixtures at low temperatures and elevated pressures. *Fuel* 181, 1074–1080. doi:10.1016/j.fuel.2016.04.116
- Cui, G., Li, Z. L., Yang, C., Zhou, Z., and Li, J. L. (2016). Experimental study of minimum ignition energy of methane-air mixtures at low temperatures and elevated pressures. *Energy fuels*. 30, 6738–6744. doi:10.1021/acs.energyfuels.6b00366
- Cui, G., Li, Z. L., and Zhao, Y. L. (2015). Design and security analysis for the liquefaction and distillation process of oxygen-bearing coal-bed methane. *RSC Adv.* 5, 68218–68226. doi:10.1039/c5ra09143h
- Dunn-Rankin, D., Barr, P. K., and Sawyer, R. F. (1988). Numerical and experimental study of “tulip” flame formation in a closed vessel. *Symposium Combust.* 21, 1291–1301. doi:10.1016/s0082-0784(88)80360-6
- Gao, T., Lin, W. S., Gu, A. Z., and Gu, M. (2010). Coalbed methane liquefaction adopting a nitrogen expansion process with propane pre-cooling. *Appl. Energy* 87, 2142–2147. doi:10.1016/j.apenergy.2009.12.010

- Hammond, G. P., and Grady, A. O. (2017). The life cycle greenhouse gas implications of a UK gas supply transformation on a future low carbon electricity sector. *Energy* 118, 937–949. doi:10.1016/j.energy.2016.10.123
- Han, J. L., Yamashita, H., and Hayashi, N. (2010). Numerical study on the spark ignition characteristics of a methane–air mixture using detailed chemical kinetics. *Combust. Flame* 157, 1414–1421. doi:10.1016/j.combustflame.2010.02.021
- Han, J. L., Yamashita, H., and Hayashi, N. (2011). Numerical study on the spark ignition characteristics of hydrogen–air mixture using detailed chemical kinetics. *Int. J. Hydrogen Energy* 36, 9286–9297. doi:10.1016/j.ijhydene.2011.04.190
- Hu, J., Rivin, B., and Sher, E. (2000). The effect of an electric field on the shape of co-flowing and candle-type methane–air flames. *Exp. Therm. Fluid Sci.* 21, 124–133. doi:10.1016/s0894-1777(99)00062-x
- Kaltayev, A. K., Riedel, U. R., and Warnatz, J. (2000). The hydrodynamic structure of a methane–air tulip flame. *Combust. Sci. Technol.* 158, 53–69. doi:10.1080/00102200008947327
- Karim, G. A., Wierzbka, I., and Boon, S. (1984). The lean flammability limits in air of methane, hydrogen and carbon monoxide at low temperatures. *Cryogenics* 24, 305–308. doi:10.1016/0011-2275(84)90139-5
- Kravchik, T., and Sher, E. (1994). Numerical modeling of spark ignition and flame initiation in a quiescent methane–air mixture. *Combust. Flame* 99, 635–643. doi:10.1016/0010-2180(94)90057-4
- Li, Z. M., Gong, M. Q., Sun, E. Y., Wu, J. F., and Zhou, Y. (2011). Effect of low temperature on the flammability limits of methane/nitrogen mixtures. *Energy* 36, 5521–5524. doi:10.1016/j.energy.2011.07.023
- Marra, F. S., and Continillo, G. (1996). Numerical study of premixed laminar flame propagation in a closed tube with a full Navier-Stokes approach. *Symposium Combust.* 26, 907–913. doi:10.1016/s0082-0784(96)80301-8
- Mikolajkov, M., Haikarainen, C., Saxen, H., and Pettersson, F. (2017). Optimization of a natural gas distribution network with potential future extensions. *Energy* 125, 848–859. doi:10.1016/j.energy.2016.11.090
- Song, R., Cui, M. M., and Liu, J. J. (2017). Single and multiple objective optimization of a natural gas liquefaction process. *Energy* 124, 19–28. doi:10.1016/j.energy.2017.02.073
- Wierzbka, I., Harris, K., and Karim, G. A. (1992). Effect of low temperature on the rich flammability limits in air of hydrogen and some fuel mixtures containing hydrogen. *Int. J. Hydrogen Energy* 17, 149–152. doi:10.1016/0360-3199(92)90205-b
- Wierzbka, I., Harris, K., and Karim, G. A. (1990). Effect of low temperature on the rich flammability limits of some gaseous fuels and their mixtures. *J. Hazard. Mat.* 25, 257–265. doi:10.1016/0304-3894(90)85082-e
- Xiao, H. H., Sun, J. H., and Chen, P. (2014). Experimental and numerical study of premixed hydrogen/air flame propagating in a combustion chamber. *J. Hazard. Mat.* 268, 132–139. doi:10.1016/j.jhazmat.2013.12.060
- Yuasa, T., Kadota, S., Tsue, M., Kono, M., Nomura, H., and Ujiie, Y. (2002). Effects of energy deposition schedule on minimum ignition energy in spark ignition of methane/air mixtures. *Proc. Combust. Inst.* 29, 743–750. doi:10.1016/s1540-7489(02)80095-5

Advantages of publishing in Frontiers



OPEN ACCESS

Articles are free to read
for greatest visibility
and readership



FAST PUBLICATION

Around 90 days
from submission
to decision



HIGH QUALITY PEER-REVIEW

Rigorous, collaborative,
and constructive
peer-review



TRANSPARENT PEER-REVIEW

Editors and reviewers
acknowledged by name
on published articles

Frontiers

Avenue du Tribunal-Fédéral 34
1005 Lausanne | Switzerland

Visit us: www.frontiersin.org

Contact us: frontiersin.org/about/contact



REPRODUCIBILITY OF RESEARCH

Support open data
and methods to enhance
research reproducibility



DIGITAL PUBLISHING

Articles designed
for optimal readership
across devices



FOLLOW US

@frontiersin



IMPACT METRICS

Advanced article metrics
track visibility across
digital media



EXTENSIVE PROMOTION

Marketing
and promotion
of impactful research



LOOP RESEARCH NETWORK

Our network
increases your
article's readership